

Second International Conference on

**COMPUTATIONAL METHODS
FOR THERMAL PROBLEMS**

September
5-7, 2011
Dalian, China

Edited by

Xikui Li

Nicola Massarotti

Perumal Nithiarasu

THERMA COMP2011

**2ND INTERNATIONAL CONFERENCE ON COMPUTATIONAL METHODS FOR
THERMAL PROBLEMS**

SEPTEMBER 5-7, 2011, DALIAN, CHINA

EDITED BY:

XIKUI LI

DEPARTMENT OF ENGINEERING MECHANICS
DALIAN UNIVERSITY OF TECHNOLOGY
DALIAN, CHINA

NICOLA MASSAROTTI

DIPARTIMENTO PER LE TECNOLOGIE
UNIVERSITÀ DEGLI STUDI DI NAPOLI "PARTHENOPE"
NAPOLI, ITALY

PERUMAL NITHIARASU

CIVIL AND COMPUTATIONAL ENGINEERING CENTRE
COLLEGE OF ENGINEERING, SWANSEA UNIVERSITY
SWANSEA SA2 8PP, UNITED KINGDOM

WITH THE SUPPORT OF:

ALESSANDRO MAURO

DIPARTIMENTO PER LE TECNOLOGIE
UNIVERSITÀ DEGLI STUDI DI NAPOLI "PARTHENOPE"
NAPOLI, ITALY

© 2011 by the authors of the abstracts

图书在版编目(CIP)数据

第二届热问题计算方法国际会议文集=Proceedings
of the Second International Conference on
Computational Methods for Thermal Problems : 英文
/ 李锡夔, (意) 马萨罗蒂 (Massarotti, N.), (英) 尼
西阿拉苏 (Nithiarasu, P.) 编. —大连 : 大连理工大学
出版社, 2011. 8

ISBN 978-7-5611-6453-2

I. ①第… II. ①李… ②马… ③尼… III. ①热学—
计算方法—国际学术会议—文集—英文 IV. ①O551

中国版本图书馆 CIP 数据核字(2011)第 165864 号

大连理工大学出版社出版

地址:大连市软件园路 80 号 邮政编码:116023

发行:0411-84708842 邮购:0411-84703636 传真:0411-84701466

E-mail:dutp@dutp.cn URL:http://www.dutp.cn

大连金华光彩色印刷有限公司印刷 大连理工大学出版社发行

幅面尺寸:168mm×238mm 印张:18.75 字数:522千字
2011年8月第1版 2011年8月第1次印刷

责任编辑:于建辉

责任校对:李云霄

封面设计:裘亚勤

ISBN 978-7-5611-6453-2

定 价:150.00元

PREFACE

It is a great pleasure to welcome all participants of the *Second International Conference on Computational Methods for Thermal Problems* (THERMACOMP2011) to Dalian. Computational and mathematical methods have had a profound impact on the understanding and advancement of engineering science and technology over the last few decades. The conference aims to convene a diverse scientific audience of mathematicians, physicists, engineers and computational scientists that have a communal interest in modelling thermal problems. It is encouraging to learn that this conference represents an interdisciplinary forum of scientists with expertise ranging from heat conduction, convection and radiation to CFD and thermo-mechanical coupling. We hope that the interaction between scientists during the conference leads to new topics of research and new collaborations.

THERMACOMP2011 consists of four plenary lectures, six keynote lectures, four organized mini-symposia and four standard sessions. We are grateful to all invited speakers for accepting our invitation.

We thank THERMACOMP2011 sponsors, supporters, mini-symposium organizers, executive, advisory and local committee members for their support.

We would also like to thank all the reviewers that helped assuring the technical quality of this Conference.

Xikui Li
China

Nicola Massarotti
Italy





Perumal Nithiarasu
United Kingdom

THERMACOMP 2011 CHAIRS

SPONSORS

 <p>NATIONAL NATURAL SCIENCE FOUNDATION OF CHINA</p>	 <p>DALIAN UNIVERSITY OF TECHNOLOGY</p>
 <p>THE STATE KEY LABORATORY FOR STRUCTURAL ANALYSIS OF INDUSTRIAL EQUIPMENT</p>	<p>ZIENKIEWICZ FOUNDATION</p>
 <p>SWANSEA UNIVERSITY</p>	 <p>UNIVERSITÀ DEGLI STUDI DI NAPOLI “PARTHENOPE”</p>

SUPPORTING ORGANIZATIONS

 <p>CHINESE SOCIETY OF THEORETICAL AND APPLIED MECHANICS</p>	 <p>CHINESE ASSOCIATION FOR COMPUTATIONAL MECHANICS</p>
 <p>DIPARTIMENTO PER LE TECNOLOGIE</p>	 <p>INTERNATIONAL ASSOCIATION FOR COMPUTATIONAL MECHANICS</p>

COMMITTEES

HONORARY CHAIR

Professor R.W. Lewis, Swansea University, UK

CO-CHAIRS

X. Li, Dalian University of Technology, China
N. Massarotti, Università degli Studi di Napoli "Parthenope", Italy
P. Nithiarasu, Swansea University, UK

INTERNATIONAL EXECUTIVE COMMITTEE

P. Cheng, Shanghai Jiao Tong University, China
G. Comini, University of Udine, Italy
G. de Vahl Davis, University of New South Wales, Australia
Y. Jaluria, Rutgers, The State University of New Jersey, USA
V. Naso, University of Naples Federico II, Italy
E. Oñate, Universitat Politècnica de Catalunya, Spain
K.N. Seetharamu, PES Institute of Technology, India
B. Sunden, Lund University, Sweden
K. Vafai, University of California, Riverside, USA

INTERNATIONAL ADVISORY COMMITTEE

F. Arpino, Università degli Studi di Cassino, Italy
A. Carotenuto, Università degli Studi di Napoli "Parthenope", Italy
S. Chang, National University of Singapore, Singapore
G. D. Cheng, Dalian University of Technology, China
R. Codina, Universitat Politècnica de Catalunya, Spain
R.M. Cotta, Universidade Federal do Rio de Janeiro, Brazil
M. J. S. de Lemos, Instituto Tecnológico de Aeronáutica, Brazil
D. Drikakis, Cranfield University, UK
D. Givoli, Technion - Israel Institute of Technology, Israel
Y. Joshi, Georgia Institute of Technology, USA
B.V.R. Kumar, Indian Institute of Technology Kanpur, India
A.G. Malan, Council for Scientific and Industrial Research, South Africa
O. Manca, Second University of Naples, Italy
J.C. Mandal, Indian Institute of Technology Bombay, India
C. Meola, University of Naples Federico II, Italy
C. Nonino, University of Udine, Italy
D. Poulikakos, ETH Zurich, Switzerland
J. Reese, University of Strathclyde, UK
B. Sarler, University of Nova Gorica, Slovenia
B. A. Schrefler, Università di Padova, Italy
W. Q. Tao, Xi'an Jiao Tong University, China
V.R. Voller, University of Minnesota, USA
H. W. Zhang, Dalian University of Technology, China
W. X. Zhong, Dalian University of Technology, China

LOCAL ORGANISING COMMITTEE

B. S. Chen, Dalian University of Technology, China
Q. L. Duan, Dalian University of Technology, China
A. Mauro, Università degli Studi di Napoli "Parthenope", Italy
M. Qu, Dalian University of Technology, China
J. B. Zhang, Dalian University of Technology, China
Y. G. Zheng, Dalian University of Technology, China
Z. Zhang, Dalian University of Technology, China

CONTENTS

PLENARY LECTURES

Challenges in the accurate numerical simulation of practical thermal processes and systems

Jaluria Yogesh

Semi-empirical models for transient heat transfer of pin-fin heat sinks subjected to non-uniform hot jet heating

Lu Tianjian, Feng S.S., Kim T.

Steps towards a real time solution of fire in tunnels

Schrefler Bernhard A., Pesavento Francesco, Chinesta Francisco, Leygue Adrien

Surrogate-based modeling and dimension reduction techniques for thermo-fluid & energy systems

Cho Young-Chang, Du Wenbo, Gupta Amit, Tseng Chien-Chou, Sastry Ann Marie, Shyy Wei

KEYNOTE LECTURES

Multiscale simulations of heat transfer and fluid flow problems

He Yaling, Tao Wenquan

Modeling of free surface flows: understanding falling drops

Biswas Gautam, Ray Bahni, Sharma Ashutosh

A meshless method for thermal problems: from theoretical developments to industrial applications

Sarler Bozidar, Lorbiecka Agnieszka Zuzanna, Kosec Gregor, Vertnik Robert

An efficient immersed boundary method for simulation of heat and mass transfer problems

Shu Chang, Ren W.W.

Numerical modeling of coupled heat/mass transport and electrochemical reactions in fuel cells

Zhao Tianshou, Yang W.W.

Micro/nano scale radiative heat transfer

Xuan Yimin, Li Qiang

MINI-SYMPOSIA

THERMO-MECHANICAL COUPLING OF INHOMOGENEOUS MEDIA AND COMPLEX STRUCTURES

MINI-SYMPOSIUM ORGANISED BY WU LINZHI

On surface models with couplings among thermal, elastic and electric fields

Chen Weiqiu, Zhu Jun

Thermal-controlled release and absorption of a hybrid gel particle

Wu Zhen, Zhong Zheng

Similarity criteria for one dimensional transient with thermo-mechanical interaction

Zhang Xiaomin, Zhang Long, Zhang Peiyuan

Numerical simulation for thermal shock resistance of thermal protection materials considering different causative environments

Li Weiguo, Li Dingyu, Wang Ruzhuan, Fang Daining

The thermal power around a blunt crack in elliptical inhomogeneity under electric loads at infinity

Song Haopeng, Gao Cunfa

Waves in a rotating random weakly conducting weakly thermal magneto-viscoelastic medium

Bhattacharyya Rabindra Kumar, Bera Rasajit Kumar

Bounds on the effective thermal conductivity of composites with spherical inclusions

Wu Linzhi

DISCRETIZATION METHODS FOR RADIATION DIFFUSION PROBLEMS AND RELATED APPLICATIONS

MINI-SYMPOSIUM ORGANISED BY YUAN GUANGWEI AND CUI XIA

A linear reconstruction algorithm for anisotropic diffusion equations

Chang Lina, Yuan Guangwei

Adaptive iteration acceleration for nonlinear parabolic-hyperbolic system

Cui Xia, Yuan Guangwei, Yue Jingyan

Finite point method for diffusion equation on irregular computational domain

Lv Guixia, Shen Longjun, Wu Hao

Fourth-order approximation for neumann boundary condition of heat conduction

Liao Honglin, Mao Lei

Boundary element method for transient radiative-conductive coupled heat transfer

Gao Xiaowei, Wang Jing

LATTICE BOLTZMANN METHOD FOR FLOW AND HEAT TRANSFER

MINI-SYMPOSIUM ORGANISED BY GUO ZHAOLI AND TANG GUIHUA

A lattice boltzmann model for variable coefficient elliptic equations

Feng Heying, Zhang Xiaoqing, Chen Huanxin

Extended thermodynamic approach for heat transfer in microfluidic structures

Zhai Guangxin, Tang Guihua, Tao Wenquan, Gu Xiaojun, Emerson David R.

Simulation of the miscible Rayleigh-Taylor instability with variable Prandtl numbers by lattice Boltzmann method

Liu Gaojie, Guo Zhaoli

Numeric solutions of thermal problems governed by fractional diffusion

Voller Vaughan, Zielinski Dan P.

High performance computation of incompressible flow by lattice boltzmann method on multi-node gpu cluster

Wang Xian, Aoki Takayuki

THERMAL-RELATED STRUCTURAL DESIGN AND OPTIMIZATION

MINI-SYMPOSIUM ORGANISED BY CHENG GENG DONG AND LIU SHUTIAN

The optimization model of the heat conduction structure

Zhang Yongcun, Liu Shutian

A deep study on topology optimization of thermo-elastic problems

Zhang Weihong, Yang Jungang

Concurrent optimization of structure composed of porous ceramic with thermal and structural objectives

Yan Jun, Deng Jiadong, Cheng Gengdong

Deformation control of thin-walled structures by applied heat flux

Zhang Junhui, Xiang Zhihai, Liu Yinghua, Xue Mingde

Temperature uniformity determination and optimization of drying ovens using experimentally validated cfd analysis and genetic algorithm

Smolka Jacek, Canibol Piotr, Olczek Piotr, Bulinski Zbigniew, Nowak Andrzej J., Rybarz Dawid

PARALLEL SESSIONS

NUMERICAL METHODS

Spectral finite difference analysis of natural convection in a triply-connected region of a nearly parallel enclosure

Mochimaru Yoshihiro

Sheared vortex-induced vibration of a circular cylinder at low Reynolds number

Singh Satya Prakash, Biswas Gautam

A smoothed finite element method for heat transfer problems

Wu Shengchuan, Liu Guirong

A generalized scheme of the Characteristic Based Split (CBS) algorithm for incompressible non-isothermal non-Newtonian fluid flows

Duan Qinglin, Li Xikui

Numerical simulation of flow inside differentially heated rotating cavity

Mandal Jadav Chandra, Sonawane Chandrakant

Fast local transient solution of multi-layered micro-channel heat sink

Beh Shiao Lin, Tio Kek Kiong, Quadir Ghulam Abdul, Seetharamu Kankanahalli Narasimhasastry

Numerical solutions of double diffusion in cavities

Arpino Fausto, Carotenuto Alberto, Massarotti Nicola, Mauro Alessandro

Analysis of flow and heat transfer characteristics in a square cavity with convective boundary condition

Aswatha As, Gowda C.J. Gangadhara, Seetharamu Kankanahalli Narasimhasastry

High order explicit solutions for transient incompressible flows

Arpino Fausto, Cortellessa Gino, Dell'isola Marco, Massarotti Nicola, Mauro Alessandro

Numerical analysis on melting in a cylindrical heat storage capsule

Sciacovelli Adriano, Verda Vittorio

High performance computing utilising fully explicit and semi-implicit characteristic based split (CBS) schemes for subject-specific modelling

Bevan Rhodri L.T., van Loon Raoul, Nithiarasu Perumal

On the small-scale anomalies in the scalar field in homogeneous and isotropic turbulence

Langella Ivan, Scalo Carlo, de Felice Giuseppe, Meola Carlo

A robust artificial compressibility algorithm for turbulent incompressible flows in urban areas

Arpino Fausto, Buonanno G., Scungio M., Massarotti Nicola, Mauro Alessandro

HEAT AND MASS TRANSFER IN POROUS MEDIA

Turbulent reacting flow in radial porous combustors

de Lemos Marcelo J.S.

Natural convection in a vertical porous annulus from two thermal sources

Do Younghae, Sankar M., Lopez Juan M.

A 3D mixed convection study in a porous cavity

Kumar Bayya Venkatesulu Rathish, Murthy S.V.S.S.N.V.G. Krishna

Double diffusive free convection process induced by boundary layer flow along a vertical surface in a doubly stratified fluid saturated porous medium with sores and dufour effects under MHD forces

Murthy S.V.S.S.N.V.G. Krishna, Magoules Frederic, Kumar Bayya Venkatesulu Rathish

Influence of porosity and electrokinetic effects on flow through microchannels

Radha Narayanan

Explicit solutions for heat and fluid flow in cylindrical porous domains

Arpino Fausto, Carotenuto Alberto, Massarotti Nicola, Mauro Alessandro

CONDUCTION, CONVECTION, RADIATION

Numerical modelling of gravitational convection in three-component gas mixtures in the cylindrical channel

Kosov Vladimir, Poyarkov Igor, Fedorenko Olga

A generalized Navier-Stokes constitution relation for multiscale gas flows

Guo Zhaoli, Zheng Chuguang

Mixed convection flow in a vertical annulus filled with variable porous material

Kaurangini Muhammad Lawan, Jha Basant K.

Benchmark solution of 3D natural convection flows with surface radiation in air-filled cavity

Hu Liyuan, Xin Shihe, Chena Yvonne Chavez, Chergui Jalel, Quere Patrick Le

Natural convection in vitreous humor during transpupillary thermotherapy (TTT) of human eye

Kumar Jha Kaushal, Sundarraaj C., Arunn Narasimhan

3D IHCP in pool boiling: mathematical formulation, efficient computational strategies and software tool

Heng Yi, Mhamdi Adel, Marquardt Wolfgang

Reconstruction of the Stefan-Boltzmann coefficients in the heat transfer process

Cheng Jin, Lu Shuai, Yamamoto Masahiro

Identification of heating source in an enclosure dynamically coupled with Thermal transport

Zhao Fuyun, Rank Ernst, Mundani Ralf-Peter, Frisch Jérôme, Liu Di, Wang Hanqing

POWER PLANTS AND EQUIPMENT SIMULATION

Numerical simulation of acoustic streaming in the piston-driven resonator by gas-kinetic BGK scheme

Feng Heying, Zhang Xiaoqing, Chen Huanxin, Peng Yehui

Particle deposition effects on heat transfer from a porous heat sink

Hooman Kamel, Odabae Mostafa, Tamayol Ali

Thermal modeling of power transformer radiators using a porous medium based CFD approach

Fdhila Rebei Bel, Kranenborg Jurjen, Laneryd Tor, Olsson Carl Olof, Samuelsson Bertil, Gustafsson Andreas, Lundin Lars Ake

Numerical investigation on thermal stratification phenomenon in a shutdown cooling system piping

Kim Sun Hye, Sung Hee Dong, Kim Young Jin, Park Jung Soon, Choi Young Hwan

Performance evaluation of heat leak to the evaporator and the effect of longitudinal heat conduction from a counter-flow cryogenic heat exchanger using finite element method

Krishna Venkataram, Pradeep Hegde, Seetharamu Kankanahalli Narasimhashastry, Seetharam Tr

Effects of aspect ratio on natural convection in a vertical annulus embedded with porous medium with different types of cold wall boundary conditions

Mukesh Patil, Pradeep Hegde, Seetharam Tr, Seetharamu Kankanahalli Narasimhashastry

Finite element applications in heat exchangers

Seetharamu Kankanahalli Narasimhashastry

PLENARY LECTURES

CHALLENGES IN THE ACCURATE NUMERICAL SIMULATION OF PRACTICAL THERMAL PROCESSES AND SYSTEMS

Yogesh Jaluria

Board Of Governors Professor, Department of Mechanical & Aerospace Engineering, Rutgers University, Piscataway, NJ 08854, USA. jaluria@jove.rutgers.edu

ABSTRACT

The numerical simulation of practical thermal processes is generally complicated because of multiple transport mechanisms and complex phenomena that commonly arise. In addition, the materials encountered are often not easily characterized and typically involve large property changes over the ranges of interest. The boundary conditions may not be properly defined and or may be unknown. The geometry and interactions between different components are also often quite complicated. However, it is important to obtain accurate and dependable numerical results from the simulation in order to study, design, and optimize most practical thermal processes of current and future interest. The models employed must be validated and the accuracy of the simulation results established if the simulation is to form the basis for improving existing systems and developing new ones in applications areas such as energy, manufacturing, environmental control, electronics cooling, and transportation. This paper focuses on the main challenges that are encountered in obtaining accurate numerical simulation results on practical thermal processes and systems. It considers a wide variety of systems, ranging from materials processing to energy and cooling. Of particular interest are concerns like verification and validation, imposition of appropriate boundary conditions, and modelling of complex, multimode transport phenomena in multiple scales. Additional effects such as viscous dissipation, surface tension, buoyancy and rarefaction that could arise and complicate the modelling are discussed. Uncertainties that arise in material properties and in boundary conditions are also important in design and optimization. Large variations in the geometry and coupled multiple regions are also discussed. The methods that may be used to meet these challenges are discussed, along with typical results for a range of important processes. Future needs in this interesting and challenging area are also outlined.

Key Words: *Thermal processes, thermal systems, numerical simulation, accuracy, challenges*

1. INTRODUCTION

Numerical modelling of thermal processes that are of interest in important applications such as those related to energy, manufacturing, transportation, aerospace, heating, cooling, and to the environment is critical to a detailed study of the resulting phenomena and to the design and optimization of the relevant systems. Most of these practical circumstances are much too complicated to be investigated by analytical methods. Also, relatively limited data are usually available from existing processes and from appropriate experimental studies, which are often expensive and time consuming. In most cases, mathematical models of the processes and systems are developed, followed by numerical modelling and simulation. The models are validated by means of available analytical and experimental results and the numerical simulation is then used to provide the extensive numerical data needed for characterizing the processes and for design, control and optimization [1-3].

Most practical thermal processes and systems involve complex, coupled, transport mechanisms and interacting subsystems that constitute the overall system. As a consequence, several challenges are commonly encountered in obtaining accurate results from the numerical simulation of these systems. Some of the most important challenges are material properties, accurate imposition of boundary

conditions, validation, combined mechanisms, complex phenomena, multiple scales, multi-objective optimization, uncertainties and other additional effects and complexities. This paper considers some of these aspects, presents examples where these considerations are of particular importance and discusses possible approaches to meet these challenges.

As examples of typical practical thermal systems, consider the systems shown in Fig. 1. This figure shows sketches of the fabrication process for a hollow optical fiber, an electronic system cooled by microchannel flow and two configurations of chemical vapour deposition (CVD) reactors for thin film fabrication. These systems involve many of the complexities mentioned above. For instance, material properties of glass in optical fiber drawing are strong functions of temperature, combined modes of radiation, conduction and convection operate at various stages in the process, non-

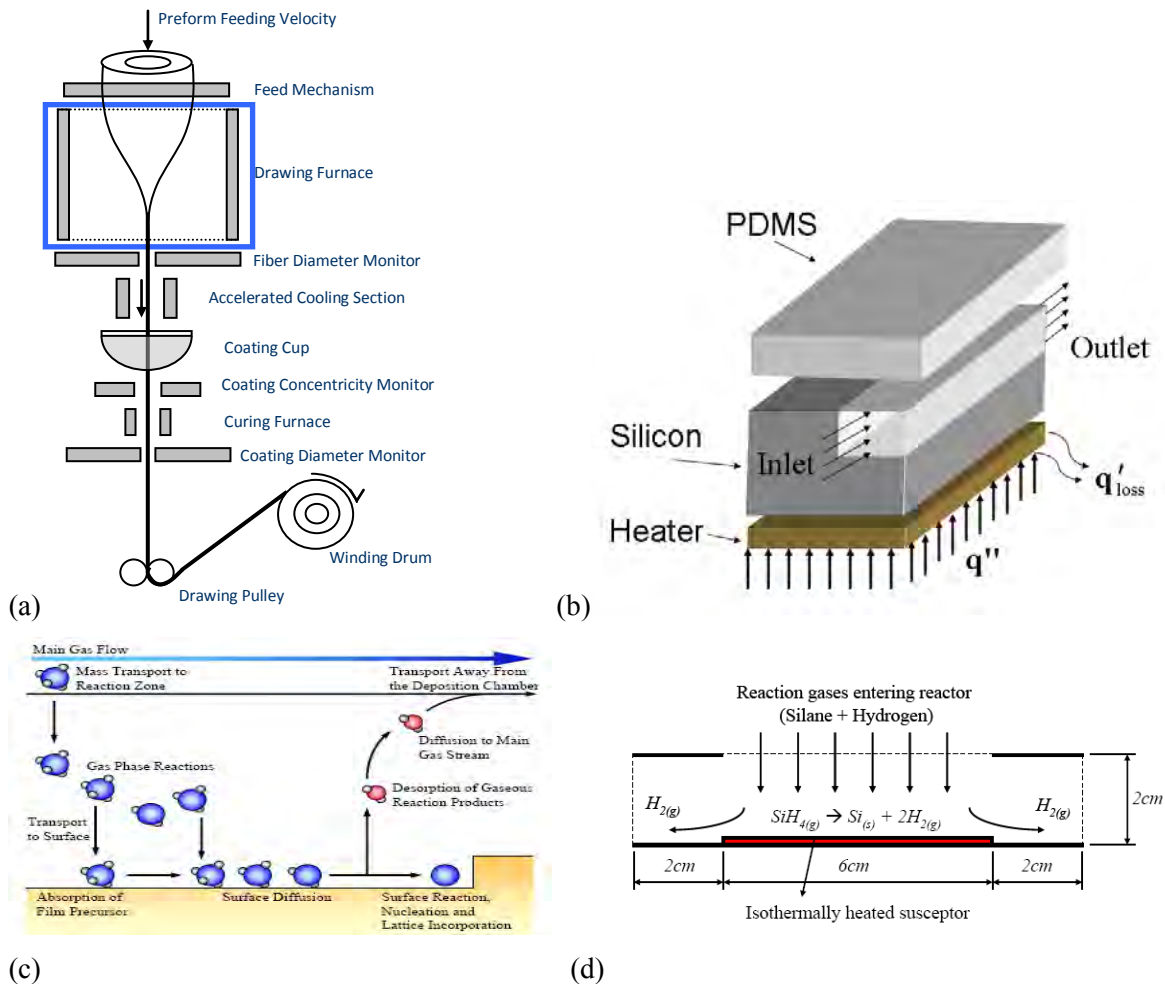


FIGURE 1. Common thermal processes and systems: (a) Hollow fiber drawing; (b) Microchannel flow for electronic cooling and (c) and (d) Chemical vapor deposition (CVD) systems for thin film fabrication.

Newtonian fluids are generally used for the fiber coating process and large changes in glass diameter occur in the draw furnace [4]. Similarly, the microchannel flow in electronic cooling is coupled with the system simulation at a much larger length scale. CVD involves chemical kinetics, which vary strongly with temperature and concentration [5]. The boundary conditions are fairly complicated in all cases and combined transport mechanisms are of interest. Similar considerations arise in other practical processes, as outlined later in this extended abstract and in the presentation.

A brief discussion of the challenges posed by the complexities in practical systems is given in this paper, considering a few selected examples such as the ones shown in Fig. 1.

2. NUMERICAL MODELING OF PRACTICAL PROCESSES

Let us consider the basic characteristics of mathematical and numerical modelling of typical thermal processes and systems. Considering the optical fiber drawing process, the flow of the glass and of the aiding purge gas in a cylindrical furnace is assumed to be axisymmetric. The governing equations for the glass and the gas are then given as,

$$\frac{\partial v}{\partial z} + \frac{1}{r} \frac{\partial(ru)}{\partial r} = 0 \quad (1)$$

$$\frac{\partial v}{\partial t} + u \frac{\partial v}{\partial r} + v \frac{\partial v}{\partial z} = -\frac{1}{\rho} \frac{\partial p}{\partial z} + \frac{1}{r} \frac{\partial}{\partial r} \left[r\nu \left(\frac{\partial v}{\partial r} + \frac{\partial u}{\partial z} \right) \right] + 2 \frac{\partial}{\partial z} \left(\nu \frac{\partial v}{\partial z} \right) \quad (2)$$

$$\frac{\partial u}{\partial t} + u \frac{\partial u}{\partial r} + v \frac{\partial u}{\partial z} = -\frac{1}{\rho} \frac{\partial p}{\partial r} + \frac{2}{r} \frac{\partial}{\partial r} \left(r\nu \frac{\partial u}{\partial r} \right) + \frac{\partial}{\partial z} \left[\nu \left(\frac{\partial v}{\partial r} + \frac{\partial u}{\partial z} \right) \right] - \frac{2\nu u}{r^2} \quad (3)$$

$$\rho C_p \left(\frac{\partial T}{\partial t} + u \frac{\partial T}{\partial r} + v \frac{\partial T}{\partial z} \right) = \frac{1}{r} \frac{\partial}{\partial r} \left(rK \frac{\partial T}{\partial r} \right) + \frac{\partial}{\partial z} \left(K \frac{\partial T}{\partial z} \right) + \Phi + S_r \quad (4)$$

Where u , v are the velocity components in the axial and radial directions, z and r , respectively, p is the local pressure, T the temperature, t the time, ν the kinematic viscosity, ρ the density, K the thermal conductivity, C_p the specific heat at constant pressure, Φ is the viscous dissipation term and S_r is the radiation source term. For glass, the material properties are strong functions of the temperature T . They also vary with composition and changes in the microstructure, the main effect being on the radiation properties. The variation in the viscosity is the most critical one for the flow, since it varies quite dramatically with temperature. An equation based on the curve fit of available data for kinematic viscosity ν is written for silica, in S.I. units, as

$$\nu = 4545.45 \exp \left[32 \left(\frac{T_{\text{melt}}}{T} - 1 \right) \right] \quad (5)$$

indicating the strong, exponential, variation of ν with temperature. Here, T_{melt} is the glass softening temperature, being around 1900 K for silica glass. The radiative source term S_r in Eq. (4) is non-zero for the glass preform/fiber because glass emits and absorbs energy. The variation of the absorption coefficient with wavelength λ can often be approximated in terms of bands with constant absorption over each band. Because of the small fiber diameter, being around 125 μm , there is a temptation to assume uniform temperature across the fiber. However, because of the high temperature dependence of the viscosity, this assumption does not yield accurate results and a large number of grid points, typically around 50, are needed across the fiber radius of around 62.5 μm to capture changes in temperature and the consequent effects on properties, viscous dissipation, thermally induced defects, and dopant movement.

Similarly, the fiber coating process may be modeled. Typical coating thicknesses are of the order of 40-50 μm and are applied to the uncoated fiber or as secondary coating to a coated fiber. The basic coating process involves drawing the fiber of diameter around 125 μm through a reservoir of coating fluid, with inlet and outlet dies. This is immediately followed by a curing process of the polymer coating material around the fiber. A balance between surface tension, viscous, gravitational, and pressure forces results in an upstream meniscus at the cup entrance, as well as a downstream meniscus at the die exit. At high speeds, the upper meniscus breaks down and air is entrained into the coating. The use of high draw

rates requires consideration of alternate pressurized applicator designs, where pressure induced motion of the coating material is used to reduce the shear at the fiber surface and helps in the establishment of a stable free surface flow. The control of the coating characteristics is of major concern in industry. These considerations have become particularly important as the coating speeds have been increased to values beyond 20 m/s to enhance productivity and as the interest in specialty fibers and fibers of different materials, including polymer fibers, has grown. The physical properties of the polymer coating materials, particularly the viscosity, and their dependence on temperature are of primary importance in the coating process. Surface tension has a significant effect on the flow near the free surface, which represents the interface between a liquid and a gas in many cases, and on the shape, stability and other characteristics of the interface.

Similarly, consider an electronic component cooled by the microchannel single-phase flow of a coolant, as shown in Fig. 1(b). Depending on the fluid, dimensions and operating conditions, the Knudsen number for the flow may be determined, leading to continuum flow, slip flow or molecular flow [6]. The overall system, on the other hand, is at engineering, or macro-scale, and can be modeled using the usual conservation equations. The typical equations are of the form:

Mass:

$$\nabla \cdot (\rho \tilde{V}) = 0 \quad (6)$$

Momentum:

$$\tilde{V} \cdot \nabla (\rho \tilde{V}) = -\nabla p + \nabla \cdot (\mu \nabla \tilde{V}) \quad (7)$$

Energy:

$$\tilde{V} \cdot \nabla (\rho C_p T) = \nabla \cdot (k \nabla T) \quad (8)$$

where μ is the dynamic viscosity, k is the fluid thermal conductivity and \tilde{V} is the velocity vector. For the solid region, the conduction equation is used, with thermal conductivity of the solid k , as

$$\frac{\partial}{\partial x_i} \left(k \frac{\partial T}{\partial x_i} \right) = 0 \quad (9)$$

For conjugate problem, the heat conduction in the solid region and the flow in the fluid region are solved separately and then coupled at the solid–fluid interface.

The chemical kinetics plays a critical role in the deposition of material from the gas phase in chemical vapor deposition systems [5]. The concentrations of the chemical species in the reactor affect the chemical kinetics, which in turn affect the deposition. In many cases, the process is chemical kinetics limited, implying that the transport processes are quite vigorous and the deposition is restricted largely by the kinetics. The chemical kinetics for several materials is available in the literature. For instance, the chemical kinetics for the deposition of Silicon from Silane (SiH₄) with Hydrogen as the carrier gas in a CVD reactor is given by the expression [7]

$$\hat{K} = \frac{K_o p_{SiH_4}}{1 + K_1 p_{H_2} + K_2 p_{SiH_4}} \quad (10)$$

where the surface reaction rate \hat{K} is in mole of Si/m²s, $K_o = A \exp (-E/RT)$, E being the activation energy, and A , K_1 , and K_2 are constants which are obtained experimentally. The p 's are the partial pressures of the two species in the reactor. However, the chemical processes are typically much more complicated, with several intermediate reactions in the gaseous phase and several at the surface. This is particularly true for the deposition of SiC and GaN.

3. RESULTS AND DISCUSSIONS

A few practical processes and systems have been mentioned in the preceding, along with some of the challenges faced in an accurate simulation. Several of these are considered in greater detail here, along with relevant examples. However, only a brief outline and a few selected examples are considered. Further details and examples will be given in the presentation.

3.1. Material properties, variations and characteristics

The accuracy of any numerical simulation is dependent on the material properties used. This is particularly critical in practical processes where the properties vary with the local conditions like temperature and pressure and where changes in the material during the process can affect the properties. However, property data are often not available to the needed accuracy and often at conditions that are different from those of the process. This is particularly problematic for the manufacture of optical fibers which strongly depends on the physical properties of silica glass and their variation with the temperature T . The exponential dependence of viscosity on temperature was given earlier. The radiation properties, such as the variation of the absorption coefficient with wavelength λ have been measured for certain compositions and glasses. But these data are often available only at room temperature, whereas the process is at much higher temperatures. Also, data may not be available for the particular glass or composition that is being simulated.

Dopants such as rare earth materials are often used to modify the transmission characteristics of optical fibers and for specialized applications. Even though accurate models may be developed for the process [8], the data on the effect of the dopants on radiation properties and on viscosity are very limited [9], as shown here.

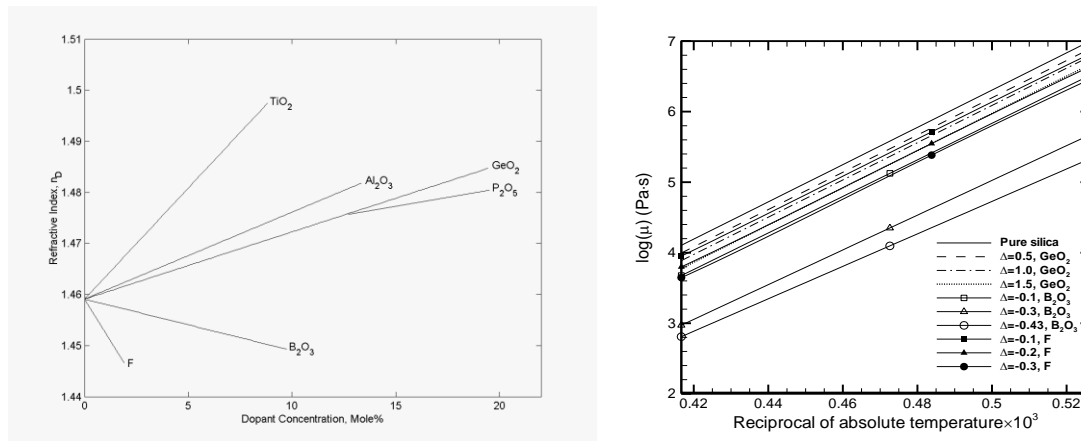


FIGURE 2. Effect of various dopants on the refractive index and viscosity of silica glass in the optical fiber drawing process.

Similarly, the coating process involves non-Newtonian materials and large material property changes. The fluid viscosity is often taken as

$$\mu = \mu_0 \left(\dot{\gamma} / \dot{\gamma}_0 \right)^{n-1} \exp(b/T) \quad (11)$$

where $\dot{\gamma}$ is the total strain rate, b the temperature coefficient of viscosity, subscript o indicates reference conditions and n is the power-law index of the fluid. The jacketing material is thus treated as a Generalized Newtonian fluid [10]. Other rheological models may also be used, depending on the fluid. Similarly, chemical kinetics play a critical role in chemical vapor deposition. Simple equations like the given earlier for Silicon are generally not available or applicable for the wide

variety of materials of practical interest. A large number of chemical reactions have to be solved in most cases and, again, the results are strongly affected by the material property and chemical kinetics employed. Lack of accurate property data is clearly a major hurdle in obtaining accurate simulation results in this case.

Besides temperature and concentration, the material properties are also often sensitive to the conditions under which the material is stored as well as the fabrication process, age and raw materials used. The properties may also change with time, resulting in different values for experiments done at different times. This is particularly of concern with biological materials, polymers and chemicals. It is therefore important to know what material and under what conditions it is being employed so that the appropriate properties can be used in simulation. Also, in some cases, properties may be measured for more accurate inputs. Interpolation may be used with available data to obtain the best estimate of the properties under the operating conditions.

3.2. Verification and validation of the mathematical and numerical models

Generally, simplifications and idealizations are employed in the modeling of practical thermal processes and systems because of the complexities that arise. Therefore, it is critical to verify and validate the mathematical and numerical models to ensure that the results obtained are applicable, realistic and accurate [11]. Unless the models are satisfactorily validated, the simulation results cannot be used as the basis for design and optimization. Among the approaches used are a consideration of the physical behavior of the results obtained, comparisons with available analytical and numerical results, particularly benchmark solutions, and comparisons with available experimental data. It is also important to ensure that the results are essentially independent of the grid and other arbitrarily chosen numerical parameters.

Because of the critical importance of validation, extensive efforts have to be made to obtain experimental data, whenever possible, for comparison with numerical predictions. In several cases, a separate, well-designed, experimental set-up may need to be fabricated to achieve this. In the modeling and simulation of single and twin-screw polymer extruders, a specially designed cam-driven thermocouple system was employed to obtain the temperature profile in the rotating screw and two rotating cylinders were used to study the mixing phenomena and thus validate the model for twin-screw extrusion [12].

In the manufacture of optical fibers, a polymer coating is applied, as shown in Fig. 1(a), for protection against abrasion and to increase strength. Typical coating thicknesses are of the order of 40-50 μm and are applied to the uncoated fiber or as secondary coating to a coated fiber. The basic coating process involves drawing the fiber of diameter around 125 μm through a reservoir of coating fluid, with inlet and outlet dies. This is immediately followed by a curing process of the polymer coating material around the fiber. At the die exit, the coating material is drawn out with the fiber, forming a downstream meniscus, which influences the coating characteristics.

Thus, an important consideration in the coating process is the exit meniscus, which represents the profile of the free surface as the fluid exits from the die due to the viscous drag from the moving wire or fiber. The governing equations are solved to obtain the temperature and flow distributions, from which the shear at the free surface is determined. The additional forces due to gravity, surface tension and external shear due to air are included to determine the overall force balance. The force imbalance is used to generate an iteration scheme, starting with a guessed profile, till the force balance is satisfied and a converged meniscus is obtained [13]. Figure 3 shows the numerical results and compares these with experimental data on the exit meniscus profile. A good agreement is observed, indicating the validity and accuracy of this approach. Overall, it is necessary to make all possible efforts to validate the mathematical/numerical models, even if it means spending considerable time and effort in developing an experimental arrangement to obtain the data needed for comparisons.

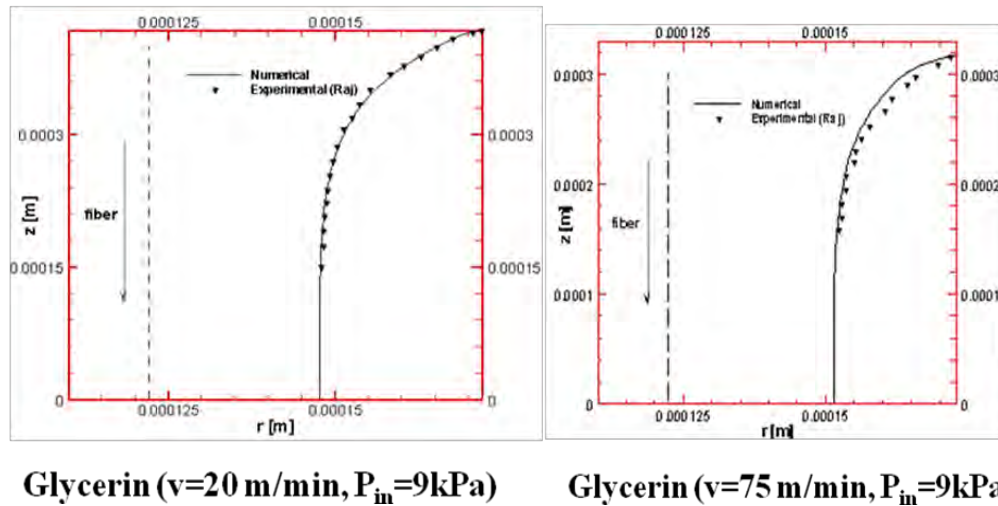


FIGURE 3. Calculated meniscus at the exit of the die in the coating process, along with experimental measurements of the profile, for glycerin at a fiber speed of (a) 20 m/min; (b) 75 m/min

3. 3. Accurate imposition of appropriate boundary conditions

The accuracy of any numerical simulation is strongly dependent on the modeling and accuracy of the imposed boundary conditions. Even though isothermal and uniform heat flux conditions are commonly used in fundamental studies, these conditions can seldom be used in practical circumstances. For example, in modeling the solidification process in an enclosed region, using the multiple-domain or the enthalpy-porosity model, the coupled conduction, or conjugate transport, in the walls of the mold is an important consideration. The effect of the imposed conditions in a practical circumstance at the outer surface of the mold on the solidification process can be obtained by solving this conjugate problem, which yields the temperature distribution in the mold as well as that in the solid and the liquid. Figure 4(a) shows the effect of conduction in the mold on the resulting temperature and velocity distributions, as well as on the solidification. For casting of metals, alloys, polymers and other materials, it has been shown in several studies that it is important to model the conjugate transport in the mold walls and in any insulation that may be used in order to obtain realistic and accurate simulation results.

Similarly, in the cooling of electronic systems, the isolated heat sources that approximate the components like electronic chips and devices are located on substrates that are conducting. Imposing adiabatic conditions on these surfaces is thus not a valid representation of the practical situation. The conduction in the walls distributes the heat input over the surface, rather than a concentrated heat source, resulting in substantial effect on the flow and the heat transfer. Figure 4(b) shows the calculated thermal and flow fields in an enclosed region with multiple heat sources that approximate electronic devices. Clearly, the walls play a very significant role in the heat transfer process and make it necessary to use the appropriate conjugate conditions.

Many such examples can be given where the appropriate imposition of boundary conditions is critical to an accurate numerical simulation of a practical thermal system. In some cases, the boundary conditions may not be accurately known and the solution of the entire system, with all its components, to obtain the relevant boundary condition may be prohibitive in terms of cost and effort. One such circumstance is the optical fiber drawing furnace, where the wall temperature distribution is a critical input to the process. But this distribution is not easily determined experimentally because of limited access to the furnace and modeling is complicated by the presence of many control and traverse subsystems in the draw furnace. An inverse calculation, using the limited temperature data obtained from a graphite rod immersed in the furnace, has been used by Issa et al. [14] to determine the wall temperature, which can then be used to accurately

simulate the draw process. For the simulations of flow in a room with an opening, the computational domain is generally extended and boundary conditions imposed far from the region of interest to ensure accurate simulation results. Other such approaches have been used in practical systems to obtain the relevant boundary conditions and thus accurately simulate the process.

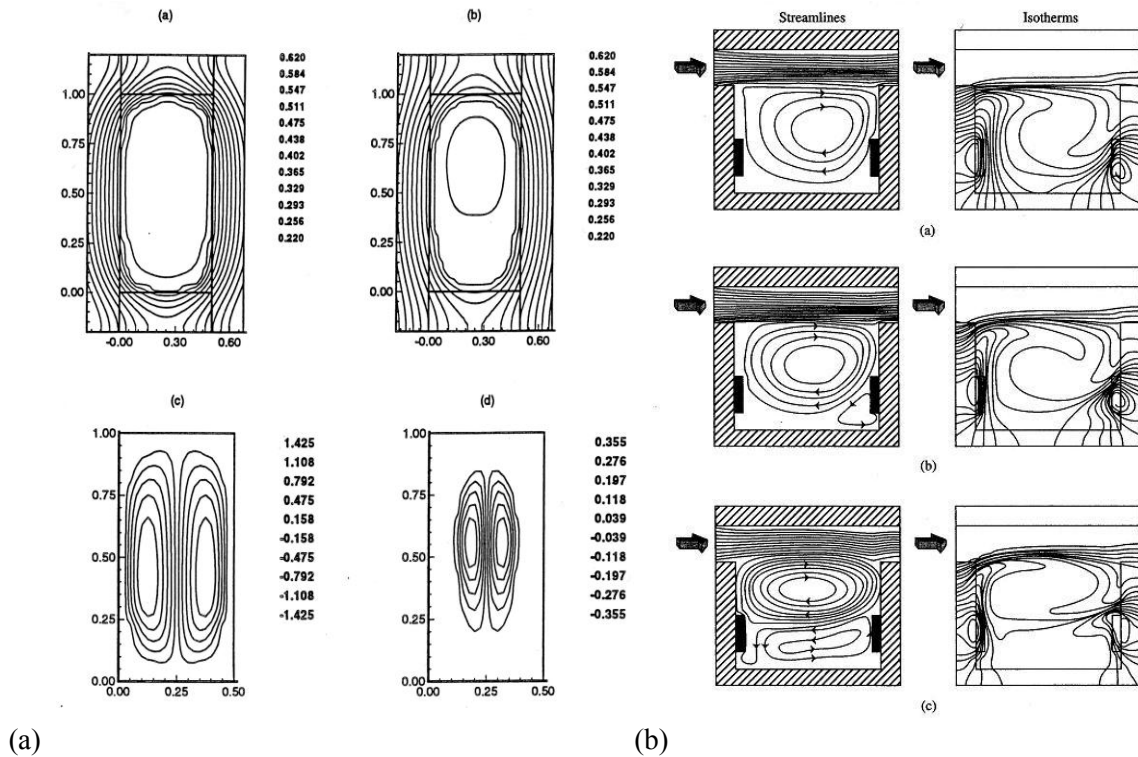


FIGURE 4. Effect of conjugate boundary conditions on the flow and heat transfer in (a) solidification process in casting; and (b) cooling of electronic devices located in an enclosed region.

3. 4. Combined mechanisms

In most practical thermal processes and systems, several coupled transport mechanisms generally arise and complicate the modeling and simulation. We considered conjugate boundary conditions in the preceding section, where the effects of combined conduction and convection were discussed. Similarly, in the furnace for optical fiber drawing, thermal radiation and convection arise as coupled mechanisms, as shown in Fig. 5(a). Convection arises both in the inert gas environment and in the glass, which is a subcooled liquid. Beyond the softening point, T_{melt} , the glass is treated as a highly viscous liquid, with viscosity obtained from an equation such as Eq. (5). Below the softening point, the viscosity is very high and the glass behaves almost like a solid. Radiation is the dominant mode of transport and the glass is largely heated up by radiation. Using radiation models such as the zonal method, the radiation transport in the glass as well as in the furnace is determined to obtain the energy absorbed. The temperature variation in the perform/fiber depends on the combined radiation and convection, including viscous dissipation in the glass. Similarly, forced and natural convection arise in the furnace drawing of hollow fibers, as shown in Fig. 5(b). Thus, the models must include the combined mechanisms to determine the resulting transport, temperature variation and the flow, as well as the free surface profile as the fiber is drawn from a cylindrical perform of several centimeters in diameter to the fiber diameter of 125 μm [15].

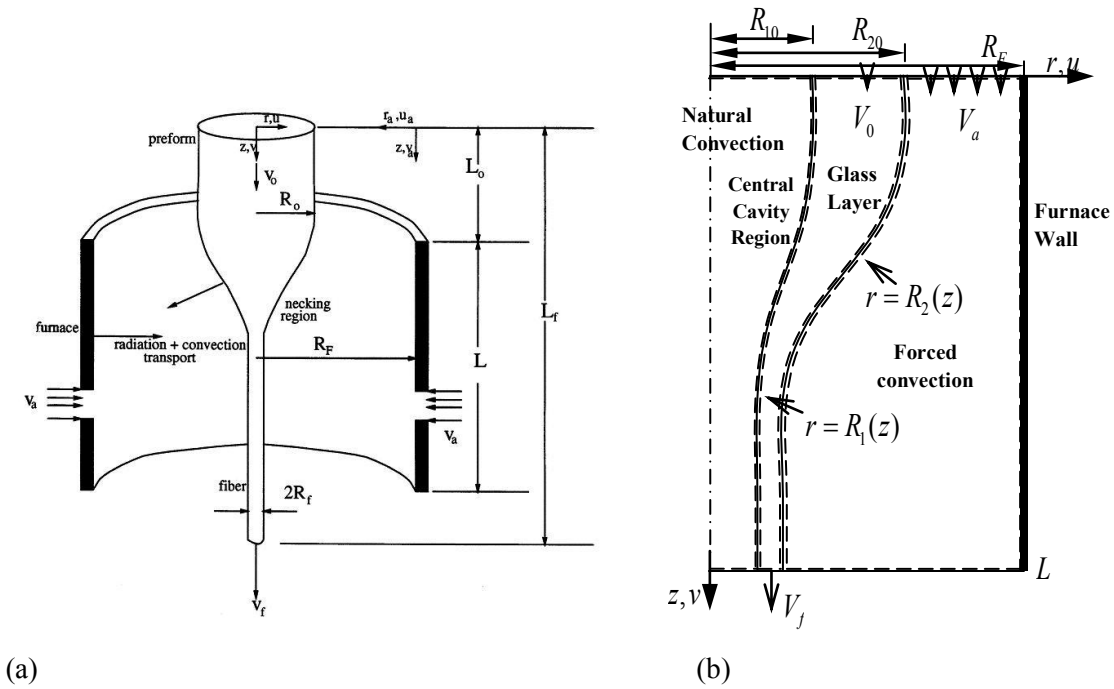


FIGURE 5. Transport mechanisms in an (a) Optical fiber drawing furnace and (b) Hollow fiber drawing process.

Another practical system that may be mentioned is that of the screw extrusion of reactive polymers like food materials. Figure 6 shows a sketch of the extruder, a simple mathematical model to obtain the domain as a channel and the boundary conditions for channel flow. The process involves convective combined heat and mass transfer and the resulting product depends on the inlet and imposed concentration C as well as the temperature T . The governing equations thus involve the flow equations along with the energy and mass transfer equations. Chemical reactions occur and give rise to source terms in the energy and mass conservation equations. The properties also vary with concentration, besides the temperature and the shear for non-Newtonian materials.

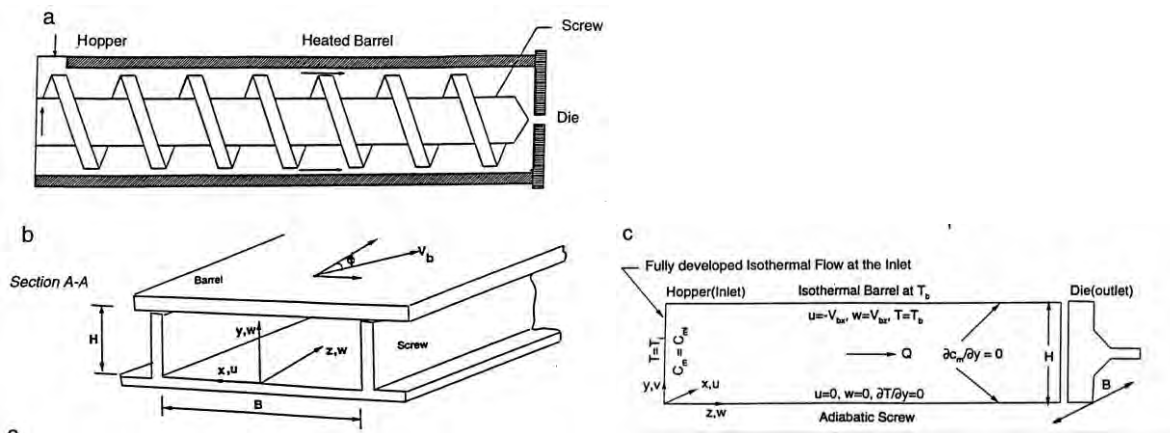


FIGURE 6. A single-screw extrusion system for reactive polymers and other chemically reactive materials such as food.

In such combined transport mechanisms, it is necessary to model the different mechanisms accurately and to ensure that the coupling effects are not neglected. For instance, in combined heat and mass transfer, the Soret and Dufour effects may not be negligible and may need to be included.

3.5. Complex transport phenomena

In most practical thermal processes, we encounter significant additional effects, such as buoyancy, complex geometry, surface tension, viscous dissipation, and free surfaces, that considerably complicate the transport phenomena being modelled. We have already considered the free surfaces that arise during fiber drawing and the menisci obtained in the coating process. As discussed earlier, the resulting shape of these free surfaces is governed by a balance of the forces due to shear, tension, gravity, and surface tension. Similarly, a force balance is used at interfaces in multi-layered fibers, along with the conservation principles, to determine the resulting profiles.

In hollow optical fiber drawing, a major concern is the collapse of the central core, which is needed for applications such as power delivery, sensors and infra-red radiation transmission. A collapse ratio C is defined to describe the collapse process of the central core as:

$$C(z) = 1 - (R_1(z) / R_2(z)) / (R_{10} / R_{20}) \quad (12)$$

Thus, $C = 0$ when the radius ratio of the final fiber equals the initial radius ratio, and $C = 1$ when the central cavity is closed. The effects of the preform feeding and fiber drawing speeds and of the furnace temperature on collapse ratio have been studied in detail [15, 16]. Because of the size of the core, surface tension is an important parameter and plays a very significant role in the collapse. Pressurizing the inner core can also be used to affect the collapse. Figure 7 shows the variation of the collapse ratio with pressure in the core and with the furnace temperature. In order to avoid the collapse of the central cavity, we can increase the drawing and feeding speeds, decrease the furnace temperature, or increase the preform radius ratio. It is seen that the collapse ratio decreases with a decrease in the pressure difference. This is because higher pressure in the central cavity tends to prevent collapse of the central cavity.

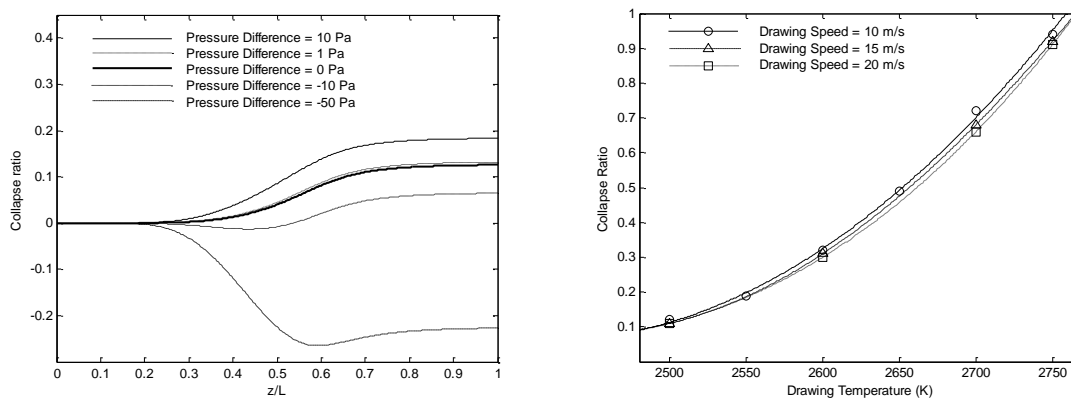


FIGURE 7. Variation of the collapse ratio in hollow optical fiber drawing with pressure in the inner core and with furnace temperature.

Thus, a wide variety of additional effects can arise in practical processes and thus complicate the transport phenomena being modeled. It is generally best to consider all the additional effects that may arise and to carry out a detailed scale analysis to determine which ones need to be retained. Then the complex process, with the important additional effects, can be modelled.

3.6. Multiple scales

A common challenge faced in the modeling of practical systems is the presence of transport processes and subsystems at different length or time scales. The governing equations for different scales in the problem may be different and thus the numerical approaches used in different regions may be quite different. As an example, consider the numerical simulation of pressure-driven nitrogen slip flow in long microchannels, with conjugate heat transfer in the walls under a uniform heat flux wall boundary condition. Figure 8(a) shows a sketch of this problem, which has not received the needed detailed investigation, despite its importance in many practical circumstances such as those related to the cooling of electronic devices and localized heat input in materials processing systems. For the gas phase, the two-dimensional momentum and energy equations are solved, considering variable properties, rarefaction, which involves velocity slip, thermal creep and temperature jump, compressibility, and viscous dissipation. For conduction in the solid region, on the other hand, the energy equation is solved with variable properties. Thus, the two regions are treated with different approaches. Figure 8(b) and (c) show the results for different substrate materials, including commercial bronze, silicon nitride, pyroceram and fused silica. The effects of substrate axial conduction, material thermal conductivity and substrate thickness are clearly seen. It is found that substrate axial conduction leads to a flatter bulk temperature profile along the channel, lower maximum temperature, and lower Nusselt number. The effect of substrate thickness on the conjugate heat transfer is very similar to that of the substrate thermal conductivity. That is, in terms of axial thermal resistance, the increase in substrate thickness has the same impact as that caused by an increase in its thermal conductivity.

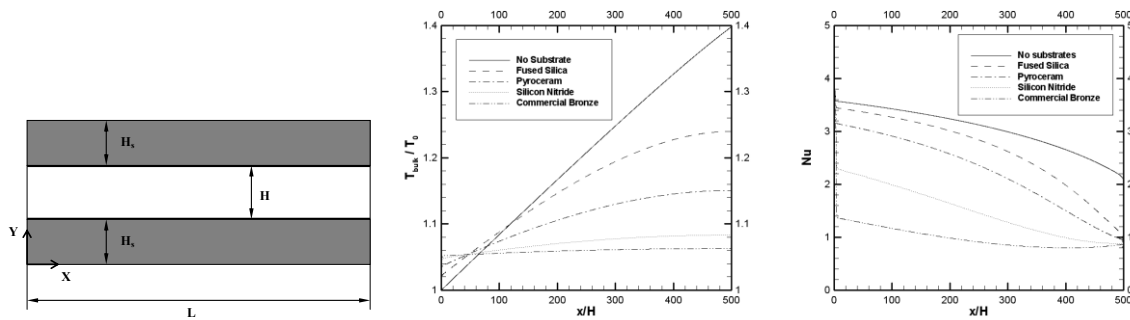


FIGURE 8. Nitrogen flow in a microchannel, with conjugate transport in the walls. (a) Sketch of the microchannel; (b) Temperature distribution for different wall materials; (c) Nusselt number for different wall materials.

In materials processing, the characteristics and quality of the material being processed are generally determined by the transport processes that occur at the micro- or nanometer scale in the material, for instance at the solid-liquid interface in casting or crystal growing, over molecules involved in a chemical reaction in chemical vapor deposition and reactive extrusion, or at sites where defects are formed in an optical fiber. However, engineering aspects are generally concerned with the commercial or macroscale, involving practical dimensions, systems and appropriate boundaries. Therefore, different scales arise and need to be solved by different methodologies, ultimately coupling the two to obtain the overall behavior. A few examples that involve these considerations are outlined here.

An area in which the changes at the molecular level are considered is that of generation of thermally induced defects in optical fiber drawing. The differential equation for the time dependence of the E' defect concentration was formulated by Hanafusa et al. [17] based on the theory of the thermodynamics of lattice vacancies in crystals. The E' defect is a point defect, which is generated at high temperature during the drawing process and which causes transmission loss and mechanical strength degradation in the fiber. It was assumed that the E' defects are generated through breaking of the Si-O band, and, at the same time, part of the defects recombine to form Si-O again. The net concentration of the E' defects is

the difference between the generation and the recombination. The equation for E' defect concentration is given as [17],

$$v \frac{dn_d}{dz} = n_p(0)v \exp\left(-\frac{E_p}{KT}\right) - n_d v \left[\exp\left(-\frac{E_p}{KT}\right) + \exp\left(-\frac{E_d}{KT}\right) \right] \quad (13)$$

where, n_d and E_d represent the concentration and activation energy of the E' defect; n_p and E_p represent those of the precursors. The initial values and constants are defined by [17]. Figure 9(a) shows the dependence of the average concentration of E' defects on the drawing temperature, indicating an increase with temperature as expected from the higher breakage of the Si-O bond. Figure 9(b) shows the results for a doped fiber. Clearly, the effect can be controlled by doping and by varying the operating conditions, particularly the furnace temperature. Again, these effects arise due to the microscopic mechanisms operating at the level of the defects.

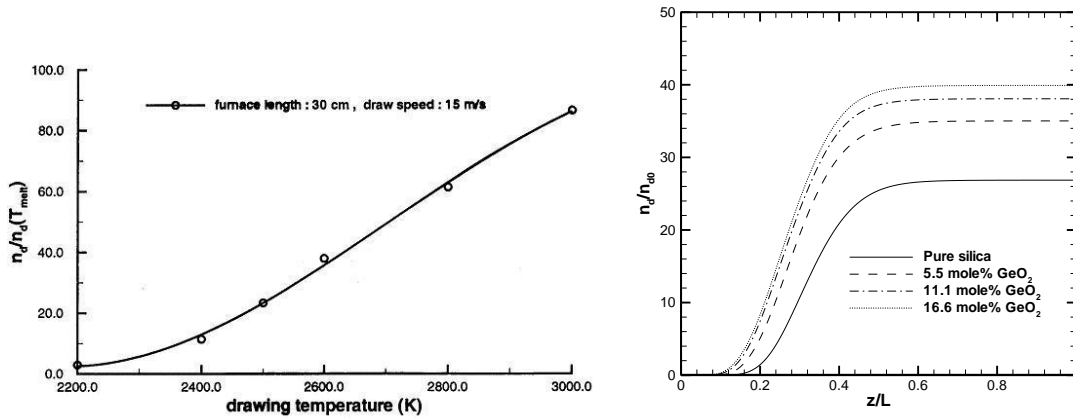


FIGURE 9. Dependence of average concentration of E' defects on furnace wall temperature; (b) Concentration of E' defects along the centerline for various GeO_2 concentrations in a doped fiber.

Similarly, in reactive thermal processing, such as food and reactive polymer extrusion, the microscopic changes in the material are linked with the operating conditions that are imposed on the system. The chemical conversion process is then represented by the chemical kinetics, which is dependent on the temperature and the concentration [18]. These microscale conversion mechanisms may be coupled with the flow and heat transfer in a screw extruder to obtain the conversion, pressure and other important quantities.

Another area where multi-scale transport is of interest is related to environmental flows, as shown in Fig. 10. The heat transfer near the source in a fire or in a polluting source involves much smaller length scales than the transport far downstream. In thermal discharges from power plants and industries, the length scale is of the order of a few meters at the source and of the order or several kilometers far downstream [19]. In room fires, the source may only be a few centimeters, with the room itself being several meters in scale. The scales are further apart in large-scale fires as in forest fires. Again, the modeling involved near the source could be quite different from that far away. For instance, radiation is particularly important near the fire source. But as one moves far away, the flow is dominated by turbulence and buoyancy. Similar considerations apply to heat and material discharges into the environment.

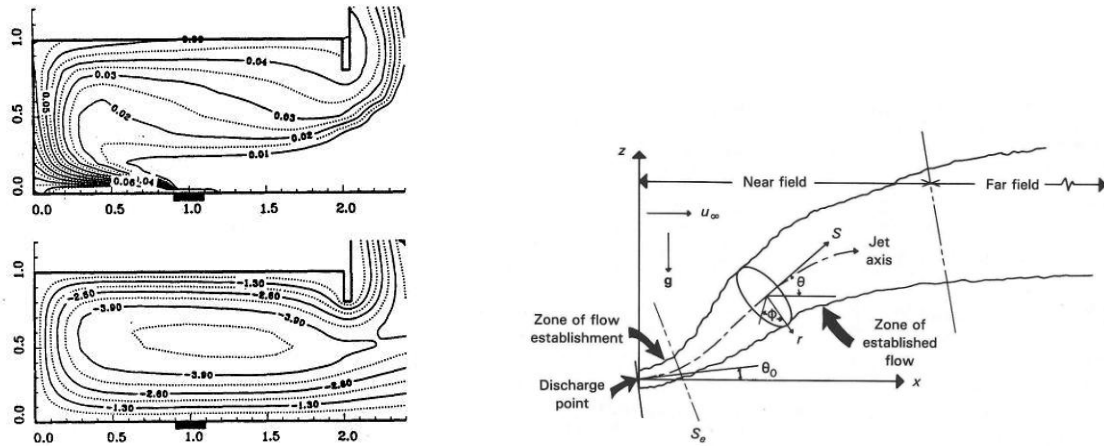


FIGURE 10. Multiple length scales in a room fire and in a thermal discharge into the environment.

3.7. Multi-objective optimization and uncertainty

Optimization is very important in most practical systems. However, multiple objective functions are generally of interest. For instance, in the cooling of electronic circuitry, typical design objectives are maximizing the heat removal rate from the components and minimizing the pressure drop. These two objectives can often be treated by considering the two objective functions separately. But this simple approach of combining the objectives into a single function simplifies the problem. Weighted sums may be employed in the development of the combined objective function [20]. If the two or more objective functions that are of interest in a given problem are considered and a strategy is developed to trade-off one objective function in comparison to the others, a set of non-dominated designs, termed the Pareto Set, which represents the best collection of designs is generated [2–22]. Then, for any design in the Pareto Set, one objective function can be improved, at the expense of the other objective function. The set of designs that constitute the Pareto Set represent the formal solution in the design space to the multi-objective optimization problem. The selection of a specific design from the Pareto Set is left to the decision maker or the engineer. A large literature exists on utility theory, which seeks to provide additional insight to the decision maker to assist in selecting a specific design. Many multi-objective optimization methods are available that can be used to generate Pareto solutions. Various quality metrics are often used to evaluate the “goodness” of a Pareto solution obtained and possibly improve the method as well as the optimal solution. The use of this approach was demonstrated by Zhao et al. [23] for an electronic system cooling problem.

A detailed study on the design and optimization of CVD systems has been carried out by Lin *et al.* [24]. Results from several trials of the numerical simulation were obtained to determine the operating conditions and examine the system performance. Response Surface Method (RSM) models were developed to study the behavior or the responses of the system with respect to the design variables. The optimization problem was formulated in terms of the RSM models, which were utilized to provide the operating conditions for higher productivity and quality of the film deposited. This is the case for deterministic optimization, with a typical result shown in Fig. 12.

However, design uncertainties arise at various points in the CVD process. Even if an optimal design is obtained from the deterministic optimization models, the uncertainties can cause unstable responses of the CVD process. For example, the compositions of the deposition species have errors

on the order of 15 %. Several researchers have estimated the randomness of the operating parameters in the CVD process. The rate constants of the chemical reactions may also have wide variances. The existence of the design uncertainties is considered in the design variables, as well as in the inlet velocity and the susceptor temperature of the CVD process [24].

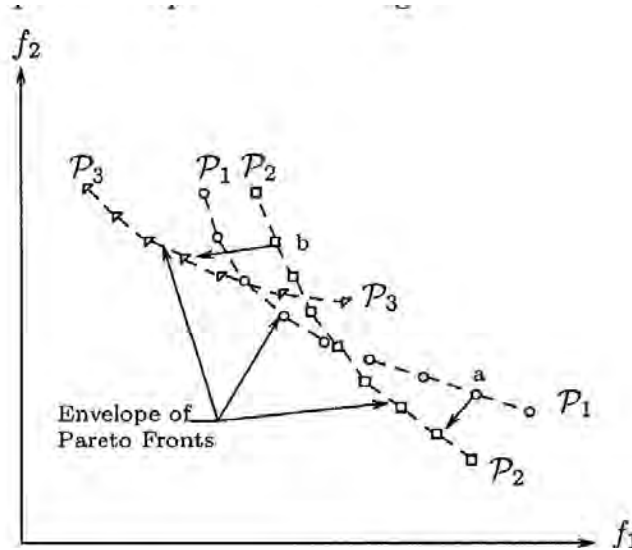


FIGURE 11. Multi-objective optimization with two objective functions f_1 and f_2 , which are to be minimized, showing the dominant designs, the Pareto Front and the envelope of Pareto Fronts for different geometric configurations.

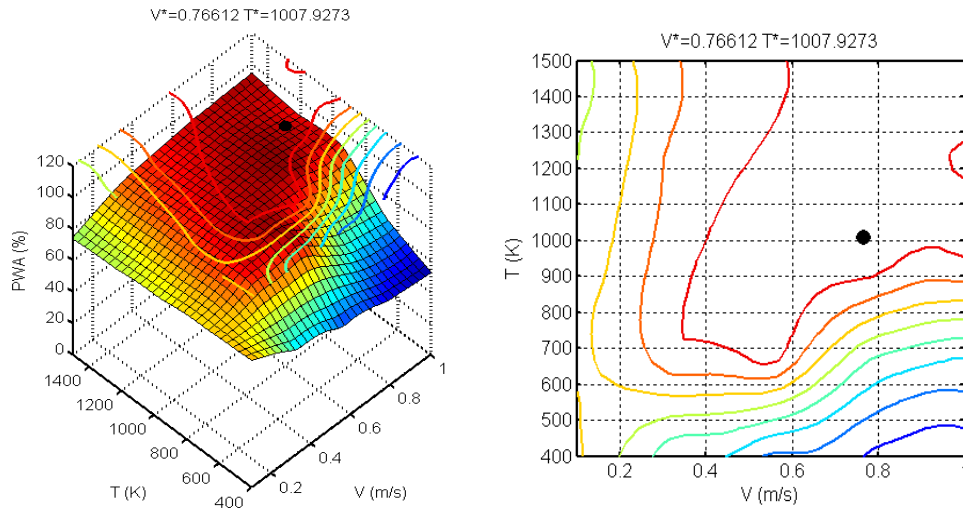


FIGURE 12. Response surface model and an optimal operating point in a typical CVD process for depositing a silicon thin film.

It was shown that, due to the existence of the design uncertainties, the traditional deterministic optimization formulation is no longer reliable to generate safe designs because it may lead to a design with high risk of system failure. The development of the Reliability-Based Design Optimization (RBDO) algorithm evaluates the probabilities of the system failures and provides a more conservative design which reaches to the optimality as the failure probabilities are subject to some acceptable level. Finally, the productions of the thermal systems are executed based on the optimal design variables. If any design uncertainties are found in the experiments, the simulations, or the mass productions, the information on the uncertainties is fed back to the formulation of the

RBDO problems and new optimal conditions can be generated by the proposed strategy. Figure 13 shows the results of optimization with some deterministic and some probabilistic or uncertainty conditions.

4. CONCLUSIONS

This paper presents a wide variety of challenges faced in an accurate numerical simulation of practical thermal systems and processes. Material properties and validation of models are well known concerns. But the accurate imposition of boundary conditions, combined transport mechanisms, uncertainties in the design variables and operating conditions for optimization, additional complexities and multiple scales are other challenges that commonly arise and must be addressed. These aspects are considered, along with practical examples where they are of particular concern, and possible approaches to meet these challenges are discussed. Since system behaviour, response, design, control and optimization are often based on numerical simulation results, particularly for practical systems, it is important to obtain accurate, realistic and valid simulation results. This paper briefly discusses the major issues that are encountered and some of the relevant solutions to these.

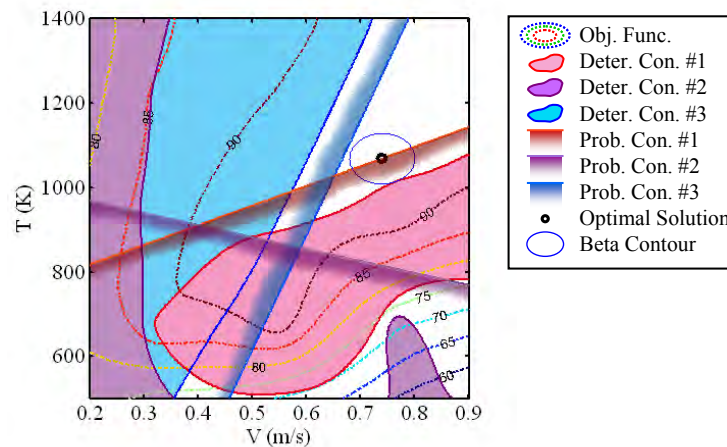


FIGURE 13. Optimization with deterministic design variables and operating conditions, as well as with uncertainties associated with these.

REFERENCES

- [1] Y. Jaluria, Thermal processing of materials: From basic research to engineering, *ASME J. Heat Transfer*, 125, 957-979, 2003.
- [2] Y. Jaluria, *Design and Optimization of Thermal Systems*, Second Edition, CRC Press, Boca Raton, FL, 2008.
- [3] A. Bejan, G. Tsatsaronis, and M. Moran, *Thermal Design and Optimization*, Wiley, New York, 1996.
- [4] U.C. Paek, Free drawing and polymer coating of silica glass optical fibers, *ASME Journal of Heat transfer*, 121, 774-788, 1999.
- [5] R.L. Mahajan, Transport phenomena in chemical vapor-deposition systems, *Advances in Heat Transfer*, 28, 339-425, 1996.
- [6] M. Gad-el-Hak, The fluid mechanics of microdevices – the Freeman scholar lecture, *J. Fluids Eng.*, 121, 5-33, 1999.

- [7] F.C. Eversteyn, P.J.W. Severin, C.H.J. Brekel, and H.L. Peek, A stagnant layer model for the epitaxial growth of silicon from silane in a horizontal reactor, *J. Electrochem. Soc.*, 117, 925-931, 1970.
- [8] C. Chen and Y. Jaluria, Effects of doping on the optical fiber drawing process *Int. J. Heat Mass Transfer*, 52, 4812-4822, 2009.
- [9] T. Izawa and S. Sudo, *Optical Fibers: Materials and Fabrication*, KTK Scientific Publishers, Tokyo, 1987.
- [10] Z. Tadmor and C. Gogos, *Principles of Polymer Processing*, Wiley, New York, 1979.
- [11] P.J. Roache, *Verification and Validation in Computational Science and Engineering*, Hermosa Publishers, Albuquerque, New Mexico, 1998.
- [12] Y. Jaluria, Heat and mass transfer in the extrusion of non-newtonian materials, *Advances in Heat Transfer*, 28, 145-230, 1996.
- [13] S.Y. Yoo and Y. Jaluria, Numerical simulation of the meniscus in the non-isothermal free surface flow at the exit of a coating die, *Numerical Heat Transfer*, 53A, 111-131, 2008.
- [14] J. Issa, Z. Yin, C.E. Polymeropoulos, and Y. Jaluria, Temperature distribution in an optical fiber draw tower furnace, *Journal of Materials Processing and Manufacturing Science*, 4, 221-232, 1996.
- [15] Y. Jaluria, Microscale transport phenomena in materials processing, *ASME J. Heat Transfer*, 131, 033111-1 to 17, 2009.
- [16] A.D. Fitt, K. Furusawa, T.M. Monro, C.P. and Please, Modeling the fabrication of hollow fibers: Capillary drawing, *J. Lightwave Tech.*, 19, 1924-1931, 2001.
- [17] H. Hanafusa, Y. Hibino, and F. Yamamoto, Formation mechanism of drawing-induced E' centers in silica optical fibers, *J. Appl. Phys.*, 58(3), 1356-1361, 1985.
- [18] S.S. Wang, C.C Chiang, A.I. Yeh, B. Zhao, and I.H. Kim, Kinetics of phase transition of waxy corn starch at extrusion temperatures and moisture contents, *J. Food Sci.*, 54, 1298-1301, 1989.
- [19] B. Gebhart, D.S. Hilder and M. Kelleher, The diffusion of turbulent jets, *Advances in Heat Transfer*, 16, 1-57, 1984.
- [20] Deb, K. (2002), *Multi-Objective Optimization Using Evolutionary Algorithms*, John Wiley & Sons, New York NY.
- [21] K.M. Miettinen, *Nonlinear Multi-objective Optimization*, Kluwer Acad. Press, Boston, MA, 1999.
- [22] J.L. Ringuest, *Multiobjective Optimization: Behavioral and Computational Considerations*, Kluwer Acad. Press, Boston, MA, 1992.
- [23] H. Zhao, T. Icoz, Y. Jaluria, and D. Knight, Application of data driven design optimization methodology to a multi-objective design optimization problem, *J. Engg. Design*, 18, 343-359, 2007.
- [24] P.T. Lin, H.C. Gea, and Y. Jaluria, Systematic strategy for modeling and optimization of thermal systems with design uncertainties, *Frontiers Heat Mass Transfer*, 1, 013003, 1-20, 2010.

SEMI-EMPIRICAL MODELS FOR TRANSIENT HEAT TRANSFER OF PIN-FIN HEAT SINKS SUBJECTED TO NON-UNIFORM HOT JET HEATING

T.J. Lu¹, S.S. Feng¹, T. Kim^{1,2}

¹MOE Key Laboratory for Strength and Vibration, Xi'an Jiaotong University, Xi'an 710049, P.R. China, tjlu@mail.xjtu.edu.cn

²School of Mechanical, Industrial, Aeronautical Engineering, University of Witwatersrand, Johannesburg, Private Bag, WITS 2050, Republic of South Africa, tongbeum@gmail.com

ABSTRACT

Jet blast deflectors (JBDs) are safety devices used on aircraft carriers to deflect aircraft exhaust upward to protect people and any equipment behind the JBD. As the cooling of the JBD is typically characterized by three-dimensional and transient heat transfer in complicated structures, JBD design using conventional CFD simulations is time-consuming and exhaustive. To address the issue, we present two cost-effective semi-empirical models, a fin analogy model and a porous medium model, to predict the heat transfer of forced air convection in pin-fin heat sinks under non-uniform heating of hot jet. Both models are experimentally validated, with excellent agreement achieved.

Key Words: *Jet Blast Deflector, Pin-Fin, Transient Heat Transfer, Non-Uniform Heating.*

1. INTRODUCTION

Jet blast deflectors are safety devices used on aircraft carriers to deflect aircraft exhaust upward to protect people and any equipment behind JBDs, see Figure 1. Due to the high level of heat of the exhaust jet, the JBDs require effective cooling. The next aircraft awaiting take-off is not allowed to roll over the JBD deck surface to avoid burning its tires (see Figure 1(a)), unless the JBD surface is cooled down to 200°F [1]. Therefore, the rapid cooling is meaningful to increase the frequency of take-off within a given period of time. Presently, cooling is actively achieved using seawater. However, the use of seawater causes extra weight, corrosion, and complex maintenance. Forced air cooling or passive cooling system has therefore attracted increasing interest.

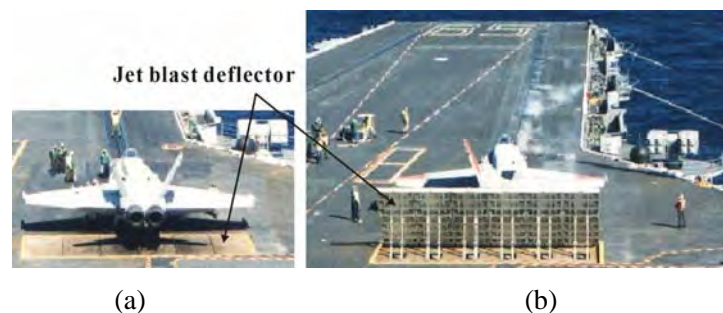


FIGURE 1. Jet blast deflector on aircraft carrier: (a) retracted position; (b) deployed to deflect the exhaust upward at take-off

Due to its simple structure and high rate of heat dissipation, pin-fins have been used in a wide range of industrial applications, such as internal cooling of turbine blades and thermal management of power electronics. Here, we propose a novel JBD consisted of a pin-fin sandwich (pin-fins array

sandwiched between two facesheets) with forced air cooling, and analyze its transient thermal behaviour when its front facesheet is exposed to localized, non-uniform heating of the jet exhaust, as shown schematically in Figure 2.

Computational Fluid Dynamics (CFD) has become a practical tool for the design of heat sinks. However, for pin-fin heat sinks under non-uniform heating of hot jet (Figure 2), the computational domain should cover at least one half of the heat sink and several million mesh elements are needed to fully realize the flow characteristics around the pin-fin units. This makes the computation time-consuming.

Alternatively, semi-empirical models can be used, such as the fin analogy model and the porous medium model widely used for extended surfaces. Whilst the fin analogy model has been successfully implemented for various metallic sandwich structures having periodic cores [2], so far only uniform thermal boundary conditions and steady heat transfer are considered, with the conjugate heat transfer in the facesheets ignored. The porous medium model has been utilized to predict the steady two-dimensional (2-D) heat transfer in pin-fin heat sinks under uniform thermal boundary conditions [3]. The paper aims to develop two semi-empirical models to predict the transient, three-dimensional (3-D) temperature fields in the pin-fin heat sink under non-uniform hot jet heating.

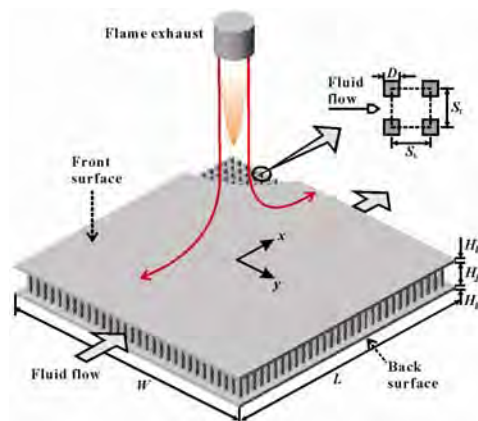


FIGURE 2. Schematic of forced air convection heat transfer in pin-fin sandwich subjected to non-uniform heating of hot jet

2. SEMI-EMPIRICAL MODELS

Fin Analogy Model

In the fin analogy model, the temperature fields in the front facesheet, in the back facesheet, in each pin-fin, and in the convective flow are described by individual governing equations.

The 3-D transient heat conduction equation is solved for both facesheets. Hot jet heating is imposed on the outer surface of the front facesheet, while natural convection and radiation boundary conditions are applied on that of the back facesheet. On the inner surface of each facesheet, forced air convection is applied to the region directly exposed to fluid flow whilst conduction boundary condition holds at the root of each pin-fin.

Heat transfer in each pin-fin is described using the classical one-dimensional (1-D) transient fin model, with the end temperatures at the two tips of each pin-fin specified as the boundary condition.

To solve for the distribution of fluid temperature in the pin-fin channel, the unit cell averaging approach is adopted, with uniform fluid temperature within each unit cell assumed. Upon analyzing

the heat balance of fluid flow in an arbitrary pin-fin unit cell, the differential equation for fluid temperature distribution in the flow plane is derived.

All the governing equations are solved iteratively with the finite volume method.

Porous Medium Model

By assuming that the pin-fin array can be modelled as a porous medium, the 2-D porous medium model with isoflux boundary conditions used by Kim et al. [3] is extended to cover 3-D transient heat transfer in pin-fin heat sink subjected to non-uniform hot jet heating. The volume-averaged Brinkman-Forchheimer model for fluid flow and the two-equation model for heat transfer are solved for the porous medium region (the pin-fins channel; Figure 2). To consider the intrinsic anisotropic heat conduction through the pin-fins array, anisotropic solid thermal conductivity is assumed in the model. Heat conduction in the facesheets is coupled with forced convection to account for lateral heat spreading in the facesheets.

3. VALIDATION

To validate the two semi-empirical models, experiments were performed to measure the temporal variation of front facesheet temperature at the impinging center ($z = 0$) for one cycle of sudden heating and cooling. The jet (circular hot air jet) exit temperature was set to be approximately 140°C. Figure 3 compares the measured data with the predictions from the two models. It is seen from Figure 3 that, for both the heat-on and heat-off processes of the hot air jet, the model predictions agree well with the experimental measurements, within the estimated experimental uncertainty of 7.3%.

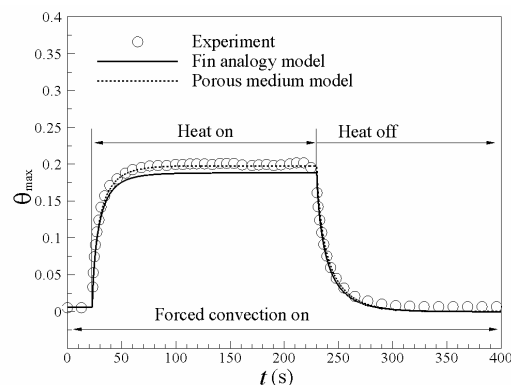


FIGURE 3. Transient temperature at impinging center: comparison between model predictions and experimental measurements

4. RESULTS

The experimentally validated semi-empirical models are used to design pin-fin sandwiches for JBD application. Note that, although in the present experiments *hot air jet* was employed to simulate the actual *flame exhaust*, the validated models can be used for many different heating conditions by modifying the boundary condition applied at the impinging surface of the front facesheet. Here, by using the non-uniform heat flux distribution of propane torch determined by Carbajal et al. [4] as the boundary condition, the instantaneous temperature contours on the front surface of the pin-fin sandwich are predicted with the fin analogy model. The results are plotted in Figure 4: the maximum temperatures coincide with the impinging center, and it is remarkable that the thermal footprints of the pin-fins on the facesheet are clearly captured by the fin-analogy model.

The fin analogy model can predict the local thermal behavior around each pin-fin in the facesheet, enabling the evaluation of thermal stresses at the pin-fin root. High thermal stresses at the roots may cause local failure. In comparison, the porous medium approach employs the volume-averaging technique, thus unable to predict local thermal distributions. Further, the fin analogy model can be extended to cover lightweight sandwich panels with periodic lattice truss cores, which are promising for JBD applications due to their combined structural load bearing and heat transfer capabilities [2].

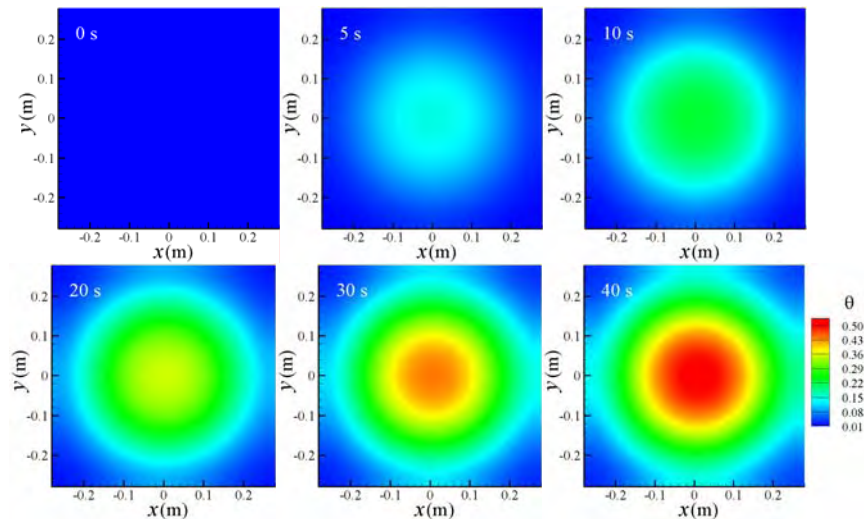


FIGURE 4. Instantaneous temperature contours on front surface of pin-fin sandwich subjected to flame jet heating: prediction with fin analogy model

4. CONCLUSIONS

Two semi-empirical models - fin analogy model and porous medium model - are developed to predict 3-D transient convective heat transfer of pin-fin heat sinks. Experimental measurements are carried out to validate the two models, with excellent agreement achieved. Amongst the two models, the fin analogy model is more attractive as it can predict local thermal behaviors around each pin-fin root, thus useful for subsequent thermomechanical analysis (e.g., calculation of thermal stresses at the pin-fin roots). In addition, it can be extended to cover the structurally efficient sandwich structures with periodic lattice truss cores that have been suggested for air-cooled JBD applications [2].

REFERENCES

- [1] F. Lavin, W. Goon, and M. Siegel, Investigations in support of Mk 7 jet blast deflector cooling module design, Naval Air Engineering Center, Philadelphia, Pennsylvania, Technical Report No. 0778537, 1972.
- [2] T.J. Lu, L. Valdevit, and A.G. Evans, Active cooling by metallic sandwich structures with periodic cores, *Progress in Materials Science*, 50, 789-815, 2005.
- [3] D. Kim, S.J. Kim, and A. Ortega, Compact modeling of fluid flow and heat transfer in pin fin heat sinks, *ASME Journal of Electronic Packaging*, 126, 342-350, 2004.
- [4] G. Carbajal, C.B. Sobhan, G.P. Peterson, D.T. Queheillalt, and H.N.G. Wadley, A quasi-3D analysis of the thermal performance of a flat heat pipe, *International Journal of Heat and Mass Transfer*, 50, 4286-4296, 2007.

STEPS TOWARDS A REAL TIME SOLUTION OF FIRE IN TUNNELS

Bernhard A. Schrefler, Francesco Pesavento

Dept. of Structural and Transportation Engineering, University of Padova, via F. Marzolo 9, 35131
– Padova, Italy, bas@dic.unipd.it, pesa@dic.unipd.it

Francisco Chinesta, Adrien Leygue

GeM: UMR CNRS-Ecole Centrale de Nantes, 1 rue de la Noe, BP 92101, F-44321 Nantes cedex 3,
France, Francisco.Chinesta@ec-nantes.fr, adrien.leygue@ec-nantes.fr

ABSTRACT

We show a solution for a realistic tunnel fire simulation using a 2D-3D coupling strategy and a full multiphysics model for concrete (2D sections), known also as three fluids model (water, vapour, dry air). The computing times are too high for a real time solution. We investigate the applicability of the proper generalized decomposition (PGD) to obtain two goals: achieve a full 3D solution for the solid domain and reduce simultaneously the computing time. The first results are encouraging.

Key Words: *Proper generalized decomposition, Fire in tunnels, Concrete.*

1. INTRODUCTION

The availability of an efficient tool for simulation of a fire scenario in a tunnel is of paramount importance for fire safety management in emergency situations, for training of fire brigades prior to emergency cases in order to be able take the right decisions when needed and to evaluate measures geared to increase the resistance of existing tunnel vaults against spalling. We have developed such a tool which takes the thermal fluid-structural coupling in a tunnel fire fully into account [1]. It appears as one of the largest coupled problems actually solved in the community of computational interaction problems. The simulation of a realistic fire scenario is still a time consuming task and the tool is not yet completely ready for the first of the above mentioned three goals. One of the bottlenecks is the heavy computational burden linked with the three fluids model for concrete. It is not possible to disregard the enormous heat sink the tunnel vault represents with the phase changes and chemical reactions going on in heated concrete. Such an omission can yield temperature fields also some 1000°C above measured ones in an experiment. On the other hand simplifications of these phenomena are not possible as highlighted in two recent companion papers [2,3]. In the existing model [1] we have chosen a 3D-2D coupling strategy where the thermally driven CFD part is solved in a three dimensional cavity i.e. the tunnel, and the concrete part is solved on 2D sections normal to the tunnel axis, at appropriate intervals, see Fig. 1. The heat flux and temperature values which serve as coupling terms between the fluid and the structural problem are interpolated between the sections. With this approximation the heat transfer in the tunnel vault in the direction of the tunnel axis is disregarded. The aim of our current research effort is twofold: realize a true 3D-3D coupling on one hand and reduce drastically the computing time on the other hand. The way for achieving this is through adoption of an extremely fast equation solver which can achieve a speed-up of up to 3600 times [4] and the adoption of the Proper Generalized Decomposition PGD [5] for a fast 3D solution of the problem of heated concrete. Steps in this direction as well as the general model will be shown.

2. FULL 3D SOLUTION OF HEATED CONCRETE WITH PGD

In the case of the complex behaviour of the tunnel vault (transient and non-linear coupled multi-physic models) we would like to avoid the above mentioned 3D to 2D dimensionality reduction.

Because of the richness of the thickness description due to many coupled physics with strong and fast evolutions in the thickness direction, a full 3D descriptions may involve millions of degrees of freedom in the solid domain that should be solved many times because of the history dependent chemo-hygro-thermo-mechanical behaviour. Today, the solution of such fully 3D models remains intractable for large size problems despite the impressive progress made in mechanical modelling, numerical analysis, discretization techniques and computer science during the last decade. New numerical techniques are needed for approaching such complex scenarios, able to proceed to the solution of fully 3D multiphysics models in geometrically complex parts. The well established mesh-based discretization techniques fail because of the excessive number of degrees of freedom involved in the fully 3D discretizations where very fine meshes are required in the thickness direction (despite its reduced dimension) and also in the in-plane directions to avoid too distorted meshes. A way to solve this problem is the adoption of the Proper Generalized Decomposition (PGD), [6]. In what follows we use the construction of the Proper Generalized Decomposition of a model defined in tunnel shell $\Xi = \Omega \times I$ with $\mathbf{x} = (x, y) \in \Omega \subset \mathfrak{R}^2$ (the tunnel transverse section) and $z \in I = [0, L]$ its axis. In the following we show an application of the 2D-3D coupling strategy for a 20MW fire in a tunnel and a PGD solution for the heat transfer problem only.

3. TUNNEL FIRE: EXAMPLE OF THE 3D-2D COUPLING STRATEGY

The structure under consideration is the tunnel of Virgolo close to Bolzano (Italy) that has been also used for an experimental test in the framework of UPTUN project [7]. We have considered the central part of the tunnel, 80 m long. Its geometry is decomposed in the fluid and the solid domains, see Fig. 1. The solid domain consists in the cross section of the tunnel vault. In the simulations five cross sections are considered at 0, 30, 40, 50, 80 meters along the longitudinal axis z . The location of fire is the section at 40 m.

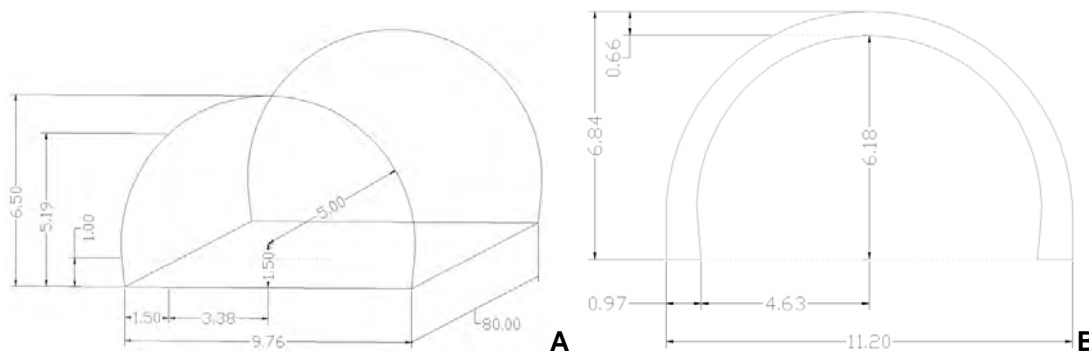


FIGURE 1. Geometry of the tunnel: (A) 3D fluid domain, (B) 2D solid domain (i.e. tunnel cross section)

The total thermal power involved by the fire is increasing in 10 minutes up to 20MW following a linear law and then kept constant. For this analysis 15300 hexaedral elements are used in the fluid domain, while each cross section is discretized with 640 quadrilateral elements with eight nodes. For further information about the properties of the fluid and the concrete used in the vault of the tunnel, the reader is referred to [1]. For sake of brevity here we report only the main result of the calculation in terms of temperature distribution in solid and fluid domain, Fig. 2.

4. HEAT TRANSFER SIMULATION IN THE TUNNEL VAULT WITH PGD

In this section we present some preliminary results of the simulation of the tunnel fire described above obtained by applying the Proper Generalized Decomposition techniques illustrated in section 2.

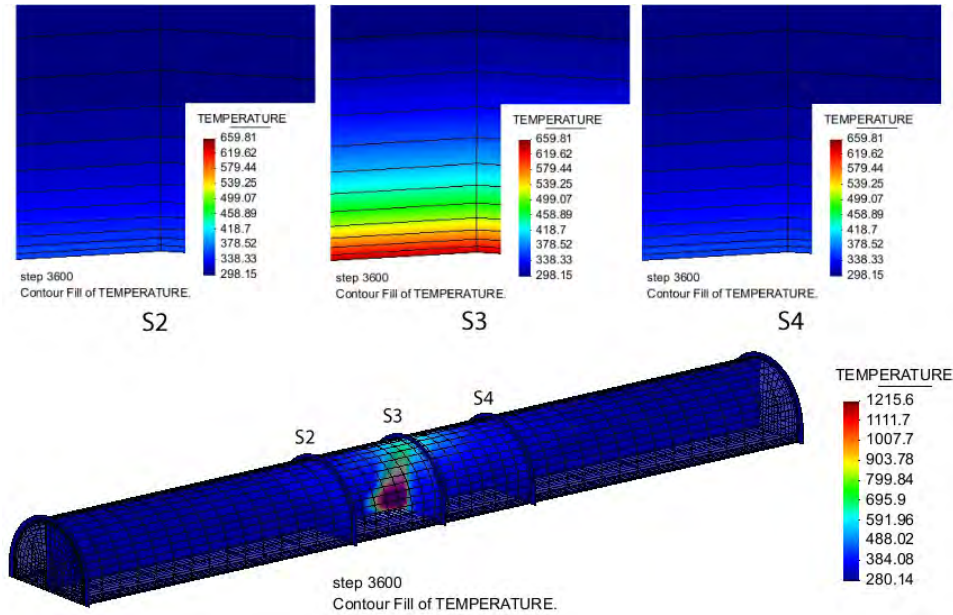


FIGURE 2. Temperature distribution (K) at $t = 3600$ s in the fluid domain and in sections S2, S3 (fire), S4

The main aim of this calculation is to demonstrate the validity of the approach considering, as initial stage of the on-going research, a simplified model limited to heat transfer through conduction. The mesh used in the same as in the previous example in the transversal section, but using nine-noded elements, while in the longitudinal direction 8000 elements have been used. The duration is 1 hour with a time step of 1 sec. As already pointed out the problem is solved assuming some simplifications as far as both the physical problem and the boundary conditions are concerned. The concrete vault is treated as a solid domain for which only the pure conductive thermal problem is considered, neglecting convective transfer of energy, phase changes and the mass transport inside the pores of the material. The boundary conditions consist in the definition of a normalized thermal flux on the inner surface of the tunnel vault according to the following formula:

$$norm. \text{ heat flux} = F_{\theta}(\theta) \times F_z(z) \times F_t(t)$$

in which the distribution functions in space and in time are shown in Figure 3B: θ is the angle (from the pavement) identifying the position of the point of the heated surface of the cross section on which the normalized flux is computed. The whole 20 MW power is applied directly to the heated surface without taking in to account the role played by air, i.e. by using Neumann condition instead of Robin condition defined trough a heat exchange coefficient α between the surface of concrete structure and the surrounding fluids. Because of this we expect a large difference in terms of temperature field between the solution obtained by means of PGD and the original one obtained by using the full model. The results of PGD analysis are depicted in Figure 4. The results shown in Figure 4 have been obtained by using 13 modes and took 2 min and 30 sec of computational time on a standard INTEL cpu based computer using MATLAB. A fast check has shown that the computed stored energy in the concrete vault after one hour equals the heat input. The time span is too short for heat flux to reach the boundary to the surrounding rocks, see the temperature gradient in Figure 4B. The surface temperatures reached are comparable to the ones obtained with the full model, [1], in the case of pure CFD simulations for which the solid domain is neglected together with the related heat exchange fluxes. In that case the temperature values were much higher than those obtained with the model of section 3 and approximately equal to 4000 K [1], that is the same order of magnitude of thermal field attained by using PGD in this work.

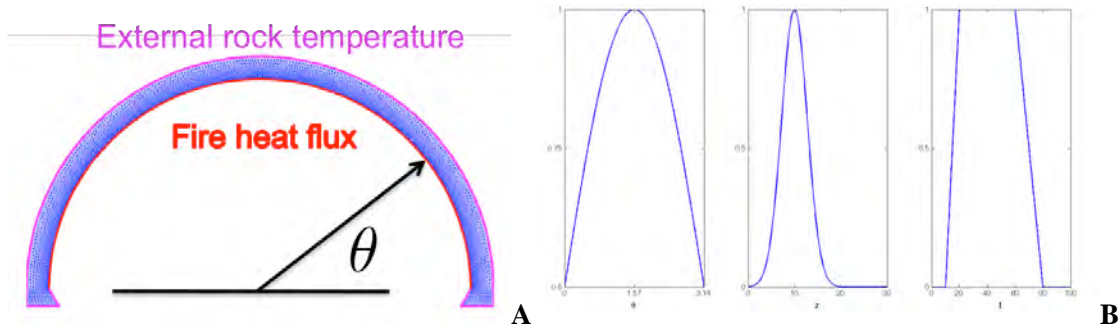


FIGURE 3. Sketch of the mesh (A) and of the bc.s (B) used in the case of tunnel fire solved by PGD

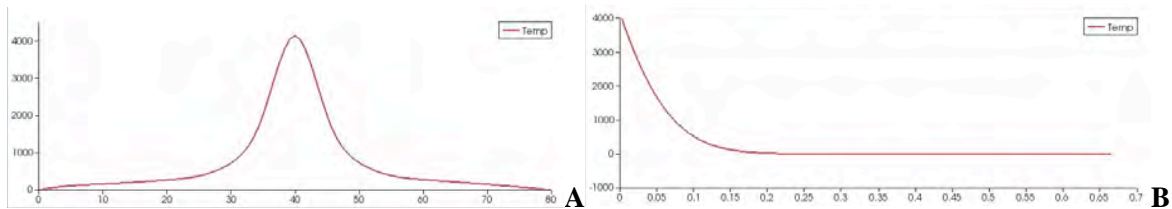


FIGURE 4. Temperature distribution along z-axis (A) and in the thickness of the central cross section of the tunnel (B) obtained from PGD analysis

5. CONCLUSIONS

We have shown a 3D-2D coupled solution for a tunnel fire simulation, taking the three fluids concrete model into account. For a fire of a duration of one hour the calculation time on a PC is well over one day. For the thermal problem in the tunnel vault a PGD approach on a full 3D solid domain model has been shown. The computing time was reduces to two and half minutes. Considering the short computational time and the fact that it is possible to obtain physically reasonable results just by introducing in PGD analysis more sophisticated physical models and physically correct bc.s (i.e. taking into account the role of the air), this set of preliminary computations are extremely encouraging.

REFERENCES

- [1] B.A. Schrefler, R. Codina, F. Pesavento, J. Principe, Thermal coupling of fluid flow and structural response of a tunnel induced by fire, *Int. J. Numer. Meth. Engng*, 87,361–385, 2011.
- [2] D. Gawin, F. Pesavento, B.A. Schrefler, What physical phenomena can be neglected when modelling concrete at high temperature? A comparative study: Part 1: physical phenomena and mathematical model, *Int. J. Solids Struct.*, 48, 1927–1944, 2011.
- [3] D. Gawin, F. Pesavento, B.A. Schrefler, What physical phenomena can be neglected when modelling concrete at high temperature? A comparative study: Part 2: comparison between models, *Int. J. Solids Struct.*, 48, 1945–1961, 2011.
- [4] A. Bertoldo, M. Bianco, and G. Pucci, A fast multifrontal solver for non-linear multi-physics problems, *Computational Science, ICCS 2004, PT 2, Book Series: Lecture Notes in Computer Science*, 3037, 614-617, 2004.
- [5] F. Chinesta, A. Ammar, E. Cueto, Recent Advances and New Challenges in the Use of the Proper Generalized Decomposition for Solving Multidimensional Models, *Archives of Computational Methods in Engineering*, 17, 327-350, 2010.
- [7] Brite EURAM Research Project, *HITECO - High Temperature Concrete*, final report, 1999.

SURROGATE-BASED MODELING AND DIMENSION REDUCTION TECHNIQUES FOR THERMO-FLUID & ENERGY SYSTEMS

Young-Chang Cho, Wenbo Du, Amit Gupta, Chien-Chou Tseng, Ann Marie Sastry

University of Michigan, Ann Arbor, MI, USA

Wei Shyy

Hong Kong University of Science and Technology, Clear Water Bay, Hong Kong weishyy@ust.hk

ABSTRACT

Successful modeling and/or design of thermo-fluid and energy systems often requires one to address the impact of multiple “design variables” on the prescribed outcome. There are often multiple, competing objectives based on which we assess the outcome of optimization. Since accurate, high fidelity models are typically time consuming and computationally expensive, comprehensive evaluations can be conducted only if an efficient framework is available. Furthermore, informed decisions of model/hardware’s overall performance rely on an adequate understanding of the global, not local, sensitivity of the individual design variables on the objectives. The surrogate-based approach, which involves approximating the objectives as continuous functions of design variables from limited data, offers a rational framework to reduce the number of important input variables, i.e., the dimension of a design or modeling space. In this paper, we discuss the fundamental issues that arise in surrogate-based analysis and optimization, highlighting concepts, methods, techniques, as well as practical implications. To aid the discussions of the issues involved, we will summarize recent efforts in investigating cryogenic cavitating flows, active flow control based on dielectric barrier discharge concepts, and Li-ion batteries.

Key Words: *Surrogate modeling, Cavitation, Dielectric barrier discharge, Lithium-ion battery.*

1. INTRODUCTION

The notion of design variables influencing system performance can be found in numerous thermo-fluid and energy systems. In the computational modeling context, the design variables can be adjustable parameters associated with a given mathematical model under different operating conditions and scaling parameters. In the hardware design context, they are often geometry, materials, and operating variables. In both situations, there are often multiple, competing objectives based on which we assess the outcome of optimization. Since accurate, high fidelity models are typically time consuming and computationally expensive, comprehensive evaluations can be conducted only if an efficient framework is available. Furthermore, informed decisions concerning a model or hardware system’s overall performance rely on an adequate understanding of the global, not local, sensitivity of the individual design variables on the objectives.

In reality, most engineering system and modeling designs are conducted as open loop, feed-forward processes. For example, for turbine design in aerospace and mechanical engineering, one design iteration for a given set of engine balance conditions may currently take up to several weeks, with just the blade geometry design sub-iteration phases taking several days each. The quest for an acceptable blade surface velocity distribution is accomplished with many ad hoc rules in what is essentially a manual trial-and-error process. A systematic approach capable of identifying design optimality and comparing possible trade-offs can significantly improve the productivity and shorten the design cycle.

Objective and efficient evaluation of advanced designs can be facilitated by development and implementation of systematic optimization and sensitivity evaluation methods. To date, the majority

of the effort in design optimization has relied on gradient-based search algorithms. These methods work iteratively through a sequence of local sub-problems, which approximate objective and constraint functions for a sub-region of the design space, e.g., by linearization using computed sensitivities. Major challenges for these optimization approaches are the robust and speedy computation of sensitivity coefficients.

Yet despite recent research advances, formal design optimization has yet to see practical use in real design scenarios. The reasons are several-fold:

- (i) The objective functions are likely to be multi-modal or discontinuous over the broad design space, rendering gradient search methods insufficient by themselves. Additionally, the usual practice to combine multiple goals into a single quantitative objective function is too restrictive. Qualitative goals are often required to correctly characterize a problem (e.g., maximizing a turbine blade's aerodynamic efficiency with a smooth, monotonic surface velocity distribution, while spreading heat load as uniformly as possible). These goals may have arisen from diverse disciplines and are usually treated sequentially by different groups.
- (ii) It is inadequate to think of the final product of a design process as a mere geometry. A "design" really encompasses a whole set of operating, manufacturing, and project level decisions.
- (iii) As the interaction between numerical simulation and physical test data becomes stronger, the future engineering knowledge base is likely to consist of various heterogeneous data sources including experimental data, past product experiences, semi-empirical modeling, and high fidelity simulations. Some data are anecdotal; others cover only small "patches" of the physical domain but are still useful for "reality checks". A unified framework needs to be constructed for representation, capturing and mining of all these data types so the response functions can be continuously improved.

The surrogate-based approach is an excellent technique for analysis and probing of such issues. It also offers a rational framework to reduce the number of important input variables, i.e., the dimension of a design or modeling space. The surrogates can be constructed using data drawn from pre-computed high-fidelity simulations and physical measurements, and provide fast evaluations of the various modeling and design scenarios, thereby making sensitivity and optimization studies feasible. As discussed by Shyy et al., they have several advantages when compared to local gradient-based methods:

- (i) They do not require calculation of the local sensitivity of each design variable,
- (ii) They can utilize the information collected from various sources and by different tools,
- (iii) They offer multi-criterion optimization,
- (iv) They can handle the existence of multiple design points and trade-offs,
- (v) They easily perform tasks in parallel, and
- (vi) They can often effectively filter the noise intrinsic to numerical and experimental data.

However, there are uncertainties in predictions using this approach, such as empiricism in computational models and surrogate model errors. We have developed methods to estimate and to reduce such uncertainties using multiple criteria because a single criterion may underestimate the error. We have advanced the techniques of using an ensemble of surrogates to reduce uncertainties in selecting the best surrogate and sampling strategy. We have also developed an averaging technique for multiple surrogates that protects against poor surrogates and performed at par with the best surrogate for many problems.

In this paper, we discuss the fundamental issues that arise in surrogate-based analysis and optimization, highlighting concepts, methods, and techniques, as well as practical implications. To aid the discussions of the issues involved, we will summarize recent efforts in investigating

cryogenic cavitating flows, active flow control based on dielectric barrier discharge concepts, and lithium-ion batteries. In cavitating flows of cryogenic fluids, such as liquid nitrogen and hydrogen, thermal effects are very important. Surrogate-based analysis has been used to investigate the importance of two adjustable parameters, which regulate the strength of the evaporation and condensation rate in the cavitation model, and the sensitivity of the thermal-sensible fluid properties, including latent heat and vapor phase density. The surrogate-based strategy has also been used to establish appropriate values for these empirical constants. For the dielectric barrier discharge (DBD) actuator, the impact of the applied voltage frequency, the insulator dielectric constant and the polarity time ratio of the voltage waveform on the net force generation and required power are examined. Multiple surrogate models consistently identify two branches of the Pareto front where a positive x-directional net force requires relatively low power, while a negative net force requires high power. Moreover, global sensitivity analysis indicates that the voltage frequency and polarity time ratio are important in only some portions of the design space, while the dielectric constant is always important. A lithium-ion battery cell has also been analyzed using a surrogate modeling framework to map the effect of cycling rate, cathode particle size, and diffusion coefficient and electrical conductivity of the solid cathode material on the energy storage. Through global sensitivity analysis the relative impact of the various parameters can be quantified under different scenarios. The design space is split into distinct regions based on characteristic discharge and diffusion time scales for separate, more refined analysis. A Pareto front is constructed to quantify the tradeoff between maximum achievable energy and power levels.

2. CONCLUSIONS

Surrogate modeling and analysis offers a unique design tool for each of these problems:

- (i) The surrogate analysis is used to assess
 - (a) the sensitivity of the cavitation model to parameters and uncertainties in the thermal-sensible material properties,
 - (b) impact of waveform, frequency and dielectric constant on DBD performance, and
 - (c) the relative importance of discharge rate, particle size, diffusivity and conductivity of battery performance.
- (ii) The surrogate models can be particularly useful in analyzing competing objectives, such as the accuracy of temperature and pressure prediction in cavitation, power input and force generation in DBD, and specific energy and power in lithium-ion batteries.
- (iii) The surrogate-based global sensitivity analysis facilitates identification of dominating and less-influential design variables. Based on the insight gained, dimensionality reduction can be conducted to reduce the complexity of the issues. This benefit is particularly significant for complex problems which are expensive to simulate/test and involve a large number of design variables. For instance, it is shown that
 - (a) the condensation term has minimal influence on the cavitation model compared to the evaporation term,
 - (b) the dielectric constant is always influential, but the importance of frequency and time ratio alternates depending on low and high power capability, and
 - (c) the dimensionality of the battery case can be reduced based on the diffusivity of the solid, which could be ignored from the analysis beyond a certain critical value.
- (iv) In addition to sensitivity analysis, surrogate tools offer the capability to identify optimal solutions in regions where competing objectives may be present. In such cases, construction of a Pareto front can assist in elucidating the gain achieved by sacrificing the other objectives. In

the context of the case studies presented, we show that multiple Pareto fronts, which may be disconnected with each other, may also exist, as evident in the case of DBD. For cavitation, it was shown that a selected value of the evaporation model parameter minimizes the pressure difference through a small penalty in the temperature difference. Since pressure prediction is more critical in design of components that may be subjected to heavy loads, the tradeoff between pressure and temperature is beneficial in this situation. In the case of lithium-ion batteries, the high slope of the Pareto front suggests that substantial gain in power, which is desirable for power-tools and automotive applications, can be achieved through minor sacrifice in energy storage.

In summary, we have developed a surrogate-based framework to assess the role of design variables on multiple competing objectives for a wide range of engineering problems. The framework allows for both local and global domain refinement strategies to be utilized in conjunction with multiple error criteria to estimate and reduce uncertainties, since a single criterion may lead to high errors. These techniques prove to be very valuable in advancing the capabilities of surrogate modeling. Similar approaches can be extended to numerous other thermo-fluid and energy systems.

KEYNOTE LECTURES

MULTISCALE SIMULATIONS OF HEAT TRANSFER AND FLUID FLOW PROBLEMS

Y.L.He, W.Q.Tao

MOE Key Laboratory of Thermo-Fluid Science and Engineering, Xi'an Jiaotong University, Xi'an, 710049, PR China, yalinghe@mail.xjtu.edu.cn, wqtao@mail.xjtu.edu.cn

ABSTRACT

The multiscale problems in the thermal and fluid science are classified into two categories: multiscale process and multiscale system. Examples are provided for multiscale process and multiscale system. The focus of this presentation is at the multiscale process. The numerical approaches for multiscale processes have been reviewed. Several numerical examples of multiscale process are presented.

Key Words: *Multiscale Simulation, Reconstruction Operator, Interface Coupling.*

1. INTRODUCTION

The multiscale problems in the thermal and fluid science are classified into two categories: multiscale process and multiscale system [1,2]. In this presentation focus is put on the simulation of multiscale process. Turbulent flow is a typical example of multiscale process which involves many different length scales of eddies. The launching process of a space craft provides another example where the fluid flow around the spacecraft experiences different gas flow regimes from the earth's surface to the outer space. The third example is the transport process in a proton exchange membrane fuel cell (PEMFC), where the fuel gas flow in polar plate channels occurs at the length scale of centimeters, the diffusion process in the gas diffusion layer and the transport of proton in the membrane occur at the order of hundreds of micrometers, while the reaction in the catalyst happens in a thickness of tens or even several micrometers. Now attention is turned to the multiscale system. By multiscale system we refer to a system that is characterized by large variation in length scales in which the processes at different length scale often have the same governing equations and are not so closely related as in the first category. The cooling of an electronic system is such a typical multiscale system[3,4]. In these two papers a top-to-down sequential multilevel simulation method with increasing fineness of grids was proposed. Since the simulation methods at the different levels in such multiscale system are all of continuum type, and [3,4] have given clear presentation, the numerical method for the multiscale system will not be further discussed in this presentation. The numerical approaches for multiscale processes have two categories: one is the usage of a general governing equation and solving the entire flow field involving a variation of several orders in characteristic geometric scale. The other is the so-called "solving regionally and coupling at the interfaces". In this approach the processes at different length level is simulated by numerical methods at different geometric scales (macro, meso and micro scales) and then information is exchanged at the interfaces between different regions. The key point is the establishment of the reconstruction operator, which transforms the data of few variables of macroscopic computation to large amount of variables of microscale or mesoscale simulation. In the following the reconstruction operators which are developed in the authors' group and for the transformation of macroscopic variables to the density distribution function in LBM are introduced and two numerical examples of multiscale simulation are presented.

2. MAJOR NUMERICAL APPROACHES FOR SIMULATING MULTISCALE PROCESS

For the numerical modeling of multiscale processes in engineering thermal and fluid science, two types of numerical approaches may be classified. They can be described as: (1) “Using uniform governing equation and solving for the entire domain”; (2) “Solving problems regionally and coupling at the interfaces”. The direct numerical simulation (DNS) is a typical example of the first numerical approach [5]. This method is very time-consuming, so we will not go further for this method. In the following focus will be put on the second approach.

The second approach is the most widely used one. In this approach the process at different length level is simulated by different numerical method and then information is exchanged at the interfaces of different regions. If the exchange of information at the interface (“hand-shaking” region) is performed via Dirichlet type, then it can be mathematically expressed by :

$$U = C_D u ; u = R_D U \quad (1)$$

where U and u are the macroscopic parameter and microscopic/mesoscopic parameter respectively. C_D and R_D are the Dirichlet compression and re-construction operators, respectively.

At the interface between different regions, there will be a mismatch in the kind and number of variables used by the different regions. The Dirichlet compression operator C_D , which extracts the macroscopic parameters from a large amount of data at micro or mesoscale level by some averaging or integrating principles, is easy to be defined, but the reconstruction operator R_D , which should prolong small amount of macroscopic parameters into a large amount of parameters at mesoscale or microscale is quite difficult to be constructed. Here we meet a one-to-many problem since the macroscopic variables have to be mapped to more LBM (DSMC or MDS) variables. The design of the compression and re-construction operators should abide by some basic physical laws or principles, such as mass conservation, momentum and energy conservation. In addition the operator should be mathematically stable, computationally efficient and easy to be implemented. In a word, the exchange of information should be conducted in a way that is physically meaningful, mathematically stable, computationally efficient and easy to be implemented. It should be noted that by the terminology “operator” we mean: (1) It is an actual mathematical formula for transferring (converting) results of different regions at the interface; or (2) It is a set of numerical treatments for transferring information which are developed from some fundamental considerations. At the present, the 2nd one is the most frequently encountered situation. In the following some existing coupling principles are presented.

3. EXAMPLES OF NUMERICAL SIMULATION OF MULTISCALE PROCESS

Coupling between MD and FDM

In 1995 O’Connel and Thompson proposed a way for coupling the simulation by MDS and by FDM [6]. This is the first paper in the literature initiating the coupled MDS-macroscale simulation. In their paper the coupling is achieved by constraining the dynamics of fluid molecules in the vicinity of the MDS-continuum interface to meet the requirement of mass and momentum continuity. The different solution regions are shown in Fig. 1 , where the interface is referred to as hybrid solution interface (HSI). The MDS portion of the computation is beyond the HSI (shown by the open circles), introducing an overlap region. Continuity of mass flux at the HSI is achieved by supplying the velocity boundary condition for the continuum region by the averaging results of the MDS over the zero bin shown in Fig. 1. Ensuring the momentum conservation in the HSI region is a more subtle issue because as indicated above in the MDS simulation there is not any constitutive equations for stress. In order to ensure the continuity of momentum (stress) it is required that in the overlap region within any bin shown in Fig. 1, following constraint should be satisfied:

$$\sum_{n=1}^{N_j} p_n - M^{(j)} v_x^{(j)} = 0 \quad (2)$$

where N_j is the total number of molecules in the j th bin and p_n is the momentum of the n th molecule in the x direction, $M(j)$ denotes the mass of the continuum fluid element corresponding to the j th bin, and $v_x^{(j)}$ is the velocity. Obviously Eq.(2) requires that in the j th bin the x -direction momentum computed from micorscale results and macrosacle results should be identical. By integrating this equation with time a holonomic constraint can be obtained and it is incorporated into Lagrange's equation for any molecule in the j th bin. This constraint is implemented for all the molecules in the bins within the overlap region, thus the momentum conservation requirement is fulfilled.

Since this pioneering work a number of MDS-continuum coupling researches have been published for different flow and heat transfer cases with focus being put on the improvement of coupling stability, accuracy, and efficiency. The details in the improvements of coupling methods are not stated here because of space limitation .

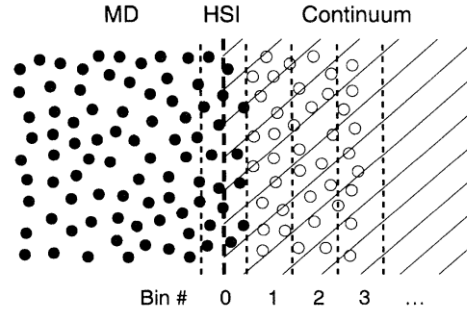


FIGURE 1. Schematic for the coupling between MD and continuum method [6] (Used with permission)

FLUID FLOW AROUND/THROUGH A POROUS MEDIA SQUARE CYLINDER SIMULATED BY COUPLED LBM/FVM

In [7] the flow around and through a porous media square cylinder is simulated by coupled FVNM and LBM (CFVLBM), fully showing the role of LBM in displaying the flow details in complicated configuration. Flow simulation results by CFVLBM is presented in Fig. 2 (a) and (b). It would be very difficult (if not impossible) for FVM to obtain such fine flow resolution. To compare the computational time for flow around a solid square cylinder, three numerical methods have been used: LBM, multi-block LBM and CFVLBM. Fig. 2 (c) shows the three-block structure used in the simulation. In the multi-block LBM the grid system in the center black region is the finest where the porous media cylinder locates and that of the outside region is the coarsest. Results show that the CFVLBM is much faster than the multi-block method. The transformation of the macro-velocity to the mesoscale parameter, the density distribution function of the LBM is conducted by the reonstrction operator proposed by the authors' group [1,2,8] :

$$f_i = f_i^{(eq)} \left[1 - \tau \Delta t U_{i\beta} c_s^{-2} \left(U_{i\alpha} \partial_{x_\alpha} u_\beta + \nu \partial_{x_\alpha}^2 u_\beta + \nu \rho^{-1} S_{\alpha\beta} \partial_{x_\alpha} \rho \right) \right] \quad (3)$$

where $f_i^{(eq)}$ is the equilibrium density distribution function; c_s is the lattice sound speed; $S_{\alpha\beta}$ is the stress tension in α, β coordinates; τ is the nondimensional relaxation time; Δt is the time step; ν is the kinematic viscosity; ρ is the fluid density; $U_{i\alpha} = c_{i\alpha} - u_\alpha$, and u_α is the velocity in α direction; $S_{\alpha\beta} = \partial_{x_\beta} u_\alpha + \partial_{x_\alpha} u_\beta$.

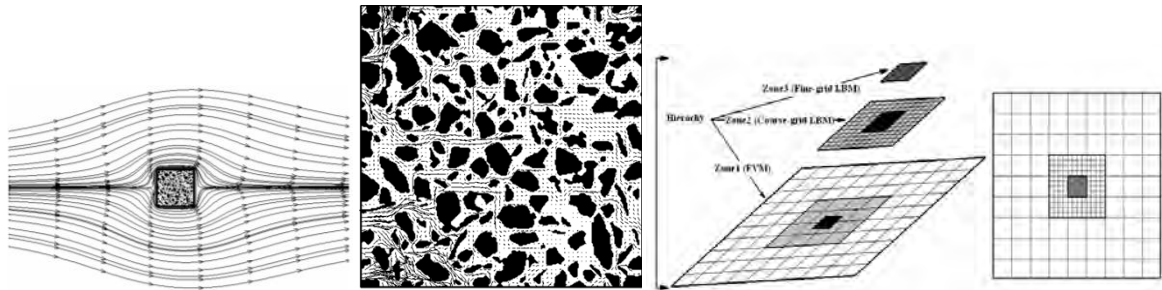


FIGURE 2. Flow around/through a porous square cylinder

4. CONCLUSIONS

Most phenomena and processes in science and engineering are multiscale in nature. With the rapid development in science and technology the importance of study from multiscale view point becomes more and more obvious. In heat transfer field multiscale problems may be classified as multiscale process and multiscale system. For the multiscale process the method of “solving regionally and coupling at the interfaces” is the most promising one. In such method the key issue is the exchange information at the interfaces. The exchange of information should be conducted in a way that is physically meaningful, mathematically stable, computationally efficient and easy to be implemented. Further researches are highly required to establish robust and quick-convergent numerical solution approaches.

REFERENCES

- [1] W.Q. Tao and Y.L. He, Recent advances in multiscale simulation of heat transfer and fluid flow problems, *Progress in Computational Fluid Dynamics*, 9(3/4/5), 151-157, 2009.
- [2] Y.L. He and W.Q. Tao, Multiscale simulations of heat transfer and fluid flow problems, to be published in *ASME Journal of Heat Transfer*.
- [3] L. Tang and Y.K. Joshi, A multi-grid based multi-scale thermal analysis approach for combined mixed convection, conduction, and radiation due to discrete heating, *ASME Journal of Heat Transfer*, 127(1), 18-26, 2005.
- [4] Q. Nie and Y. K. Joshi, Multiscale thermal modeling methodology for thermoelectrically cooled electronic cabinets, *Numerical Heat Transfer, Part A: Applications*, 53(3), 225-248, 2008.
- [5] P. Moin and K. Mahesh, Direct numerical simulation: a tool in turbulence research, *Ann Rev Fluid Mec.*, 30, 39-78, 1998.
- [6] S.T.O. Connel and P.A.Thompson. Molecular dynamics-continuum hybrid computations: A tool for studying complex fluid flows, *Physics Review E*, 52 (6), R5792-R5795, 1995.
- [7] H.B. Luan, H. Xu, L. Chen L., D.L. Sun and W.Q.Tao, Evaluation of the coupling finite volume method and lattice Boltzmann method for fluid flows around complex geometries, *International Journal of Heat and Mass Transfer*, 54, 1975-1985, 2011.
- [8] H. Xu, *Lattice Boltzmann model for turbulent fluid flow simulations and its application in multiscale analysis*, Ph. D. dissertation, Xi'an Jiaotong University, Xi'an, 2009.

MODELING OF FREE SURFACE FLOWS: UNDERSTANDING FALLING DROPS

G. Biswas¹, B. Ray, A. Sharma

Indian Institute of Technology Kanpur, Kanpur, 208016, India

¹CSIR-Central Mechanical Engineering Research Institute, Durgapur, 713209, India

ABSTRACT

Our study deals with the understanding of drop dynamics during partial coalescence. When liquid 1 drop falls through liquid 2 to eventually hit the liquid 2-liquid 1 interface, its initial impact on the interface can produce daughter droplets of liquid 1. Results show that inertia and interfacial surface tension forces largely govern the process of partial coalescence. Below the specified lower bound and above the specified upper bound, the partial coalescence is suppressed by the viscous force and gravity force, respectively. The process of partial coalescence is also observed for multiple drop impact where the process of pinch off is different.

Key Words: *Partial Coalescence, Secondary drops, Ohnesorge number.*

1. INTRODUCTION

Multi-fluid systems play an important role in many natural and industrial processes such as bubble column reactor, boiling, ink jet printing, painting, biological systems, rain drop impact phenomenon etc to mention few. A full understanding of the behavior of multiphase flows is still lacking, although a number of experimental, theoretical analysis and numerical studies have addressed this problem. The various numerical techniques used to solve these multi-fluid systems are like volume of fluid method (VOF), level set method (LS), coupled level set and volume of fluid method (CLSVOF), front tracking method (FT) etc. We have used the CLSVOF method [1] to explore the partial coalescence phenomena during drop impact on liquid-liquid interface. When a drop of liquid 1 impacts a liquid 1-liquid 2 interface, the impact either generates a daughter/secondary droplet of liquid 1 or the impacting drop is absorbed without engendering a secondary droplet. The first case will be referred to as a partial coalescence and the later as complete coalescence. Generation of secondary drop is observed for systems of lower Ohnesorge number for liquid 1, lower and intermediate Ohnesorge number for liquid 2 and for low and intermediate values of Bond number. Whenever the horizontal momentum in the liquid column is more than the vertical momentum, secondary drop is formed. A transition regime between partial and complete coalescence with increasing Ohnesorge number is defined. In this regime the neck oscillates twice before collapsing into the liquid. For further increase in Ohnesorge number the oscillation again reduces to one. In order to have secondary droplets in the complete coalescence regime, when multiple drops are made to impact then again the partial coalescence phenomena occurs.

2. MAIN BODY

Complete numerical simulation of the processes of partial coalescence is performed for two-dimensional incompressible flow which is described in axisymmetric coordinates as shown in Figure 1.

The mass and momentum conservation equations for the incompressible Newtonian fluids for the two liquid phases are given by,

$$\nabla \cdot \vec{V} = 0 \quad (1)$$

$$\rho \left(\frac{\partial \vec{V}}{\partial t} + \nabla \cdot \vec{V} \vec{V} \right) = -\nabla P + \rho \vec{g} + \nabla \cdot \left[\mu \left(\nabla \vec{V} + (\nabla \vec{V})^T \right) \right] + \sigma \kappa \vec{n} \delta_s \quad (2)$$

where σ is the surface tension force, \vec{n} is the unit normal vector at the interface, κ is the curvature of the interface, δ_s is the surface delta function.

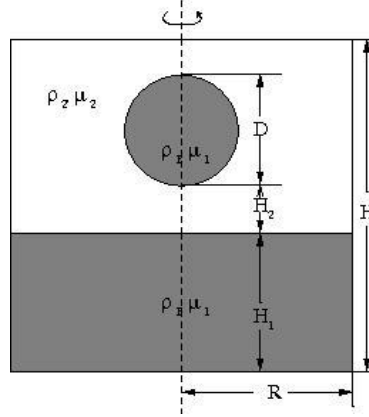


FIGURE 1. Computational domain

The level-set function chosen here is maintained as the signed distance from the interface close to it. The unit normal vector and the mean curvature are simply, $\vec{n} = (\nabla \phi / |\nabla \phi|)$ and $\kappa = -\nabla \cdot (\nabla \phi / |\nabla \phi|)$ respectively. Using the level-set formulation the momentum equation for incompressible two-phase flow becomes

$$\rho(\phi) \left(\frac{\partial \vec{V}}{\partial t} + \nabla \cdot (\vec{V} \vec{V}) \right) = -\nabla P + \rho(\phi) \vec{g} + \nabla \cdot \left[\mu(\phi) \left(\nabla \vec{V} + (\nabla \vec{V})^T \right) \right] + \sigma \kappa(\phi) \nabla H(\phi) \quad (3)$$

The interface is captured by solving the advection for the level-set function ϕ and for the volume fraction F in its conservative form, $\frac{\partial \phi}{\partial t} + \nabla \cdot (\vec{V} \phi) = 0$, $\frac{\partial F}{\partial t} + \nabla \cdot (\vec{V} F) = 0$.

Void fraction F is introduced as the fraction of the liquid inside a control volume (cell), where the void fraction taking the values 0 for lighter liquid (liquid 2), 1 for heavier liquid (liquid 1) cell and between 0 and 1 for a two-phase cell. The boundary conditions are symmetry or free slip condition at the left and right boundaries. Outflow boundary conditions are used on the top surface of the domain. No slip and impermeability (wall) conditions are used on the bottom surface of the domain.

3. RESULTS

Charles & Mason [2] have suggested that the partial coalescence was due to a Rayleigh-Plateau instability. Blanchette & Bigioni [3] have argued that it is the convergence of the capillary waves on the drop apex which leads to secondary drop pinch off. Recently Gilet et al. [4] have shown that the convergence of the capillary waves cannot be the only mechanism responsible for partial coalescence. They showed that when Oh_1 is high, a mechanism is responsible for enhancing the emptying of the droplet, resulting in a premature total coalescence. Inversely, when Oh_2 is high, another mechanism has to aid the horizontal collapse. However, when Oh_2 is too large, it has an opposite effect of weakening of the horizontal collapse. From our simulations it is seen that the important criterion for partial coalescence is the increasing horizontal momentum of the drop relative to the vertical momentum. This can be accomplished either by changing the viscosity or by

changing the gravity within limits. Figure 2 depicts the dominant movement in six different cases. The dotted line indicates the initial liquid/liquid interface. When $Oh_1 \approx Oh_2$, the liquid column is stretched upwards to a long height and liquid 2 forces inwards to promote pinch off. For $Oh_1 < Oh_2$, the height of the liquid column is lower due to the higher viscosity of liquid 2, but the higher viscosity increases the horizontal collapse. So the drop pinches off before collapsing. During the case, $Oh_1 \ll Oh_2$, at very high viscosity of liquid 2, the pinch off is prevented and viscous liquid 2 pushes the entire drop to coalesce completely. For $Oh_1 > Oh_2$, due to the high viscosity of liquid 1, the capillary waves get damped out and the drop coalesces totally. It can be concluded that for a low Oh_1 value ($= 0.0058$), when $(Oh_1/Oh_2) \approx 1$, the pinch off of secondary drop occurs. As this ratio decreases to 0.1, the partial coalescence phenomenon still occurs but as the ratio is further decreased to 0.01, there is no more pinch off. In contrast, for a low Oh_2 value ($= 0.0058$), as Oh_1 is increased by a small amount, $Oh_1 = 0.0412$ ($Oh_1/Oh_2 \approx 10$), the drop completely coalesces. In the case of a high viscosity of liquid 1, more mass of liquid 2 is displaced. Hence as Oh_1 is increased, an additional movement is induced which tends to accelerate the emptying of the droplet. More viscous diffusion leads to vertical collapse of the liquid column. In liquid 2, such an induced movement enhances the horizontal collapse. When Oh_2 is intermediate, the horizontal collapse is confined to regions lower than the equator of the initial droplet, and this leads to partial coalescence. In contrast, when Oh_2 is high, the viscous diffusion entrains liquid 1 at higher latitudes and the vertical extension of the horizontal collapse is greater, so the coalescence becomes total. For $Oh_1 \approx Oh_2$ and intermediate Bo , the pinch off is similar to that in the first case, but as can be seen from the figure, the necking is below the initial liquid/liquid interface due to more downward pull. When $(Oh_1 \approx Oh_2, \text{ high } Bo)$ shows the total collapse of the drop due to the large downward vertical movement of the drop for high gravitational pull.

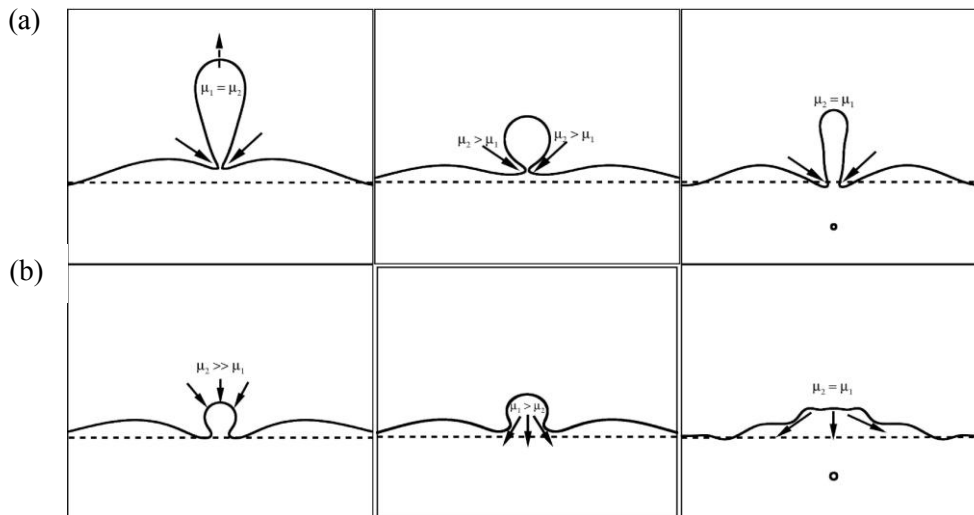


FIGURE 2. The different flows during (a) partial coalescence and (b) complete coalescence.

Thus it is seen that whether the drop will completely coalesce or it will pinch off secondary droplet depends on the dominant direction of flows acting on the drop. The detailed parametric study is done and reported in Ray *et al.* [5]. The partial coalescence phenomenon occurs for low impact velocity of the impacting drop. The free surface deformation is shown in Figure 3(a), along with the experiments of Chen *et al.* [6]. Complete coalescence can be prevented when another drop impacts the liquid during the coalescing process of the first drop as shown in Figure 3(b).

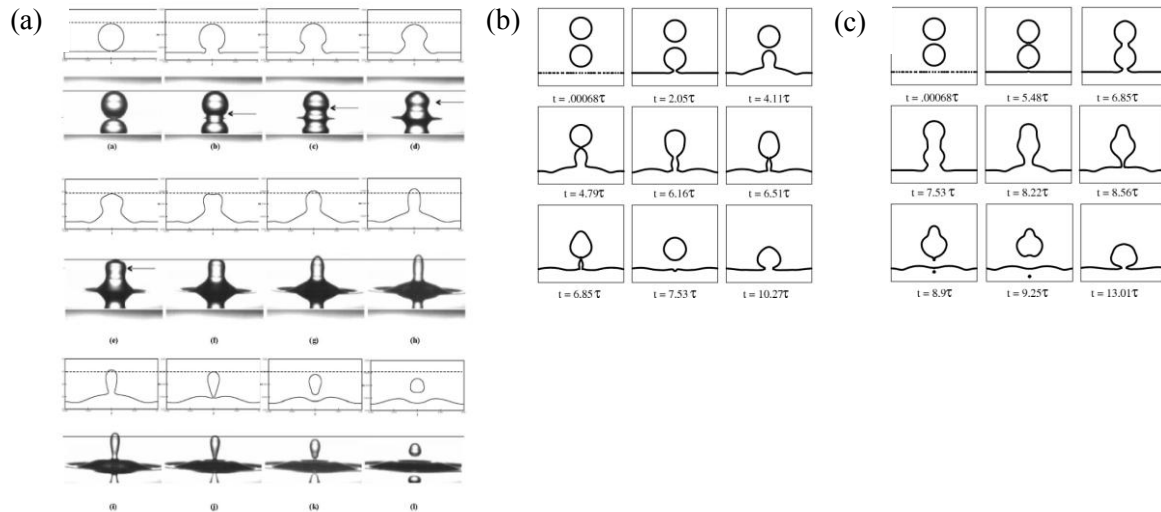


FIGURE 3. Partial coalescence phenomena with
 (a) single drop impact, (b) multiple drop impact, (c) coalesced drop impact.

In some cases partial coalescence also occurs when two drops coalesce before impacting to the liquid surface. On impact the liquid from the coalesced drop drains in the liquid. Due to more horizontal momentum by the surrounding liquid necking occurs leading the pinch off.

4. CONCLUSIONS

In the present work we have numerically established that it is the competition between the horizontal and vertical momentum of the drop which determines the transition between the two regimes of coalescence. The capillary wave converges at the drop apex. Furthermore, when the horizontal momentum exceeds the vertical momentum, a daughter drop pinches out. Different forces for different flow parameters determine the outcome. Multiple drop impact also exhibits partial coalescence phenomena when the drops fall one after another within very small time gap with low impact velocity.

REFERENCES

- [1] D. Gerlach, G. Tomar, G. Biswas and F. Durst, Comparison of volume-of-fluid methods for surface tension-dominant two-phase flows, *International Journal of Heat and Mass Transfer*, 49, 740–754, 2006.
- [2] G.E. Charles and S.G. Mason, The coalescence of liquid drops with flat liquid/liquid interfaces, *Journal of Colloid Science*, 15, 236–267, 1960.
- [3] F. Blanchette and T.P. Bigioni, Partial coalescence of drops at liquid interfaces, *Nature Physics*, 2, 254-257, 2006.
- [4] T. Gilet, K. Mulleners, J.P. Lecomte, N. Vandewalle and S. Dorbolo, Critical parameters for the partial coalescence of a droplet, *Physical Review E*, 75, 036303(1)-036303(14), 2007.
- [5] B. Ray, G. Biswas and A. Sharma, Generation of secondary droplets in coalescence of a drop at a liquid/liquid interface, *Journal of Fluid Mechanics*, 655, 72-104, 2010.
- [6] X. Chen, S. Mandre and J.J. Feng, Partial coalescence between a drop and a liquid-liquid interface, *Physics of Fluids*, 18, 051705(1)-051705(4), 2006.

A MESHLESS METHOD FOR THERMAL PROBLEMS: FROM THEORETICAL DEVELOPMENTS TO INDUSTRIAL APPLICATIONS

Božidar Šarler, Agnieszka Zuzanna Lorbiecka, Gregor Kosec, Robert Vertnik

University of Nova Gorica, Vipavska 13, SI-5000 Nova Gorica, Slovenia, bozidar.sarler@ung.si, agnieszka.zuzanna.lorbiecka@ung.si, gregor.kosec@ung.si, robert.vertnik@ung.si

ABSTRACT

Structure of a new meshless solution method for calculation of one-domain coupled macroscopic heat, mass, momentum and species transfer problems as well as phase field concepted models and cellular automata models of microstructure evolution is represented. The solution procedure is defined on a set of nodes which can be non-uniformly distributed. The domain and boundary of interest are divided into overlapping influence areas. On each of them, the fields are represented by the multiquadrics radial basis functions collocation or least squares approximation on a related subset of nodes. The transition rules are defined for a set of nodes on the influence area in case of cellular automata (CA) modelling. The time-stepping is performed in an explicit way. All governing equations are solved in their strong form, i.e. no integrations are performed. The polygonisation is not present. The possible growth of the domain (like in the problems of die casting or continuous casting) is described by activation of additional nodes and by the movement of the boundary nodes through the computational domain, respectively. The solution can be easily and efficiently adapted in node redistribution and/or refinement sense, which is of utmost importance when coping with fields exhibiting sharp gradients (phase field variable or enthalpy, for example). Step by step theoretical developments and benchmarking of the method has been performed, followed by industrial examples such as the dendritic growth, grain structure formation in continuous casting of steel and turbulence modelling with solidification. The results of the new approach are compared with the analytical solutions, recent well documented bench-mark solutions, and commercial packages. The method turns out to be extremely simple to code, accurate, inclusion of the complicated physics can easily be looked over. The coding in 2D or 3D is almost identical.

Key Words: *Thermal Problems, Multiphysics and Multiscale Modelling, Meshless Methods.*

1. INTRODUCTION

The most popular discrete approximate methods, such as for example the finite element method, are nowadays based on some sort of polygonization of the computational domain. Despite the powerful features of these methods, there are often substantial difficulties in applying them to realistic, geometrically complex three-dimensional transient problems. The meshing is often the most time consuming part of the solution process and is far from being fully automated. This is even more pronounced in solving thermal problems with phase changes, where in the front tracking approach, the polygons need to fit to the moving boundary, and in the one-domain approach, the polygons have to be refined in the vicinity of the moving boundary jumps and/or gradients. Regular mesh structure on the other hand introduces anisotropy in discretization and is not suitable for simulation of microstructures such as dendrites. In the last decade, there is a strong development of the meshless methods which rely on discretization by nodes without polygons between them. The present paper describes one of the most simple, versatile and efficient among them [1], based on the collocation with radial basis functions. The first developments of the described method started in 2006 and the method has been up to now applied to most complicated benchmark tests and industrial applications. It is out of the scope of this extended abstract to describe all of them.

2. FORMULATION

The basis of the method, applicable in macroscopic multi-physics simulations as well as in the microscopic phase-field method, can be described as follows. The suitable model equation for this purpose is the general transport equation, defined on a fixed domain Ω with boundary Γ

$$\frac{\partial}{\partial t}(\rho\Phi) + \nabla \cdot (\rho\mathbf{v}\Phi) = \nabla \cdot (\mathbf{D}\nabla\Phi) + S \quad (1)$$

with $\rho, \Phi, t, \mathbf{v}, \mathbf{D}$, and S standing for density, transport variable, time, velocity, diffusion matrix and source, respectively. The solution of the governing equation for the transport variable at the final time $t_0 + \Delta t$ is sought, where t_0 represents the initial time and Δt the positive time increment.

The initial value of the transport variable $\Phi(\mathbf{p}, t)$ at a point with position vector \mathbf{p} and time t_0 is defined through the known function Φ_0 . The boundary Γ is divided into not necessarily connected parts $\Gamma = \Gamma^D \cup \Gamma^N \cup \Gamma^R$ with Dirichlet, Neumann and Robin type boundary conditions, respectively. At the boundary point \mathbf{p} with normal \mathbf{n}_Γ and time $t_0 \leq t \leq t_0 + \Delta t$, these boundary conditions are defined through known functions $\Phi_\Gamma^D, \Phi_\Gamma^N, \Phi_\Gamma^R, \Phi_{\Gamma^{ref}}^R$. The representation of function over a set l of (in general) non-equally spaced ${}_lN$ nodes ${}_l\mathbf{p}_n; n=1,2,\dots,{}_lN$ is made in the following way $\Phi(\mathbf{p}) \approx \sum_{k=1}^{{}_lK} {}_l\psi_k(\mathbf{p}) {}_l\alpha_k$, where ${}_l\psi_k$ stands for the shape functions, ${}_l\alpha_k$ for the coefficients of the shape functions, and ${}_lK$ represents the number of the shape functions. The left lower index on entries of summation expression represents the sub-domain ${}_l\omega$ on which the coefficients ${}_l\alpha_k$ are determined. The sub-domains ${}_l\omega$ are overlapping. Each of the sub-domains ${}_l\omega$ includes ${}_lN$ grid-points of which ${}_lN_\Omega$ are in the domain and ${}_lN_\Gamma$ are on the boundary. The coefficients can be calculated from the sub-domain nodes in two distinct ways. The first way is collocation (interpolation) and the second way is approximation by the least squares method. Only the simpler collocation version for calculation of the coefficients is explicitly considered in this extended abstract. Let us assume the known function values ${}_l\Phi_n$ in the nodes ${}_l\mathbf{p}_n$ of sub-domain

${}_l\omega$. The collocation implies $\sum_{k=1}^{{}_lK} {}_l\psi_k({}_l\mathbf{p}_n) {}_l\alpha_k = \Phi({}_l\mathbf{p}_n)$. For the coefficients to be computable by collocation, the number of the shape functions has to match the number of the grid-points, and the collocation matrix has to be non-singular $\sum_{k=1}^{{}_lK} {}_l\psi_k({}_l\mathbf{p}_n) {}_l\alpha_k = \Phi({}_l\mathbf{p}_n); {}_lK = {}_lN$. This system of equations can be written in a matrix-vector form and the coefficients ${}_l\boldsymbol{\alpha}$ can be computed by inverting it ${}_l\underline{\Psi} {}_l\boldsymbol{\alpha} = {}_l\boldsymbol{\Phi}; {}_l\underline{\Psi}_{kn} = {}_l\psi_k({}_l\mathbf{p}_n), {}_l\Phi_n = \Phi({}_l\mathbf{p}_n), {}_l\boldsymbol{\alpha} = {}_l\underline{\Psi}^{-1} {}_l\boldsymbol{\Phi}$. By taking into account the expressions for the calculation of the coefficients ${}_l\boldsymbol{\alpha}$, the collocation representation of function $\Phi(\mathbf{p})$ and the first derivatives can be expressed as (in Cartesian system)

$$\Phi(\mathbf{p}) \approx \sum_{k=1}^{{}_lK} {}_l\psi_k(\mathbf{p}) \sum_{n=1}^{{}_lN} {}_l\underline{\psi}_{kn}^{-1} {}_l\Phi_n, \quad \frac{\partial}{\partial p_\zeta} \Phi(\mathbf{p}) \approx \sum_{k=1}^{{}_lK} \frac{\partial}{\partial p_\zeta} \psi_k(\mathbf{p}) \sum_{n=1}^{{}_lN} {}_l\underline{\psi}_{kn}^{-1} {}_l\Phi_n; \zeta = x, y, z \quad (2)$$

The required second derivatives are calculated principally the same as the first ones. The radial basis functions, such as multi-quadrics $\psi_k(\mathbf{p}) = [(\mathbf{p} - \mathbf{p}_k) \cdot (\mathbf{p} - \mathbf{p}_k) + c^2]^{1/2}$ can be used for the

shape function, where c represents the shape parameter, determined to match a suitable condition number of the collocation matrix. The equation (1) can be transformed into following expression, by considering the explicit discretization, from which the unknown function values are calculated

$$\Phi = (\rho_0 / \rho) \Phi_0 - (\Delta t / \rho) \nabla \cdot (\rho_0 \mathbf{v}_0 \Phi_0) + (\Delta t / \rho) \nabla \cdot (\mathbf{D}_0 \nabla \Phi_0) + (\Delta t / \rho) S_0 \quad (3)$$

3. SPECTRA OF APPLICATIONS

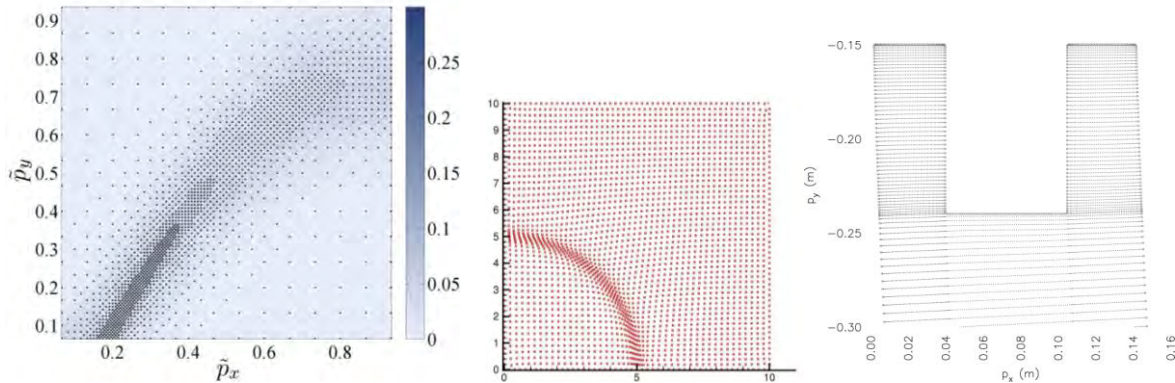


FIGURE 1. Left: h-node refinement settings [1]. Centre: r-node refinement [11]. Right: non-uniform node distribution - industrial example [10].

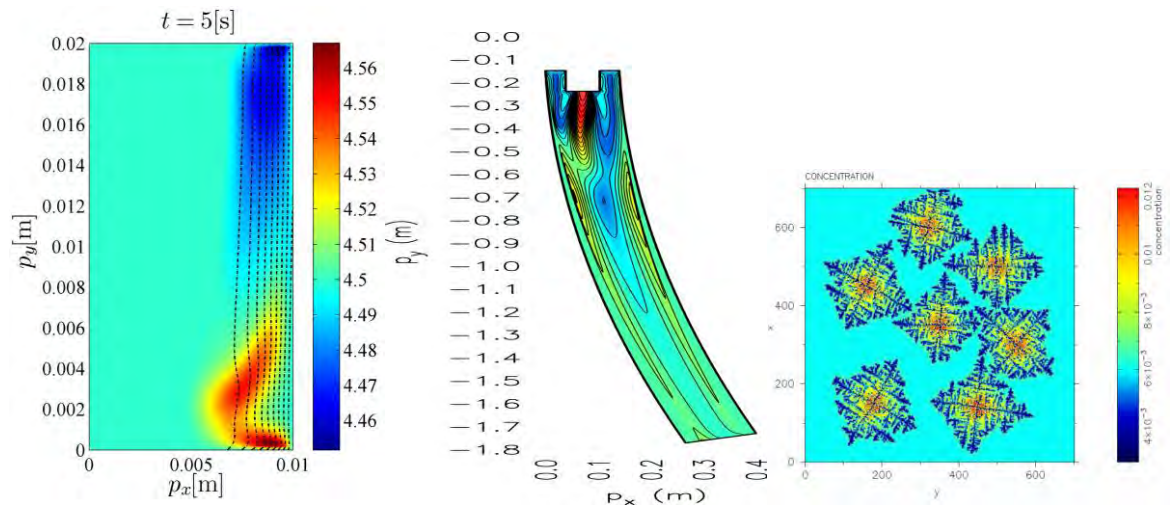


FIGURE 2. Left: Macroseggregation test simulation [6]. Center: industrial continuous casting simulation [10]. Right: dendritic growth simulation by the point automata method [12].

The method has been first successfully applied to diffusion problems [2], convection-diffusion problems [3], the classical De Vahl Davis problem [4], melting of pure substance [5], solidification of binary alloy [6], turbulent flow [7,8]. Industrial applications on the macro-scale include solution of the thermal model of the direct chill casting of aluminium alloys [9] and continuous casting of steel [10] on moving (growing) computational domains. The convection dominated situations involve a special adaptive upwind strategy. The method has been on the micro level applied for solving dissolution of primary particles in aluminium alloys [11] and dendritic growth in Fe-C steel [12]. A multi-scale grain growth model for describing grain structure in steel billets is given in [13].

4. CONCLUSIONS

This paper shows basic elements and reviews applicability of the entirely new generation of numerical methods for solving thermo-fluid problems on multiple scales. The numerical tests, performed until now in the cited references, show much higher accuracy of the method as compared with the classical approaches. The method can cope with very large problems, since the computational effort grows approximately linear with the number of the nodes. The method appears efficient, because it does not require a solution of large systems of equations. Instead, small systems of linear equations have to be solved in each time-step for each node and associated sub-domain, probably representing the most natural and automatic domain decomposition. Respectively, the method is straightforwardly suitable for parallelization. Different types of refinements can be easily implemented. Complicate physics can be coped with in a transparent way.

ACKNOWLEDGEMENT: Financial support from the Slovenian Research Agency in the framework of the Programme P2-0379 is kindly acknowledged.

REFERENCES

- [1] B. Šarler, From Global to local radial basis function collocation method for transport phenomena, in: V.M.A. Leitao, C.J.S. Alves, C. Armando-Duarte, *Advances in Meshfree Techniques*, (Computational Methods in Applied Sciences, Vol.5), Springer-Verlag, Dordrecht 257-282, 2006.
- [2] B. Šarler, and R. Vertnik, Meshfree explicit local radial basis function collocation method for diffusion problems. *Comput. Math. Applic.*, 51, 1269-1282, 2006.
- [3] R. Vertnik, and B. Šarler, Meshless local radial basis function collocation method for convective-diffusive solid-liquid phase change problems, *Int. J. Nume. Methods for Heat and Fluid Flow*, 16, 617-640, 2006.
- [4] G. Kosec, and B. Šarler, Solution of thermo-fluid problems by collocation with local pressure correction, *Int. J. Numer. Methods Heat & Fluid Flow*, 18, 868-882, 2008.
- [5] G. Kosec, and B. Šarler, Solution of phase change problems by collocation with local pressure correction. *Comput. Model. Eng. Sci.*, 47, 191-216, 2009.
- [6] G. Kosec, M. Založnik, B. Šarler, and H. Combeau, A meshless approach towards solution of macrosegregation phenomena, *Comput. Mater. Cont.*, 2011 (in review).
- [7] R. Vertnik, B. Šarler, Solution of incompressible turbulent flow by a mesh-free method, *Comput. Model. Eng. Sci.*, 44, 65-95, 2009.
- [8] R. Vertnik, and B. Šarler, Local collocation approach for solving turbulent combined forced and natural convection problems. *Adv. Appl. Math. Mech.*, 3, 259-279, 2011.
- [9] R. Vertnik, M. Založnik, and B. Šarler, Solution of transient direct-chill aluminium billet casting problem with simultaneous material and interphase moving boundaries by a meshless method, *Eng. Anal. Bound. Elem.*, 30, 847-855, 2006.
- [10] R. Vertnik, B. Šarler, Simulation of continuous casting of steel by a meshless technique. *Int. J. Cast. Met. Res.*, 22, 311-313, 2009.
- [11] I. Kovačević, and B. Šarler, Solution of a phase field model for dissolution of primary particles in aluminium alloys by an r-adaptive mesh-free method, *Mat. Sci. Eng.*, 414, 423-428, 2005.
- [12] A.Z. Lorbiecka, and B. Šarler, Simulation of dendritic growth with different orientation by using a novel point automata method, *Comput. Mater. Cont.*, 18, 69-103, 2010.
- [13] A.Z. Lorbiecka, R. Vertnik, H. Gjerkeš, G. Manojlovič, B. Senčič, J. Cesar, and B. Šarler, Numerical modeling of grain structure in CC of steel. *Comput. Mat. Cont.*, 8, 195-208, 2009.

AN EFFICIENT IMMERSSED BOUNDARY METHOD FOR SIMULATION OF HEAT AND MASS TRANSFER PROBLEMS

C. Shu, W.W. Ren

Department of Mechanical Engineering, National University of Singapore
10 Kent Ridge Crescent, Singapore 117576, mpeshuc@nus.edu.sg

ABSTRACT

A boundary condition-enforced immersed boundary method is presented in this work for simulation of heat and mass transfer problems. The heat source/sink is introduced into the energy equation to model the effect of immersed boundary. Different from the previous works, in this work, the heat source/sink is not pre-calculated. Instead, it is determined implicitly in such a way that the temperature at the immersed boundary interpolated from the corrected temperature field accurately satisfies the boundary condition. In addition, the work proposes two simple and efficient ways to compute the average Nusselt number. Numerical experiments for both forced convection and natural convection problems are conducted to demonstrate the capability and efficiency of present method, and proposed two ways to calculate the average Nusselt number.

Key Words: *heat transfer, immersed boundary method, Nusselt number*

1. INTRODUCTION

The immersed boundary method (IBM) [1] has been proven to be an effective technique for the study of flow characteristics with complex geometries. It models the effect of the immersed boundary to the surrounding fluid through the introduction of forcing terms in the momentum equations. In this regard, IBM has a difficulty to be directly applied to heat transfer problems since they also involve the energy equation. Currently, very few work is available in the literature to apply IBM for thermal flow problems. Among available works in the literature, a heat source term is usually introduced in the energy equation to consider the effect of the immersed boundary. However, like the conventional IBM, the heat source term is computed explicitly and is pre-calculated, and there is no mechanism to enforce the boundary condition for temperature. Consequently, the boundary condition for temperature is not accurately satisfied. In this work, we target on this issue and present an improved IBM for simulation of thermal flow problems. The central idea is that the heat source/sink is not calculated in advance, but considered as unknown and determined implicitly in such a way that the temperature at the boundary interpolated from the corrected temperature field is just the given value (boundary condition for temperature is enforced). For the thermal flow problem, accurate and effective calculation of average Nusselt number is a critical issue. This paper also presents two simple and efficient ways to compute the mean Nusselt number directly from the temperature correction at Eulerian points and heat flux at Lagrangian points.

2. BOUNDARY CONDITION-ENFORCED IMMERSSED BOUNDARY METHOD FOR THERMAL FLOW PROBLEMS

In the application of IBM, two sets of points are used. One is called Eulerian point where the governing equations of heat and flow are solved. The other is termed as Lagrangian point which is used to model the immersed boundary. Note that the physical boundary condition is applied at the Lagrangian point.

The boundary condition-enforced immersed boundary method was first proposed by Shu et al [2], Wu and Shu [3] for simulation of isothermal flow problems. This technique can still be used to solve continuity and momentum equations in the thermal flow problems. In addition, we need to extend this technique for the solution of energy equation. Following the work of [2-3], the solution of energy equation by boundary condition-enforced IBM can be obtained by the following Predictor-Corrector steps,

$$\text{Predictor Step: } \rho c_p \left(\frac{\partial T}{\partial t} + (\mathbf{u} \cdot \nabla) T \right) = k \nabla^2 T \quad (1)$$

$$\text{Corrector Step: } \rho c_p \frac{\partial T}{\partial t} = q \quad (2)$$

Here, \mathbf{u} and T denote velocity vector and temperature. ρ , k and c_p are the fluid density, thermal diffusivity at reference temperature $T = T_\infty$, and specific heat at constant pressure, respectively. q is the heat source/sink transferred to the fluid from the heat flux $Q(\mathbf{X}(s), t)$ at the immersed boundary, which can be expressed as

$$q(\mathbf{x}, t) = \int_{\Gamma} Q(\mathbf{X}(s), t) \delta(\mathbf{x} - \mathbf{X}(s, t)) ds \quad (3)$$

If we define the solution from Eq. (1) as intermediate temperature $T^*(\mathbf{x}, t)$ and solution from Eq.(2) as temperature correction $\delta T(\mathbf{x}, t)$, the corrected temperature field is

$$T(\mathbf{x}, t) = T^*(\mathbf{x}, t) + \delta T(\mathbf{x}, t) \quad (4)$$

Substituting Eq. (3) into Eq. (2) and writing the resultant equation in discrete form leads to

$$\delta T(\mathbf{x}_j, t) = \sum_i \frac{Q(\mathbf{X}_B^i, t) \delta t}{\rho c_p} D(\mathbf{x}_j - \mathbf{X}_B^i) \Delta s_i \quad (i=1, 2, \dots, M; j=1, 2, \dots, N) \quad (5)$$

where \mathbf{X}_B^i and \mathbf{x}_j represent boundary (Lagrangian) points and fluid mesh (Eulerian) points respectively. Δs_i is the arc length of boundary segment and $D(\mathbf{x}_j - \mathbf{X}_B^i)$ is the discrete delta function. Note that the unknowns in Eq. (5) are the boundary heat fluxes $Q(\mathbf{X}_B^i, t)$. To satisfy the physical boundary condition, we have to make sure that the temperature at the boundary point interpolated from the corrected temperature field by the delta function D_{ij} (abbreviation for $D(\mathbf{x}_j - \mathbf{X}_B^i)$) is equal to the specified temperature $T_B(\mathbf{X}_B^i, t)$, that is,

$$T_B(\mathbf{X}_B^i, t) = \sum_j T(\mathbf{x}_j, t) D(\mathbf{x}_j - \mathbf{X}_B^i) h^2 \quad (6)$$

Substituting Eqs. (4) and (5) into Eq. (6) gives

$$\begin{aligned} T_B(\mathbf{X}_B^i, t) &= \sum_j T^*(\mathbf{x}_j, t) D(\mathbf{x}_j - \mathbf{X}_B^i) h^2 \\ &+ \sum_j \sum_k \frac{Q(\mathbf{X}_B^k, t) \delta t}{\rho c_p} D(\mathbf{x}_j - \mathbf{X}_B^k) \Delta s_k D(\mathbf{x}_j - \mathbf{X}_B^i) h^2 \end{aligned} \quad (7)$$

This is the equation system for boundary heat fluxes Q_B^i . After Q_B^i at all Lagrangian points are obtained, they are substituted into Eq. (6) to obtain the temperature correction δT_j , which are further substituted into Eq. (4) to get the corrected temperature T_j .

3. EVALUATION OF AVERAGE NUSSOLT NUMBER

From the energy conservation law, two simple and efficient ways are presented to compute the mean Nusselt number from temperature correction at Eulerian points and boundary heat flux at Lagrangian points, which completely avoid evaluation of temperature gradients at the boundary points. These two methods are

- Method 1: evaluation of mean Nusselt number from temperature correction at Eulerian points

$$\overline{Nu} = \frac{\sum_j \rho c_p \frac{\delta T_j}{\delta t} \Delta x_j \Delta y_j}{kL(T_w - T_\infty)} L_c \quad (j=1, \dots, N) \quad (8)$$

- Method 2: evaluation of mean Nusselt number from heat flux at Lagrangian points

$$\overline{Nu} = \frac{\sum_i Q_B^i \Delta s_i}{kL(T_w - T_\infty)} L_c \quad (i=1, \dots, M) \quad (9)$$

Here Δx_j and Δy_j are the Eulerian mesh size, L_c and L are the reference length and the total length of the immersed boundary. N is the total number of Eulerian points while M is the total number of Lagrangian points.

3. SOME NUMERICAL RESULTS

The present method and proposed two ways to compute average Nusselt number are validated by their application to solve following two thermal flow problems.

3.1 Forced Convection over A Stationary Isothermal Circular Cylinder

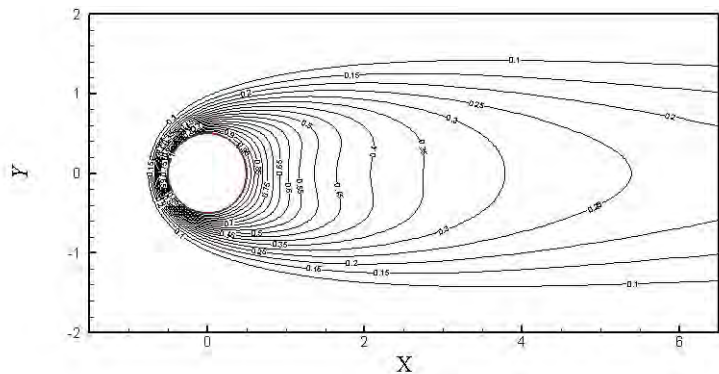


FIGURE 1 Isotherms for flow over a heated stationary cylinder at $Pr = 0.7, Re = 40$

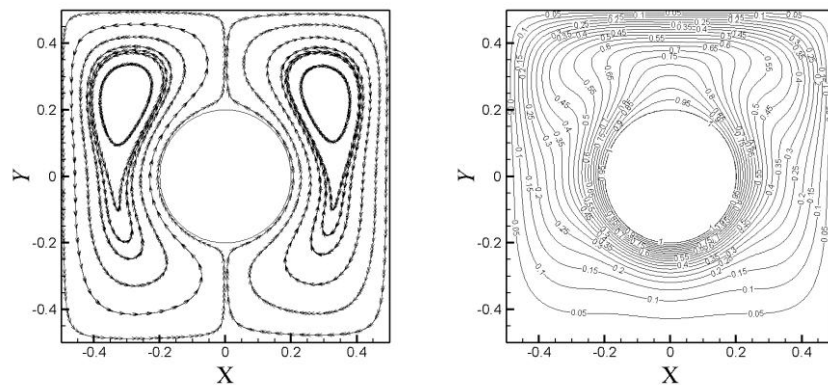
\overline{Nu}	References				
	Present		Lange et al. [4]	Soares et al. [5]	Bharti et al. [6]
	Method 1	Method 2			
	3.3519	3.3518	3.2805	3.2000	3.2825

TABLE 1 Comparison of average Nusselt number

The case of $Re = 40$, $Pr = 0.7$ is simulated. Here the Reynolds number $Re = \rho UD / \mu$ is based on the free stream velocity U and the cylinder diameter D , and Prandtl number is defined as $Pr = \mu c_p / k$. Fig. 1 shows isotherms in the vicinity of the cylinder. As can be seen, the temperature contours (isotherms) cluster heavily in the front surface of the cylinder, indicating a large temperature gradient there. The average Nusselt number on the cylinder surface is presented in Table 1. It is obvious that the average Nusselt numbers obtained by the two methods are almost the same and basically agree well with reference data in the literature [4-6].

3.2 Natural Convection in A Concentric Annulus Between A Square Outer Cylinder and A Circular Inner Cylinder

To further test the capability of proposed method, the natural convection in a concentric annulus between a square outer cylinder (with length L) and a heated circular inner cylinder (with radius r), in which the velocity and temperature fields are strongly coupled, is simulated. The case of $Pr = 0.7$, $L/(2r) = 2.5$ and $Ra = 10^5$ (based on length of square outer cylinder L) is studied, and the numerical results are shown in Fig. 2. It is observed clearly from Fig. 2 that the flow and thermal fields are symmetric about the vertical central line through the center of the annulus and a plume appears on top of the inner cylinder. Table 2 shows the average Nusselt numbers calculated by the two methods and their comparison with reference data [7-8] in the literature. Clearly, the present results agree very well with the reference data.

FIGURE 2 Streamlines (left) and isotherms (right) for $Pr = 0.7, L/(2r) = 0.25, Ra = 1 \times 10^5$

Case		Source			
Ra	$L/(2r)$	Present		Shu and Zhu [8]	Moukalled and Acharya [7]
		Method 2	Method 3		
	2.5	4.836	4.836	4.86	5.08

TABLE 2 Comparison of computed average Nusselt number

4. CONCLUSIONS

A boundary condition-enforced immersed boundary method is developed for simulation of heat and mass transfer problems. The heat source/sink incorporated into the energy equation to model the heated immersed boundary is evaluated implicitly by enforcing the isothermal boundary condition. In the meantime, two simple ways for computing average Nusselt number is proposed. Two numerical examples, including both forced convection and natural convection problems, are chosen to validate the proposed method. Numerical results demonstrate that the present boundary condition-enforced IBM can well solve thermal flow problems.

REFERENCES

- [1] C.S. Peskin, Flow patterns around heart valves: a numerical method, *J. Comp. Phys.*, 10, 252-271, 1972.
- [2] C. Shu, N.Y. Liu, Y.T. Chew, A novel immersed boundary velocity correction-lattice Boltzmann method and its application to simulate flow past a circular cylinder, *J. Comp. Phys.*, 226, 1607-1622, 2007.
- [3] J. Wu, C. Shu, Implicit velocity correction-based immersed boundary-lattice Boltzmann method and its applications. *J. Comp. Phys.*, 228, 1963-1979, 2009.
- [4] C.F. Lange, F. Durst, M. Breuer, Momentum and heat transfer from cylinders in laminar crossflow at $10^{-4} \leq Re \leq 200$, *Int. J. Heat Mass Transf.*, 41, 3409-3430, 1998.
- [5] A.A. Soares, J.M. Ferreira, R.P. Chhabra, Flow and forced convection heat transfer in crossflow of non-Newtonian fluids over a circular cylinder, *Industrial Engineering Chemistry Research*, 44, 5815-5827, 2005.
- [6] R.P. Bharti, R.P. Chhabra, V. Eswaran, A numerical study of the steady forced convection heat transfer from an unconfined circular cylinder, *Heat Mass Transfer*, 43, 639-648, 2007.
- [7] F. Moukalled, S. Acharya, Natural convection in the annulus between concentric horizontal circular and square cylinders, *J. Thermophys Heat Transfer*, 10, 524-531, 1996.
- [8] C. Shu, Y.D. Zhu, Efficient computation of natural convection in a concentric annulus between an outer square cylinder and an inner circular cylinder, *Int. J. Numer. Methods Fluids*, 38, 429-445, 2002.

NUMERICAL MODELING OF COUPLED HEAT/MASS TRANSPORT AND ELECTROCHEMICAL REACTIONS IN FUEL CELLS

T. S. Zhao*, W. W. Yang

Department of Mechanical Engineering, The Hong Kong University of Science and Technology, Clear Water Bay, Kowloon, Hong Kong SAR, China, metzhao@ust.hk

ABSTRACT

A two-dimensional two-phase mass transport model for a liquid-feed DMFC is presented. The two-phase mass transport in the anode and cathode porous regions is formulated based on the classical multiphase flow in porous media without invoking the assumption of constant gas pressure in the unsaturated porous medium flow theory. The two-phase flow behavior in the anode flow channel is modeled by utilizing the drift-flux model, while in the cathode flow channel the homogeneous mist-flow model is used. In addition, a micro-agglomerate model is developed for the cathode catalyst layer. The model also accounts for the effects of both methanol and water crossover through the membrane. The integrated model formed by integrating the models in the different regions is solved numerically using a home-written computer code and validated against the experimental data in the literature. The model can be used to investigate the effects of various operating and structural parameters, such as methanol concentration, anode flow rate, porosities of both anode and cathode electrodes, the rate of methanol crossover, and the agglomerate size, on cell performance.

Key Words: *Direct methanol fuel cell, two-phase, mass transport*

1. INTRODUCTION

Because of its unique advantages, the direct methanol fuel cell (DMFC) has been identified as one of the most promising power sources for portable and mobile applications. Although promising, this technology is facing some challenging technical issues. For given electrolyte and electrode materials, the performance and operating stability of a DMFC are determined by the mass transport of different species in the cell. As such, more and more attentions are turned to the management of the supply/removal of the reactants /products inside the DMFC, i.e. the mass transport related issues. Understanding of mass transport behaviors in DMFCs is thus essential. However, the opaque materials that form the constituent components of the fuel cell prevent experimental access for revealing the real-world details of how different species are transported and distributed inside the cell. Mathematical modeling, therefore, plays an important role in elucidating the complicated transport mechanism and limitations in DMFCs.

To date, many DMFC models have been developed, most are based on single-phase approach. Although useful, the single-phase approach is incompetent to reveal the real-world details of transport behaviours in DMFC because of the bold assumption involved. It is necessary to develop two-phase mass transport model for DMFC. Although realistic, developing a sound two-phase DMFC model is challenging. During the past few years, great efforts have been made to develop two-phase DMFC models. The two-phase mass transport phenomena in a DMFC were often modelled by a so-called multiphase mixture model [1]. This model was obtained by reformulating the classical multi-phase theory with introducing multiphase mixture properties, among which, a mixture pressure of liquid and gas in a the porous medium has to be boldly defined. More importantly, the liquid and gas are usually assumed to be in thermodynamic equilibrium by the multiphase mixture model, which thus ignores the interfacial mass exchange at phase interface.

Clearly, there is a need to develop a sound DMFC model that can realistically simulate the liquid-gas two-phase flow and mass transport phenomena in a DMFC. In this work, we developed an isothermal two-phase mass transport model for a liquid-feed DMFC. As compared with conventional models, the present two-phase mass transport model in the anode and cathode porous regions eliminates (a) the assumption of constant gas pressure in the unsaturated porous-medium flow theory; (b) the definition of the liquid-gas mixture pressure in the multiphase mixture model; and (c) the assumption of thermodynamic equilibrium condition between phases in the multiphase mixture model. Besides, sub-models were also developed for other regions. Each describes the specific mass transport processes that occur in the corresponding region.

2. MODEL FORMULATION

Consider a DMFC, as illustrated in Fig. 1, which consists of anode channel, anode diffusion layer (ADL), anode catalyst layer (ACL), membrane (MEM), cathode catalyst layer (CCL), cathode diffusion layer (CDL) and cathode channel. For convenience of description, the domain shown in Fig. 1 is divided into the cathode porous region (CDL and CCL), anode porous region (ADL and ACL), polymer electrolyte membrane, cathode channel and anode channel. To save space, in the following, we only present the models for anode and cathode porous regions.

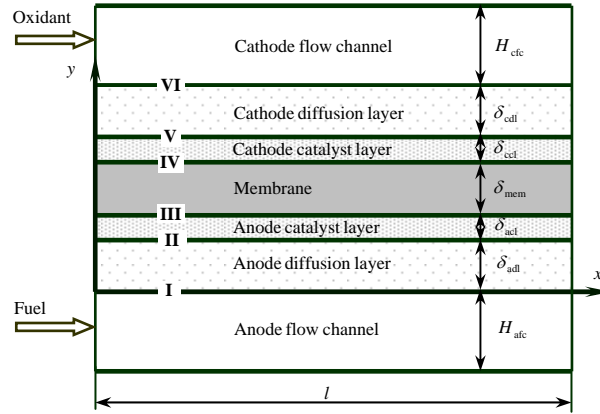


FIGURE 1. Schematic of a liquid-feed DMFC and the coordinate system

2.1 Model for two-phase mass transport in the anode porous region

On the DMFC anode, methanol is supplied in the anode flow channel, transfers through the ADL to the ACL, where part of methanol is electro-chemically oxidized to form gas carbon dioxide and current, while the remainder of methanol permeates the membrane to the cathode. The produced carbon dioxide transfers back to the anode flow channel, and is finally removed by the methanol solution stream. In the anode porous region, we are interested in four major variables, including liquid methanol concentration ($C_{M,l}$), liquid pressure (p_l), gas-void fraction ($1-s_l$) and methanol vapor concentration ($C_{M,v,g}$). The governing equations corresponding to each of these variables can be given by:

$$C_{M,l}: \quad \nabla \cdot \left[\left(-\frac{Kk_{rl}}{\mu_l} \nabla p_l \right) C_{M,l} - D_{M,l}^{\text{eff}} \nabla C_{M,l} \right] = \dot{R}_{M,l} \quad (1)$$

$$p_l: \quad \nabla \cdot \left(-\frac{Kk_{rl}}{\mu_l / \rho_l} \nabla p_l \right) = \dot{m}_l \quad (2)$$

$$1 - s_1 : \quad \nabla \cdot \left[\left(-\frac{Kk_{rg}}{\mu_g / \rho_g} \right) \left(\left[\frac{d p_c}{d(1-s_1)} \right] \nabla(1-s_1) + \nabla p_1 \right) \right] = \dot{m}_g \quad (3)$$

and

$$C_{MV,g} : \quad \nabla \cdot \left[\left(-\frac{Kk_{rg}}{\mu_g} \nabla p_g \right) C_{MV,g} - D_{MV,g}^{eff} \nabla C_{MV,g} \right] = \dot{R}_{MV,g} \quad (4)$$

The interfacial transfer rate of methanol between the liquid and gas in the anode porous region is given by:

$$\tilde{R}_M = A_{lg} h_{lg} s_1 (1-s_1) \frac{(P_{MV}^{sat} - P_{MV})}{RT} \quad (5)$$

Eqs. (1) to (5) form the model for the two-phase mass transport in the anode porous region. Note that the interfacial exchange of methanol between phases is considered, opposing to the assumption of thermodynamic equilibrium between phases employed in other DMFC models [1-2].

2.2 Model for two-phase mass transport in the cathode porous region

On the DMFC cathode, oxygen in the flow channel transfers through the CDL to the CCL, where the oxygen reduction reaction (ORR) takes place to form water. The produced water, along with the water permeated from the anode, flows back through the cathode porous region to the cathode channel. This two-phase mass transport in the cathode porous region is related to four major variables: oxygen concentration ($C_{O_2,g}$), gas pressure (p_g), liquid saturation (s_1) and water vapor concentration ($C_{wv,g}$). The governing equations corresponding to the four variables are:

$$C_{O_2,g} : \quad \nabla \cdot \left[\left(-\frac{Kk_{rg}}{\mu_g} \nabla p_{g,c} \right) C_{O_2,g} - D_{O_2,g}^{eff} \nabla C_{O_2,g} \right] = \dot{R}_{O_2,g} \quad (6)$$

$$p_g : \quad \nabla \cdot \left[\left(-\frac{Kk_{rg}}{\mu_g / \rho_g} \right) \nabla p_g \right] = \dot{m}_g \quad (7)$$

$$s_1 : \quad \nabla \cdot \left[\left(-\frac{Kk_{rl}}{\mu_l / \rho_l} \right) \left(-\frac{d p_c}{d s} \nabla s_1 + \nabla p_g \right) \right] = \dot{m}_1 \quad (8)$$

and

$$C_{wv,g} : \quad \nabla \cdot \left[\left(-\frac{Kk_{rg}}{\mu_g} \nabla p_g \right) C_{wv,g} - D_{wv,g}^{eff} \nabla C_{wv,g} \right] = \dot{R}_{wv,g} \quad (9)$$

To account for the effect of water evaporation and condensation, the interfacial transfer rate of water between the liquid and gas phase is given by:

$$\tilde{R}_w = \begin{cases} k_e \frac{\varepsilon s_1 \rho_l}{M_{H_2O}} (y_{wv} p_g - P_{wv}^{sat}) & y_{wv} p_g < P_{wv}^{sat} \\ k_c \frac{\varepsilon (1-s_1) y_{wv}}{RT} (y_{wv} p_g - P_{wv}^{sat}) & y_{wv} p_g > P_{wv}^{sat} \end{cases} \quad (10)$$

Note that the interfacial transfer of water between the phases is embodied in the source terms on the right-hand sides of Eqs. (7-9).

Eqs. (6) to (10) form the model for simulating the two-phase mass transport in the cathode porous region. It is noticed that unlike the unsaturated porous-medium flow theory, the present model eliminates the assumption of constant gas pressure assumption. As implied by Eq. (8), the constant gas pressure assumption in the unsaturated porous medium flow model will exclude the liquid flux caused by the gas phase motion that counters the capillarity-induced liquid phase motion. Moreover, the assumption of constant gas pressure will cause the corresponding convective transfer of gas species to be neglected. Another feature of the present model is that there is no need to introduce a so-called liquid-gas mixture pressure as defined in the multiphase mixture model. More importantly, the present model considers the interface mass exchange between liquid and gas, eliminating the assumption of thermodynamic equilibrium between phases in the multiphase mixture model.

Besides, specific sub-models were also constructed to simulate the specific mass transport processes occurred in other regions. Those include the drift-flux model for simulating the two-phase flow in the anode channel, the homogenous model for cathode flow channel, the microscopic agglomerate model for the CCL, and the model for simulating the transport of dissolved species through the membrane. The present model was formed by integrating those sub-models for different regions. The information on the two-phase mass transport in a DMFC can be obtained by solving the governing equations with corresponding boundary conditions, specific physicochemical properties and the information of the electrochemical kinetics.

3. RESULTS

To validate the model, we compare the numerical results predicted by the present model with the data reported in the open literature. Figure 2 compares the global cell performance for 0.25 M, 0.5 M, 1 M and 2 M methanol solutions that predicted by the present model with the data experimentally measured [3]. Those experimental data were collected at 75 °C with air fed to the cathode at an extremely high flow rate of 1000 ml min⁻¹ to avoid the effects of the oxygen depletion and the presence of liquid water along the channel. It is seen that the predicted polarization curves are in reasonable agreement with the experimental data. As can be seen, in the low current density region the cell voltage decreases with methanol concentration due to the increased mixed potential as a result of the increased rate of methanol crossover. The numerical results also reveal that the limiting current density increases with methanol concentration for the cases when methanol concentration is lower than 1 M, proving that the limiting current density is caused by the methanol transport limitation. However, for the case when methanol concentration increases to 2 M, the cell voltage decreases almost linearly with current density toward zero with no mass transport limitation. All these polarization behaviors are consistent with those revealed by experiments [3].

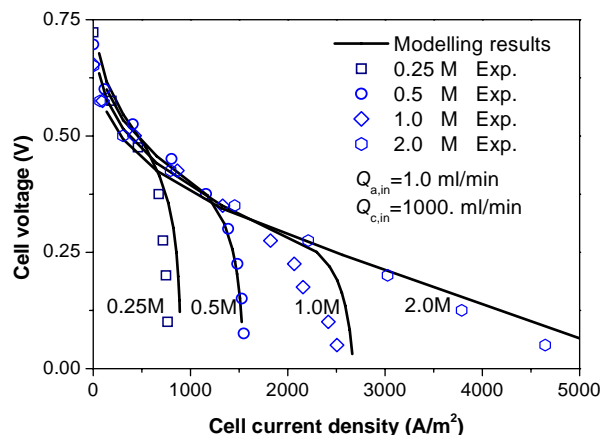


FIGURE 2. Cell performance predicted by the present model and experimental data [3]

Figure 3 shows the rate of methanol crossover as a function of current density for various methanol concentrations ranging from 0.25 M to 3 M. For the cases when methanol concentration is lower than 2 M, the rate of methanol crossover decreases with current density and becomes zero when reaching limiting current density, at which the mole flow rate of methanol equals the rate of the MOR in the anode catalyst layer. However, the rate of methanol crossover at 3 M shows a different behaviour: it increases slightly with current density, reaches a maximum, and decreases afterward. Generally speaking, the trend in methanol crossover as function of current density is similar to those measured [4] or calculated [5].

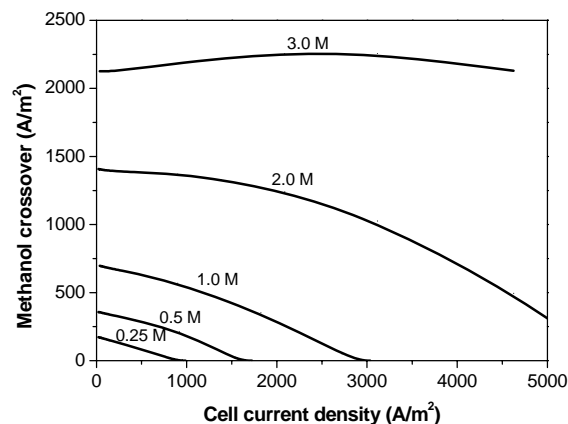


FIGURE 3. Effect of methanol concentration on methanol crossover

4. CONCLUSIONS

Mathematical modeling is essential to shed light on the mass transport processes in the DMFC. This work describes the development and validation of a two-phase mass transport model for liquid-feed DMFCs. As compared with conventional models, the present two-phase mass transport model in the porous structures eliminates the following assumptions: (a) the assumption of constant gas pressure in the unsaturated porous medium flow theory; (b) the definition of the liquid-gas mixture pressure in the multiphase mixture model; and (c) the assumption of thermodynamic equilibrium condition between phases in the multiphase mixture model. In addition, the drift-flux and homogeneous theories were employed to simulate, respectively, the flow in the anode and cathode channels. Moreover, a microscopic agglomerate model was developed to describe the effect of microstructure of the catalyst layer. Finally, this integrated model is solved numerically using a home-written computer code and validated against the data reported in the open literature. It is indicated that the present model can predict the cell performance with fairly good accuracy.

REFERENCES

- [1] Z.H. Wang, C.Y. Wang, Mathematical modelling of liquid-feed direct methanol fuel cells, *J. Electrochem. Soc.*, 150, A508, 2003.
- [2] E. Birgersson, J. Nordlund, M. Vynnychy, C. Picard, G. Lindbergh, Reduced two-phase model for analysis of the anode of a DMFC, *J. Electrochem. Soc.*, 151, A2157, 2004.
- [3] C. Xu, Y.L. He, T.S. Zhao, R. Chen, Q. Ye, Analysis of mass transport of methanol at the anode of direct methanol fuel cell, *J. Electrochem. Soc.*, 153, A1358, 2006.
- [4] R.Z. Jiang, D. Chu, Comparative studies of methanol crossover and cell performance for a DMFC, *J. Electrochem. Soc.*, 151, A69, 2004.
- [5] J.B. Ge, H.T. Liu, A three-dimensional mathematical model for liquid-fed direct methanol fuel cells, *J. Power Sources*, 160, 413, 2006.

MICRO/NANO SCALE RADIATIVE HEAT TRANSFER

Yimin Xuan, Qiang Li

School of Energy and Power Engineering, Nanjing University of Science & Technology, 210094,
ymxuan@mail.njust.edu.cn

ABSTRACT

The mechanism of the radiative heat transfer in micro/nano scale structures is different from that of the traditional one, and the "near-field effects" are needed to be considered. Several examples of calculation model are introduced here to describe the radiative properties of the structured surface with the characteristic length smaller than the incident wavelength.

Key Words: *Micro/Nano structure, FDTD, Near-field radiative theory.*

1. INTRODUCTION

As a basic way of energy transfer, thermal radiation exists commonly in nature. In the area of engineering technology such as the energy, power, aerospace, optoelectronics, military technology, optical technology, mechanical and electrical systems, the thermal radiation plays an important role. Since the 1920s, research of the basic theory and application of thermal radiation has been made considerable progress, and has become very active in the field of thermal science.

The process of radiation heat transfer is generally divided into emission, absorption, scattering and transmission. When the characteristic length of the object involved in the thermal radiation heat transfer is much larger than the wavelength of thermal radiation, the radiant energy transfer process can be simulated using the methods of ray-tracing or geometrical optics approximately. These problems are named as "far-field radiative heat transfer problem". When the characteristic length of the object is close to or smaller than the wavelength, the wave characteristics ignored in traditional radiation heat transfer equation stand out, and the effect of the surface properties of the object on radiation heat transfer process is more obvious, i.e., the "near field" significantly affects the whole process of energy radiation. Such problems are called as "near-field radiative heat transfer problem."

Microscale radiation effects don't only show on micro-structured surface, when the distance between two objects is close to or smaller than the wavelengths of radiation, the radiation transfer process between the objects also shows strong microscale effect. For the enhanced near-field radiation effects, the traditional theory of radiation heat transfer could not be analyzed and resolved.

In this paper, based on the FDTD method and near-field radiative theory, several examples of calculation model are introduced to describe the radiative properties of the micro/nano structured surface. In addition, near-field radiative theory is used to study the mechanism of near field effect between magnetic and non-magnetic materials.

2. FDTD METHOD AND NEAR-FIELD RADIATIVE THEORY

FDTD method is a direct time-domain method for solving Maxwell differential equations. The basic idea of FDTD method is: Using the Yee cell as discrete units, the Maxwell's equations are converted to a set of central difference equations to solve in each Yee unit cell. Based on the results of the solution of Maxwell's equations, it is needed to analysis the energy penetrating into the system in a certain time, and its reflection, transmission and absorption in different directions, then to obtain the spectral properties of the thermal radiation.

The near-field radiative theory is a direct method to deal the radiative heat transfer in microscale, in which the magnitude of the heat flux is directly achieved. It is mainly assumed that the thermal radiation is due to the fluctuating electromagnetic field result from the fluctuating electric and magnetic current sources in the medium. By combination of the stochastic Maxwell's equations and the correlation functions between these sources given by fluctuation-dissipation theorem (FDT), the heat flux described by the time-averaged Poynting vector is achieved.

3. EXAMPLES

3.1 Structure color of tropical Morpho butterflies

Structure color of tropical Morpho butterflies is one of very hot topics. It is commonly accepted that their brilliant and iridescent color is principally due to optical interference. The calculation models based on morpho's microstructure is presented here, and characteristics of structure color from such ridge microstructures were simulated by using the FDTD method in order to explore the color mechanism of the butterfly. Explorations were offered to explain structure color of Morpho butterflies according to our simulations. Our analysis meets with other's experiment results very well, and which shows our method is very feasible to investigate the structure color of morpho butterflies.

3.2 One-dimensional Si/SiO₂ photonic crystals for thermophotovoltaic filter

The one-dimensional PC filter for the spectral control of photons in order to maximize the conversion efficiency and power density of a TPV system is proposed (as shown in Fig 1) [1]. The filter structure has been designed as 4 periods and 8 layers (4 pairs) by using SiO₂ and Si material pair, and the thicknesses of SiO₂ and Si layer have been determined to be equal to 0.204 and 0.194 μm in the first period and 0.408 and 0.176 μm in the other three periods. The physical vapor deposition (PVD) process has successfully been used to fabricate the filter. The normal transmittance performance of the filter has been measured with two spectrophotometers within the spectral range from 0.7 to 3.3 μm . It shows that the reflectivity of the filter is over 92% in the wavelength range 1.8—3.3 μm and the averaged transmissivity reaches 90% in the wavelength range 0.9—1.8 μm . The theoretical prediction has also given the identical results. The estimated spectral efficiency of the TPV increases with the emitter temperature. For example, the spectral efficiency of the TPV system with such a filter reaches 53%. The temperature-withstanding experiment has indicated that the fabricated 8-layer matching one-dimensional Si/SiO₂ PC filter can normally work at the temperature environment below 600.



FIGURE 1. Sample of PC Si/SiO₂

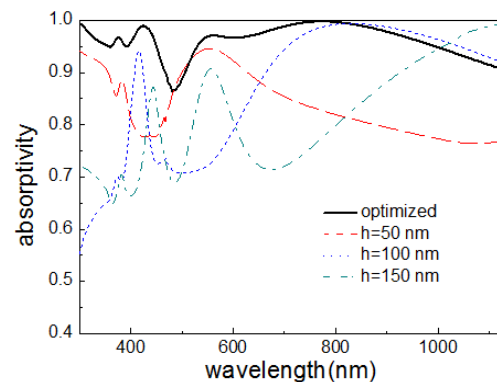


FIGURE 2. Absorptance of the assembly grating structure compared with the monotone structure surfaces

3.3 Absorption enhancement of solar cells with an assembly grating structure

Figure 2 illustrates the spectral absorptance of the assembly structure of the gratings. For the purpose of comparison, the surface absorptance of three conventional monotone grating structures is included. It is clear that the absorptance spectrum of the assembly grating structure is much higher than those of the three conventional ones, especially in the visible spectrum. It is found that the absorptance of the assembly structure surface is greater than 0.85 throughout the wave-band, which is also higher than those of the nanostructured surface [2]. Such an absorption property of the assembly structure is beneficial for improving the conversion efficiency of solar cells.

3.4 Spectral properties of multilayer hole arrays

The spectral properties of the symmetric metal-insulator-metal hole arrays consisting of an air or MgF₂ core layer sandwiched between two silver layers with rectangular hole arrays have been investigated using FDTD Sin-Cos method. Numerical investigation has revealed that the structural parameters and the physical parameters of the dielectric core layer affect the optical properties of the structure. The absorption and EOT peaks in absorptance and transmittance spectra are mainly attributed to the internal- and external-SPPs excited in metal-dielectric multilayer system. Compared with other SPPs modes, the external-SPPs (1, 0) mode has a greater contribution to the strong absorption and EOT phenomena. From the spectra maps, an important feature can be found that the absorptance can reach more than 90% if the internal- and external-SPPs are simultaneously excited. By selecting the suitable structural parameters, the metal-insulator-metal film hole arrays structure can reach a higher EOT peak than single metallic 2DHAs. Therefore, these features can be applied to design the novel optical-electronic devices.

3.5 Spectral properties of 2D Ag micro-cavity arrays and the application in narrow-band emitter

To investigate spectral properties of structured silver surface with periodic rectangular hollow cavities, numerical computation is conducted to obtain spectral distribution of surface absorptance with different structural parameters using the finite-difference time-domain (FDTD) method [3]. By means of numerical examples, the effects of structural parameters, incident angle and azimuthal angle on the spectral features of the structured surface are discussed. It is found that the structured surface shows the characteristics of the peak absorption in the vicinity of resonant wavelength of rectangular cavity. For some special structure parameters, the peak absorptance of the incident plane wave can reach as high as above 80% due to the excitation of microcavity effect. The optimal narrow-band absorption can be achieved by the rational design of the structural parameters of rectangular cavity. The directional dependence of spectral absorptance is also analyzed and the results reveal that the absorption peak positions are incident-angle-independent. The results show that the microscaled rectangular cavities fabricated on the low-emissivity silver surface are very efficient for selective improvement of the radiative features, which provides guidance for the design of narrow-band infrared thermal emitters.

3.6 The near field radiative heat transfer between magnetic and non-magnetic materials

So far, most investigations of near field radiative heat transfer were restricted to the assumption of nonmagnetic substances. From these researches, it was clear that excitation of surface waves in TM polarization would enhance the near-field radiative heat transfer and made it monochromatic [4]. With the development of the metamaterials, the surface waves in TE polarization might be excited. In order to discuss the effect of the excitation of surface waves in TE polarization on the near-field radiative heat transfer, we developed the theory of near-field radiative heat transfer to deal with near-field radiative heat transfer for layered magnetic media (involving metamaterials). According to the theory, we calculated the near-field radiative heat transfer between two semi-infinite bodies (made by identical nonmagnetic/magnetic materials) separated by different vacuum gap, as shown in Fig. 3. It should be pointed that except the relative permeability is 1, the other conditions is same as that for magnetic materials.

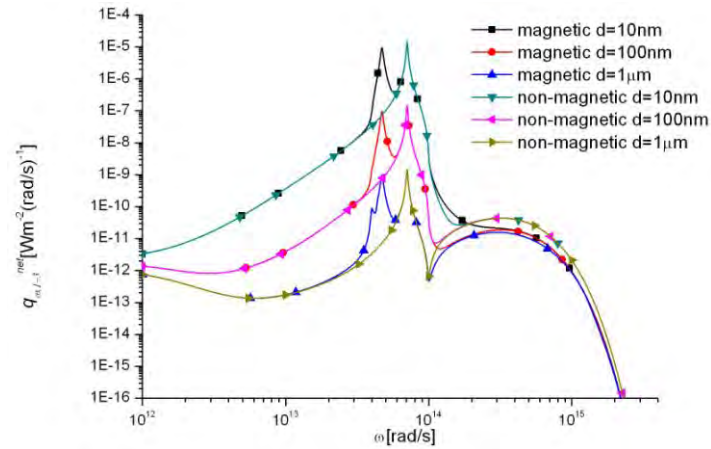


FIGURE 3. Spectral radiative energy flux between magnetic and non-magnetic materials

As shown in Fig. 8, the different behaviours for the radiative heat transfer were observed for magnetic and nonmagnetic materials. Although there exists a peak $\omega = 7.0705 \times 10^{13}$ rad/s for both magnetic and nonmagnetic media due to the effect excitation of surface waves in TM polarization, there is an additional peak around $\omega = 4.7134 \times 10^{13}$ rad/s due to the effect of excitation of surface waves in TE polarization for the magnetic media as the dispersion relation for surface polaritons in TE polarization could be satisfied, which will further enhance the heat transfer between the two bodies. By comparison of the contributions of TE and TM waves to the heat flux, it might be found that the main difference between the magnetic and nonmagnetic materials is that the surface wave would be excited in TE polarization, resulting the enhancement of the contributions of TE waves to the heat flux and little effect on the contributions of TM waves to it.

4. CONCLUSIONS

In this paper, the near-field effects in radiation are considered adequately by solving Maxwell equations directly. The results show great influence of the near-field effects on heat radiation of the micro/nano-structured surface. By adjusting micro/nano-scale structure, the radiative heat transfer can be greatly enhanced or suppressed. Therefore, the mechanism of the radiative heat transfer in micro/nano scale structures can provide a good guidance in the control of heat radiation.

ACKNOWLEDGEMENTS

This work is sponsored by the National Natural Science Foundation of China (Grant No. 50936002).

REFERENCES

- [1] G.P. Liu, Y.M. Xuan, Y.G. Han, Q. Li. Investigation of one-dimensional Si/SiO₂ photonic crystals for thermophotovoltaic filter. *Science in China Series E: Technological Sciences*, 51, 2031-2039, 2008.
- [2] L. Tsakalakos, J. Balch, J. Fronheiser, et al. Strong broadband optical absorption in silicon nanowire films, *J. Nanophotonics*, 1, 013552, 2007.
- [3] J.G. Huang, Y.M. Xuan, Q. Li. Narrow-band spectral features of structured silver surface with rectangular resonant cavities. *Journal of Quantitative Spectroscopy & Radiative Transfer*, 112, 839-846, 2011.
- [4] Z.H. Zheng, Y.M. Xuan. Theory of near-field radiative heat transfer for stratified magnetic media. *International Journal of Heat and Mass Transfer*, 54, 1101-1110, 2011.

MINI-SYMPOSIA

ON SURFACE MODELS WITH COUPLINGS AMONG THERMAL, ELASTIC AND ELECTRIC FIELDS

W. Q. Chen, J. Zhu

Department of Engineering Mechanics, Zhejiang University, Hangzhou 310027, China

ABSTRACT

We report a novel method to derive surface models of different orders, which account for the couplings among thermal, elastic and electric fields. The derivation is based on the state-space formalism, during which an operational interpretation of related partial differential operators is needed. For the degenerated case of a plane surface boundary of an elastic body, the results are identical to the well-known surface model proposed by Gurtin and Murdoch when the residual surface stresses are absent. Numerical results are given to show the surface effect on the propagation characteristics of the Bleustein-Gulyaev waves in a surface electroded piezoelectric half-space.

Key Words: *Surface Theory, Multi-field Coupling, State-space Formalism.*

1. INTRODUCTION

There is an increasing academic interest in the mechanical behavior of bodies of small size because some size-dependent phenomena have been observed experimentally or through molecular dynamics simulation [1,2]. Continuum mechanics has demonstrated very powerful to explain these particular phenomena in a relatively simple theoretical framework by accounting for the so-called surface effects. There are two main ways to establish the continuum surface theories. One is to treat the surface of a body as a material surface of zero thickness and extend the conventional continuum mechanics concepts. This is accomplished by Gurtin and Murdoch [3] for an arbitrary deformable curved surface. The other assumes a surface layer of a small thickness, which has material properties different from the bulk. This is initially suggested by Mindlin [4] and later explored by Tiersten [5] in the wave propagation analysis. Recently, it has become a main stream to study the surface effects in solids by employing the Gurtin-Murdoch theory [6,7]. However, the Mindlin-Tiersten approach has also been followed by several authors in the wave propagation analyses [8,9].

In this paper, we will follow the Mindlin-Tiersten treatment, but adopt a new method to develop the surface models of bodies in which there are interactions among elastic, electric and thermal fields. This is an extension of our previous short paper which studies the surface effect on surface shear waves in a horizontally polarized piezoelectric half-space [10].

2. STATE EQUATION

Only linear problems are of interest here. It has been shown recently that the state-space formulation can play a very effective and important role in the study of laminated structures [11]. For a deformable body with couplings among thermal, elastic and electric fields, Tarn [12] derived the following state equation:

$$\frac{\partial}{\partial x_2} \begin{Bmatrix} \mathbf{u} \\ \boldsymbol{\tau}_2 \end{Bmatrix} = \begin{bmatrix} \mathbf{D}_{11} & \mathbf{C}_{22}^{-1} \\ \mathbf{D}_{21} & \mathbf{D}_{11}^T \end{bmatrix} \begin{Bmatrix} \mathbf{u} \\ \boldsymbol{\tau}_2 \end{Bmatrix} + \begin{Bmatrix} \mathbf{C}_{22}^{-1} \boldsymbol{\beta}_2 \\ \mathbf{L}_1^T \boldsymbol{\beta}_1 \end{Bmatrix} T + \frac{\partial^2}{\partial t^2} \begin{Bmatrix} \mathbf{0} \\ \mathbf{K}_p \mathbf{u} \end{Bmatrix}, \quad (1)$$

where $\mathbf{u} = [u_1, u_2, u_3, \phi]^T$ and $\boldsymbol{\tau}_2 = [\sigma_{12}, \sigma_{22}, \sigma_{23}, D_2]^T$ are the generalized displacement vector and generalized stress vector; \mathbf{D}_{ij} and \mathbf{L}_1 are operator matrices, containing derivatives with respect to x_1 and x_3 ; and other symbols in Eq. (1) are well defined in Ref. [12] and are omitted here.

3. NEW METHOD TO ESTABLISH SURFACE MODELS

We first rewrite Eq. (1) in the form of $\partial \mathbf{V} / \partial x_2 = \mathbf{M} \mathbf{V} + \mathbf{g} T$, here $\mathbf{V} = [\mathbf{u}^T, \boldsymbol{\tau}_2^T]^T$ is the state vector; \mathbf{M} is an operator matrix, which further includes the time derivatives; and \mathbf{g} is an operator vector. Then, by treating the differential operators as parameters [13], we may obtain the following solution:

$$\mathbf{V}(x_2) = \exp(\mathbf{M}x_2)\mathbf{V}(0) + T \int_0^{x_2} \exp[\mathbf{M}(x_2 - t)]\mathbf{g} dt, \quad (2)$$

Now we confine ourselves to a plane surface, which is seen as a thin layer with different material properties from the bulk. The coordinates are set up as shown in Fig. 1.

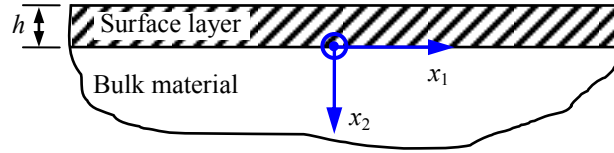


FIGURE 1. The surface layer model.

Setting $x_2 = -h$ in Eq. (2) leads to

$$\mathbf{V}(-h) = \exp(-\mathbf{M}h)\mathbf{V}(0) + T \int_0^{-h} \exp[-\mathbf{M}(h+t)]\mathbf{g} dt, \quad (3)$$

The exponential matrix can be expressed in a series as follows

$$\exp(-\mathbf{M}h) = \mathbf{I} - \mathbf{M}h + \frac{1}{2}\mathbf{M}^2h^2 + \dots + \frac{(-1)^n}{n!}\mathbf{M}^nh^n + O(h^{n+1}). \quad (4)$$

Since the thickness h is small, we can truncate the above series to any order, depending on the accuracy requirement of the problem. If we retain only the first two terms in Eq. (4), we obtain from Eq. (3)

$$\mathbf{V}(-h) = (\mathbf{I} - \mathbf{M}h)\mathbf{V}(0) + T \int_0^{-h} [\mathbf{I} - \mathbf{M}(h+t)]\mathbf{g} dt, \quad (5)$$

Now making use of the continuity conditions at the interface $x_2 = 0$ between the surface layer and the bulk, as well as the boundary conditions at $x_2 = -h$, we can derive a set of differential relation between the state variables at $x_2 = 0$. These are the equations governing the surface, and can be used to approximate the effect of the surface layer. We will give a simple description of such a procedure for a particular wave propagation problem in the next section.

4. SURFACE EFFECT ON BG WAVE

Recently, the propagation of Bleustein-Gulyaev (BG) type surface shear wave in a piezoelectric half-space with surface effect was considered [10], with the assumption that the surface of the half-space is open-circuited. Here we consider another case, i.e. the surface of the half-space is covered with an electrode which is grounded. For the BG wave without thermal effect, we have $\mathbf{u} = [u_3, \phi]^T$ and $\boldsymbol{\tau}_2 = [\sigma_{23}, D_2]^T$, and

$$\mathbf{M} = \begin{bmatrix} \mathbf{0} & \mathbf{A} \\ \mathbf{B} & \mathbf{0} \end{bmatrix}, \quad \mathbf{A} = \begin{bmatrix} \frac{\varepsilon_{11}}{\alpha} & \frac{e_{15}}{\alpha} \\ \frac{e_{15}}{\alpha} & -\frac{c_{44}}{\alpha} \end{bmatrix}, \quad \mathbf{B} = \begin{bmatrix} \rho \frac{\partial^2}{\partial t^2} - c_{44} \frac{\partial^2}{\partial x_1^2} & -e_{15} \frac{\partial^2}{\partial x_1^2} \\ -e_{15} \frac{\partial^2}{\partial x_1^2} & \varepsilon_{11} \frac{\partial^2}{\partial x_1^2} \end{bmatrix}, \quad \mathbf{g} = \mathbf{0}. \quad (6)$$

Thus, we obtain from Eq. (5) the following first-order surface theory:

$$\phi(0) - \frac{e_{15}^s}{\alpha^s} \sigma_{23}(0) + \frac{c_{44}^s}{\alpha^s} D_2(0) = 0, \quad \sigma_{23}(0) - \rho^s \frac{\partial^2 u_3(0)}{\partial t^2} + c_{44}^s \frac{\partial^2 u_3(0)}{\partial x_1^2} + e_{15}^s \frac{\partial^2 \phi(0)}{\partial x_1^2} = 0, \quad (7)$$

where the superscript s denotes the surface parameters, and these can be found in Ref. [10]. We have made use of the continuity conditions at $x_2 = 0$ and the boundary conditions at $x_2 = -h$. It can be easily shown that the second in Eq. (7) is identical to the one derived by Gurtin and Murdoch in the pure elastic case. In view of Eq. (7), the characteristic equation for the BG wave can be derived as

$$\begin{vmatrix} \frac{e_{15}^s}{\varepsilon_{11}} + \frac{e_{15}^s}{\alpha^s} \bar{c} k_2 & 1 + \frac{(e_{15}^s e_{15} + c_{44}^s \varepsilon_{11})}{\alpha^s} k_1 \\ \bar{c} k_2 + \left(c_{44}^s + \frac{e_{15}^s e_{15}}{\varepsilon_{11}} \right) k_1^2 - \rho^s \omega^2 & e_{15} k_1 + e_{15}^s k_1^2 \end{vmatrix} = 0, \quad (8)$$

where k_1 is the wave number along the x_1 axis, and $k_2 = \sqrt{k_1^2 - \rho \omega^2 / \bar{c}} > 0$, with $\bar{c} = c_{44} + e_{15}^2 / \varepsilon_{11}$. If the surface effect is absent, Eq. (8) becomes identical to that available in literature [14].

For numerical calculation, we consider a PZT-4 half-space, for which $c_{44} = 25.6 \times 10^9 \text{N/m}^2$, $e_{15} = 12.7 \text{C/m}^2$, $\varepsilon_{11} = 646.4 \times 10^{-11} \text{F/m}$, and $\rho = 7500 \text{kg/m}^3$. To study the surface effect, we artificially assume a surface layer of thickness 2mm, which has material properties $c_{44}^s = r_1 c_{44}$, $e_{15}^s = r_1 e_{15}$, $\varepsilon_{11}^s = r_1 \varepsilon_{11}$, and $\rho^s = r_2 \rho$, with r_1 and r_2 being two scaling factors. Figure 2 depicts the phase velocity spectrum, where the dimensionless phase velocity V and wave number χ are defined respectively as $V = v / v_0$ and $\chi = k_1 H$, with $v_0 = \sqrt{c_{44} / \rho}$ and $H = 1 \text{m}$. As we can see that, when there is no surface effect, the BG wave propagates at a constant velocity, and hence is non-dispersive. If the surface effect is involved, then the wave is slightly dispersive, and becomes slower when the wave number increases. In the calculation, we have taken $r_1 = 2$ and $r_2 = 20$, which indicate a slow surface layer (i.e. v_0 in the layer is slower than that in the half-space).

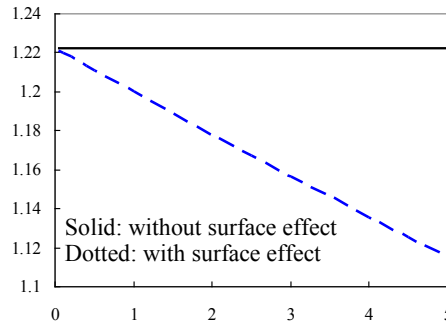


FIGURE 2. Phase velocity versus wave number.

5. CONCLUSIONS

This paper outlines a new approach to derive the governing equations of continuum surface models which involve the couplings among thermal, elastic and electric fields. An example of wave propagation in a piezoelectric half-space with surface electrode is presented and the surface effect is illustrated.

ACKNOWLEDGEMENTS

The work was supported by the National Natural Science Foundation of China (Nos. 11090333, 10832009 and 10725210).

REFERENCES

- [1] R.C. Cammarata, Surface and interface stress effects in thin films, *Progress in Surface Science*, 46, 1-38, 1994.
- [2] R.E. Miller and V.B. Shenoy, Size-dependent elastic properties of nanosized structural elements. *Nanotechnology*, 11(3), 139-147, 2000.
- [3] M.E. Gurtin and A.I. Murdoch, A continuum theory of elastic material surfaces, *Archive for Rational Mechanics and Analysis*, 57, 291-323, 1975.
- [4] R. D. Mindlin, High frequency vibrations of plated, crystal plates, In: *Progress in Applied Mechanics*, pp. 73-84, MacMillan, New York, 1963.
- [5] H. F. Tiersten, Elastic surface waves guided by thin films, *Journal of Applied Physics*, 40, 770-789, 1969.
- [6] L.H. He and Z.R. Li, Impact of surface stress on stress concentration, *International Journal of Solids and Structures*, 43, 6208-6219, 2006.
- [7] W.Q. Chen and Z.C. Zhang, Anti-plane shear Green's functions for an isotropic elastic half-space with a material surface, *International Journal of Solids and Structures*, 47, 1641-1650, 2010.
- [8] A.J. Niklasson, S.K. Datta and M.L. Dunn, On approximating guided waves in plates with thin anisotropic coatings by means of effective boundary conditions, *Journal of the Acoustical Society of America*, 108, 924-933, 2000.
- [9] K. Mauritssona, A. Boström and P.D. Folkow, Modelling of thin piezoelectric layers on plates, *Wave Motion*, 45, 616-628, 2008.
- [10] W.Q. Chen, Surface effect on Bleustein-Gulyaev wave in a piezoelectric half-space, *Theoretical and Applied Mechanics Letters*, 1, 041001, 2011.
- [11] H.J. Ding and W.Q. Chen, *Three Dimensional Problems of Piezoelasticity*, Nova Science Publishers, New York, 2001.
- [12] J.Q. Tarn, A state space formalism for piezothermoelasticity, *International Journal of Solids and Structures*, 39, 5173-5184, 2002.
- [13] A.I. Lur'e, *Three-Dimensional Problems of the Theory of Elasticity*, Interscience Publishers, New York, 1964.
- [14] J.S. Yang, *An Introduction to the Theory of Piezoelectricity*, Springer, New York, 2005.

THERMAL-CONTROLLED RELEASE AND ABSORPTION OF A HYBRID GEL PARTICLE

Zhen Wu, Zheng Zhong*

School of Aerospace Engineering and Applied Mechanics, Tongji University, Shanghai 200092, China, *Email: zhongk@tongji.edu.cn

ABSTRACT

The thermal-controlled swelling process of a gel particle is of great importance for applications in drug delivery. In this work, we study a hybrid structure where a poly(N-isopropylacrylamide) gel particle is coated by an elastic membrane. Our results show that in such a hybrid gel particle, the thermal-controlled release and absorption process can be tuned by changing the elastic property of the elastic membrane.

Key Words: *PNIPAM Gel, Core-shell Structure, Thermal-induced Deformation.*

1. INTRODUCTION

Poly(N-isopropylacrylamide) (PNIPAM) gels have been widely used in drug delivery due to their thermal-responsive swelling (or deswelling). In these applications, the controlling of the amount of solvent molecules that the PNIPAM gel releases (or absorbs) in response to temperature changes is of great importance, which motivates researchers to fabricate new species of PNIPAM gels with hybrid structures. This work studies a core-shell gel particle where a PNIPAM microgel is enclosed by an elastic membrane, and shows that the thermal-controlled release and absorption process in this hybrid gel particle can be tuned by changing the elastic property of the membrane.

2. HYBRID GEL PARTICAL

Figure 1 illustrates a hybrid gel particle, where a spherical core of PNIPAM gel is coated by a membrane of phospholipid bilayer. The structure can be prepared by polymerizing a solution of PNIPAM inside a phospholipid giant unilamellar vesicle. The phospholipid membrane, which is compliant and permeable to water, separates the PNIPAM core from the external pure water. The procedure of the preparation of this gel particle is conducted at a constant room temperature T_0 , which is much lower than the volume transition temperature T_{tr} of the PNIPAM gel (Fig. 1a).

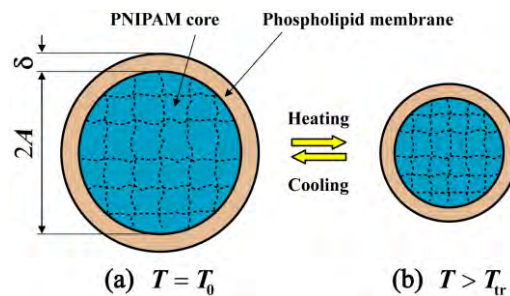


FIGURE 1. A hybrid gel particle

At the instant when the particle has been prepared, the phospholipid membrane is a shell of thickness δ ; meanwhile, the core gel is a sphere with radius A and swells by an isotropic stretch λ_0 relative to its dry network. We assume that the outer surface of the core gel is fully bounded with the inner surface of the membrane. We also assume that the membrane has no physical or chemical

interaction with the solvent and is un-sensitive to temperature but allows the solvent molecules to diffuse freely.

Subsequently, the temperature is allowed to vary. When the temperature is elevated, the hybrid gel particle first shrinks remarkably and then keeps its volume constant at temperatures above the volume transition temperature of PNIPAM gels (Fig. 1b). The process is reversible. When the temperature is cooled back to room temperature again, the hybrid gel particle re-swells and recovers its initial shape. Interestingly, it is observed that during the volume transition, the phospholipid membrane is compliant and is strongly bonded to the PNIPAM core [1]. Compared with a stand-alone PNIPAM microgel, the presence of this elastic membrane in this hybrid gel particle should affect the thermal-responsive behaviour of the PNIPAM core. Thus, an understanding of the effects of the elastic membrane is of great importance, especially when such hybrid gel particles are used in controlled release systems. However, few theoretical analyses exist to account for such effects.

In this paper, we develop a theoretical model to show that the thermal-responsive behaviour of the hybrid gel particle can be altered by changing the material property of the membrane. Here the preparation state (Fig. 1a) is chosen as the reference state. With reference to Figs. 1a and b, an element of the gel particle, which is at distance R from the centre in the reference state, deforms to a position at distance r from the centre in the current state. For simplicity, the deformation of the hybrid particle is taken to retain spherical symmetry, so that the deformation of the structure can be fully specified by the function $r(R)$. Since the membrane is fully bounded with the core gel, the expansion or the shrink of the core gel produces an internal stress distributed uniformly over the interface between the membrane and the core. This internal stress plays a similar rule as that of a hydrostatic stress, so that the deformation field, as well as the solvent concentration, in the core gel is homogeneous. Consequently, the deformation (and hence the solvent concentration) of the core gel is then fully determined by the inner radius of the membrane. For convenience, we introduce superscripts “m” and “c” to distinguish quantities associated with the membrane from those associated with the PNIPAM core. Denote the stretches of the membrane in the radial direction and in the circumferential direction as

$$\lambda_r^m = dr^m/dR^m, \quad \lambda_\theta^m = r^m/R^m. \quad (1)$$

By definition, the deformation gradient of the membrane is

$$\mathbf{F}^m = \begin{bmatrix} \lambda_r^m & & \\ & \lambda_\theta^m & \\ & & \lambda_\theta^m \end{bmatrix}. \quad (2)$$

Here we regard the phospholipid membrane as a layer of rubber-like elastomer, the free-energy density of which takes the classical neo-Hookean form [2]

$$W^m = \frac{1}{2} \mu^m \left[\text{Tr}(\mathbf{C}^m) - 3 - \log \det(\mathbf{C}^m) \right]. \quad (3)$$

Here μ^m is the shear modulus of the membrane, “Tr” stands for trace, and $\mathbf{C}^m = \mathbf{F}^{mT} \mathbf{F}^m$ is the right Cauchy-Green strain tensor, where \mathbf{F}^{mT} is the transpose of the deformation gradient \mathbf{F}^m defined in (2). Define the nominal stress as the work conjugate to the deformation gradient, namely

$$s_r^m = \partial W^m / \partial \lambda_r^m, \quad s_\theta^m = \frac{1}{2} \partial W^m / \partial \lambda_\theta^m. \quad (4)$$

In equilibrium, the two nominal stresses s_r^m and s_θ^m are required to satisfy the condition of mechanical equilibrium

$$\frac{ds_r^m}{dR^m} + 2\frac{s_r^m - s_\theta^m}{R^m} = 0. \quad (5)$$

A combination of the above equations yields the specialized mechanical equilibrium equation

$$\frac{d^2 r^m}{dR^{m2}} \left[\left(\frac{dr^m}{dR^m} \right)^{-2} + 1 \right] + \frac{2}{R^m} \left[\frac{dr^m}{dR^m} - \left(\frac{dr^m}{dR^m} \right)^{-1} - \frac{r^m}{R^m} + \frac{R^m}{r^m} \right] = 0. \quad (6)$$

This equation is a nonlinear second-order differential equation that governs the field of deformation in the membrane, $r^m(R^m)$. Denote the uniform internal stress acting on the interface by P . On the outer surface of the membrane, no mechanical constraint acts, so that the radial stress $s_r^m(A + \delta)$ vanishes and (4) becomes

$$\left[\frac{dr^m}{dR^m} - \left(\frac{dr^m}{dR^m} \right)^{-1} \right]_{R^m=A+\delta} = 0. \quad (7)$$

On the inner surface of the membrane, the radial stress $s_r^m(A)$ equals the uniform stress P , so that (4) now gives

$$\mu^m \left[\frac{dr^m}{dR^m} - \left(\frac{dr^m}{dR^m} \right)^{-1} \right]_{R^m=A} = P. \quad (8)$$

Now let us consider the PNIPAM core. Under the uniform stress P , the PNIPAM core establishes a homogeneous field of stress in equilibrium, $s_r^c = s_\theta^c = P$, which in turn results in a homogenous field of stretch, denoted by λ_h . This homogenous stretch λ_h is equal to the ratio of the radius of the PNIPAM core in current state to that in the reference state, $\lambda_h = r^c(A)/A$. Since the membrane and the core are fully bonded at the interface, the radius of the PNIPAM core should equal the inner radius of the membrane, $r^c(A) = r^m(A)$, which gives

$$\lambda_h = r^m(A)/A. \quad (9)$$

The free-energy function of a uniformly deformed PNIPAM gel takes the form [3]

$$W^c = \frac{\mu^c}{2\lambda_0^3} \left[3\lambda_h^2/\lambda_*^2 - 3 - \log \det(\lambda_h^2/\lambda_*^2) \right], \quad (10)$$

where μ^c is the shear modulus of the PNIPAM gel, λ_0 is the initial stretch of the PNIPAM gel in the reference state. The stretch λ_* is temperature dependent and takes the form $\lambda_* = A(T)/A(T_0)$. Here $A(T)$ is the stretch of a stress-free PNIPAM gel in a state at temperature T relative to that in the state when the volume transition is completed. An empirical formula of $A(T)$ is

$$A(T) = \begin{cases} 1 + \beta(1 - T/T_{tr})^\alpha, & \text{for } T < T_{tr} \\ 1, & \text{for } T \geq T_{tr} \end{cases}. \quad (11)$$

Here $\alpha=0.255$ and $\beta=1.968$, which are obtained by fitting experimental data. Similar to (4), the homogenous stress inside the PNIPAM core is defined as $s^c = \partial W^c / \partial \lambda_h = P$. Using (10) we obtain

$$P = \frac{\mu^c}{\lambda_0^3} \left[\frac{r^m(A)}{A} \frac{A^2(T_0)}{A^2(T)} - \frac{A}{r^m(A)} \right]. \quad (12)$$

Eliminating P from (8) and (12) we finally find

$$\mu^m \left[\frac{dr^m}{dR^m} - \left(\frac{dr^m}{dR^m} \right)^{-1} \right] \Big|_{R^m=A} = \frac{\mu^c}{\lambda_0^3} \left[\frac{r^m(A)}{A} \frac{A^2(T_0)}{A^2(T)} - \frac{A}{r^m(A)} \right]. \quad (13)$$

Equations (7) and (13) determine two boundary conditions for solving the differential equation (6). Once the function $r^m(R^m)$ is solved, the degree of swelling λ_h^3 of the core gel can be determined by (9).

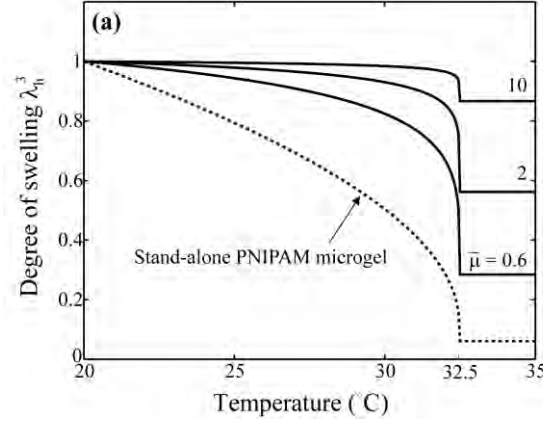


FIGURE 2. Variation of the degree of swelling λ_h^3 with the temperature T

3. RESULTS

Figure 2 plots the variation of the degree of swelling λ_h^3 with the temperature T at several values of the relative elastic modulus $\bar{\mu} = \mu^m / \mu^c$. In plotting this figure, we have set $\mu^c = 10^4$ N/m², $T_0 = 20^\circ$ C, $T_{tr} = 32.5^\circ$ C and $\lambda_0 = 1.3$. As expected, the PNIPAM core shrinks substantially as the temperature rises during the volume transition (i.e., $T < T_{tr}$), but keeps its volume unchanged when the volume transition is complete (i.e., $T \geq T_{tr}$). This trend is in good consistency with experiment observation [1].

4. CONCLUSIONS

In this work, a theoretical model was developed to account for the thermal-controlled swelling process in a hybrid particle based on PNIPAM gels. Our results show that the thermal-responsive behaviour of the hybrid gel particle can be tuned by changing the mechanical properties of the elastic membrane.

REFERENCES

- [1] C.C. Campillo, B. Pepin-Donat and A. Viallat, Responsive viscoelastic giant lipid vesicles filled with a poly(N-isopropylacrylamide) artificial cytoskeleton, *Soft Matter*, 3, 1421-1427, 2007.
- [2] Y. Sawa, K. Urayama, T. Takigawa, A. Desimone and L. Teresi, Thermally driven giant bending of liquid crystal elastomer films with hybrid alignment, *Macromolecules*, 43, 4362-4369, 2010.
- [3] X. Zhao, W. Hong and Z. Suo, Inhomogeneous and anisotropic equilibrium state of a swollen hydrogel containing a hard core, *Applied Physics Letters*, 92, 51903-51904, 2008.

SIMILARITY CRITERIA FOR ONE DIMENSIONAL TRANSIENT WITH THERMO-MECHANICAL INTERACTION

Xiaomin Zhang¹, Long Zhang, Peiyuan Zhang

Department of Engineering Mechanics, Chongqing University, 400044, xiaomin@cqu.edu.cn

ABSTRACT

To counter micro-structure materials has measurable relaxation time and obey C-V non-Fourier law of heat conduction, similarity criteria for one dimensional transient with thermo-mechanical interaction was discussed to provide basis for application of numerical calculation and model experiment result.

Key Words: *Similarity criterion, Thermo-mechanical interaction, Non-Fourier law.*

1. INTRODUCTION

Laminated structures have been used in a large number of structures due to their excellent characteristics, such as heat shield plates and shells made of the laminates. For example, the face sheet are generally made up of the perfect heat resistance solid media, while the cores are lightweight materials, such as honeycombs materials, in order to increase stiffness and strength. There exist the wave propagation with thermo-mechanical interaction in laminated structure under the thermal and/or mechanical shock. For the design calculation, the one dimensional transient with thermo-mechanical interaction would be taken as a model to give the numerical results corresponding to the typical load. Because there is so important engineering background [1-3]. How to spread the achievements to applications would be a valuable works. To counter micro-structure materials that has measurable relaxation time and obey C-V non-Fourier law of heat conduction[4], similarity criteria for one dimensional transient with thermo-mechanical interaction was discussed to provide basis for application of numerical calculation and model experiment result.

2. MAIN BODY

Suppose media in each layer are continuum and transversely isotropic homogeneous materials. Taking ox_3 axis along the thickness direction, and the coordinate plane x_1, x_2 is the transversely isotropic plane. Thus the constitutive equation and heat conductivity laws in each sheet are given as :

$$\sigma_{11} = a_{1111}\epsilon_{11} + a_{1122}\epsilon_{22} + a_{1133}\epsilon_{33} - \beta_{11}\theta, \quad \sigma_{12} = \sigma_{21} = 2a_{1212}\epsilon_{12} \quad (1.1)$$

$$\sigma_{22} = a_{1122}\epsilon_{11} + a_{1111}\epsilon_{22} + a_{1133}\epsilon_{33} - \beta_{11}\theta, \quad \sigma_{23} = \sigma_{32} = 2a_{1313}\epsilon_{23} \quad (1.2)$$

$$\sigma_{33} = a_{1133}\epsilon_{11} + a_{1133}\epsilon_{22} + a_{3333}\epsilon_{33} - \beta_{33}\theta, \quad \sigma_{31} = \sigma_{13} = 2a_{1313}\epsilon_{13} \quad (1.3)$$

$$q_1^{(e)} + t_{01}^{(e)}\dot{q}_1 = -k_1\theta_{,1}, \quad q_2 + t_{01}\dot{q}_2 = -k_1\theta_{,2}, \quad q_3 + t_{03}\dot{q}_3 = -k_3\theta_{,3} \quad (2)$$

Here, the partial derivative available are introduced, for example $\theta_{,2} = \partial\theta/\partial x_2$, $\dot{q}_3 = \partial q_3/\partial t$ and $\sigma_{ji}, \epsilon_{ji}, \theta_{,j}, q_j, \theta$ are the stress, strain, temperature gradient, heat flux vector components and the temperature increase, respectively. The θ is the increase of update temperature T relative to the uniform reference temperature T_0 , namely, $T = T_0 + \theta \geq 0$. β_{11}, β_{33} are the temperature coefficient of the stress. $a_{1111}, a_{1122}, a_{1133}, a_{3333}, a_{1212}, a_{1313}$ are the five independent components of elastic

constants, some of them satisfied with the following relationship $a_{1111} - a_{1122} = 2a_{1212}$. There is measurable relaxation time in micro-structure materials that reach several seconds for some porous media. In accordance with this phenomenon the C-V type non-Fourier heat transfer law(2) has been introduced [4]. The equivalent quantities t_{01} and t_{03} are relaxation times. If the equivalent relaxation times is equal to zero, k_1 , k_3 will become two independent Fourier coefficients. The eq. (1-2) have to be taken are the equivalent constitutive equation of the continuum model to describe the laminated structure with the core cellular materials. Here, 11 equivalent constants are involved. Different sub-layer has different ones. In condition of one dimensional deformation and heat conduction along the thickness direction, $q_1 = q_2 = 0$, $\varepsilon_{22} = \varepsilon_{33} = \varepsilon_{12} = \varepsilon_{23} = \varepsilon_{31} = 0$, hence, $\sigma_{12} = \sigma_{23} = \sigma_{31} = 0$, equation (1, 2) can be simplified as the following:

$$\sigma_{11} = a_{1133}\varepsilon_{33} - \beta_{11}\theta, \sigma_{22} = a_{1133}\varepsilon_{33} - \beta_{11}\theta, \sigma_{33} = a_{3333}\varepsilon_{33} - \beta_{33}\theta \quad (3)$$

$$q_3 + t_{03}\dot{q}_3 = -k_3\theta_3 \quad (4)$$

Considering the geometric equations, momentum equations and thermal equilibrium equation^[5], the partial differential equations can be given with the strain ε_{33} and the temperature increase θ :

$$0 \leq x \leq l, \quad 0 \leq t < \Delta t:$$

$$\frac{a_{3333}}{\rho} \frac{\partial^2 \varepsilon_{33}(x,t)}{\partial x^2} - \frac{\partial^2 \varepsilon_{33}(x,t)}{\partial t^2} - \frac{\beta_{33}}{\rho} \frac{\partial^2 \theta(x,t)}{\partial x^2} + \frac{\partial f_3(x,t)}{\partial x} = 0 \quad (5)$$

$$\frac{T\beta_{33}}{\rho C} \left[\frac{\partial^2 \varepsilon_{33}(x,t)}{\partial t^2} + \frac{1}{t_{03}} \frac{\partial \varepsilon_{33}(x,t)}{\partial t} \right] + \frac{\partial^2 \theta(x,t)}{\partial t^2} + \frac{1}{t_{03}} \frac{\partial \theta(x,t)}{\partial t} - \frac{k_3}{\rho C t_{03}} \frac{\partial^2 \theta(x,t)}{\partial x^2} - \frac{1}{\rho C} \left[\frac{\partial R(x,t)}{\partial t} + \frac{1}{t_{03}} R(x,t) \right] = 0 \quad (6)$$

Where $f_3(x,t)$ and $R(x,t)$ are body force component and the intensity of body heat source, respectively, ρ , C are the density and the specific heat per mass measured in the state of constant strain. Using eqs.(8, 9), $\varepsilon_{33}(x,t)$ and $\theta(x,t)$ can be calculated out. Then taken them into eq. (3), the stress components σ_{33} , $\sigma_{11}(=\sigma_{22})$ can be derived. Here the spread interval size l and spread duration time Δt are introduced, combined with the parameters a_{3333} , a_{1133} , β_3 , β_1 , k_3 , ρ , C , t_{03} and T_0 , the one-dimensional thermal mechanical interaction model with C-V type non-Fourier heat transfer medium can be constituted to seek the unknown functions $\varepsilon_{33}(x,t)$ and $\theta(x,t)$.

3. RESULTS

Suppose the model B_m is similar with model B in geometric, and they are C-V type non-Fourier heat conduction medium. Moreover, one dimensional transient with thermo-mechanical interaction has taken place on them, respectively. Two groups parameters $a_{3333}^{(m)}$, $a_{1133}^{(m)}$, $\beta_{11}^{(m)}$, $\beta_{33}^{(m)}$, $\rho^{(m)}$, $C^{(m)}$, $k^{(m)}$, $T_0^{(m)}$, $t_0^{(m)}$, $\Delta t^{(m)}$, $l^{(m)}$ and a_{3333} , a_{1133} , β_{11} , β_{33} , ρ , C , k , T_0 , t_0 , Δt , l have been taken to describe them. For introduced both the double 11 parameters, the functions ε_{33} , θ , displacement u_3 , two quantities f_3 , R , variables x and t , the 16 similarity ratios can be defined as follows:

$$\alpha_l = x/x^{(m)} = l/l^{(m)}, \quad \alpha_t = t/t^{(m)} = \Delta t/\Delta t^{(m)}, \quad \alpha_f = f_3/f_3^{(m)}, \quad \alpha_R = R/R^{(m)}, \quad \alpha_\varepsilon = \varepsilon_{33}/\varepsilon_{33}^{(m)}, \quad \alpha_\theta = \theta/\theta^{(m)},$$

$$\alpha_{a3} = a_{3333}/a_{3333}^{(m)}, \quad \alpha_{\beta3} = \beta_{33}/\beta_{33}^{(m)}, \quad \alpha_\rho = \rho/\rho^{(m)}, \quad \alpha_C = C/C^{(m)}, \quad \alpha_k = k/k^{(m)}, \quad \alpha_T = T_0/T_0^{(m)}, \quad \alpha_{t0} = t_0/t_0^{(m)} \quad (7)$$

and

$$\alpha_u = u/u^{(m)}, \quad \alpha_{a1} = a_{1133}/a_{1133}^{(m)}, \quad \alpha_{\beta1} = \beta_{11}/\beta_{11}^{(m)} \quad (8)$$

Here, the 16 similarity ratios are divided into two groups. 13 similarity ratios listed in eq. (7) are related to the control eq. (5, 6), 3 similarity ratios listed in eq.(8) are related to $u_3, \sigma_{11}, \sigma_{22}$. Considering the eq. (7), the eq. (5, 6) can be expressed by the physical quantities of model B_m ,

$$0 \leq x^{(m)} \leq l^{(m)}, \quad 0 \leq t^{(m)} < \Delta t^{(m)} :$$

$$\frac{\alpha_{a3} \alpha_\varepsilon}{\alpha_\rho \alpha_l^2} \frac{a_{3333}^{(m)}}{\rho^{(m)}} \frac{\partial^2 \varepsilon_{33}^{(m)}(x^{(m)}, t^{(m)})}{\partial x^{(m)} \partial x^{(m)}} - \frac{\alpha_\varepsilon}{\alpha_t^2} \frac{\partial^2 \varepsilon_{33}^{(m)}(x^{(m)}, t^{(m)})}{\partial t^{(m)} \partial t^{(m)}} - \frac{\alpha_{\beta 3} \alpha_\theta}{\alpha_\rho \alpha_l^2} \frac{\beta_{33}^{(m)}}{\rho^{(m)}} \frac{\partial^2 \theta^{(m)}(x^{(m)}, t^{(m)})}{\partial x^{(m)} \partial x^{(m)}} + \frac{\alpha_f}{\alpha_l} \frac{\partial f_3^{(m)}(x^{(m)}, t^{(m)})}{\partial x^{(m)}} = 0 \quad (9)$$

$$\frac{\alpha_r \alpha_{\beta 3} \alpha_\varepsilon}{\alpha_\rho \alpha_c \alpha_l^2} \frac{T^{(m)} \beta_{33}^{(m)}}{\rho^{(m)} C^{(m)}} \left[\frac{\partial^2 \varepsilon_{33}^{(m)}(x^{(m)}, t^{(m)})}{\partial t^{(m)} \partial t^{(m)}} + \frac{\alpha_l}{\alpha_{t_0}} \frac{1}{t_{03}^{(m)}} \frac{\partial \varepsilon_{33}^{(m)}(x^{(m)}, t^{(m)})}{\partial t^{(m)}} \right] + \frac{\alpha_\theta}{\alpha_l^2} \left[\frac{\partial^2 \theta^{(m)}(x^{(m)}, t^{(m)})}{\partial t^{(m)} \partial t^{(m)}} + \frac{\alpha_l}{\alpha_{t_0}} \frac{1}{t_{03}^{(m)}} \frac{\partial \theta^{(m)}(x^{(m)}, t^{(m)})}{\partial t^{(m)}} \right] - \frac{\alpha_k \alpha_\theta}{\alpha_\rho \alpha_c \alpha_{t_0} \alpha_l^2} \frac{k_3^{(m)}}{\rho^{(m)} C^{(m)} t_{03}^{(m)}} \frac{\partial^2 \theta^{(m)}(x^{(m)}, t^{(m)})}{\partial x^{(m)} \partial x^{(m)}} - \frac{\alpha_R}{\alpha_\rho \alpha_c \alpha_l} \frac{1}{\rho^{(m)} C^{(m)}} \left[\frac{\partial R^{(m)}(x^{(m)}, t^{(m)})}{\partial t^{(m)}} + \frac{\alpha_l}{\alpha_{t_0}} \frac{1}{t_{03}^{(m)}} R^{(m)}(x^{(m)}, t^{(m)}) \right] = 0 \quad (10)$$

For the model body B_m , the same equations like as eq. (5, 6) should also be satisfied, namely,

$$0 \leq x^{(m)} \leq l^{(m)}, \quad 0 \leq t^{(m)} < \Delta t^{(m)} :$$

$$\frac{a_{3333}^{(m)}}{\rho^{(m)}} \frac{\partial^2 \varepsilon_{33}^{(m)}(x^{(m)}, t^{(m)})}{\partial x^{(m)} \partial x^{(m)}} - \frac{\partial^2 \varepsilon_{33}^{(m)}(x^{(m)}, t^{(m)})}{\partial t^{(m)} \partial t^{(m)}} - \frac{\beta_{33}^{(m)}}{\rho^{(m)}} \frac{\partial^2 \theta^{(m)}(x^{(m)}, t^{(m)})}{\partial x^{(m)} \partial x^{(m)}} + \frac{\partial f_3^{(m)}(x^{(m)}, t^{(m)})}{\partial x^{(m)}} = 0 \quad (11)$$

$$\frac{T^{(m)} \beta_{33}^{(m)}}{\rho^{(m)} C^{(m)}} \left[\frac{\partial^2 \varepsilon_{33}^{(m)}(x^{(m)}, t^{(m)})}{\partial t^{(m)} \partial t^{(m)}} + \frac{1}{t_{03}^{(m)}} \frac{\partial \varepsilon_{33}^{(m)}(x^{(m)}, t^{(m)})}{\partial t^{(m)}} \right] + \left[\frac{\partial^2 \theta^{(m)}(x^{(m)}, t^{(m)})}{\partial t^{(m)} \partial t^{(m)}} + \frac{1}{t_{03}^{(m)}} \frac{\partial \theta^{(m)}(x^{(m)}, t^{(m)})}{\partial t^{(m)}} \right] - \frac{k_3^{(m)}}{\rho^{(m)} C^{(m)} t_{03}^{(m)}} \frac{\partial^2 \theta^{(m)}(x^{(m)}, t^{(m)})}{\partial x^{(m)} \partial x^{(m)}} - \frac{1}{\rho^{(m)} C^{(m)}} \left[\frac{\partial R^{(m)}(x^{(m)}, t^{(m)})}{\partial t^{(m)}} + \frac{1}{t_{03}^{(m)}} R^{(m)}(x^{(m)}, t^{(m)}) \right] = 0 \quad (12)$$

Comparing eq. (11, 12) with eq. (9, 10), the normalized conditions will be given by:

$$\frac{\alpha_{a3} \alpha_l^2}{\alpha_\rho \alpha_l^2} = 1, \quad \frac{\alpha_{\beta 3} \alpha_\theta \alpha_l^2}{\alpha_\rho \alpha_l^2 \alpha_\varepsilon} = 1, \quad \frac{\alpha_l^2 \alpha_f}{\alpha_l \alpha_\varepsilon} = 1, \quad \frac{\alpha_r \alpha_{\beta 3} \alpha_\varepsilon}{\alpha_\rho \alpha_c \alpha_\theta} = 1, \quad \frac{\alpha_l}{\alpha_{t_0}} = 1, \quad \frac{\alpha_k \alpha_l^2}{\alpha_\rho \alpha_c \alpha_{t_0} \alpha_l^2} = 1, \quad \frac{\alpha_R \alpha_l}{\alpha_\rho \alpha_c \alpha_\theta} = 1 \quad (13)$$

According to the 5th formula in (13), the following can be obtained:

$$\alpha_l = \alpha_{t_0} \quad \text{OR} \quad t_{03} / \Delta t = t_{03}^{(m)} / \Delta t^{(m)} \quad (14)$$

For the body B , the following parameters can be introduced

$$V_1 = \sqrt{a_{3333} / \rho}, \quad V_2 = \sqrt{k_3 / \rho C t_{03}}, \quad V_\beta = \sqrt{\beta_{33} T_0 / \rho^2 C} \quad (15)$$

Where V_1 and V_2 represent the propagation speed of the simplex one dimension elastic longitudinal wave and the simplex heat waves along the thickness direction, respectively. V_β is the speed dimensional physical quantity relating to the degree of thermal-mechanical interaction. The "simplex" refers to the eq. (15) is derived in absence of thermal-mechanical coupling. Four non-dimensional quantities are defined as:

$$S_0 = t_{03}/\Delta t, \quad S_1 = \frac{V_1^2}{(l/\Delta t)^2}, \quad S_2 = \frac{V_2}{l/t_{03}} \frac{V_2}{l/\Delta t}, \quad S_\beta = \frac{V_\beta^2}{(l/\Delta t)^2} \quad (16)$$

Analogously, for the body B_m , the parameters $V_1^{(m)}, V_2^{(m)}, V_\beta^{(m)}$ and non dimensional quantity $S_0^{(m)}, S_1^{(m)}, S_2^{(m)}, S_\beta^{(m)}$ are introduced. According to the normalization conditions (13), the similarity criterions can be conducted from the formula (13):

$$S_1 = S_1^{(m)}, \quad S_2 = S_2^{(m)}, \quad S_\beta = S_\beta^{(m)} \quad (17)$$

The 4th similarity criterion can be conducted from eq. (14),

$$S_0 = S_0^{(m)} \quad (18)$$

According to the conditions (13), the similarity conditions of body force and body heat source, and the relationship between similarity ratios of field components u_3, ε_{33} and θ are both obtained:

$$\frac{\alpha_f}{\alpha_\varepsilon} = \frac{\alpha_l}{\alpha_t^2}, \quad \frac{\alpha_R}{\alpha_\theta} = \frac{\alpha_\rho \alpha_C}{\alpha_l} \quad (19)$$

$$\frac{\alpha_\theta}{\alpha_\varepsilon} = \frac{\alpha_T \alpha_{\beta 3}}{\alpha_\rho \alpha_C} = \frac{\alpha_\rho \alpha_l^2}{\alpha_{\beta 3} \alpha_t^2}, \quad \frac{\alpha_u}{\alpha_\varepsilon} = \alpha_l \quad (20)$$

Here the geometric equation $\varepsilon_{33} = u_{3,3}$ has been used.

4. CONCLUSIONS

The necessary conditions of the similarity between two phenomenons with thermal mechanical interaction for one-dimensional propagation is that the 4 non-dimensional quantities S_0, S_1, S_2, S_β should be equal, respectively. Strictly speaking, it is a set of rigor conditions, since phenomena of one dimensional transient with thermo-mechanical interaction should be contained in these criterions. While if to preserve S_1, S_β only, i.e. to abandon the criterions S_0, S_2 , the similarity criterions will suite to the macro-scale thermal mechanical interaction, and it will be satisfied easily to some extend in practice.

REFERENCES

- [1] Q.H. Qin and T.J. Wang, A theoretical analysis of the dynamic response of metallic sandwich beam under impulsive loading, *Eur J Mech/Solids*, 28, 1014-25, 2009.
- [2] Y. Frostig and O.T. Thomsen, Non-linear thermal response of sandwich panels with a flexible core and temperature dependent mechanical properties, *Composites Part B*, 39(1), 165-184, 2008.
- [3] X.M. Zhang, X.H. Peng and P.Y. Zhang, Theory of couple stresses of temperature gradient medium---thermal mismatch of multiphase solid mixture, *Chinese Journal of Applied Mechanics*, 25(3), 361-365, 2008.
- [4] K.K.Tamman and X.M. Zhou, Macroscale and Microscale Thermal Transport and Thermo-Mechanical Interactions: Some Noteworthy Perspectives, *Journal of Thermal Stresses*, 21, 405-449, 1998.
- [5] Y.C. Fung, *Foundations of Solid Mechanics*, PRENTICE HALL.INC, 404-405, 1965.

NUMERICAL SIMULATION FOR THERMAL SHOCK RESISTANCE OF THERMAL PROTECTION MATERIALS CONSIDERING DIFFERENT CAUSATIVE ENVIRONMENTS

Weiguo Li, Dingyu Li, Ruzhuan Wang

College of Resource and Environment Science of Chongqing University, Chongqing 400030, China
wgli@cqu.edu.cn, lidingyu@cqu.edu.cn, wrz@cqu.edu.cn

Daining Fang

LTCS and College of Engineering of Peking University, Beijing 100871, China,
fangdn@pku.edu.cn

ABSTRACT

Based on the sensitivities of material properties to temperature and the complexity of service environment of thermal protection system on the spacecraft, ultra-high-temperature ceramics (UHTCs), which are used as thermal protection materials, cannot simply consider thermal shock resistance (TSR) of the material its own, but need to take the external constraint conditions and the thermal environment into full account. Through a numerical simulation on hafnium diboride (HfB_2), a detailed study of the effects of the different external constraints and thermal environments on the TSR of UHTC had been made. This study can provide a more intuitively understanding of the evolution of the TSR of UHTCs during actual operation conditions.

Key Words: *Ultra-high-temperature ceramics, thermal shock resistance, thermal environment, numerical simulation, constraint.*

1. INTRODUCTION

Ultra-high-temperature ceramics (UHTCs) is a family of materials that have melting points higher than 3000°C , and can be potentially used at temperatures above 2000°C in an oxidizing environment. As important ceramics and promising candidates for high temperature applications of thermal protection systems (TPS), UHTCs are attracting growing attention.

Current research shows that thermal shock resistance (TSR) of ceramic materials is poor because of their inherent brittleness. Thermal shock is the cause of damage of ceramic materials [1]. The TSR performance of ceramic materials depends on the mechanical properties and thermal properties of the materials [1,2]. Moreover, the effects of the geometry of components and environmental media are also very important points because the properties of the materials are sensitive to the temperatures and the complex thermal environments experienced by the spacecraft surface. At present, the research of TSR mostly focuses on experimental way [2-3]. And several evaluation theories of TSR have been reported [1,4,5]. Moreover, Song etc. enhanced thermal shock resistance of ceramics through biomimetically inspired nanofins which had proved to be a very effective way [6]. However, few experiments have considered the influences of temperature of the cooling medium and the different external constraint conditions as they are difficult to conduct. And the current experiment is difficult to simulate the thermal environment and external constraint conditions suffered by the UHTCs in the actual operation and difficult to reveal the changes of the TSR of the thermal protection materials in the operating process. Moreover, such experiments cannot meet the demand of the comprehensively understanding of the TSR of materials.

Thus hafnium diboride (HfB_2) is used to study the effects of the external constraint conditions and different thermal environment on the TSR of the UHTC in detail through numerical simulation. The

study provides a more comprehensive understanding of the changes of TSR in the course of the entire service of the material. Furthermore, this paper provides some possible ways for the application design, improving the TSR and reliability of the thermal protection materials.

2. FINITE ELEMENT ANALYSIS MODEL

In order to simulate the effects of different external constraint conditions on the TSR performance of the UHTC thermal protection materials, the geometric model and the finite element mesh are employed, as shown in Figure 1. Assumed that, 1) the UHTC material is isotropic; 2) there is no initial stress in the material at thermal shock initial temperature; 3) The connection between the UHTC material and the external constraints (the frame) is perfect; 4) The temperature of the external constraint (the frame) is constant.

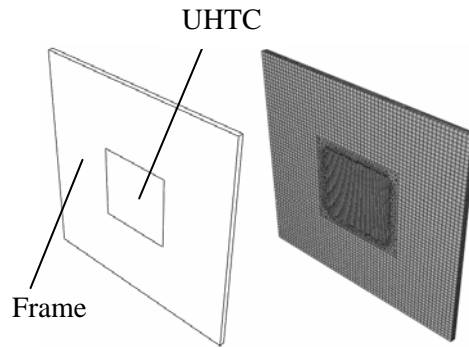


FIGURE 1. Geometric model and the finite element mesh

Hafnium diboride (HfB_2) is used for simulation example with material properties [5,7,8] shown in Table 1.

Material parameters	Values and expressions
T_m (°C)	3400
E (GPa)	$E = E_0 - BT e^{-\frac{T_m}{T}} + B_1 (T - B_2 T_m + T - B_2 T_m) e^{-\frac{T_m}{T}}$
E_0 (GPa), B_0 , B_1 , B_2	441, 2.54, 1.9, 0.363
α (°C ⁻¹)	$(2\ln(T)-5) \times 10^{-6}$
k (W·(m·°C) ⁻¹)	$-8.3455 \times \ln(T) + 127.68$
ν	0.12
$C_p(T)$ (cal/mol)	$73.346 + 7.824 \times 10^{-3}T - 2.301 \times 10^{-6}T^2$
ρ (g·cm ⁻³)	10.5

TABLE 1. Temperature-dependent material properties of HfB_2

3. RESULTS AND DISCUSSION

Tensile stress is formed at the surface of ceramic materials during the cooling process, which is more dangerous than the heating process. Therefore, this paper takes the calculation of cooling process as a model for analysis. Single-sided cooling of the UHTC plate in various cooling rates with different constraint conditions (corresponding to different frame material's Young's modulus) and thermal shock initial temperatures are also simulated.

Figure 2 shows that, in the same constraint, the critical fracture temperature difference that UHTCs can withstand rapidly decreases initially and slowly rises as the cooling rate increases. Therefore, there is a dangerous zone of cooling rate where the TSR is lowest when the cooling rate is relatively minor. From this result, the previous conclusion, that the higher the cooling rates the smaller the critical temperature difference that the material can withstand, is considered one-sided. This is due to restrictions of experimental methods. Experiments cannot reproduce the whole real and complex processes of thermal shock that the thermal protection materials suffered during the causative processes. The common experimental methods are also so simple and harsh that the understanding of TSR of materials is extremely one-sided. This is especially true for the UHTC thermal protection materials, which suffer from a wide and drastic temperature change. In addition, it can be seen from the figure that either the higher or the lower thermal shock initial temperature corresponds to the higher critical temperature.

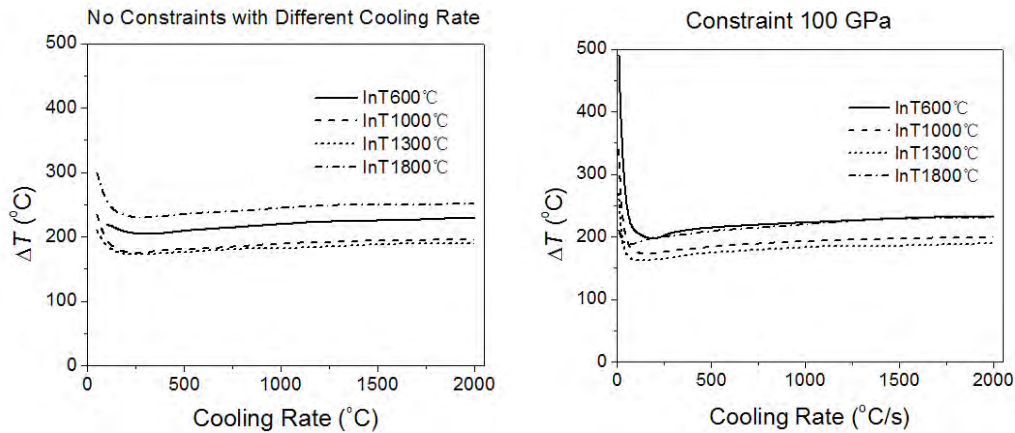


FIGURE 2. Relationship between critical fracture temperature ΔT corresponding to different thermal shock initial temperature (in the figure is $\ln T$) and cooling rate

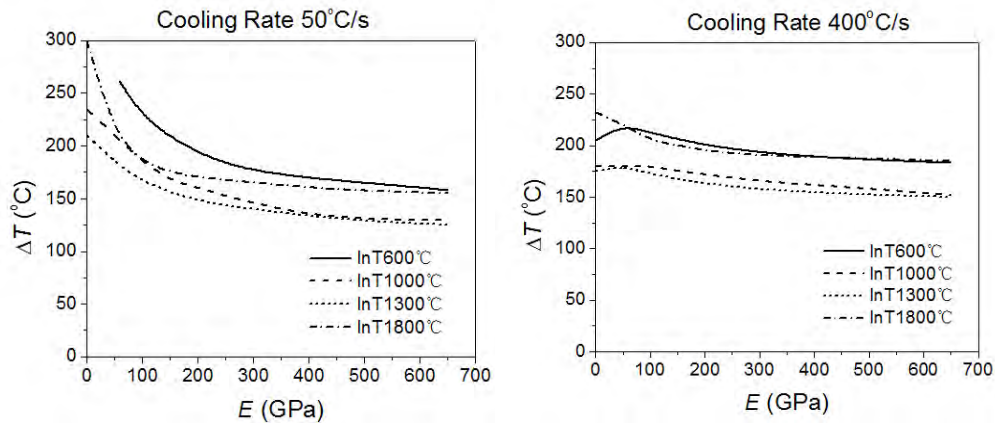


FIGURE 3. Relationship between critical fracture temperature corresponding to different thermal shock initial temperature with the same cooling rate and the Young's modulus of constraint material

As the figure 3 shows, when the cooling rate is 50 °C/s, the critical fracture temperature difference of the material corresponding to the same initial temperature of thermal shock decreases monotonically as the external constraints are enhanced. While the cooling rate is high, with the enhancement of external constraints, the critical fracture temperature difference of the material initially increases and then decreases. Moreover, if some certain constraints are imposed upon the materials, the materials can withstand the more critical fracture temperature difference. And the critical fracture temperature difference is sensitive to external constraints when these constraints are small; however, with the increase of external constraints, the sensitivity decreases rapidly. The

lower the cooling rate, the more sensitive the critical fracture temperature difference is to the changes of external constraints. From these results, the reasonable adjustments to the connections between the thermal protection materials and the main structure in the corresponding causative environment can significantly improve the TSR of the thermal protection materials.

4. CONCLUSIONS

A reasonable finite element model was established by considering the factors of external constraints and thermal environment in this paper. The result shows that when considering the external constraints and the thermal environment, the TSR of UHTC thermal protection materials is no longer the TSR of the material its own. There is a dangerous zone of cooling rate where the TSR is lowest when certain constraints are applied upon the material. The critical fracture temperature difference is sensitive to external constraints when the constraints are small, however, with the increase of the external constraints, the sensitivity decreases rapidly. In addition, in the role of external constraints, when the temperature change rate reaches a certain value, the higher the temperature change rate, the greater the critical fracture temperature difference. That is to say reasonable adjustments in the connections between the thermal protection materials and the main structures can significantly improve the TSR of thermal protection materials, which provides new ideas for structural optimization.

ACKNOWLEDGMENTS

The authors are grateful for support from the National Natural Science Foundation of China under grants Nos. 10702035, 90916009 and 90505015.

REFERENCES

- [1] W.D. Kingery, Factors affecting thermal stress resistance of ceramic materials, *Journal of the American Ceramic Society*, 38, 3-15, 1955.
- [2] J.C. Han and B.L. Wang, Thermal shock resistance of ceramics with temperature-dependent material properties at elevated temperature, *Acta Material*, 59, 1373-82, 2011.
- [3] S.H. Meng, H. Jin, J. An, G.H. Bai and W.H. Xie, Mechanism analysis of thermal shock properties for ZrB₂-20%SiCp-10%AlN ultra-high temperature ceramic with the surface defects, *Solid State Sciences*, 12, 1667-71. 2010.
- [4] D.P.H. Hasselman, Unified theory of thermal shock fracture initiation and crack propagation in brittle ceramics, *Journal of the American Ceramic Society*, 52, 600-4, 1969.
- [5] W.G. Li, F. Yang and D.N. Fang, Thermal shock Modeling of Ultra-High Temperature Ceramics under active cooling. *Computers and Mathematics with Application*, 58, 2373-8. 2009.
- [6] F. Song, S.H. Meng, X.H. Xu and Y.F. Shao, Enhanced Thermal Shock Resistance of Ceramics through Biomimetically Inspired Nanofins. *Physical Review Letters*, 104, 125502, 2010.
- [7] M.M. Opeka, I.G. Talmy, E.J. Wuchina, J.A. Zaykoski and S.J. Causey, Mechanical, thermal, and oxidation properties of refractory hafnium and zirconium compounds. *Journal of the European Ceramic Society*, 19, 2405-14, 1999.
- [8] E.J. Wuchina, M.M. Opeka, S. Causey, J. Spain, A. Cull, J. Routbort and F. Guitierrez-Mora, Designing for ultrahigh-temperature applications: The mechanical and thermal properties of HfB₂, HfCx, HfNx and aHf(N). *Journal of Materials Science*, 39, 5939-49, 2004.

THE THERMAL POWER AROUND A BLUNT CRACK IN ELLIPTICAL INHOMOGENEITY UNDER ELECTRIC LOADS AT INFINITY

Haopeng Song, Cunfa Gao

College of Aerospace Engineering, Nanjing University of Aeronautics & Astronautics, Nanjing
210016, China, shp305@163.com

ABSTRACT

The thermal power around a blunt crack in elliptical inhomogeneity under electric loads at infinity is dealt with. Utilizing the Muskhelishvili complex variable method, the closed form solutions are derived. The results show that the thermal power concentrate is more severe in the crack tip when the inhomogeneity became larger. However, the thermal power decreases with the increase of the distance and the angle.

Key Words: *thermal power, interfacial blunt crack.*

1. INTRODUCTION

Many facilities, in which accidents and failures caused by thermal environments and thermal loading conditions play a fatal role in the assurance of safety, stimulate the subject of thermal fracture analysis of structural components to develop at an ever higher rate [1-3]. In the area of plane thermoelasticity, basic singular solutions have been developed for an infinite medium, a semi-infinite medium, a crack in an infinite medium and other kinds of geometries under the effect of a point thermal inclusion or a point heat source [4-5].

When electric loads are applied to a conductor which there are cracks inside, the current concentrate occurs, meanwhile the corresponding thermal power concentrate would produce thermal stress, change the microstructure of the material and even leads to material failure.

Hence, the thermal effect around a blunt crack in elliptical inhomogeneity under electric loads at infinity is discussed in this paper. The closed form solutions are derived, and the thermal power concentrate is discussed in detail.

2. SOLUTION

Consider an infinite matrix with electroelastic modulus $\mathbf{M}_2 = \begin{bmatrix} C_{44}^2 & e_{15}^2 \\ e_{15}^2 & -d_{11}^2 \end{bmatrix}$ containing an elliptical

cylindrical inhomogeneity with electroelastic modulus $\mathbf{M}_1 = \begin{bmatrix} C_{44}^1 & e_{15}^1 \\ e_{15}^1 & -d_{11}^1 \end{bmatrix}$ with a confocal elliptical

hole. The two materials are assumed to be perfectly bonded along the interface, the elliptical hole surfaces are considered traction-free.

The transform function

$$z = \omega(\zeta) = \frac{c}{2} \left(R\zeta + \frac{1}{R\zeta} \right), \quad \zeta = G(z) = \frac{z}{Rc} \left\{ 1 + \left[1 - \left(\frac{c}{z} \right)^2 \right]^{\frac{1}{2}} \right\} \quad (1)$$

which can map the elliptic contours $x^2/a^2 + y^2/b^2 = 1$ and $x^2/a_1^2 + y^2/b_1^2 = 1$ in the z -plane on to the circles $|\zeta|=1$ and $|\zeta|=R/r$ in the ζ -plane (Fig. 1). Here $R = \sqrt{(a+b)/(a-b)}$, $r = \sqrt{(a_1+b_1)/(a_1-b_1)}$, $c = \sqrt{a^2-b^2} = \sqrt{a_1^2-b_1^2}$, and a and b are, respectively, the lengths of the major semi-axis and minor semi-axis of the elliptical inhomogeneity, a_1 and b_1 are, respectively, the lengths of the major semi-axis and minor semi-axis of the elliptical hole.

Under the action of the remote applied loadings Γ , the complex potential in the ζ -plane can be obtained as

$$\frac{df_1(\zeta)}{d\zeta} = \mathbf{N}^{-1}cR^3\Gamma - \frac{\mathbf{N}^{-1}cRr^2\bar{\Gamma}}{\zeta^2} \quad (2)$$

$$\frac{df_2(\zeta)}{d\zeta} = \frac{cR}{2}\Gamma - \frac{(\mathbf{M}_2\mathbf{M}_1^{-1} + \mathbf{I})\mathbf{N}^{-1}cRr^2\bar{\Gamma}}{2\zeta^2} - \frac{(\mathbf{M}_2\mathbf{M}_1^{-1} - \mathbf{I})\mathbf{N}^{-1}cR^3\bar{\Gamma}}{2\zeta^2} \quad (3)$$

where $\mathbf{N}^{-1} = (\mathbf{M}_2\mathbf{M}_1^{-1} + \mathbf{I})R^2 + (\mathbf{M}_2\mathbf{M}_1^{-1} - \mathbf{I})r^2$, $\Gamma = -i \begin{bmatrix} \sigma_{yz}^\infty \\ D_y^\infty \end{bmatrix}$.

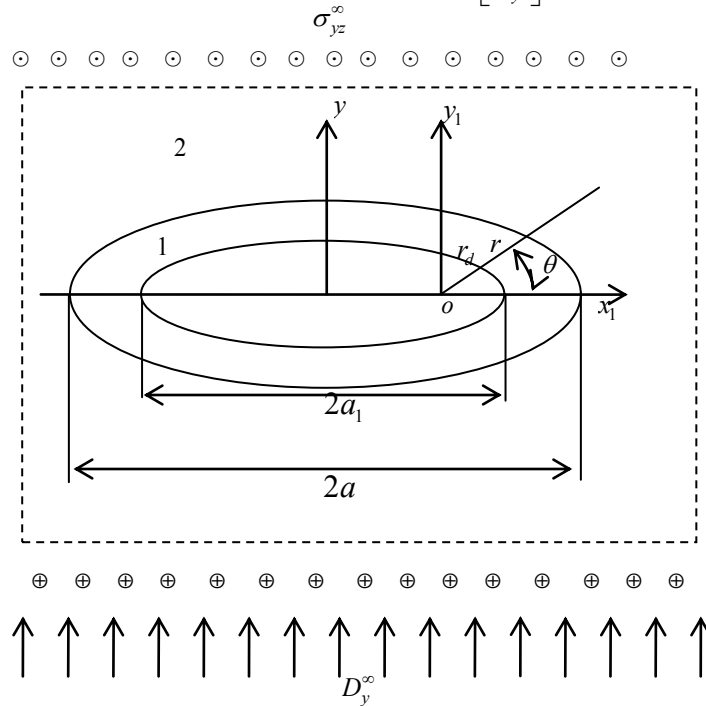


FIGURE 1. The blunt crack in elliptical inhomogeneity

From Eqs. (1)- (2), the complex potential in the z -plane can be derived.

$$\frac{df_1(z)}{d\zeta} = \mathbf{N}^{-1}cR^3\Gamma - \frac{\mathbf{N}^{-1}cRr^2\bar{\Gamma}}{G^2(z)} \quad (4)$$

$$\frac{df_2(z)}{d\zeta} = \frac{cR}{2}\Gamma - \frac{(\mathbf{M}_2\mathbf{M}_1^{-1} + \mathbf{I})\mathbf{N}^{-1}cRr^2\bar{\Gamma}}{2G^2(z)} - \frac{(\mathbf{M}_2\mathbf{M}_1^{-1} - \mathbf{I})\mathbf{N}^{-1}cR^3\bar{\Gamma}}{2G^2(z)} \quad (5)$$

The total stress fields and electric displacements produced by the remote applied loadings are

$$\begin{bmatrix} \sigma_{xz1} - i\sigma_{yz1} \\ D_{x1} - iD_{y1} \end{bmatrix} = \frac{d\mathbf{f}_1(z)}{dz} = \frac{d\mathbf{f}_1(z)}{d\zeta} \frac{d\zeta}{dz} = \frac{z + \sqrt{z^2 - c^2}}{Rc\sqrt{z^2 - c^2}} \left[\mathbf{N}^{-1}cR^3\mathbf{\Gamma} - \frac{\mathbf{N}^{-1}cRr^2\bar{\mathbf{\Gamma}}}{G^2(z)} \right] \quad (6)$$

$$\begin{aligned} \begin{bmatrix} \sigma_{xz2} - i\sigma_{yz2} \\ D_{x2} - iD_{y2} \end{bmatrix} &= \frac{d\mathbf{f}_2(z)}{dz} = \frac{d\mathbf{f}_2(z)}{d\zeta} \frac{d\zeta}{dz} \\ &= \frac{z + \sqrt{z^2 - c^2}}{Rc\sqrt{z^2 - c^2}} \left[\frac{cR}{2} \mathbf{\Gamma} - \frac{(\mathbf{M}_2\mathbf{M}_1^{-1} + \mathbf{I})\mathbf{N}^{-1}cRr^2\bar{\mathbf{\Gamma}}}{2G^2(z)} - \frac{(\mathbf{M}_2\mathbf{M}_1^{-1} - \mathbf{I})\mathbf{N}^{-1}cR^3\bar{\mathbf{\Gamma}}}{2G^2(z)} \right] \end{aligned} \quad (7)$$

The current density around the blunt crack can be expressed as

$$J_{x1} - iJ_{y1} = \frac{\gamma_1}{d_{11}^1} (D_{x1} - iD_{y1}) = \frac{\gamma_1}{d_{11}^1} \frac{z + \sqrt{z^2 - c^2}}{Rc\sqrt{z^2 - c^2}} \begin{bmatrix} 0 \\ 1 \end{bmatrix}^T \left[\mathbf{N}^{-1}cR^3\mathbf{\Gamma} - \frac{\mathbf{N}^{-1}cRr^2\bar{\mathbf{\Gamma}}}{G^2(z)} \right] \quad (8)$$

$$\begin{aligned} J_{x2} - iJ_{y2} &= \frac{\gamma_2}{d_{11}^2} (D_{x2} - iD_{y2}) \\ &= \frac{\gamma_2}{d_{11}^2} \frac{z + \sqrt{z^2 - c^2}}{Rc\sqrt{z^2 - c^2}} \begin{bmatrix} 0 \\ 1 \end{bmatrix}^T \left[\frac{cR}{2} \mathbf{\Gamma} - \frac{(\mathbf{M}_2\mathbf{M}_1^{-1} + \mathbf{I})\mathbf{N}^{-1}cRr^2\bar{\mathbf{\Gamma}}}{2G^2(z)} - \frac{(\mathbf{M}_2\mathbf{M}_1^{-1} - \mathbf{I})\mathbf{N}^{-1}cR^3\bar{\mathbf{\Gamma}}}{2G^2(z)} \right] \end{aligned} \quad (9)$$

where $\gamma_i (i = 1, 2)$ is the electric conductivity.

The thermal power which produced by the current can be expressed as

$$Q_1 = \int_{-h}^h \frac{1}{\gamma_1} (J_{x1}^2 + J_{y1}^2) dz = \frac{2h}{\gamma_1} \left| \frac{\gamma_1}{d_{11}^1} \frac{z + \sqrt{z^2 - c^2}}{Rc\sqrt{z^2 - c^2}} \begin{bmatrix} 0 \\ 1 \end{bmatrix}^T \left[\mathbf{N}^{-1}cR^3\mathbf{\Gamma} - \frac{\mathbf{N}^{-1}cRr^2\bar{\mathbf{\Gamma}}}{G^2(z)} \right] \right|^2 \quad (10)$$

$$\begin{aligned} Q_2 &= \int_{-h}^h \frac{1}{\gamma_2} (J_{x2}^2 + J_{y2}^2) dz = \frac{2h}{\gamma_2} \\ &\left| \frac{\gamma_2}{d_{11}^2} \times \frac{z + \sqrt{z^2 - c^2}}{Rc\sqrt{z^2 - c^2}} \begin{bmatrix} 0 \\ 1 \end{bmatrix}^T \left[\frac{cR}{2} \mathbf{\Gamma} - \frac{(\mathbf{M}_2\mathbf{M}_1^{-1} + \mathbf{I})\mathbf{N}^{-1}cRr^2\bar{\mathbf{\Gamma}}}{2G^2(z)} - \frac{(\mathbf{M}_2\mathbf{M}_1^{-1} - \mathbf{I})\mathbf{N}^{-1}cR^3\bar{\mathbf{\Gamma}}}{2G^2(z)} \right] \right|^2 \end{aligned} \quad (11)$$

3. RESULTS

Assuming that matrix material is PZT-5H and inhomogeneity material is PZT-4. The electro-elastic properties of PZT-5H and PZT-4 are:

$$\mathbf{M}_1 = \begin{bmatrix} 2.3 \times 10^{10} \text{ N/m}^2 & 17 \text{ C/m}^2 \\ 17 \text{ C/m}^2 & 150.4 \times 10^{-10} \text{ C/Vm} \end{bmatrix}, \quad \mathbf{M}_2 = \begin{bmatrix} 2.56 \times 10^{10} \text{ N/m}^2 & 12.7 \text{ C/m}^2 \\ 12.7 \text{ C/m}^2 & 0.646 \times 10^{-10} \text{ C/Vm} \end{bmatrix}$$

Fig.2 shows the normalized thermal power Q_1/Q_0 versus z/a_1 with different b at $a_1 = 10^{-3}$, $b_1 = 10^{-4}$, where Q_0 is the thermal power of the right endpoint of a blunt crack inside infinite PZT-4 matrix. It is seen that the thermal power concentrate in the crack tip is more severe for a large inhomogeneity. However, the thermal power decreases with the increase of the distance.

Fig.3 shows the normalized thermal power Q_1/Q_0 versus θ with different b at $a_1 = 10^{-3}$, $b_1 = 10^{-4}$, where Q_0 is the thermal power of the right endpoint of a blunt crack inside infinite PZT-4 matrix. It is seen that the thermal power decrease with the increase of $|\theta|$.

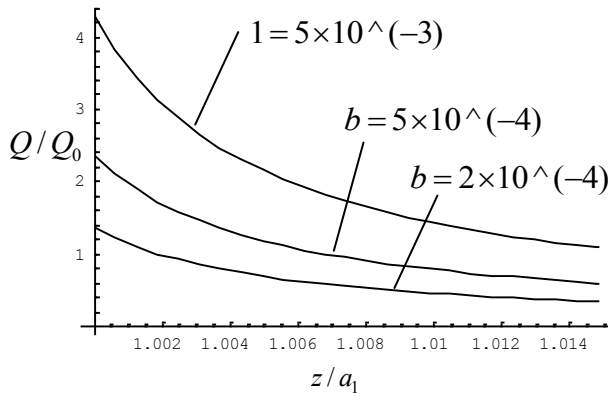


FIGURE 2. Curves for Q/Q_0 versus z/a_1

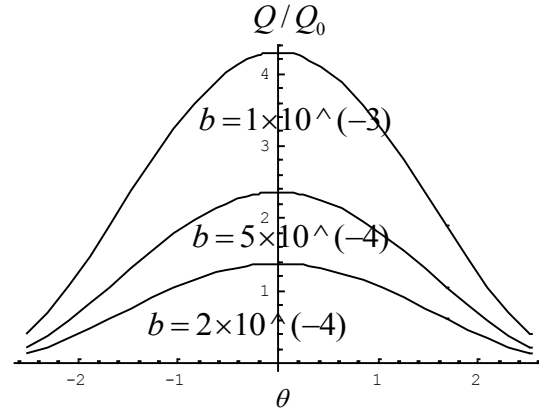


FIGURE 3. Curves for Q/Q_0 versus θ

4. CONCLUSIONS

The thermal power around a blunt crack in elliptical inhomogeneity under electric loads at infinity is dealt with. Utilizing the Muskhelishvili complex variable method, the closed form solutions are derived. The results show that the thermal power concentrate is more severe in the crack tip when the inhomogeneity became larger. The thermal power decreases with the increase of the distance and the modulus of the angle.

REFERENCES

- [1] A.L.Florence, J.N.Goodier, *Journal of Applied Mechanics*, 27, 635-639, 1960.
- [2] N.Hasebe, A.Tomida and T.Nakamura, *Journal of Thermal Stresses*, 11, 381-391, 1988.
- [3] N.Hasebe, H.Irikura, T. Nakamura, *Journal of Applied Mechanics*, 113, 996-1000, 1991.
- [4] W.Nowacki, *Thermoelasticity*, Pergamon, Oxford (1986).
- [5] X.Z. Zhang, N.Hasebe, Basic singular thermoelastic solutions for a crack, *International Journal of Fracture*, 62, 97-118, 1993.
- [6] Y.W. Liu, H.P. Song, Q.H. Fang, Shielding effect and emission condition of a screw dislocation near a blunt crack in elliptical inhomogeneity, *Meccanica*, 45, 519-530, 2010.

WAVES IN A ROTATING RANDOM WEAKLY CONDUCTING WEAKLY THERMAL MAGNETO-VISCOELASTIC MEDIUM

R.K. Bhattacharyya

Department of Applied Mathematics, Calcutta University,
Calcutta 700009, India. E-Mail: rabindrakb@yahoo.com

R.K. Bera

Department of Mathematics, Heritage Institute of Technology
Calcutta 700107, India. E-Mail: rasajit@yahoo.com

ABSTRACT

The problem of wave propagation in an interacting rotating random inhomogeneous magneto-thermo-visco-elastic medium has been studied. The perturbation technique relevant to stochastic differential equations has been employed to obtain the relation connecting displacement amplitudes of waves propagating in the interacting media. The medium has been assumed to be weakly thermal and electrically weakly conducting. A more general coupled dispersion relation for longitudinal and transverse waves has been deduced to determine the effects of thermal and magneto-viscoelastic parameters, rotation and conductivity on the phase velocity of the coupled waves. The equations have been analyzed for a particular form of thermo-mechanical coupling auto-correlation function. Cases of low and high frequencies have also been studied.

Key Words: *Magneto-thermo-viscoelastic, Random, Rotating, Auto-correlation*

1. INTRODUCTION

In recent years, considerable interest has been shown in the study of plane thermoelastic, magneto-thermoelastic, and magneto-thermo-visco-elastic wave propagation in an infinite non-random or random and non-rotating and rotating media by many authors.

It has been found important to study the effects of random inhomogeneities of media, viewed as a departure from the deterministic models [1]. In the most recent study, Chottopadhyay and Bhattacharyya have been able to compute Green's tensor for a conducting magneto-viscoelastic medium [2] and employ the same to investigate wave propagation in random conducting, magneto-thermo-viscoelastic medium [3]. In the present paper, however, the problem of wave propagation in a rotating, random magneto-thermo-visco-elastic medium [4] has been investigated following classical theory of heat conduction. The resulting magnetic field is $\vec{H}_0 + \vec{h}$, where \vec{H}_0 is the external magnetic field and \vec{h} , the small perturbation in the magnetic field. The dispersion relation is evaluated, when the conductivity (σ) and other material constants undergo small random variations.

The mathematical study of the phenomena of wave propagation in random elastic and electromagnetic materials was carried out by Keller [5] and Karal and Keller [6]. The smooth perturbation method has been employed for the solution of the resulting stochastic differential equations. The field equations are put in the form

$$LV = f \tag{1}$$

where L is the random linear operator, V is the field quantity, and f is the source term.

Assuming that

$$L(\vec{x}) = L_0 + \varepsilon L_1(\vec{x}) + \varepsilon^2 L_2(\vec{x}) \quad (2)$$

Keller [5] has shown that the mean field quantity $\langle V(\vec{x}, t) \rangle$ satisfies the mean field equation

$$[L_0 + \varepsilon \langle L_1 \rangle + \varepsilon^2 \langle L_2 \rangle + \varepsilon^2 \{ \langle L_1 \rangle L_0^{-1} \langle L_1' \rangle - \langle L_1 L_0^{-1} L_1' \rangle \}] \langle V(\vec{x}, t) \rangle = f \quad (3)$$

where L_0^{-1} is obtained by solving

$$L_0 G_{ij}(\vec{x}, \vec{x}') = \delta(\vec{x}, \vec{x}') \delta_{ij} \quad (4)$$

where G_{ij} is the appropriate Green's tensor for L_0 .

2. FORMULATION OF THE PROBLEM AND BASIC EQUATIONS

An infinite isotropic, homogeneous (thermally as well as electrically) conducting random magneto-thermo-viscoelastic medium with density ρ at uniform initial temperature θ_0 has been considered.

The medium is rotating with an angular velocity $\vec{\Omega} = \Omega \hat{n}$, where \hat{n} is a unit vector representing the direction of the axis of rotation. Let \vec{u} be the dynamic displacement vector measured from a steady state deformed position and supposed to be small. Let \vec{H} be the magnetic vector and \vec{j} the current density vector of the electromagnetic field. Assuming

$$(\vec{u}, \vec{h}, \theta) = (\vec{u}, \vec{h}, \theta) e^{-i\omega t} \quad (5)$$

in the magnetic perturbation field equation, the displacement equation of motion in the rotating magneto-thermo-visco-elastic medium and the energy equation, one gets the three field equations, after dropping the bars, as

$$i\nu\omega\vec{h} = -\frac{1}{\sigma} [\vec{\nabla} \{ \frac{1}{\nu} (\vec{\nabla} \nu \cdot \vec{h}) \} + \nabla^2 \vec{h}] - i\omega \nu [\vec{H}_0 (\vec{\nabla} \cdot \vec{u}) - (\vec{H}_0 \cdot \vec{\nabla}) \vec{u}] - i\omega (\vec{\nabla} \nu \cdot \vec{u}) \vec{H}_0 \quad (6)$$

$$(\lambda + \mu) \vec{\nabla} (\vec{\nabla} \cdot \vec{u}) + \mu \nabla^2 \vec{u} + \vec{\nabla} \lambda (\vec{\nabla} \cdot \vec{u}) + \vec{\nabla} \mu (\vec{\nabla} \times \vec{u}) + 2(\vec{\nabla} \mu \cdot \vec{\nabla}) \vec{u} - \nu \vec{H}_0 \times (\vec{\nabla} \times \vec{h}) - \vec{\nabla} (m\theta) = \rho [-\omega^2 \vec{u} + \vec{\Omega} \times (\vec{\Omega} \times \vec{u}) - 2i\omega \vec{\Omega} \times \vec{u}] \quad (7)$$

$$-\gamma\omega\theta = \vec{\nabla} \cdot (\eta \vec{\nabla} \theta) + i\omega m \theta_0 (\vec{\nabla} \cdot \vec{u}) \quad (8)$$

with $\vec{\nabla} \nu \cdot \vec{H}_0 = 0$, $\lambda = (\gamma_v - \gamma_s)/3$, $\mu = \gamma_s/2$.

The field equations (6)-(8) can now be put in the

$$L(\vec{x})V(\vec{x}) = 0 \quad (9)$$

$$L = \begin{bmatrix} M & P & K \\ N & Q & 0 \\ R & 0 & S \end{bmatrix} \quad V = \begin{bmatrix} \vec{u} \\ \vec{h} \\ \theta \end{bmatrix} \quad (10)$$

and M, P, K, N, Q, R and S are determined from the governing equations assuming that

$$(\lambda, \mu, \nu, \gamma, \eta, \rho) = (\lambda_0, \mu_0, \nu_0, \gamma_0, \eta_0, \rho_0) + \varepsilon(\lambda_1, \mu_1, \nu_1, \gamma_1, \eta_1, \rho_1)(\vec{x}) \quad (11)$$

$$\sigma = \varepsilon\sigma_1(\vec{x}), \quad m = \varepsilon m_1(\vec{x}) \quad (12)$$

such that

$$\langle \sigma_1 \rangle = \sigma_1^0 \neq 0, \quad \langle m_1 \rangle = m_1^0 \neq 0 \quad (13)$$

$$[\langle \lambda_1 \rangle, \langle \mu_1 \rangle, \langle \nu_1 \rangle, \langle \gamma_1 \rangle, \langle \eta_1 \rangle, \langle \rho_1 \rangle] = 0 \quad (14)$$

3. SOLUTION OF THE PROBLEM

Let the mean field quantity

$$\langle V(\vec{x}) \rangle = \begin{bmatrix} \vec{A} & \vec{B} & D \end{bmatrix}^T e^{i\vec{k}\cdot\vec{x}} \quad (15)$$

satisfy the integro-differential equation (3) with $f = 0$.

The appropriate Green's tensor corresponding to L_0^{-1} have already been evaluated [7]. Also

$$G_3(r) = \frac{1}{4\pi r} e^{i\beta r}, \quad \beta = \sqrt{\frac{\omega \nu_0 \sigma_1^0}{2\mu_0}} (1+i). \quad (16)$$

Substitution of (15) into (3) yields three equations. Eliminating \vec{B} and D one gets

$$\begin{aligned} & M'_0 - i\nu_0 \vec{H}_0 \times [\vec{k} \times \{ \frac{\varepsilon \omega \nu_0 \sigma_1^0}{k^2} \vec{k} \times (\vec{A} \times \vec{H}_0) + \varepsilon^2 \Psi + \varepsilon^2 \frac{(\omega \nu_0 \sigma_1^0)^2}{k^2} \vec{k} \times (\vec{A} \times \vec{H}_0) \}] \\ & - \varepsilon^2 \frac{i\omega \theta_0 m_1^0 (\vec{A} \cdot \vec{k}) \vec{k}}{i\omega \gamma_0 - \eta_0 k^2} - \varepsilon^2 i\omega \theta_0 m_1^0 (\vec{A} \cdot \vec{k}) \vec{k} \int G_3(r) e^{-i\vec{k}\cdot\vec{r}} d\vec{r} + \varepsilon^2 \int f_1 \vec{A} e^{-i\vec{k}\cdot\vec{r}} d\vec{r} = 0, \end{aligned}$$

where

$$M'_0 = -(\lambda_0 + \mu_0)(\vec{k} \cdot \vec{A})\vec{k} + (\rho_0 \omega^2 - \mu_0 k^2)\vec{A} + \rho_0[\Omega^2 \vec{A} - (\vec{\Omega} \cdot \vec{A})\vec{\Omega} + 2i\omega \vec{\Omega} \times \vec{A}],$$

$$e^{i\vec{k}\cdot\vec{x}} (f_1 \vec{A}) \equiv \langle M_1 G_0 M'_1 + M_1 G_1 N'_1 + P_1 G_2 N'_1 + K_1 G_3 R'_1 \rangle (A e^{i\vec{k}\cdot\vec{x}}),$$

$$\begin{aligned} \Psi &= \omega[\langle \sigma_1 \nu_1 \rangle \{ \vec{k} \times (\vec{A} \times \vec{H}_0) \} - i\vec{H}_0 \langle \sigma_1 \vec{\nabla} \nu_1 \rangle \cdot \vec{A}] \\ &- [(\omega \nu_0 \sigma_1^0)^2 \{ \vec{k} \times (\vec{H}_0 \times \vec{A}) \} \int \{ G_1(r)(H_0 \vec{k}) + iG_2(r) \} e^{-i\vec{k}\cdot\vec{r}} d\vec{r} + \int G_1(r) \vec{A} e^{-i\vec{k}\cdot\vec{r}} d\vec{r}. \end{aligned} \quad (17)$$

4. RESULTS

Equation (17) represents the relation connecting displacement amplitudes for waves propagating in the interacting rotating random magneto-thermo-viscoelastic medium. The term M'_0 contains the

rotating parameter Ω . It may be noted that this equation does not include any term involving cross-correlation functions between magnetic and thermal parameters. If the terms to the order ε only are retained, the equation (17) reduces to

$$\begin{aligned} & -(\lambda_0 + \mu_0)(\vec{k} \cdot \vec{A})\vec{k} + (\rho_0\omega^2 - \mu_0k^2)\vec{A} + \rho_0[\Omega^2\vec{A} - (\vec{\Omega} \cdot \vec{A})\vec{\Omega} + 2i\omega\vec{\Omega} \times \vec{A}] \\ & - \varepsilon i\omega v_0^2 \sigma_1^0 [(\vec{k} \cdot \vec{H}_0)\{(\vec{H}_0 \cdot \vec{A})\vec{k} - (\vec{H}_0 \cdot \vec{k})\vec{A}\} - (\vec{k} \cdot \vec{A})\{H_0^2\vec{k} - (\vec{H}_0 \cdot \vec{k})\vec{H}_0\}] = 0 \end{aligned} \quad (18)$$

The terms representing the effect of the thermal field do not appear in (18), while the effect of the magnetic field is discernible to the first order of ε . This indicates that in an interacting field of the type described here, the effect of the magnetic field is stronger than that of the thermal field. To study the effect of the presence of a thermal field, we assume for equation (17) that [8]

$$R_{mm}(r) = \langle m_1(\vec{x})m_1(\vec{x}') \rangle \neq 0 \quad (19)$$

and the other correlation functions vanish. After lengthy calculations it was shown that the effect of randomness to the ε – order term is to increase attenuation of longitudinal type waves. The attenuation coefficient was computed. Many other cases were discussed and numerical computations made. Low and high frequency waves were considered for both Maxwell and Voigt type of viscoelastic medium. Effects of randomness as also of rotation were enumerated; graphs were drawn.

REFERENCES

- [1] H. Sato and M.C. Fehler, *Seismic wave propagation and scattering in the heterogeneous earth*, AIP Press, Springer, 1998.
- [2] G. Chattopadhyay. and R.K.Bhattacharyya, Determination of Green's tensor for a conducting magneto-viscoelastic medium, *Proc. 6th Int. conf. on math. and num. aspects of wave propagation*, Jyvaskyla, Finland, INRIA (France), Springer, 2003.
- [3] R.K. Bhattacharyya and G. Chattopadhyay, Wave propagation in a random conducting magneto-thermo-viscoelastic medium, *Proc. 6th Int Congress on Thermal Stresses and Related Topics*, Vienna, Austria, 667-670, 2005.
- [4] M. Schoenberg and D. Censor, Elastic waves in rotating media, *Quarterly of Applied Maths.* 31, 115-125, 1973.
- [5] J. B. Keller, Stochastic equations and wave propagation in random media, *Proc. Symp. App. Math.*, Vol 16, p 145, Amer. Math. Soc., Providence, RI, 1964.
- [6] F.C. Karal and J. B. Keller, Elastic, electro-magnetic and other waves in a random medium, *J. Mathematical Physics* 5, 537-547, 1964.
- [7] R.K. Bera, Study of Green's Tensor in Magneto-Visco-elastic media, *Appl. Math. Lett.* 9(5), 111-115 (1996).
- [8] P.L. Chow, Thermo-elastic wave propagation in a random medium and some related problems, *Int. J. Eng. Sci.* II, 953, 1973.

BOUNDS ON THE EFFECTIVE THERMAL CONDUCTIVITY OF COMPOSITES WITH SPHERICAL INCLUSIONS

Linzhi Wu

Center for Composite Materials, Harbin Institute of Technology, 150001, wlz@hit.edu.cn

ABSTRACT

A new model is put forward to bound the effective thermal conductivity of composites with spherical inclusions. According to the principles of minimum potential energy and minimum complementary energy, the rigorous upper and lower bounds on the effective thermal conductivity of composites with spherical inclusions are derived. The effects of the distribution of spherical inclusions on the effective thermal conductivity of composites are analyzed in details.

Key Words: *Bounds, Effective thermal conductivity, Spherical inclusions, Composites.*

1. INTRODUCTION

The problem of determining the effective physical properties of statistically homogeneous two-phase composites has an extensive history. Several methods have been developed to derive bounds on effective parameters of composites. Hashin and Shtrikman (1963, 1962) have derived bounds for effective elastic moduli and magnetic permeability for statistically homogeneous and isotropic materials by introducing polarization fields and applying variational principles, respectively. These bounds are expressed in terms of the volume fraction, which is the simplest statistical information related to the effective properties of two-phase composites. Phan-Thien and Milton (1982) have derived the third- and fourth-order bounds for the effective thermal conductivity of composites in terms of the perturbation solution to the effective thermal conductivity problem for an N-component material.

2. UPPER BOUND

For the two-phase composite with spherical inclusions shown in Fig.1, it is assumed that the interfaces between spherical inclusions and matrix are perfectly bonded and spherical inclusions are non-touching unless the volume fraction of spherical inclusions is equal to 1. This implies that the matrix is not disconnected by spherical inclusions. To make the temperature field in the composite continuous, we introduce the α -th transition region situated in the matrix for the α -th spherical inclusion, which has the inner radius r_α and outer radius R_α , respectively. Thus, the composite with spherical inclusions is divided into three kinds of regions denoted by $V_{\bar{M}}$, V_T and V_I , respectively. They are called as the regions of remnant matrix, transition layers and spherical inclusions, respectively. For the present model, the temperature fields in these three kinds of regions are constructed as follows.

1) *In the remnant matrix*

$$T^{\bar{M}}(\mathbf{x}) = -E_i^0 x_i, \quad \mathbf{x} \in V_{\bar{M}} \quad (1)$$

where E_i^0 is the uniform temperature gradient and $T^{\bar{M}}(\mathbf{x})$ denotes the temperature field in the remnant matrix $V_{\bar{M}}$. Without loss of generalization, it is assumed that spherical inclusions do not

intersect with the surface S . Thus, the temperature field given by Eq. (1) satisfies the homogeneous boundary condition.

2) In the spherical inclusions

$$T^\alpha(\mathbf{x}) = (E_i^\alpha - E_i^0)x_i^\alpha - E_i^\alpha x_i, \quad \mathbf{x} \in V_\alpha, \quad (\alpha = 1, 2, \dots, N) \quad (2)$$

where $T^\alpha(\mathbf{x})$ and E_i^α are the temperature field and constant temperature gradient components in the α -th spherical inclusion, respectively, x_i^α denotes the coordinate of the center of the α -th spherical inclusion, and V_α is the volume of the α -th spherical inclusion.

3) In the transition layers

$$\tilde{T}^\alpha(\mathbf{x}) = -E_i^0 x_i - (E_i^\alpha - E_i^0)(x_i - x_i^\alpha) \frac{R_\alpha - \rho}{h_\alpha}, \quad \mathbf{x} \in \tilde{V}_\alpha, \quad \rho \in [r_\alpha, R_\alpha] \quad (3)$$

where $\tilde{T}^\alpha(\mathbf{x})$ is the temperature field in the α -th transition layer, r_α and R_α are the inner and outer radii of the α -th concentric spherical shell, respectively, and $h_\alpha = R_\alpha - r_\alpha$ and \tilde{V}_α are the thickness and volume of the α -th concentric spherical shell, respectively.

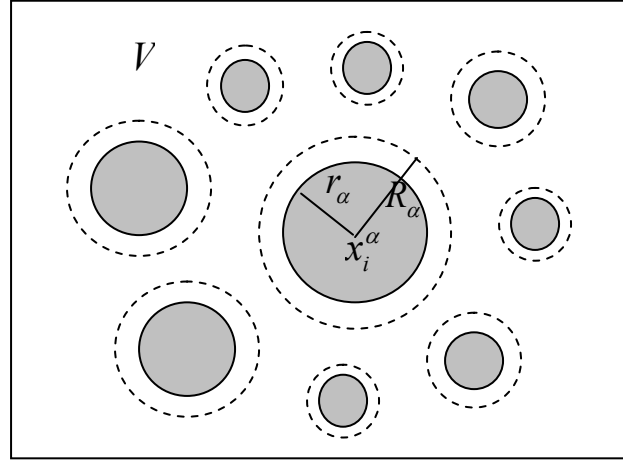


FIGURE 1 The representative volume V where the transition region is located in the matrix.

From Eqs (1)-(3), it is easily verified that the temperature field in the composite is continuous. For the temperature field given in Eqs (1)-(3), we can obtain the temperature gradient fields in three kinds of regions. Application of classical variational principles for steady state conduction in conjunction with linear admissible temperature can yield the corresponding upper bound.

$$\sigma_e \leq c_I \sigma_I + c_M \sigma_M - \frac{c_I (\sigma_I - \sigma_M)^2}{\sigma_I - \sigma_M + \sigma_M (\lambda^5 - 1) / (5(\lambda - 1)^2)} \quad (4)$$

where σ_e is the effective thermal conductivity of composites, σ_I and σ_M are the thermal conductivities of inclusions and matrix, respectively, and c_I and c_M are the volume fractions of inclusions and matrix, respectively. Here, the parameter λ is defined in Wu (2010).

3. LOWER BOUND

For the present model, three kinds of new potential functions in the remnant matrix, transition layers and spherical inclusions are constructed to make the normal components of heat flux vector continuous on interfaces between remnant matrix and transition layers and between transition layers and spherical inclusions. The heat flux $Q_i(\mathbf{x})$ can be determined by the differentiation of potential function $\psi(\mathbf{x})$ with respect to variable x_i .

$$Q_i(\mathbf{x}) = \psi_{,i}(\mathbf{x}), \quad \mathbf{x} \in V \quad (5)$$

These three kinds of potential functions are expressed as the following forms.

1) *In the remnant matrix*

$$\psi^{\bar{M}}(\mathbf{x}) = Q_i^0 x_i, \quad \mathbf{x} \in V_{\bar{M}} \quad (6)$$

where $\psi^{\bar{M}}(\mathbf{x})$ and Q_i^0 are the potential function and constant heat flux components in $V_{\bar{M}}$, respectively.

2) *In the spherical inclusions*

$$\psi^\alpha(\mathbf{x}) = Q_i^\alpha x_i, \quad \mathbf{x} \in V_\alpha, \quad (\alpha = 1, 2, \dots, N) \quad (7)$$

where $\psi^\alpha(\mathbf{x})$ and Q_i^α are the potential function and constant heat flux components in the α -th spherical inclusion, respectively.

3) *In the transition layers*

$$\tilde{\psi}^\alpha(\mathbf{x}) = Q_i^0 x_i + (Q_i^\alpha - Q_i^0)(x_i - x_i^\alpha) f_\alpha(\rho), \quad \mathbf{x} \in \tilde{V}_\alpha, \quad \rho \in [r_\alpha, R_\alpha] \quad (8)$$

where $\tilde{\psi}^\alpha(\mathbf{x})$ is the potential function in the α -th transition layer and $f_\alpha(\rho)$ is a function of variable ρ in the α -th concentric spherical shell.

For the potential functions given in Eqs (6)-(8), we can obtain the heat flux fields in these three kinds of regions. Thus, the heat flux field in the remnant matrix satisfies the homogeneous boundary condition. Application of classical variational principles for steady state conduction in conjunction with constant admissible heat flux can yield the corresponding lower bound.

$$\left[\frac{c_I + \frac{c_M}{\sigma_I} - \frac{c_I(\sigma_I^{-1} - \sigma_M^{-1})^2}{\sigma_I^{-1} - \sigma_M^{-1} + 3\zeta^3 / (2\sigma_M(\zeta^3 - 1))}}{\sigma_I} \right]^{-1} \leq \sigma_e \quad (9)$$

Here, the parameter ζ is defined by Wu (2010).

4. RESULTS AND DISCUSSIONS

To calculate the effective thermal conductivity of composites, we need to determine the geometric parameters λ and ζ . They are expressed as by two new parameters ν and η

$$\nu = c_M / (c_I(\lambda^3 - 1)), \quad \eta = c_M / (c_I(\zeta^3 - 1)) \quad (10)$$

To compare the present bounds with Hashin-Shtrikman (1962) bounds, the upper bound for $\nu = 5$ and the lower bound for $\eta = 1$ are given, respectively. From Fig.2, it can be seen that the upper bound for $\nu = 5$ provides a significant improvement over Hashin-Shtrikman (1962) upper bound

and the lower bound for $\eta=1$ coincides with Hashin-Shtrikman lower bound. Since Hashin-Shtrikman (1962) lower bound is the same as the CSA (composite spheres assemblage) result of Hashin (1962), it is believed to be best possible in terms of volume fractions.

From Fig.3, it can be observed that the upper bound decreases and the lower bound increases with the decreasing of geometrical parameters ν and η . It is interesting that the upper bound is very close to the lower bound which coincide with the CSA result of Hashin (1962) when $\nu = \eta = 1$. Right now, the distribution of spherical inclusions is consistent with the composite spheres assemblage.

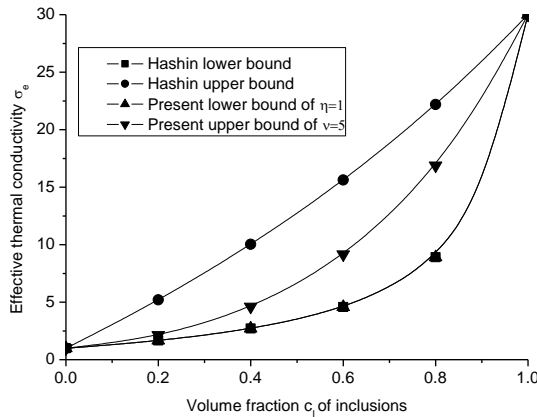


FIGURE 2 Comparison of the present bounds with Hashin-Shtrikman bounds.

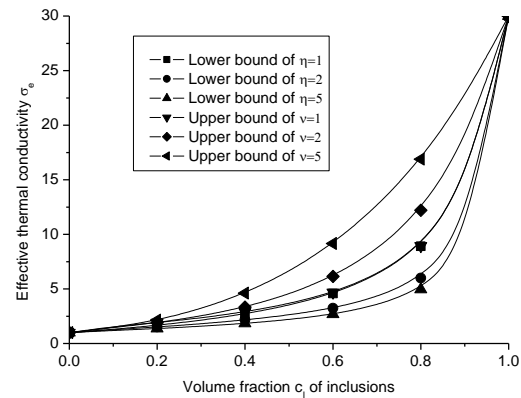


FIGURE 3 Variations of the present bounds with the volume fraction of inclusions.

5. CONCLUSIONS

A new model is developed to bound the effective thermal conductivity of composites with spherical inclusions. Based on the principles of minimum potential energy and minimum complementary energy, the upper and lower bounds are rigorously derived. In contrast to Hashin-Shtrikman (1962) bounds and higher-order bounds, the present bounds still are finite when the thermal conductivity of spherical inclusions tends to infinity and zero. As we saw before, the present upper bound offers a substantial improvement over Hashin-Shtrikman upper bound. In comparison with higher-order bounds which involve the complicated integrals of multi-point correlation functions, the present bounds are rigorous and only are related to simple calculations.

REFERENCES

- [1] Z. Hashin, S. Shtrikman, A variational approach to the theory of the elastic behaviour of multiphase materials, *Journal of the Mechanics and Physics of Solids*, 11, 127-140, 1963.
- [2] Z. Hashin, S. Shtrikman, A variational approach to the theory of the effective magnetic permeability of multiphase materials, *Journal of Applied Physics*, 33, 3125-3131, 1962.
- [3] N. Phan-Thien, G.W. Milton, New bounds on the effective thermal conductivity of N-phase materials, *Proceedings of the Royal Society of London*, A380, 333-348, 1982.
- [4] L.Z. Wu, Rigorous bounds on the effective thermal conductivity of composites with ellipsoidal inclusions, *International Journal of Engineering Science*, 48, 417-428, 2010.

A LINEAR RECONSTRUCTION ALGORITHM FOR ANISOTROPIC DIFFUSION EQUATIONS

Lina Chang, Guangwei Yuan

National Key Laboratory of Science and Technology on Computational Physics, Institute of Applied Physics and Computational Mathematics, Beijing 100088, China, changln@iapcm.ac.cn

ABSTRACT

A reconstruction algorithm is designed for constructing cell-centered finite volume schemes on skewed meshes for solving anisotropic diffusion problems. We show that a balance point can be found for each edge on polygonal meshes. At this point, the edge unknowns are reconstructed accurately with a simple linear interpolation formula. The scheme accuracy is demonstrated by the numerical results.

Key Words: *Anisotropic diffusion, Finite volumes, Reconstruction.*

1. INTRODUCTION

Skewed or non-orthogonal meshes arise in various fields, e.g., grid generation on physical domains with complex geometry, or numerical solutions of diffusion problems in Lagrangian radiation hydrodynamics. In the construction of cell-centered finite volume schemes for diffusion problems, due to the skewness of the grids, auxiliary unknowns defined at the vertices or edges are often introduced in addition to the primary unknowns at the cell centers. However, the introduction of auxiliary unknowns leads to greater computational costs or more complex algorithms than those with cell-centered unknowns only, especially when the diffusion scheme is used to solve the diffusion equation in a coupled radiation hydrodynamic problem.

An efficient and accurate reconstruction algorithm is proposed in [1]. With this algorithm, edge unknowns are defined at a balance point on the edge, instead of at the midpoint. In this way, the edge unknowns can be approximated accurately with a simple linear interpolation formula in which only the two adjacent cells are used as interpolation stencils. Here we extend the reconstruction algorithm to anisotropic diffusion problems. The location of the balance point is calculated by imposing the flux continuity condition for anisotropic problems. So the heterogeneous tensor can be dealt with strictly.

Moreover, the reconstruction algorithm is used for approximating the gradients of the cells with edge unknowns. In a previous paper [2] the edge unknowns are defined at mid-points in IDC (improved deferred correction) scheme. The scheme accuracy is improved when the mid-points are replaced by our balance points. Moreover, the IDC scheme with our new reconstruction algorithm is generalized to be suitable for anisotropic problems.

2. RECONSTRUCTION ALGORITHM AND DISCRETIZATION OF FLUX

The diffusion problem under consideration is:

$$-\nabla \cdot (\kappa \nabla u) = f \quad \text{in } \Omega \quad (1)$$

$$u = g \quad \text{on } \partial\Omega \quad (2)$$

where Ω is an open bounded subset of R^2 and $\partial\Omega$ its boundary, κ is the anisotropic diffusion tensor, f is the intensity of sources, and u is a scalar unknown function. In case of heat diffusion, u denotes the temperature.

The diffusion flux on the edge is defined as

$$\mathbf{F} = -\int_{\sigma} \kappa \nabla u \cdot \vec{n}_{\sigma} dl = -\int_{\sigma} \nabla u \cdot \vec{n}_{\kappa,\sigma} dl \quad (3)$$

where

$$\vec{n}_{\kappa,\sigma} = \kappa^T \vec{n}_{\sigma}.$$

For any given point l on the edge, we have

$$\vec{n}_{\kappa,\sigma} = \lambda_{\kappa,l} \vec{\xi}_l + \beta_{\kappa,l} \vec{t}_{\sigma} \quad (4)$$

where $\vec{\xi}_l = KI/d_{kl}$, K is the cell center, \vec{t}_{σ} is the unit tangential vector of the edge, $\lambda_{\kappa,l}$ and $\beta_{\kappa,l}$ are the coefficients whose values depend on the geometry and the diffusion tensor.

Multiplying both sides of (4) with ∇u^- , we have

$$\nabla u^- \cdot \vec{n}_{\kappa,\sigma}^- = \lambda_{\kappa,l}^- \frac{u_l^- - u_k^-}{d_{k,l}} + \beta_{\kappa,l}^- \nabla u^- \cdot \vec{t}_{\sigma}^- \quad (5)$$

The superscripts - and + indicate the limits of a function from the left and right hand of the edge respectively. Integrating both sides of (5) over the edge, we obtain the discretization of the flux

$$F_{\sigma}^- = -\left(\lambda_{\kappa,l}^- \frac{u_l^- - u_k^-}{d_{k,l}} S_{\sigma} + \beta_{\kappa,l}^- \int_{\sigma} \nabla u^- \cdot \vec{t}_{\sigma}^- dl \right). \quad (6)$$

Using similar notations, we also have

$$F_{\sigma}^+ = -\left(\lambda_{\kappa,l}^+ \frac{u_l^+ - u_L^+}{d_{L,l}} S_{\sigma} + \beta_{\kappa,l}^+ \int_{\sigma} \nabla u^+ \cdot \vec{t}_{\sigma}^+ dl \right). \quad (7)$$

The continuity condition of the normal flux can be written as

$$F_{\sigma}^- + F_{\sigma}^+ = 0 \quad (8)$$

Combining (6)-(8), we eliminate the auxiliary unknowns and obtain

$$F_{\sigma}^- = -\frac{\tau_{\sigma}^- \tau_{\sigma}^+}{\tau_{\sigma}^- + \tau_{\sigma}^+} \left(u_L - u_k + \left(\frac{\beta_{\kappa,l}^-}{\tau_{\sigma}^-} + \frac{\beta_{\kappa,l}^+}{\tau_{\sigma}^+} \right) \int_{\sigma} \nabla u \cdot \vec{t}_{\sigma} dl \right) \quad (9)$$

where

$$\tau_{\sigma}^- = \frac{(\vec{n}_{\kappa,\sigma}^- \cdot \vec{n}_{\sigma}^-) S_{\sigma}}{d_{k,\sigma}}, \quad \tau_{\sigma}^+ = \frac{(\vec{n}_{\kappa,\sigma}^+ \cdot \vec{n}_{\sigma}^+) S_{\sigma}}{d_{L,\sigma}}.$$

Moreover, certain balance point J_r is obtained with (6)-(8) per edge. At this point, the edge unknowns can be calculated accurately using the linear interpolation formula

$$u_{J_r} = \frac{\tau_{\sigma}^- \tau_{\sigma}^+}{\tau_{\sigma}^- + \tau_{\sigma}^+} (\tau_{\sigma}^- u_K + \tau_{\sigma}^+ u_L). \quad (10)$$

The location of J_r and its value can be used to obtain the approximation of ∇u in (9).

3. NUMERICAL RESULTS

Consider the problem (1)-(2) in the unit square $(0,1)^2$. Dirichlet boundary condition is imposed. The diffusion tensor is given by $\kappa = RDR^T$ and

$$R = \begin{pmatrix} \cos \theta & -\sin \theta \\ \sin \theta & \cos \theta \end{pmatrix}, \quad D = \begin{pmatrix} \kappa_1 & 0 \\ 0 & \kappa_2 \end{pmatrix},$$

where $\theta = \frac{5\pi}{12}$, $\kappa_1 = 1 + 2x^2 + y^2$ and $\kappa_2 = 1 + x^2 + 2y^2$. The exact solution is

$$u(x, y) = \sin(\pi x) \sin(\pi y).$$

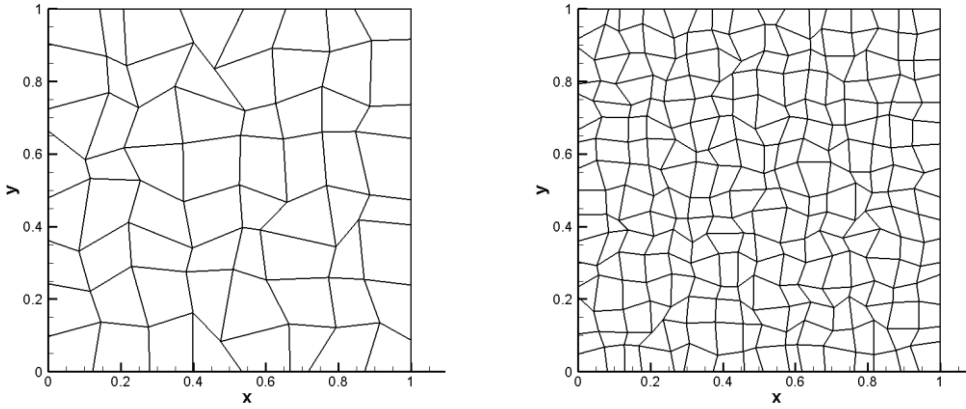


FIGURE 1. The 8×8 (left) and 16×16 (right) random grids.

Cell number	8×8	16×16	32×32	64×64	128×128
BP method					
L2 error	0.117E-1	0.288E-2	0.651E-3	0.181E-3	0.472E-4
rate	-	2.02	2.15	1.84	1.94
MP method					
L2 error	0.122E-1	0.130E-1	0.142E-1	0.154E-1	0.149E-1
rate	-	-0.09	-0.13	-0.11	0.04

TABLE 1. Convergence on a sequence of random meshes.

Calculations are performed on a sequence of random grids. Two of them are shown in Figure 1. We compare the numerical results obtained by our new reconstruction method (denoted by BP method) and that obtained by the method used in [2] (denoted by MP method). The L_2 -norm of the error on the random grids is given in Table 1. It shows that the convergence rate is close to 2 if the BP method is adopted. For the MP method, however, the errors do not reduce as the grids are refined.

4. CONCLUSIONS

The IDC scheme is extended to handle anisotropic diffusion problems in this paper. For reconstructing the gradients in the scheme, a new method is proposed, and its accuracy is demonstrated by the numerical results.

ACKNOWLEDGEMENTS

This work was partially supported by the National Nature Science Foundation of China (10801018, 11071024), and the Foundation of National Key Laboratory of Computational Physics. The authors thank Prof. T.X. Gu for providing us with the package of linear equation solvers.

REFERENCES

- [1] L.N. Chang and G.W. Yuan, An efficient and accurate reconstruction algorithm for the formulation of cell-centered diffusion schemes, submitted.
- [2] P. Traorea, Y. Ahipo and C. Louste, A robust and efficient finite volume scheme for the discretization of diffusive flux on extremely skewed meshes in complex geometries, *J. Comput. Phys.*, 228, 5148-5159, 2009.

ADAPTIVE ITERATION ACCELERATION FOR NONLINEAR PARABOLIC-HYPERBOLIC SYSTEM

Xia Cui, Guang-Wei Yuan, Jing-Yan Yue

National Key Laboratory of Science and Technology on Computational Physics,
Institute of Applied Physics and Computational Mathematics, Beijing 100088, China,
cuixia09@gmail.com, yuan_guangwei@iapcm.ac.cn, yue_jingyan@iapcm.ac.cn

ABSTRACT

A new iteration scheme named adaptive Picard-Newton iteration is studied for a nonlinear coupled parabolic-hyperbolic system. It can accelerate the resolving procedure with flexible adjustment of the adaptive parameter. It includes Picard iteration and Picard-Newton iteration as special cases. Theoretical analysis shows its solution has super-linear convergence rate to the solution of the nonlinear discrete scheme of the original problem, and second order spatial and temporal approximations to the real solution of the problem. Numerical tests verify its high accuracy and efficiency. Accelerating factors are picked up by comparisons of several iterations, and significant synthesis acceleration is gained.

Key Words: *Coupled Parabolic-Hyperbolic System, Nonlinearity, Adaptive Iteration Acceleration.*

1. INTRODUCTION

Coupled parabolic-hyperbolic systems are often used in describing high-temperature and high-pressure radiation (magnetic) hydrodynamics in many application fields. In this paper, iteration method is studied for solving a nonlinear coupled parabolic-hyperbolic system as follows.

$$\begin{aligned} u_t - \nabla \cdot (A(x, y, t, u, v) \nabla u) &= f(x, y, t, u, v, u_x, u_y, v_x, v_y), \\ v_{tt} - \nabla \cdot (B(x, y, t, u, v) \nabla v) &= g(x, y, t, u, v, u_x, u_y, v_x, v_y, v_t). \end{aligned}$$

Adaptive iteration acceleration is designed and theoretical analysis is made. As an essential component of radiation hydrodynamics, radiation diffusion has the character of nonlinearity and strong coupling. For nonlinear coupled problem, fully implicit scheme has the merits of being able to cancel the restriction on time step size needed in explicit scheme and operator time-splitting method without accuracy loss [1]. Hence it is favourable for transient problems. However it needs enormous calculations. For nonlinear schemes, proper iterations are necessary to fulfil fast and accurate numerical solution [2]. In this paper, the difficulty coming from nonlinearity is overcome by using implicit solution and inductive hypothesis reasoning, and another difficulty from the strong coupling is overcome by compatibly considering the features of different equations and using comprehensive analysis. Numerical experiment results are presented to verify theoretical analysis.

2. ADAPTIVE ITERATION ACCELERATION DESIGNED FOR COUPLED SYSTEM

Adaptive iteration method appropriate for the fully implicit solution of coupled system is proposed. The traditional way for solving nonlinear PDE is the so-called discretization-linearization approach: firstly, discretize the PDE and get a nonlinear algebraic system (NAS), then linearize this NAS, and finally solve the derived linear AS. It is very difficult, sometimes even impossible, to build Newton linearization for complex practical applications. A revelatory way named as LD (linearization-discretization) is put forward to overcome such difficulty [2]: first, linearize the nonlinear PDE, then discretize the derived linear PDE and get linear AS to be solved finally. In this way, it is more

convenient to construct new iteration schemes. E.g., Picard-Newton (PN) iteration can be built with additional high-order approximation terms in an existing Picard iteration, various discrete iteration schemes can be designed by different discretizations for temporal and spatial operators. In this paper, by using LD approach, introducing medium variant to diminish the approximation template, and approximating the spatial and temporal operators with second-order discretization, an adaptive Picard-Newton (APN) iteration acceleration scheme is designed for the first time, which has second-order uniform accuracy in both space and time.

$$\begin{aligned}
& 3/2(U_{ij}^{n+1(s+1)} - U_{ij}^n)/\tau - 1/2(U_{ij}^n - U_{ij}^{n-1})/\tau - \delta(A^{n+1(s)}(U, V)\delta U^{n+1(s+1)})_{ij} \\
& - \theta\delta(\{A_u^{n+1(s)}(U, V)[U^{n+1(s+1)} - U^{n+1(s)}] + A_v^{n+1(s)}(U, V)[V^{n+1(s+1)} - V^{n+1(s)}]\}\delta U^{n+1(s)})_{ij} \\
& = f_{ij}^{n+1(s)}(U, V) + \theta L(f'^{n+1(s+1)}(U, V)[U, V])_{ij}, \\
& 3/2(W_{ij}^{n+1(s+1)} - W_{ij}^n)/\tau - 1/2(W_{ij}^n - W_{ij}^{n-1})/\tau - \delta(B^{n+1(s)}(U, V)\delta V^{n+1(s+1)})_{ij} \\
& - \theta\delta(\{B_u^{n+1(s)}(U, V)[U^{n+1(s+1)} - U^{n+1(s)}] + B_v^{n+1(s)}(U, V)[V^{n+1(s+1)} - V^{n+1(s)}]\}\delta V^{n+1(s)})_{ij} \\
& = g_{ij}^{n+1(s)}(U, V, W) + \theta L(g'^{n+1(s+1)}(U, V, W)[U, V, W])_{ij}, \\
& 3/2(V_{ij}^{n+1(s+1)} - V_{ij}^n)/\tau - 1/2(V_{ij}^n - V_{ij}^{n-1})/\tau = W_{ij}^{n+1(s+1)},
\end{aligned}$$

where θ is the adaptive iteration parameter, which can be adjusted automatically according to predicted adaptive rules in the program. Picard, PN and other iterations can be acquired with different choices of this parameter, i.e. 0, 1, and a figure between 0 and 1. The adaptive rules in this study depend on the amounts of Newton iterations executed, physical background (spatial gradient and temporal gradient), and the property of algebraic matrix (diagonal dominance).

Notice that slight variations of the APN iteration can derive other iteration schemes, such as the Partly Newton iteration (namely NewtonL or NewtonR) with only diffusion terms or reaction terms Newton linearized, i.e. , only the adaptive parameters on the left or right hands equal to 1 and others are 0. Also algorithms with iteration decoupling and variant updating (DU) can be gained for Picard and PN iterations.

3. THEORETICAL ANALYSIS

Discrete equation achieved by LD approach has similar appearance with the original equation, which makes it available to carry out theoretical analysis. Specially, it is feasible to study the convergence property of the iteration solution to the real solution of the original problem, i.e. to make error estimate. Difficulties arising from the nonlinearity and coupling between parabolic and hyperbolic equations are overcome, by different choices of test functions for different equations, and an ingenious use of the method of energy estimation and inductive hypothesis reasoning and comprehensive analysis. Complete theoretical result is obtained. It shows that the APN iteration solution has second-order spatial and temporal error estimate to the real solution of the original problem, and it generally has super-linear convergence ratio except linear and quadratic ratio for Picard and PN iterations respectively. In the theoretical analysis, the error estimate and convergence ratio are proved respectively with the help of the convergence and stability property [3] of the full implicit discrete scheme.

4. NUMERICAL TESTS AND ANALYSIS

Abundant numerical experiments are carried out. By comparison calculation, accelerative factors are ascertained, theoretical results are verified, and synthesis acceleration effects are assessed. E.g., iterations with different temporal accuracy are compared, which demonstrates the second-order

scheme in this paper is more accurate and efficient than a first-order counterpoint [4]. Various adaptive parameters are chosen in tests, which confirms the error order of the iteration solution to the real solution is about 2 in all seven variant function norms (as shown in Tables 1 and 2). Average amounts of iterations and iteration convergent errors in each time step are searched, which concludes the respective super-linear, linear and quadratic convergence ratio of APN, Picard and PN iterations (Table 3). Also APN, Picard and PN iterations are further compared, which shows that they have similar desirable accuracy; as to efficiency, APN iteration is superior to PN, while the latter is superior to Picard (Table 4, only a few additional time for adaptive judgment is needed for APN iteration). APN, Picard, PN, NewtonR and NewtonL iterations are compared for three different problems, which again show the merits of APN iteration (Table 5). Algorithms with and without iteration decoupling and variant updating are compared, which indicates the former can shrink the scale of calculation hence save computational cost (Table 6). Various adaptive rules as mentioned in Section 2 are designed and realized and their influences on computation efficiency are observed. By collective utilization of the methods of high accuracy scheme, PN iteration, iteration decoupling and updating, adaptive adjustment of iteration parameters, the total iteration amounts and computation time are greatly eliminated with same accuracy guaranteed, and decades of acceleration effects are acquired (as shown in Table 7, only about 1/30 original cost is needed for similar computation accuracy after acceleration).

θ	8×8	16×16	32×32	64×64	ord1	ord2	ord3	ord
0	1.4175e-2	3.6171e-3	9.3008e-4	2.2171e-4	1.97	1.96	2.07	2.00
0.2	1.4187e-2	3.6213e-3	1.0166e-3	2.1896e-4	1.97	1.83	2.22	2.01
0.4	1.4186e-2	3.6560e-3	9.1739e-4	2.1501e-4	1.96	1.99	2.09	2.01
0.6	1.4186e-2	3.6399e-3	9.1920e-4	2.5159e-4	1.96	1.99	1.87	1.94
0.8	1.4185e-2	3.6176e-3	9.1564e-4	2.5179e-4	1.97	1.98	1.86	1.94
1.0	1.4184e-2	3.6177e-3	9.1502e-4	2.3585e-4	1.97	1.98	1.96	1.97

TABLE 1. Approximation errors and orders of the iteration solution to the real solution u

θ	u	v	w	∇u	∇v	u_t	v_t
0	2.00	2.01	1.98	1.97	1.97	1.97	1.97
0.2	2.01	2.01	2.00	1.99	1.99	1.99	1.99
0.4	2.01	2.03	1.98	1.98	1.98	1.98	1.98
0.6	1.94	1.92	1.92	1.91	1.91	1.91	1.91
0.8	1.94	1.92	1.90	1.90	1.90	1.90	1.90
1.0	1.97	1.90	2.00	2.00	2.00	2.00	2.00

TABLE 2. Approximation orders of the iteration solutions to the real solutions

θ	8×8			16×16			32×32			64×64		
	out	in	errstop	out	in	errstop	out	in	errstop	out	in	errstop
0	10.9	19.7	3.36e-13	9.9	26.7	3.17e-13	8.6	22.8	3.00e-13	7.3	25.0	3.22e-13
0.2	10.0	29.6	4.87e-13	9.2	32.6	3.77e-13	7.9	28.2	3.84e-13	6.8	28.9	3.42e-13
0.4	9.4	33.7	2.22e-13	8.5	30.1	2.44e-13	7.4	32.2	2.64e-13	6.4	26.9	2.69e-13
0.6	8.4	29.5	2.43e-13	7.6	28.8	2.82e-13	6.7	28.5	3.27e-13	5.9	25.2	2.73e-13
0.8	7.2	24.9	1.80e-13	6.5	27.1	3.01e-13	6.1	25.3	1.49e-13	5.4	23.2	1.62e-12
1.0	3.4	9.6	1.41e-13	3.0	10.0	3.83e-14	3.0	10.1	6.94e-14	3.0	11.2	8.74e-14

TABLE 3. Average iteration numbers and iteration convergent errors in each time step

	N72	P72	APN72	N80	P80	APN80
Out-it	431	1196	431	682	1289	494
Inner-it	2016	5265	2016	3661	5650	2335

Time	1592.766	4427.656	1599.250	6294.297	11428.531	4530.047
uemax	2.0738e-4	1.8401e-4	2.0738e-4	1.8879e-4	1.5026e-4	1.8879e-4

TABLE 4. Comparison of Newton, Picard and APN iterations

	APN	PN	Picard	NewtonR	NewtonL
1	840.063	833.922	2836.547	1082.25	3387.016
2	633.687	1472.235	1515.813	1583.906	2213.625
3	500.859	879.578	1364.75	972.329	1433.953

TABLE 5. Computation time for various iterations

	DUP	DUPN	Picard	PN
Out-it	1842	1022	1853	770
Inner-it	9522	4602	6392	2857
Time	1765.859	991.937	3755.609	1669.703
uemax	2.298e-4	2.274e-4	2.217e-4	2.358e-4

TABLE 6. Comparisons of decoupling and no-decoupling, Picard and PN iterations

	τ	uemax	vemax	time
DUPN2	1/24	2.54e-4	3.80e-4	372.140
P1	1/288	3.68e-4	4.59e-4	10958.469

TABLE 7. Synthesis acceleration

5. CONCLUSION

In this paper, adaptive Picard-Newton iteration acceleration with high accuracy is designed by using LD approach. By theoretical analysis and numerical experiments, various iteration acceleration methods are analyzed. Remarkable acceleration effects are acquired. This method can be extended to three-dimensional problems. Its methodology, theoretical and experimental results, and program modules can serve as reference and technical support for solving nonequilibrium radiation diffusion and radiation transfer problems.

ACKNOWLEDGEMENT This study is supported by the National Natural Science Foundation of China (60973151, 10871029, 11071024), the Science Foundation of CAEP (2010A0202010), the Foundation of National Key Laboratory of Science and Technology on Computational Physics, and the Defense Industrial Technology Development Program (B1520110011).

REFERENCES

- [1] P.N. Brown, C.S. Woodward, Preconditioning strategies for fully implicit radiation diffusion with material-energy transfer, *SIAM Journal on Scientific Computing*, 23:2, 499-516, 2001.
- [2] G.W. Yuan, X.D. Hang, Z.Q. Sheng, J.Y. Yue, Progress in numerical methods for radiation diffusion equations, *Chinese Journal of Computational Physics*, 26:4, 475-500, 2009.
- [3] X. Cui, J.Y. Yue, G.W. Yuan, Nonlinear scheme with high accuracy for nonlinear coupled parabolic-hyperbolic system, *Journal of Computational and Applied Mathematics*, 235:12, 3527-3540, 2011.
- [4] X. Cui, J.Y. Yue, A nonlinear iteration method for solving a two-dimensional nonlinear coupled system of parabolic and hyperbolic equations, *Journal of Computational and Applied Mathematics*, 234:2, 343-364, 2010.

FINITE POINT METHOD FOR DIFFUSION EQUATION ON IRREGULAR COMPUTATIONAL DOMAIN

Guixia Lv, Longjun Shen, Hao Wu

National Key Laboratory of Science and Technology on Computational Physics, Institute of Applied Physics and Computational Mathematics, Beijing 100088, China, lv_guixia@iapcm.ac.cn

ABSTRACT

In this paper, a finite point method for 2D diffusion equation is developed. The method is based on directional derivatives, and is applicable to irregular computational domain. Spatial discretization is performed by employing numerical formulae of directional derivatives. A new method for selecting steady distribution neighboring point set is presented. An example to show the convergence of the method is also included.

Key Words: *diffusion equation, irregular computational domain, finite point method.*

1. INTRODUCTION

In the last few decades, meshless method, as a new generation of numerical methods, has drawn much attention. Among such methods, the strong-form meshless methods are well known as being simple and straightforward. To guarantee numerical accuracy and stability, a well designed method for selecting neighboring points is always required. In this area, many approaches employ a great number of points which always result in an overdetermined system of equations solved by a least square procedure (e.g. [1],[2]). In the present paper, we will develop a new method for selecting five proper neighboring points only, which facilitate obtaining explicit formulae to approximate directional derivatives and subsequently performing spatial discretization.

The following section includes spatial discretization method and selecting neighboring points method. Section 3 presents an example to show the performance of the method. Conclusions are drawn in Section 4.

2. FINITE POINT METHOD FOR DIFFUSION EQUATION

In this paper, we consider the 2D diffusion equation in the form as follows:

$$-\nabla \cdot (\kappa \nabla u) = f, \quad \text{in } \Omega \quad (1)$$

with proper boundary conditions, where κ, f are given smooth functions, and Ω is computational domain.

2.1 Spatial discretization for diffusion operator

Given three non-parallel directions $\vec{l}_1, \vec{l}_2, \vec{l}_3$, the diffusion operator $-\nabla \cdot (\kappa \nabla u)$ can be reformed as

$$-\nabla \cdot (\kappa \nabla u) = \left(\frac{\overline{(23)}}{(12)(31)} \frac{\partial}{\partial l_1} \kappa \frac{\partial u}{\partial l_1} + \frac{\overline{(31)}}{(12)(23)} \frac{\partial}{\partial l_2} \kappa \frac{\partial u}{\partial l_2} + \frac{\overline{(12)}}{(23)(31)} \frac{\partial}{\partial l_3} \kappa \frac{\partial u}{\partial l_3} \right)$$

where $(i j) = \sin(l_i, l_j)$, $\overline{(i j)} = \cos(l_i, l_j)$.

Suppose that there are five proper neighboring points indexed by “1, 2, 3, 4, 5” around point O , and “1” is the midpoint of the line connecting point 1 and O . Expanding $(\kappa \frac{\partial u}{\partial l_1})_{1'}$ at point O along direction \vec{l}_1 gives

$$(\kappa \frac{\partial u}{\partial l_1})_{1'} = (\kappa \frac{\partial u}{\partial l_1})_o + \frac{\Delta l_1}{2} (\frac{\partial}{\partial l_1} (\kappa \frac{\partial u}{\partial l_1}))_o + O(\Delta l_1^2). \quad (2)$$

Δl_1 is the distance between point 1 and O . Approximating $(\kappa)_{1'}$ by $(\kappa_o + \kappa_1)/2$ and $(\frac{\partial u}{\partial l_1})_{1'}$ by $(u_1 - u_o)/\Delta l_1$ in Eqn. (2) results in

$$\left(\frac{\partial}{\partial l_1} \kappa \frac{\partial u}{\partial l_1} \right)_o = \frac{2}{\Delta l_1} \left[\frac{\kappa_o + \kappa_1}{2} \frac{u_1 - u_o}{\Delta l_1} - \kappa_o \left(\frac{\partial u}{\partial l_1} \right)_o \right] + O(\Delta l_1),$$

where $(\frac{\partial u}{\partial l_1})_o$ can be approximated by the formulae of directional derivatives (see [3]), that is

$$\left(\frac{\partial u}{\partial l_1} \right)_o = \frac{1}{M \Delta l_1} \sum_{j=1}^5 a_{1j} (u_j - u_o) + O(\Delta l_1^2),$$

M, a_{1j} are some combinations of algebraic areas of triangles spanned by point O and its neighbors, and $M \neq 0$ is the so-called solvability condition.

The discretization for $(\frac{\partial}{\partial l_2} \kappa \frac{\partial u}{\partial l_2})_o$ and $(\frac{\partial}{\partial l_3} \kappa \frac{\partial u}{\partial l_3})_o$ are analogous. Therefore, the diffusion operator is fully discretized.

2.2 Selecting neighboring points

To guarantee the numerical process stable, a method for selecting steady distribution neighboring point set is desired which requires $|M|$ to be greater than some positive number for all points in computing domain. Rewrite M as

$$M = M^* \Delta l_1 \Delta l_2 \Delta l_3 \Delta l_4 \Delta l_{15} \Delta l_{25} \Delta l_{35} \Delta l_{45},$$

where

$$M^* = (23)(41)(125)(345) - (12)(34)(235)(415)$$

and Δl_{i5} ($i = 1, 2, 3, 4$) denote the distances between “i” and “5”.

Obviously, the size of M^* which mirrors angle measure is equivalent for different problems. Therefore, using M^* to discuss the neighboring point distribution is an appropriate approach.

For any point i , its neighbors should be chosen in an appropriate point set denoted by G_i , which is neither too large nor too small, in general, it is proper to include 20 points or so in it. For the fixed discrete points in computing process, background grids can be adopted to divide the discrete point set into many small scale point sets which can be chosen as G_i .

For any point i , select its neighbour points 1, 2, 3, 4, 5 in the local set G_i contained point i in turn as follows:

Step 1: select a nearest point to “i” in G_i as “1.”

Step 2: select a nearest point to “i” in G_i as “2” which satisfies $(1,2) \geq \alpha_0$, where α_0 is a parametric angle.

Step 3: select a nearest point to “i” in G_i as “3” which satisfies $(2,3) \geq \alpha_0$ and $(1,3) \neq 0$, otherwise, go to step 1 to select a secondary nearest point as “1”, and repeat step 2 and step 3 until “3” is selected.

Step 4: select a nearest point to “i” in G_i other than “1”, “2” and “3” as “4.”

Step 5: select a nearest point to “i” in G_i other than “1”, “2”, “3” and “4” as “5” which satisfies $M^*(1,2,3,4,5) \geq C_0$, where C_0 is a positive constant always given by $C_0 = 0.1$ in practical application.

3. RESULTS

Example 1. To solve the diffusion equation as follows

$$\begin{cases} \Delta u = e^x \tanh^3\left(\frac{y}{\sqrt{2}}\right), & (x, y) \in \Omega, \\ u = g(x, y), & (x, y) \in \partial\Omega, \end{cases}$$

where $\partial\Omega$ is the boundary of Ω , and $g(x, y)$ is given by the exact solution $u(x, y) = e^x \tanh\left(\frac{y}{\sqrt{2}}\right)$. The computational domain Ω is the so-called C-type domain shown in Figure 1.

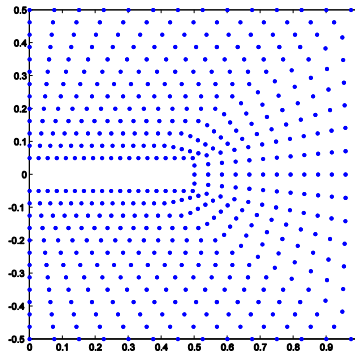


FIGURE 1. C-type computational domain

Define the discrete norm error by

$$\begin{aligned} AL_2 &= \left\{ \sum_{i=1}^N |U_i - u(x_i, y_i)|^2 / N \right\}^{1/2}, \\ RL_2 &= \left\{ \sum_{i=1}^N |(U_i - u(x_i, y_i)) / u(x_i, y_i)|^2 / N \right\}^{1/2}, \\ AL_\infty &= \max_{1 \leq i \leq N} |U_i - u(x_i, y_i)|, \\ RL_\infty &= \max_{1 \leq i \leq N} |(U_i - u(x_i, y_i)) / u(x_i, y_i)|, \end{aligned}$$

where U_i denotes the numerical solution at (x_i, y_i) , and N is the total number of discrete points. The corresponding numerical results are presented in Table 1-2.

N	AL_2	RL_2	AL_∞	RL_∞
120	1.4856E-4	5.4931E-4	6.4180E-4	2.5668E-3
480	4.1929E-5	2.3084E-4	1.2877E-4	1.1381E-3
2000	9.3024E-6	4.8277e-5	3.1864E-5	1.8086E-4
8000	2.3509E-6	1.2048e-5	1.0331E-5	6.6279E-5
Convergence Rate	1.9939	1.8369	1.9857	1.7560

TABLE 1. The errors of u on C-type computational domain

N	AL_2	RL_2	AL_∞	RL_∞
120	1.6464E-3	6.2064E-3	6.3845E-3	2.6233E-2
480	3.8567E-4	2.4712E-3	2.1656E-3	3.0703E-2
2000	1.1980E-4	5.2036e-4	1.8580E-3	7.8485E-3
8000	2.9723E-5	1.2946e-4	2.1791E-4	1.3841E-3
Convergence Rate	1.9305	1.8611	1.6243	1.4148

TABLE 2. The errors of u_x on C-type computational domain

From Table 1-2, we can see that the method obtain almost second-order convergence to the numerical solutions, and more than first-order convergence to the first order derivatives.

4. CONCLUSIONS

In this paper, a finite point method based on directional derivatives is developed for diffusion equation. Spatial discretization scheme and a new method for selecting steady distribution neighboring point set are presented, which are simple, straightforward, and applicable to irregular computational domain.

Acknowledgments: This research was supported by the National Natural Science Foundation of China(10871029, 11071025), the Foundation of CAEP(2010A0202010) and the Foundation of LCP.

REFERENCES

- [1] E. Onate, S. Idelsohn, O.C. Zienkiewicz, and R. L. Taylor, A finite point method in computing mechanics application to convective transport and fluid flow, *Internat. J. Numer. Methods Engrg.*, 39, 3839-3866, 1996.
- [2] D. Sridar and N. Balakrishnan, An upwind finite difference scheme for meshless solvers, *J. Comput. Phys.*, 189, 1-29, 2003.
- [3] L.J. Shen, G.X. Lv and Z.J. Shen, A Finite Point Method based on directional differences, *SIAM Journal on Numerical Analysis*, 47(3), 2224-2242, 2009.

FOURTH-ORDER APPROXIMATION FOR NEUMANN BOUNDARY CONDITION OF HEAT CONDUCTION

Hong-lin Liao

Department of Mathematics, Southeast University, Nanjing, 210096, China, and Department of
Applied Mathematics and Physics, Institute of Sciences, PLAUST, Nanjing, 211101, China,
liaohl2003@yahoo.com.cn

Lei Mao

Department of Applied Mathematics and Physics, Institute of Sciences, PLAUST, Nanjing, 211101,
China, maolei1981@126.com

ABSTRACT

A three-level compact difference scheme is proposed for the heat conduction equation with Neumann boundary conditions. By using the discrete energy method, it shows that the new method is uniquely solvable, unconditionally stable and uniformly convergent with the fully accuracy of second-order in time and fourth-order in space. A numerical example is presented to support the theoretical results.

Key Words: *Heat Transfer Equation, Neumann Boundary Data, Compact Scheme, Convergence*

1. INTRODUCTION

Compared with some low-order methods such as the well-known Crank-Nicolson scheme, high-order compact schemes can achieve higher order accuracies with narrower grid stencils such that they have been considered better suited for numerical simulations, see [1-5] for related discussions. As noted in [3,4], most existing high-order compact schemes are constructed for the Dirichlet boundary-value problems but fewer schemes have been considered for the Neumann problems, which are much more difficult to handle than the Dirichlet problems.

In this report, we construct a new fourth-order compact difference scheme for the heat conduction problem with Neumann boundary conditions. The interesting virtue of the new scheme is that it is fourth-order accurate in space at all grid points, both interior and boundary points. The fourth-order approximations at the boundary points are constructed by transferring the spatial derivatives in the truncation error to temporal derivatives by using the original equation and approximating the resulting terms. For accurate approximations of the time derivatives with second-order temporal accuracy, the resulting scheme involves three time levels.

For simplicity of presentation, we consider the model problem

$$u_t - u_{xx} = f(x, t), \quad 0 \leq x \leq 1, \quad 0 < t \leq T, \quad (1)$$

$$u_x(0, t) = \alpha(0, t), \quad u_x(1, t) = \alpha(1, t), \quad 0 < t \leq T, \quad (2)$$

$$u(x, 0) = \phi(x), \quad 0 \leq x \leq 1. \quad (3)$$

It is to assume that the initial value $\phi(x)$, the boundary values $\alpha(0, t)$, $\alpha(1, t)$, and the source term $f(x, t)$ are regular enough such that the heat equation (1) admits a smooth solution.

For the finite difference approximation, let $h = 1/M$ for a positive integer M , $x_i = ih$ ($0 \leq i \leq M$) and the spatial grid $\Omega_h = \{x_i | 0 \leq i \leq M\}$. Given a grid function $v_h = \{v_i | 0 \leq i \leq M\}$, denote

$v_{i-\frac{1}{2}} = (v_i + v_{i-1})/2$, $\delta_x v_{i-\frac{1}{2}} = (v_i - v_{i-1})/h$ and $\delta_x^2 v_i = (\delta_x v_{i+\frac{1}{2}} - \delta_x v_{i-\frac{1}{2}})/h$. For integer K , take $\tau = T/K$, $t_k = k\tau$ ($0 \leq k \leq K$), $t_{k-1/2} = (t_k + t_{k-1})/2$ and the mesh $\Omega_\tau = \{t_k | 0 \leq k \leq K\}$. Given grid function $\omega^\tau = \{\omega^k | 0 \leq k \leq K\}$, denote $\omega^{k-1/2} = (\omega^k + \omega^{k-1})/2$, $\delta_t \omega^{k-1/2} = (\omega^k - \omega^{k-1})/\tau$, $\omega^{\bar{k}} = (\omega^{k+1} + \omega^{k-1})/2$, $D_t \omega^k = (\omega^{k+1} - \omega^{k-1})/(2\tau)$ and $\delta_t^2 \omega^k = (\omega^{k+1} - 2\omega^k + \omega^{k-1})/\tau^2$.

Let $\{u_i^k | 0 \leq i \leq M, 0 \leq k \leq K\}$ be a grid function on $\Omega_h \times \Omega_\tau$. We consider the following three-level compact difference scheme for solving the model problem (1)-(3)

$$\frac{1}{12}(D_t u_{i-1}^k + 10D_t u_i^k + D_t u_{i+1}^k) - \delta_x^2 u_i^{\bar{k}} = F_i^k, \quad 1 \leq i \leq M-1, 1 \leq k \leq K-1, \quad (4)$$

$$D_t u_0^k + \frac{h}{3}(\alpha_t)_{\bar{0}}^k + \frac{h^2}{12}\delta_t^2 u_0^k + \frac{h^3}{60}(\alpha_u)_{\bar{0}}^k - \frac{2}{h}(\delta_x u_{1/2}^{\bar{k}} - \alpha_0^{\bar{k}}) = F_0^k, \quad 1 \leq k \leq K-1, \quad (5)$$

$$D_t u_M^k - \frac{h}{3}(\alpha_t)_M^{\bar{k}} + \frac{h^2}{12}\delta_t^2 u_M^k - \frac{h^3}{60}(\alpha_u)_M^{\bar{k}} - \frac{2}{h}(\alpha_M^{\bar{k}} - \delta_x u_{M-1/2}^{\bar{k}}) = F_M^k, \quad 1 \leq k \leq K-1, \quad (6)$$

$$u_i^1 = \phi(x_i), \quad 0 \leq i \leq M; \quad u_i^0 = \phi(x_i), \quad 0 \leq i \leq M, \quad (7)$$

where,

$$F_i^k = \frac{1}{12}(f_{i-1}^k + 10f_i^k + f_{i+1}^k), \quad 1 \leq i \leq M-1,$$

$$F_0^k = f_0^k + \frac{h}{3}(f_x)_0^k + \frac{h^2}{12}[(f_t)_0^k + (f_{xx})_0^k] + \frac{h^3}{60}[(f_{xt})_0^k + (f_{xxx})_0^k],$$

$$F_M^k = f_M^k - \frac{h}{3}(f_x)_M^k + \frac{h^2}{12}[(f_t)_M^k + (f_{xx})_M^k] - \frac{h^3}{60}[(f_{xt})_M^k + (f_{xxx})_M^k],$$

$$\phi(x) = \phi(x) + \tau[\phi_{xx}(x) + f(x, 0)] + \frac{\tau^2}{2}[\phi_{xxxx}(x) + f_{xx}(x, 0) + f_t(x, 0)].$$

By using the discrete energy method, it shows that the compact difference method (4)-(7) is uniquely solvable, unconditionally stable and convergent of $O(\tau^2 + h^4)$. The theoretical results of the difference scheme are described in the next section. Section 3 devotes to examining numerically the theoretical results in our analysis. Some comments are presented in the concluding section.

2. STABILITY AND CONVERGENCE OF DIFFERENCE SCHEME

For the theoretical analysis of the fourth-order compact scheme (4)-(7), denote

$$\|v\| = \sqrt{\frac{h}{2} \sum_{i=1}^M (v_{i-1}^2 + v_i^2)}, \quad \|\delta_x v\| = \sqrt{h \sum_{i=1}^M (\delta_x v_{i-1/2})^2}, \quad \|v\|_\infty = \max_{0 \leq i \leq M} |v_i|.$$

We consider firstly the following lemma of a priori estimation.

LEMMA 2.1. Let $\{\omega_i^k\}$ be the solution of the following difference system

$$\frac{1}{12}(D_t \omega_{i-1}^k + 10D_t \omega_i^k + D_t \omega_{i+1}^k) - \delta_x^2 \omega_i^{\bar{k}} = g_i^k, \quad 1 \leq i \leq M-1, 1 \leq k \leq K-1, \quad (8)$$

$$D_t \omega_0^k - \frac{2}{h} \delta_x \omega_{1/2}^k + \frac{h^2}{12} \delta_t^2 \omega_0^k = g_0^k, \quad 1 \leq k \leq K-1, \quad (9)$$

$$D_t \omega_M^k + \frac{2}{h} \delta_x \omega_{M-1/2}^k + \frac{h^2}{12} \delta_t^2 \omega_M^k = g_M^k, \quad 1 \leq k \leq K-1, \quad (10)$$

$$\omega_i^1 = \psi_i, \quad \omega_i^0 = \varphi_i, \quad 0 \leq i \leq M. \quad (11)$$

Then it holds that

$$E^k + \frac{1}{6T} \|\omega^{k-1/2}\|^2 \leq E^1 + \frac{1}{3T} \|\omega^{1/2}\|^2 + \tau \sum_{l=1}^{k-1} \|g^l\|^2, \quad 1 \leq k \leq K,$$

where the energy norm

$$E^k = \frac{1}{2} \left(\|\delta_x \omega^k\|^2 + \|\delta_x \omega^{k-1}\|^2 \right) + \frac{h^3}{12} \left[\left(\delta_t \omega_0^{k-1/2} \right)^2 + \left(\delta_t \omega_M^{k-1/2} \right)^2 \right], \quad 1 \leq k \leq K.$$

Applying Lemma 2.1, it easy to prove the unique solvability, the unconditional stability and the unconditional convergence of the suggested method, as stated in the following theorems.

THEOREM 2.2. *The compact difference scheme (3)-(7) is uniquely solvable.*

THEOREM 2.3. *The compact difference scheme (3) -(7) is unconditionally stability.*

THEOREM 2.4. *The solution of the three-level compact difference scheme (3)-(7) is unconditionally convergent with the convergence order $O(\tau^2 + h^4)$ in the maximum norm.*

3. NUMERICAL EXPERIMENTS

In this section, an example is presented to examine the numerical stability and accuracy of the proposed three-level compact difference scheme. To show the effectiveness of the fourth-order approximations of boundary conditions of Neumann-type (list as 4-order Approx. in the tables), the numerical solutions are compared with those of the following fourth-order compact difference scheme with the one-order ($\chi=0$) and second-order ($\chi=1$) discretizations of Neumann boundary data (list as 1-order Approx. and 2-order Approx. respectively in the tables),

$$\begin{aligned} \frac{1}{12} (\delta_t u_{i-1}^{k-1/2} + 10\delta_t u_i^{k-1/2} + \delta_t u_{i+1}^{k-1/2}) - \delta_x^2 u_i^{k-1/2} &= \frac{1}{12} (f_{i-1}^{k-1/2} + 10f_i^{k-1/2} + f_{i+1}^{k-1/2}), \\ \delta_t u_0^{k-1/2} + \frac{\chi h}{3} \delta_x \delta_t u_{1/2}^{k-1/2} - \frac{2}{h} (\delta_x u_{1/2}^{k-1/2} - \alpha_0^{k-1/2}) &= f_0^{k-1/2} + \frac{\chi h}{3} \delta_x f_{1/2}^{k-1/2}, \quad 1 \leq k \leq K, \\ \delta_t u_M^{k-1/2} - \frac{\chi h}{3} \delta_x \delta_t u_{M-1/2}^{k-1/2} - \frac{2}{h} (\alpha_M^{k-1/2} - \delta_x u_{M-1/2}^{k-1/2}) &= f_M^{k-1/2} - \frac{\chi h}{3} \delta_x \delta_t f_{M-1/2}^{k-1/2}, \quad 1 \leq k \leq K, \\ u_i^0 &= \phi(x_i), \quad 0 \leq i \leq M. \end{aligned}$$

We consider the heat equation $u_t - u_{xx} = e^{x+2t}$ with the Neumann boundary data such that it has solution $u(x, t) = \exp(x + 2t)$. The solution errors in the maximum norm and the experimental rates are listed in Tables 1-2. The results of Theorems 2.3 and 2.4 are supported by observing that the new compact difference method is stable and convergent with the accuracy of second-order in time and fourth-order in space. The fourth-order compact scheme with one-order ($\chi=0$) boundary treatment is convergent with second-order spatial accuracy. The second-order approximation ($\chi=1$) generates third-order accurate solutions. Compared with the lower order approximations of Neumann boundary data, the superiority of our discretizations is seen.

M	K	1-order Approx.		2-order Approx.		4-order Approx.	
		error	Rate	error	Rate	error	Rate
80	80	1.67e-04	---	1.53e-04	---	6.19e-04	---
160	160	4.21e-05	1.99	3.85e-05	1.99	1.55e-04	2.00
320	320	1.05e-05	2.00	9.65e-06	2.00	3.87e-05	2.00

TABLE 1. Convergence of the solution at $T = 1$ for the spacing $h = \tau$

M	K	1-order Approx.		2-order Approx.		4-order Approx.	
		error	Rate	error	Rate	error	Rate
80	6400	3.22e-04	---	1.34e-06	---	9.61e-08	---
160	25600	8.07e-05	2.00	1.69e-07	2.98	5.99e-09	4.00
320	102400	2.02e-05	2.00	2.12e-08	3.00	3.33e-10	4.17

TABLE 2. Convergence of the solution at $T = 1$ for the time step $\tau = h^2$.

4. CONCLUSIONS

Focusing on the fourth-order approximations for the Neumann boundary conditions, we develop a new compact difference scheme that is fourth-order accurate in space at all grid points for solving the one-dimensional heat problem. The unique solvability, unconditional stability and uniform convergence of the difference scheme are theoretically verified by the energy method. Numerical experiments are included to support the error analysis and to exhibit the superiority of the proposed method to other similar approaches.

REFERENCES

- [1] W.Y. Liao, J.P. Zhu and A.Q.M. Khaliq, A fourth-order compact algorithm for nonlinear reaction-diffusion equation with Neumann boundary conditions, *Numerical Methods for Partial Differential Equations*, 22(3), 600-616, 2006.
- [2] J. Zhao, W.Z. Dai and T.C. Niu, Fourth-order compact schemes of a heat conduction problem with Neumann boundary conditions, *Numerical Methods for Partial Differential Equations*, 23(5), 949-959, 2007.
- [3] J. Zhao, W.Z. Dai and S.Y. Zhang, Fourth-order compact schemes for solving multidimensional heat problems with Neumann boundary conditions, *Numerical Methods for Partial Differential Equations*, 24, 165-178, 2008.
- [4] Z.Z. Sun, On the compact difference scheme for heat equation with Neumann boundary conditions, *Numerical Methods for Partial Differential Equations*, 25, 1320-1341, 2009.
- [5] W.Z. Dai, A new accurate finite difference scheme for Neumann (insulated) boundary condition of heat conduction, *International Journal of Thermal Sciences*, 49, 571 - 579, 2010.

BOUNDARY ELEMENT METHOD FOR TRANSIENT RADIATIVE- CONDUCTIVE COUPLED HEAT TRANSFER

Xiao-Wei Gao

State Key Laboratory of Structural Analysis for Industrial Equipment, Dalian University of
Technology, Dalian, 116024, P.R. China, xwgao@dlut.edu.cn

Jing Wang

Department of Engineering Mechanics, School of Civil Engineering, Southeast University, Nanjing ,
210096, P. R. China, wangjing060730@qq.com

ABSTRACT

A boundary-only formulation for transient radiative-conductive coupled heat transfer problems is presented. Heat radiation and conduction are coupled together by radiative heat source, and nonlinear material properties and arbitrary non-linear boundary conditions can be considered. The Green's function for the Laplace equation is adopted in deriving basic heat transfer integral equations. Domain integrals appearing in integral equations are transformed into boundary integrals using the radial integration method (RIM). The Newton-Raphson iteration method is applied to solve the nonlinear algebraic equations, in which the resulted linear set of equations is solved using REBSM. A numerical example is given to demonstrate the efficiency of the presented method.

Key Words: *Heat Radiation, Heat Conduction, Boundary Element Method, Radial Integration Method, REBSM.*

1. INTRODUCTION

Coupled radiation and conduction heat transfer is importantly significant in applications to semi-transparent mediums under high temperature. Some studies have been conducted [1]. Siegel [2] gave a detailed review of the literatures on this subject over the past 40 years. In the recent years, Wellele et al. [3] solved numerically the coupled radiation-conduction heat transfer problems in semi-transparent orthotropic materials, where both the radiation and conduction problems are solved using finite-volumes. Matthew et al.[4] simulated 3D transient radiation and conduction heat transfer inside thin glass sheets undergoing high temperature processing. Blobner et al.[5] developed a novel boundary-only formulation for transient temperature fields in bodies of non-linear material properties and self-irradiating boundary conditions using the dual reciprocity method.

The Boundary Element Method (BEM) [6] is very efficient for solving heat transfer problems. One of the advantages is that the boundary elements in BEM can be directly served as the heat radiative surface. The classical formulation of BEM for radiative heat transfer equations requires volume integrations [7]. Recently, a new transformation technique, called radial integration method (RIM), has been developed by Gao [8], which can transform any domain integrals to the boundary. In this paper, RIM is applied to convert domain integrals appearing in integral equations into equivalent boundary integrals. Two heat transfer modes are coupled by radiation heat source term, which forms the final nonlinear system of equations. The Newton-Raphson iteration scheme is used to solve the nonlinear equation set. A numerical example is provided to illustrate the accuracy and effectiveness of the developed technique.

2. HEAT CONDUCTION EQUATIONS

The transient energy equation (governing equation) for heat conduction in participating media for combined conduction and radiation [9] is

$$\frac{\partial}{\partial x_i} \left(k(T) \frac{\partial T(\mathbf{x}, t)}{\partial x_i} \right) + q_v^r(\mathbf{x}, t) = \rho c \frac{\partial T(\mathbf{x}, t)}{\partial t} \quad \mathbf{x} \in \Omega, \quad t > 0 \quad (1)$$

Where, $k(T)$ is the thermal conductivity, q_v^r the radiative heat source, ρ the density of the media, c the heat capacity of the medium. A weight function $G(\mathbf{x}, \mathbf{y})$ is introduced to Eq. (1) and the Gauss's divergence theorem is applied to derive the following boundary-domain integral equations [8]:

$$\begin{aligned} k(T(\mathbf{y}, t))T(\mathbf{y}, t) = & \int_{\Gamma} G(\mathbf{x}, \mathbf{y})q^c(\mathbf{x}, t)d\Gamma(\mathbf{x}) - \int_{\Gamma} k(T)T(\mathbf{x}, t) \frac{\partial G(\mathbf{x}, \mathbf{y})}{\partial n} d\Gamma(\mathbf{x}) \\ & + \int_{\Omega} G(\mathbf{x}, \mathbf{y})q_v^r(\mathbf{x}, t)d\Omega + \int_{\Omega} \frac{\partial k(T)}{\partial x_i} T(\mathbf{x}, t) \frac{\partial G(\mathbf{x}, \mathbf{y})}{\partial x_i} d\Omega(\mathbf{x}) - \int_{\Omega} G(\mathbf{x}, \mathbf{y})\rho c \left(\frac{\partial T(\mathbf{x}, t)}{\partial t} \right) d\Omega \end{aligned} \quad (2)$$

In this paper, the weight function $G(\mathbf{x}, \mathbf{y})$ is chosen as the Green's function [8].

3. HEAT RADIATION EQUATIONS

The radiative heat transfer and heat source equations can be written as:

$$\begin{aligned} & q^r(\mathbf{y}) + \varepsilon(\mathbf{y})e_b(\mathbf{y}) \\ & = \varepsilon(\mathbf{y}) \int_{\Gamma} \left[e_b(\mathbf{x}) + \frac{1 - \varepsilon(\mathbf{x})}{\varepsilon(\mathbf{x})} q^r(\mathbf{x}) \right] K(\mathbf{x}, \mathbf{y}) \exp(-a|\mathbf{x} - \mathbf{y}|) d\Gamma(\mathbf{x}) \\ & + \varepsilon(\mathbf{y}) \int_{\Omega} a e_b(\mathbf{x}') K_y(\mathbf{x}', \mathbf{y}) \exp(-a|\mathbf{x}' - \mathbf{y}|) d\Omega(\mathbf{x}') \end{aligned} \quad (3)$$

$$\begin{aligned} & q_v^r(\mathbf{y}) + c' a e_b(\mathbf{y}) \\ & = a \int_{\Gamma} \left[e_b(\mathbf{x}) + \frac{1 - \varepsilon(\mathbf{x})}{\varepsilon(\mathbf{x})} q^r(\mathbf{x}) \right] K_x(\mathbf{x}, \mathbf{y}) \exp(-a|\mathbf{x} - \mathbf{y}|) d\Gamma(\mathbf{x}) \\ & + a \int_{\Omega} a e_b(\mathbf{x}') K_0(\mathbf{x}', \mathbf{y}) \exp(-a|\mathbf{x}' - \mathbf{y}|) d\Omega(\mathbf{x}') \end{aligned} \quad (4)$$

where, $e_b = \sigma T^4$ is the blackbody emissive power, $c' = 4$ for internal point and $c' = \alpha / \pi$ for boundary point with α being the geometry angle around the boundary point, i.g., for a smooth point $\alpha = 2\pi$. Functions, such as $K(\mathbf{x}, \mathbf{y})$ are the kernels of heat radiation which can be found in [7].

4. COUPLING SYSTEM OF EQUATIONS

All domain integrals in Eqs.(2)-(4) are transformed into boundary integrals using RIM [8], resulting in integral equations formulated in terms of boundary integrals only. Discretizing the boundary of the problem into boundary elements and evaluating all integrals in Eq.(2), the following algebraic equation can be formed:

$$[H]\{kT\} - [G]\{q^c\} = [Q]\{q_v^r\} + [V]\{T\} - [C] \left\{ \frac{\partial T}{\partial t} \right\} \quad (5)$$

Similarly, algebraic equations from Eqs.(3) and (4) can be expressed, respectively, as

$$[A]\{e_b\} + [B]\{q^r\} + [W]\{e_b\} = 0 \quad (6)$$

$$\{q^r\} = [M]\{e_b\} + [N]\{q^r\} + [W']\{e_b\} \quad (7)$$

After some operations on Eqs.(5) to (7) and noticing that $e_b = \sigma T^4$, the final system of equations can be written as

$$[H]\{kT\} - [G]\{q\} + [\bar{Q}]\{\sigma T^4\} = [V]\{T\} - [C]\left\{\frac{\partial T}{\partial t}\right\} \quad (8)$$

where $\{q\} = \{q^c\} - \{q^r\}$, $[\bar{Q}] = -[Q][\bar{M}] + [G][B]^{-1}[A]$ and $[\bar{M}] = [\bar{M}] - [N][B]^{-1}[A]$.

Equation (8) is the final system of equations formulated in terms of the temperature T and boundary heat flux q . Since it is a nonlinear equation set about T , an iterative solution scheme is needed to solve unknown temperatures and fluxes by imposing initial and boundary conditions. In this paper, the Newton-Raphson iterative scheme is adopted to solve this system.

For transient problems, the time-marching technique is used to compute the time derivative term with a finite difference method.

5. NUMERICAL EXAMPLE

A computer code, called RIBEM, has been developed using formulations presented in this paper. To verify the correctness of the presented formulations, a numerical example is presented in the paper. The example considered is a $1\text{m} \times 1\text{m}$ plate (FIGURE 1). The left and right sides are insulated, the top wall is imposed with temperature 100K , while the bottom wall exchanges energy with environment with convection coefficient $h = 200\text{W}/(\text{m}^2 \cdot \text{K})$ and emissivity $\varepsilon = 1$. The parameters used are $k(T) = (15 + 0.01T^2)$ ($\text{W}/(\text{m} \cdot \text{K})$), $c = 100\text{J}/(\text{kg} \cdot \text{K})$, $\rho = 100\text{kg}/\text{m}^3$, and the absorption of the medium $a = 1$. Initial temperature is $T_0 = 100\text{K}$ for whole model. The computational model is as shown in Fig.2. Temperatures at 81 internal points are investigated.

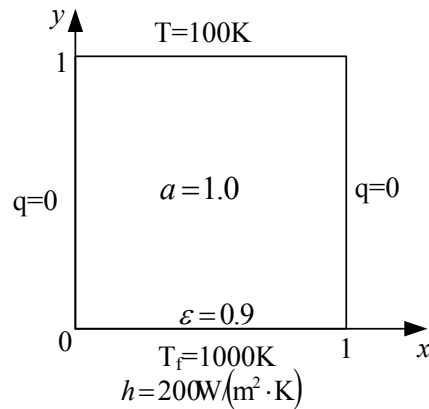


FIGURE 1. Dimensions and conditions of the plate

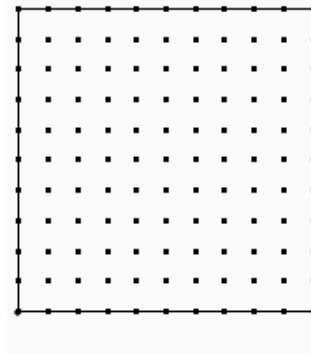


FIGURE 2. BEM model of the plate

Fig.3 shows the computed temperature curves along y -direction in the left side of the plate by using the heat conduction only and conduction-radiation coupling together. It can be seen that the speed of heat transfer is faster in participate of the radiation. This is accordant with the physical analysis.

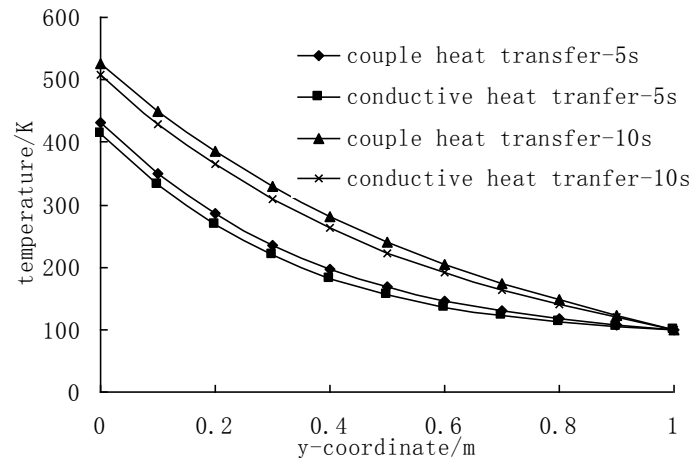


FIGURE 3. Temperature curves along y-direction

6. CONCLUSIONS

An efficient boundary-only numerical technique is presented for solving transient nonlinear radiative-conductive coupled heat transfer problems. The technique is capable of dealing with heat transfer problems with non-linear conductivity and medium radiation. The radial integration method is used to transform the domain integrals appearing in the derived basic boundary-domain integral equations into boundary integrals, which results in a pure boundary element analysis algorithm.

REFERENCES

- [1] D. Lacroix, G. Parent, F. Asllanaj and G. Jeandel, Coupled radiative and conductive heat transfer in a non-grey absorbing and emitting semitransparent media under collimated radiation, *J. Quant. Spectrosc. Radiat. Transfer*, 75, 589-609, 2002.
- [2] R. Siegel, Transient thermal effects of radiant energy in translucent materials, *Journal of Heat Transfer*, 120, 4-23, 1998.
- [3] O. Wellele and H.R.B. Orlande, Coupled Conduction-radiation in Semi-transparent Materials at High Temperatures, *Journal of Physics and Chemistry of Solids*, 67, 2230-2240, 2006.
- [4] M.R. Jones and V.P. Solovjoy, Green's Function Approach to Nonlinear Conduction and Surface Radiation Problems, *Journal of Heat Transfer*, 132, 024502-1, 2010.
- [5] J. Blobner and R.A. Bialecki, et al., Transient Non-linear Heat Conduction-radiation Problems- A Boundary Element Formulation, *Int. J. Nume. Meth. Engng*, 46, 1865-1882, 1999.
- [6] E.A. Divo and A.J. Kassab, Boundary Element Methods for Heat Conduction, With Applications in Non-homogeneous Media. WIT Press: Southampton, 2003.
- [7] R.A. Bialecki, *Solving Heat Radiation Problems Using the Boundary Element Method*. Computational Mechanics Publications 1993.
- [8] X.W. Gao, A meshless BEM for isotropic heat conduction problems with heat generation and spatially varying conductivity, *Int. J. Numer. Meth. Engng*. 66, 1411-1431, 2006.
- [9] B. Mondal and S.C. Mishra, The lattice Boltzmann method and the finite volume method applied to conduction-radiation problems with heat flux boundary conditions, *Internal journal for numerical methods in engineering*, 78, 172-195, 2009.

A LATTICE BOLTZMANN MODEL FOR VARIABLE COEFFICIENT ELLIPTIC EQUATIONS

Heying Feng, Xiaoqing Zhang, Huanxin Chen

School of Energy and Power Engineering, Huazhong University of Science and Technology, Wuhan, 430074, Hubei, P. R. China, fengheyings1983@163.com; zhangxq@mail.hust.edu.cn

ABSTRACT

A lattice Boltzmann model is proposed to solve elliptic equations with variable coefficient. Compared with the previous model, the present model is a more effective solver to the ellipse equation with variable coefficient, and the ellipse equation is exactly recovered to order $O(\varepsilon^2)$. The relaxation time τ is not fixed and is defined by the coefficient of the equation. The limited numerical results show that the present model is valid for ellipse equations.

Key Words: *Lattice Boltzmann model, variable coefficient elliptic equation, Chapman-Enskog expansion.*

1. INTRODUCTION

The n-dimension ellipse-type equation considered in this paper can be written as

$$-\nabla \cdot [\alpha(x)\nabla \phi] = F(x, \phi) \quad (1)$$

where ∇ is the gradient operator with respect to the spatial coordinate x , ϕ is a scalar function of position x , $\alpha(x) \geq \alpha_0 > 0$ is the coefficient dependent on position x and function $F(x, \phi)$ is the source term. There are many numerical methods for the solution of equation (1), such as finite difference method, finite element method, boundary element method, etc.

The lattice Boltzmann method (LBM) is a new computational tool for the study of fluid dynamics and physical problems with partial differential equations. It has been developed as an alternative method for computational fluid dynamics (CFD), see Refs. [1-3]. Recently, LBM has been applied to simulate linear and nonlinear partial differential equations, see Refs. [4-8] and reference therein. Especially, Ref. [6] presented a better lattice Boltzmann model solver for the Poisson equation and the transient term derived by previous models [5] is already eliminated.

In this paper, simulated by the idea in [6], a lattice BGK model is presented to solve the elliptic equation with variable coefficient. Compared with the model of Ref. [6], this present model is capable of dealing with elliptic equations with variable coefficient through a variable relaxation time determined by the coefficient of the elliptic equation. Additionally, this model can avoid the too large relaxation time value τ by introducing a new parameter in arithmetical.

2. LATTICE BOLTZMANN MODEL

The present Lattice Boltzmann model is based on $DnQb$ lattice with b velocity direction in nD space. The evolution equation of the distribution function in the model is described as

$$f_j(x + c_j \Delta t, t + \Delta t) = f_j(x, t) - \frac{1}{\tau} [f_j(x, t) - f_j^{eq}(x, t)] + Rc_s^2 \Delta t^2 F_j(x, t), \quad j = 0, \dots, b-1, \quad (2)$$

where $\{c_j, j=0,1,\dots,b-1\}$ is a set of discrete velocity directions, Δt the time step, τ the dimensionless relaxation time, $f_j^{eq}(x,t)$ the equilibrium distribution function, c_s the sound velocity, R a constant controlling the relaxation time τ , and $F_j(x,t)$ the distribution function for the source term. The Knudsen number ε is assumed to be equal to the time step Δt [9]. With parameter ε , the lattice Boltzmann Eq. (2) can be rewritten as

$$f_j(x+c_j\varepsilon,t+\varepsilon) = f_j(x,t) - \frac{1}{\tau} [f_j(x,t) - f_j^{eq}(x,t)] + Rc_s^2\varepsilon^2 F_j(x,t), \quad j=0,\dots,b-1. \quad (3)$$

Using the Taylor expansion to Eq. (3), yields

$$f_j(x+c_j\varepsilon,t+\varepsilon) - f_j(x,t) = \sum_{n=1}^2 \frac{\varepsilon^n}{n!} \left(\frac{\partial}{\partial t} + c_j \frac{\partial}{\partial x} \right)^n f_j(x,t) + O(\varepsilon^3). \quad (4)$$

With the assumption of small Knudsen number ε , applying the Chapman-Enskog expansion to $f_j(x,t)$ and ∂_t , that is

$$f_j = f_j^{eq} + \varepsilon f_j^{(1)} + \varepsilon^2 f_j^{(2)} + O(\varepsilon^3), \quad \partial_t = \partial_{t0} + \varepsilon \partial_{t1} + \varepsilon^2 \partial_{t2} + O(\varepsilon^3) \quad (5)$$

Substitute Eqs. (4) and (5) into Eq. (3) and retain and rearrange those terms with order ε and ε^2 , and thus gives

$$D_{0j} f_j^{eq} = -\frac{1}{\tau} f_j^{(1)}, \quad \partial_{t1} f_j^{eq} + D_{0j} f_j^{(1)} + \frac{1}{2} D_{0j}^2 f_j^{eq} = -\frac{1}{\tau} f_j^{(2)} + Rc_s^2 F_j(x,t), \quad (6)$$

where $D_{0j} = (\partial_{t0} + c_j \bullet \nabla)$. Setting $\sum_j f_j = \sum_j f_j^{eq} = 0$ and $\sum_j c_j f_j^{eq} = 0$, and considering Eq. (5), obtains $\sum_j f_j^{(1)} = \sum_j f_j^{(2)} = 0$. Therefore, above equations yield

$$-\frac{1}{\tau} \sum_j c_j f_j^{(1)} = \nabla \bullet \left(\sum_j c_j c_j f_j^{eq} \right). \quad (7)$$

Considering Eqs. (6) and (7), obtains

$$\sum_j D_{0j}^2 f_j^{eq} = -\nabla \bullet \left(\frac{1}{\tau} \sum_j c_j f_j^{(1)} \right) = (\nabla \nabla) : \left(\sum_j c_j c_j f_j^{eq} \right). \quad (8)$$

Summing the second equation in (6) over j and combining Eqs. (7) and (8), yields

$$\nabla \bullet \left\{ (0.5 - \tau) \nabla \bullet \sum_j c_j c_j f_j^{eq} \right\} = Rc_s^2 \sum_j F_j(x,t). \quad (9)$$

Setting $\sum_j c_j c_j f_j^{eq} = c_s^2 \phi I$, $F_j(x,t) = \lambda_j F(x,\phi)$ and $\sum_j \lambda_j = 1$, one has from Eq. (9) that

$$-\nabla \bullet [(\tau - 0.5) \nabla \phi] = RF(x,\phi).$$

Therefore, taking $\tau = 0.5 + R\alpha(x)$, one recovers the Eq.(1) to order $O(\varepsilon^2)$.

Remark If R is set as $R = [\max\{\alpha(x) : x \in \Omega\}]^{-1}$, then $0.5 + \alpha_0 [\max\{\alpha(x) : x \in \Omega\}]^{-1} \leq \tau \leq 1.5$, which is an efficient range for lattice Boltzmann method. Specially, if $\alpha(x)$ is constant in Ω , then the model in this paper is reduced to the one presented in Ref. [6].

3. NUMERICAL EXPERIMENTS

For the limit on the page, we only consider the following two examples:

Example 1. $\alpha(x) = e^x$, $F(x) = 2e^{2x}(\sin \pi x + \pi \cos \pi x) + e^{2x}(\pi \cos \pi x - \pi^2 \sin \pi x)$, and the analytical solution $\phi^* = e^x \sin \pi x$ in the internal $[0,1]$.

Example 2. $\alpha(x, y, z) = e^{xyz}$, $F(x, y, z) = e^{xyz}(3 \sin(x + y + z) - (yz + xz + xy) \cos(x + y + z))$, and the analytical solution is $\phi^* = \sin(x + y + z)$ on the computational region $\Omega = [0,1]^3$.

In the numerical experiments, the equilibrium distribution function f_j^{eq} is defined as follows [6]:

$$\begin{cases} f_0^{eq} = (\omega_0 - 1)\phi, \\ f_j^{eq} = \omega_j\phi, \quad j = 1, \dots, b. \end{cases}$$

The distribution functions $f_j(x, t)$ are initialized as $f_j^{eq}(x, t)$, and ϕ is set zero at $t = 0$ except on the boundary. The non-equilibrium extrapolation scheme [11] is adopted. Additionally, the global relative error $GRE = \frac{\sum |\phi - \phi^*|}{\sum |\phi^*|}$ is used to test the accuracy of the present model in this paper, where ϕ and ϕ^* are the numerical solution and analytical solution, respectively. Moreover, D1Q3 and D3Q13 are applied to 1-dimension and 3-dimension problems, respectively.

First, we verify the proposed model is a second order scheme on precision by applying the model to the Example 1 with knots $NX = 20, 40, 50, 80, 100, 120, 150,$ and 200 respectively. We obtain the relation of GRE with lattice space, which can be described by a line. The slope of the line is about 1.9818, which is same as the results in Ref. [6].

Then the given two examples are numerical solved on 100 and $100 \times 100 \times 100$ lattice, respectively. The numerical results are listed in Table 1, where NS, AS and ABSerror denote the numerical solution, analytical solution and absolute error, respectively. For Example 1, the max absolute error is $1.99837e-4$ on these knots. And the max absolute error on knots is $4.20666e-5$ for Example 2. These facts imply the presented model is valid.

Example 1				Example 2			
x_i	NS	AS	ABSerror	(x_i, y_i, z_i)	NS	AS	ABSerror
0.1	0.34155	0.341517	3.54046e-5	(0.1,0.1,0.1)	0.295516	0.295520	4.20666e-5
0.2	0.71790	0.717923	2.55283e-5	(0.2,0.2,0.2)	0.564632	0.564642	1.04734e-5
0.3	1.09200	1.092059	5.87153e-5	(0.3,0.3,0.3)	0.783310	0.783327	1.69096e-5
0.4	1.41876	1.418810	4.95998e-5	(0.4,0.4,0.4)	0.932018	0.932039	2.10860e-5
0.5	1.64872	1.648721	1.27070e-6	(0.5,0.5,0.5)	0.997473	0.997495	2.19866e-5
0.6	1.73302	1.732938	8.20414e-5	(0.6,0.6,0.6)	0.973829	0.973848	1.86309e-5
0.7	1.62936	1.629160	1.99837e-4	(0.7,0.7,0.7)	0.863198	0.863209	1.13666e-5

0.8	1.30853	1.308140	3.89863e-4	(0.8,0.8,0.8)	0.675463	0.675463	1.80551e-7
0.9	0.76075	0.760059	6.88839e-4	(0.9,0.9,0.9)	0.427398	0.427380	1.81198e-5

TABLE 1. Comparison between numerical and analytical solution two examples

Additionally, we find that the effect of parameter R on the precision is significant. For Example 1, the GRE is $1.32892e-3$ for $R = 1$, but $1.90219e-4$ for the R defined in the remark.

4. CONCLUSIONS

In this paper, a lattice Boltzmann model is proposed to solve variable coefficient ellipse equations. And the ellipse equation is exactly recovered to order $O(\varepsilon^2)$. The relaxation time τ in the present model is not fixed and is defined by the coefficient of the equation. Moreover, τ can be controlled in the interval $\left[0.5 + \frac{\alpha_0}{\max\{\alpha(x) : x \in \Omega\}}, 1.5\right]$, in which the lattice Boltzmann method is very efficient. Additionally, the parameter R effects the precision and performance greatly. The limited numerical results show that the present model is valid for variable coefficient ellipse equations.

Nevertheless, some important issues, such as how to choose suitable R and how to modify the model for more general elliptic equations need further studies.

REFERENCES

- [1] R. Benzi, S. Succi, M. Vergassola, The lattice Boltzmann equation: theory and applications, *Phys. Rep.* 222:147-197, 1992.
- [2] Z.L. Guo, B.C. Shi, N.C. Wang, Lattice BGK model for incompressible Navier-Stokes equation, *J. Comput. Phys.* 165:288-306, 2000.
- [3] B.C. Shi, Z.L. Guo, N.C. Wang, Lattice Bhatnagar-Gross-Krook simulation for turbulent natural convection in a Cavity, *Chin. Phys. Lett.*, 19:515-521, 2002.
- [4] M. Hirabayashi, Y. Chen, H. Ohashi, The lattice BGK model for the Poisson equation, *JSME Int. J. Ser. B*, 44(1):45-52, 2001.
- [5] J. Wang, M. Wang, Z. Li, Lattice Poisson-Boltzmann simulations of electro-osmotic flows in microchannels, *J. Colloid. Interface Sci.*, 296:729-736, 2006.
- [6] Z.H. Chai and B.C. Shi, A novel lattice Boltzmann model for the Poisson equation, *Applied Mathematical Modelling*, 32:2050-2058, 2008.
- [7] Z.H. Chai, B.C. Shi, L. Zheng, A unified lattice Boltzmann model for some nonlinear partial differential equations, *Chaos, Solitons and Fractals*, 36:874-882, 2008.
- [8] B.C. Shi, Z.L. Guo, Lattice Boltzmann model for nonlinear convection-diffusion equations, *Phys. Rev. E* 79. 016701, 2009.
- [9] G. W. Yan, A lattice Boltzmann equation for waves, *J. Comput. Phys.* 161:61-69, 2000.
- [10] S.P. Dawson, S. chen, D.G. Doolen, Lattice Boltzmann Computations for reaction-diffusion equation, *J. Chem. Phys.* 98(2):1514-1523, 1993.
- [11] Z.L. Guo, C.G. Zheng, B.C. Shi, Non-equilibrium extrapolation method for velocity and pressure boundary conditions in the lattice Boltzmann method. *Chin. Phys.* 11:366-374, 2002.

EXTENDED THERMODYNAMIC APPROACH FOR HEAT TRANSFER IN MICROFLUIDIC STRUCTURES

Guangxin Zhai, Guihua Tang, Wenquan Tao

MOE Key Laboratory of Thermo-Fluid Science and Engineering, School of Energy and Power Engineering, Xi'an Jiaotong University, Xi'an 710049, PRC, ghtang@mail.xjtu.edu.cn

Xiaojun Gu, David R. Emerson

Computational Science and Engineering Department, STFC Daresbury Laboratory, Warrington WA4 4AD, UK, xiaojun.gu@stfc.ac.uk; david.emerson@stfac.ac.uk

ABSTRACT

Gases in microfluidic structures or devices are often in a non-equilibrium state. The conventional thermodynamic models for fluids and heat transfer break down and the Navier-Stokes-Fourier equations are no longer accurate or valid. In this paper, the extended thermodynamic approach is employed to study the heat transfer in microstructures. It is shown that the heat transfer in the non-equilibrium state no longer obeys the Fourier gradient transport law and the 26 moment equations are able to predict the velocity, pressure, and temperature profiles in the early transition regime.

Key Words: *Heat Transfer, Non-equilibrium, Moment Method.*

1. INTRODUCTION

Due to the rapid development in fabrication technology for constructing micro-electro-mechanical-systems (MEMS), fluid flow at the micro- and nano-scale has received considerable attention. A basic understanding of the nature of flow and heat transfer in these devices or structures is considered essential for efficient design and control of MEMS. Gas flows in micro-scale devices suffer from non-equilibrium effects when the gas molecular mean free path is the same order as the characteristic length of the device. The degree of non-equilibrium of a gas is generally expressed through the Knudsen number ($Kn=\lambda/L$) which is the ratio of the molecular mean free path, λ , to a typical dimension of the flow field, L . The different rarefaction regimes can be summarised according to the value of the Knudsen number. Most MEMS operate at the slip and early transition regime ($Kn < 1$). Different approaches have been employed by various researchers to capture and describe the non-equilibrium phenomena that arise due to an insufficient number of molecular collisions occurring under rarefied conditions. Microscopically, the Boltzmann equation provides an accurate description of a dilute gas at all degrees of rarefaction and describes its state through a molecular distribution function that treats the gas as a large number of interacting molecules, colliding and rebounding according to prescribed laws. However, solutions of the Boltzmann equation, either directly [1] or through the direct simulation Monte Carlo (DSMC) method [2], entail significant mathematical complexity and can be computationally expensive, particularly for low-speed, low Knudsen number flows in the slip and transition regime. Due to the difficulties associated with solving the Boltzmann equation, there is significant effort being made to construct alternative solution strategies that can provide an accurate description of a gas with Knudsen numbers that extend into the early transition regime, such as the lattice Boltzmann method [3]. The extended thermodynamic equations developed with the method of moments have been used to predict the hydrodynamic quantities successfully [4-6]. In this paper, the regularised 26 moment equations are briefly introduced. They are employed to study heat transfer between two parallel plates of different temperatures and flow characteristics of pressure-driven flow through a long microchannel with different outlet Knudsen numbers. The predicted results are compared with DSMC data [7] and LBM data [8]. It is shown that the extended thermodynamic model is able to capture a range of non-equilibrium phenomena, such as the non-uniform pressure between the plates and the existence of a normal stress without any velocity gradient.

2. EXTENDED THERMODYNAMIC APPROACH: 26 MOMENT EQUATIONS

The Boltzmann equation is the central equation in kinetic theory, the properties of which can be used to guide the development of kinetic and macroscopic models for rarefied gas flow. Once the distribution function, f , is known, its moments with respect to ξ can be determined. For example, the density, ρ , and the momentum, ρu_i , can be obtained from

$$\rho = \int f d\xi \quad \text{and} \quad \rho u_i = \int \xi_i f d\xi \quad (1)$$

where ξ_i and u_i represent the particle and fluid velocity, respectively. It is convenient to introduce the intrinsic or peculiar velocity as $c_i = \xi_i - u_i$, so that the moments with respect to c_i can be conveniently calculated. A set of N moments are then used to describe the state of the gas through

$$\rho_{i_1 i_2 \dots i_N} = \int c_{i_1} c_{i_2} \dots c_{i_N} f d\xi \quad (2)$$

Any moment can be expressed by its trace and traceless part [4]. For example, the pressure tensor can be separated as follows:

$$p_{ij} = \int c_i c_j f d\xi = p \delta_{ij} + p_{<ij>} = p \delta_{ij} + \sigma_{ij}, \quad (3)$$

where δ_{ij} is the Kronecker delta function, $p = p_{kk}/3$ is the pressure, and $\sigma_{ij} = p_{<ij>}$ is the deviatoric stress tensor. The angular brackets are used to denote the traceless part of a symmetric tensor. Furthermore, the thermal energy density, ε , is given by

$$\rho \varepsilon = \frac{1}{2} \int c^2 f d\xi = \frac{3}{2} \rho R T. \quad (4)$$

The temperature, T , is related to the pressure and density by the ideal gas law, $p = \rho R T$ where R is the gas constant. The heat flux vector is

$$q_i = \int c^2 c_i f d\xi / 2. \quad (5)$$

The molecular distribution function, f , can be reconstructed from the values of its moments. Grad expressed f in Hermite polynomials as:

$$f = f_M \lim_{N \rightarrow \infty} \sum_{n=0}^N \frac{1}{n!} a_A^{(n)} H_A^{(n)} \quad (6)$$

where $H_A^{(n)}$ is the Hermite polynomials and $a_A^{(n)}$ the coefficients, which are linear combinations of the moments. f_M is the Maxwellian distribution function.

To accurately describe the state of a gas an infinite number of moments ($N \rightarrow \infty$) is required to reconstruct the distribution function. However, for gases not too far from equilibrium, a finite number of moments should provide an adequate approximation. When $N=4$, a 26 moment system is constructed. Instead of using of the gradient transport assumption for heat flux and stress to close the conservation equations, their governing equations as well as higher moment equations are derived from the Boltzmann equation. The details of the extended thermodynamic model can be found in Ref. [4], which is able to capture many non-equilibrium phenomena, such as Knudsen layer, Knudsen minimum. In the present study, it is employed to predict the thermal characteristics between two parallel plates with different temperatures and the flow characteristics of pressure-driven flow through a long microchannel with different outlet Knudsen numbers.

3. RESULTS

The heat transfer between two parallel planar plates with different temperatures is studied with the extended thermodynamic model. To be consistent with the DSMC simulation setup [7], the lower wall with a temperature of 263K sits at $y=0$ and the other wall with a temperature of 283K at $y=L$. All the derivatives in the x -direction parallel to the walls are zero. Both walls are stationary. The

Knudsen number is calculated on a reference temperature of 273K and different reference pressures, as given in Ref. [7]. The predicted temperature profiles at different Knudsen numbers are shown in figure 1 in comparison with the DSMC data [7]. When $Kn=0.0475$ in the slip regime, both NSF and extended thermodynamic models can predict the temperature between the plates accurately, except that the NSF equations cannot capture the thermal Knudsen layer close the walls as shown in figure

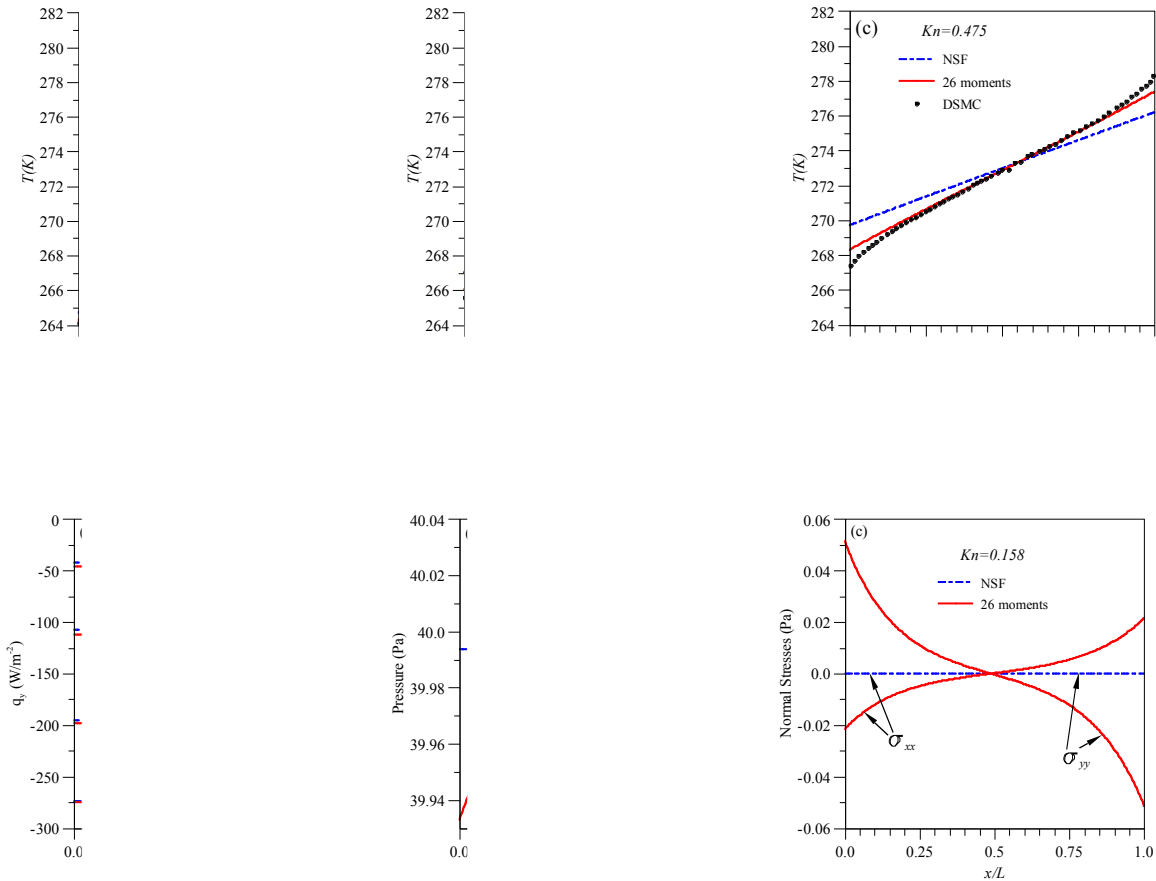


FIGURE 2. Characteristics of the non-equilibrium heat transfer between the parallel plates with different temperatures. (a) Normal heat flux; (b) Pressure; (c) Normal stresses

The normal heat flux, q_y , between the two plates is a constant as shown in figure 2(a). However the NSF equations underpredict the value of heat flux as the value of the Knudsen number increases. The NSF equations predict a constant pressure distribution between the two plates. However, the 26 moment equations show that the pressure close to the hot wall is higher than that close to the cold wall, as demonstrated in figure 2(b). More interestingly, the normal stresses, σ_{xx} and σ_{yy} are not equal to zero without any velocity gradient and the NSF equations completely fail to capture this non-equilibrium effect as indicated in figure 2(c).

The gas flows through a long microchannel with different Knudsen numbers at the outlet are also studied with the extended thermodynamic model. The walls with a temperature of 273K sit at $y=0$ and $y=L$ separately. The height of the channel, L , is 1 μ m and the ratio of the channel length to height keeps at 100. Pressure ratio of the inlet to outlet is 2.0. Knudsen number is calculated on the temperature of 273K and the pressure at the outlet. The predicted velocity and pressure profiles at

different Knudsen numbers are shown in figure 3 in comparison with the DSMC and LBM data given in Ref. [8]. The results from 26 moment equations are in good agreement with DSMC and LBM data. Deviation of pressure distribution from a linear pressure can also be captured by the extended thermodynamic model.

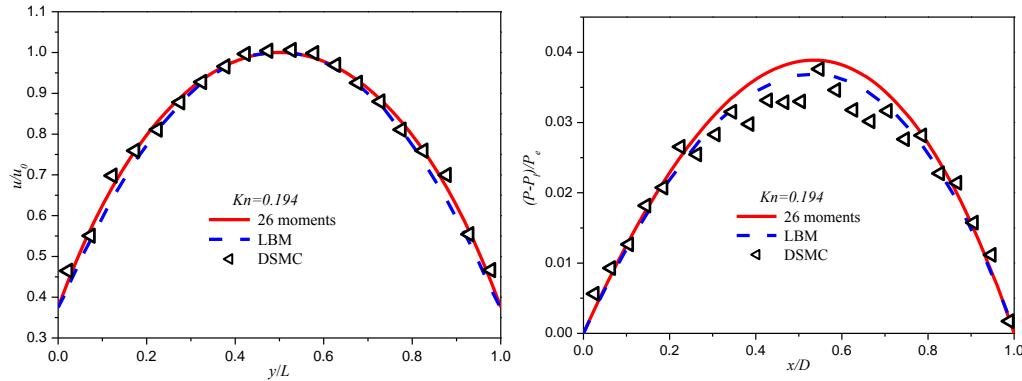


FIGURE 3. Streamwise velocity at the outlet and pressure deviation of pressure-driven flow through a long microchannel when $Kn=0.194$

4. CONCLUSIONS

The 26 moment equations are employed to study the temperature distribution at different Knudsen numbers between two parallel planar plates with different temperatures, and the flow characteristics of pressure-driven flow through a long microchannel with different outlet Knudsen numbers. It is found that the extended thermodynamic approach can predict heat transfer and the deviation of pressure distribution from a linear pressure in the non-equilibrium state in the early transition regime. The results are fairly accurate in comparison with the DSMC data with substantially low computational cost.

This work is supported by the National Natural Science Foundation of China under grant number 51076125 (GXZ, GHT and WQT) and Collaborative Computational Project 12 of the Engineering and Physical Sciences Research Council (XJG and DRE).

REFERENCES

- [1] L. Mieussens, Discrete-velocity models and numerical schemes for the Boltzmann-BGK equation in plane and axisymmetric geometries, *J. Comput. Phys.*, 162, 429-66, 2000.
- [2] G. Bird, *Molecular Gas Dynamics and the Direct Simulation of Gas Flows*, Clarendon Press, Oxford, 1994.
- [3] G.H. Tang, Y.H. Zhang, X.J. Gu, and D.R. Emerson, Lattice Boltzmann modelling Knudsen layer effect in non-equilibrium flows, *Europhys. Lett.*, 83, 40008, 2008.
- [4] X.J. Gu and D.R. Emerson, A high-order moment approach for capturing non-equilibrium phenomena in the transition regime, *J. Fluid Mech.*, 636, 177-216, 2009.
- [5] X.J. Gu, D.R. Emerson, and G.H. Tang, Kramers' problem and the Knudsen minimum: A theoretical analysis using a linearised 26-moment approach, *Contin. Mech. Thermodyn.*, 21, 345-360, 2009.
- [6] P. Taheri and H. Struchtrup, An extended macroscopic transport model for rarefied gas flows in long capillaries with circular cross section, *Phys. Fluids*, 22, 112004, 2010.
- [7] M.A. Gallis, D.J. Rader, and J.R. Torczynski, Calculations of the near-wall thermophoretic force in rarefied gas flow, *Phys. Fluids*, 14, 4290-4301, 2002.
- [8] Q. Li, Y.L. He, G.H. Tang, and W.Q. Tao, Lattice Boltzmann modeling of microchannel flows in the transition flow regime, *Microfluid. Nanofluid.*, 10, 607-18, 2011.

Simulation of the miscible Rayleigh-Taylor Instability with variable Prandtl numbers by Lattice Boltzmann Method

Gaojie Liu, Zhaoli Guo

National Laboratory of Coal Combustion, Huazhong University of Science and Technology, Wuhan,
People's Republic of China

E-mail addresses: liugj.hust@gmail.com, zlguo@hust.edu.cn

ABSTRACT

In this paper, the characteristics of a two-dimensional Rayleigh-Taylor instability in incompressible and miscible flows with variable Prandtl numbers are studied numerically by the lattice Boltzmann method (LBM). Since previous works study the Rayleigh-Taylor instability with constant Prandtl number with emphasis on the interfacial dynamics, we use double distribution function LBM model to investigate the effects of variable Prandtl numbers on mixing in both absolute time and dimensionless time. The numerical results reveal that the mixing-zone grows differently with various Prandtl numbers in absolute time, but Prandtl numbers do not affect mixing growth in dimensionless time.

Key Words: *Lattice Boltzmann method, miscible, Rayleigh-Taylor instability.*

1. INTRODUCTION

Rayleigh-Taylor instability occurs as a heavier fluid is put on a lighter one. The small disturbance at the interface will increase and develop into turbulence finally. Numerical simulation have been shown to be a powerful tool for analyzing the dynamics of Rayleigh-Taylor instability, which can provide detailed information which is difficult to obtain in experiments. As an effective and stable approach, the lattice Boltzmann equation (LBE) method has some advantages in simulating such complicated phenomena. The LBE has been used to study the Rayleigh-Taylor instability of immiscible fluids, with emphasis on the interfacial dynamics. In this paper we investigate the effects of variable Prandtl numbers on mixing in both absolute time and dimensionless time. The numerical results reveal the mixing-zone grows differently with various Prandtl numbers in absolute time, but Prandtl numbers do not affect mixing growth in dimensionless time.

2. PROBLEM DESCRIPTION AND THE CONTROL EQUATIONS

In this study, we consider a layer of heavy fluid placed on top of another layer of light fluid in a gravitational field with gravity pointing downward in a two-dimensional cavity. The fluids are supposed to be incompressible and miscible. Periodic boundary condition is applied in the horizontal direction, while the temperatures at the top and bottom plates are fixed at T_1 and T_2 ($T_1 < T_2$), respectively. The initial interface to be at height $y = 0$, the cavity extending up to $y = L_y/2$ above and $y = -L_y/2$ below as shown in Figure 1. In the two half volumes we then fix two different temperature homogeneous fluids, with the corresponding density

$$\rho_i = \rho_0[1 - \beta(T_i - T_0)], \quad i = 1, 2. \quad (1)$$

where T_0 is the average fluid density.

The control equations for the fluids read

$$\nabla \cdot \mathbf{u} = 0, \quad (2)$$

$$\frac{\partial \mathbf{u}}{\partial t} + \nabla \cdot (\mathbf{u}\mathbf{u}) = -\nabla P + \nu \nabla^2 \mathbf{u} - \mathbf{g}\beta(T - T_0), \quad (3)$$

$$\frac{\partial T}{\partial t} + \mathbf{u} \cdot \nabla T = D \nabla^2 T, \quad (4)$$

where $\mathbf{u} = (u, v)$ is the velocity vector, P is the pressure, β is the thermal expansion coefficient and T_0 is the average fluid temperature. A is the Atwood number, $A = (\rho_1 - \rho_2)/(\rho_1 + \rho_2)$. Pr is Prandtl number, $Pr = \nu/D$, Ra is Rayleigh number, $Ra = g\beta L^3(T_2 - T_1)/\nu D$, where L is the width of the domain, ν is kinematic viscosity and D is the thermal diffusivity.

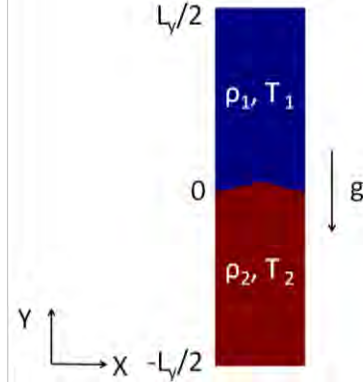


FIGURE 1. Fluids configuration with a heavier fluid of (ρ_1, T_1) placed on top of a lighter one of (ρ_2, T_2) , $\rho_1 > \rho_2$ and $T_1 < T_2$.

3. Lattice Boltzmann Model

DDF-LBE model uses two distribution functions to describe the evolution of the temperature and velocity field respectively. As fluids are supposed to be incompressible, all fluid properties can be considered as constant except the body force term so that the Boussinesq approximation is adopted.

In order to solve the incompressible flow equations, Guo et al. construct the following D2Q9 DDF-LBE model [1]

$$f_i(\mathbf{x} + \mathbf{c}_i \delta_t, t + \delta_t) = f_i(\mathbf{x}, t) - \frac{1}{\tau_1} [f_i(\mathbf{x}, t) - f_i^{(eq)}(\mathbf{x}, t)] + \delta_t F_i, \quad i = 0, 1, \dots, 8. \quad (5)$$

$$g_i(\mathbf{x} + \mathbf{c}_i \delta_t, t + \delta_t) = g_i(\mathbf{x}, t) - \frac{1}{\tau_2} [g_i(\mathbf{x}, t) - g_i^{(eq)}(\mathbf{x}, t)], \quad i = 1, 2, 3, 4. \quad (6)$$

where $f_i(\mathbf{x}, t)$ and $g_i(\mathbf{x}, t)$ are density and temperature distribution functions with velocity \mathbf{c}_i at position \mathbf{x} and time t , respectively. τ_1 and τ_2 are the dimensionless relaxation times. $f_i^{(eq)}(\mathbf{x}, t)$ and $g_i^{(eq)}(\mathbf{x}, t)$ are the equilibrium distribution functions corresponding to $f_i(\mathbf{x}, t)$ and $g_i(\mathbf{x}, t)$, which are defined as

$$f_i^{(eq)} = \begin{cases} -4\sigma \frac{P}{c^2} + s_0(\mathbf{u}) & i = 0 \\ \lambda \frac{P}{c^2} + s_i(\mathbf{u}) & i = 1, 2, 3, 4 \\ \gamma \frac{P}{c^2} + s_i(\mathbf{u}) & i = 5, 6, 7, 8 \end{cases} \quad (7)$$

$$T_i^{(eq)} = \frac{T}{4} \left[1 + 2 \frac{\mathbf{c}_i \cdot \mathbf{u}}{c^2} \right], \quad i = 1, 2, 3, 4 \quad (8)$$

where the parameters of $f_i^{(eq)}$ are set as

$$s_i(\mathbf{u}) = \omega_i \left[\frac{\mathbf{c}_i \cdot \mathbf{u}}{c_s^2} + \frac{(\mathbf{c}_i \cdot \mathbf{u})^2}{2c_s^4} - \frac{u^2}{2c_s^2} \right], \quad (9)$$

with the weight coefficients $\omega_0 = 4/9, \omega_{1,4} = 1/9, \omega_{5,8} = 1/36$. The parameters σ , λ , and γ are satisfied with the following conditions

$$\lambda + \gamma = \sigma, \quad \lambda + 2\gamma = \frac{1}{2}. \quad (10)$$

The fluid macroscopic velocity, pressure and temperature are defined as follows:

$$\mathbf{u} = \sum_{i=1}^8 \mathbf{c}_i f_i, \quad P = \frac{c^2}{4\sigma} \left[\sum_{i=1}^8 f_i + s_0(\mathbf{u}) \right], \quad T = \sum_{i=1}^4 g_i, \quad (11)$$

the force item F_i is given by

$$F_i = \begin{cases} -\frac{\mathbf{c}_i \cdot \mathbf{g}}{2c^2} \beta(T - T_0), & i = 2, 4, \\ 0, & \text{other.} \end{cases} \quad (12)$$

Obviously, $\sum_i F_i = 0$, $\sum_i \mathbf{c}_i F_i = \mathbf{F} \equiv -\mathbf{g} \beta(T - T_0)$, $\sum_i \mathbf{c}_i \mathbf{c}_i F_i = 0$. The kinematic viscosity ν and the thermal diffusivity D are calculated by

$$\nu = c_s^2 \left(\tau_1 - \frac{1}{2} \right) \delta_t, \quad D = c^2 \left(\tau_2 - \frac{1}{2} \right) \delta_t. \quad (13)$$

Hence, the corresponding Prandtl number is $Pr = \frac{2}{3} (2\tau_1 - 1) / (2\tau_2 - 1)$.

4. RESULTS

We use the above model to simulate Rayleigh-Taylor instability with variable Prandtl numbers. The parameters are set as $\tau_1 = 1.8$, $Ra = 6.4 \times 10^7$, the dimensionless temperature of T_1 and T_2 are set to be -0.5 and 0.5. In the simulations, the system size is $N_x \times N_y = 256 \times 1024$.

To measure the growth of the mixing zone, the temperature is averaged in the horizontal direction, [2]

$$\bar{T}(y) = \frac{1}{L_x} \int_{L_x} T(x, y, t) dx. \quad (14)$$

The penetration length of the spikes and bubbles $h_s(t)$ and $h_b(t)$ are defined as the y-distances for which $\frac{\bar{T}(y) - T_1}{T_2 - T_1} \leq 1 - \varepsilon$ and $\frac{\bar{T}(y) - T_1}{T_2 - T_1} \geq \varepsilon$, respectively, with $\varepsilon = 0.05$.

As shown in Figure 2, the variation of Pr number has a significant influence on the mixing growth in absolute time. When Pr number is changed from 0.71 to 7.1, the speeds of mixing growth are different. As Pr number increases, the mixing growth slows down.

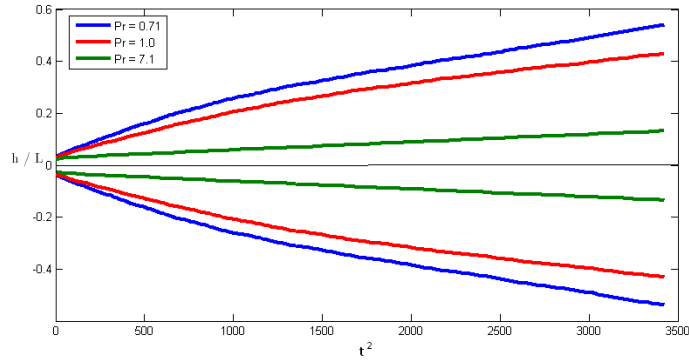


FIGURE 2. Penetration penetration length of the spikes and bubbles $h_s(t)$ and $h_b(t)$ vs. t^2 in absolute time.

As shown in Figure 3, the variation of Pr number nearly has no impact on the mixing growth in dimensionless time with a normalization time scale chosen as

$$\tau = \sqrt{\frac{L}{Ag}}. \quad (15)$$

We can see that with Pr number increasing from 0.71 to 7.1, the mixing-zone growths are almost the same. Because with variable Pr numbers, the normalized time steps are different although the time steps of each Pr number are the same. It can be deduced that Pr number only effects the absolute time of mixing-zone growth. When Pr number increases, it cost more time to develop the mixing-zone of the fluids, and the mixing processes are the same in dimensionless time.

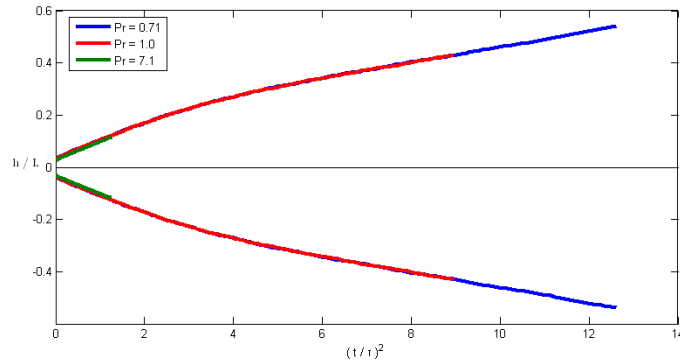


FIGURE 3. Penetration penetration length of the spikes and bubbles $h_s(t)$ and $h_b(t)$ in dimensionless time.

5. CONCLUSIONS

In this paper, we investigate the characteristics of a two-dimensional Rayleigh-Taylor instability in incompressible and miscible flows with variable Prandtl numbers. The numerical results reveal some features of Rayleigh-Taylor instability. The mixing-zone grows differently with various Prandtl numbers in absolute time, but the mixing processes are the same in dimensionless time.

REFERENCES

- [1] ZL. Guo, BC. Shi, and CG. Zheng, A coupled lattice BGK model for the Boussinesq equations, *International Journal for Numerical Methods in Fluids*, 39(4): 325-342, 2002.
- [2] A.W. Cook, and P.E. Dimotakis, Transition stages of Rayleigh-Taylor instability between miscible fluids, *Journal of Fluid Mechanics* 443: 69-99, 2001.

NUMERIC SOLUTIONS OF THERMAL PROBLEMS GOVERNED BY FRACTIONAL DIFFUSION

V.R. Voller, D.P Zielinski

Department of Civil Engineering, University of Minnesota, Minneapolis, MN 55455

volle001@umn.edu, ziel0064@umn.edu

ABSTRACT

The concept of a fractional diffusion equation is introduced. Two novel numerical solutions are introduced. The first is based on a weighting of non-local finite difference approximation of the flux. The other is based on a Monte-Carlo simulation with step sizes selected from an appropriate α stable Lévy distribution. The performance of these two schemes are compared on a steady-state problem. Close agreement between the schemes and with available analytical solutions is observed.

Key Words: *Fractional Diffusion, Finite Difference Scheme, Monte Carlo Scheme*

1. INTRODUCTION

In recent times there has been a growing interest in modeling transport systems that exhibit non-locality. In a heat transfer setting such considerations will become important when the maximum length scale of the heterogeneities in the system is of the order of the domain size. If the sizes of the heterogeneities are power-law distributed a formal treatment of this type of problem leads to the definition of flux at a particular point in terms of a combination of convolution integrals

$$\theta(x) = k \left[\frac{1+\beta}{2} \left[- \int_a^x \Psi(x-\xi) \frac{\partial T(\xi)}{\partial \xi} d\xi \right] + \frac{1-\beta}{2} \left[\int_x^b \Psi(\xi-x) \frac{\partial T(\xi)}{\partial \xi} d\xi \right] \right] \quad (1)$$

where k is thermal conductivity (assumed constant here), the problem domain is $x \in [a, b]$, and $-1 \leq \beta \leq 1$ is a parameter that biases the non-locality between the upstream and downstream directions. If the convolution kernel function is set as a power law, with the form

$$\Psi(z) = z^{-\alpha}, \quad 0 < \alpha \leq 1 \quad (2)$$

the expression in equation (1) can be associated with fractional order Caputo fractional derivatives to the left and right [1], i.e.,

$$\theta(x) = \frac{1+\beta}{2} k \left[- \frac{\partial^\alpha T}{\partial x^\alpha} \right] + \frac{1-\beta}{2} k \left[\frac{\partial^\alpha T}{\partial (-x)^\alpha} \right] = \frac{1+\beta}{2} q_x^L + \frac{1-\beta}{2} q_x^R \quad (3)$$

In these expressions the term $0 < \alpha \leq 1$, which gives the fractional order of the derivative, is an expression of the locality in the problem; note when $\alpha \rightarrow 1$ locality is expressed and the flux in equation (3) takes the conventional form $\theta \propto \partial T / \partial x$. In this way a non-local (fractional) version of the Fourier heat conduction equation, in a two-dimensional domain, can be established by using the general flux definitions of the form in equation (3) in the heat balance

$$\rho c \frac{\partial T}{\partial t} = - \frac{\partial}{\partial x} \left(\frac{1+\beta}{2} q_x^L + \frac{1-\beta}{2} q_x^R \right) - \frac{\partial}{\partial y} \left(\frac{1+\beta}{2} q_y^L + \frac{1-\beta}{2} q_y^R \right) \quad (4)$$

Recently building on and from previous numerical schemes [2-5], Voller, Paola and Zielinski [6] have developed a finite-difference based scheme for (4) referred to as the Control Volume Weight Flux Scheme (CVWFS). The object of the current work is to outline the key ingredients in the CVWFS and establish its validity by comparing CVWFS results for steady-state heat conduction problems with results from an alternative Monte-Carlo (random-walk) method.

2. THE CVWFS

The key features in the CVWFS scheme can best be observed by considering the finite difference solution of a steady-state one-dimensional fractional heat condition equation

$$\frac{d}{dx} \left(\frac{1+\beta}{2} \frac{d^\alpha T}{dx} - \frac{1-\beta}{2} \frac{d^\alpha T}{d(-x)^\alpha} \right) = 0, \quad 0 \leq x \leq 1 \quad (5)$$

with boundary conditions $T(0)=1$, $T(1)=0$. Recognize that once an effective finite difference scheme is developed for (5) it can be readily adapted—through using conventional finite difference approaches—for the more general solution of the two-dimensional problem in (4).

The CVWFS solution of (5) is constructed on a grid of $n+1$ equally spaced node points. At internal node $1 < I < n+1$ the discrete form of (5) is written as

$$\frac{1+\beta}{2} \frac{d^\alpha T}{dx} \Big|_{in-I} - \frac{1-\beta}{2} \frac{d^\alpha T}{d(-x)^\alpha} \Big|_{in-I} - \frac{1+\beta}{2} \frac{d^\alpha T}{dx} \Big|_{out-I} + \frac{1-\beta}{2} \frac{d^\alpha T}{d(-x)^\alpha} \Big|_{out-I} = 0 \quad (6)$$

The various fractional derivatives in (6) are evaluated in terms of the following weighted sums of the approximated gradients at neighboring points

$$\frac{d^\alpha T}{dx^\alpha} \Big|_{in-I} = \sum_{j=1}^{I-1} W_j \left[\frac{T_{I-j} - T_{I+1-j}}{\Delta x} \right] \quad (7a)$$

$$\frac{d^\alpha T}{dx^\alpha} \Big|_{out-I} = \sum_{j=1}^I W_j \left[\frac{T_{I+1-j} - T_{I+2-j}}{\Delta x} \right]$$

$$\frac{d^\alpha T}{d(-x)^\alpha} \Big|_{in-I} = \sum_{j=1}^{n+2-I} W_j \left[\frac{T_{I+j-2} - T_{I+j-1}}{\Delta x} \right] \quad (7b)$$

$$\frac{d^\alpha T}{d(-x)^\alpha} \Big|_{out-I} = \sum_{j=1}^{n+1-I} W_j \left[\frac{T_{I+j-1} - T_{I+j}}{\Delta x} \right]$$

where, following the work in [6], the weights are given by

$$W_j = (1-\alpha)[(j-\mu)\Delta x]^{-\alpha} \Delta x \quad \text{with } 0 < \mu = (1-\Gamma(1-\alpha)^{\frac{1}{\alpha}}) < 1 \quad (8)$$

where $\Gamma(x)$ is the gamma function. This choice of weights is made to ensure that (i) they sum to unity, and (ii) recover locality as $\alpha \rightarrow 1$, i.e., a flux expressed by local quantities

$$-\frac{d^\alpha T}{dx^\alpha} \Big|_{in-I} = \left[\frac{T_{I-1} - T_I}{\Delta x} \right]. \quad \text{Note also that the sum upper limits in (7) differ by one between the "in" and "out" components, a device that ensures that the resulting coefficient matrix (which in general will be non-sparse) will be diagonally dominant; a device that is similar in nature to the one-shift Grünwald weight schemes [2-4]. Further recognize that the summations are truncated, thereby avoiding the calling on nodes beyond the domain. Finally note that the fixed value conditions for$$

equation (5) are readily incorporated in equation (7). If fixed flux conditions are required then an iterative procedure can be used to set the boundary temperature so that the expressions in (7) (applied at the boundary nodes) recover the correct flux value. Solution of the resulting finite difference equation can be accomplished through a false time step iterative approach, see [6].

3. RESULTS

Various CVWFS results for a range of choices of bias β and locality α values are shown, as broken lines, in Figure 1. Also shown in this figure, as a continuous line, is the analytical solution for the case $\alpha = .3$, $\beta = 1$, viz., $T = 1 - x^\alpha$, and as symbols results from an alternative Monte-Carlo (MC) solution; this latter solution following similar lines to a standard heat condition MC scheme. Here, however, random walk step sizes in the MC scheme are chosen from an appropriate α stable Lévy distribution; a pdf that can exhibit thick-power law tails and can also be directly associated with the Caputo derivatives in equation (3). There are two observations

- (1) The non-local behavior in the solution is readily observed by the wide range of departures from the straight line ($T = 1 - x$) local (integer) solution of (5).
- (2) The proposed CVWFS produces excellent agreement with the available analytical and alternative MC solutions.

Further work will be aimed at demonstrating and validating extensions of the CVWFS to multi-dimensional and transient problems including more specialized heat transfer problems, e.g., fractional Stefan problems [7].

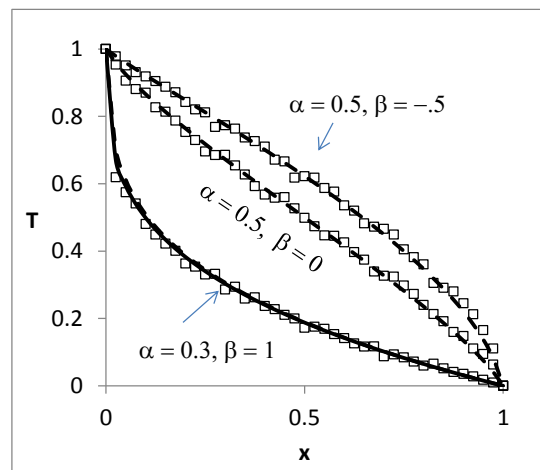


FIGURE 1. Results for the CVWFS and Monte-Carlo Scheme for various values of bias and non-locality

REFERENCES

- [1] I. Podlubny, *Fractional Differential Equations. An Introduction to Fractional Derivatives, Fractional Differential Equations, to Methods of Their Solution and Some of Their Applications*, Academic Press, San Diego 1998.
- [2] M.M. Meerschaert, C. Tadjeran, Finite difference approximations for two-sided space-fractional partial differential equations, *Appl. Numer. Math.*, 56, 80-90, 2006.
- [3] M.M. Meerschaert and C. Tadjeran, Finite difference approximations for fractional advection-dispersion flow equations, *J. Comput. App. Math.*, 172, 65-77, 2004.

- [4] C. Tadjeran, M.M. Meerschaert, H.P. Scheffler, A second-order accurate numerical approximation for the fractional diffusion equation, *J. Comp. Phys.*, 213, 205-213, 2006.
- [5] X. Zhang, M. Lv, J.W. Crawford, and I.M. Young, The impact of boundary on the fractional advection-dispersion equation for the solute transport in soil: Defining the fractional dispersive flux with Caputo derivatives, *Advances in Water Resources*, 30, 1205-1217, 2007.
- [6] V.R. Voller, C. Paola, and D.P. Zielinski, The control volume weighted flux scheme (CVWFS) for non-local diffusion and its relationship to fractional calculus, *Numerical Heat Transfer B*, 59, 421-441, 2011.
- [7] V.R. Voller, An exact solution of a limit case Stefan problem governed by a fractional diffusion equation, *Int. J. Heat Mass Transfer*, 53, 5622-5625, 2010.

HIGH PERFORMANCE COMPUTATION OF INCOMPRESSIBLE FLOW BY LATTICE BOLTZMANN METHOD ON MULTI-NODE GPU CLUSTER

Xian Wang, Takayuki Aoki

Global Scientific Informational and Computing Center, Tokyo Institute of Technology, 2-12-1, Meguro-ku, Tokyo, 152-8550, Japan. wang@sim.gsic.titech.ac.jp

ABSTRACT

GPGPU has drawn much attention on accelerating non-graphic applications. The simulation by D3Q19 model of Lattice Boltzmann method was executed successfully on multi-node GPU cluster by using CUDA programming and MPI library. Comparison and analysis were made among the parallel results by 1D, 2D and 3D domain decompositions. With $384 \times 384 \times 384$ mesh system and 96 GPUs, the performance by 3D decomposition is about 3~4 times higher than that of 1D decomposition. In order to hide the communication time, we introduced the overlapping technique between computation and communication. Using 8-96 GPUs, the performances increase by a factor about 1.1~1.3 with overlapping mode. As large-scaled computation of a flow around a sphere at $Re=13000$ was carried on successfully using mesh system $2000 \times 1000 \times 1000$ and 100 GPUs. As a result, 6.0 hours were used for processing 100,000 time steps. Under this condition, the computational time (2.79 hours) and data communication time (3.06 hours) are almost same.

Key Words: *GPGPU, Lattice Boltzmann method, Computation, Communication.*

1. INTRODUCTION

Recently, the use of GPU (Graphical Processing Unit) to accelerate non-graphic computations has drawn much attention. GPU has been further used for general purpose with the release of CUDA (Compute Unified Device Architecture) by NVIDIA[1]. However, there are few large-scaled CFD applications for engineering purpose, which requires spare memory access and has relatively less arithmetic operations than the memory access. In computational fluid dynamics (CFD), Lattice Boltzmann method (LBM) is widely used currently as an alternative numerical scheme for simulating fluid flows governed by the Navier-Stokes equations[2]. Since GPU has many computational units and the weak correlations among adjacent computational points in solving the LB equation well match the data-parallel SIMT (Single-Instruction Multiple-Thread) characteristic of GPU, it is expected to obtain high efficiency of GPU on the LBM solver.

2. MAIN BODY

The completely discretized form of Boltzmann equation with BGK model is

$$f_i(x + e_i \delta t, t + \delta t) - f_i(x, t) = -\frac{1}{\tau} [f_i(x, t) - f_i^{eq}(x, t)] ;$$

It is usually solved with its standard form by assuming $\delta t = 1$ according to the following two steps.

$$\text{Collision step: } \bar{f}_i(x, t) = f_i(x, t) - \frac{1}{\tau} [f_i(x, t) - f_i^{eq}(x, t)] ;$$

$$\text{Streaming step: } f_i(x + e_i, t + 1) = \bar{f}_i(x, t) .$$

Figure 1 shows the architecture of CUDA-ready GPU. On GPU chip, there are many processors named multiprocessor (MP), each of them contains 8 streaming processor (SP) cores. CUDA

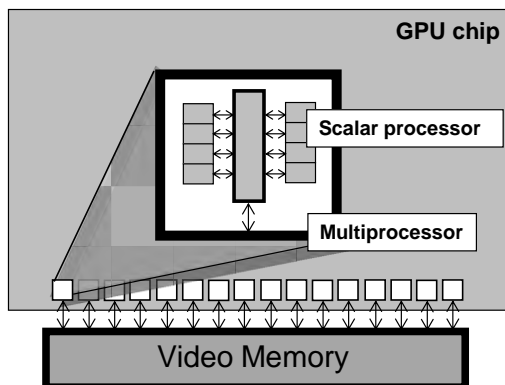


FIGURE 1. The architecture of CUDA-ready GPU

extends C by allowing the programmer to define C functions, called kernels, which run on GPU. When the kernels are called, they are executed N times in parallel by N different CUDA threads. The threads of a thread block execute concurrently on one MP and the MP employs the architecture of SIMT to map each thread on one SP. Each thread is executed on SP independently. On the other hand, for LBM, the dominant equation for the collision step is purely local, and the streaming step is a uniform data shifting and requires little computational effort, which makes LBM straightforward for parallel computation. In LBM, the two steps are solved in a successive and repeating way, the order for processing them is not important. To use the GPU on-chip memory (register) efficiently, we set two kernels for the 3D-LBM solvers as follows.

```
__global__ void stream_collide (...);
__global__ void boundary (...);
dim3 block (thread_x, thread_y, thread_z);
dim3 grid (nx/block.x, ny/block.y, 1);
stream_collide <<< grid, block >>> (...);
boundary <<< grid, block >>> (...);
```

With LBM D3Q19 model, we made a computation of lid-driven cavity flow with $96 \times 96 \times 96$ lattice nodes using a single GPU (NVIDIA GeForce GTX280). The performance of 270 MLUPS and 87 speedup over CPU (Xeon E5420 (2.5GHz)) computation were obtained. Here, it should be declared that for all the computations in the present work, the single-precision floating-point variables were used.

The present multi-node GPU computations were performed on Tsubame, the HPC of Tokyo Institute of Technology. GPUs cannot control the data transfer between themselves, the data communication process should be realized via CPUs. First, the data are copied from GPU to CPU by CUDA API `cudaMemcpy(..., cudaMemcpyDeviceToHost)`. Then the data are exchanged between corresponding CPUs using parallel tool like MPI (Message Passing Interface) et al. Finally, the exchanged data are copied from CPU to GPU by `cudaMemcpy(..., cudaMemcpyHostToDevice)`.

3. RESULTS

Figure 2 shows the performance of LBM solver by 1D, 2D and 3D decompositions for the mesh systems of $384 \times 384 \times 384$. The ideal line is drawn based on the data of 3D decomposition. The thread number we used is 96, 1 and 2 in x, y, and z directions respectively, totally 192 threads. The computation is cavity lid driven flow at $Re=1000$.

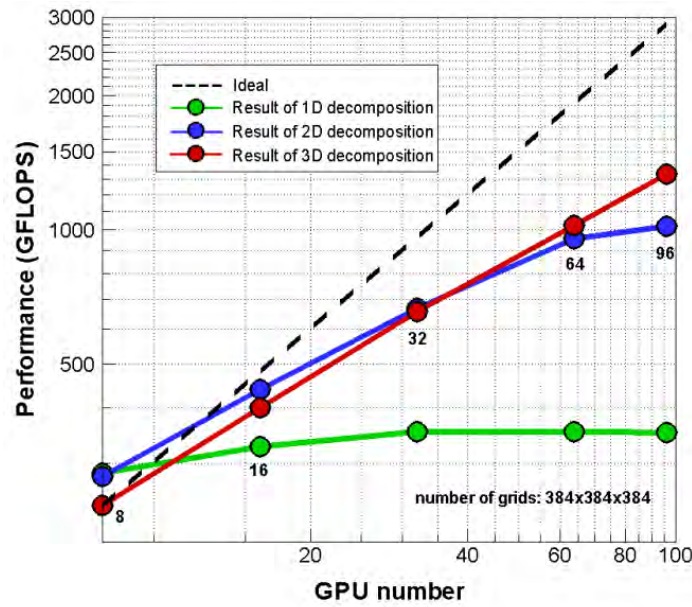


FIGURE 2. Performance of LBM solver by 1D, 2D and 3D decompositions for the mesh systems $384 \times 384 \times 384$

It can be seen from Fig.2, using 1D decomposition, the performance does not increase when the number of GPUs is larger than 32 and even decreases slightly when the number of GPUs equals to 96. That means the parallel efficiency drops greatly with the increase in GPU number for 1D decomposition. For 2D and 3D decompositions, the performances increase all along till 96 GPUs. This is because the amount of data for communication does not change for 1D decomposition with the increase in GPU number, but it decreases for 2D and 3D decompositions. However, the computational load decreases with GPU number in spite of the domain decomposition way.

For multi-GPU computation, decreasing data communication time is the key point to enhance parallel efficiency. As for above computations, GPUs are idle when data transfer is being done. If the two processes can be done simultaneously, the communicational time is hidden. CUDA provides an overlapping mode to make it possible simultaneously executing a kernel and copying data between Host and Device. In our computation, using 8-96 GPUs, the performances increase by a factor about 1.1~1.3 with overlapping mode.

Finally, a 3D large-scaled computation to simulate the air flow in an urban city was performed using multi-node cluster: Tsubame 2 in Tokyo Institute of Technology. Tsubame 2 includes 1408 compute nodes are all equipped with three NVIDIA Tesla M2050 GPU accelerators, each of which consists of 448 small power-efficient processing cores with 3GB of high-bandwidth GDDR5 memory. The simulation was done at $Re=10000$ using mesh system $3072 \times 1536 \times 768$ with 288 GPUs. The buildings are simulated by 47 rectangular blocks. Using 3D domain decomposition, the corresponding data size for communication for one GPU is 16.4 Mb. Figure 3 shows the iso-surfaces of second invariant of velocity gradient tensor behind the buildings at time step = 20000. Large amount of vortex yields in disorder at such a high Re . As a result, 1965s was consumed for the computation of 20,000 time steps, in which the computational time is 1383s and the data communicational time is 582s. The achieved performance is 122 TFLOPS.

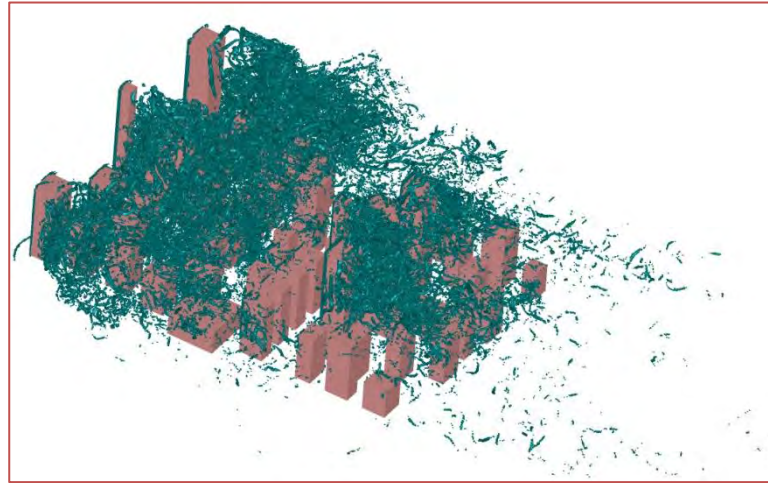


FIGURE 3. Iso-surface of second invariant of velocity gradient tensor at $Re=10000$ using $3072 \times 1536 \times 768$ mesh system and 288 GPUs

4. CONCLUSIONS

Lattice Boltzmann method is very suitable for parallel computation due to the local property of the dominant equations. The drawback of multi-GPU computation is GPU cannot control the data transfer between them, the data communication must be via CPUs, which makes data communication quite time-consuming. When GPU number is large, 3D decomposition can decrease the data size for communication greatly and obtain higher performance than 1D and 2D ones. Besides, the GPU performance can be extracted by increasing the computational load. Multi-GPU computation is more suitable for very large-scaled computation.

REFERENCES

- [1] nVIDIA, NVIDIA CUDA Compute Unified Device Architecture programming Guide Version 2.0, nVIDIA, 2008.
- [2] S.Y. Chen and G.D. Doolen, Lattice Boltzmann method for fluid flows, *Annual Review of Fluid Mechanics* 30, 329-364, 1998.

THE OPTIMIZATION MODEL OF THE HEAT CONDUCTION STRUCTURE

Yongcun Zhang, Shutian Liu

State Key Laboratory of Structural Analysis for Industrial Equipment, Department of Engineering Mechanics, Dalian University of Technology, Dalian 116024, China, yczhang@dlut.edu.cn, stliu@dlut.edu.cn

ABSTRACT

An optimization model which considers a novel thermal performance index as the objective function is proposed for minimizing the highest temperature in this paper. Firstly, the performance of the conventional heat conduction optimization model, with the dissipation of heat transport potential capacity as the objective function, is evaluated by a one-dimensional heat conduction problem in a planar plate exchanger. Then, a new thermal performance index, named the geometric average temperature, is introduced. The new heat conduction optimization model, with the geometric average temperature as the objective function, is developed and the corresponding finite element formula is presented. The results show that the geometric average temperature is an ideal thermal performance index and the solution of the new model is close to the theoretical optimal solution.

Key Words: *Optimization; Heat Conduction Structure; Dissipation of Heat Transport Potential Capacity; Geometric Average Temperature; Planar Plate Exchanger.*

1. INTRODUCTION

Statistical data show that the failure of real devices with a fraction of 55% is caused by the high temperature and this fraction increases exponentially with increasing temperature. Thus, the highest temperature is a primary factor that induces the failure of practical cooling structure and should be well controlled. In practice, it is natural to define the highest temperature as an objective function of the optimization model. However, the location of the highest temperature usually changes with the change of material distribution in the optimization process and is a discontinuous function of design variables, which may introduce numerical difficulties in optimization. Therefore, instead of a directing optimization of the highest temperature, it is more convenient to define another proper thermal performance index as the objective function in an optimization model to accomplish indirectly the goal of minimizing the highest temperature.

In the optimization model of heat conduction structure, the objective function can be selected as

$$f(\mathbf{X}) = \int_{\Omega} \frac{1}{2} (-\mathbf{q}(\mathbf{X}) \nabla T(\mathbf{X})) d\Omega \quad (1)$$

where \mathbf{X} is the design variable used to describe the distribution of material, $\mathbf{q}(\mathbf{X})$ is the flux density and $\nabla T(\mathbf{X})$ is the temperature gradient. Using the finite element formulation, Eq. (1) is defined as the dissipation of heat transport potential capacity (DHTPC), Using the DHTPC (or the heat dissipation efficiency) as a thermal performance index, some good design results have been obtained. However, this index can only tell us the heat dissipative capability rather than the highest temperature. How much difference between DHTPC and the present design goal, that is, the control of the highest temperature? Is there any better thermal performance index? Answers to these questions are the motivation of this study.

2. MAIN BODY

To evaluate the quality of two commonly used models--Minimization of the highest temperature and Minimization of the highest temperature, a one-dimensional heat conduction problem for a planar plate is presented, which can be solved analytically.

2.1 Problem description

A rectangular planar plate exchanger, with length l , width W ($W \gg l$) and thickness t , is embedded in the heater. The heat generated by heater flows into the exchanger uniformly. The heat flowing into the exchanger is q'' per unit time and area. Only one side along the width direction of exchanger contacts with a thermostat with a constant temperature T_0 and others are adiabatic. This problem can be described as a planar heat conduction model with uniform heat source, as shown in Fig. 1. Furthermore, this model can be simplified into a one-dimensional heat transfer problem because the thickness t and the internal heat source q'' do not change along the width direction. The goal is to obtain the optimal heat conduction performance by designing the thickness t along the length direction of exchanger.

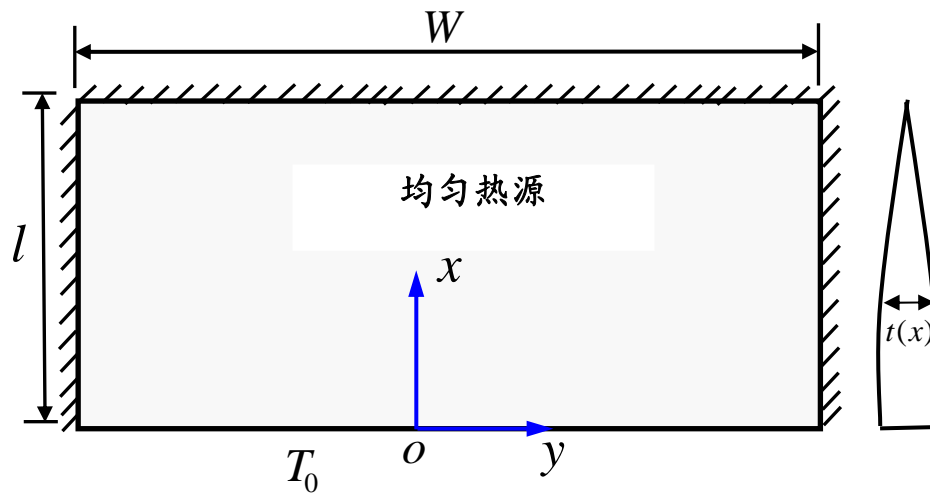


FIGURE 1. A theoretical model of a planar plate exchanger.

2.2 Comparisons of two different optimization models

The dimensionless thermal conductivity fields and the corresponding dimensionless temperature distributions from the two different optimization models are shown in Fig. 2. It can be found that the temperature distribution from the model with an objective function of the DHTPC has an obvious reduction in the internal exchanger when compared with the temperature field from the model with a uniform thermal conductivity field. However, these two models give the same highest temperature. In addition, when compared with the model with an objective function of the highest temperature, large differences in thermal conductivity field can be found and the highest temperature increases by 12.5%, which indicates that the optimization model with an objective function of the DHTPC sometimes cannot fulfill the present design goal. Thus, it is necessary to propose new thermal performance indexes for the optimization model.

A new thermal performance index called the geometric average temperature T_{geoav} is proposed, which can be expressed as

$$T_{\text{geoav}} = \left(\frac{1}{|\Omega|} \int_{\Omega} (T(x))^n dx \right)^{1/n}, x \in \Omega \quad (2)$$

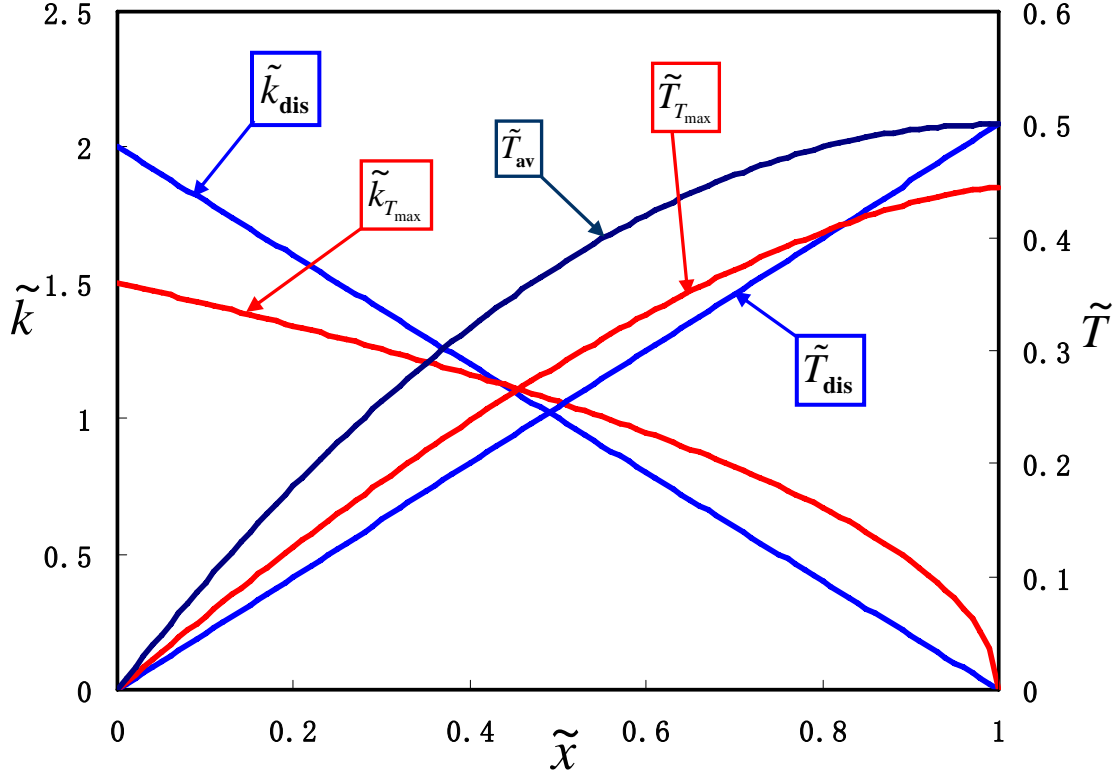


FIGURE 2. Comparisons of thermal conductivity fields and temperature distributions from different optimization models. av: the uniform conductivity field; dis: the dissipation of heat transport potential capacity; T_{max} : the highest temperature.

Where $|\Omega|$ denotes the area (or volume) over the design region. Theoretically, the geometric average temperature is close to the highest temperature when n is infinitely large, i.e. $T_{\text{geoav}} \xrightarrow{n \rightarrow \infty} T_{\text{max}}$. Thus, the geometric average temperature is an appropriate approximation of the highest temperature.

3. RESULTS

The obtained thermal conductivity field (material distribution) and the corresponding temperature distribution are shown in Fig. 3. To facilitate comparisons, the solutions of the optimization models with the DHPC and the highest temperature as objective functions are also shown in Fig. 3.

4. CONCLUSIONS

In this paper, we have discussed how to minimize the highest temperature of a heat conduction structure by designing the material distribution with a specified material volume (conductivity ability). The large error sometimes occurs between the results by the usual optimization model with an objective function of the DHTPC and the theoretical optimal design. A geometric average temperature has been proposed, which is a better thermal performance index as the objective

function. The solution of the new model with the geometric average temperature as the objective function is close to the theoretical optimal solution.

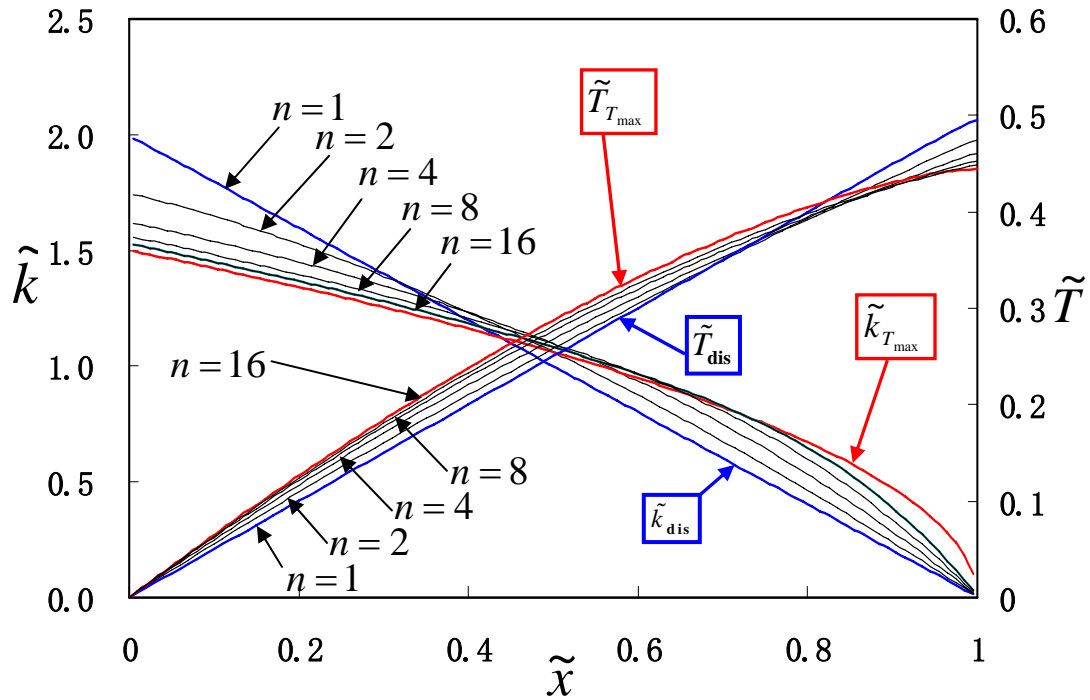


FIGURE 3. The solutions of the optimization model based on the geometric average temperature with different power indexes. Results from other models are also shown for comparison.

REFERENCES

- [1] Z.Y. Guo, X.G. Cheng, and Z.Z. Xia, Least dissipation principle of heat transport potential capacity and its application in heat conduction optimization. *Chinese Science Bulletin*, 48(4), 406-410, 2003.
- [2] Y.C. Zhang and S.T. Liu, Design of conducting paths based on topology optimization. *Heat and Mass Transfer*, online; DOI 10.1007/s00231-007-0365.

A DEEP STUDY ON TOPOLOGY OPTIMIZATION OF THERMO-ELASTIC PROBLEMS

Weihong ZHANG*, Jungang YANG

Engineering Simulation and Aerospace Computing (ESAC), The Key Laboratory of Contemporary Design and Integrated Manufacturing Technology, Northwestern Polytechnical University, Xi'an, China, 710072, zhangwh@nwpu.edu.cn

ABSTRACT

In this paper, alternative formulations are proposed to deal with topology optimization of thermo-elastic problems. The basic mathematical formulations of the thermo-elastic problems are presented and the classical 3-bar problem is used to show the difference between the elastic strain energy and the compliance. Then different topology optimization formulations are used to show the importance to distinguish the strain energy and the mean compliance in the formulations.

Key Words: *topology optimization, thermo-elastic, strain energy.*

1. INTRODUCTION

Topology optimization is now recognized as an advanced methodology for the layout design of lightweight structures. The traditional way is to formulate the problem as a compliance-oriented problem subjected to volume constraint because the structural compliance is commonly known to be a global measure reflecting the stiffness of the considered structure only bearing mechanical loads.

However, in the simultaneous presence of mechanical and thermal loads, the validity of the current formulation is doubtful. From illustrative examples of closed-form solutions, it can theoretically be seen that a meaningless solution with complete void over the design domain will produce a minimum compliance design if only thermal load is involved. The basic fact is that the thermal load related to temperature effect that causes thermal stress are design-dependent and will vary with the material layout unlike mechanical loads.

In this paper, alternative formulations are addressed to deal with this kind of problem. Physically, the designable domain is interpreted as an elastic support whose topology optimization can be carried out for different aims, e.g., reductions of thermal stress, strain energy or compliance to fulfil practical design needs. Comparisons are made among different solutions to show the effects of these formulations.

2. MATHEMATICAL FORMULATIONS

To have a clear idea, it is necessary to reminder some basic mathematical formulations of the thermo-elastic problems. The elastic strain energy is expressed as

$$\Phi = \frac{1}{2} \int (\boldsymbol{\varepsilon} - \boldsymbol{\varepsilon}_{th})^T D (\boldsymbol{\varepsilon} - \boldsymbol{\varepsilon}_{th}) dV = \frac{1}{2} \int \boldsymbol{\varepsilon}^T D \boldsymbol{\varepsilon} dV - \int \boldsymbol{\varepsilon}^T D \boldsymbol{\varepsilon}_{th} dV + \frac{1}{2} \int \boldsymbol{\varepsilon}_{th}^T D \boldsymbol{\varepsilon}_{th} dV \quad (1)$$

The total potential energy of discrete form is expressed as

$$\Pi = \Phi - U^T F_m = \frac{1}{2} U^T K U - U^T F_t + \frac{1}{2} \int \boldsymbol{\varepsilon}_{th}^T D \boldsymbol{\varepsilon}_{th} dV - U^T F_m \quad (2)$$

By applying the variational principle, the stationary condition of $\frac{\partial \Pi}{\partial U} = 0$ results in the well-known finite element equation

$$KU = F_m + F_t \quad (3)$$

The mean compliance of the structure is defined as

$$C = \frac{1}{2}(F_m + F_t)^T U = \frac{1}{2}F_m^T K^{-1} F_m + \frac{1}{2}F_t^T K^{-1} F_t + F_t^T K^{-1} F_m \quad (4)$$

It can easily be proved that the strain energy consists of two independent parts contributed from the mechanical and thermal loads, respectively.

$$\Phi = \Phi_m + \Phi_t \quad (5)$$

$$\Phi_m = \frac{1}{2} F_m^T K^{-1} F_m, \quad \Phi_t = -\frac{1}{2} F_t^T K^{-1} F_t + \frac{1}{2} \int \varepsilon_{th}^T D \varepsilon_{th} dV \quad (6)$$

Therefore, the strain energy is different from the mean compliance. Notice that the subscripts m and t denote the mechanical and thermal parts in all above expressions.

To clarify the notations, consider a 3-bar problem loaded by a uniform temperature and vertical load as shown in Fig. 1.

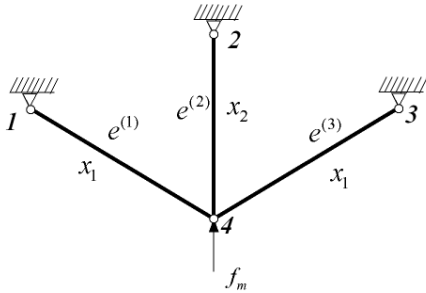


FIGURE 1. Three-bar problem

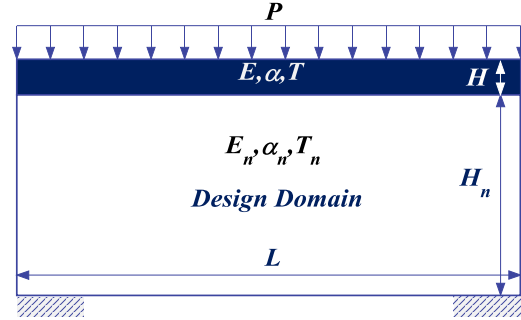


FIGURE 2. Beam problem

It follows that

$$C = \frac{L(E\alpha\Delta T(x_1 + x_2) - f_m)^2}{E(x_1 + 2x_2)}, \quad \Phi_m = \frac{L f_m^2}{E(x_1 + 2x_2)}, \quad \Phi_t = \frac{(\alpha\Delta T)^2 EL x_1 x_2}{2(x_1 + 2x_2)} \quad (7)$$

Clearly, both the mean compliance and strain energy are not monotonous functions of x_1 and x_2 when the thermal load related to ΔT exists. The mean compliance is equal to the strain energy when the thermal load is omitted.

3. FORMULATIONS OF TOPOLOGY OPTIMIZATION PROBLEMS

For this kind of problem, different formulations can be used depending upon the strength, stiffness or compliance requirements of the structure as well as the loading cases. It is important to distinguish the strain energy and the mean compliance in the formulation. In certain cases, it is also important to distinguish different parts involved in the strain energy and compliance contributed from the mechanical and thermal loads.

For example, if the compliance or the strain energy is used as the objective function in the following formulation, respectively subjected to the volume constraint, the optimal solution may be completely different.

$$\begin{aligned} & \text{Min } C, \Phi \\ & V \leq \bar{V} \end{aligned} \quad (8)$$

4. NUMERICAL RESULTS OF TOPOLOGY OPTIMIZATION OF A 2D PROBLEM

Consider a 2D rectangular domain with the top layer loaded by a uniform pressure and temperature distribution as shown in Fig. 2. This problem is similar to a typical TPS design problem. The top layer is non-designable while the bottom region will be designed in configuration to act as an elastic support. Suppose that $E = E_n = 2.0 \times 10^5 \text{GPa}$, $\alpha = \alpha_n = 1.0 \times 10^{-4}$, $H = 2\text{m}$, $H_n = 0.8\text{m}$, $L = 3$, $T = 100^\circ\text{C}$, $T_n = 0^\circ\text{C}$, $P = 5\text{N/m}$. Different topology optimization formulations and corresponding design results are shown in Fig. 3. In all the formulations, σ_i denotes the equivalent Von-mises stress of element i of the top layer, vf denotes the volume fraction. In the first formulation, the compliance is used as constraint, so both the vertical and horizontal deformations are limited, which will result in the increasing of thermal stress. In the second formulation, only the vertical displacement is controlled by the constraint. Therefore, the maximum stress of the second formulation will be lower than that in the first formulation.


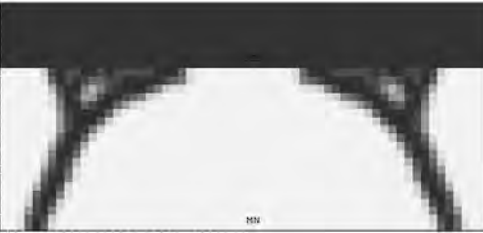

Optimization model	Material layout of topology optimization result
$\begin{cases} \text{Min } \text{Max}_{i \in I} \{\sigma_i\} \\ \text{s.t. } C \leq \bar{C} \\ V \leq vf\bar{V} \end{cases}$	 <p data-bbox="781 1192 1247 1234">$\bar{C} = 10, vf = 0.2, \text{Max } \sigma_i = 516.157, C = 9.8903$</p>
$\begin{cases} \text{Min } \text{Max}_{i \in I} \{\sigma_i\} \\ \text{s.t. } \mathbf{P}^T \mathbf{U} \leq \bar{\phi}_y \\ V \leq vf\bar{V} \end{cases}$	 <p data-bbox="691 1520 1338 1562">$\bar{\phi}_y = 30, vf = 0.2, \text{Max } \sigma_i = 317.766, \Phi_m = 30.28974, C = 97.8207$</p>
$\begin{cases} \text{Min } \mathbf{P}^T \mathbf{U} \\ \text{s.t. } \sigma_i \leq \bar{\sigma} \quad i \in I \\ V \leq vf\bar{V} \end{cases}$	 <p data-bbox="691 1856 1338 1898">$\bar{\sigma} = 550, vf = 0.2, \text{Max } \sigma_i = 524.826, \Phi_m = 15.0596, C = 27.1877$</p>

FIGURE 3. Different formulations and corresponding design results

5. CONCLUSIONS

In this paper, topology optimization of structures under thermo-elastic load is investigated. Variant optimization formulations are mainly addressed to highlight their differences. A compromise way is to find the solution that matches the effect between thermal load and mechanical load.

ACKNOWLEDGEMENTS

This work is supported by the National Natural Science Foundation of China (10925212, 90916027) and 973 Program (2011CB610304).

REFERENCES

- [1]. N. Noda, R.B. Hetnarski, Y. Tanigawa Thermal stress second edition Taylor & Francis New York London
- [2]. P. Pedersen and N.L. Pedersen, Strength optimized designs of thermoelastic structures. *Struct Multidisc Optim*, DOI 10.1007/s00158-010-0535-5
- [3]. T. Gao and W.H. Zhang, Topology optimization involving thermo-elastic stress loads. *Struct Multidisc Optim*, DOI 10.1007/s00158-010-0527-5
- [4]. B. Chen and L. Tong, Thermo-mechanically coupled sensitivity analysis and design optimization of functionally graded materials. *Comput Methods Appl Mech Eng*, 194, 1891-1911, 2005
- [5]. Q. Li, G.P. Steven and Y.M. Xie, Displacement minimization of thermo-elastic structures by evolutionary thickness designs. *Comput Methods Appl Mech Eng*, 179, 361-378, 1999.
- [6]. Q. Li, G.P. Steven and Y.M. Xie, Thermo-elastic topology optimization for problems with varying temperature fields. *J Therm Stress*, 24, 347-366, 2001.
- [7]. P. Pedersen, Some general optimal design results using anisotropic power law non-linear elasticity. *Struct Optim*, 15, 73-80, 1998.
- [8]. P. Pedersen, Analytical stiffness matrices with Green-Lagrange strain measure. *Int J Numer Methods Eng*, 62, 334-352, 2005.
- [9]. N.L. Pedersen and P. Pedersen, Design of notches and grooves by means of elliptical shapes. *J Strain Anal Eng Des*, 43(1), 1-14, 2008.
- [10]. H. Rodrigues and P. Fernandes P, A material based model for topology optimization of thermoelastic structures. *Int J Numer Methods Eng*, 38, 1951-1965, 1995.
- [11]. D.A. Tortorelli, G. Subraman, S.C.Y. Lu and R.B. Haber, Sensitivity analysis for coupled thermo-elastic systems. *Int J Solids Struct*, 27(12), 1477-1497, 1991.
- [12]. Q. Xia and M.Y. Wang, Topology optimization of thermo-elastic structures using level set method. *Comput Mech*, 42, 837-857, 2008.

CONCURRENT OPTIMIZATION OF STRUCTURE COMPOSED OF POROUS CERAMIC WITH THERMAL AND STRUCTURAL OBJECTIVES

Jun Yan*, Jiadong Deng, Gengdong Cheng

State Key Lab of Structural Analysis for Industrial Equipment and Department of Engineering Mechanics, Dalian University of Technology, Dalian, 116024, P.R. China, yanjun@dlut.edu.cn

ABSTRACT

The optimization formulations are studied for the concurrent optimization of the load carrying spacecraft structures composed of porous ceramic materials, which combine high stiffness with low thermal expansion in a predefined domain. The optimal results of single objective and multi-objective models are compared and the merits of the multi-objective models are explained. To realize the concurrent optimization of the structures composed of porous ceramic material, the independent macro and micro densities are introduced as the design variables and penalization approaches are adopted in both scales, i.e. SIMP (Solid Isotropic Material Penalization) in micro material scale and PAMP (Porous Anisotropic Material Penalization) in macro structure scale. A sandwich elliptically curved shell is optimized to verify the concurrent multi-scale design of structure configuration and microstructure of porous ceramic. And the axial symmetric and 3D concurrent optimization results are shown. The numerical examples demonstrate that the porous material is conducive to enhance the thermal and load carrying performances of sandwich shells.

Key Words: *Multi-objective Optimization, Porous Ceramic, Multi Geometrical Scale, Thermal Structure.*

1. INTRODUCTION

Ultra-light design is the eternal pursuit of aero-spatial structures carrying with mechanical loads. Many such loading carrying structures often experience large temperature changes, 2000K in some high speed cases, which lead to an extreme thermal stress/deformation and activate structural failure or reduce the equipmental precision. Experiments have shown that ultra-high temperature ceramics (also know as porous functional ceramics), which are utilized as non-ablative thermal protective material, are one of the most competitive materials used in the mechanical and thermal loads bearing spacecraft structures. The porous ceramic material contains myriad of open or closed pores formed during the high temperature agglomerating process which characterized the materials with structural characters in micro scale [1]. Reference [2] evaluates the virtue of the porous ceramic in ultra light, manufacture and process facility and survival ability in high temperature environments are emphasized. However, it also points out that its large thermal expansion may cause incompatible deformation between the adjacent components. So it is important to design the structural configuration and material property to optimize the load carrying capacity and structural thermal expansion. With a single objective to minimize the structural compliance, article [3] probes into the concurrent design of the structure and its material under uniform temperature field and mechanical loads. It is found that results from this single objective optimization depend on the relative ratio of the mechanical load and the thermal loads. What's more, with the structural compliance as the single objective, the optimum configuration of the macro structure is prone to

separate abnormally when the available material fraction is specified relatively higher. To cope with the above problems, a novel multi-objective optimization model are established to design the structural configuration and microstructure of porous ceramic concurrently to obtain the combined properties of high stiffness with low thermal expansion in a predefined domain.

2. DESCRIPTION OF CONCURRENT AND MULTI-OBJECTIVE OPTIMIZATION MODEL

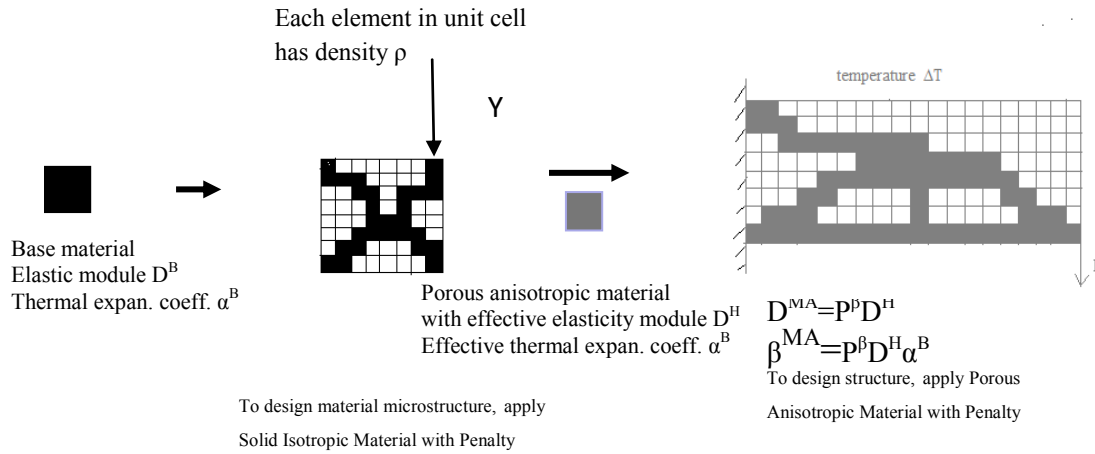


FIGURE 1 Penalization-based concurrent optimization with two classes of density design variables

Figure 1 schematically shows the idea of the concurrent topology optimization of the macro structure and its material micromaterial in the two geometrical scales. The macro and micro design domain are meshed into N and n elements respectively in order to numerically solve this mathematical problem via the Finite Element Method. Each element is then assigned a unique density value varying between 0 and 1, e.g. $P_i(\Omega)(i = 1, 2, \dots, N)$ for the i th element in macro scale and $\rho_j(Y)(j = 1, 2, \dots, n)$ for the j th element in micro-scale. While implementing, topology optimization based on SIMP(Solid Isotropic Material Penalization) is adopted in micro material scale to obtain an optimum material microstructure comprised of solid isotropic material for porous ceramic, and topology optimization based on PAMP (Porous Anisotropic Material Penalization) is introduced in macro structural scale to find the optimum configuration of structures composed of the “optimum” porous material. Optimizations of the two geometrical scales are integrated into one system through homogenization theory based on the assumption of the homogeneity of the material in structural scale. Through optimizing the distribution of material on the two scales, the concurrent optimum design of the macro structure and its micro material configuration are obtained. The volume preserving nonlinear density filtering based on Heaviside step function is used together with the penalization approaches to prevent checkerboard pattern and to obtain a clear design.

Two objectives, the structural compliance under mechanical loads and the thermal expansion in a predefined domain under thermo loads, are both normalized and then jointed through weighted coefficients to establish the multi-objective optimization model. The adjoint method is utilized to obtain the sensitivity of objective and the SQP method is adopted to solve and find the Pareto optimum of the bi-objective optimization. In this article, the compliance and the thermo expansion are normalized into a multi-objective function optimization problem so that the optimum results is

more flexible and adaptable, because final optimum topology configuration shows no dependence on the relative intensity of the mechanical and thermo load under the linear elastic assumption.

3. RESULTS

We apply the proposed multi-objective optimization model to a sandwich elliptically curved shell composed of porous ceramic to investigate effectiveness of the proposed concurrent optimization method at the two geometric scales. The core between the exterior and interior solid areas of the sandwich structure is composed of porous CSi ceramic material and is defined as the design domain. The configurations of the macro sandwich core and the microstructure of ceramics are concurrently optimized with topology optimization. The total objective contains both the normalized compliance when uniform pressure is considered and the normalized the summation of the deformation of the edge of the exterior solid surface when only thermal load applies which are joined with weighting coefficients w_1 and w_2 , and then is minimized. Table 1 presents the optimization results under different w_1 and w_2 . We also investigate the influences of “optimum” material volume fraction constraint and thickness of surface sheets on the optimal designs.





w_1/w_2	Structural Topology	Microstructural Topology 4×4 arrays	Objective
Initial design: Obj1=3.69406, Obj2=0.01218			
$\frac{w_1}{w_2} = \frac{1}{0}$			Obj1=0.1101
Only mechanical load is considered			Obj2=0.01138
$\frac{w_1}{w_2} = \frac{0}{1}$			Obj1=6.7034
Only thermo load is considered			Obj2=0.008588

TABLE 1 Multi-objective multi-scale design results under different weight coefficients

The denotation obj1, obj2 inside table 2 are the unnormalized structural compliance and the thermo expansion of the surface.

When only structural compliance is taken into account, the optimum design of the core presents a “branch-like” configuration to link the exterior and interior surface sheets. And more material is distributed on the top area of the core to resist the deformation caused by the mechanical load where the mechanical load is larger because the angle between the uniform mechanical load direction and the direction of the outer normal of the exterior solid sheets becomes larger near the top area of the core. As expected the optimum micro material configuration is isotropic solid. However, when we only consider 1% percent thermo expansion of the outer surface, the optimum macro structural topology differs with that from the single structural compliance optimization. What’s more, the weighting coefficient of the thermo objective, 1%, can be apprehended as the scope of the temperature field receding to 80-160°C (because F_2 is the summation of the squared summation of

the nodal thermo expansion, 1% of the original thermo objective means the scope of the temperature field reduced to 10% of the original value equivalently) while the mechanical load remains unchanged. Consequently, more load cases can be covered through the adjusting the weighting coefficients.

In the case of $w_1/w_2 = 0/1$ (only thermo load are considered), as can be observed from Table 2, the optimum micro material configuration is porous with “diamond-shaped” holes. And the optimum configuration of the core of the sandwich structure presents many “reinforced ribs” connecting the exterior and interior surface sheets. And the “reinforced ribs” will coordinate their thermo expansion to minimize the deformation of outer surface. What’s more, the material tends to distribute near the interior surface sheet and lower part of the core of sandwich structure. This is because the temperature of the lower part of the core is much lower and thus the thermo load is relatively weak. At the same time, the distribution of material near the interior surface will not cause significant thermo expansion of the exterior surface which is conducive to the heat protection and heat insulation of the design of the interior surface sheet.

4. CONCLUSIONS

When the available amount of material is insufficiently given, the optimum micro material configuration is porous with the optimization model which combines the structural compliance and thermo deformation as the objective function. The extraordinary properties of the porous ceramic material, such as high specific stiffness ratio, high specific strength ratio, high wave transmitting and the high temperature stabilization render it extremely promising for multi-disciplinary applications. When both the structural compliance and thermo deformation are considered in the objective function, an “optimum” material volume fraction is observed contrary to the minimization structural compliance design where the material is “the more, the better”. This provides us new idea in the lightweight design of the thermo elastic structures. The configuration of the structure and its effective material properties can influence the temperature field. Combining the coupling effect will be the focus of our future research.

ACKNOWLEDGEMENTS

The financial support for this research was provided by the Program (90816025, 10902018) of NSFC, the National Basic Research Program of China(2011CB610304), the Major National Science and Technology Project (2011ZX02403-002) and the Science Research Foundation of Dalian University of Technology(DUT11LK05). These supports are gratefully appreciated.

REFERENCES

- [1] S.J. Xu, G.J. Qiao, H.J. Wang, D.C. Li, T.J. Lu, Microstructure Evolution and Reaction Mechanism of Microporous Carbon Derived SiC Ceramic. *Journal of Inorganic Materials*,24(2), 291-296, 2009. (in Chinese)
- [2] G. Jefferson, T. A. Parthasarathy, R.J. Kerans. Tailorable thermal expansion hybrid structures. *International Journal of Solids and Structures*, 46, 2372-2387, 2009.
- [3] J. Yan, G.D. Cheng, L. Liu, A Uniform Optimum Material Based Model for Concurrent Optimization of Thermoelastic Structures and Materials. *International Journal for Simulation and Multidisciplinary Design Optimization*, 2, 259-266, 2008.

DEFORMATION CONTROL OF THIN-WALLED STRUCTURES BY APPLIED HEAT FLUX

Junhui Zhang, Zhihai Xiang, Yinghua Liu, Mingde Xue

AML, Tsinghua University, Beijing 100084, China, E-mail: xiangzhihai@tsinghua.edu.cn

ABSTRACT

The thermally-induced deformation of flexible space structures could be suppressed by controlling the temperature difference on certain cross-sections of these kinds of thin-walled structures. For this purpose, one must optimize the applied heat flux to control the temperature difference and deformation of thin-walled structures. This optimization procedure could be very time consuming, because the radiation analysis has to be conducted in each iteration step. However, this problem can be greatly remedied with the help of the Fourier temperature finite element, which has been proposed in our early work. Based on this element, this paper develops a heat flux optimization method to control the thermally-induced deformation of thin-walled structures. A numerical example demonstrates the validity and efficiency of the proposed method.

Key Words: *Thin-walled Structures, Finite Elements, Thermally-induced deformation, Control.*

1. INTRODUCTION

Large Flexible Space Structures (LFSS), such as satellite antennas, solar arrays and reflectors are widely used in space technology. These thin-walled structures are likely to undergo thermally-induced responses due to the temperature change in orbit. Sometimes these responses are harmful to the system performance, such as the most famous accident of Hubble Space Telescope (HST) [1]. People have tried to use thermal actuators to achieve the shape control of the LFSS [2, 3]. Those actuators generate control forces due to the thermal gradient in the actuator or the mismatch of thermal expansion coefficients on the interface of the structure. However, this paper just uses a simpler idea that suppresses the structural deformation by controlling the temperature difference on certain cross-sections of the structure.

To control the structural deformation, one can apply certain heat flux on the structure, which can be determined by certain optimization method iteratively. In each iteration step, a transient temperature problem with the radiation boundary condition has to be solved. Usually, this time-dependent and strong nonlinear problem is very time consuming. However, for these kinds of thin-walled structures, Xue et al. proposed a Fourier temperature finite element [4], which is characterized by the decomposition of the temperature into an average part and a perturbation part on the cross-section of the structure. Owing to the orthogonality of shape functions, the average temperature and the perturbation temperature can be decoupled into two equations. Thus, the detailed transient temperature field can be efficiently solved. Based on the Fourier temperature element, this paper proposes an optimization scheme that can determine the desired heat flux to control the deformation of the structure.

2. OPTIMIZATION ALGORITHM

2.1 Fourier-temperature finite element subjected to heat flux loads

The LFSS is usually made of thin-walled beams with closed or open sections, as shown in Figure 1. The temperature $T(x, s, t)$ of a beam should satisfy a nonlinear partial differential equation [4]:

$$c\rho \frac{\partial T}{\partial t} - \frac{\partial}{\partial x} \left(k_x \frac{\partial T}{\partial x} \right) - \frac{\partial}{\partial s} \left(k_s \frac{\partial T}{\partial s} \right) + \frac{\varepsilon\sigma}{t_s} (T^4 - T_\infty^4) - \frac{\alpha_s}{t_s} \bar{q}(s, x, t) - \frac{a_s}{t_s} \bar{q}_c(s, x, t) = 0 \quad (1)$$

where c is the specific heat; ρ is the material density; k_x and k_s are thermal conductivities along the axial and circumferential directions, respectively; ε is the emissivity of the external surface of the beam; α_s is the absorptivity on the surface of the beam; σ is the Stefan–Boltzman constant; $\bar{q}(s, x, t)$ and $\bar{q}_c(s, x, t)$ are the space heat flux and the controlled local heat flux normal to the surface of the beam, respectively.

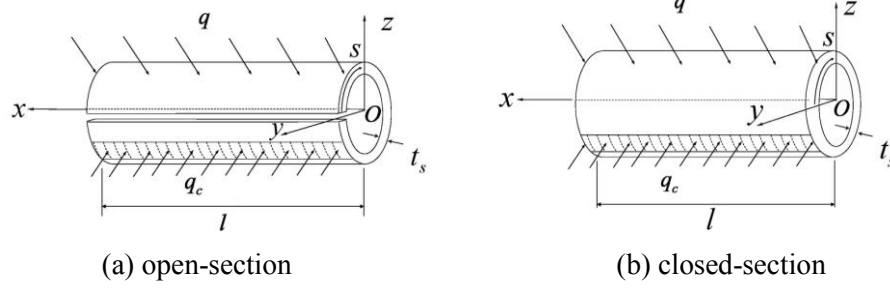


FIGURE 1. Thin-walled beams subjected to controlled local heat flux q_c and space heat flux q

Supposing M sets of controlled heat flux $\bar{q}_c^{(m)}$ ($m = 1, 2, \dots, M$) act on the surface of the thin-walled beam at circumferential position $s_p^{(m)}$ in length of $s_a^{(m)}$. The absorbed heat flux is:

$$\bar{q}_c = \sum_{m=1}^M \delta_c^{(m)} \bar{q}_c^{(m)} \quad (2)$$

where

$$\delta_c^{(m)} = \begin{cases} 1 & s_p^{(m)} - s_a^{(m)} / 2 < s^{(m)} < s_p^{(m)} + s_a^{(m)} / 2 \\ 0 & s^{(m)} \leq s_p^{(m)} - s_a^{(m)} / 2 \quad \text{or} \quad s^{(m)} \geq s_p^{(m)} + s_a^{(m)} / 2 \end{cases} \quad (3)$$

The temperature $T(x, s, t)$ on the beam cross-section can be decomposed into an average part T_i^0 and a perturbation part T_i^n and is interpolated by the values at two element nodes:

$$T(x, s, t) \approx \sum_{i=1}^2 \left[T_i^0(t) + \sum_n T_i^n(t) N^n(s) \right] N_i(x) \quad (4)$$

Because of the orthogonality between the shape function in axial direction $N_i(x)$ and the shape function in circumferential direction $N^n(s)$, the conductivity equations of the whole structure can be decoupled into the following two finite element equations:

$$C\dot{T}^0 + K^0 T^0 + R^0(T^0) = P^0(t) + P_c^0(t) \quad (5)$$

$$C\dot{T}^n + [K^n + R^n(T^0)] T^n = P^n(t) + P_c^n(t) \quad (6)$$

where C is the specific heat matrix; K^0 and K^n are the conductivity matrices; R is the radiation vector or matrix; P^0 and P^n are thermal loading vectors due to the space heat flux; P_c^0 and P_c^n are thermal loading vectors due to the controlled local heat flux; superscripts 0 and n are corresponding to the average temperature and the perturbation temperature, respectively. In this way, the perturbation temperature vector T^n can be solved after obtaining the average temperature

vector \mathbf{T}^0 , which greatly improves the computational efficiency [4]. After obtaining the temperature $T(x, s, t)$, the deformation \mathbf{u} of structures subjected to controlled local heat flux \mathbf{q}_c and space heat flux \mathbf{q} can be obtained by solving the following equation:

$$\mathbf{K}\mathbf{u} = \mathbf{F}(\mathbf{T}) \quad (7)$$

where \mathbf{K} is the stiffness matrix; \mathbf{F} is the equivalent nodal force vector due to thermal strain.

2.2 Optimize the controlled local heat flux

Take the magnitude of the controlled local heat fluxes as design parameters \mathbf{p} , which can be determined through the following optimization formulation:

$$\begin{aligned} \text{Min} \quad & f(\mathbf{p}, \mathbf{u}) = \mathbf{W}^T \mathbf{W} \\ \text{S.t.} \quad & \mathbf{C}\dot{\mathbf{T}}^0 + \mathbf{K}^0 \mathbf{T}^0 + \mathbf{R}^0(\mathbf{T}^0) = \mathbf{P}^0(t) + \mathbf{P}_c^0(t) \\ & \mathbf{C}\dot{\mathbf{T}}^n + [\mathbf{K}^n + \mathbf{R}^n(\mathbf{T}^0)] \mathbf{T}^n = \mathbf{P}^n(t) + \mathbf{P}_c^n(t) \\ & \mathbf{K}\mathbf{u} = \mathbf{F}(\mathbf{T}) \end{aligned}$$

where $\mathbf{W} = (\mathbf{u}^* - \mathbf{S}\mathbf{u})$ is the residual vector; \mathbf{u}^* are the desired deformation; and \mathbf{S} is a selective matrix that specifies the location of desired deformation. This Least-Squares problem can be efficiently solved by the Gauss-Newton method iteratively [5]:

$$\mathbf{p}^k = \mathbf{G}(\mathbf{p}^{k-1}) = \mathbf{p}^{k-1} \left[(\mathbf{J}^{k-1})^T \mathbf{J}^{k-1} \right]^{-1} (\mathbf{p}^{k-1})^T \mathbf{W}^{k-1} \quad k = 1, 2, \dots \quad (8)$$

where $\mathbf{J} = -\mathbf{S}\partial\mathbf{u}/\partial\mathbf{p}$ can be obtained by the following sensitivities analysis.

2.3 Sensitivities analysis

Differentiating Eqs. (5), (6) and (7) with respect to the k th design parameter p_k , obtains:

$$\mathbf{C}\dot{\mathbf{T}}_{,p_k}^0 + (\mathbf{K}^0 + \mathbf{R}_{,T^0}^0) \mathbf{T}_{,p_k}^0 = \mathbf{P}_{c,p_k}^0 \quad (9)$$

$$\mathbf{C}\dot{\mathbf{T}}_{,p_k}^n + (\mathbf{K}^n + \mathbf{R}^n) \mathbf{T}_{,p_k}^n = \mathbf{P}_{c,p_k}^n - \mathbf{H}_R \mathbf{T}^n \quad (10)$$

$$\mathbf{K}\mathbf{u}_{,p_k} = \mathbf{F}_{,T^0} \mathbf{T}_{,p_k}^0 + \mathbf{F}_{,T^n} \mathbf{T}_{,p_k}^n \quad (11)$$

Solving the linear ordinary differential equations (9) and (10) step by step by the Wilson- θ method, one can obtain $\mathbf{T}_{,p_k}^0, \mathbf{T}_{,p_k}^n$. Substituting $\mathbf{T}_{,p_k}^0$ and $\mathbf{T}_{,p_k}^n$ into Eq. (11), $\mathbf{u}_{,p_k}$ can be obtained, and thus one can calculate $\mathbf{J} = -\mathbf{S}\partial\mathbf{u}/\partial\mathbf{p}$.

3. NUMERICAL EXAMPLE

In this section, the proposed deformation control method is used to suppress the deformation of the HST solar array subjected to solar heat flux. The schematic view of the HST solar array is shown in Figure 2. The geometric dimensions and material properties can be found in [1]. This structure will undergo certain thermal deformation subjected to the suddenly applied solar heat flux $q_0 = 1350 \text{ W/m}^2$ along the negative Y -direction. To suppress this deformation, the controlling

heat flux q_c is applied on small part of the surfaces but throughout the whole length of the thin-walled booms (see FIGURE 2, where $\theta_p = \pi$ and $\theta_c = \pi/6$). With the proposed method, the optimal q_c can be easily obtained as $q_c = 2.048 \times 10^3 (W/m^2)$ by minimizing the deformation in Y -direction at position A .

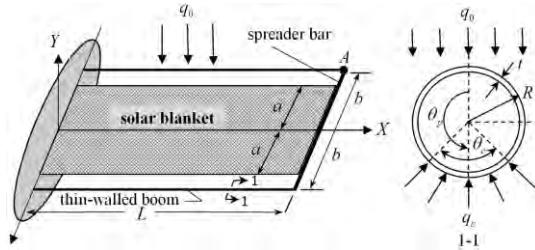


FIGURE 2. Model of the HST solar array

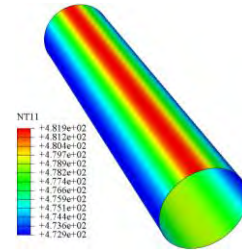


FIGURE 4. Temperature field of the boom

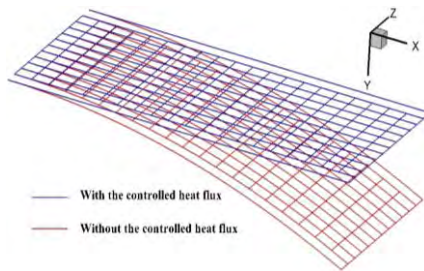


FIGURE 3. Model of the HST solar array

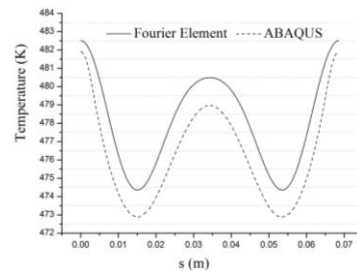


FIGURE 5. Section-temperatures of the boom

The deformations of the HST solar array subjected to solar flux with and without the controlling heat flux are shown in Figure 3. It observes that the HST solar array is well kept to its original shape with the controlling heat flux. The corresponding temperature field of the thin-walled boom is shown in Figure 4. Figure 5 is the comparison between section-temperatures of the thin-walled boom obtained by ABAQUS shell element model and the Fourier temperature element with the same controlled heat flux. The differences are less than 0.2%. However, there are 13072 nonlinear equations in ABAQUS model, while there are only 401 nonlinear equations and 2406 linear equations in the Fourier temperature element model, which greatly saves the computational time.

4. CONCLUSIONS

Based on the Fourier temperature element, this paper develops a method to control the deformation of thin-walled structures by changing the temperature field of the structure. The numerical example demonstrates the effectiveness and efficiency of using this method to solve engineering problems.

REFERENCES

- [1] E.A. Thornton and Y.K. Kim, Thermally Induced Bending Vibrations of a Flexible Rolled-Up Solar Array, *Journal of Spacecraft and Rockets*, 30, 438-448, 1993.
- [2] L.E. Donald, Control of Flexible Structures by Applied Thermal Gradients, *AIAA Journal*, 25, 877-883, 1987.
- [3] H. Tirschik and U. Pichler, Dynamic shape control of solids and structures by thermal expansion strains, *Journal of Thermal Stresses*, 24, 565-576, 2001.
- [4] M.D. Xue and Y. Ding, Two Kinds of Tube Elements for Transient Thermal-Structural Analysis of Large Space Structures, *International Journal for Numerical Methods in Engineering*, 59, 1335-1353, 2004.

TEMPERATURE UNIFORMITY DETERMINATION AND OPTIMIZATION OF DRYING OVENS USING EXPERIMENTALLY VALIDATED CFD ANALYSIS AND GENETIC ALGORITHM

Jacek Smolka*, **Piotr Canibol**, **Piotr Olczek**, **Zbigniew Bulinski**, **Andrzej J. Nowak**
Institute of Thermal Technology, Silesian University of Technology, Konarskiego 22, 44-100
Gliwice, Poland, *corresponding author: jacek.smolka@polsl.pl

Dawid Rybarz

Pol-Eko-Aparatura Sp.J., Kokoszycka 172C, Wodzislaw Slaski, Poland

ABSTRACT

The present paper discusses experimental and computational studies of the flow and thermal processes in a laboratory drying oven with a natural air circulation to improve temperature uniformity inside the storage chamber. The device is mainly used in the laboratories of the food and chemical industry to store products and samples at a constant, spatially uniform temperature. The actual device has been assessed according to a certification procedure and then numerically simulated on the basis of the mathematical model developed, including all heat transfer modes, temperature-dependent air properties and local heat transfer coefficients on the external walls, etc. In this study, a source of the non-uniformity of the temperature field was identified. As a result, a configuration of the electrical heaters were modified. Furthermore, a shape and location of the modified heaters were optimized using genetic algorithm coupled with CFD computations of the 3-D model of the drying oven.

Key Words: *Heat Transfer, CFD, Drying oven, Temperature uniformity, Genetic algorithm.*

1. INTRODUCTION

Drying ovens and thermostatic cabinets are devices that are broadly installed in laboratories of chemical, food and pharmaceutical industry to store products and samples in a desired uniform temperature. This means that the temperature distribution in such devices is controlled very precisely. A typical solution for smaller storage capacities are the units with natural air circulation, where the fresh air is sucked from ambient through intake holes located in a back wall of the devices. Then the air heated by the electrical heaters flows through the distribution gaps into the storage chamber. From this region the air flows out of the oven through the main outlet equipped with a valve controlling the air change rate in the chamber. Configuration of the device is shown in Figure 1(a).

The quality of such devices is measured taking into account the temperature uniformity inside the main chamber. Such studies are well known in the literature [6-9]. In the experiments, the temperatures are captured by the sensors located in the corners and in the center of the main chamber. Therefore, companies producing these devices continuously improve products experimentally changing a configuration of the distribution gaps for a fixed configuration of the electrical coil heaters. This method may be successful, however, it is very time and cost consuming. Another disadvantage is that the temperatures are only monitored instead of flow field.

The aim of this study is to build a three-dimensional geometrical model of the device, formulate a mathematical model taking all the thermal and flow processes occurring in the chamber, and finally identify the problem of the non-uniform temperature distribution, especially at higher values. In the second stage, the experimental tests were performed for the modified heaters. These were followed

by the optimization process of the heater positions using the genetic algorithms [4]. Similar studies were already published for the heat generating parts of the electrical transformer [5]. In this case, the objective function in the optimization procedure was the temperature uniformity defined as a temperature difference of the centre and particular corner value.

2. COMPUTATIONAL MODEL AND EXPERIMENTAL TESTS

To analyze the flow and the temperature field within a drying oven, a three-dimensional model was created based on technical documentation provided by a drying oven manufacturer. The overall dimensions of the device are width 0.440 m, depth 0.342 m, and height 0.480 m. The volume of the storage space is 15 L. The main target of this research was to stabilize the temperature distribution within the storage chamber. This means that all elements that may influence both flow field and heat transfer are geometrically modeled. In general, the device being produced consists of a back internal wall with a few rows of intake gaps in the upper part, side internal walls and two electrical coil-shaped heaters placed below the bottom internal wall with intake gaps and the insulated external walls. A geometrical model of the currently produced device is shown in Figure 1.

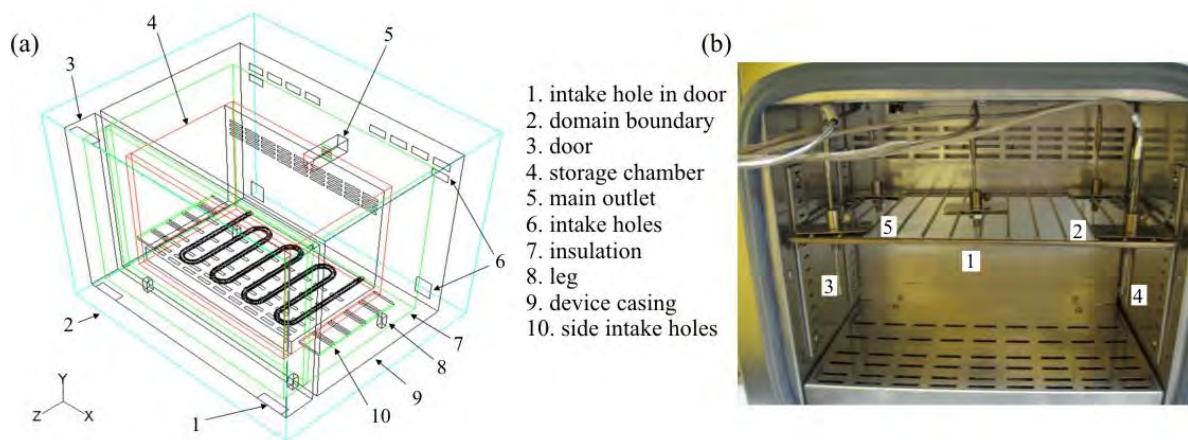


FIGURE 1. A drying oven with a natural air circulation (a) geometrical model, and (b) photo with a location of the temperature sensors.

The formulated mathematical model included equations for the pressure, velocity, temperature, radiative heat fluxes and turbulence. All the air properties were defined as temperature-dependent values [2], while those for solid materials originated from the specifications delivered.

To define realistic boundary conditions, the model also consists of the secondary chamber between the main chamber and the insulation layer. Moreover, computational domain was also enlarged by a volume of ambient air surrounding the device. In this way, the most important heat transfer mode, i.e. natural convection was also considered outside the drying oven.

The second mode influencing the temperature field in the device was thermal radiation occurring between internal chamber walls, and between these walls and heaters. Furthermore, it was also important to take heat conduction into consideration.

Computational results obtained using this CFD model [1] were used to determine a quite low temperature uniformity obtained in experimental tests. These measurements were performed according to the certificate procedure for such devices. This means that the sensors captured temperatures on centre plane (12 cm from the internal bottom wall) in the corners and in the centre of the storage chamber are listed in Table 1, while the PT-100 sensor locations are shown in Figure 1(a). As shown in first three rows of this table for the case of temperature level of 170°C, the difference between corner and centre values is unacceptable.

Parameter	Sensor number				
	1	2	3	4	5
Mean temperature, ℃	186.0	190.6	176.6	185.7	175.6
Standard deviation, ℃	0.6	0.5	0.2	0.5	0.2
Temperature uniformity, ℃	0.0	4.6	9.4	0.3	10.4
Mean temperature, ℃	150.4	148.9	153.0	150.2 <td 153.8	
Standard deviation, ℃	0.2	0.1	0.2	0.2	0.1
Temperature uniformity, ℃	0.0	1.5	2.6	0.2	3.4

TABLE 1. Experimental results of the temperature field inside the chamber of the drying oven for two heater types. A location of the sensor numbers is shown in Figure 1(b).

3. RESULTS

Computational tests were performed for different numerical and physical parameters such as higher discretization orders, two levels of mesh size, various turbulence models, wall emissivities and effective thermal conductivities for electrical heaters. Results obtained for one of these computations is presented in Figure 2(a). As shown, computational results are qualitatively different than those obtained from the experiments. In general, all the numerical results showed a very high temperature uniformity. Therefore, it was necessary for perform additional experimental tests in which temperature of the heater was measured using infrared camera. As illustrated in Figure 2(b), heat generated is definitely non-uniform along a wire of the heater. As a results, a single heater including eight straight segments was replaced with the four heaters with two segments. Results of the temperature uniformity in the chamber obtained for this case are shown in the second three rows of Table 1. Hence, the main conclusion of this part of the study was that the quality of the heater is mainly responsible for the temperature distribution.

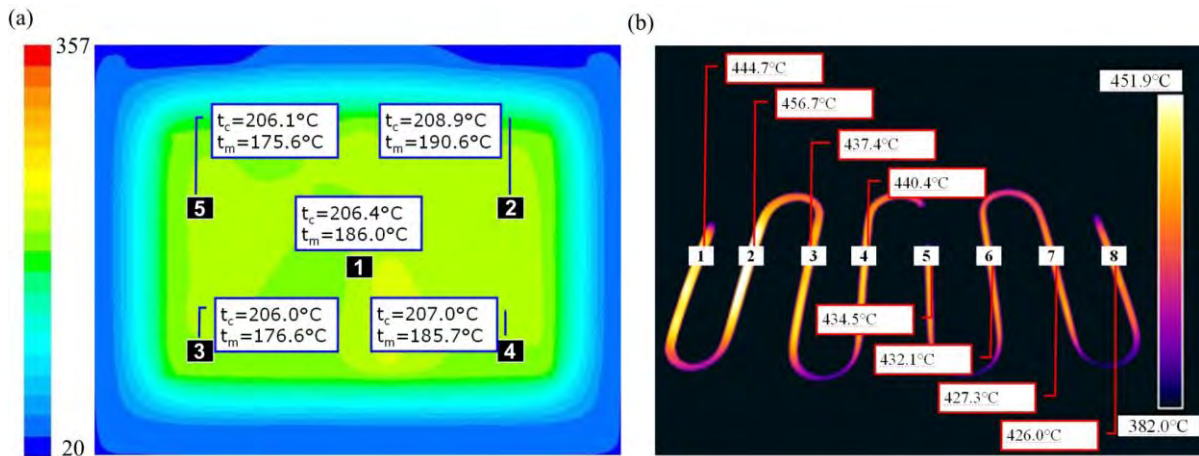


FIGURE 2. (a) Comparison of temperature field obtained from experiments (subscript m) and computations (subscript c).

In the second part of this research, an optimization procedure based on genetic algorithm (GA) was applied to improve a temperature uniformity in the main chamber. This parameter was defined as an objective function that was computed using CFD analysis performer in Ansys Fluent code [3]. The optimized parameters were geometrical parameters defining a position of each electrical heater. The GA code written in Fortran was automatically executed in a parallel manner calling particular Ansys Fluent jobs.

Results of the optimization will be shown during the conference.

4. CONCLUSIONS

In this paper, experimental and computational studies of the flow and thermal processes in a laboratory drying oven with a natural air circulation were performed. As a result, the temperature uniformity inside the storage chamber was modified in two stages. In the first one, based on CFD model and infrared measurements, the main problem of a low uniformity was identified and eliminated. In the second part of this research, a further calibration of the heater was carried out using optimization procedure. The coupled CFD and GA procedure allowed the authors to improve the 3-D temperature distribution in the device.

REFERENCES

- [1] J.D Anderson, *Computational Fluid Dynamics. The Basics with Applications*, McGraw Hill, 1995.
- [2] Y.A. Cengel, *Heat and Mass Transfer. A Practical Approach*, McGraw-Hill, New York, 2007.
- [3] Computational Fluid Dynamics Software. User's manual, Release 6.3, Ansys Inc, www.ansys.com, 2006.
- [4] M. Mitchell, *An Introduction to Genetic Algorithms*, Cambridge, MA: The MIT Press, 1998.
- [5] J. Smolka, A.J. Nowak, Shape optimization of coils and cooling ducts in dry-type transformers using CFD and GA, *IEEE Transactions on Magnetics*, 99, 1-1, 2011.
- [6] J. Smolka, A.J. Nowak, D. Rybarz, Improved 3-D temperature uniformity in a laboratory drying oven based on experimentally validated CFD computations, *Journal of Food Engineering*, 97, 373-383, 2010.
- [8] P. Verboven, A.K. Datta, N.T. Anh, N. Scheerlinck, B.M. Nicolai, Computation of airflow effects on heat and mass transfer in a microwave oven, *Journal of Food Engineering*, 59, 181-190, 2003.
- [7] P. Verboven, N. Scheerlinck, J. De Baerdemaeker, B.M. Nicolai, Computational fluid dynamics modelling and validation of the temperature distribution in a forced convection oven, *Journal of Food Engineering*, 43, 61-73, 2000.
- [9] L. Wang, D.-W. Sun, Recent developments in numerical modelling of heating and cooling processes in the food industry - a review, *Trends in Food Science and Technology*, 14, 408-423, 2003.

PARALLEL SESSIONS

SPECTRAL FINITE DIFFERENCE ANALYSIS OF NATURAL CONVECTION IN A TRIPLY-CONNECTED REGION OF A NEARLY PARALLEL ENCLOSURE

Yoshihiro Mochimaru

Department of International Development Engineering, Tokyo Institute of Technology
 Tokyo 152-8550, JAPAN, ymochima@o.cc.titech.ac.jp

ABSTRACT

Steady-state two-dimensional laminar natural convection around a triply-connected region is analyzed numerically, using a spectral finite difference scheme. The region is assumed to be of infinite extension consisting of two nearly parallel horizontal walls with two nearly circular cylinders. A boundary-fitted conformal map is generated analytically. In addition, transformation of a variable is adopted to support the condition at an artificially generated boundary.

Key Words: *Conformal Mapping, Spectral Analysis, Natural Convection*

1. INTRODUCTION

Analysis of natural convection heat transfer is one element of heat and fluid flow problems, e.g. heat transfer to liquid metals from cylinders [2], to air from cylinders [1]. Recently-developed spectral finite difference schemes [5] are very effective to analytical or numerical treatment of heat and/or fluid flow problems in two-dimensional or in axisymmetric solutions, but not restricted to them. Mathematical introduction of multiply-connectedness is required as shown in [7] (doubly-connected), [6] (triplly-connected), and [8] (quadruply-connected). The spectral finite difference scheme has the following property: mathematically exact spatial spectral decomposition, high spatial resolution, high speed computation, and accepting non-uniform grid spacing.

2. ANALYSIS

2.1. GENERAL

Steady-state two-dimensional laminar natural convection around a triply-connected region in a nearly parallel horizontal enclosure is analyzed numerically, using a spectral finite difference scheme. The region is assumed to be of infinite extension with two nearly circular cylinders as shown in Figure 1, supplemented with no slip flow and uniform surface temperatures along walls and nearly-circular cylinders. Under a boundary-fitted conformal mapping coordinate system (α, β) , dimensionless Cartesian coordinate system (x, y) (y : vertically upward), and a Boussinesq approximation neglecting dissipation terms, the dimensionless governing equations (vorticity transport equation, relation between vorticity and a stream function, and energy equation; ψ : dimensionless stream function based on UL , ζ : dimensionless vorticity based on U/L , T : dimensionless temperature \equiv (local temperature $-T_L$)/ ΔT , t : dimensionless time based on L/U) are

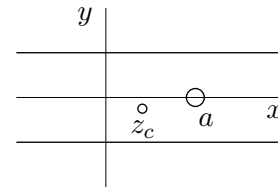


FIGURE 1. Schematic configuration in case of $p > 0$

$$J \frac{\partial \zeta}{\partial t} + \frac{\partial(\zeta, \psi)}{\partial(\alpha, \beta)} = \frac{1}{\sqrt{Gr}} \left(\frac{\partial^2}{\partial \alpha^2} + \frac{\partial^2}{\partial \beta^2} \right) \zeta + \frac{\partial(T, y)}{\partial(\alpha, \beta)}, \quad (1)$$

$$J \zeta + \left(\frac{\partial^2}{\partial \alpha^2} + \frac{\partial^2}{\partial \beta^2} \right) \psi = 0, \quad J \equiv \frac{\partial(x, y)}{\partial(\alpha, \beta)}, \quad (2)$$

$$J \frac{\partial T}{\partial t} + \frac{\partial(T, \psi)}{\partial(\alpha, \beta)} = \frac{1}{Pr \sqrt{Gr}} \left(\frac{\partial^2}{\partial \alpha^2} + \frac{\partial^2}{\partial \beta^2} \right) T \quad (3)$$

respectively, where Gr , Pr stand for a Grashof number (based on ΔT and L) and a Prandtl number, and L : width faraway, $U \equiv (\nu/L)\sqrt{Gr}$, ν : kinematic viscosity, $\Delta T (> 0)$: reference temperature difference, T_L : reference temperature. Coordinates x and y are based on L .

2.2. MAPPING FUNCTION

Introduced is the following mapping function:

$$-\frac{1}{2\pi} \ln \left\{ 1 - (1 - k^2) \left(i \tanh \frac{\alpha + i\beta}{2} + p \right)^2 \right\} = z + b + \frac{\delta^2}{z - a}, \quad (4)$$

where $z \equiv x + iy$; b, p : real, $0 < k < 1, a > 0, \delta > 0, \delta \ll 1, -\pi \leq \beta \leq \pi$. Consequently, it is assumed that one of the two nearly-circular cylinders are specified by $\alpha = 0$, i.e., $|z - a| = \delta$, and the second nearly-circular cylinder is specified by $\alpha = \alpha_0 (< 0), |\beta| \leq \pi$ such that $e^{\alpha_0} \ll 1$ and to be separated from each other

$$\left| a + b + \frac{1}{2\pi} \ln \left\{ 1 - (1 - k^2) (i - p)^2 \right\} \right| \gg \delta + \frac{2(1 - k^2)}{\pi} \left| \frac{i - p}{1 - (1 - k^2)(i - p)^2} \right| e^{\alpha_0}.$$

Finally, the closed field region is specified by $\alpha_0 \leq \alpha \leq 0, |\beta| \leq \pi$. Jacobian J becomes

$$\frac{\sqrt{J}}{e^\alpha} = \frac{2(1 - k^2)}{\pi} \left| \frac{i \tanh \frac{\alpha + i\beta}{2} + p}{1 - (1 - k^2) \left(i \tanh \frac{\alpha + i\beta}{2} + p \right)^2} \right| \left/ \left| \left(e^\alpha + i\beta + 1 \right)^2 \left\{ 1 - \frac{\delta^2}{(z - a)^2} \right\} \right| \right|. \quad (5)$$

2.3. TRANSFORMATION OF A VARIABLE β

In case of $\alpha = 0$, $\tanh \frac{\alpha + i\beta}{2} = i \tan \frac{\beta}{2}$, so that the following is introduced independently of α :

$$\tan \frac{\omega}{2} \equiv \tan \frac{\beta}{2} - p; \quad -\pi \leq \omega \leq \pi. \quad (6)$$

Consequently

$$\frac{\partial}{\partial \beta} = \left(1 + \frac{p^2}{2} + p \sin \omega + \frac{p^2}{2} \cos \omega \right) \frac{\partial}{\partial \omega}, \quad d\beta = \frac{d\omega}{1 + \frac{p^2}{2} + p \sin \omega + \frac{p^2}{2} \cos \omega}. \quad (7)$$

2.4. MULTIPLY-CONNECTEDNESS

Multiply-connectedness leads at every circumference C_j ($j = 1, 2$; for $j = 1, z \approx a$ ($\alpha = 0$), $\omega_1 \leq |\omega| \leq \omega_2$; for $j = 2, z \approx z_c \equiv -b - \frac{1}{2\pi} \ln \{ 1 - (1 - k^2)(i - p)^2 \}$, ($\alpha = \alpha_0, |\omega| \leq \pi$) of the isolated configuration to

$$\oint_{C_j} \frac{\partial p_0}{\partial \beta} d\beta = 0,$$

which becomes

$$\frac{1}{\sqrt{Gr}} \oint_{C_j} \frac{\partial \zeta}{\partial \alpha} d\beta + \oint_{C_j} T \frac{\partial y}{\partial \beta} d\beta = 0 \quad (8)$$

(under a no-slip flow condition at a stationary wall), where p_0 stands for local pressure, and

$$\omega_j \equiv 2 \tan^{-1} \left[\frac{1 - \exp 2\pi \{ (-1)^{j-1} 2\delta - a - b \}}{1 - k^2} \right]^{1/2}, \quad (j = 1, 2), \quad a + b - 2\delta > 0.$$

2.5. BOUNDARY CONDITIONS AT PHYSICAL BOUNDARIES

As dynamic boundary conditions, no slip flow at nearly-parallel walls and physical cylinder boundaries is assumed; without loss of generality ($\omega_3 \equiv \pi - 2 \tan^{-1} \sqrt{1 - k^2}$)

$$\psi(0, \omega) = 0, \quad \pi > |\omega| > \omega_3; \quad \psi = \psi_j \text{ (constant to be determined on } C_j, j = 1, 2), \quad (9)$$

$$\frac{\partial}{\partial \alpha} \psi(0, \omega) = 0, \quad \pi > |\omega| > \omega_3; \quad \frac{\partial \psi}{\partial \alpha} = 0 \text{ on } C_j (j = 1, 2). \quad (10)$$

For thermal boundary conditions, Dirichlet type surface boundary conditions are assumed, without loss of generality

$$T(0, \omega) = 0, \quad \pi > |\omega| > \omega_3; \quad T(0, \omega) = 1, \quad \omega_1 < |\omega| < \omega_2, \quad (11)$$

$$T(\alpha_0, \omega) = T_1, \quad (0 < T_1 < 1), \quad |\omega| \leq \pi. \quad (12)$$

2.6. AUXILIARY CONDITIONS AT $\alpha = 0, |\omega| \in (0, \omega_1) \cup (\omega_2, \omega_3)$

At $\alpha = 0$ and $\Im(z) = 0$, for any scalar ϕ from the continuity of scalar quantity and its gradient,

$$\phi_+ = \phi_- , \quad \frac{1}{\sqrt{J_+}} \frac{\partial \phi_+}{\partial \alpha} = - \frac{1}{\sqrt{J_-}} \frac{\partial \phi_-}{\partial \alpha} , \quad (13)$$

where $\phi_+ = \phi(\omega), \phi_- = \phi(-\omega), J_+ = J(\omega), J_- = J(-\omega), \omega > 0$. In Eq.(13) arguments should be regarded as ω instead of β . The second part of Eq.(13) becomes

$$\frac{\partial}{\partial \alpha} \left\{ \frac{1}{2} (\phi_+ + \phi_-) \right\} = \frac{\sqrt{J_+} - \sqrt{J_-}}{\sqrt{J_+} + \sqrt{J_-}} \frac{\partial}{\partial \alpha} \left\{ \frac{1}{2} (\phi_+ - \phi_-) \right\} . \quad (14)$$

The first part of Eq.(13) is just $(\phi_+ - \phi_-) / 2 = 0$, which applies to ψ, ζ , and T for ϕ .

2.7. SPECTRAL DECOMPOSITION

Spectral decomposition of variables is based on Fourier series:

$$\begin{bmatrix} \psi(\alpha, \beta, t) \\ \zeta(\alpha, \beta, t) \\ T(\alpha, \beta, t) \end{bmatrix} = \sum_{n=1}^{\infty} \begin{bmatrix} \psi_{sn}(\alpha, t) \\ \zeta_{sn}(\alpha, t) \\ T_{sn}(\alpha, t) \end{bmatrix} \sin n\omega + \sum_{n=0}^{\infty} \begin{bmatrix} \psi_{cn}(\alpha, t) \\ \zeta_{cn}(\alpha, t) \\ T_{cn}(\alpha, t) \end{bmatrix} \cos n\omega , \quad (15)$$

where $-\pi \leq \omega \leq \pi$.

2.8. DISCRETIZATION AND TIME INTEGRATION

Numerical integration schemes are as follows: the system of Eqs.(1)-(3) with respect to ω are decomposed into the corresponding Fourier components of ω , discretized in time and space using a finite difference scheme with respect to α , together with a mixed type of boundary conditions at $\alpha = 0$, [3]. Although any non-uniform grid spacing in α can be accepted, the following may work for the n -th grid point $\alpha_n (0 \leq n \leq M + 1; M$: suitably chosen integer, $M + 1$ for $\alpha = 0$).

$$\alpha_n = -h \left\{ \frac{\sinh \gamma (M - n)}{\sinh \gamma} + 1 \right\} , \quad h \equiv (-\alpha_0) / \left(\frac{\sinh \gamma M}{\sinh \gamma} + 1 \right) , \quad (16)$$

where γ is a real parameter (> 0), and the limit $\gamma \rightarrow 0$ corresponds to a uniform grid spacing in α . The larger the value of γ is, the finer the relative grid spacing near the surface of the cylinder at $\alpha = 0$ is. As the initial thermal field the pure heat conduction field is adopted, and an initial stationary flow field is assumed, which is integrated semi-implicitly with respect to time to get a steady-state solution, applying a diagonal dominant form. Total force F_j acting on the stationary surface (with uniform temperature) $C_j (j = 1, 2)$ (excluding stationary buoyancy force) is given by

$$F_j = \frac{1}{\sqrt{Gr}} \oint_{C_j} \zeta dz - \frac{1}{\sqrt{Gr}} \oint_{C_j} \frac{\partial \zeta}{\partial \alpha} \left(z / \frac{dz}{d\alpha} \right) dz , \quad (17)$$

where as usual integration is carried out in the counter-clockwise direction. Mean Nusselt number Nu_m at the surface C_j is given by

$$Nu_j = \pm \oint_{C_j} \frac{\partial T}{\partial \alpha} d\beta / \oint_{C_j} \sqrt{J} d\beta , \quad (18)$$

where + sign applies for C_1 and - for C_2 . For the estimate of denominator

$$\oint_{C_1} \sqrt{J} d\beta = 2\pi\delta , \quad \oint_{C_2} \sqrt{J} d\beta \approx 4(1 - k^2) \left| \frac{i - p}{1 - (1 - k^2)(i - p)^2} \right| e^{\alpha_0} . \quad (19)$$

3. RESULTS AND DISCUSSIONS

3.1. FIELD CHARACTERISTICS

Figures 2 and 3 show an example of steady-state streamlines and isotherms respectively at $Gr = 1000, Pr = 0.7$ for $a = 1, b = -0.463, p = 1, \delta = 0.1, k = 1/\sqrt{2}, \alpha_0 = -1.86, T_1 = 0.5$, which are strongly influenced by the mutual cylinder configuration and T_1 . $\delta\psi$ and δT stand for the difference of streamlines and isotherms respectively. Examples of global quantities corresponding to Figures 2 and 3 are $F_1 \approx -0.02 + 0.004i$ and $Nu_1 = 1.22$.

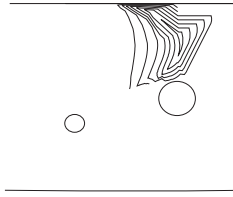


FIGURE 2. Streamlines at $Gr = 10^3$, $Pr = 0.7$; $\delta\psi = 2.5 \times 10^{-5}$, minimum of $\psi \approx -1.8 \times 10^{-4}$

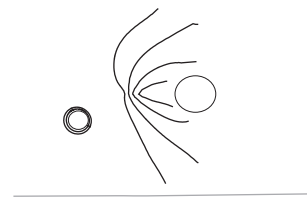


FIGURE 3. Isotherms at $Gr = 10^3$, $Pr = 0.7$; $\delta T = 0.2$.

3.2. TOTAL CHARACTERISTICS

Under the same configuration with Figure 2, mean Nusselt number Nu_1 varies with Gr as

$$Nu_1(Gr = 0.1) = 0.70, Nu_1(Gr = 10) = 0.95, Nu_1(Gr = 10^3) = 1.22 .$$

As far as the above mentioned configurations and a thermal boundary condition is concerned, the absolute value |minimum of $\psi|/\sqrt{Gr}$ (for a low Grashof number case) is 6×10^{-6} ($Gr = 1000$, $Pr = 0.7$, $p = 1$, $e^{\alpha_0} = 0.156$, $T_1 = 0.5$), which is nearly the same order as that in a closed contour case 10^{-6} with completely different closed configuration (elliptic cylinder) and thermal boundary conditions [4]. The maximum degree of Fourier series used in Figures 2 – 3 is 25 for both sine and cosine components.

4. CONCLUSIONS

Introduction of multiply-connectedness leads to a reasonable analysis of natural convection for two isolated objects in a parallel enclosure, using a spectral finite difference scheme with a suitably chosen conformal mapping function.

REFERENCES

- [1] S.C. Hyman, C.F. Bonilla, S.W. Ehrlich, Natural Convection Transfer Processes: I. Heat Transfer to Liquid Metals and Nonmetals at Horizontal Cylinders, *Chem. Eng. Prog. Sym. Ser.*, 49, 21–31, 1953.
- [2] B. Gebhart and L. Pera, Mixed Convection from Long Horizontal Cylinders, *J. Fluid Mech.*, 45, 49–64, 1970.
- [3] Y. Mochimaru, Effectiveness of a spectral finite difference scheme, *Computational Fluid Dynamics Review 1998*, Vol.1, 379–394, 1998.
- [4] Y. Mochimaru and M-W. Bae, Natural convection heat transfer in a doubly-connected region, using a spectral finite difference scheme, *International J. Pure and Applied Mathematics*, 32, 51–60, 2006.
- [5] Y. Mochimaru and M-W., Bae, Spectral finite difference analysis in a triply-connected region, *International J. Computational and Numerical Analysis and Applications*, 4, 91–104, 2003.
- [6] Y. Mochimaru, A Spectral Finite Difference Scheme and its Effectiveness, *Proc. 26th Ann. Iranian Mathematics Conference*, 245–254, 1995.
- [7] Y. Mochimaru, Global instability of natural convection in an elliptic cavity, using a Fourier spectral difference method, *Proc. Seventh International Colloquium on Differential Equations*, 243–252, 1997.
- [8] Y. Mochimaru, Spectral finite difference analysis of natural convection in a multiply-connected region, *International Electronic Journal of Pure and Applied Mathematics*, 2, 7–15, 2010.

SHEARED VORTEX-INDUCED VIBRATION OF A CIRCULAR CYLINDER AT LOW REYNOLDS NUMBER

S. P. Singh

Simulation and Modelling Lab., CSIR-CMERI, Durgapur, 713 209, India, sp_singh@cmeri.res.in

G. Biswas

Department of Mechanical Engineering, Indian Institute of Technology, Kanpur, India,
gtm@iitk.ac.in, On deputation at Central Mechanical Engineering Research and Institute,
(CSIR-CMERI), Durgapur, 713 209, India

ABSTRACT

Sheared vortex-induced vibration (*VIV*) of a circular cylinder is simulated using stabilized finite element (SUPG and PSPG) methods at low *Reynolds number* (*Re*). The cylinder is allowed to oscillate in in-line and transverse directions. Sheared parameter (β) is defined as GD/U_C where G is constant velocity gradient (dU/dy), D and U_C are the diameter of the cylinder and the incoming velocity at the centre of the domain respectively. In the present work, flow of *VIV* are simulated for $\beta=0\%$, 2%, 10%, 20%, 30% and 40%. Structural damping coefficient, ζ , is kept constant to zero so that the displacement responses can be maximized. In the present simulation, *Re* is varied from 70-500 and the value of the reduced velocity, U^* , is kept constant. Two hysteretic loops are observed at $Re \sim 83$ and 325. However, second hysteretic loop is not observed for $\beta=40\%$. The two hysteretic loops are observed for responses such as *rms* (root mean square) variation of in-line displacement, transverse displacement, lift and drag coefficients as *Re* is varied. However, *rms* variation of transverse displacement does not show the second hysteretic loop for all values of β . $2S$, $C(2S)$ and $S+P$ modes of vortex shedding are observed for various cases.

Key Words: *Vortex-induced vibrations, Stabilized Finite Element Methods, Circular Cylinder, Sheared Flow.*

1. INTRODUCTION

A spring-mounted cylinder undergoes vibrations due to unsteady forces acting upon it in transverse and in-line directions. Response of a cylinder depends upon the low or high value of mass-damping ($m^*\zeta$) where m^* is the non-dimensional mass ratio ($4m/\pi\rho_\infty D^2$). *Lock-in/synchronization* and *hysteresis* are phenomena which take place in vortex-induced vibrations.

Khalak and Williamson (1999) have done *VIV* experiments for low value of $m^*\zeta$ and only transverse oscillations of the cylinder are allowed. Three response branches are observed. These branches are named as the initial amplitude branch, upper and lower branch. Mode of vortex shedding is $2S$ and $2P$ for various branches. Singh and Mittal (2005) have simulated vortex-induced vibration of a circular cylinder at low *Re* for low value of m^* ($=10$). The cylinder is allowed to move in both the directions i.e., in-line and transverse directions. Two sets of computations are carried out to see the effect of *Re* and reduced natural frequency, $F_n (= 1/U^* = f_n D/U)$. First set of simulation consists of the variation of U^* at fixed $Re=100$. In the second set of simulation, *Re* is varied as U^* is kept constant. $2S$, $C(2S)$ and $P+S$ are the modes of vortex shedding at various *Re*.

Lei et al. (2000) have solved the incompressible 2D Navier-Stokes equations for the flow of a stationary circular cylinder with the shear introduced at the inlet for $Re=80$ to 1000 and for shear parameter, $\beta = 0.25$. Mukhopadhyaya et al. have simulated 3D linearly sheared flow past a stationary cylinder for mean $Re = 131.5$ and for $\beta = 0.02$.

2. GOVERNING EQUATIONS AND BOUNDARY CONDITIONS

Navier-Stokes and continuity equations are solved using stabilized finite element methods. Stress tensor is expressed as the sum of its isotropic and deviatoric parts. Details about the methods can be found out in Tezduyar *et al.* (1992). A spring-mounted solid body immersed in the fluid experiences unsteady forces and it may exhibit rigid body motion. The equations to the motion of the body along in-line and transverse directions are written. Unknowns are acceleration, velocity and displacement in both the directions. To accommodate the motion of the cylinder and the deformation of the mesh, the employed formulation can handle moving boundaries and interfaces.

The boundary of the cylinder is assigned no slip condition. The equation to the motions is solved and the location of the cylinder and the flow velocity on the cylinder surface are updated at each time step. Sheared inflow is assigned at the inlet. The viscous stress vector is set to zero at the exit. At the top and bottom boundaries, velocity in transverse direction and stress vector along the boundaries are assigned to zero.

3. RESULTS

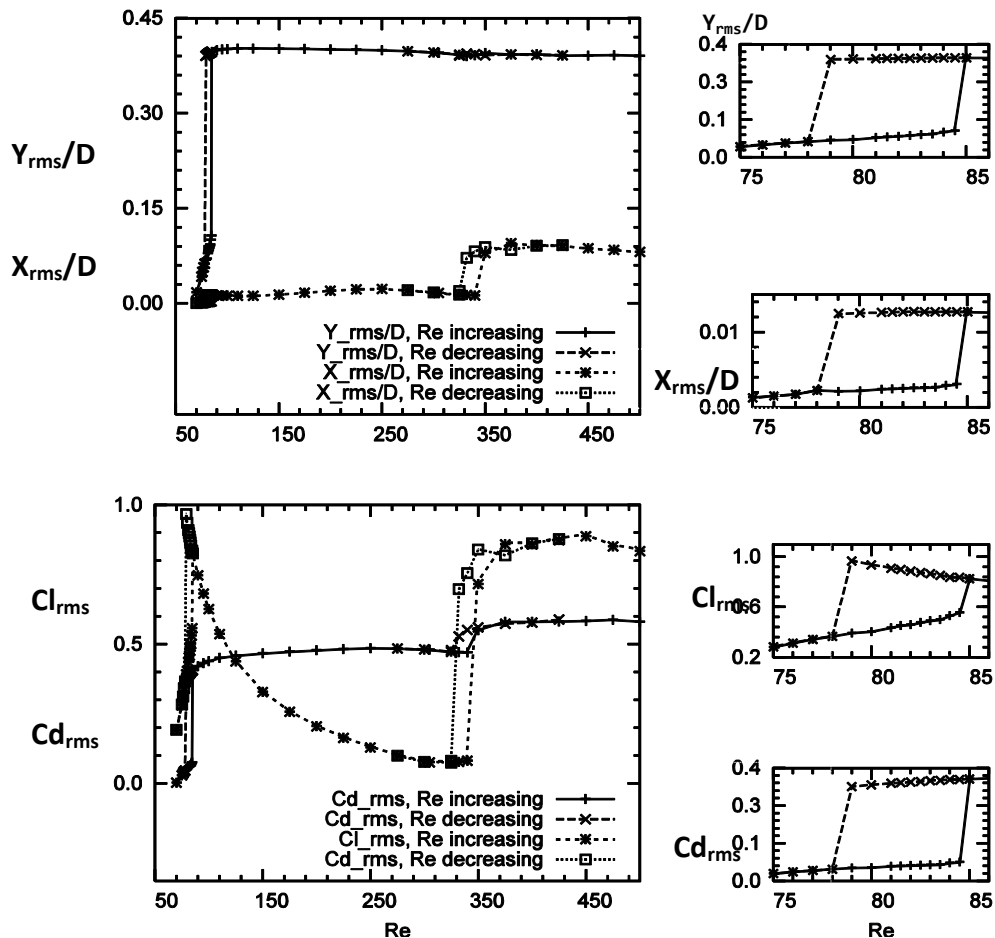


FIGURE 1. Sheared Vortex-induced vibration for $U^*=4.92$ and $\beta=20\%$: variation of *rms* in-line displacement, transverse displacement, lift and drag coefficient of the cylinder with Re .

Figure 1 shows the variation of *rms* values of various parameters for $\beta=20\%$. First hysteresis loop occurs around $Re \sim 80$. Zoomed views of the variations are shown for $Re = 75-85$ in the second

column. Second hysteresis loops are observed for $Re \sim 340$. The absence of this loop for Y_{rms}/D can be observed. However this loop exists for the variation of Y_{max}/D . Figure 2 shows the same variations for $\beta=30\%$. First hysteresis loop is similar to the previous case. But the range of the second loop is different and it is spread over $Re = 225 - 325$. For $Re = 75 - 85$ (first hysteresis), variation of Y_{rms}/D is almost similar for $\beta=20\%$, 30% . Its value after the sudden jump at $Re \sim 85$ is about 0.38 for both the values of β . But the value of X_{rms}/D after the sudden jump at $Re \sim 85$ is about 0.012 and 0.018 for $\beta=20\%$ and 30% respectively.

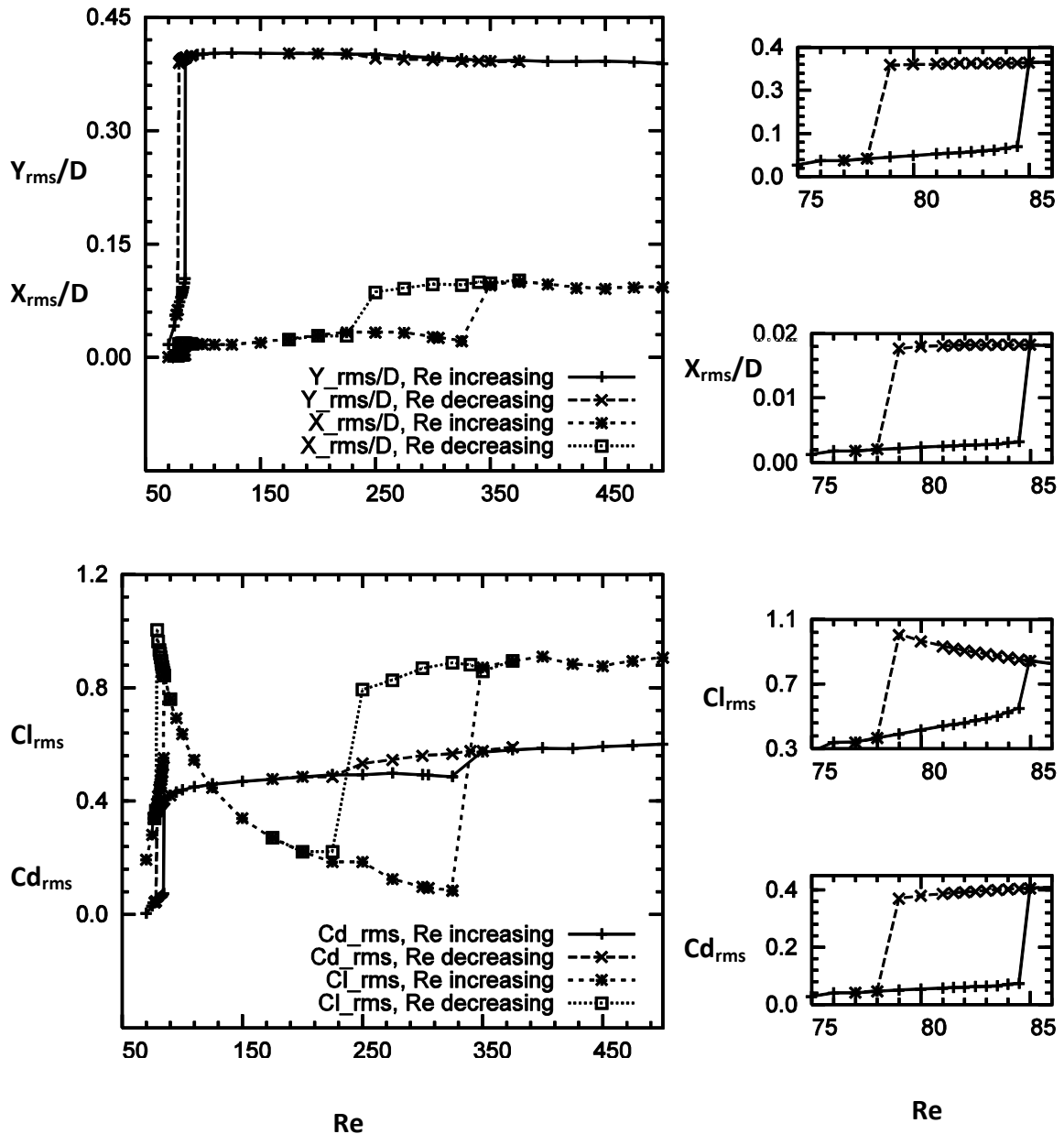


FIGURE 2. Vortex-induced vibration with sheared inflow for $U^* = 4.92$ and $\beta=30\%$: variation of *rms* in-line displacement, transverse displacement, lift and drag coefficient of the cylinder with Re .

Figure 3 shows that the mode of vortex shedding for $Re = 82$ (increasing as well as decreasing Re case), 325 and 400 and for $\beta = 30\%$. The various modes are described by Williamson and Roshko

(1988). It is observed that mode of shedding is $2S$ for $Re = 82$ while it is $C(2S)$ for $Re = 82$ (decreasing Re case). For $Re = 325$ (decreasing Re) and 400, it is $S+P$ mode of vortex shedding. In $S+P$ mode of vortex shedding, one single vortex and two counter-rotating vortices are shed alternately. However, it is somewhat disorganized in the far wake for $Re = 400$.

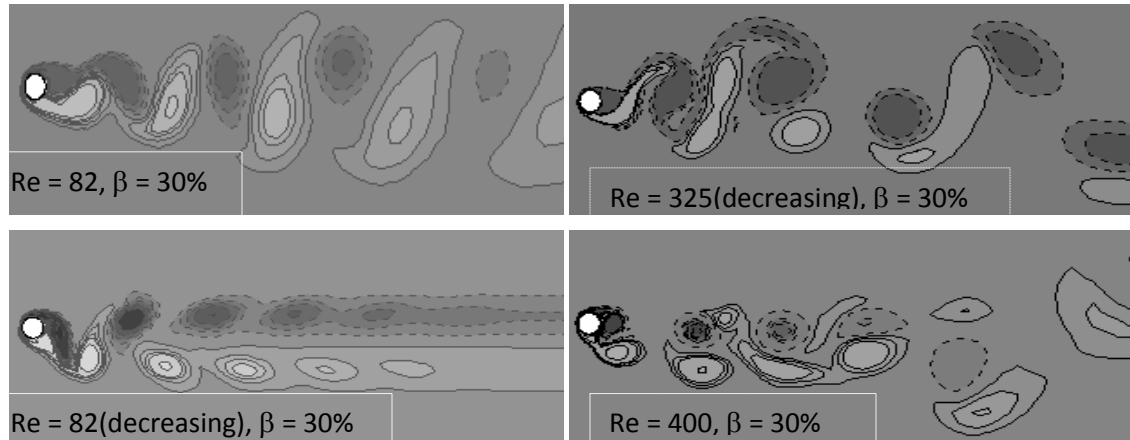


FIGURE 3: Vortex-induced vibrations with sheared inflow for $U^* = 4.92$: instantaneous vorticity field for $\beta = 30\%$ for different Re . Flow fields are shown at the time instant where the lift coefficient is maximum.

4. CONCLUSIONS

It is observed that the introduction of the shear at the inlet does not have an effect on the maximum displacement in the transverse direction. Range of Re , for which the two hysteresis loops are observed, depend upon the value of β . Maximum in-line displacement when the sudden jump occurs at $Re \sim 85$, depends on β .

REFERENCES

- [1] A. Khalak and C.H.K. Williamson, Motions, force and mode transitions in vortex-induced vibrations at low mass-damping, *Journal of Fluids and Structures*, 13:813-851, 1999.
- [2] S.P. Singh and S. Mittal, Vortex-induced oscillations at low Reynolds numbers: Hysteresis and vortex shedding modes. *Journal of Fluids and Structures*, 20, 1085-1104, 2005.
- [3] C. Lei, L. Cheng, and K. Kavanagh, A finite difference solution of the shear flow over a circular cylinder. *Ocean Engineering*, 27:271-290, 2000.
- [4] A. Mukhopadhyay, P. Venugopal, and S.P. Vanka, Oblique vortex shedding from a circular cylinder in linear shear flow. *Computers and Fluids*, 31:1-24, 2002.
- [5] T.E. Tezduyar, M. Behr, and J. Liou, A new strategy for finite element computations involving moving boundaries and interfaces – the deforming-spatial-domain/space-time procedure:I. The concept and the preliminary tests. *Computer Methods in Applied Mechanics and Engineering*, 94(3):339-351, 1992.
- [6] C.H.K. Williamson and A. Roshko, Vortex formation in the wake of an oscillating cylinder, *Journal of Fluids and Structures*, 2:355-381, 1988.

A SMOOTHED FINITE ELEMENT METHOD FOR HEAT TRANSFER PROBLEMS

S.C. Wu, G.R. Liu

Centre for Advanced Materials Joining & Simulations (AMJS), Hefei University of Technology, Hefei 230009, PR China, wushengchuan@gmail.com

ABSTRACT

By smoothing, a family of smoothed FEM (S-FEM) has been developed recently. It possesses the advantages of both meshfree methods and the standards FEM, and works well with triangular and tetrahedral types of background cells/elements. This paper presents the general formulation of S-FEM for thermal problems in one, two and three dimensions. To examine our formulation, computational results are compared with those obtained using other established means.

Key Words: *Meshfree Methods, Gradient Smoothing Technique, Transient Heat Transfer.*

1. INTRODUCTION

It is well-known that the compatible displacement-based FEM can result in significant accuracy loss in solution due to the so-called overly stiff phenomena and the mesh distortion [1]. Meshfree methods have thus been proposed in the new direction of establishing “softer” models [2]. One of main issues in many meshfree methods is the “spatial” instability due to the inadequate integration of the weak form inherent in the nodal integration [3]. To remove this type of instability, the strain smoothing technique was further generalized [4] to functions in the G space [5]. Wu *et al.* [6] achieved the findings on accuracy, efficiency and convergence of solutions in both temperature and its gradient and heat flux. They also carried out the thermoelastic analyses using the NS-FEM [7]. Mohammad used the gradient smoothing technique for the smoothed fixed grid FEM (SFGFEM) [8] and the nonlinear inverse geometry thermal problems were analyzed in detail. The proposed SFGFEM is shown more accurate and facilitates integration over boundary intersecting elements.

It is well-known that a spatially stable model always produces a unique and convergent solution for steady heat transfer problems when functions are bounded at least in G^1 norms [5]. However, this does not guarantee a temporal stability for unsteady thermal problems. The instability may be restored by added a stabilization term into the smoothed potential energy functional of the original NS-FEM [9]. More effectively, such instability can be suppressed by constructing the smoothing integration domain based on element edges.

Wu *et al.* [10] has formulated the ES-PIM for heat transfer problems, and evaluated the heat transfer process of a practical cooling system of the rapid direct manufacturing. The ES-FEM was further used for solving dynamic nonlinear heat transfer problems [11], which gives better understanding of realistic physical thermal systems and processes. Wu *et al.* [12] has also established an ES-FEM for incremental heat transfer equilibrium equations. To reduce the computational efforts, a quasilinearization scheme is adopted to linearize the nonlinear algebra equations, and the Euler backward method is used for time integration for its unconditional stability allowing larger time steps. Li *et al.* [13] then used the ES-FEM to conduct the research of 2D and 3D hyperthermia treatment for the first time. The use of the close-to-exact ES-FEM is clearly advantageous.

2. SMOOTHED GALERKIN WEAK FORM

Detailed constructions of the gradient smoothed domain based on surface triangles can be found in [12]. For three-dimensional spaces, the smoothed temperature gradients are given by

$$\left[\bar{\mathbf{B}}_l^{\Omega_k} \right]^T = [\bar{b}_{l1} \quad \bar{b}_{l2} \quad \bar{b}_{l3}] \quad (1)$$

$$\bar{b}_{lp} = \frac{1}{V_k} \int_{\Gamma_k} \varphi_l(\mathbf{x}) n_p(\mathbf{x}) d\Gamma \quad (p=1, 2, 3) \quad (2)$$

To solve the time-dependent nonlinear system, the Euler backward unconditionally stable method is used by

$$\frac{\partial({}^{t+\Delta t}T^{(i)})}{\partial t} = \frac{({}^{t+\Delta t}T^{(i-1)} + \Delta T^{(i)} - {}^tT)}{\Delta t} \quad (3)$$

Using the smoothed temperature gradient, we obtain the temperature variation of practical system inside each edge-based smoothing domain in the following set of smoothed algebraic equations

$$\left[{}^t\mathbf{C} / \Delta t + {}^t\bar{\mathbf{K}}^k + {}^t\mathbf{K}^c + {}^t\mathbf{K}^r \right] \Delta \mathbf{T}^{(i)} = {}^{t+\Delta t}\mathbf{Q}^v + {}^{t+\Delta t}\mathbf{Q}^s + {}^{t+\Delta t}\bar{\mathbf{Q}}^k(i-1) + {}^{t+\Delta t}\mathbf{Q}^c(i-1) + {}^{t+\Delta t}\mathbf{Q}^r(i-1) + {}^{t+\Delta t}\mathbf{Q}^C(i-1) \quad (4)$$

The terms in the left-hand side can be found in the dissertation [12]. Note that the foregoing discretized system equations are obtained based on a number of smoothing domains created using the face-based smoothed technique. The global stiffness and vector are then assembled based on these smoothing domains that are similar to elements used in FEM.

3. RESULTS

As illustrated in Figure 1, the exterior surfaces of weldment exchanges heat with the air, and the front surface is continuously heated through the hot fluid flow. The right surface of substrate is prescribed with constant heat flux, and bottom surface is specified with room temperature. The temperature of the lower pass is 1000°C and 2000°C for the upper pass. Several points are also sampled to check the accuracy of numerical solutions of the present ES-FEM.

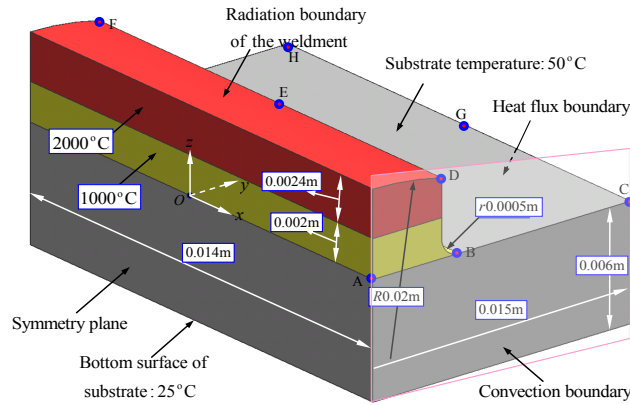


FIGURE 1. Computational model subjected to complex nonlinear convection and radiation boundary conditions.

Computational parameters are taken as: $k_{0x}=k_{0y}=k_{0z}=40\text{W}/(\text{m}\cdot^\circ\text{C})$, $\rho_0=6000\text{kg}/\text{m}^3$, $c_0=50\text{J}/(\text{kg}\cdot^\circ\text{C})$, $h_{c0}=1500\text{W}/(\text{m}^2\cdot^\circ\text{C})$, $q_1=1000\text{W}/\text{m}^2$, $T_r=25^\circ\text{C}$, $T_b=200^\circ\text{C}$, $\varepsilon=1$ (black body assumed), $\sigma=5.67\times 10^{-8}\text{W}/(\text{m}^2\cdot^\circ\text{C}^4)$, $\beta_1=0.006/^\circ\text{C}$, $\beta_2=0.008/^\circ\text{C}$, $\beta_3=0.005/^\circ\text{C}$, $\beta_4=-0.0002/^\circ\text{C}$ and $\beta_5=0.001/^\circ\text{C}$. In nonlinear transient analysis, the time step Δt is selected to 0.005 sec for both ES-FEM and standard FEM and the cooling system approaches the steady state at $t=3.0$ sec or so.

The following Figure 2 confirms the bound property of the close-to-exact ES-FEM model for more complicated nonlinear problems of heat transfer. It can be clearly observed that the present ES-FEM

performs much softer than linear FEM and converges to the reference solution from below. The ES-FEM solution is bounded from two sides respectively by FEM and NS-FEM. The results of equivalent energy norms also show that the temperature result of ES-FEM is more accurate than that of FEM and worse than that of linear NS-FEM using the same sets of nodes.

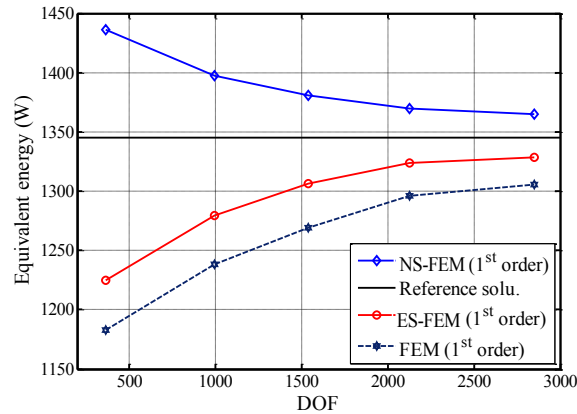


FIGURE 2. Equivalent energy converging to the reference solution for the two-pass weldments with the increasing of DOF using the same tetrahedral mesh ($T_r=0^\circ\text{C}$).

The ES-FEM is then used to analyze the nonlinear transient heat transfer problems and the contours plotted in Fig. 4 demonstrate the temperature distributions at $t=1.5\text{s}$. The background tetrahedrons used in analyses of ES-FEM and FEM are generated automatically with total 1437 nodes. The reference solution is obtained using the higher order Solid 90 based on the ANSYS package.

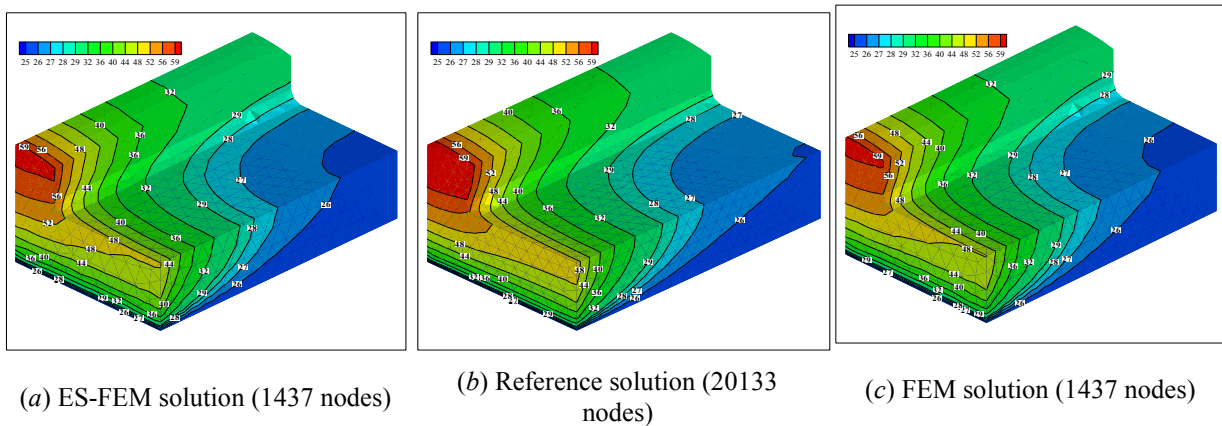


FIGURE 3. Comparison of computed temperature distributions at $t=1.5$ sec.

It can be clearly seen that the present ES-FEM formulation can give more accurate solution in temperature compared with linear FEM using the same 4-node tetrahedral mesh especially in the high gradient region. This finding will be further confirmed numerically by checking nodal temperature.

Note that in present analysis only linear polynomial basis is used to interpolate the temperature field. It has been found in Ref [15] that for the 3D linear problems the present ES-FEM is significantly more accurate than FEM using the same mesh but takes a longer time to solve. However, the ES-FEM for 3D problems is found to be more efficient than the 4-node tetrahedral FEM in terms of CPU time for the same accuracy in both energy and displacement error norms.

4. CONCLUSIONS

From this study, some remarks can be made as follows:

1. The ES-FEM works well with tetrahedral meshes that can be easily generated thanks to the softening effects on the conductivity matrix.
2. The ES-FEM formulation can effectively analyze the nonlinear transient problems of heat transfer with complex geometry and boundary conditions.
3. The ES-FEM models perform much softer than those of FEM model and stiffer than that of NS-FEM model, which indicates the present ES-FEM model can achieve much accurate temperature solutions than standard FEM using the same linear meshes in solving transient nonlinear heat transfer problems.

REFERENCES

- [1] R.W. Lewis, K. Morgan, H.R. Thomas and *et al.*, *The Finite Element Method in Heat Transfer Analysis*, John Wiley & Sons, New York, USA, 1996.
- [2] G.R. Liu, *Meshfree Methods: Moving Beyond the Finite Element Method*, CRC Press, Boca Raton, USA, 2002.
- [3] M.A. Puso, J.A. Solberg, A stabilized nodally integrated tetrahedral, *International Journal for Numerical Methods in Engineering*, 67(6), 841-67, 2006.
- [4] G.R. Liu, A generalized gradient smoothing technique and the smoothed bilinear form for Galerkin formulation of a wide class of computational methods, *International Journal of Computational Methods*, 5(2), 199-236, 2008.
- [5] G.R. Liu, On a G space theory, *International Journal of Computational Methods*, 6(2), 257-89, 2009.
- [6] S.C. Wu, G.R. Liu, H.O. Zhang and *et al.*, A node-based smoothed point interpolation method (NS-PIM) for three-dimensional heat transfer problems, *International Journal of Thermal Sciences*, 48(6), 1154-65, 2009.
- [7] S.C. Wu, G.R. Liu, H.O. Zhang and *et al.*, A node-based smoothed point interpolation method (NS-PIM) for three-dimensional thermoelastic problems, *Numerical Heat Transfer A-Applications*, 54(12), 1121-47, 2008.
- [8] J.K. Mohammad, D. Farhang, Solution of geometric inverse heat conduction problems by smoothed fixed grid finite element method, *Finite Elements in Analysis and Design*, 45(10), 599-611, 2009.
- [9] Z.Q. Zhang, G.R. Liu, Temporal stabilization of the node-based smoothed finite element method and solution bound of linear elastostatics and vibration problems, *Computational Mechanics*, 46(2), 229-46, 2010.
- [10] S.C. Wu, G.R. Liu, X.Y. Cui and *et al.*, An edge-based smoothed point interpolation method (ES-PIM) for heat transfer analysis of rapid manufacturing system, *International Journal of Heat and Mass Transfer*, 53(5-6), 1938-50, 2010.
- [11] J.N. Reddy, *An Introduction to Nonlinear Finite Element Analysis*, Oxford University Press, New York, USA, 2004.
- [12] Z.B. Zhang, S.C. Wu, G.R. Liu and *et al.*, Nonlinear transient heat transfer problems using the meshfree ES-PIM, *International Journal of Nonlinear Science & Numerical Simulation*, 11(12), 1077-91, 2010.
- [13] E. Li, G.R. Liu, V. Tan, Simulation of hyperthermia treatment using the edge-based smoothed finite element method, *Numerical Heat Transfer Part A: Applications*, 57(11), 822-47, 2010.
- [14] G.R. Liu, H.X. Nguyen, T.T. Nguyen, A theoretical study on the smoothed FEM (S-FEM) models: Properties, accuracy and convergence rates, *International Journal for Numerical Methods in Engineering*, 84(10), 1222-56, 2010.
- [15] T.T. Nguyen, G.R. Liu, K.Y. Lam and *et al.*, A face-based smoothed finite element method (FS-FEM) for 3D linear and geometrically nonlinear solid mechanics problems using 4-node tetrahedral elements, *International Journal for Numerical Methods in Engineering*, 78(3), 324-353, 2009.

A GENERALIZED SCHEME OF THE CHARACTERISTIC BASED SPLIT (CBS) ALGORITHM FOR INCOMPRESSIBLE NON-ISOTHERMAL NON-NEWTONIAN FLUID FLOWS

Qinglin Duan, Xikui Li

Department of Engineering Mechanics, Dalian University of Technology, Dalian 116024, P.R. China, qinglinduan@dlut.edu.cn, xikuili@dlut.edu.cn

ABSTRACT

A generalized scheme of the Characteristic Based Split (CBS) algorithm for numerical simulation of incompressible non-isothermal non-Newtonian fluid flows is presented. The generalization is twofold: one is that it extends the CBS algorithm from Eulerian description to Arbitrary Lagrangian-Eulerian (ALE) description; the other is that two parameters α and β are introduced such that the classical CBS algorithm is a special case of this generalized scheme with $\alpha=1$ and $\beta=0$. Numerical results of the non-isothermal Poiseuille flow problem with the power-law fluid model show that, by tuning these two introduced parameters, such generalized scheme may perform better than the classical CBS algorithm in a wide range of Reynolds and thermal Peclet numbers. With the adaptive coupled finite element (FE) and meshfree (MF) method for spatial discretizations, the performance and the capability of the proposed scheme is further validated by the thermal 4:1 contraction and the injection moulding problems.

Key Words: CBS, non-isothermal non-Newtonian, Convection dominated, Injection moulding, ALE.

1. INTRODUCTION

Numerical modelling of incompressible flows with the standard Galerkin method, i.e. the traditional finite element method, the element-free Galerkin method et al, often shows oscillatory solutions due to two main sources. The first attributes to the mixed character of the incompressible N-S equation which results in a reducible mixed formulation in its discretized form and then restricts the choice of interpolation spaces for the velocity and pressure fields. The second is associated with the convective character of the equations which induces oscillations particularly in convection dominated cases. Strategies to circumvent the LBB (or the inf-sup) condition stemming from the first problem are, among others, the PSPG formulation of Hughes et al, the Fractional Step Algorithm (FSA) originally derived by Chorin, the PGP method of Codina and Blasco. Li and Duan [1] further improved the pressure stability of the fractional step algorithm by using the Finite Increment Calculus (FIC) theory. The resulting Pressure Stabilized FSA (PS-FSA) is similar to the PGP method mentioned above.

The methods developed to overcome the instabilities associated with the hyperbolic nature of the equations emanating from the second problem have also been extensively investigated in the literature, such as the SUPG method of Brooks and Hughes and the Taylor-Galerkin method of Donea. It is widely accepted that the standard Galerkin method is optimal for self-adjoint operator equations which is not the case for the N-S equation due to the presence of the convective term. However, the self-adjoint property can be recovered if the N-S equation is derived in terms of material (Lagrangian) point instead of spatial (Eulerian) point. This requires the discretization of the temporal derivative along the characteristic (the particle trajectory). Based on this idea, Zienkiewicz and Codina first introduced into this method the idea of approximating the characteristics by using a Taylor expansion and combined it with a split scheme of the fractional step algorithm that results in the well-known Characteristic Based Split (CBS) algorithm widely used in computational fluid dynamics, such as for viscoelastic flow by Nithiarasu [2]. Codina [3] generalized the derivation of the method in the sense that the reference time can be arbitrary within the time step and used it to

solve the incompressible N-S equation. However, only the Eulerian description and the explicit approximations of the characteristics are used in his derivation and only the Newtonian flow is considered in his work.

The purpose of this paper is to develop a generalized scheme of the CBS algorithm in an ALE framework for incompressible non-isothermal non-Newtonian fluid flows. The motivation of using an ALE description is that our final goal is to simulate injection moulding problems and we will use the ALE technique to track the moving free surface. We give a general derivation for the numerical approximation of the characteristics in the ALE description which introduces two parameters into the method and combine it with the Pressure Stabilized FSA mentioned above to form the proposed scheme. Numerical simulation of the injection moulding process is achieved by using this scheme, along with an ALE free surface tracking technique and the adaptive coupled finite element and meshfree method for spatial discretizations.

2. DERIVATION OF THE GENERALIZED SCHEME OF THE CBS ALGORITHM

Let $\mathbf{x}(t)$ be the trajectory of the particle we follow and obviously $\mathbf{x}(t_{n+1}) \neq \mathbf{x}(t_n)$. To numerically solve the governing equations with the discretization of the temporal derivative along the characteristic, for a given physical variable φ , we need approximate $\varphi(\mathbf{X}(t_{n+1}), t_{n+1})$ and $\varphi(\mathbf{X}(t_n), t_n)$ in terms of $\varphi(\mathbf{X}(\bar{t}), t_{n+1})$ and $\varphi(\mathbf{X}(\bar{t}), t_n)$ respectively and consequently all the terms of the governing equations can be evaluated at the same reference point $\boldsymbol{\chi} = \mathbf{X}(\bar{t})$, where $\bar{t} = t_{n+\alpha} = t_n + \alpha\Delta t$ is the reference time within the time step $[t_n, t_{n+1}]$, α is arbitrarily taken within the range $0 \leq \alpha \leq 1$. In an ALE method, the motion of the mesh is independent of the motion of the material, i.e. $\mathbf{c} = \mathbf{u} - \hat{\mathbf{u}}$, where \mathbf{c} , \mathbf{u} and $\hat{\mathbf{u}}$ are, respectively, the convective, material and mesh velocities. Therefore, we can approximate $\mathbf{X}(t_{n+1})$ and $\mathbf{X}(t_n)$ in terms of $\boldsymbol{\chi}$, as

$$\mathbf{X}(t_{n+1}) = \boldsymbol{\chi} + (1-\alpha)\Delta t \mathbf{c}^{n+\beta} + O(\Delta t^2) \quad \mathbf{X}(t_n) = \boldsymbol{\chi} - \alpha\Delta t \mathbf{c}^n + O(\Delta t^2) \quad (1)$$

where $\beta = 0$ stands for an explicit expression for $\mathbf{X}(t_{n+1})$ which is used by Codina [11], and $0 < \beta \leq 1$ the implicit ones. From Eq.(1), we can approximate $\varphi(\mathbf{X}(t_{n+1}), t_{n+1})$ and $\varphi(\mathbf{X}(t_n), t_n)$ as

$$\varphi(\mathbf{X}(t_{n+1}), t_{n+1}) = \varphi^{n+1} + (1-\alpha)\Delta t \mathbf{c}^{n+\beta} \cdot \nabla \varphi^{n+\beta} + O(\Delta t^2) \quad \varphi(\mathbf{X}(t_n), t_n) = \varphi^n - \alpha\Delta t \mathbf{c}^n \cdot \nabla \varphi^n + O(\Delta t^2) \quad (2)$$

By using central difference technique, Eqs.(1-2) can be approximated one order higher as

$$\mathbf{X}(t_{n+1}) = \boldsymbol{\chi} + (1-\alpha)\frac{\Delta t}{2}[(1+\alpha)\mathbf{c}^{n+1} + (1-\alpha)\mathbf{c}^n] + (1-\alpha)^2\frac{\Delta t^2}{2}\mathbf{c}^{n+\beta} \cdot \nabla \mathbf{c}^{n+\beta} + O(\Delta t^3) \quad (3)$$

$$\mathbf{X}(t_n) = \boldsymbol{\chi} - \alpha\frac{\Delta t}{2}[\alpha\mathbf{c}^{n+1} + (2-\alpha)\mathbf{c}^n] + \alpha^2\frac{\Delta t^2}{2}\mathbf{c}^n \cdot \nabla \mathbf{c}^n + O(\Delta t^3) \quad (4)$$

$$\varphi(\mathbf{X}(t_{n+1}), t_{n+1}) = \varphi^{n+1} + (1-\alpha)\frac{\Delta t}{2}[(1+\alpha)\mathbf{c}^{n+1} + (1-\alpha)\mathbf{c}^n] \cdot \nabla \varphi^{n+1} + (1-\alpha)^2\frac{\Delta t^2}{2}\mathbf{c}^{n+\beta} \cdot \nabla (\mathbf{c}^{n+\beta} \cdot \nabla \varphi^{n+\beta}) + O(\Delta t^3) \quad (5)$$

$$\varphi(\mathbf{X}(t_n), t_n) = \varphi^n - \alpha\frac{\Delta t}{2}[\alpha\mathbf{c}^{n+1} + (2-\alpha)\mathbf{c}^n] \cdot \nabla \varphi^n + \alpha^2\frac{\Delta t^2}{2}\mathbf{c}^n \cdot \nabla (\mathbf{c}^n \cdot \nabla \varphi^n) + O(\Delta t^3) \quad (6)$$

Based on the PS-FSA, the proposed CBS scheme is obtained by taking the velocity and temperature as φ and discretizing the momentum and energy equation along the characteristics through Eqs.(1-6), where the energy equation to compute the temperature has the following form

$$\begin{aligned} \frac{\rho c}{\Delta t} [T^{n+1} - T^n] + \rho c c_j^{n+1/2} \frac{\partial T^{n+1-\alpha}}{\partial x_j} &= \tau_{ij}^{n+1/2} \dot{\epsilon}_{ji}^{n+1/2} + \frac{\partial}{\partial x_j} \left(k \frac{\partial T^{n+1/2}}{\partial x_j} \right) \\ &+ (2\alpha - 1) \frac{\Delta t}{2} c_k^{n+\beta} \frac{\partial}{\partial x_k} \left[\rho c c_j^{n+\beta} \frac{\partial T^{n+\beta}}{\partial x_j} - \tau_{ij}^{n+\beta} \dot{\epsilon}_{ji}^{n+\beta} - \frac{\partial}{\partial x_j} \left(k \frac{\partial T^{n+\beta}}{\partial x_j} \right) \right] \end{aligned} \quad (7)$$

Note that α and β are introduced into Eq.(7) and it can reduce to classical characteristic form by setting $\alpha=1$ and $\beta=0$.

3. RESULTS

The first example is a thermal plane Poiseuille flow problem. Table 1 gives the maximum time step sizes Δt_{\max} allowed by the proposed CBS algorithm with different α_u for the velocity-pressure field and α_T for the thermal field under different Reynolds and thermal Peclet numbers. Note that $\alpha=0.5$ and $\alpha=1.0$ correspond to the classical Crank-Nicolson scheme and the classical CBS algorithm, respectively. Obviously, the classical Crank-Nicolson scheme can not handle convection dominated problems as its Δt_{\max} is unacceptably small for problems with high Reynolds or high Peclet numbers. The other two schemes can be used for the whole range of the tested cases. Note that the scheme with $\alpha=0.8$ allows larger Δt_{\max} than the classical CBS algorithm, especially for the thermal field where its Δt_{\max} is two times of Δt_{\max} allowed by the classical CBS algorithm.

	Re=1	Re=10	Re=10 ²	Re=10 ³		Pe=1	Pe=10	Pe=10 ²	Pe=10 ³
$\alpha_u = 1.0$	0.04	0.04	0.04	0.04	$\alpha_T = 1.0$	0.3	0.3	0.3	0.3
$\alpha_u = 0.8$	0.05	0.05	0.05	0.05	$\alpha_T = 0.8$	0.6	0.6	0.6	0.6
$\alpha_u = 0.5$	0.8	0.3	0.03	0.005	$\alpha_T = 0.5$	1.0	1.0	0.001	Hard to converge

TABLE 1. Comparison of maximum time step sizes with different Reynolds and Peclet numbers

The second example is the thermal 4:1 contraction problem. We run this example by using the proposed CBS scheme with $\alpha=0.8$ and the adaptive coupled finite element and meshfree method for spatial discretizations. Fig.1 shows the finite element and meshfree coupling region, the obtained streamline and pressure field. The solution is smooth and no oscillation is present. Fig.2 illustrates the isotherms for different thermal Peclet numbers. The shapes of the isotherms agree well with the reference results in the literature.

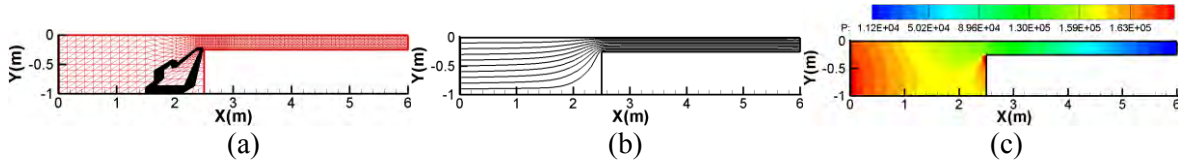


FIGURE 1. The thermal 4:1 contraction problem: (a) Coupling region (black); (b) Streamline; (c) Pressure contours

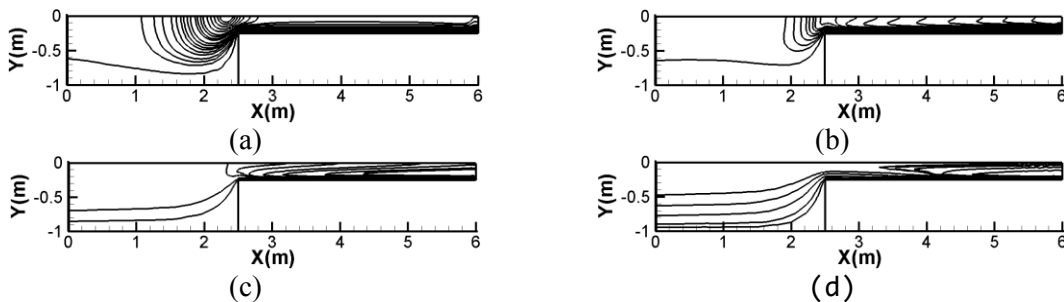


FIGURE 2. Isotherm plots for the thermal 4:1 contraction problem: (a) Pe=1; (b) Pe=10; (c) Pe=100; (d) Pe=1000.

The last example is the simulation of the filling process of a typical mould cavity. Fig.3 shows the evolutions of the velocity distributions, the pressure and the temperature contours over the zones filled with molten polymer in the mould cavity at different discrete time levels which clearly demonstrate the ability of the proposed method for simulating the injection moulding process with non-isothermal non-Newtonian molten polymers.

4. CONCLUSIONS

A generalized scheme of the CBS algorithm for incompressible non-isothermal non-Newtonian fluid flow is developed. The numerical results demonstrate a better performance of the proposed scheme than the classical one in a wide range of Reynolds and Peclet numbers. Modelling of the injection moulding process with non-isothermal non-Newtonian molten polymers is also achieved by using the proposed scheme.

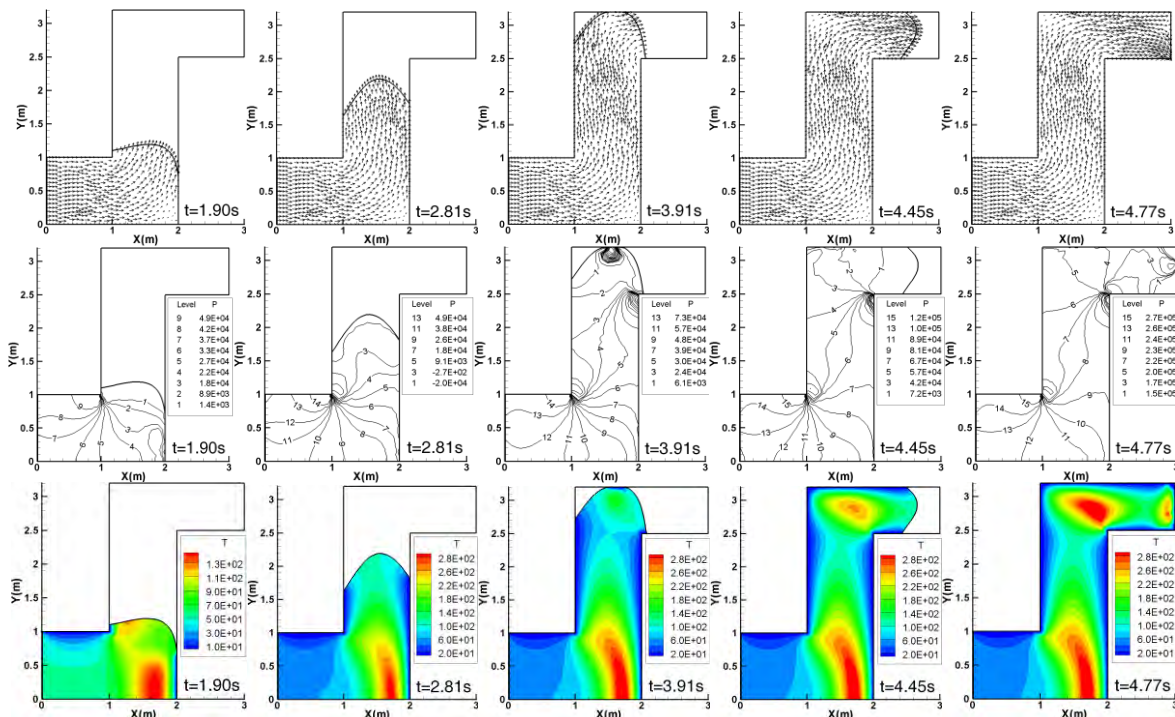


FIGURE 3. Evolution of the velocity distributions, the pressure and the temperature contours within the filled domains.

REFERENCES

- [1] Xikui Li and Qinglin Duan, Meshfree iterative stabilized Taylor-Galerkin and characteristic-based split (CBS) algorithms for incompressible N-S equations, *Comput. Methods Appl. Mech. Engrg.*, 195, 6125-6145, 2006.
- [2] P. Nithiarasu, A fully explicit characteristic based split (CBS) scheme for viscoelastic flow calculations, *Int. J. Numer. Methods Engrg.*, 60, 949-978, 2004.
- [3] R. Codina, Numerical solution of the incompressible Navier-Stokes equations with Coriolis forces based on the discretization of the total time derivative, *Journal of Computational Physics*, 148, 467-496, 1999.

NUMERICAL SIMULATION OF FLOW INSIDE DIFFERENTIALLY HEATED ROTATING CAVITY

J C Mandal, C R Sonawane

Aerospace Engineering Department, IIT Bombay - 400076, India,

mandal@aero.iitb.ac.in

Key Words: *Rotating cavity, artificial compressibility approach, inertial and non-inertial frames, ALE.*

1. INTRODUCTION

Flows inside differentially heated rotating cavity has wide range of applications in the study of geophysical and astrophysical flows as well as in practical engineering applications like manufacturing of single wafer crystal for semiconductor industries and numerous metallurgical processes. Due to rotation the heat transfer characteristic of the flow becomes complex and thereby, makes it very challenging in terms of numerical and experimental investigations.

It is observed that numerical simulations of rotating cavity flows reported in literature usually model the flow in non-inertial (rotating) frame of reference, in which the effect of rotation is considered indirectly through source terms (like centrifugal, Coriolis and Euler forces) in the Navier-Stokes (NS) equations. Numerical treatment of these source terms can sometime become troublesome and tricky, and it remains an area of research till date. We, therefore, consider mathematical modelling of the differentially heated rotating cavity problem in inertial frame of reference in order to avoid the above source terms. In the later case, the rotation of the cavity directly influence the flow and heat transfer phenomena inside it as in the real situation.

In present study, we simulate an orthogonal rotating cavity (i.e. rotation axis and gravity axis are orthogonal to each other) problem [1] using both inertial and non-inertial frame of references. The incompressible Navier-Stokes equations in both inertial and non-inertial frames are written in Artificial-Compressibility (AC) formulations before discretization. The spatial part is discretized using finite volume method based on HLLC-AC scheme [2, 3], whereas time part is discretized using dual time stepping. In case of inertial model, Arbitrary Lagrangian Eulerian (ALE) approach is used to tackle the moving boundary.

2. GOVERNING EQUATIONS

Initially the cavity is rotated at a constant angular speed ω about an axis through the centre of the cavity. Then, temperatures of two opposite side walls AB and CD are suddenly raised and lowered to $T_h = T_0 + \Delta T/2$ and $T_c = T_0 - \Delta T/2$, while other two opposite walls AD and BC are kept thermally insulated (refer to figure 1).

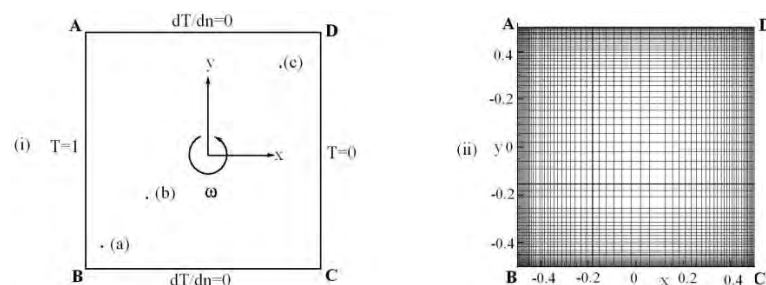


FIGURE 1 (i) Schematic of rotating cavity (ii) Computational mesh.

As the gravitational, centrifugal and Coriolis accelerations all lie within the cross-sectional plane of the cavity, the problem can be analyzed as a two-dimensional flow problem. Integral form of 2D NS equations in artificial compressibility formulation with dual time stepping approach can be written for both inertial as well as non-inertial frame of references as

$$\iint_{\Omega} \frac{d}{dt} \left[\mathbf{W} \right] d\Omega + \iint_{\Omega} \frac{d}{dt} \left[\mathbf{W} \right] d\Omega = \iint_{\Omega} \mathbf{S} d\Omega \quad (1)$$

where l_x, l_y are direction cosines for face area ΔA , which is enclosing the cell volume ΔV . The variables t and τ are real time and pseudo time respective y . The matrices $\mathbf{I}^M, \mathbf{M}^M$ in (1) are given as

$$\mathbf{I}^M = \begin{pmatrix} 0 & 0 & 0 & 0 \\ 0 & 1 & 0 & 0 \\ 0 & 0 & 1 & 0 \\ 0 & 0 & 0 & 1 \end{pmatrix}, \quad \mathbf{M} = \begin{pmatrix} \rho & 0 & 0 & 0 \\ 0 & 1 & 0 & 0 \\ 0 & 0 & 1 & 0 \\ 0 & 0 & 0 & 1 \end{pmatrix}$$

The expressions for $\mathbf{W}, \mathbf{E}^c, \mathbf{E}^v$ and $\mathbf{G}^c, \mathbf{G}^v$ for two different frames of reference are given below.

2.1 Mathematical formulation in inertial frame of reference and discretization. For inertial frame of reference, the field vector in equation (1), $\mathbf{W}=(p, u_l, v_l, T)^T$ with u_l and v_l as the component of velocity vector, V_l . The convective flux vectors are $\mathbf{E}^c=(U, u_l U+p, v_l U, u_l T)^T$, $\mathbf{G}^c=(V, u_l V, v_l V+p, v_l T)^T$; and diffusive fluxes $\mathbf{E}^v=(0, \sigma_{xx}, \sigma_{xy}, \frac{\partial T}{\partial x})^T$, $\mathbf{G}^v=(0, \sigma_{yx}, \sigma_{yy}, \frac{\partial T}{\partial y})^T$; and the source term $\mathbf{S}=(0, 0, -g\Delta T, 0)^T$. The terms $U=u_l - x_t$ and $V=v_l - y_t$, where x_t and y_t are the grid velocities in x and y directions respectively.

An ALE method is used to take care of moving cavity, where whole grid is rotated as solid body. The detailed description of discretization and solution methodology for ALE formulation can be found in reference [3].

2.2 Mathematical formulation in non-inertial frame of reference and discretization. For non-inertial frame of reference, the field vector in equation (1), $\mathbf{W}=(p, u_r, v_r, T)^T$ with u_r and v_r are the component of velocity, V_r . Note that the velocity vector V_l in the inertial frame is related to the velocity vector V_r in the non-inertial frame as $V_l=V_r+(\omega \times r)$. The convective flux vectors in non-inertial frame are defined as $\mathbf{E}^c=(u_r, u_r^2+p, v_r u_r, u_r T)^T$, $\mathbf{G}^c=(v_r, u_r v_r, v_r^2+p, v_r T)^T$; and the diffusive fluxes are $\mathbf{E}^v=(0, \sigma_{xx}, \sigma_{xy}, \frac{\partial T}{\partial x})^T$, $\mathbf{G}^v=(0, \sigma_{yx}, \sigma_{yy}, \frac{\partial T}{\partial y})^T$; the source term is

$$\mathbf{S} = \begin{pmatrix} 0 \\ 2\omega v_r - \beta_t \Delta T \omega^2 x + \beta_t \Delta T g \sin(\omega t) + \omega^2 x - g \sin(\omega t) \\ -2\omega u_r - \beta_t \Delta T \omega^2 y + \beta_t \Delta T g \cos(\omega t) + \omega^2 y - g \cos(\omega t) \\ 0 \end{pmatrix}$$

In non-inertial frame of reference, the grid is treated as stationary. The detailed description of discretization and solution methodology can be found in [2].

3. NUMERICAL RESULTS

In this paper the numerical results obtained over a non-uniform mesh (refer figure 1) of 70 x 70 grid points, which has the minimum spacing of 0.0032 near the walls and maximum spacing of 0.04 near the center of the cavity, is presented. The HLLC-AC upwind scheme [2, 3] with dual time stepping approach is applied to both inertial and non-inertial formulations to simulate the mixed convective heat transfer in square cavity undergoing orthogonal rotation. The numerical codes developed have been validated with the results from reference [1].

As boundary conditions on all the four walls of the rotating cavity, $(u, v)_{wall}=(x_t, y_t)_{wall}$ is specified in case of formulation with inertial frame of reference, whereas $(u, v)_{wall}=0$ is specified for formulation

with non-inertial frame of reference. Temperature T is specified at the walls AB and CD, while Neumann boundary conditions $\frac{\partial T}{\partial n} = 0$ are applied for the other two walls AD and BC (refer figure 1). The pressure gradients are specified at all the wall depending on the angular rotation of the cavity wall. The space-average Nusselt number at both the cold and hot walls has been calculated using the relation,

$$\overline{Nu} = - \int_{-h}^h \frac{\partial \theta}{\partial n} dn ; \quad \text{where } \theta \text{ is temperature difference at wall and } n \text{ is unit normal to the wall}$$

In the present work, two test cases [1] are studied with two different sets of Prandtl no. (Pr), Rayleigh no. (Ra), Rotational Rayleigh no. (Ra_w), Taylor no. (Ta) and rotational speeds (ω).

3.1 Case I: $Pr=0.01$, $Ra=10^7$, $Ta=8.16$, $Ra_w=1.02 \times 10^2$. In this case, a low rotational speed with non-dimensional value $\omega^* = \omega H^2 / \alpha = 0.014$ is considered, where H is width of cavity and α is thermal diffusivity. Due to the small rotational speed and large difference in Ra and Ra_w , the thermal buoyancy is the dominating force over the rotational buoyancy and Coriolis force. Figure 2 shows the comparison of numerical results produced by the present code using inertial frame of reference with ALE formulation, and the code using non-inertial frame of reference. The results from literature [1] is also shown here for validation. It can be seen that the isotherms (normalized temperature difference contour) show thin boundary layers near isothermal walls with stable stratification of the core.

Figure 3 shows time histories of the spatially averaged Nu for hot and cold wall, which clearly shows oscillatory heat transfer at both the walls with a temporal mean value of 9.0 approximately for non-inertial frame and that of Baig *et al.* [1] results, whereas near 10 for inertial frame of reference.

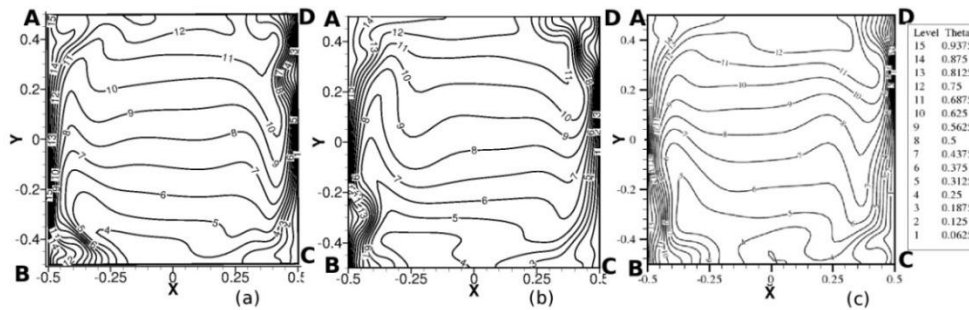


FIGURE 2 Comparison of temperature difference contours at time $t=0.4$ (a)ALE (Present), (b)Non-inertial frame (Present), (c) Baig *et al.* [3] for $Ra=10^7, Ta=8.16, Ra_w=102$.

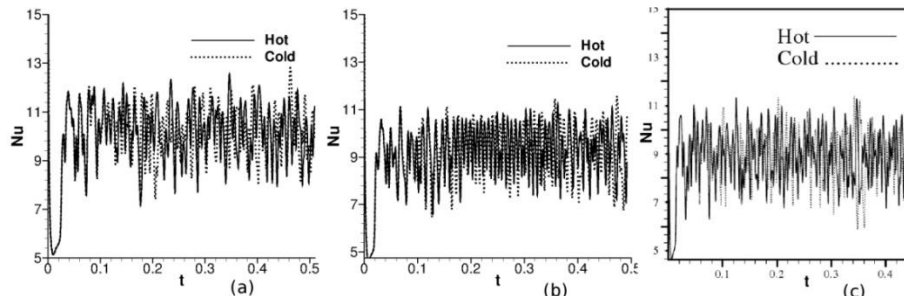


FIGURE 3 Comparison of time history of Nusselt number, Nu (a)ALE (Present), (b)Non-inertial frame (Present), (c) Baig *et al.* [3] for $Ra=10^7, Ta=8.16, Ra_w=102$.

3.2 Case II: $Pr=0.01$, $Ra=10^5$, $Ta=8.16 \times 10^4$, $Ra_w=1.02 \times 10^4$. In this case, higher value of rotational speed with $\omega^* = 1.428$ is used. The isotherms (normalized temperature difference contours), shown in figure 4, depict thick boundary layers near the isothermal walls with stable stratification in the core of the enclosure. The time histories of the spatially averaged Nu obtained

by present calculations shown in figure 5 indicate that the flow becomes asymptotically steady with steady heat transfer at walls with a value of $Nu=2.96$ for non-inertial frame and $Nu=3.13$ for inertial frame, which is contrary to the results given in reference [1].

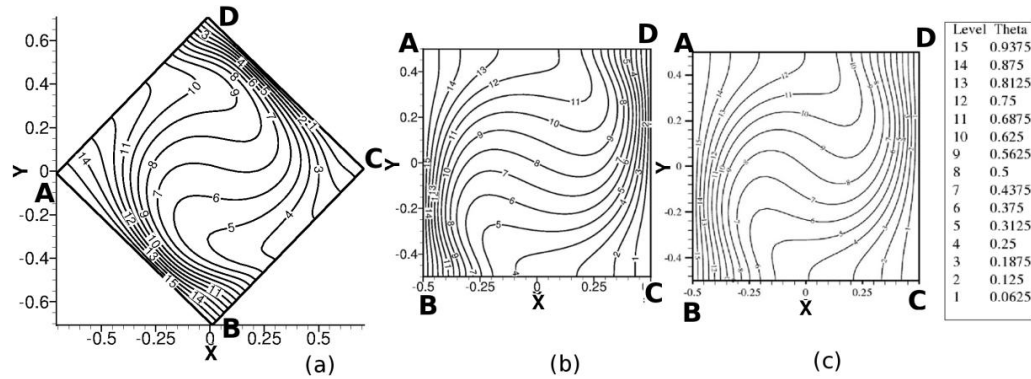


FIGURE 4 Comparison of temperature difference contours at time $t=0.8$ (a)ALE (Present), (b)Non-inertial frame (Present), (c) Baig *et al.* [3] for $Ra=10^5$, $Ta=8.16 \times 10^4$, $Ra_w=1.02 \times 10^4$

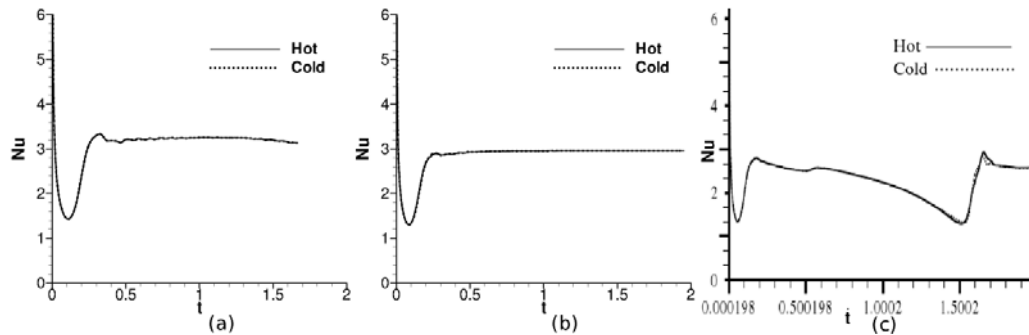


FIGURE 5 Comparison of time history of Nusselt number, Nu (a)ALE (Present), (b)Non-inertial frame (Present), (c) Baig *et al.* [3] for $Ra=10^5$, $Ta=8.16 \times 10^4$, $Ra_w=1.02 \times 10^4$

4. CONCLUSIONS

The flows inside differentially heated rotating cavity have been successfully simulated by solving Navier-stokes equation in artificial compressibility formulations using both inertial and non-inertial frames of references. The results are compared with that available in literature and found to be in good agreement, except for time history of Nusselt no. for the case II. Since non-inertial formulation may face computational difficulties in case of stiffness of the source terms for high rotations, an alternate formulation with inertial frame of reference is tried out in the present work. The alternate formulation for the rotating cavity is found to produce excellent results and hence, recommended for future applications.

REFERENCES

- [1] M. Zunaid and M.F. Baig, Numerical simulation of liquid metals in differentially heated enclosure undergoing orthogonal rotation, *Int. J. Heat & Mass Trans.*, 49, 3500-3513, 2006.
- [2] J.C. Mandal and A.S. Iyer, An Upwind Method for Incompressible Flows With Heat Transfer, *Int. J. Numer. Meth. Heat Fluid Flow*, 21(5), 518-534, 2011.
- [3] J.C. Mandal, C.R. Sonawane, A.S. Iyer and S.J. GosaviInamdar, Incompressible flow computations over moving boundary using a novel upwind method, *Comput. & Fluids*, 46, 348-352, 2011.

FAST LOCAL TRANSIENT SOLUTION OF MULTI-LAYERED MICRO-CHANNEL HEAT SINK

S.L. Beh, K.-K. Tio

Multimedia University, Melaka, Malaysia, slbeh@mmu.edu.my

G.A. Quadir

University Malaysia Perlis, Perlis, Malaysia, gaquadir@gmail.com

K.N. Seetharamu

PES Institute of Technology, Bangalore, India, knseetharamu@yahoo.com

ABSTRACT

Thermal analyses of one-, two- and three-layered micro-channels have been carried out. Finite element method (FEM) and asymptotic waveform evaluation (AWE) are used to obtain the transient response equation of one node. When the transient response graph is smooth and monotonic towards steady state temperature, AWE approximates this graph well even at small number of moments. However, if the transient response graph shows irregular pattern towards steady state temperature, higher number of moments are required to obtain a good approximation. Results indicate that three-layered micro-channel gives significant reduction in thermal resistance.

Key Words: *Asymptotic waveform evaluation, finite element, micro-channel, local transient solution.*

1. INTRODUCTION

The solution using conventional FEM gives the transient response of all nodes of the domain. If the transient response of only a few nodes is of interest, the computational effort for the other nodes will be wasted. Therefore AWE can be employed if the transient responses of only a few nodes of interest are required.

2. MODELLING AND FORMULATIONS

The schematic sketch and modelling of one-layered micro-channel is given in Figure 1. Two- and three-layered micro-channels are described in Figure 2. In total, there is one configuration for one-layered, two for two-layered and four for three-layered micro-channels. The heat transfer governing equations of the micro-channel (wall and fluid) are given in Eqs. (1-4).

$$\text{Horizontal wall: } k \frac{\partial^2 T}{\partial x^2} + k \frac{\partial^2 T}{\partial y^2} - \frac{h}{t_H} (T - T_f)_H = c \frac{\partial T}{\partial t} \quad (1)$$

$$\text{Vertical wall: } k \frac{\partial^2 T}{\partial y^2} + k \frac{\partial^2 T}{\partial z^2} - \frac{h}{t_V} (T - T_f)_V = c \frac{\partial T}{\partial t} \quad (2)$$

$$\text{Top channel: } \dot{m} c_f \frac{\partial T_f}{\partial y} + \rho_f c_f W H \frac{\partial T_f}{\partial t} = h H (T - T_f)_V + h W (T - T_f)_H \quad (3)$$

$$\text{Bottom and middle channels: } \dot{m} c_f \frac{\partial T_f}{\partial y} + \rho_f c_f W H \frac{\partial T_f}{\partial t} = h H (T - T_f)_V + h W (T - T_f)_H + h W (T - T_f)_H \quad (4)$$

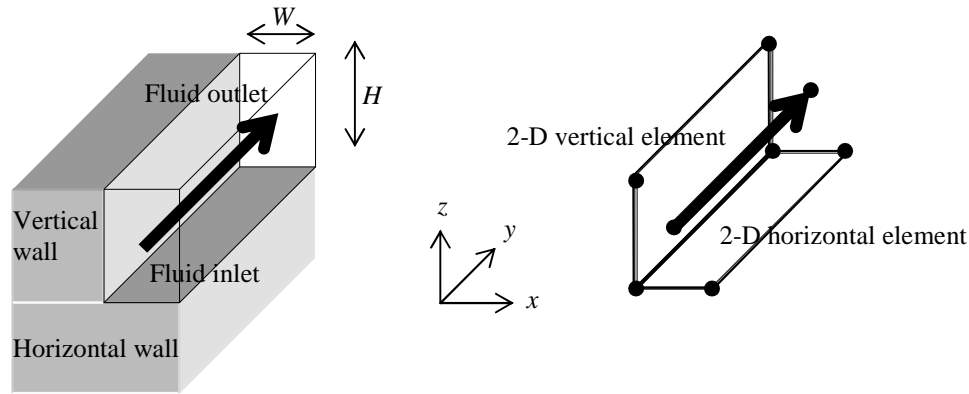


FIGURE 1. One-layered micro-channel: nomenclatures, nodes and elements used to represent the simplified model

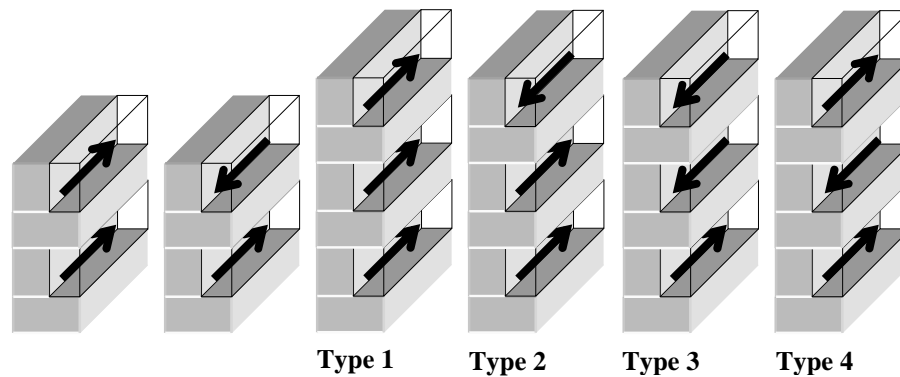


FIGURE 2. Two-layered micro-channels: parallel-flow and counter-flow, and three-layered micro-channels: parallel-flow (Type 1) and counter-flows (Types 2, 3 and 4)

The symbols used Eqs. (1-4) are explained as follows: k , T , and c are thermal conductivity, temperature, density and specific heat of the wall respectively; T_f , ρ_f and c_f are the temperature, density and specific heat of the fluid respectively; W and H are the width and height of channel, h is the heat transfer coefficient, t is the time, \dot{m} is the fluid mass flow rate in the channel.

Next, the formulations are divided into two parts: FEM followed by AWE. The micro-channels are discretised into nodes and elements as shown in Figure 3. The discretisation is independent on the flow configuration, which will be taken into consideration only when applying the boundary conditions. The FEM formulation is based on the Galerkin's weighted residual [1]. Eqs. (1-4) are then combined to become Eq. (5).

The AWE formulation applies Laplace transform to Eq. (5) to obtain Eq. (6). After that the formulation is separated into parts: zero-state response (ZSR) and zero-input response (ZIR). Each response computes its respective poles and zeros which are combined to form a general equation as shown in Eq. (7). Eq. (7) is the transient response of the temperature of the node of interest. Detailed FEM and AWE formulations are available in reference [2].

$$[C] \left\{ \frac{dT}{dt} \right\} + [K] \{T\} = \{0\} \quad (5)$$

$$[C] \{s(s) - s_0\} + [K] \{s(s)\} = \{b\} \quad (6)$$

$$\left(\right) = \left(\sum_{i=0}^q \frac{k_i}{p_i} (\exp(p_i) - 1) \right)_{ZSR} + \left(\sum_{i=0}^q k_i \exp(p_i) \right)_{ZIR} \quad (7)$$

3. RESULTS AND DISCUSSIONS

The accuracy and convergence of AWE are first presented in Figures 3, using one-layered micro-channel as the subject of verification. Figure 3 (left) shows that the transient response has converged even with small number of moments. The transient response is also verified using conventional FEM. Figure 3 (right) shows the effect of increasing the number of unit cells (discretisation of the domain) towards the accuracy of the results. It also shows convergence at small discretisation (10 unit cells).

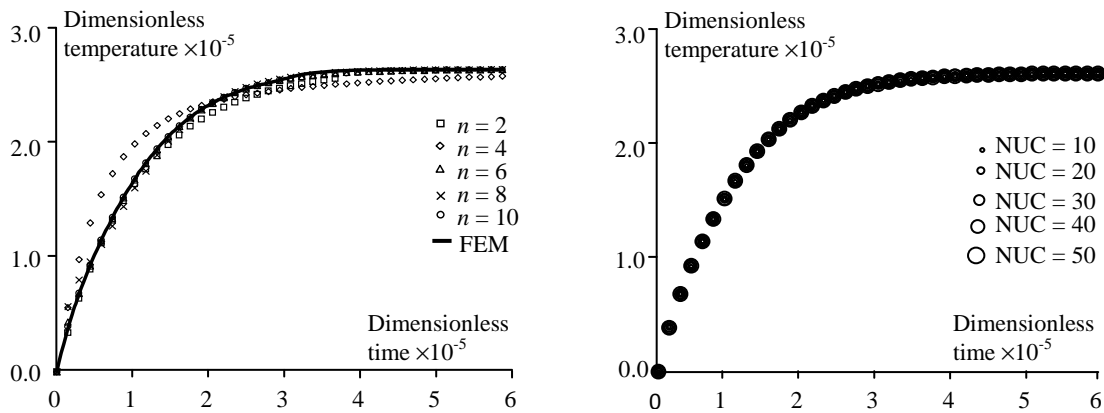


FIGURE 3. One-layered micro-channel: transient response of the maximum temperature for different number of moments n and different number of unit cells NUC.

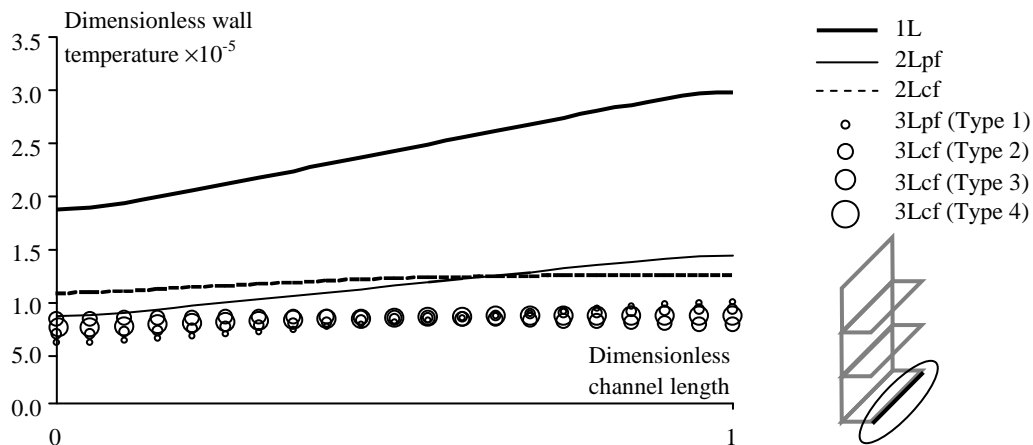


FIGURE 4. All micro-channels: steady state temperature profile of bottom wall centreline

Table 1 shows the comparison of thermal resistance of all micro-channel models using the same total flow rate in each micro-channel. Thus the flow rate in each channel of a two-layered micro-channel is half of one-layered; three-layered micro-channel is one third of one-layered. Qualitatively, one-layered gives the highest thermal resistance and the lowest for three-layered. Between two-layered micro-channels, parallel-flow is higher than counter-flow. Among the three-layered, parallel-flow is the highest, followed by Type 2, Type 4 and Type 3 of counter-flow.

Quantitative discussion focuses on the percentage of reduction of thermal resistance relative to one-layered. Generally, three-layered has higher reduction compared to two-layered, except the case of two-layered counter-flow having a higher reduction (42.0%) compared to three-layered parallel-flow (40.2%). Even so, the performance of two-layered counter-flow micro-channel is comparable to any types of three-layered micro-channels based on the thermal resistance values.

Micro-channel	Thermal resistance, K/W	Reduction of thermal resistance relative to one-layered, %
One-layered	0.497	-
Two-layered parallel-flow	0.338	32.0
Two-layered counter-flow	0.288	42.0
Three-layered parallel-flow (Type 1)	0.297	40.2
Three-layered counter-flow (Type 2)	0.273	45.1
Three-layered counter-flow (Type 3)	0.267	46.3
Three-layered counter-flow (Type 4)	0.271	45.5

TABLE 1. All micro-channels: comparison of thermal resistance using the same total flow rate

Figure 4 shows the steady state temperature profile of bottom wall centreline. One-layered micro-channel has the highest temperature profile which increases from fluid inlet to outlet. For two-layered micro-channels, the temperature profile of counter-flow is more evenly distributed than parallel-flow, based on the observation that the inlet temperature of parallel-flow is lower than counter-flow, but is reversed at the fluid outlet. The same pattern can be observed when comparing among the three-layered micro-channels, where counter-flow Type 4 is the most evenly distributed.

4. CONCLUSIONS

The convergence of the transient response equations using AWE have been verified by using different number of moments n to obtain the equations. The graphs generated have been shown to be close to each other even for small n . Meanwhile the accuracy has also been checked with the transient response graph using the FEM results, and AWE graphs have shown to be close to FEM results. The percentage of reduction in thermal resistance for two- and three-layered micro-channels relative to one-layered are also calculated. Having analysed the temperature of the micro-channels at various key locations, a decision can be made regarding the type of micro-channel suitable to be used in practice with similar operating conditions. With the incorporation of AWE in the analysis, the results can be obtained fast by solving the temperature only at these locations and not the whole domain.

REFERENCES

- [1] R.W. Lewis, P. Nithiarasu and K.N. Seetharamu, *Fundamentals of the finite element method for heat and fluid flow*, John Wiley and Sons, 2004.
- [2] S.L. Beh, K.-K. Tio, G.A. Quadir and K.N. Seetharamu, Fast transient solution of a two-layered counter-flow microchannel heat sink, *International Journal of Numerical Methods for Heat and Fluid Flow*, 19(5), 595-616, 2009.

NUMERICAL SOLUTIONS OF DOUBLE DIFFUSION IN CAVITIES

Fausto Arpino

Dipartimento di Meccanica Strutture Ambiente e Territorio (DiMSAT), Università di Cassino, Via G. Di Biasio 43, 03043 Cassino (FR), Italy. E-mail: f.arpino@unicas.it

Alberto Carotenuto, Nicola Massarotti, Alessandro Mauro

Dipartimento per le Tecnologie (DiT), Università degli Studi di Napoli "Parthenope", Centro Direzionale, Isola C4, 80143 Napoli, Italy. E-mail: alberto.carotenuto@uniparthenope.it, nicola.massarotti@uniparthenope.it, alessandro.mauro@uniparthenope.it

ABSTRACT

In this work, steady-state thermosolutal convection in a square cavity, subject to horizontal temperature and concentration gradients, is numerically simulated by using a new efficient matrix inversion free numerical procedure. The algorithm is based on the explicit Artificial Compressibility (AC) version of the Characteristic Based Split (CBS) scheme, opportunely stabilized by the authors to solve Double Diffusion problems. Rectangular cavities with different aspect ratios, subject to Dirichlet and Neumann boundary conditions, have been considered as computational domain. The thermal and solutal buoyancy forces acting on the fluid have been taken into account in case of aiding and opposing flow condition. All the results presented in this paper have been validated against the numerical and experimental data available from the literature.

Key Words: *AC-CBS, stability, double diffusive, mass transfer, concentration.*

1. INTRODUCTION

Many numerical and experimental studies on fluid flow in cavities have been carried out during the last decades. A number of these studies deal with natural convection induced by only temperature gradients. More recently, a great deal of attention has been posed on fluid motion generated by buoyancy forces due to simultaneous temperature and concentration gradients. This phenomenon, known as Double Diffusion (DD), is encountered in many physical problems, such as geothermal reservoirs, contaminant flow in rooms, vapour transport, food processing, alloys solidification.

First experiments on double diffusive flows of electrolyte solutions in shallow enclosures [1] showed that multilayer flow structures can be observed. Weaver and Viskanta [2] studied the DD problem of binary gases in cavities, both experimentally and numerically, by using the finite difference discretization technique. Nithiarasu *et al.* [3] employed for the first time the generalized porous medium model to study DD in saturated porous media, by using a finite element semi-implicit solver to obtain the numerical solution. Unsteady DD natural convection in the laminar and turbulent flow regime has been studied numerically in an asymmetric enclosure, a typical configuration of greenhouse-type solar stills, by employing a finite volume code, based on a successive over-relaxation method [4]. Recently, Chen *et al.* [5] investigated the influence of the buoyancy forces ratio and aspect ratio on DD in vertical annuluses, by using a Lattice Boltzmann (LB) model. Very recently Chen and Du [6] carried out a numerical study of entropy generation for turbulent DD natural convection in rectangular cavity, by employing a large eddy simulation (LES) based LB method.

To the authors' knowledge, fully explicit finite element based solutions of DD natural convection in rectangular cavities are still not available in literature. The present work introduces for the first time the Artificial Compressibility (AC) Characteristic Based Split (CBS) scheme, based on the finite

element discretization procedure, for the solution of natural convection driven by buoyancy forces due to both temperature and concentration gradients. Rectangular cavities with different aspect ratios have been taken into account, imposing both temperature and concentration values and thermal and solutal fluxes on the vertical side walls. Horizontal walls have been considered impermeable and adiabatic, or linear temperature variation has been imposed on them. All the presented results have been validated against other numerical or experimental data available from the literature.

2. GOVERNING EQUATIONS

The non-dimensional form of the equations solved in this paper for DD natural convection, in vector notation, can be written as:

$$\frac{\partial \mathbf{W}}{\partial t} + \frac{\partial \mathbf{F}_j}{\partial x_j} - \frac{\partial \mathbf{G}_j}{\partial x_j} = \mathbf{S} \quad (1)$$

with

$$\mathbf{W} = \begin{pmatrix} \rho \\ u_1 \\ u_2 \\ T \\ C \end{pmatrix}, \quad \mathbf{F}_j = \begin{pmatrix} \rho u_j \\ u_1 u_j + p \delta_{1j} \\ u_2 u_j + p \delta_{2j} \\ T u_j \\ C u_j \end{pmatrix}, \quad \mathbf{G}_j = \begin{pmatrix} 0 \\ \tau_{1j} \\ \tau_{2j} \\ \frac{\partial T}{\partial x_j} \\ \frac{1}{Le} \frac{\partial T}{\partial x_j} \end{pmatrix}, \quad \mathbf{S} = \begin{pmatrix} 0 \\ 0 \\ 0 \\ Ra Pr (T + R_\beta C) \\ 0 \end{pmatrix}$$

The non-dimensional form of the deviatoric stress is defined by $\tau_{ij} = Pr \left(\frac{\partial u_i}{\partial x_j} + \frac{\partial u_j}{\partial x_i} - \frac{2}{3} \frac{\partial u_k}{\partial x_k} \delta_{ij} \right)$.

The scales and the parameters used to derive the above non-dimensional equations are:

$$\begin{aligned} x_i &= \frac{x_i^*}{L}; \quad u_i = \frac{u_i^* L}{\alpha}; \quad t = \frac{t^* \alpha}{L^2}; \quad p = \frac{p^* L^2}{\rho \alpha^2}; \quad T = \frac{T^* - T_c}{T_h - T_c}; \\ C &= \frac{C^* - C_c}{C_h - C_c}; \quad \alpha = \frac{\lambda}{\rho c_p}; \quad \nu = \frac{\mu_f}{\rho}; \quad Pr = \frac{\nu}{\alpha}; \quad Le = \frac{D}{\nu}; \\ Ra &= \frac{g \beta_r (T_h - T_c) L^3}{\nu \alpha}; \quad R_\beta = \frac{\beta_c (C_h - C_c)}{\beta_r (T_h - T_c)}; \end{aligned} \quad (2)$$

3. STABILITY ANALYSIS FOR THE AC-CBS SCHEME FOR DOUBLE DIFFUSION

The stability analysis of the conservation equations, performed on the basis of the order of magnitude of all the terms [7], is here extended to efficiently solve DD problems. The stability conditions are derived by observing that the order of magnitude of each term must be smaller than one. This approach is applied to the steps of the AC-CBS scheme. The time-step restrictions obtained by adopting the present analysis are shown in the followings:

$$\begin{aligned}
 \text{Step 1: } \Delta t_{conv} &= \frac{h}{u_{conv}^n}; \Delta t_{diff} = \frac{h^2}{2Pr}; \Delta t_b = \frac{h}{Ra Pr T^n \Delta t^n}; \\
 \text{Step 2: } \beta &= u_{conv}^n + \frac{h}{\min(\Delta t_{conv}, \Delta t_{diff}, \Delta t_b)}; \Delta t_2 = \min\left(\frac{p^n \varepsilon h}{\beta^2 \tilde{u}^{n+1}}, \sqrt{\frac{\rho_f h^2}{2\beta^2}}\right) \\
 \text{Step 3: } \Delta t_3 &= \frac{h}{\beta}; \text{ Step 4: } \Delta t_{convT} \leq \frac{h}{u_{conv}^n}; \Delta t_{diffT} \leq \frac{h^2}{2}; \text{ Step 5: } \Delta t_{convC} \leq \frac{h}{u_{conv}^n}; \Delta t_{diffC} \leq \frac{h^2 Le}{2}
 \end{aligned} \tag{3}$$

4. RESULTS

The AC-CBS scheme is successfully applied to the benchmark problem of DD natural convection in rectangular cavities with different aspect ratios, imposing temperature and concentration values on the vertical walls, and employing different boundary conditions on horizontal walls (see Figure 1), for which numerical solutions are available in the literature [2, 5]. The thermal and concentration buoyancy forces have been considered in both aiding and opposing flow. In the first case, the buoyancy ratio R_β assumes a positive value, while, in the second case, a negative one. Figure 2 shows the non-dimensional concentration profiles at mid-height of the cavity for an aiding buoyancy case and non-dimensional temperature profiles at three x-coordinate of the cavity for an opposing buoyancy case. The present results compare excellently with the numerical and experimental solutions available in the literature [2, 5]. Figure 3 present the concentration and temperature contours for the same case of Figure 2 (right).

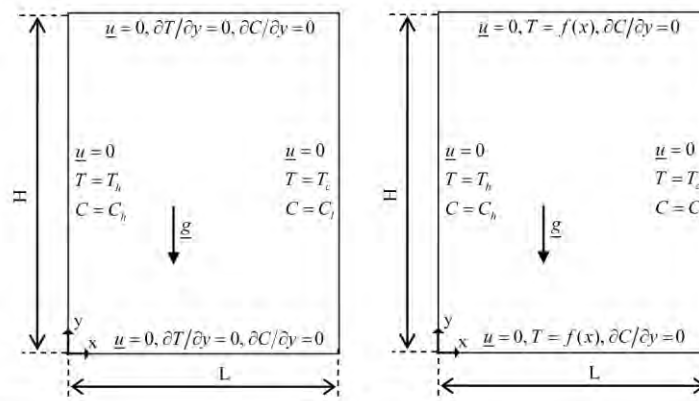


FIGURE 1. Computational domain and boundary conditions employed: (left) adiabatic horizontal walls; (right) linear temperature on horizontal walls.

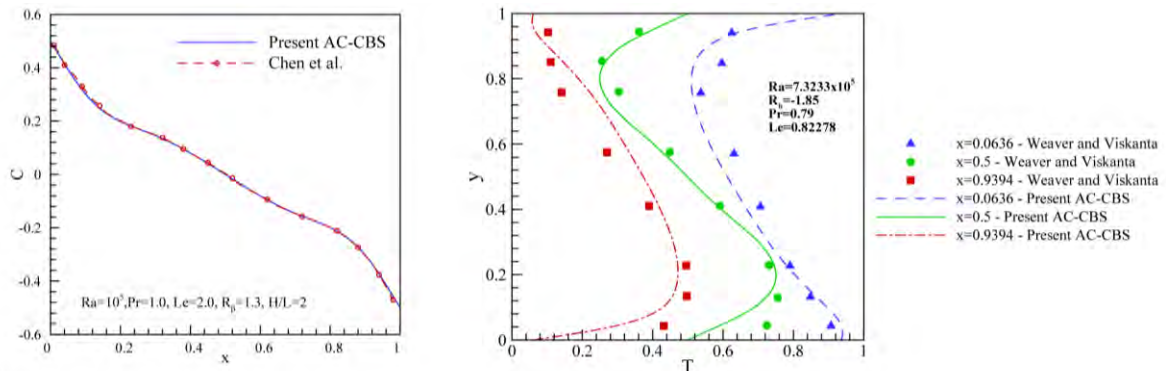


FIGURE 2. DD natural convection: (left) concentration and (right) temperature profiles.

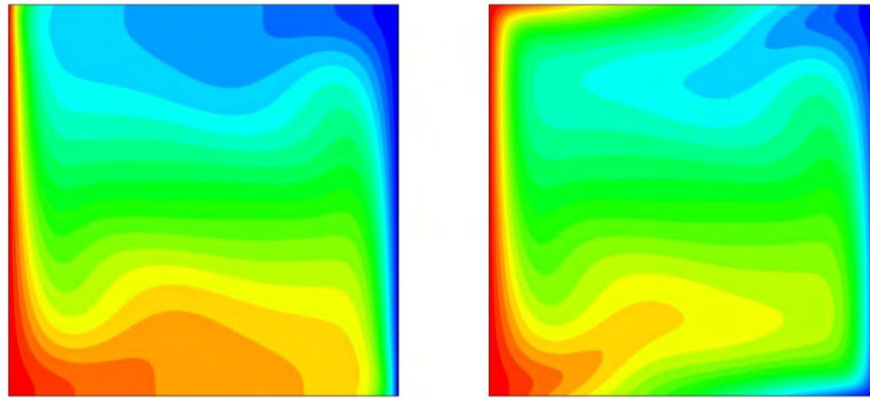


FIGURE 3. DD natural convection: (left) concentration and (right) temperature contours.

5. CONCLUSIONS

The new stabilized AC-CBS scheme has been presented for the solution of Double Diffusion natural convection in cavities with different aspect ratios. Aiding and opposing buoyancy forces have been taken into account in the present simulations. The influence of different boundary conditions on the fluid dynamic, thermal and solutal field in the cavity has been analyzed. The present results have been successfully verified and validated against numerical and experimental data available from the literature for well known problems.

REFERENCES

- [1] Y. Kamotani, L.W. Wang, S. Ostrach, H.D. Jiang, Experimental study of natural convection in shallow enclosures with horizontal temperature and concentration gradients. *International Journal of Heat and Mass Transfer*, 28, 165-173, 1985.
- [2] J.A. Weaver, R. Viskanta, Natural convection in binary gases due to horizontal thermal and solutal gradients, *Journal of Heat Transfer*, 113, 141-147, 1991.
- [3] P. Nithiarasu, T. Sundararajan, K.N.Seetharamu, Double-diffusive natural convection in a fluid saturated porous cavity with a freely convecting wall, *International communications in Heat and Mass Transfer*, 24, 1121-1130, 1997.
- [4] E. Papanicolaou, V. Belessiotis, Double-diffusive natural convection in an asymmetric trapezoidal enclosure: unsteady behavior in the laminar and the turbulent-flow regime, *International Journal of Heat and Mass Transfer*, 48, 191-209, 2005.
- [5] S. Chen, J. Tolke, M. Krafczyk, Numerical investigation of double-diffusive (natural) convection in vertical annuluses with opposing temperature and concentration gradients, *International Journal of Heat and Fluid Flow*, 31, 217-226, 2010.
- [6] S. Chen, R. Du, Entropy generation of turbulent double-diffusive natural convection in a rectangle cavity, *Energy*, doi:10.1016/j.energy.2010.12.056, 2011.
- [7] F. Arpino, N. Massarotti, A. Mauro, A stable explicit fractional step procedure for the solution of heat and fluid flow through interfaces between saturated porous media and free fluids in presence of high source terms, *International Journal for Numerical Methods in Engineering*, 83: 671-692, 2010.

ANALYSIS OF FLOW AND HEAT TRANSFER CHARACTERISTICS IN A SQUARE CAVITY WITH CONVECTIVE BOUNDARY CONDITION

Aswatha

Department of Mechanical Engineering, Bangalore Institute of Technology, Bangalore - 560004,
India, aswath_bit@yahoo.co.in

C. J. Gangadhara Gowda

Department of Mechanical Engineering, PES College of Engineering, Mandya - 571401, India,
cjb_gowda@yahoo.com

K. N. Seetharamu

Department of Mechanical Engineering, PES Institute of Technology, Bangalore - 560085, India,
seetharamukn@yahoo.com

ABSTRACT

Natural convection flow in a square cavity has been analyzed using finite volume based numerical procedure. The enclosure used for flow and heat transfer analysis has been bounded by adiabatic top wall, constant temperature cold vertical walls and a horizontal bottom wall. The bottom wall is subjected to convective heat transfer ranging from $0.1 \text{ W/m}^2 \text{ K}$ to $10,000 \text{ W/m}^2 \text{ K}$. The analysis is carried out for Rayleigh numbers (Ra) ranging from 10^3 to 10^7 and Prandtl number varied from 0.7 to 17. It is observed from this study that the effect of changes of parameters have been observed for heat transfer coefficient upto $50 \text{ W/m}^2 \text{ K}$. The average Nusselt numbers increases monotonically with Rayleigh number. As the Biot number increases, the average Nusselt number increases and reaches an asymptotic value equal to the average Nusselt number value obtained with the constant temperature boundary condition for a given Rayleigh number.

Key Words: *Natural Convection, Cavities, Convective Boundary Conditions, Numerical Heat Transfer.*

1. INTRODUCTION

Natural convection in a square cavity is prototype of many problems of engineering interest. Applications include design of energy efficient buildings, cooling of electronic cabinets, operation and safety of nuclear reactors, cryogenic storage, furnace design and others.

In the open literature, detailed review of natural convection in cavities is dealt in Ostrach [1]. Corcione [2] studied natural convection in a rectangular cavity heated from below and cooled from top as well as sides for variety of thermal boundary conditions. Numerical results are reported for several values of aspect ratios and Rayleigh numbers. Lo *et al.* [3] studied convection in cavities heated from left vertical wall and cooled from opposite vertical wall with both horizontal walls insulated using differential quadrature method.

Numerical results are reported for several values of width-to-height aspect ratio of enclosure and Rayleigh number. Basak *et al.* [4] have studied the effect of uniform and non uniform temperature at bottom wall on natural convection in a square cavity for Rayleigh numbers from 10^3 to 10^5 using Penalty finite element method. They reported that the uniform temperature gives more heat transfer than the non-uniform temperature. Natural convection flows in a trapezoidal enclosure with uniform and non-uniform heating of bottom wall is investigated numerically by Natarajan *et al.* [5]. Sinusoidal heating of the bottom wall produces greater heat transfer rate at the center of the bottom

wall than uniform heating case for all Rayleigh numbers. However, average Nusselt number shows lower heat transfer rate for non-uniform heating case.

Nomenclatures:

Bi_T	Thermal Biot number	u	x- component of velocity, m/s
g	Acceleration due to gravity, m/s^2	v	y- component of velocity, m/s
h	Heat transfer coefficient, $W/m^2 K$	<i>Greek Symbols</i>	
k	Thermal conductivity, $W/m K$	α	Thermal diffusivity, m^2/s
L	Length of the cavity, m	β	Volume expansion coefficient, K^{-1}
Nu	Local Nusselt number	θ	Dimensionless temperature
\overline{Nu}	Average Nusselt number	γ	Kinematic viscosity, m^2/s
p	Dimensional pressure, Pa	ρ	Density, kg/m^3
p_r	Prandtl number	Ψ	Stream function, m^2/s
R^2	Regression coefficient	<i>Subscripts</i>	
Ra	Rayleigh number	b	bottom wall
T	Temperature, K	S	side wall
T_c	Temperature of cold vertical wall, K	T	thermal

Recently, Aswatha [6] performed numerical study of natural convection in enclosures subjected to different temperature boundary conditions at bottom wall for cavity aspect ratio ranging from 1 to 3. It is found that the average Nusselt number is increased with increase of aspect ratio at bottom wall and it is decreased for side walls.

The objective of this study is to investigate the flow and heat transfer characteristics in a square cavity subjected to convective boundary conditions varying from $0.1 W/m^2 K$ to $10,000 W/m^2 K$ at the bottom wall, symmetrically cooled side walls with constant temperature and insulated top wall (see Fig. 1) for the range of Ra from 10^3 to 10^7 . p_r ranging from 0.7 to 17.08.

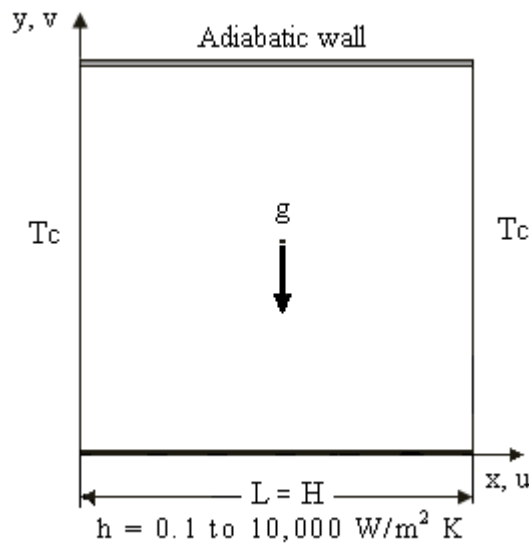


FIGURE 1. Geometry of the cavity

2. MATHEMATICAL FORMULATION

The governing equations for natural convection flow are conservation of mass, momentum and energy equations which can be written as in Basak *et al.* [4]:

No-slip boundary conditions are specified at all walls and ambient temperature is T_h .

$$\text{Bottom wall: } T(x, 0) = 0.1 \text{ W / m}^2 \text{ K to } 10000 \text{ W / m}^2 \text{ K}$$

$$\text{Top wall: } \frac{\partial T}{\partial y}(x, H) = 0 \quad (1)$$

$$\text{Sidewalls: } T(0, y) = T(L, y) = T_c$$

The fluid is assumed to be Newtonian and its properties are constant. Only the Boussinesq approximation is invoked for the buoyancy term. The changes of variables are as follows:

$$\theta = \frac{T - T_c}{T_h - T_c}, \quad p_r = \frac{\gamma}{\alpha}, \quad Bi_T = \frac{hL}{k}, \quad Ra = \frac{g\beta(T_h - T_c)L^3 p_r}{\gamma^2} \quad (2)$$

2.1 Numerical Procedure

In the present investigation, the set of governing equations are integrated over the control volumes, which produces a set of algebraic equations. The PISO (Pressure Implicit with Splitting of Operators) algorithm developed by Issa [7] is used to solve the coupled system of governing equations. The set of algebraic equations are solved sequentially by ADI. A second-order upwind differencing scheme is used for the formulation of the convection contribution to the coefficients in the finite-volume equations. Central differencing is used to discretize the diffusion terms. The computation is terminated when all of the residuals reach below 10^{-5} . The computations are carried out using the FLUENT 6.3 commercial code.

2.2 Nusselt Number

In order to determine the local Nusselt numbers on the cold walls, the temperature profiles are fit with quadratic, cubic and bi-quadratic polynomials and their gradients at the walls are determined. It has been observed that the temperature gradients at the surface are almost the same for all the polynomials considered. Hence only a quadratic fit is made for the temperature profiles to extract the local gradients at the walls to calculate the local heat transfer coefficients from which the local Nusselt numbers are obtained. Integrating the local Nusselt number over each side, the average Nusselt number for each side wall is obtained as

$$\overline{Nu_s} = \int_0^H Nu_s dy \quad (3)$$

3. RESULTS AND DISCUSSION

3.1. Verification of the Present Methodology with Experimental Results

The grid independence study has been made with different grids and biasing to yield consistent values [3]. The present methodology is compared with Lo *et al.* [3], Different grid sizes of 31×31 , 41×41 , 51×51 and 61×61 uniform mesh as well as biasing have been studied. The grid 41×41 biasing ratio (BR) of 2 (The ratio of maximum cell to the minimum cell is 2, thus making cells finer near the wall) gave results identical to that of 61×61 uniform mesh. In view of this, 41×41 grid with biasing ratio 2 is used in all further computations.

Computations are performed for cavity configuration with aspect ratio 5 for which the experimental results are available in the form of a correlation for the average Nusselt number as a function of the Rayleigh number as in equation 4,

$$\overline{Nu} = \max \left(\sqrt[3]{1 + \left(\frac{0.193 \sqrt[4]{Ra}}{1 + (1800/Ra)^{1.289}} \right)^3}, 0.0605 \sqrt[3]{Ra} \right) \quad (4)$$

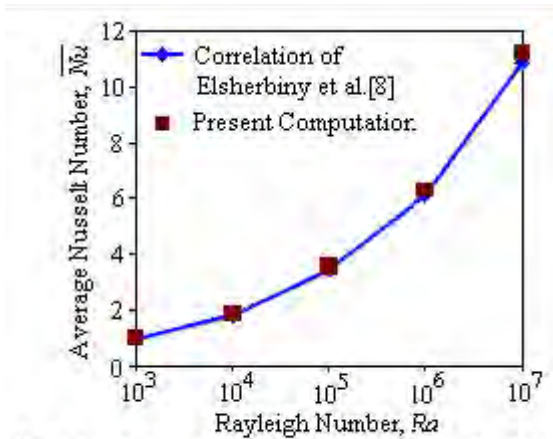


FIGURE 2. Comparison of present results with that of Elshebiny *et al.* [8].

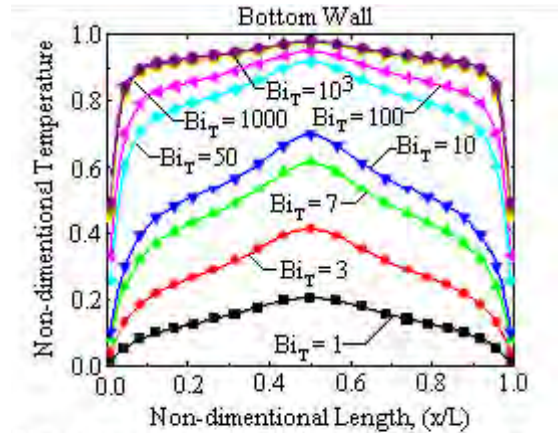


FIGURE 3. Non-dimensional temperature variation for $Ra = 10^5$.

The average Nusselt numbers computed by the present code for values of Ra ranging from 10^3 to 10^7 are compared with the correlation of [4] in Fig. 2. The agreement is found to be excellent with a maximum discrepancy of about 3%, which validates the present computations.

Fig. 3 shows the variations of non-dimensional temperature at the bottom wall. It can be observed that as Bi_T increases, the temperature at the bottom wall will tend to be more uniform. Simultaneously as Bi_T increases, it will approach a non-dimensional temperature of 1.0 at the bottom wall.

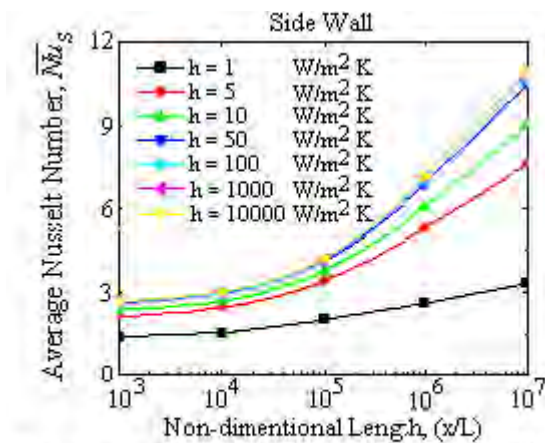


FIGURE 4. Variations of \overline{Nu} for side wall for different convective boundary conditions at bottom wall.

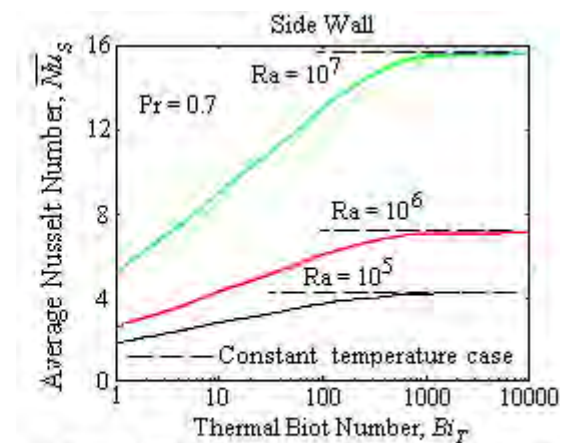


FIGURE 5. \overline{Nu} variation with Bi_T for different Rayleigh numbers.

Fig. 4 shows the variation of average Nusselt number for the case of convective boundary conditions for side walls. It can be observed that the average Nusselt number increases with Rayleigh number as expected. The average Nusselt numbers remain invariant for $h \geq 50 \text{ W/m}^2 \text{ K}$ for the range of Ra studied. Fig. 5 shows the average Nusselt number variation with the Biot number. As the Biot number (heat transfer coefficient) increases, the Nusselt number increases and reaches an asymptotic value equal to the Nusselt number value obtained with the constant temperature boundary condition for a given Ra , as expected.

Pr	Ra range	h W/m ² K	Side Wall		
			Correlation	R ²	% Error
0.7	10 ⁴ to 10 ⁷	1	$\overline{Nu}_s = 0.567 Ra^{0.109}$	0.999	<0.20
		5	$\overline{Nu}_s = 0.528 Ra^{0.165}$	0.999	<0.20
		10	$\overline{Nu}_s = 0.518 Ra^{0.177}$	0.998	<0.30
		50	$\overline{Nu}_s = 0.543 Ra^{0.183}$	0.999	<0.20
		100	$\overline{Nu}_s = 0.548 Ra^{0.184}$	1.000	<0.10
		1000	$\overline{Nu}_s = 0.535 Ra^{0.186}$	0.999	<0.20
		6.08	10 ⁴ to 10 ⁷	1	$\overline{Nu}_s = 0.280 Ra^{0.163}$
5	$\overline{Nu}_s = 0.234 Ra^{0.197}$			0.998	<0.20
10	$\overline{Nu}_s = 0.250 Ra^{0.202}$			0.997	<0.35
50	$\overline{Nu}_s = 0.312 Ra^{0.212}$			0.997	<0.35
100	$\overline{Nu}_s = 0.353 Ra^{0.213}$			0.999	<0.35
1000	$\overline{Nu}_s = 0.379 Ra^{0.221}$			0.996	<0.60
17.08	10 ⁴ to 10 ⁷	1	$\overline{Nu}_s = 0.252 Ra^{0.171}$	0.997	<0.50
		5	$\overline{Nu}_s = 0.227 Ra^{0.199}$	0.998	<0.20
		10	$\overline{Nu}_s = 0.239 Ra^{0.206}$	0.997	<0.30
		50	$\overline{Nu}_s = 0.297 Ra^{0.216}$	0.997	<0.40
		100	$\overline{Nu}_s = 0.331 Ra^{0.218}$	0.999	<0.30
		1000	$\overline{Nu}_s = 0.337 Ra^{0.227}$	0.997	<0.40

TABLE 1. Correlation of \overline{Nu} with Ra for side wall.

Table 1 show the correlations developed and error involved for side wall. The range of convection domination is different for different thermal boundary conditions. The conduction domination occurs up to $Ra \leq 104$. The maximum error involved in correlating average Nusselt number with Rayleigh number is less than 0.6 % in the range of Ra studied.

4. CONCLUSIONS

The following conclusions have been observed during the present study.

- i) It is observed that the heat transfer characteristics like temperature variations, temperature contours, stream function contours, local and average Nusselt numbers remains same for $h > 50 \text{ W/m}^2 \text{ K}$.
- ii) The contours of stream functions and isotherms are symmetric about vertical central line.
- iii) The average Nusselt number increases monotonically with increase of Ra for side wall.

- iv) It observed that as Bi_T increases, the temperature at the bottom wall will tend to be more uniform.
- v) It is seen that as Bi_T increases, it will approach a non-dimensional temperature of 1.0 at the bottom wall.

REFERENCES

- [1] S. Ostrach, Natural convection in enclosures, *Advances in Heat Transfer*, 8, 161-227, 1972.
- [2] M. Corcione, Effects of the thermal boundary conditions at the sidewalls upon natural convection in rectangular enclosures heated from below and cooled from above. *Int. J. of Thermal Sciences*, 42(2), 199-208, 2003.
- [3] D.C. Lo, D.L. Young, and C.C. Tsai, High resolution of 2D natural convection in a cavity by the DQ method. *J. of Computational and Applied Mathematics*, 203(1), 219-236, 2007.
- [4] T. Basak, S.Roy, and A.R. Balakrishnan, An effect of thermal boundary conditions on natural convection flows with in a square cavity. *Int. J. of Heat and Mass Transfer*, 49(23-24), 4525-4535, 2006.
- [5] E. Natarajan, T. Basak and S. Roy, Natural convection flows in a trapezoidal enclosure with uniform and non-uniform heating of bottom wall, *Int. J. of Heat and Mass Transfer*, 51, 747-756, 2008.
- [6] Aswatha, C.J. Gangadhara Gowda, S.N. Sridhara, K.N. Seetharamu. Effect of different thermal boundary conditions at bottom wall on natural convection in cavities. *J. of Engineering Science and Technology*, 6(1), 61-82, 2011.
- [7] R.I. Issa, Solution of the implicitly discretized fluid flow equations by operatorsplitting, *J. Comput. Phys.*, 62, 40-65, 1985.
- [8] S.M. Elsherbiny, G.D. Raithby and K.G. T. Hollands, Heat transfer by natural convection across vertical and inclined air layers. *Transactions of ASME, J. of Heat Transfer*, 104(1), 96-102, 1982.

HIGH ORDER EXPLICIT SOLUTIONS FOR TRANSIENT INCOMPRESSIBLE FLOWS

F. Arpino, G. Cortellessa, M. Dell'Isola

Department of Mechanics, Structures and Environment (DiMSAT), University of Cassino, Via G. Di Biasio 43, 03043 Cassino (FR), Italy. E-mail: f.arpino@unicas.it, g.cortellessa@unicas.it, dellisola@unicas.it

N. Massarotti, A. Mauro

Department for Technologies (DiT), University of Napoli "Parthenope", Isola C4, Centro Direzionale di Napoli, 80143 Napoli, Italy. E-mail: nicola.massarotti@uniparthenope.it, alessandro.mauro@uniparthenope.it

ABSTRACT

In the present paper, the results of the Artificial Compressibility version of the Characteristic Based Split algorithm (AC-CBS) are analysed for both forced and natural convection incompressible flows. A dual time-stepping procedure is used to recover the real transient solution. The true transient term is discretized explicitly up to the fourth order of approximation, allowing the adoption of larger true time steps, and resulting in a more robust and efficient algorithm.

Key Words: *Natural convection, Cavity, Vortex shedding, Transient problems.*

1. INTRODUCTION

Fully explicit time step schemes are becoming popular for the study of transient behaviour of both compressible and incompressible fluid-dynamic problems due to their simplicity and increasing robustness [1-4]. Since density variation is negligible in many fluid problems, the time term in the mass conservation equation can be ignored. In such a case, the explicit incompressible flow calculation can still be performed by replacing the density term by an equivalent pressure term which is related to density via an Artificial Compressibility (AC) parameter [1]. Unfortunately, many of the standard AC schemes available in literature present convergence or accuracy issues and a proper stability analysis becomes then crucial. In the present paper the performance of the AC version of the Characteristic Based Split algorithm (AC-CBS) [2] is discussed for transient problems. On the basis of the stabilization approach presented by the authors in some of their recent papers [3], a new stabilization constraint has been derived for the transient term. The use of the third and fourth order approximations for the transient term allowed the adoption of larger real time steps, resulting in a more robust and efficient algorithm.

2. DUAL TIME-STEPPING PROCEDURE FOR A REAL TRANSIENT SOLUTION

The governing equations for incompressible flows [2] have been solved numerically by using the AC-CBS algorithm, which is based on the temporal discretization along characteristics, and standard Galerkin spatial discretization procedure [1]. Application to the CBS of the principle of recovering the transient solution has been proposed only recently [1,4]. Since the artificial compressibility parameter makes the solution reliable only when steady state condition is reached, the dual time-stepping approach splits a problem into several instantaneous steady states. The true transient term is added to the first or third step of the CBS algorithm [1,4] and is usually written to get a second order of approximation over the real time step size:

$$\Delta u_i^n = \frac{3u_i^n - 4u_i^{n-\Delta\tau} + u_i^{n-2\Delta\tau}}{2} \quad (1)$$

where $\Delta\tau$ represents the real time step size, n is the pseudo time step level and u_i is the velocity. Nevertheless, when severe pseudo time steps restriction are adopted, significant limitation is also imposed to the real time step size in order to get an adequate accuracy. Such a limitation can be reduced employing a four-points third order approximation:

$$\Delta u_i^n = \frac{11u_i^n - 18u_i^{n-\Delta\tau} + 9u_i^{n-2\Delta\tau} - 2u_i^{n-3\Delta\tau}}{6} \quad (2)$$

or a five-points fourth order approximation:

$$\Delta u_i^n = \frac{25u_i^n - 48u_i^{n-\Delta\tau} + 36u_i^{n-2\Delta\tau} - 16u_i^{n-3\Delta\tau} + 3u_i^{n-4\Delta\tau}}{12} \quad (3)$$

The explicit nature of the true transient term introduces a limitation on the pseudo time step size to ensure the required stability of the method. On the basis of the order of magnitude analysis [3] it has been derived that $\Delta t \leq \Delta\tau/4$ when a second order of approximation is adopted, $\Delta t \leq 3\Delta\tau/20$ for a third order of approximation, and $\Delta t \leq 3\Delta\tau/32$ when a fourth order of approximation is employed. At the same time, the admissible maximum real time step size depends on the pseudo time step in order to ensure an adequate accuracy of the method. As a consequence, the choice of the computational grid size represents a crucial issue. In fact, very refined grids result in very small pseudo time-step sizes, reducing the scheme accuracy when large true time step size is adopted.

3. RESULTS

Vortex Shedding behind a circular cylinder

The first benchmark case analysed in this paper is the vortex shedding behind a circular cylinder. The computational domain, boundary conditions and the results in terms of x-velocity contours are available in FIGURE 1. FIGURE 2 presents the variation with time of the vertical velocity component at the Q-point (FIGURE 1), obtained by employing a dual time-stepping based on second, third and fourth order true time approximation and for a real time step size of 0.166 (left) and 0.083 (right). Results have been compared to data from literature [5] in terms of amplitude and frequency of oscillations. For $\Delta\tau = 0.166$ and when the three-point second order approximation is employed, oscillations start later and their amplitude is smaller if compared to reference data [5]. For the same real time step size, oscillations start earlier when higher order of approximation is employed and also their amplitude increases, resulting in a better agreement with the reference data. When $\Delta\tau = 0.083$, second order scheme substantially reproduces the results obtained using the third order approximation for $\Delta\tau = 0.166$ (so still underestimates the oscillations amplitude), while the four-point approximation presents a good agreement with [5] in terms of both oscillations frequency and amplitude when $\Delta\tau = 0.083$ is adopted. Results obtained when the fourth order of approximation is used are also in good agreement with reference data, even though the stability restrictions on the pseudo time step resulted in a larger number of iterations for each instantaneous steady state condition, resulting in a larger computational time with respect to the third order of approximation approach. These results confirm that the use of real time higher order of approximation allows significant reduction of the true time steps number for a given temporal interval under investigation.

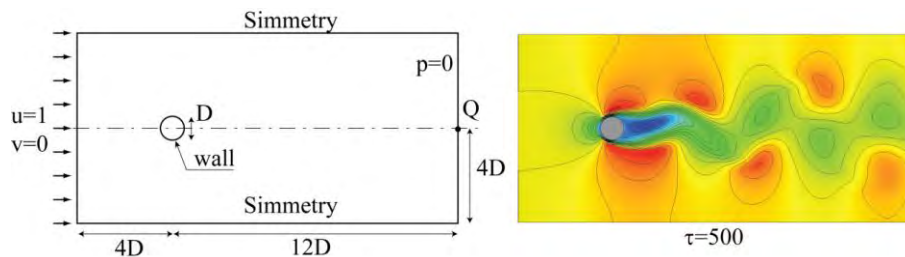


FIGURE 1. Vortex shedding behind a circular cylinder: computational domain and boundary conditions (left) and x-velocity contours (right) at a real time of 500.

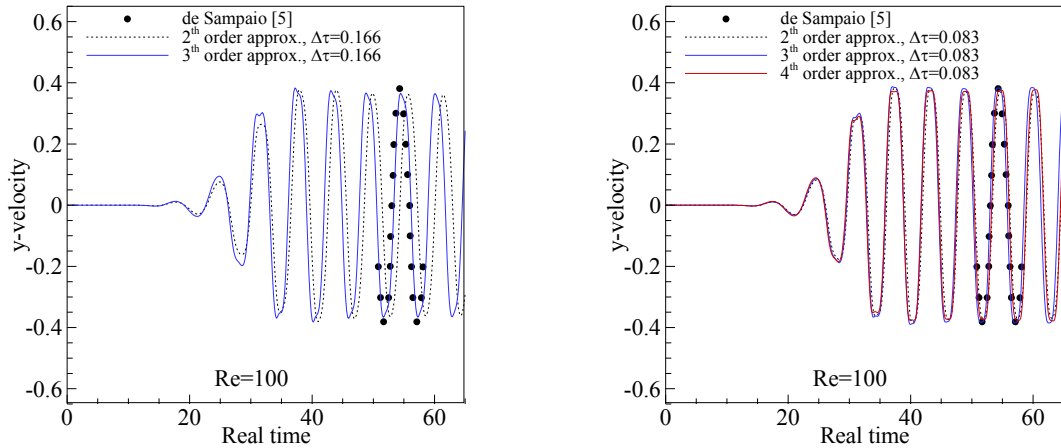


FIGURE 2. y -velocity at the Q-point (FIGURE 1) for $\Delta\tau = 0.166$ (left) and $\Delta\tau = 0.083$ (right).

Buoyancy driven enclosure

Performance of the AC-CBS for transient problems has been investigated for a buoyancy driven enclosure problem. The computational domain and the boundary conditions imposed are available in Figure 3 (left). The enclosure aspect ratio H/W is equal to 8. The gravity vector is directed in the

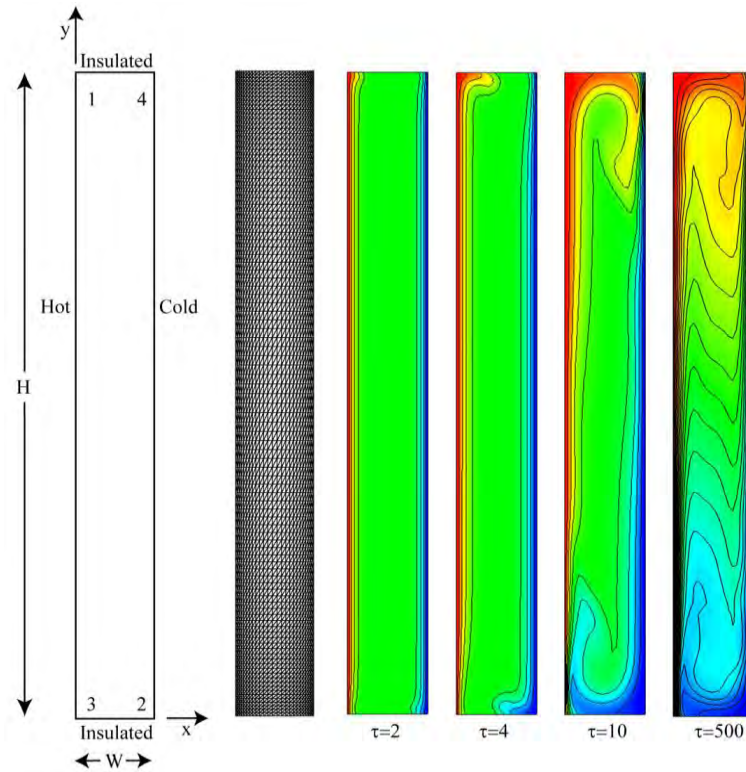


FIGURE 3. Buoyancy driven enclosure problem. From left to right: problem definition, computational grid, temperature contours at a real time of 2, 4, 10 and 500.

negative y -coordinate direction. The calculations have been performed for Prandtl number $Pr=0.71$ and Rayleigh number $Ra=3.4 \times 10^5$, using a computational grid composed by 2626 nodes and 5000 triangular elements (Figure 3). The obtained results, in correspondence of a statistically steady state condition, have been compared to data available in [6] at the point 1 (Figure 3). In particular, the results obtained from the AC-CBS scheme using a second and third approximation order and for a

real time step size of 0.1 and 0.01, have been compared to the mean x-velocity and temperature, together with their oscillation amplitudes. From the obtained results, it can be observed that the use of the third order of approximation allows a better agreement with the results obtained by most of the authors considered in [6], especially in terms of oscillation amplitude for both velocity and temperature. It should be pointed out that the data available in [6] present a significant dispersion. For instance, the mean velocity value at point 1 ranges from 0.05400 to 0.06537 for different authors, while the mean temperature value ranges from 0.264820 to 0.275000. However, as mentioned, the present data are in good agreement with the most commonly found values.

Corresponding author	\bar{u}_1	u'_1	$\bar{\theta}_1$	θ'_1
Christon-II (Ref. 8 of [6])	0.065370	0.064320	0.267100	0.050040
Ambrosini (Ref. 4 of [6])	0.060800	0.080000	0.275000	0.050000
Comini-I (Ref. 1 of [6])	0.059800	0.074540	0.265440	0.056920
Bruneau (Ref. 9 of [6])	0.059630	0.066160	0.268500	0.051380
Le Quéré (Ref. 22 of [6])	0.056356	0.054828	0.265480	0.042740
Chan-II (Ref. 7 of [6])	0.059290	0.083100	0.264820	0.063580
Kim (Ref. 5 of [6])	0.054000	0.000480	0.265000	0.000260
AC-CBS 2 nd order approx. $\Delta\tau=0.1$	0.0569	0.0493	0.2660	0.0392
AC-CBS 2 nd order approx. $\Delta\tau = 0.01$	0.0589	0.0630	0.2661	0.0492
AC-CBS 3 rd order approx. $\Delta\tau=0.1$	0.0580	0.0569	0.2658	0.0450
AC-CBS 3 rd order approx. $\Delta\tau = 0.01$	0.0594	0.0661	0.2662	0.0514

TABLE 1. Comparison of AC-CBS results calculated at point 1 (Figure 3) with reference data available in [6].

4. CONCLUSIONS

The paper investigates the performance of the Artificial Compressibility version of the Characteristic Based Split algorithm (AC-CBS) for the solution of unsteady flow problems with higher order approximation of transient terms, discretized up to fourth order. The results are in good agreement with literature data, even for large real time step size when higher order of approximation is employed, reducing the number of time iterations needed.

REFERENCES

- [1] P. Nithiarasu, An efficient artificial compressibility (AC) scheme based on split (CBS) method for incompressible flows, *International Journal for Numerical Methods in Engineering*, 56, 1815-1845, 2003.
- [2] O.C. Zienkiewicz and R.L. Taylor, *The Finite Element Method, Vol 3, Fluid Dynamics*, Butterworth and Heinemann, 2000.
- [3] F. Arpino, N. Massarotti, and A. Mauro, High Rayleigh Number Laminar-Free Convection in Cavities: New Benchmark Solutions, *Numerical Heat Transfer, Part B: Fundamentals*, 58(2), 73-97, 2010.
- [4] A.G. Malan, R.W. Lewis, and P. Nithiarasu, An improved unsteady, unstructured, artificial compressibility, finite volume scheme for viscous incompressible flows: part I. Theory and implementation, *International Journal for Numerical Methods in Engineering*, 54, 695-714, 2002.
- [5] P.A.B. de Sampaio, P.R.M. Lyra, K. Morgan, and N.P. Weatherill, Petrov-Galerkin solutions of the incompressible Navier Stokes equations in primitive variables with adaptive remeshing, *Computer Methods in Applied Mechanics and Engineering*, 106, 143-178, 1993.
- [6] M.A. Christon, P.M. Gresho, and S.B. Sutton, Computational predictability of time-dependent natural convection flows in enclosures (including a benchmark solution), *International Journal for Numerical Methods in Fluids*, 40, 953-980, 2002.

NUMERICAL ANALYSIS ON MELTING IN A CYLINDRICAL HEAT STORAGE CAPSULE

Adriano Sciacovelli

Politecnico di Torino Dipartimento di Energetica, c.so Duca degli Abruzzi 24, Torino, Italy,
adriano.sciacovelli@polito.it

Vittorio Verda

Politecnico di Torino Dipartimento di Energetica, c.so Duca degli Abruzzi 24, Torino, Italy,
vittorio.verda@polito.it

ABSTRACT

The present paper describes the application of computational fluid-dynamics (CFD) for the analysis of melting process in a cylindrical enclosure heated from the side. The 2D model is based on a finite-volume numerical procedure that adopts the enthalpy method to take in account the phase change phenomenon. The time-dependent simulations show the melting phase front and melting fraction of the PCM and incorporate the fluid flow in the liquid phase. The obtained temperature profiles are compared to a set of experimental data available on a web site for public access. The results show that during the melting process natural convection within the PCM has non negligible effects on the behavior of the system. The paper also discusses the effects on the phase-change processes of the main operating conditions, including inlet temperature and mass flow rate of the heat transfer fluid.

Key Words: *Phase change, CFD, Natural convection, Melting*

1. INTRODUCTION

Thermal energy storage plays a key role when is necessary to store excess energy that would be otherwise wasted and to match demand and supply. This is an important problem in renewable energy systems and cogeneration systems. Latent heat storage systems are able to store heat at nearly constant temperature, corresponding to the phase transition temperature of the phase change material (PCM) [1]. On the other hand, the main disadvantage is represented by the low thermal conductivity of many PCMs, causing poor charging and discharging rates. Therefore the advance of LHTS requires the understanding of heat transfer in the PCM during the phase transition. The aim of this work is to solve transient complete conservation equations for the melting process occurring in a vertical cylindrical enclosure . In particular the buoyancy-driven fluid motion within the melted PCM is explicitly computed. The results provide a detailed description of the heat transfer process occurring in the system.

2. MAIN BODY

The experimental set up of Jones *et al.* [2] is here considered, as shown in Figure 1. The phase change material (PCM) is placed inside a cylindrical shell made of polycarbonate, an acrylic base and an acrylic block on the top. The outer surface of the cylinder is kept at a constant temperature by immersion in a hot water bath. Therefore uniform temperature T_H on the cylinder can be adopted as boundary condition for use in a numerical model. The top of the cylinder can be assumed adiabatic due to the presence of the acrylic block. Finally, Jones *et al.* [2] imposed a fixed temperature T_B of 32°C along the acrylic base. The PCM chosen is a paraffin wax: *n*-eicosane, The wax is initially at ambient temperature ($T_i = 23^\circ\text{C}$). At the start of the computation the outer

surface cylinder temperature is set to T_H . The resulting heat flux conducted through the wall causes PCM melting. The charging process is completed when PCM is completely liquid.

Three thermocouple racks are placed inside the PCM, as depicted in Figure 1. Each rack contain six thermocouples. Temperature measurements are made available by Jones *et al.* [2] on a public web site.

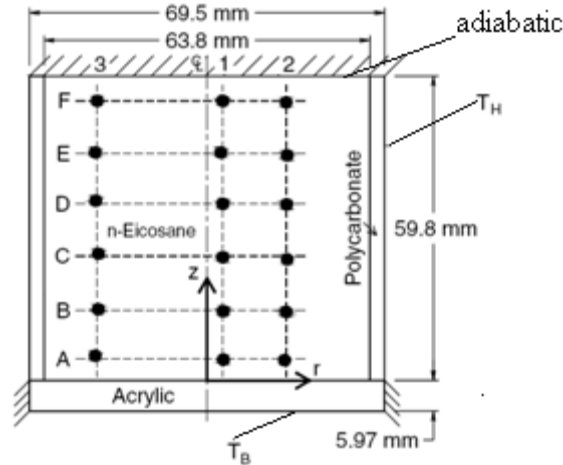


FIGURE 1. System geometry and Thermocouples positions [2].

The governing equations for the transient analysis of the melting of the phase change materials include Navier-Stokes equation, the continuity equation and the energy equation. Density variation due to phase change is neglected; the Boussinesq approximation is applied. Thus density change within the liquid PCM which drives natural convection in the liquid phase is considered in the body force terms. Governing equations used here for the PCM are [3]:

Continuity:

$$\frac{\partial \rho}{\partial t} + \nabla \cdot (\rho \vec{V}) = 0 \quad (1)$$

Momentum:

$$\rho \frac{\partial \vec{V}}{\partial t} + \rho (\vec{V} \cdot \nabla) \vec{V} = -\nabla p + \mu \nabla^2 \vec{V} + \rho \vec{g} \beta (T - T_0) + \frac{(1-\gamma)^2}{(\gamma^3 + \epsilon)} A_{mushy} \vec{V} \quad (2)$$

Energy:

$$\frac{\partial}{\partial t} (\rho h) + \nabla \cdot (\rho \vec{V} h) = \nabla \cdot (k \nabla T) \quad (3)$$

where ρ is the density, \vec{V} the velocity of the liquid PCM, p is the pressure, μ the dynamic viscosity, \vec{g} the gravity vector, β the thermal expansion coefficient, T_0 the reference temperature. In order to deal with the phase change problem, the enthalpy-porosity approach has been used since it does not require and explicit tracking of the solid-liquid interface [3]. The presence of the solid or liquid phase is instead monitored by using a quantity known as liquid fraction γ . The enthalpy-porosity formulation treats different phases as porous media by means of the last term of the right hand side of Eq. (2). The computational constant ϵ is a small number typically around 10^{-3} to avoid the division by zero and A_{mush} is the mushy zone constant which describe how steeply the velocity are reduced to zero when the material solidifies. The value here used for the computations is $10^5 \text{ kg}/(\text{m}^3 \text{ s})$. The modeling has been conducted by using a finite-volume CFD code. In this particular application a segregated solver has been used to address the problem. SIMPLE algorithm has been used to solve the pressure-velocity coupling. Furthermore, the LHTS system geometry allows to adopt a 2D axial-symmetric model.

3. RESULTS

The different scenarios have been considered corresponding to $T_H = 70^\circ\text{C}$, 55°C and 45°C for sake of simplicity a detailed analysis of the CFD results is presented for the case characterized $T_H = 70^\circ\text{C}$. Figure 2 illustrates the comparison between the numerical and experimental melt front positions at three different times. It can be observed that the melt layer thickness varies significantly along the vertical direction: This behavior indicates that buoyancy-driven currents play an important role in the upper part of the system. It is clear from Fig. 2 that buoyancy currents enhance the melting process starting from the top of the cylinder. As time progress, melting front moves downward where conduction heat transfer play a dominant role for a longer time. The agreement between numerical and experimental melt front position is quite good. Some discrepancies are observed at early time, this can be in good part attributed to the interactions between PCM and the pipes constituting the thermocouples racks.

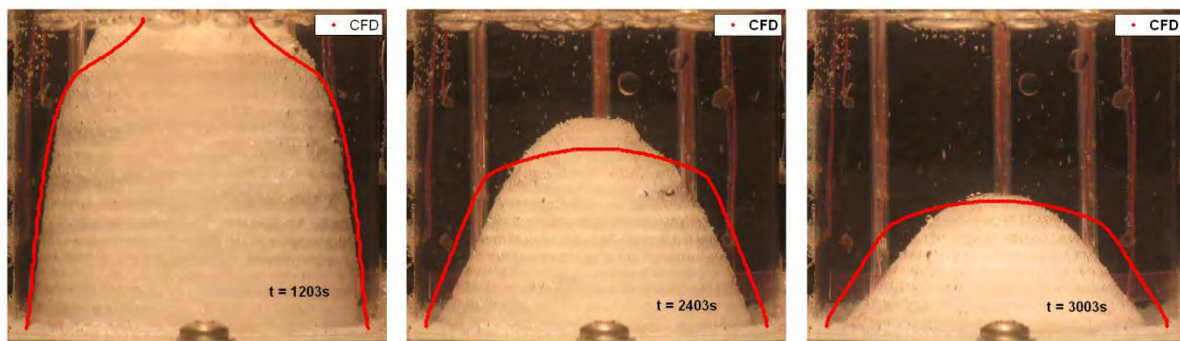


FIGURE 2. Melt front evolution.

Figure 3 illustrates streamlines and temperature contours obtained by the numerical model at the same times considered in Figure 2. Streamlines pattern allows to understand the role of natural convection in the liquid PCM: the molten liquid rises upward along the cylinder wall and the solid PCM, while the colder liquid moves downward along the solid PCM. Consequently a buoyancy driven vortex can be observed which moves downward as time passes. This fluid-dynamics structures promotes the PCM melting since it enhances the heat transfer between the hot wall and the solid-liquid interface; thus natural convection plays a major role in the system here considered. Furthermore, from the streamlines distribution is also possible to observe that buoyancy is not particularly marked where liquid PCM has already reached the axis of the cylinder. In absence of natural convection the melting process is controlled by thermal-diffusion. As a consequence, at early stages of the melting process temperature contours are more aligned with the x -axis. This is more evident in the lower part of the cylinder where natural convection is less relevant.

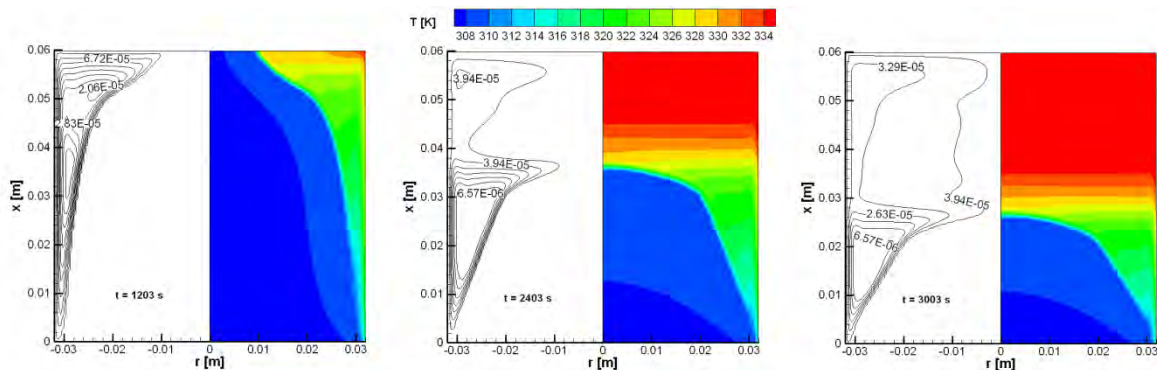


FIGURE 3. Streamlines and temperature contours.

As the buoyancy starts to affect the melting process, thermal stratification can be noticed. Vertical temperature gradients are observed in the proximity of the region where the vortex is located. Where PCM melting is complete, further energy is stored as sensible heat. Consequently liquid PCM temperature raises up to wall temperature.

Time-dependent variations of computed temperature and the experimental results for three thermocouples are compared in Figure 4: good agreement is achieved in the details of the melting process. In each plot reported in Fig. 4 a sharp temperature increase can be observed at different time frames depending on the position considered. This phenomenon is due to the passage of the melting front through the thermocouple position. Some discrepancies can be observed in the bottom part of the cylinder (position B3), at this position the numerical prediction of melt front progression is slower compared to experimental data.

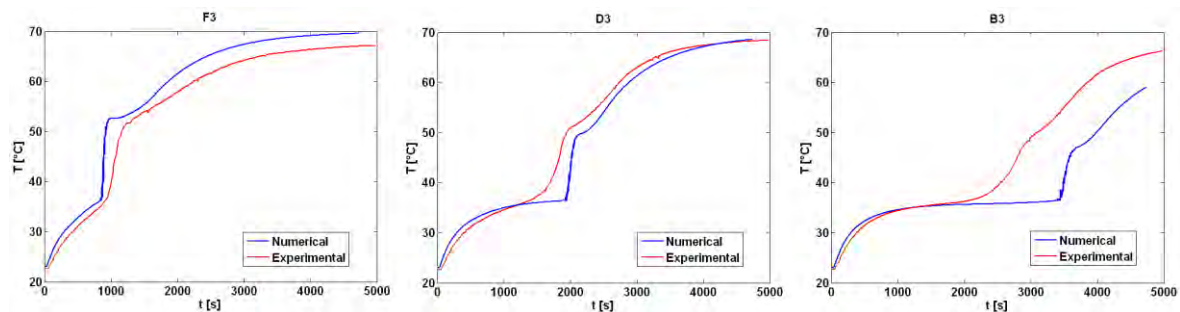


FIGURE 4. Comparison of computed and experimental temperatures inside the PCM.

4. CONCLUSIONS

In this paper the melting process occurring in a cylindrical enclosure is studied. A paraffin wax is considered as phase change material (PCM) and water acts as heat transfer fluid. The analysis is conducted by means of a 2D axial-symmetric CFD model. In particular buoyancy-driven fluid flow is fully solved within the PCM domain. Temperature and phase fields are also computed by means of the numerical model. The comparison between numerical results and experimental data available in literature reveals a good agreement. The results indicate that only very early stages of the charging process are dominated by conduction heat transfer. During the later stages, melting is affected significantly by natural convection. It can be concluded that the numerical modelling of latent heat storage systems should carefully take in account the effect of buoyancy in order to correctly predict system behaviour.

REFERENCES

- [1] Agyenim, F., Hewitt, N., Eames, P., Smyth, M. A review of materials, heat transfer and phase change problem formulation for latent heat thermal energy storage systems (LHTESS), *Renewable and sustainable Energy Reviews* 2010; 14: 615-628
- [2] Jones BJ, Sun B, Krishnan S, Garimella SV. Experimental and numerical investigation of melting in a cylinder. *International Journal of Heat and Mass Transfer* 2006; 49:2724-38.
- [3] Tan F.L., Hosseinizadeh S.F., Khodadadi J.M., Fan L. Experimental and computational study of constrained melting of phase change materials (PCM) inside a spherical capsule. *International Journal of Heat and Mass Transfer* 2009; 52:3464-3472.

HIGH PERFORMANCE COMPUTING UTILISING FULLY EXPLICIT AND SEMI-IMPLICIT CHARACTERISTIC BASED SPLIT (CBS) SCHEMES FOR SUBJECT-SPECIFIC MODELLING

Rhodri L.T. Bevan, Raoul van Loon and Perumal Nithiarasu

Civil and Computational Engineering Centre, Swansea University, SA2 8PP, UK,
R.Bevan@Swansea.ac.uk

ABSTRACT

In this work, we examine the potential advantages of the choice of a CBS scheme for patient-specific modelling. With a timely solution often sought, it is necessary to consider both the computational implementation and accuracy trade off of each scheme. From the initial results, it is clear that the semi-implicit scheme can produce solutions at a marginally greater accuracy in a significantly reduced (7x) time

Key Words: *Parallelisation, Computational Fluid Dynamics, CBS, Domain Decomposition.*

1. INTRODUCTION

Patient-specific modelling is a complex and time consuming operation. When investigating problems such as atherosclerosis, it is however necessary in order to deliver the pertinent wall shear stress field. Thus, the scheme employed for modelling the blood flow must deliver a timely solution. Recent work [1] has utilised the explicit scheme due to the ease and efficiency of parallelisation.

The characteristic based split (CBS) schemes employed in this work has become well established in the field [2]. Although the schemes have been previously compared in two dimensions [3], this work is intended to assess the three dimensional behaviours of the relevant scheme, assessing both accuracy and computational runtime in benchmark problems, before application to a patient-specific problem. The scalability of the two schemes in parallelisation is also contrasted for an identically subdivided domain.

2. NUMERICAL SCHEMES

The CBS approach adopted in this work, starts with a solution to an intermediate velocity field. This intermediate velocity field is then corrected, once the pressure field is obtained from a pressure (continuity) equation. It is in the determination of the pressure field that the semi-implicit and explicit approaches differ. In the explicit scheme, the concept of artificial compressibility (AC) is introduced [4] along with local timestepping as an iterative mechanism. To recover transient solutions in this approach, a dual time-stepping technique must be employed.

2.1 Semi-implicit CBS scheme

Ignoring third and higher order terms, the three steps of the CBS scheme are defined respectively as

$$u_i^\dagger = u_i^n - \Delta t \left(\frac{\partial u_j u_i}{\partial x_j} \right)^n + \Delta t \frac{\partial}{\partial x_j} \left(\frac{1}{Re} \frac{\partial u_i}{\partial x_j} \right)^n + \frac{\Delta t^2}{2} u_k \frac{\partial}{\partial x_k} \left(\frac{\partial u_j u_i}{\partial x_j} \right)^n \quad (1)$$

$$0 = \frac{\partial}{\partial x_i} \left(u_i^\dagger - \Delta t \left(\frac{\partial p}{\partial x_i} \right)^{n+1} \right) \quad (2)$$

$$u_i^{n+1} = u_i - \Delta t \left(\frac{\partial p}{\partial x_i} \right)^{n+1} + \frac{\Delta t^2}{2} u_k \frac{\partial}{\partial x_k} \left(\frac{\partial p}{\partial x_i} \right)^n \quad (3)$$

A numerical solution to the second step of the semi-implicit scheme is determined using a preconditioned conjugate gradient solver.

2.2 Explicit CBS-AC scheme

The three steps for the explicit approach are given below. As can be seen, the first step is identical in both cases, however with the use of a dual timestepping mechanism, the third step includes an additional component.

$$u_i^\dagger = u_i^n - \Delta t \left(\frac{\partial u_j u_i}{\partial x_j} \right)^n + \Delta t \frac{\partial}{\partial x_j} \left(\frac{1}{Re} \frac{\partial u_i}{\partial x_j} \right)^n + \frac{\Delta t^2}{2} u_k \frac{\partial}{\partial x_k} \left(\frac{\partial u_j u_i}{\partial x_j} \right)^n \quad (4)$$

$$p^{n+1} = p^n - \beta^2 \Delta t \rho \frac{\partial}{\partial x_i} \left(u_i^\dagger - \Delta t \left(\frac{\partial p}{\partial x_i} \right)^n \right) \quad (5)$$

$$u_i^{n+1} = u_i - \Delta t \left(\frac{\partial p}{\partial x_i} \right)^n + \frac{\Delta t^2}{2} u_k \frac{\partial}{\partial x_k} \left(\frac{\partial p}{\partial x_i} \right)^n - \frac{\Delta \mathbf{U}_i^\tau}{\Delta \tau} \quad (6)$$

where $\Delta \tau$ is the real time step. $\Delta \mathbf{U}_i^\tau$ can be calculated using the backward differentiation formulae (BDF). For a 3rd order BFD, this is

$$\Delta \mathbf{U}_i^\tau = \frac{11\mathbf{U}_i^n - 18\mathbf{U}_i^{m-1} + 9\mathbf{U}_i^{m-2} - 2\mathbf{U}_i^{m-3}}{6} \quad (7)$$

In the above equation the nth term denotes the solution from the previous pseudo time step and mth term denotes the solution from the respective mth real time level. Due to its implicit nature, no time step restrictions are placed on the real time step.

2.3 Time step calculation

In both schemes, the time step employed is subject to time step limitations. In the semi-implicit scheme, a global time step value must be determined. In both cases, however, it is first necessary to compute the local time step. The local time step is determined using

$$\Delta t = \min(\Delta t_c, \Delta t_d) \quad (8)$$

where the diffusive component is defined as

$$\Delta t_d = \frac{h^2 Re}{2} \quad (9)$$

where the convective component of the local time step is defined as

$$\Delta t_c = \frac{h}{\max(\sqrt{u_i u_i})} \quad (10)$$

for the semi-implicit scheme and

$$\Delta t_c = \frac{h}{\max(\sqrt{u_i u_i} + \beta)} \quad (11)$$

for the explicit approach. The element size h can either be determined using

$$h = \frac{3A_e}{L_{opp}} \quad (12)$$

where A_e is the area of the element and L_{opp} denotes the opposite edge length. An alternative method of calculating the local element size using the stream line direction can also be employed.

$$h = \frac{2}{\sum_{r=1}^{N_p} |\mathbf{S} \cdot \nabla \mathbf{N}_r|} \quad (13)$$

where N_p is the number of nodes within the element, r is a local node, \mathbf{S} is the unit vector in the direction of local velocity at node r and \mathbf{N}_r represents the shape function.

Whereas the explicit scheme utilises the local timestep as a means of accelerating convergence to a numerical solution, the semi-implicit scheme utilises the minimum value of the local time step as a global time step.

3. COMPUTATIONAL IMPLEMENTATION

The explicit CBS scheme requires no solution of simultaneous equations and as such is readily parallelisable. The Jacobi preconditioned conjugate gradient solver utilised in the semi-implicit scheme is also straightforward to parallelise. The computational codes were written in Fortran 90 and parallelisation was undertaken using MPI, with domain decomposition carried out prior to the CFD analysis. The parallel implementation, as mentioned, utilises MPI in a single program multiple data (SPMD) format. Only information on interface nodes is passed between processors when necessary, reducing delays due to data transfer. The implementation of both schemes demonstrates linear speedup as the number of processors increases.

4. NUMERICAL SIMULATION

A typical benchmark utilised to examine the accuracy and robustness of a scheme is the transient flow around a cylinder at $Re=100$ in 3D. Some selected results are shown in Figure (1) and further results will be discussed in the presentation. Shown in Figure (1a) is u_1 contours at the non-dimensional real time of 150 for the semi-implicit case. In Figure (1b) the vertical velocity component is shown for the exit midpoint downstream of the cylinder. From this, it is possible to calculate the Strouhal number. In the semi-implicit case the error in the Strouhal number was 4% (compared to experimental solution of 0.16667) and 6% in the explicit case. With further mesh

refinement these errors should decrease significantly. It is in the computational run times that the semi-implicit scheme stands out. The explicit computation took 7x longer to achieve a solution of less accuracy.

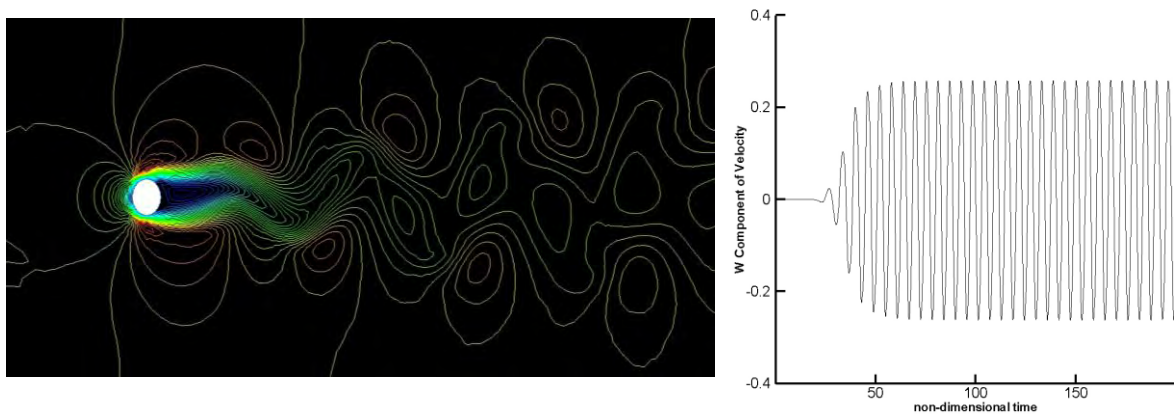


FIGURE 1. a) Horizontal Velocity Contours b) U_3 Velocity Component

5. CONCLUSIONS

This short paper outlines two alternative methods that can be parallelised in order to achieve timely solutions for biomedical problems. From initial results, the parallelised semi-implicit scheme has significant speed advantages over the explicit CBS scheme when running transient simulations. Work is ongoing in the analysis of further problems and model refinement.

REFERENCES

- [1] R.L.T. Bevan, P. Nithiarasu, R. Van Loon, I. Sazonov, H. Luckraz, and A. Garnham. Application of a locally conservative Galerkin (LCG) method for modelling blood flow through a patient-specific carotid bifurcation. *International Journal for Numerical Methods in Fluids*, DOI: 10.1002/flid.2313.
- [2] P. Nithiarasu, R. Codina, and O.C. Zienkiewicz. The characteristic based split scheme - a unified approach to fluid dynamics. *International Journal for Numerical Methods in Engineering*, 66:1514-1546, 2006.
- [3] N.Massarotti, F. Arpino, R.W. Lewis, and P. Nithiarasu. Explicit and semi-implicit CBS procedures for incompressible viscous flows. *International Journal for Numerical Methods in Engineering*, 66:1618-1640, 2006.
- [4] P. Nithiarasu. An efficient artificial compressibility (AC) scheme based on the characteristic based split (CBS) method for incompressible flows. *International Journal for Numerical Methods in Engineering*, 56:1815-1845, 2003.

ON THE SMALL-SCALE ANOMALIES IN THE SCALAR FIELD IN HOMOGENEOUS AND ISOTROPIC TURBULENCE

Ivan Langella¹, Carlo Scalo², Giuseppe de Felice³, Carlo Meola⁴

Università degli studi di Napoli - Federico II, Piazzale Tecchio, Naples, Italy^{1,3,4},
ivanlang87@gmail.com¹, giudedefel@unina.it³, cmeola@unina.it⁴

Queen's University, 130 Stuart St., Kingston, Canada, cscalo.ca@gmail.com²

ABSTRACT

In this work we use data from Direct Numerical Simulations (DNS) of a passive scalar field in forced homogenous and isotropic turbulence to gain some insight on the origin of intermittency. The Navier-Stokes (NS) and passive scalar conservation equation are solved in a L^3 -periodic box with a classic pseudo-spectral approach implemented in MATLAB, exploiting the efficiency of the latest FFTW libraries and multithreading capabilities. The code has been extensively validated against several numerical and experimental results available in literature. Our analysis will focus on the case of a unitary Schmidt number scalar in a turbulent flow for $Re_\nu = 50$ and $Re_\nu = 70$, respectively solved with 96^3 and 128^3 grid points. Classic results regarding inertial-range intermittency are reproduced such as non-Gaussian behaviour of passive scalar statistics, loss of local isotropy, multi-fractal scaling of scalar structure functions. Also, a preliminary Lagrangian analysis, used to test the classical theories of Taylor and Richardson, reveals disagreement only in the dissipation range (small-scales anomalies). A new interpretation of intermittency is proposed here based on the loss of regularity of the evolution equation of the scalar gradient; the unboundedness of the scalar gradient magnitude is not ruled out by the mathematical properties of the scalar conservation equation.

Key Words: *Scalar transport, Intermittency, Isotropic turbulence.*

1. INTRODUCTION

Recent progress in the field of the passive scalar has shown that, when it is introduced into a sustained turbulent field, the classical return-to-isotropy model suggested by the Kolmogorov-Obukhov-Corrsin (KOC) theory breaks down for a wide range of Reynolds numbers [1]. The evolution of the scalar concentration field, θ , is governed by well-known conservation laws yielding a linear PDE in θ . In spite of the linearity of such equation, when the transporting velocity field is turbulent, isosurfaces of scalar concentration stretch and fold decreasing the contribution of the large scales to the scalar variance, progressively transferring it to smaller scales [2]. In this process the scalar gradients can grow (despite the monotonicity of the scalar conservation equation) and local discontinuities can arise in the gradient field, influencing the passive scalar phenomenology. Kraichnan (1994, [3]) has shown that even when the velocity field is strictly Gaussian (non-intermittent and statistically self-similar), the transported passive scalar field exhibits several anomalies including loss of isotropy at the smallest scales and inertial range intermittency. These features are visible both in statistical quantities such as skewness and kurtosis, and in instantaneous events. The loss of local isotropy is testified by the presence of order-one derivative skewness (in the scalar field), ramp-cliff structures in the passive scalar signals and large fronts separating sharply 'hot' and 'cold' regions as well as sub-linear scaling of the high-order structure functions exponents. Exponential tails in the passive scalar gradients and passive scalar differences PDFs (present both in the dissipation and inertial range), independently of the velocity field probabilistic structure, are also a signature of this phenomenon.

2. MAIN BODY

The aim of the present work is exploiting numerical simulations (as well as theoretical results for a the governing PDEs) in order to assess whether the NS equations in their incompressible form are a suitable model to study intermittency effects. The *possible* presence of discontinuities in a turbulent flow may threaten the regularity of the solution. However, these irregularities are not contemplated by the incompressible model. Also, being the passive scalar dynamics driven by the velocity field, we investigate if the monotonicity property is still satisfied. In the limit of zero diffusivity, by re-writing the passive scalar conservation equation in the Lagrangian form, we show that monotonicity is verified, as each particle transports the same (constant) value. However, if turbulent mixing is present, no one can guarantee that particles transporting very different values can end up, at a certain time, one next to the other. In such a case, even if the transport equation seems rather straightforward to manage, we should question the derivability of such equation. We therefore suggest to search for entropic equations which allow us to asses rigorously the limits of the mathematical model in spite of the obvious phenomenology. In the first step of this analysis we shall consider the governing equation for the scalar gradient magnitude:

$$\frac{Dg^2}{Dt} + \boxed{2g \cdot (\nabla u)^S \cdot g} = 2\alpha \nabla \cdot [g \cdot (\nabla g)^S] - 2\alpha \nabla g : (\nabla g)^S, \quad g = \nabla \theta$$

As we can see, even if the passive scalar energy must decay in time, the scalar gradient can still sustain itself due to the additional term, indicated with a box on the left-hand side. This term could cause local discontinuities in the passive scalar gradient field, which can alter the structure of the passive scalar field itself generating intermittency phenomena and therefore is responsible of the non-Gaussianity of the passive scalar gradient PDFs.

We developed a Matlab code in order to verify these speculations in the framework of the classic turbulence modelling via the incompressible NS model. Our numerical model is based on a 3D pseudo-spectral approach, implemented in MATLAB in a triply-periodic box. A linear forcing term (i.e. a mean gradient in the x_1 direction with β and B as the constant mean gradient intensity for the scalar and velocity field, respectively) has been added on the right-hand side of the momentum equations, solved for the velocity fluctuations only. Non-linear terms are treated with the 3/2 de-aliasing rule. Initial conditions are pseudo-randomly generated in the spectral space satisfying the divergence-free constraint; the linear forcing guarantees that the stationary state is independent of the initial condition [4]. Time-advancement scheme is a *fractional step* method with a third-order, memory-saving RK for the prediction step.

3. RESULTS

All statistics have been extracted in a statistically steady time range of 80 turnover times for both simulations. The initial parameters are presented in Table 1.

N^3	L	ν	Sc	B	β	CFL
96^3	2π	$2.8 \cdot 10^{-3}$	1	0.1333	-0.1333	0.3
128^3	2π	$1.272 \cdot 10^{-2}$	1	1	-1	0.3

TABLE 1. Simulation parameters

The same parameters have been used for both the velocity and the scalar field so that the respective equations are identical except for the pressure gradient term. This will allow to isolate the intrinsic differences of the two fields. Only the most relevant results are shown here.

First of all, strong non-Gaussian behaviours are present in time and space derivatives of θ and u_i , as visible in the exponential tails of PDFs in Figure 1. In particular, we notice that the passive scalar exhibits a more intermittent behaviour in both simulations, and that intermittency effects increase with the Reynolds number. On the other hand, PDFs of θ and u_i appear perfectly Gaussian (not shown), and this supports our hypothesis that non-Gaussian behaviours in the gradient field are due to the additional term appearing in scalar gradient equation.

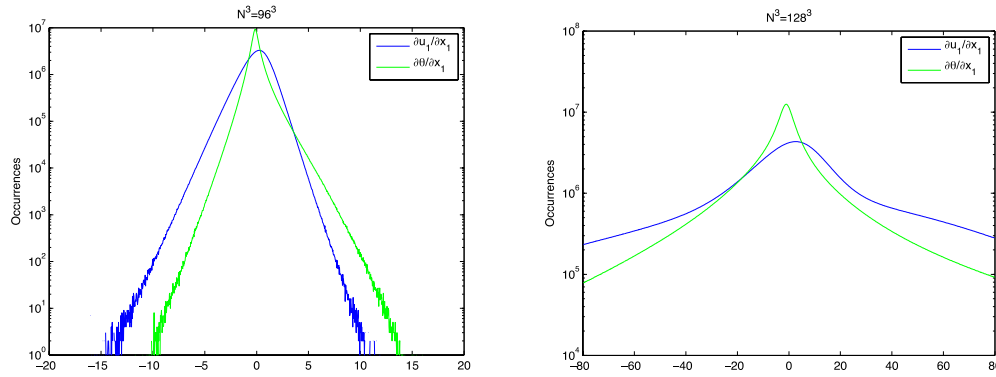


FIGURE 1. PDFs of space derivatives

Intermittency effects extend also in the inertial ranges, despite the rather low Reynolds numbers investigated here. These are evident in the PDF of the scalar differences (not shown). At small scales non-Gaussian behaviours are prevalent, and there is a fast tendency towards Gaussianity as for larger scales. This result is consistent with the calculated scalar intermittency exponents (not shown) for these cases that are slightly lower than values present in literature (that, however, refer to much higher Reynolds numbers).

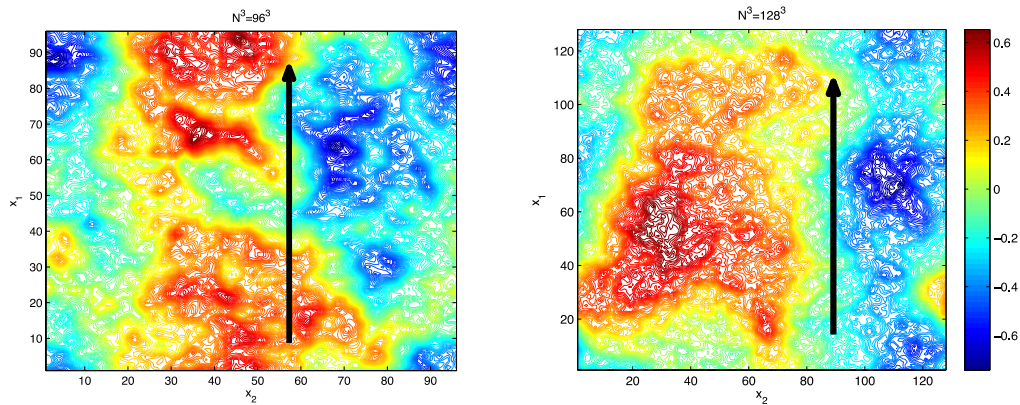


FIGURE 2. ‘Hot-cold’ fronts aligning along the mean gradient direction (arrows direction)

Loss of isotropy at small scales is also evident. Statistics at small scales depend in fact on the particular direction, as the passive scalar derivative skewness is of order one along the mean gradient direction and of order Re_τ^{-1} (KOC theory) along the orthogonal directions. Indeed, we have found a scalar derivative skewness of 1.5 in the $N=96^3$ simulation, and 1.4 in the $N=128^3$ simulation. Another proof of small-scale anisotropy is given by presence of ‘hot-cold’ fronts which originate in the passive scalar field along the mean gradient direction. In Figure 2 an isocontour of the mean field is reported, and we see that the front becomes more marked as Reynolds number increases.

Moreover, our results are in good agreement with literature for what concerns the anomalous scaling. Skewness of the scalar differences function tends to a plateau of order one at small scales, while the kurtosis of the same function tends to the Gaussian value of 3 only at large scales (not shown). Moreover, plotting the scaling exponents V_n in function of the order n we see perfect agreement with results in figure 11 of [1].

Finally, a preliminary Lagrangian analysis has been carried out to compare our predictions with the theories of Taylor for the diffusion of a single particle and Richardson for the diffusion of two particles [4]. The paths of 50 particles have been analyzed with starting positions inside a sphere of a radius corresponding to half the Kolmogorov length scale. Our results are in good agreement for middle and large scales. However, at small scales, our results differ a lot from prediction of Richardson theory, as we can see in Figure 3. We speculate that this is the result of existing anomalies at small scales, but more accurate simulations and at higher Reynolds are needed to assess this.

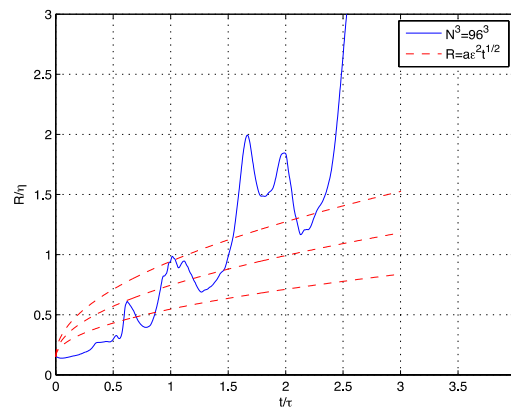


FIGURE 3. Relative distances covered by particles at small scales. Dotted lines represent Richardson theory predictions for $a=1$, $a=1.5$ and $a=2$.

4. CONCLUSIONS

We have performed a study on intermittency effects with DNS of a unitary-Schmidt-number scalar in a turbulent flow for $Re_\eta = 50$ and $Re_\eta = 70$. Classic results regarding inertial-range intermittency are reproduced such as non-Gaussian behaviour of passive scalar statistics, loss of local isotropy, multi-fractal scaling of scalar structure functions. A new approach is proposed here based on the interpretation of intermittency in terms of loss of regularity, at smallest scales, of the evolution equation of the scalar gradient. We designate, as a successful pathline to follow, the analysis of the boundedness properties of the scalar gradient transport equation which shows different regularity properties than the scalar concentration equation itself, from which it originates.

REFERENCES

- [1] Z. Warhaft, Passive scalars in turbulent flows, *Annu. Rev. Fluid Mech.*, 32, 203-240, 2000.
- [2] A. N. Kolmogorov, Dissipation of energy in locally isotropic turbulence, *Dokl. Akad. Nauk SSSR*, 32, 19-21, 1941.
- [3] R. H. Kraichnan, Anomalous scaling of a randomly advected passive scalar, *Physical Review Letters*, 72, 1016-1019, 1994.
- [4] C. Rosales and C. Meneveau, Linear forcing in numerical simulations of isotropic turbulence: Physical space implementations and convergence properties, *Physics of fluids*, 17, 095106, 2005.

A ROBUST ARTIFICIAL COMPRESSIBILITY ALGORITHM FOR TURBULENT INCOMPRESSIBLE FLOWS IN URBAN AREAS

F. Arpino, G. Buonanno, M. Scungio

Department of Mechanics, Structures and Environment (DiMSAT), University of Cassino, Via G. Di Biasio 43, 03043 Cassino (FR), Italy. E-mail: f.arpino@unicas.it, buonanno@unicas.it, m.scungio@unicas.it

N. Massarotti, A. Mauro

Department for Technologies (DiT), University of Napoli "Parthenope", Isola C4, Centro Direzionale di Napoli, 80143 Napoli, Italy. E-mail: nicola.massarotti@uniparthenope.it, alessandro.mauro@uniparthenope.it

ABSTRACT

In the present paper the results of the Artificial Compressibility version of the Characteristic Based Split algorithm (AC-CBS) and the one equation Spalart-Allmaras (SA) turbulence model are presented for incompressible turbulent flows. The proposed model has been employed for the simulation of a turbulent flow in a street-canyon. The one-equation SA model is expected to be advantageous in term of CPU time, if compared to the commonly employed two-equation turbulence models for the simulation of complex three-dimensional turbulent flows in urban areas.

Key Words: *Fully explicit, Finite Elements, Vortex.*

1. INTRODUCTION

Microscale Computational Fluid Dynamics (CFD) models have become an efficient simulation tool for many engineering applications. In the last period air quality prediction in indoor environments and urban areas has become of great interest. In fact, traffic pollution in urban areas represents the major concern for public health, since emissions from non-traffic sources have been constantly reduced [1]. Especially in low ventilation areas, human activities led to pollution levels much higher than the admissible limits. Also, it has to be considered that even for relatively high ambient wind conditions the building aggregates represent artificial obstacles to the wind flow, causing stagnant conditions in the city. A typical configuration is the so-called street canyon, formed along a street in densely built urban areas [2]. The turbulent behaviour of the flow requires an adequate turbulence model to be coupled to the mass, momentum and energy conservation equations. Despite considerable progress in the last century in understanding turbulence behaviour in both compressible and incompressible flows, still a significant research activity is needed since many aspects of the problem are supposed to remain unresolved for the foreseeable future [3].

Over the last years, CFD using Reynolds Averaged Navier-Stokes (RANS) have become a standard simulation tool for the investigation of atmospheric flow and pollutant dispersion, and one of the most used turbulence model is the well known two equations κ - ε model. In the present paper, the one equation Spalart-Allmaras (SA) model is proposed for the solution of a two-dimensional street-canyon problem. The governing equations are solved fully explicitly by employing the Artificial Compressibility (AC) Characteristic Based Split (CBS) algorithm [4]. All the terms of the partial differential equations have been stabilized on the basis of a order of magnitude analysis [4]. The obtained results have been compared to the experimental and numerical data available in the literature and the proposed model has been proven to be robust and reliable. The analysis of different RANS models characteristic does not represent the objective of this paper. The use of a

one-equation model is expected to be advantageous in terms of computational requirements when complex three-dimensional problems are investigated.

2. GOVERNING EQUATIONS

In the present paper, incompressible viscous flow of a single phase fluid in forced convection turbulent regime is mathematically described through the RANS equations of motion, written in the follows in conservative non-dimensional form.

Mean-continuity

$$\frac{1}{\beta^2} \frac{\partial \bar{p}}{\partial t} + \rho \frac{\partial \bar{u}_i}{\partial x_i} = 0 \quad (1)$$

Mean-momentum

$$\frac{\partial \bar{u}_i}{\partial t} + \frac{\partial (\bar{u}_i \bar{u}_j)}{\partial x_j} + \frac{\partial \bar{p}}{\partial x_i} = \frac{\partial}{\partial x_j} \left[\left(\frac{1 + \nu_T}{\text{Re}} \right) \left(\frac{\partial \bar{u}_i}{\partial x_j} + \frac{\partial \bar{u}_j}{\partial x_i} - \frac{2}{3} \frac{\partial \bar{u}_k}{\partial x_k} \delta_{ij} \right) \right] \quad (2)$$

Spalart-Allmaras (SA) scalar equation

$$\frac{\partial \hat{v}}{\partial t} + \frac{\partial (\bar{u}_j \hat{v})}{\partial x_j} = c_{b1} \hat{S} \hat{v} + \frac{1}{\text{Re} \sigma} \frac{\partial}{\partial x_i} \left[(1 + \hat{v}) \frac{\partial \hat{v}}{\partial x_i} \right] + \frac{c_{b2}}{\text{Re} \sigma} \left(\frac{\partial \hat{v}}{\partial x_i} \right)^2 - \frac{c_{w1} f_w}{\text{Re}} \left(\frac{\hat{v}}{y} \right)^2 \quad (3)$$

Where \bar{u}_i is the averaged velocity, \bar{p} is the pressure, Re represents the Reynolds number and ν_T is the turbulent eddy viscosity. The scales and parameters used to derive the above non-dimensional equations and the constants of the SA model are available in the literature [3].

3. THE NUMERICAL PROCEDURE

The set of Partial Differential Equations (PDEs) presented in the previous section has been solved numerically by using the Artificial Compressibility Characteristic Based Split (AC-CBS) algorithm, which is based on the temporal discretization along characteristics, and spatial discretization procedure based on standard Galerkin. The core of the algorithm is based on three successive steps that are well described in the literature [3-5]. In addition to the basic AC-CBS steps, a fourth step is here added to explicitly solve the SA scalar equation at each time step. The required stability is achieved deriving the time-step limit for each term of the SA equation on the basis of an order of magnitude analysis [4].

3. RESULTS

Turbulent flow past a backward facing step

The correctness of the obtained results has been proved by comparison with the numerical and experimental data available in the literature. One standard test case is the turbulent flow past a Backward Facing Step (BFS). The computational domain and the boundary conditions employed for the simulations are available in Figure 1(a). The simulations have been performed using an unstructured grid composed by 33726 triangular elements, refined in correspondence of the solid walls. All the domain dimensions are normalized with respect to the step height. The velocity profile at the inlet section, located at a distance of four times the step height from the step itself, is obtained from experimental data from Denham et al. [6]. For the Spalart-Allmaras model a fixed value of 0.05 of the eddy viscosity is prescribed at the inlet section, while the scalar turbulent variable is set to zero on the walls. The velocity field obtained for Re=3025 is available in Figure 1(b), while the velocity profiles at a distance of two and four times the step height from the step are

reported in Figure 2, compared to the experimental data form Denham et al. [6], showing a good agreement with the experiments.

Two dimensional simulation of a street-canyon

The term "Street Canyon" (SC) refers to a relatively narrow street with buildings along both sides. The dimensions of a street canyon are usually expressed by its aspect ratio H/W , where H is the

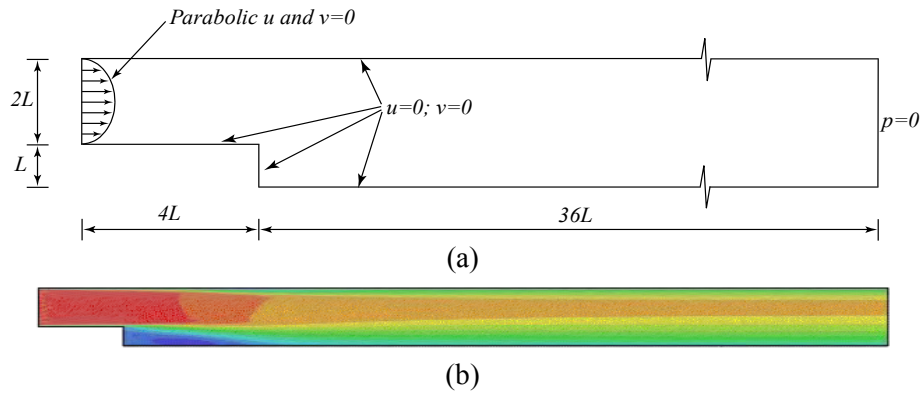


FIGURE 1. Turbulent flow over a BFS: (a) problem definition; (b) x-velocity contours. $Re=3025$.

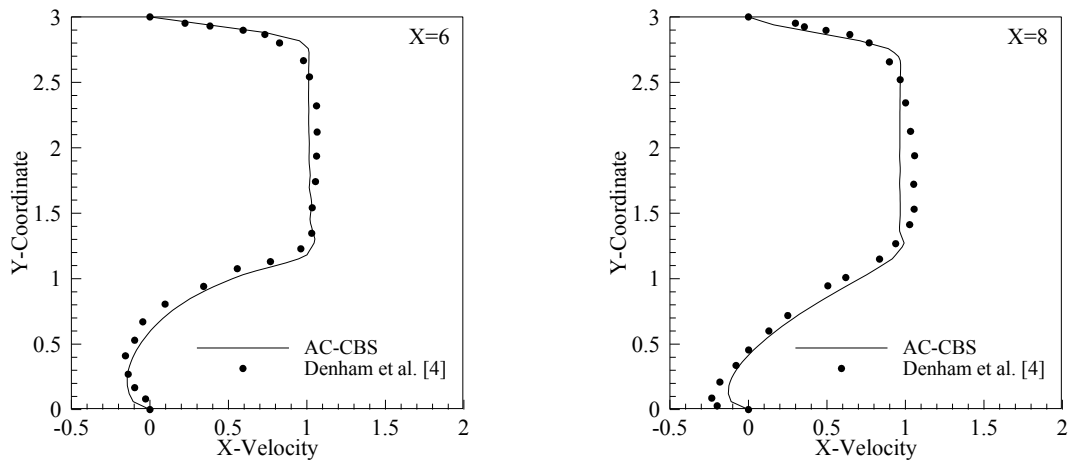


FIGURE 2. Turbulent flow over a BFS: velocity profiles compared to experiments. $Re=3025$.

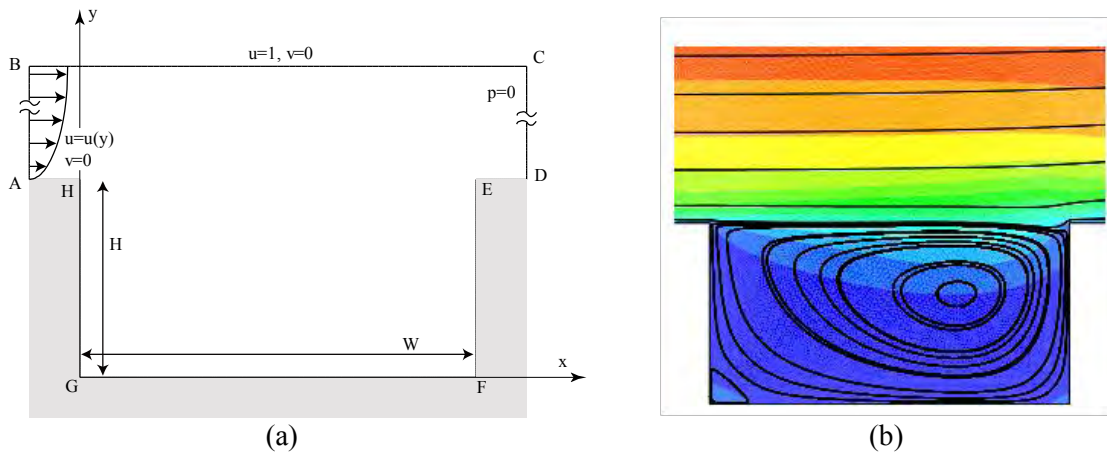


FIGURE 3. Turbulent flow in a SC: (a) problem definition and boundary conditions; (b) x-velocity field and streamlines. $Re=50000$.

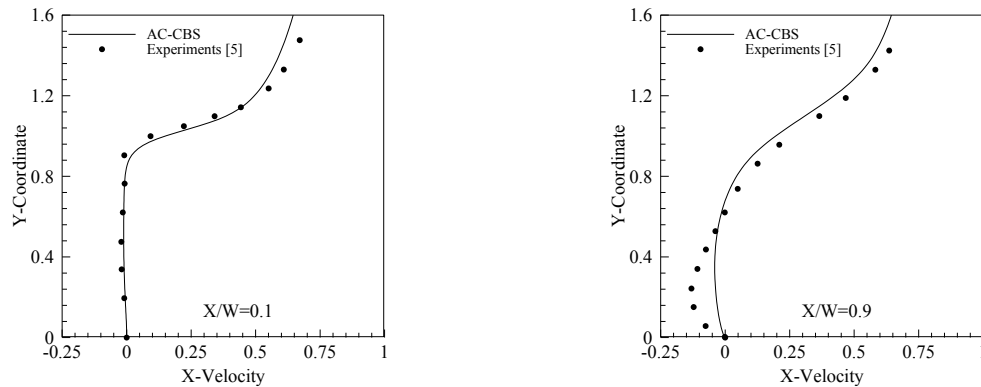


FIGURE 4. Turbulent flow in a SC: x- velocity profiles compared to experiments. $Re=50000$.

height of the canyon and W is its width. In this paper a street canyon with an aspect ratio equals to 0.5 has been considered. The computational domain and the boundary conditions employed are available in Figure 3(a). A known velocity profile obtained from experiments [7] has been imposed at the "AB" section. An horizontal velocity equal to 1 is imposed to the "BC" side, while no slip condition has been assumed for the "DEFGHA" boundary. The simulations have been performed for a Reynolds number, referred to the H dimension, equals to 50000. The horizontal velocity field and the streamlines are reported in Figure 3(b), while the horizontal velocity profiles compared to the experiments [7] are available in Figure 4. From the obtained results, it is evident that the proposed model is able to reasonably predict the velocity field in a street canyon, offering the advantage of a lower computational cost, referred to the commonly used two-equations models.

4. CONCLUSIONS

In the present paper the performance of the Artificial Compressibility version of the Characteristic Based Split algorithm (AC-CBS) and the one-equation Spalart-Allmaras (SA) model are investigated for turbulent incompressible flows. The results are in good agreement with the experiments from the literature. The use of the SA model is expected to significantly reduce the CPU time for complex 3D problems, compared to the commonly employed two-equations models.

REFERENCES

- [1] G. Buonanno, F.C. Fuoco, and L. Stabile, Influential parameters on particle exposure of pedestrians in urban microenvironments, *Atmospheric Environment*, 45, 1434-1443, 2011.
- [2] S. Vardoulakis, B.E.A. Fisher, K. Pericleous, and N. Gonzalez-Flesca, Modelling air quality in street canyons: a review, *Atmospheric Environment*, 37, 155-182, 2003.
- [3] P. Nithiarasu, C.-B. Liu, and N. Massarotti, Laminar and turbulent flow calculations through a model human upper airway using unstructured meshes, *Communications in Numerical Methods in Engineering*, 23, 1057-1069, 2007.
- [4] F. Arpino, N. Massarotti, and A. Mauro, High Rayleigh Number Laminar-Free Convection in Cavities: New Benchmark Solutions, *Numerical Heat Transfer, Part B: Fundamentals*, 58(2), 73-97, 2010.
- [5] N. Massarotti, F. Arpino, R.W. Lewis, and P. Nithiarasu, Explicit and semi-implicit CBS procedures for incompressible viscous flows, *International Journal For Numerical Methods In Engineering*, 66, 1618-1640, 2006.
- [6] M.K. Denham, P. Briard, and M.A. Patrick, A directionally-sensitive laser anemometer for velocity measurements in highly turbulent flows, *Journal of Physics E: Scientific Instruments*, 8, 681-683, 1975.
- [7] P. Sahm, P. Louka, M. Ketzler, E. Guilloteau, and J.-F. Sini, Intercomparison of numerical urban dispersion models - part I: street canyon and single building configurations, *Water, Air, and Soil Pollution: Focus*, 2, 587-601, 2002.

TURBULENT REACTING FLOW IN RADIAL POROUS COMBUSTORS

Marcelo J.S. de Lemos

Departamento de Energia - IEME
 Instituto Tecnológico de Aeronáutica - ITA
 12228-900 - São José dos Campos - SP - Brazil
 Fellow ASME, E-mail: delemos@ita.br

ABSTRACT

This paper presents two-dimensional numerical simulations of combustion of an air/methane mixture in porous materials using a mathematical model that explicitly considers the intra-pore levels of turbulent kinetic energy. Transport equations are written in their time-and-volume averaged form and a volume-based statistical turbulence model is applied to simulate turbulence generation due to the porous matrix. A cylindrical porous combustor is analyzed, in which the mixture flows inside it in the axial direction, being the flue gases ejected through the lateral surface. Combustion is modelled via a unique simple closure. For high excess air, the flame front moves towards the lateral exit of the burner. Also, increasing the inlet flow rate for stoichiometric mixture pushes the flame out of the porous material.

Key Words: *Porous Media, Turbulent Combustion.*

1. INTRODUCTION

The advantages of having a combustion process inside an inert porous matrix are today well documented in the literature [1-8], including a recent review on lean-combustion porous burners [9]. Hsu *et al* (1993) [10] points out some of its benefits including higher burning speed and volumetric energy release rates, higher combustion stability and the ability to burn gases of a low energy content. Driven by this motivation, the effects on porous ceramics inserts have been investigated in Peard *et al* (1993) [11], among others.

Turbulence modeling of combustion within inert porous media has been conducted by Lim & Matthews (1993) [12] on the basis of an extension of the standard $k-\varepsilon$ model of Jones & Launder (1972) [13]. Work on direct simulation of premixed flames, for the case when the porous dimension is of the order of the flame thickness, has also been reported in Sahraoui & Kaviany (1995) [14].

The objective of this paper is to present a mathematical model for simulation of reacting flows in porous materials.

2. MATHEMATICAL MODEL

The fundamentals of the mathematical model used here is presented in detail in the open literature [15], and for that only the basic equations are presented next. They read:

$$\nabla \cdot \rho \bar{\mathbf{u}}_D = 0 \quad (1)$$

where, $\bar{\mathbf{u}}_D$ is the average surface velocity (also known as seepage, superficial, filter or Darcy velocity) and ρ is the fluid density. Equation (1) represents the macroscopic continuity equation for the gas phase.

$$\nabla \cdot \left(\rho \frac{\bar{\mathbf{u}}_D \bar{\mathbf{u}}_D}{\phi} \right) = -\nabla \cdot (\phi \langle \bar{p} \rangle^i) + \mu \nabla^2 \bar{\mathbf{u}}_D + \nabla \cdot \left(-\rho \phi \langle \bar{\mathbf{u}}' \mathbf{u}' \rangle^i \right) + \phi \rho \mathbf{g} - \left[\frac{\mu \phi}{K} \bar{\mathbf{u}}_D + \frac{c_F \phi \rho \bar{\mathbf{u}}_D / \bar{\mathbf{u}}_D}{\sqrt{K}} \right] \quad (2)$$

where the last two terms in equation (2), represent the Darcy and Forchheimer contributions. The symbol K is the porous medium permeability, $c_F = 0.55$ is the form drag coefficient, $\langle p \rangle^i$ is the intrinsic (fluid phase averaged) pressure of the fluid, μ represents the fluid viscosity and ϕ is the porosity of the porous medium.

Turbulence is handled via a macroscopic $k - \varepsilon$ model given by,

$$\nabla \cdot (\rho \bar{\mathbf{u}}_D \langle k \rangle^i) = \nabla \cdot \left[\left(\mu + \frac{\mu_{t\phi}}{\sigma_k} \right) \nabla (\phi \langle k \rangle^i) \right] - \rho \langle \bar{\mathbf{u}}' \mathbf{u}' \rangle^i : \nabla \bar{\mathbf{u}}_D + c_k \rho \frac{\phi \langle k \rangle^i |\bar{\mathbf{u}}_D|}{\sqrt{K}} - \rho \phi \langle \varepsilon \rangle^i \quad (3)$$

$$\begin{aligned} \nabla \cdot (\rho \bar{\mathbf{u}}_D \langle \varepsilon \rangle^i) = & \nabla \cdot \left[\left(\mu + \frac{\mu_{t\phi}}{\sigma_\varepsilon} \right) \nabla (\phi \langle \varepsilon \rangle^i) \right] + c_1 \left(-\rho \langle \bar{\mathbf{u}}' \mathbf{u}' \rangle^i : \nabla \bar{\mathbf{u}}_D \right) \frac{\langle \varepsilon \rangle^i}{\langle k \rangle^i} \\ & + c_2 c_k \rho \frac{\phi \langle \varepsilon \rangle^i |\bar{\mathbf{u}}_D|}{\sqrt{K}} - c_2 \rho \phi \frac{\langle \varepsilon \rangle^i}{\langle k \rangle^i} \end{aligned} \quad (4)$$

Gas energy:

$$(\rho c_p)_f \nabla \cdot (\mathbf{u}_D \langle \bar{T}_f \rangle^i) = \nabla \cdot \{ \mathbf{K}_{eff,f} \cdot \nabla \langle \bar{T}_f \rangle^i \} + h_i a_i (\langle \bar{T}_s \rangle^i - \langle \bar{T}_f \rangle^i) + \phi \Delta H S_{fu}, \quad (5)$$

Solid energy:

$$0 = \nabla \cdot \{ \mathbf{K}_{eff,s} \cdot \nabla \langle \bar{T}_s \rangle^i \} - h_i a_i (\langle \bar{T}_s \rangle^i - \langle \bar{T}_f \rangle^i), \quad (6)$$

where, $a_i = A_i / \Delta V$ is the interfacial area per unit volume, h_i is the film coefficient for interfacial transport, $\mathbf{K}_{eff,f}$ and $\mathbf{K}_{eff,s}$ are the effective conductivity tensors for fluid and solid, respectively

Transport equation for the fuel reads,

$$\nabla \cdot (\bar{\mathbf{u}}_D \langle \bar{m}_{fu} \rangle^i) = \nabla \cdot \mathbf{D}_{eff} \cdot \nabla (\phi \langle \bar{m}_{fu} \rangle^i) - \phi S_{fu} \quad (7)$$

where $\langle \bar{m}_{fu} \rangle^i$ is the mass fraction for the fuel. The effective mass transport tensor, \mathbf{D}_{eff} , is defined as:

$$\mathbf{D}_{eff} = \underbrace{\mathbf{D}_{disp}}_{dispersion} + \underbrace{\mathbf{D}_{diff}}_{diffusion} + \underbrace{\mathbf{D}_t + \mathbf{D}_{disp,t}}_{turbulence} = \mathbf{D}_{disp} + \frac{1}{\rho} \left(\frac{\mu_\phi}{Sc_\ell} + \frac{\mu_{t\phi}}{Sc_{\ell,t}} \right) \mathbf{I} = \mathbf{D}_{disp} + \frac{1}{\rho} \left(\frac{\mu_{\phi,ef}}{Sc_{\ell,ef}} \right) \mathbf{I} \quad (8)$$

where Sc_ℓ and $Sc_{\ell,t}$ are the laminar and turbulent Schmidt numbers for species ℓ , respectively, and “*ef*” denotes an effective value. The dispersion tensor is defined such that,

$$-\rho \langle \bar{\mathbf{u}} \bar{m}_{fu} \rangle^i = \rho \mathbf{D}_{disp} \cdot \nabla \langle \bar{m}_{fu} \rangle^i \quad (9)$$

In this work, for simplicity, the chemical exothermic reaction is assumed to be instantaneous and to occur in a single step.

3. RESULTS

The problem here analyzed consists in simulating turbulent flow and thermal fields in a radial porous combustor, which is depicted in Figure 1a. The mixture of methane and air enters through a

central hole on the left side, of radius $r_i = 0.017m$, permeating in the radial direction across the ceramic material. The porous cylinder has length $L=0.1m$. At the outside radius, $R=0.05m$, flue gases leave the combustor where radiation heat flux is accounted for by considering the difference in temperature between the porous matrix and the environment.

Figure 1.b) shows the position of the heat generation rate for distinct inlet velocities and for a stoichiometric mixture, $\Psi=0$. In the text to follow, we assume that the heat generation rate is related to the flame location. One can see that the flame position moves towards the lateral exit as the inlet mass flow rate is increased. At very high rates ($u_{in}=75\text{ m/s}$), the flame opens up and unburnt gases leave the combustor. Also, as pressure builds up at the left plate, the flame starts to tilt at positions close to left side.

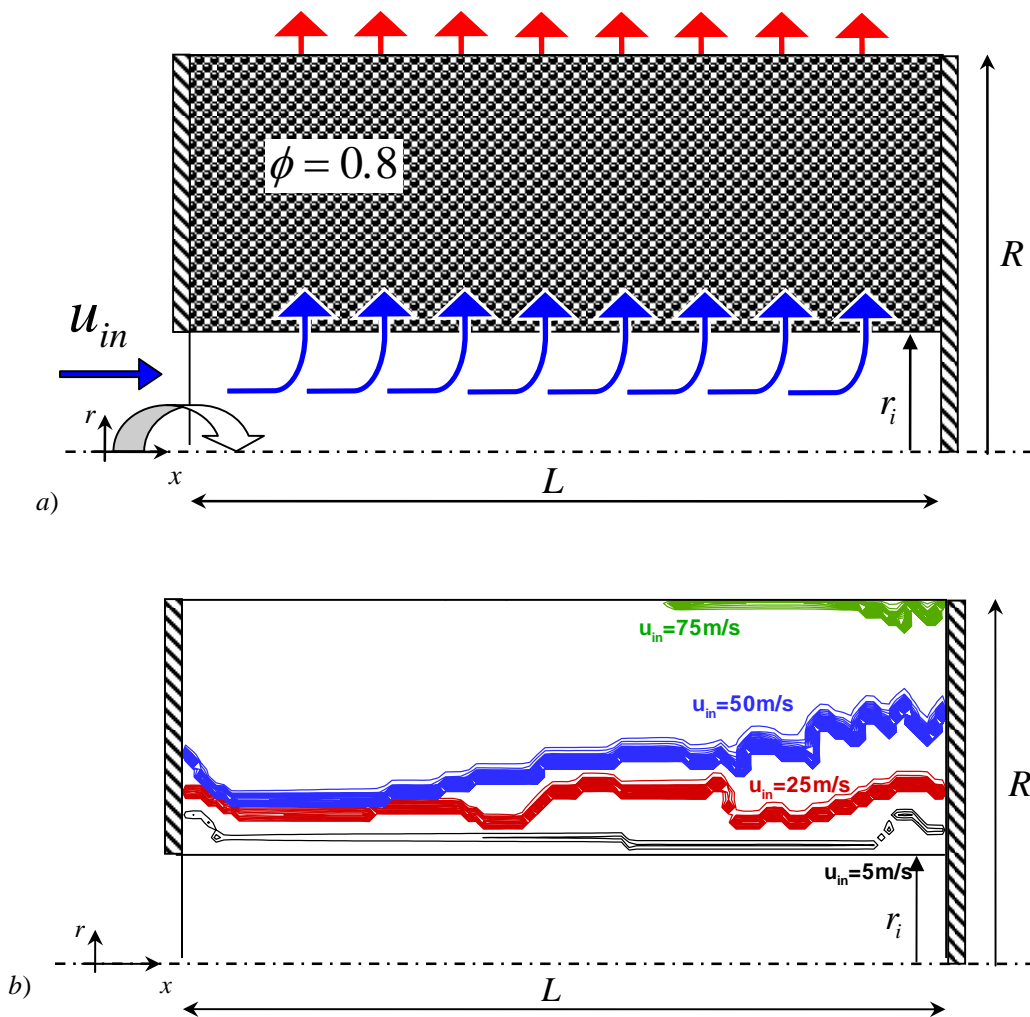


FIGURE 1 – a) Radial porous combustor, $L = 0.1m$, $R = 0.05m$, $r_i = 0.017m$. , b) Effect of inlet velocity U_{in} on the flame front position in the (x,r) plane for excess air $\Psi = 0$.

4. CONCLUSIONS

This paper presented two-dimensional simulations for a mixture of air and methane burning in a porous radial combustor. Results indicate that a much higher power modulation is possible when stoichiometric mixtures are burned. Also, although not shown here, as the inlet mass flow rate increases, the flame is pushed towards the burner exits and such effect is more pronounced as the amount of air increases.

REFERENCES

1. Howell, J.R., Hall, M.J., Ellzey, J.L., 1996, Combustion of Hydrocarbon Fuels within Porous Inert Media, *Progress in Energy and Combustion Science* 22 (2): 121-145.
2. Oliveira A.A.M, Kaviany M., 2001, Non Equilibrium in the Transport of Heat and Reactants in Combustion in Porous Media, *Progress in Energy and Combustion Science* 27 (5): 523-545.
3. Henneke, M.R., Ellzey, J.L., 1999, Modeling of Filtration Combustion In A Packed Bed, *Combustion and Flame* 117 (4), p. 832-840.
4. Bouma, P. H., De Goey L. P.H., Premixed Combustion On Ceramic Foam Burners, *Combustion and Flame* 119 (1-2): 133-143 Oct 1999
5. Babkin Vs., Filtrational Combustion Of Gases - Present State Of Affairs And Prospects, *Pure and Applied Chemistry* 65 (2): 335-344 Feb 1993.
6. Leonardi S. A., Viskanta R, Gore J.P., Analytical and Experimental Study of Combustion and Heat Transfer in Submerged Flame Metal Fiber Burners/Heaters, *Journal of Heat Transfer*, 125 (1): 118-125 Feb 2003
7. Lammers F.A., De Goey, L.P.H, 2003, A Numerical Study of Flash Back of Laminar Premixed Flames in Ceramic-Foam Surface Burners., *Combustion and Flame* 133 (1-2): 47-61.
8. Mohamad A.A., Ramadhyani S, Viskanta R, 1994, Modeling of Combustion and Heat-Transfer in a Packed-Bed with Embedded Coolant Tubes, *Int. J Heat Mass Transfer* 37 (8): p. 1181-1191.
9. S. Wood, A.T. Harries, Porous burners for lean-burn applications, *Prog. Energy Comb. Science*, 34 (2008) 667-684.
10. Hsu, P.-F., Howell, J.R., Matthews, R.D., 1993, A Numerical Investigation of Premixed Combustion Within Porous Inert Media, *J. Heat Transfer*, v.115, p. 744-750.
11. Peard, T.E., Peters, J.E., Brewster, Buckius, R.O., Radiative heat Transfer Augmentation in Gas-Fired radiant Tube Burner By Porous Inserts: Effect on Insert Geometry, *Exp. Heat Transfer*, v. 6, pp. 273-286 (1993).
12. Lim, I- G., Matthews, R.D., 1993, Development of a Model for Turbulent Combustion Within Porous Inert Media, *Trensp. Phenm. Therm. Eng., Begell House Inc. Publ.*, pp 631-636
13. Jones, W.P., Launder, B.E., 1972, The Prediction of Laminarization with Two-Equation Model of Turbulence , *Int. J. Heat & Mass Transfer*, vol. 15, pp. 301 – 314,
14. Sahraoui, M., Kaviany, 1995, Direct simulation vs Time-Averaged Treatment of Adiabatic, Premixed Flame in a Porous Medium, *Int. J. Heat Mass Transfer*, v.18, pp. 2817-2834.
15. de Lemos, M.J.S., 2006, *Turbulence in Porous Media: Modeling and Applications*, Elsevier, Amsterdam, ISBN: 0-08-044491-1, 384 pgs.

NATURAL CONVECTION IN A VERTICAL POROUS ANNULUS FROM TWO THERMAL SOURCES

Younghae Do, M. Sankar

Department of Mathematics, Kyungpook National University,
1370 Sangyeok-Dong, Buk-Gu, Daegu 702-701, Republic of Korea
(manisankarir@yahoo.com, yhdo@knu.ac.kr)

Juan M. Lopez

School of Mathematical and Statistical Sciences, Arizona State University,
Tempe, AZ 85287, USA (lopez@math.asu.edu)

ABSTRACT

The effects of discrete heating on natural convection heat transfer in a vertical porous annulus are investigated numerically. The inner wall of the annulus has two discrete flush-mounted heat sources, the outer wall is isothermally cooled at a lower temperature, and the top and bottom walls are thermally insulated. The governing equations are solved using an implicit finite difference technique. The influence of discrete heating on the flow and heat transfer in the porous annulus are investigated for a wide range of parameters. We found that the heat transfer rate is always higher at the bottom heater. Further, the rate of heat transfer increases with radius ratio (curvature) but decreases with Darcy number.

Key Words: *Natural Convection, Discrete Heating, Finite Difference, Porous Medium.*

1. INTRODUCTION

Natural convection in porous annulus enclosures is of practical interest in many engineering, agriculture, geothermal, medical and biological sciences. Examples include the storage of grain, transpiration cooling, ground water pollution, food technology, radioactive waste management, and certain biological materials [1,2]. Natural convection in a differentially heated vertical porous annulus has been investigated widely, owing to its importance in high performance insulation for building, porous heat exchangers, and many others applications [3-5].

Previous works on natural convection in a vertical porous annulus are limited to uniform heating of the inner wall by either isothermal or isoflux wall-heating conditions. However, in many practical applications, heating takes place over a portion of one of the vertical walls, where the heating segment may significantly affect the heat transport process in the annular enclosure filled with a fluid-saturated porous media. Although the annular porous enclosure with discrete heating is employed in many practical applications, most studies have been in rectangular enclosures, in which the effects of curvature are missing. Here, we examine the effects of isoflux discrete heaters on the natural convective flows in a porous annular cavity, and in particular explore the effects of curvature.

2. MATHEMATICAL FORMULATION AND NUMERICAL METHOD

Consider a cylindrical annular enclosure of inner and outer radii r_i and r_o , and height h , filled with a fluid-saturated porous medium. Two discrete heat sources are placed at the inner wall of the annular cavity, while the unheated portions of the inner wall, top and bottom walls are kept at adiabatic. The outer wall of the annulus is isothermally cooled at a lower temperature providing a heat sink. The lengths of both heaters and the unheated portions of the inner wall are kept fixed at a value of $h/5$. The fluid is assumed to be Newtonian with negligible viscous dissipation and all physical properties

are taken to be constant, except for the density in the buoyancy term. Employing the Boussinesq approximation, the dimensionless governing equations in vorticity stream function form are:

$$\frac{\partial T}{\partial \tau} + \frac{U}{A} \frac{\partial T}{\partial r} + \frac{W}{A} \frac{\partial T}{\partial z} = \nabla^2 T, \quad (1)$$

$$\frac{\partial \zeta}{\partial \tau} + \frac{U}{A} \frac{\partial \zeta}{\partial r} + \frac{W}{A} \frac{\partial \zeta}{\partial z} - \frac{U}{A} \left(\frac{d}{rd+r_i} \right) \zeta = \text{Pr} \nabla^2 \zeta - \text{Pr} \left(\frac{d}{rd+r_i} \right)^2 \zeta + Ra \frac{\partial T}{\partial r} - \frac{\text{Pr}}{Da} \zeta, \quad (2)$$

$$\zeta = \frac{1}{\text{Pr}} \left(\frac{r_i}{rd+r_i} \right) \frac{\partial^2 \psi}{\partial r^2} - \left(\frac{d}{rd+r_i} \right) \frac{\partial \psi}{\partial r} + \frac{1}{A^2} \frac{\partial^2 \psi}{\partial z^2}, \quad (3)$$

$$U = \left(\frac{r_i}{rd+r_i} \right) \frac{\partial \psi}{\partial z}, \quad W = - \left(\frac{r_i}{rd+r_i} \right) \frac{\partial \psi}{\partial r}, \quad (4)$$

where $d = r_o - r_i$ and $\nabla^2 = \frac{\partial^2}{\partial r^2} + \left(\frac{d}{rd+r_i} \right) \frac{\partial}{\partial r} + \frac{1}{A^2} \frac{\partial^2}{\partial z^2}$.

The non-dimensional variables used in the above equations are:

$$U = \frac{ud}{\kappa} A, W = \frac{wh}{\kappa A}, T = \frac{k(\theta - \theta_c)}{(q_h d)}, r = \frac{r^* - r_i}{d}, z = \frac{z^*}{h}, \tau = \frac{t\kappa}{d^2}, \zeta = \frac{\zeta^* d^2}{\nu}, \psi = \frac{\psi^*}{r_i \kappa}.$$

The equations (1)-(4) are solved using the Alternating Direction Implicit (ADI) and Successive Line Over Relaxation (SLOR) methods. For brevity, the details of the method are not given, and the same can be found in [5,6].

3. RESULTS

The range of the modified Rayleigh number ($Ra = g\beta q_h d^4 / k\nu\kappa$) and Darcy number ($Da = K / d^2$) considered are $10^3 \leq Ra \leq 10^7$ and $10^{-6} \leq Da \leq 10^{-1}$, while the radius ratio ($\lambda = r_o / r_i$) is varied over $1 \leq \lambda \leq 10$. The Prandtl number ($\text{Pr} = \nu / \kappa$) and the aspect ratio ($A = h / d$) are held constant respectively at $\text{Pr} = 0.71$ and $A = 1$. In the expressions of Ra and Da , the variables g, β, k, ν, κ and K are respectively the gravity, thermal expansion coefficient, thermal conductivity, kinematic viscosity, thermal diffusivity and the permeability of the porous medium.

Figure 1 shows the streamlines and isotherms inside the porous annulus for Darcy numbers 10^{-6} and 10^{-2} , corresponding to the limits of Darcy and viscous flows. At $Da = 10^{-6}$, the resistance from the boundary friction is significant and adds to the bulk frictional drag induced by the solid matrix, slowing down the convective motion in the annulus. In the limit of $Da \rightarrow 0$, the Brinkman model reduces to the Darcy regime. However, as the Darcy number is increased from 10^{-6} to 10^{-2} , the permeability of the porous medium increases and hence the boundary frictional resistance becomes gradually reduced, and in turn the fluid circulation is significantly enhanced. Indeed, increasing the Brinkman term implies that the balance between the Darcy term and the buoyancy force in the boundary layer is progressively replaced by the balance between a viscous force and the buoyancy force. The resulting viscous force increases the velocity at high Darcy numbers. For small Darcy number, a circulating flow pattern centred about the middle of the cavity results. As the Darcy number is increased, the streamlines show that the meridional circulation is more confined to boundary layers on the annulus walls, with the centre of circulation near the outer cylindrical wall, where the flow is fastest. Generally, increasing the Darcy number (permeability) helps the flow to penetrate deeper into the porous layer.

Figure 2 reveals the influence of radius ratio (larger λ corresponds to larger curvature) on the heat transfer rate for different values of modified Rayleigh and Darcy numbers. The figure reveals that the heat transfer increases with radius ratio for fixed values of Ra and Da . Similarly, for a fixed value of λ , the heat transfer rate increases with the modified Rayleigh and Darcy numbers. In particular, the rate of heat dissipated from the bottom heater is found to be higher compared to the top heater at all radius ratios, Darcy and modified Rayleigh numbers. At small Darcy numbers, the fluid flow experiences more resistance, and hence the average Nusselt number is almost flat at all radius ratios. It is also observed that the heat transfer rate increases sharply for $Da > 10^{-5}$, while the steep increase in the Nusselt number curve is delayed for the top heater. The variation of maximum temperature or hot spots at all values of Ra is illustrated in Figure 3 for three different values of Da . The maximum temperature appears on the top heater at all values of Ra and Da . However, the maximum temperature decreases rapidly with Ra for $Da > 10^{-5}$, due to enhanced convection strength.

4. CONCLUSIONS

Natural convection in a vertical porous annulus has been numerically investigated in the presence of two discrete thermal sources. The results reveal that the rate of heat transfer is higher at the bottom heater, while the maximum temperature appears on the top heater. An increase in radius ratio (curvature) produces a higher heat transfer in the annulus. Further, the presence of porous medium delays the onset of convection in the porous annulus. More results will be presented in the full length version of the paper.

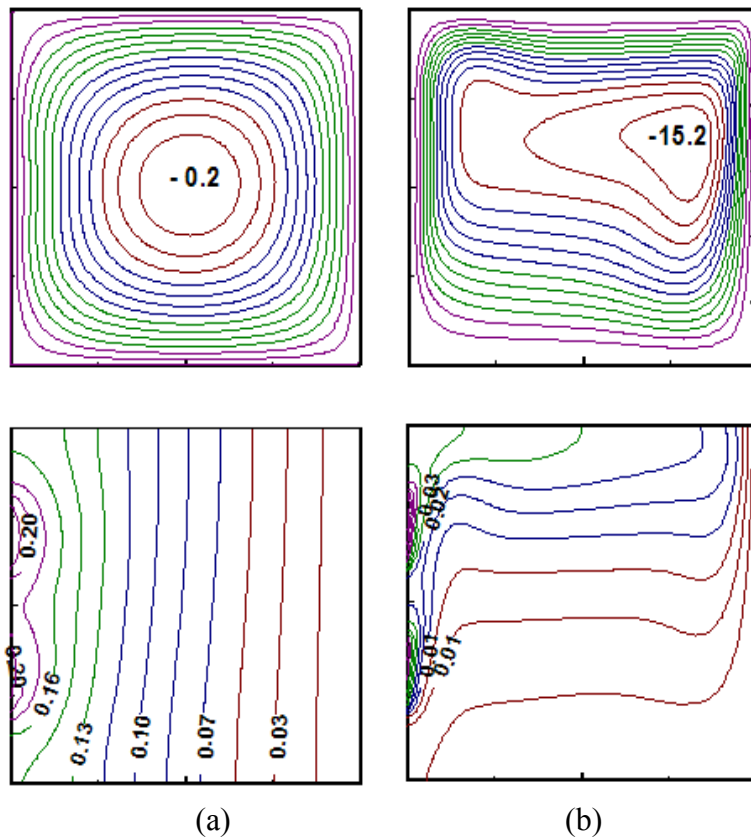


FIGURE 1. Streamlines and isotherms for $Ra=10^6$, $\lambda=2$, (a) $Da=10^{-6}$ and (b) $Da=10^{-2}$.

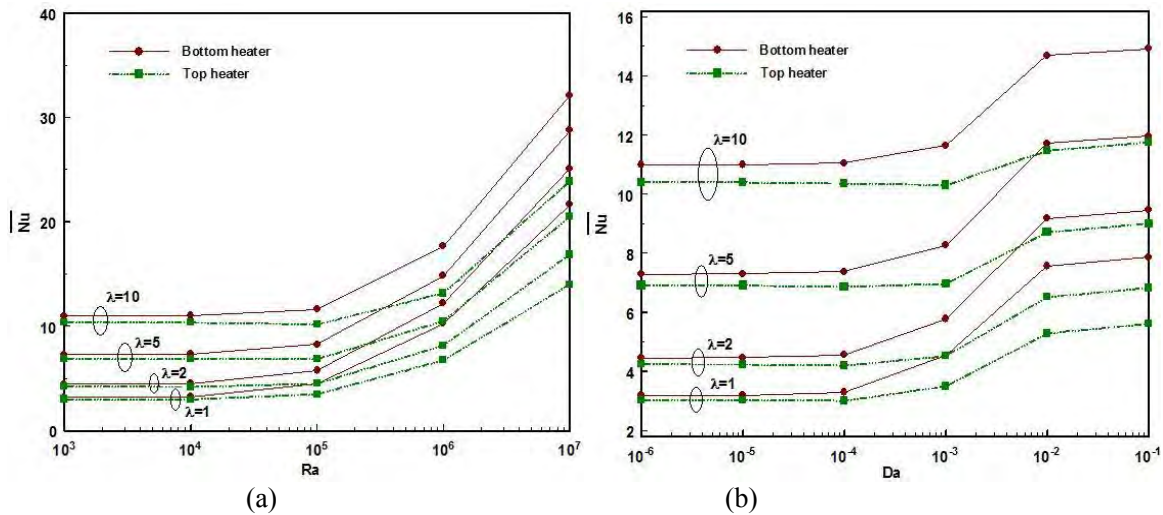


FIGURE 2. Effect of radius ratio on the heat transfer rate for different values of (a) Ra and (b) Da.

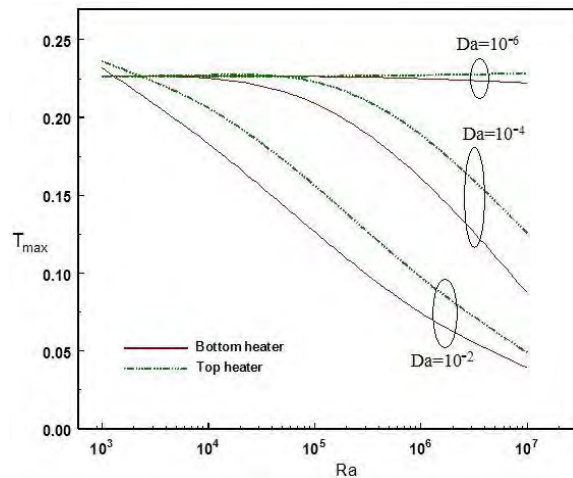


FIGURE 3. Variation of maximum temperature with different values of Ra and Da.

REFERENCES

- [1] D.A. Nield and A. Bejan, *Convection in Porous Media*, 3rd Edition, Springer, New York, 2006.
- [2] K. Vafai, *Handbook of Porous Media*, 2nd Edition, Taylor & Francis, New York, 2005.
- [3] V. Prasad, Numerical study of natural convection in a vertical, porous annulus with constant heat flux on the inner wall, *Int. J. Heat Mass Transfer*, 29, 841-853, 1986.
- [4] S. Kiwan, and M.S. Al-Zahrani, Effect of porous inserts on natural convection heat transfer between two concentric vertical cylinders, *Numer. Heat Transfer Part A: Appl.*, 53, 870-889, 2008.
- [5] M. Sankar, Y. Park, J.M. Lopez, and Y. Do, Numerical study of natural convection in a vertical porous annulus with discrete heating. *Int. J. Heat and Mass Transfer*, 54, 1493-1505, 2011.
- [6] M. Sankar, and Y. Do, Numerical simulation of free convection heat transfer in a vertical annular cavity with discrete heating. *Int. Comm. Heat Mass Transfer*, 37, 600-606, 2010.

A 3D MIXED CONVECTION STUDY IN A POROUS CAVITY

B. V. Rathish Kumar¹, Mohit Nigam²

Department of Mathematics, Indian Institute of Technology, Kanpur -208016, India,
bvrk@iitk.ac.in

S. V. S. S. N. V. G. Krishna Murthy³

Applied Mathematics and Systems Lab, Ecole Centrale Paris, 92295, France,
drsomanchikmurthy@gmail.com, krishnas@ecp.fr,

ABSTRACT

The aim of this work is to investigate the fully nonlinear coupled nonlinear partial differential equations governing the steady mixed convection in a 3D porous enclosure are solved numerically by Galerkin Finite Element Method (FEM). The forced flow conditions are imposed by providing an inlet with injection at the bottom surface and an outlet with suction on the top surface. The free convection is induced by a centrally buried isothermal cubical body together with Boussinesq approximation on density variable. In view of the large size of the linear systems encountered in the 3D FE calculations, a numerical scheme based on segregated variable approach is followed to carry out the numerical simulations. Detailed numerical computations are carried out for a wide range of governing parameters such as Rayleigh Number (Ra), suction/injection velocity (a), suction /injection width (D/H), cubical hot object of length L_h , as fraction of the length of the square enclosure and the results are analyzed by tracing the isotherms and streamlines on different 2D horizontal and vertical cross sections of the domain. Also local heat fluxes along the isothermal buried structure are presented in the form of Nusselt Number for different values of the governing parameters.

Key Words: *Mixed Convection, Suction/Injection, Porous Medium, Finite Element Method.*

1. INTRODUCTION

The practical applications of studies in mixed convection are not only vast and diverse but also of considerable importance, like in many of the engineering applications such as solar central receivers exposed to wind currents, electronic devices cooled by fans, heat exchangers, vented enclosures filled with micro spheres, Coal gasification, geothermal heating due to nuclear waste disposal, migration of moisture through air contained in fibrous insulations, porous gas burners, IC engines, thermal insulation of buildings, environmental chambers, oil extraction which require a detailed study on mixed convection process the spatial location of inlet / outlet windows become very vital [1-9]. Based on the need for three-dimensional solution, the physical system has been modeled mathematically by writing mass and energy balances on a differential volume of a porous medium. Darcys law has been used as the force balance equation. The equations are simplified by neglecting the temperature dependence of the fluid properties, except for the density in Darcy's equation. The equations have been formulated in terms of a vector potential, which is the three dimensional analog of the stream function, see Holst and Aziz [9] for reference. System of equations have been solved using finite element method in a sparse format by taking advantage of the sparsity of assembled mass matrix. Detailed numerical simulations are carried out by Galerkin finite element method for a wide range of parameters such as Rayleigh Number (Ra), suction/injection velocity (a), suction /injection width (D/H), cubical hot object of length L_h . Results have been shown in the form of Nusselt number, temperature and velocity vector plots.

So far not much work has been reported on Darcy mixed convection in a cubical porous enclosure. In particular mixed convection in fluid saturated porous enclosure under the influence of Suction/Injection effect with a centrally buried isothermal cubical structure which becomes very relevant in the context of electronic devices, environmental chamber for bacterial culture preservation etc., have not been considered so far.

2. MAIN BODY

Fig 1 represents a three-dimensional cubical porous enclosure of length L and a cubical hot object of length L_h with a uniform temperature higher than the ambient temperature at the center of the enclosure. All the faces of the porous enclosure are assumed at ambient temperature including the outlet portion at the top surface. The forced flow conditions are imposed by providing an inlet at the bottom of the surface and an outlet with suction at the top of the surface for out flow. It is assumed that 'D' is the width of the inlet and outlet, H is the height of the Cavity. The inflow is considered to be at ambient temperature. We assume x and z co-ordinates to lie on the plane of the paper and y coordinate to be in the perpendicular plane. Flow is assumed to be steady and three dimensional. Darcy flow model is considered for the momentum equation and Boussinesq approximation for density is assumed to be valid for this equation. Using the non-dimensional variables and introducing the Boussinesq approximation, $\rho = \rho_0 \{1 - \beta(t - t_0)\}$ the three-dimensional mass, momentum and energy equations for this system can be written as follows in the non-dimensional form

$$\nabla^2 \phi_1 = Ra \frac{\partial T}{\partial Y}, \quad (1)$$

$$\nabla^2 \phi_2 = -Ra \left[\frac{\partial T}{\partial Z} + \frac{\partial T}{\partial X} \right], \quad (2)$$

$$\nabla^2 \phi_3 = Ra \frac{\partial T}{\partial Y}, \quad (3)$$

$$\nabla^2 T = U \frac{\partial T}{\partial X} + V \frac{\partial T}{\partial Y} + W \frac{\partial T}{\partial Z} \quad (4)$$

The appropriate boundary conditions in non-dimensional form are:

$$\frac{\partial \phi_1}{\partial X} = \phi_2 = \phi_3 = 0, \text{ on left and right faces, } X=0,1,$$

$$\frac{\partial \phi_2}{\partial Y} = \phi_1 = \phi_3 = 0, \text{ on front and back faces, } Y=0,1,$$

$$\frac{\partial \phi_3}{\partial Z} = \phi_1 = \phi_2 = 0, \text{ on top and bottom faces, } Z=0,1,$$

$$T = 0, \text{ on all the six faces}$$

and

$$\begin{aligned} \phi_1 = \phi_2 = \phi_3 = 0, T = 1 \text{ for } (0.5 - \frac{L_h}{2}) \leq X, Y, Z \leq (0.5 + \frac{L_h}{2}) \\ \phi_1 = -\frac{a}{2} (X + Y), \phi_2 = \frac{a}{2} (X + Y), \phi_3 = 0, T = 0 \text{ Bottom Slit} \\ \phi_1 = -\frac{a}{2} (X + Y), \phi_2 = \frac{a}{2} (X + Y), \phi_3 = 0, \frac{\partial T}{\partial Z} = 0 \text{ Top slit} \end{aligned} \quad (5)$$

The velocity components (U, V, W) are given as follows in terms of vector potential, ϕ :

$$U = \frac{\partial \phi_3}{\partial Y} - \frac{\partial \phi_2}{\partial Z}, V = \frac{\partial \phi_1}{\partial Z} - \frac{\partial \phi_3}{\partial X}, W = \frac{\partial \phi_2}{\partial X} - \frac{\partial \phi_1}{\partial Y}$$

3. RESULTS

The above three dimensional FEM scheme based on the vector potential and temperature formulation has been developed to simulate the mixed convection in 3-D fluid saturated porous enclosures. In view of the large size of the linear systems resulting from the finite element analysis, the scheme is evolved in a de-coupled framework, where in one can solve separately for components of vector potential function and temperature field. In the current study parallel Bi-CGM solver has been used to handle the large scale linear systems resulting from the Finite Element formulation of Eq. (1)-(5). First, to check the correctness of the code, solutions have been compared and found to be in perfect agreement. Isotherms for the case of convection in a cubical enclosure due to bottom heating are considered for $Ra = 100$. The results are in good agreement with those of Zhao et al. [1]. In Fig 2 isotherms on $X = Y = Z = 0.5$ cross sections of the cubical porous enclosure are presented for the cases with increasing size of hot cubical structure. Clearly, the temperature fields on each of these cross section remain symmetric about the centrally embedded hot object but vary in magnitudes. However the conical nature of the downward facing plume like structure gradually changes to a rectangular plume like structure with the increase in the size of the embedded hot object. Clearly the isotherm pattern in Fig 3 is very sensitive to the magnitude of Ra . With increasing values of Ra a downward stretching plume like structure manifests under the bottom horizontal wall and it gets prominent with increasing Ra . The isotherms which are circular and centered about the hot body at small values of Ra , get set into interesting complex symmetric circulation patterns centered about the plume like structure as Ra increases. This variation in the isotherm pattern is fully in tune with the changes noticed in circulation rolls in the flow field. The plume manifestation can be attributed to the intensified mixing of hot and cold fluids due to flow circulation intensification.

4. CONCLUSIONS

3-D mixed convection in a fluid saturated porous enclosure with a hot body embedded at its center under I/S effects has been analyzed for various values of Rayleigh number, different sizes of isothermal cubical hot objects for different I/S velocities. Prominent circulation zones are seen to manifest adjacent to the four vertical faces to the hot object. When $Ra < 100$ 3-D symmetry is observed in the flow and temperature distribution fields. A downward drift in the eye of the circulations and flow intensification is noticed with the increase in Ra beyond 100. For When $Ra > 100$, prominent downward stretching thermal plumes are seen manifest under the embedded hot body.

REFERENCES

- [1] C.Zhao, B.E. Hobbs, H.B. Muhlhaus, A. Ord, and G. Lin, Finite element modelling of three-dimensional convection problems in fluid-saturated porous media heated from below, *Commun. Numer. Meth. Engng.*, 17, 101-114, 2001.
- [2] S. Mahmud and I. Pop, Mixed Convection in Square Vented Enclosure Filled with a Porous Medium, *International Journal of Heat and Mass Transfer*, 49, 2190-96, 2006.
- [3] B.V.R. Kumar, S.S. Belouettar, S.K. Murthy, V. Sangwan and M. Nigam, A 3-D Finite Element Computation of Free Convection from a Cubical structure Buried in a Fluid Saturated Porous Enclosure on ANU-Cluster, *Engineering Applications of Computational Fluid Mechanics*, 2(3), 319-330, 2008.
- [4] G.H. Hirasaki and J.D. Hellums, A general formulation of the boundary conditions on the vector potential in three-dimensional hydrodynamics, *Q. Appl. Math.*, 16, 331-336, 1968.

- [5] B.V.R. Kumar, S.V.S.S.N.V.G.Krishna Murthy, V. Sangwan, M. Nigam, P. Chandra, Non-Darcy Mixed Convection in a Fluid Saturated Square Porous Enclosure Under Suction Effect :I, 13(6), 537-554, 2010.
- [6] K. Aziz and J.D. Hellums, Numerical solution of the three dimensional equations of laminar natural convection, *Physics Fluids*, 10, 314-324, 1967.
- [7] L. Brevdo, Three-dimensional absolute and convective instabilities at the onset of convection in a porous medium with inclined temperature gradient and vertical through flow, *Journal of Fluid Mechanics*, 641, 475-487, 2009.
- [8] M.N. Ouarzazi, F. Mejni, A. Delache and G. Labrosse, Nonlinear global modes in inhomogeneous mixed convection flows in porous media, *Journal of Fluid Mechanics*, 595, 367-377, 2008.
- [9] P.H. Holst and K. Aziz, Transient three-dimensional natural convection in confined porous media. *Int. J. Heat MassTransfer*, 15, 73-90, 1972.

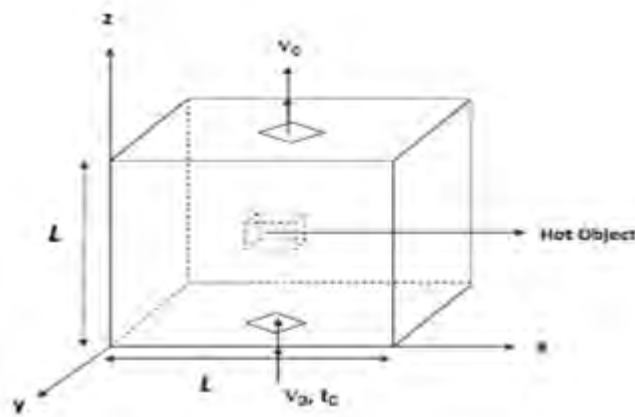


FIGURE 1. Porous Enclosure with a Cubical Hot Object in the center with the physical co-ordinates

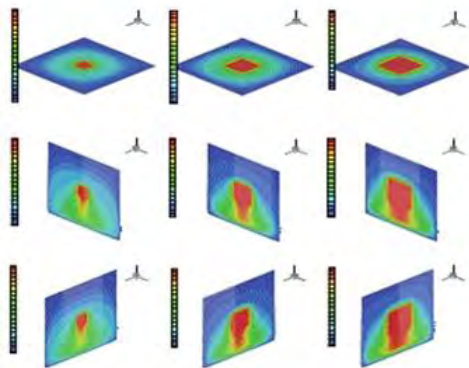


FIGURE 2. Isotherm plots while increasing size of cubical structure when $Ra = 250$ for the XY plane when (a) $L_h = 0.1$ (b) $L_h = 0.2$ (c) $L_h = 0.3$: Corresponding YZ and XZ plane vector plots are in (d-f) and (g-i) respectively

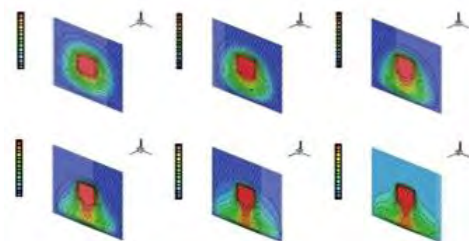


FIGURE 3. Isotherm plots while fixing $a = 0.5$, $L_h = 0.2$ on the YZ plane for (a) $Ra = 25$ (b) $Ra = 50$ (c) $Ra = 100$ (d) $Ra = 250$ (e) $Ra = 500$ (f) $Ra = 750$

DOUBLE DIFFUSIVE FREE CONVECTION PROCESS INDUCED BY BOUNDARY LAYER FLOW ALONG A VERTICAL SURFACE IN A DOUBLY STRATIFIED FLUID SATURATED POROUS MEDIUM WITH SORET AND DUFOUR EFFECTS UNDER MHD FORCES

S. V. S. S. N. V. G. Krishna Murthy¹, Frédéric Magoulès²

Applied Mathematics and Systems Lab, Ecole Centrale Paris, 92295 Châtenay Malabry Cedex, France

E-mail addresses¹: drsomanchikmurthy@gmail.com, krishnas@ecp.fr,

E-mail addresses²: frederic.magoules@hotmail.com (F. Magoulès),

B. V. Rathish Kumar³

Department of Mathematics and Statistics, Indian Institute of Technology, Kanpur -208016, India

E-mail addresses: bvrk@iitk.ac.in

ABSTRACT

This paper details a study of the combined effect of heat and mass transfer in a two-dimensional magnetohydrodynamic free convection flow along a vertical semi-infinite flat surface immersed in a thermal and mass stratified Darcy porous medium under the influence of Soret and Dufour effect. The resulting nonlinear partial differential equations governing the problem under consideration have been transformed by a similarity transformation into a system of ordinary differential equations which are solved numerically by finite difference scheme following the Keller Box approach. A comparison with previously published work is performed and the results are found to be in good agreement. The numerical results are demonstrated graphically for various values of the parameters involved in the problem like: Magnetic parameter(M_g), Buoyancy ratio(B), Lewis number(Le), Soret(S_r) and Dufour(D_f) numbers, presence of Thermal(S_T) and Mass(S_C) stratification. Local and Average Nusselt(Nu) number and Sherwood(Sh) number plots are presented in all cases..

Key Words: *MHD, Darcy porous medium, Dufour & Soret effect, Thermal & Mass stratification.*

1. INTRODUCTION

Boundary layer flow on a continuous moving surface is a significant type of flow occurring in a variety of technological applications. Aerodynamic extrusion of plastic sheets, cooling of an infinite metallic plate in a cooling bath, the boundary layer along a liquid film in condensation processes and polymer sheet, continuous filament extrusion from a dye, the fluid dynamics of a long thread traveling between a feed roll and a wind-up roll are only few pertinent examples of practical applications of continuous stretching flows from flat surfaces. In all these technologies, the quality of final product is strongly influenced by the rate of heat transfer at the stretching surface. Magnetohydrodynamics(MHD) can be regarded as a combination of fluid mechanics and electro-magnetism, that is, the behaviour of electrically conducting fluid in the presence of magnetic and electric fields. The study of magnetohydrodynamic natural convection flow and heat transfer of an electrically conducting fluid past a heated semi-infinite vertical porous plate finds useful applications in many engineering problems like: MHD generator, Plasma studies, nuclear reactors, geothermal extractions and the boundary layer control in the field of aeronautics and aerodynamics. It serves as the basis for understanding some of the important phenomena occurring in heat exchanger devices. In addition to this the industrial applications include the cooling of metallic plates in a cooling bath, the aerodynamic extrusion of plastic sheets, drawing, annealing and tinning of copper wires, etc., which require a detailed study on natural convection process induced by boundary layer flow along a vertical surface in a doubly stratified fluid saturated porous medium with Soret and Dufour effects under MHD forces become very vital [1-11].

So far not much work has been reported on the present work. In the present study we aim to consider the free convection process in a thermal and mass stratified fluid-saturated porous medium under the boundary layer assumption.

2. THE METHOD

We consider a magnetohydrodynamic(MHD) free convective heat and mass transfer boundary layer flow along a vertical semi-infinite surface embedded in a doubly stratified fluid saturated porous medium in the presence of Soret and Dufour effects. The origin of the coordinate system is placed at the leading edge of the vertical surface where the x-axis is measured along the plate, a uniform magnetic field of strength m_d is applied in the y- direction that is normal to the streamwise direction. The induced magnetic field due to the motion of the electrically-conducting fluid is negligible. It is also assumed that the external electrical field is zero and the electric field due to the polarization of charges is negligible. The semi infinite vertical surface is considered at constant temperature t_w and constant mass concentration c_w of some constituent in the fluid. Sufficiently far from the vertical wall, the ambient temperature and concentration are considered as $t_{\infty,x}$ and $c_{\infty,x}$ respectively, where $t_{\infty,x}$ and $c_{\infty,x}$ are defined as:

$$t_{\infty,x} = t_{\infty,0} + s_t x, \quad s_t = \frac{dt_{\infty,x}}{dx},$$

$$c_{\infty,x} = c_{\infty,0} + s_c x, \quad s_c = \frac{dc_{\infty,x}}{dx}.$$

It is also assumed that pressure gradient, viscous and electrical dissipation are neglected. To obtain the volume averaged conservation equations the following assumptions are made:

- The flow is electrically conducting, steady, laminar, incompressible and two-dimensional.
- The flow and the solid matrix are everywhere in local thermal equilibrium.
- The thermophysical properties of the fluid are homogeneous and isotropic.
- the properties of the fluid and porous medium are constants except for density variations with temperature and concentration, which are considered only in the body force term.

Using the non-dimensional variables and introducing the Boussinesq approximation, $\rho = \rho_0 \{1 - [\beta_t(t - t_\infty) + \beta_c(c - tc_\infty)]\}$ is valid and the boundary-layer approximation is applicable, then system of governing equations can be written as follows in the non-dimensional form

$$\frac{\partial^2 \Psi}{\partial X^2} + \frac{\partial^2 \Psi}{\partial Y^2} + M_g \frac{\partial^2 \Psi}{\partial Y^2} = Ra \left(\frac{\partial T}{\partial Y} + B \frac{\partial C}{\partial Y} \right) \quad (1)$$

$$\left[\frac{\partial^2 T}{\partial X^2} + \frac{\partial^2 T}{\partial Y^2} \right] + D_f \left[\frac{\partial^2 C}{\partial X^2} + \frac{\partial^2 C}{\partial Y^2} \right] = \frac{\partial \Psi}{\partial Y} \frac{\partial T}{\partial X} + S_T \frac{\partial \Psi}{\partial Y} - \frac{\partial \Psi}{\partial X} \frac{\partial T}{\partial Y} \quad (2)$$

$$\frac{1}{Le} \left[\frac{\partial^2 C}{\partial X^2} + \frac{\partial^2 C}{\partial Y^2} \right] + S_r \left[\frac{\partial^2 T}{\partial X^2} + \frac{\partial^2 T}{\partial Y^2} \right] = \frac{\partial \Psi}{\partial Y} \frac{\partial C}{\partial X} + S_C \frac{\partial \Psi}{\partial Y} - \frac{\partial \Psi}{\partial X} \frac{\partial C}{\partial Y} \quad (3)$$

The appropriate boundary conditions in non-dimensional form are:

$$\Psi = 0, \quad T = 1 - S_T X, \quad C = 1 - S_C X \quad \text{on } Y = 0$$

$$\frac{\partial \Psi}{\partial Y} \rightarrow 0, \quad T \rightarrow 0, \quad C \rightarrow 0 \quad \text{as } Y \rightarrow \infty, \quad (4)$$

The above non-dimensional governing equations have been converted to non-dimensional form by considering non dimensional stream function Ψ is defined as Ψ is defined as: $u = \frac{\partial \Psi}{\partial y}$ and $v = -\frac{\partial \Psi}{\partial x}$

3. RESULTS

We now assume that the Rayleigh number (Ra) is large so that free convection takes place within a boundary layer whose cross-stream width is substantially smaller than the ($O(1)$). Thus using the scale analysis we obtain the following transformation:

$$\xi = X, \quad Y = \xi^{1/2} Ra^{-1/2} \eta, \quad \Psi = Ra^{1/2} \xi^{1/2} f(\xi, \eta). \quad (5)$$

where, (ξ, η) are the transformed coordinate variables and f is the non-similar stream function. Substituting transformation (5) into equations (1)-(4) and in the limiting case $Ra \rightarrow \infty$, we obtain the

transformed boundary layer equations. The non-similar boundary layer equations together with boundary conditions are solved by using two-point local non-similarity method [3, 4]. The resulting coupled non-linear partial differential equations subjected to the boundary conditions are solved by using an implicit finite difference scheme developed by following the box approach of Isaacson, Keller and Cebeci [2, 5]. Convergence is ensured at each fixed ξ , by repeating iteration process to obtain an accuracy of 10^{-10} , using double precision arithmetic throughout. Maximum η -length (η_∞) is chosen as 20 as it is found to lie well outside the boundary layer. A uniform step size of 0.05 is used in ξ -direction, $0 \leq \xi \leq 10$ and a non-uniform grid of 500 points is used in η -direction, $0 \leq \eta \leq 20$, with more points concentrated towards $\eta = 0$. The computational grid of size 200×500 is found to be more than adequate for carrying out the detailed simulations. The influence of magnetic field parameter, Soret and Dufour effect and Lewis number on heat and mass transfer process in the presence of both thermal and mass stratification plots are presented in Fig 1(a - d) for $Le = 1$, $B = 1$, $S_T = S_C = 0.025$, $D_f = S_r = 0.02$, and for $0 \leq M_g \leq 100$. From Fig 1(a)-(d) one can notice that on increasing the magnetic field parameter Local Nu and Sh, Average Nu and Sh decreases along the wall. In Fig 1(a) and 1(c) at large values of M_g Local Heat Flux(LHFLX) curves tend to get parallel to ' ξ ' coordinate axis. From the plots in Fig 2 (a-d) one can notice that in the presence of thermal or concentration stratification the horizontal Local Nu and Local Sh curves, observed at zero thermal and mass stratification levels, gradually drop down as one marches along ξ axis away from the leading edge of the surface. Increasing levels of thermal or concentration stratification tend to decrease the Local and Average Nu and Sh all along the vertical surface.

4. CONCLUSIONS

The combined influence of Soret and Dufour effect and double diffusion on the Magnetohydrodynamic(MHD) free convection process in a fluid saturated Darcian porous medium in the presence of mass and thermal stratification has been analysed under boundary layer assumptions using two-point non-similarity transformation on the governing equations and later applying Keller Box method on the modified equations. Heat and mass fluxes are found to be sensitive to the governing parameters related to Magnetohydrodynamic forces(M_g), thermal and mass stratification(S_T , S_C), Lewis number(Le), Buoyancy ratio(B), Soret(S_r) and Dufour(D_f) numbers.

REFERENCES

- [1] D.A. Nield, A. Bejan, Convection in porous media, 3rd edition, Springer, New York, 2006.
- [2] E. Isaacson, and H.B. Keller, Analysis of Num. Methods, J. Wiley, New York, 1966.
- [3] E.M. Sparrow, H. Quack, and C.J. Boerner, *Local nonsimilarity boundary-layer solutions*, AIAA Journal 8(11), 1936-1942, 1970.
- [4] E.M. Sparrow, and H.S. Yu, *Local non similarity thermal boundary layer solutions*, ASME J. Heat Transfer, 93, 328-334, 1971.
- [5] H. B. Keller and T. Cebeci, Lecture Notes in Physics, Springer Verlag, New York, 8, 91-100, 1971.
- [6] C. Geindreau and J.L. Auriault, *Magnetohydrodynamic flows in porous media*, Journal of Fluid Mechanics, 329, 445-450 2001.
- [7] C. Geindreau and J.L. Auriault, *Magnetohydrodynamic flows in porous media*, Journal of Fluid Mechanics, 466, 343-363, 2002.
- [8] A. Postelnicu, *Influence of a magnetic field on heat and mass transfer by natural convection from vertical surfaces in porous media considering Soret and Dufour effects*, Int. J. Heat and Mass Transfer, 47, 1467-1472, 2004.
- [9] B.V.R. Kumar, S. Belouettar, S.V.S.S.N.V.G.K. Murthy, et al., *Soret and Dufour effect on double diffusive natural convection in a wavy porous enclosure in porous media*: Heat and Mass Transfer(NOVA Publisher:ISBN:978-1-60692-437-2), 2008.
- [10] A. Mahdy, *MHD non-Darcian free convection from a vertical wavy surface embedded in porous media in the presence of Soret and Dufour effect*, Int. Communications in Heat and Mass Transfer, 36, 1067-1074, 2009.
- [11] T. Hayat, M. Mustafa, I. Pop, *Heat and mass transfer for Soret and Dufours effect on mixed convection boundary layer flow over a stretching vertical surface in a porous medium filled with a viscoelastic fluid*, Commun. Nonlinear Sci. Numer. Simulat. 15, 1183-1196, 2010.

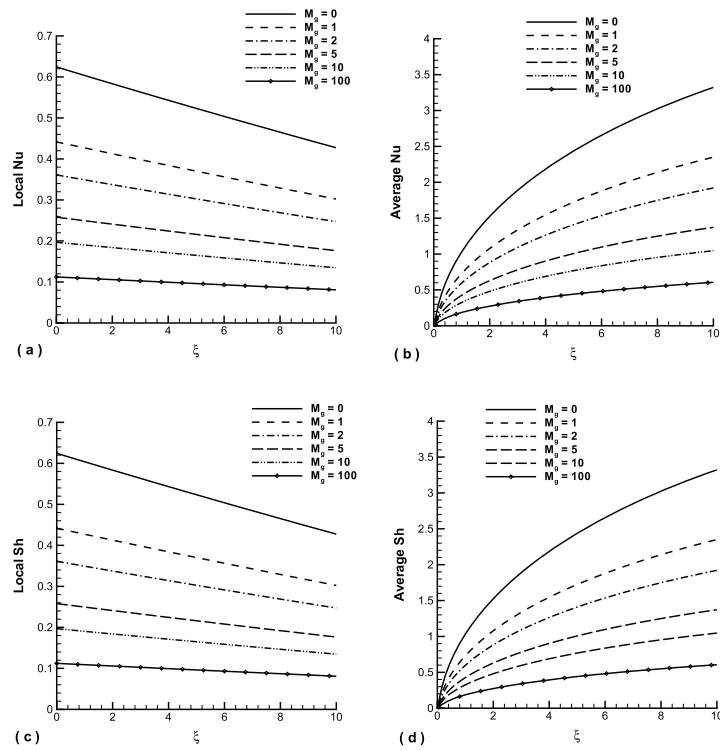


FIGURE 1. When fixing $Le = 1$, $B = 1$, $S_r = D_f = 0.02$, $S_T = S_C = 0.025$ (a) Local Nu (b) Avg Nu (c) Local Sh (d) Avg Sh plots along the vertical wall for varying M_g .

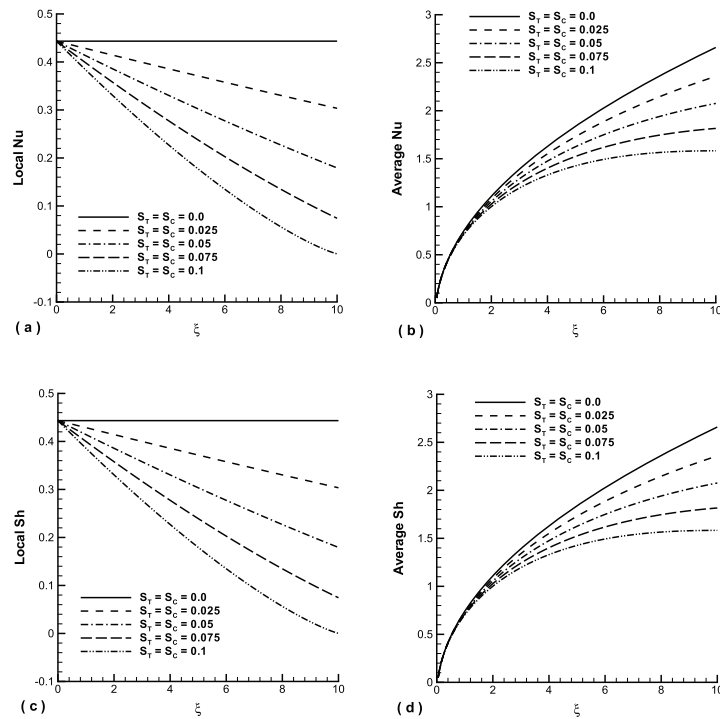


FIGURE 2. When fixing $B = 1$, $Le = 1$, $M_g = 1$, $D_f = S_r = 0.005$ (a) Local Nu (b) Avg Nu (c) Local Sh (d) Avg Sh plots along the vertical wall for varying S_T and S_C .

INFLUENCE OF POROSITY AND ELECTROKINETIC EFFECTS ON FLOW THROUGH MICROCHANNELS

Radha Narayanan

Dept.of Electronics, Christ University, Bangalore, India

ABSTRACT

The influence of porosity and electrokinetic effects on flow through microchannels is studied in this paper. The brinkman model for porous media is modified to take into account electrokinetic effects. The model is solved numerically and Debye –huckel linear approximation is used for electric potential.

Key Words: *heat transfer,porosity,zeta potential ,flow.*

1. INTRODUCTION

Micro electromechanical systems involve fluid flow in microchannels. Flow through microchannels is important in designing microfluidic devices like cooling system of chips due to their higher heat transfer coefficient as discussed by Zhang *et al.* [1]. In flow through microchannels interfacial effects are important. For example, electrolytic flow in microchannels can be different from nonelectrolytic flows. The study of flow through porous media has applications in nuclear cooling system, geophysics and petroleum engineering. Moreover human lung, small blood vessels are examples of flow through porous medium. Hence a numerical analysis of influence of porosity and electrokinetic effects is presented here.

The present work deals with modification of brinkman equations taking into account electrokinetic effects and numerically solving them using numerical method. The brinkman model of equations for porous media is applied to an infinite parallel channel. Debye –huckel linear approximation is used for electric potential.

The equations are solved numerically with the following assumptions

1. The flow is laminar, incompressible, steady, fully developed.
2. Gravity forces are ignored.
3. The fluid is Newtonian and its properties are independent of local field strength.
4. The ions are point charges, with no concentration gradients.
5. Zeta potential is assumed to be uniform.
6. Viscous dissipation is neglected.
7. The fluid is continuum.

The electrostatic potential Ψ is related to the local net charge density ρ by Poissons equation

$$\partial^2\Psi/\partial y^2 = -\rho/\epsilon$$

Following A.Jain *et al.* [2] the nonlinear dimensional second order equation is

$$d^2\Psi/dy^2 = 2ze_n/\epsilon \sinh(ze\Psi/kT)$$

which is the boltzmann equation.

2. DEBYE–HUCKEL APPROXIMATION

Debye –huckel parameter k depends only on liquid properties. At small electrolyte concentrations \sinh can be approximated and equation reduces to

$$d^2\Psi/dy^2=k^2\Psi$$

The solution of the above equation is

$$\Psi = \zeta/\sinh(k) \sinh(ky)$$

Increased zeta potential increases relative charge density of ions near the walls which produces higher potential.

3. SOLUTION OF THE GOVERNING EQUATIONS

The nondimensional brinkman model equation for the flow through a channel with porous media using the non-dimensional parameters is

$$d^2U/dY^2 - \sigma^2U - Qd^2\Psi/dY^2 + \Gamma = 0$$

where $\sigma = a^2/K, Q=2n\epsilon a^2\zeta/\mu UL$ $\Gamma = -a^2/\mu U$. The equations are solved numerically using the boundary conditions

$$d\Psi/dY=dU/dY=0 \text{ at } Y=0, U=0, \Psi=\zeta \text{ at } Y=1$$

4. RESULTS

The influence of porous media , electrokinetic effects and pressure are illustrated in the graphs. The presence of EDL decreases the fluid velocity. As porosity increases flow rate decreases further. In the presence of porosity higher value of pressure gradient shows that the flow is constant and only decreases near the wall.

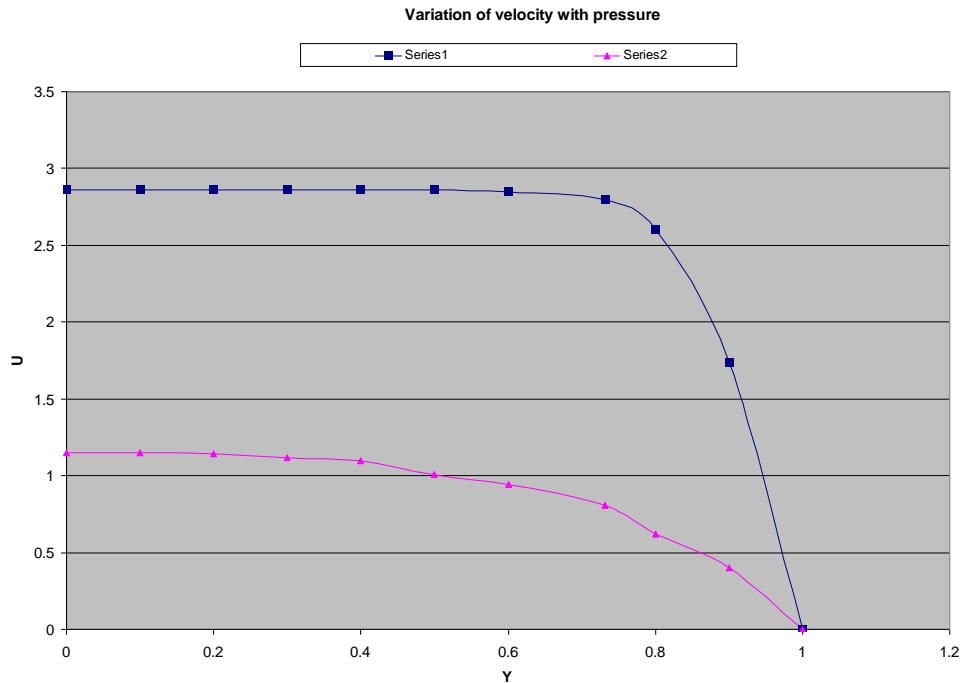


FIGURE 1 Variation of velocity with pressure

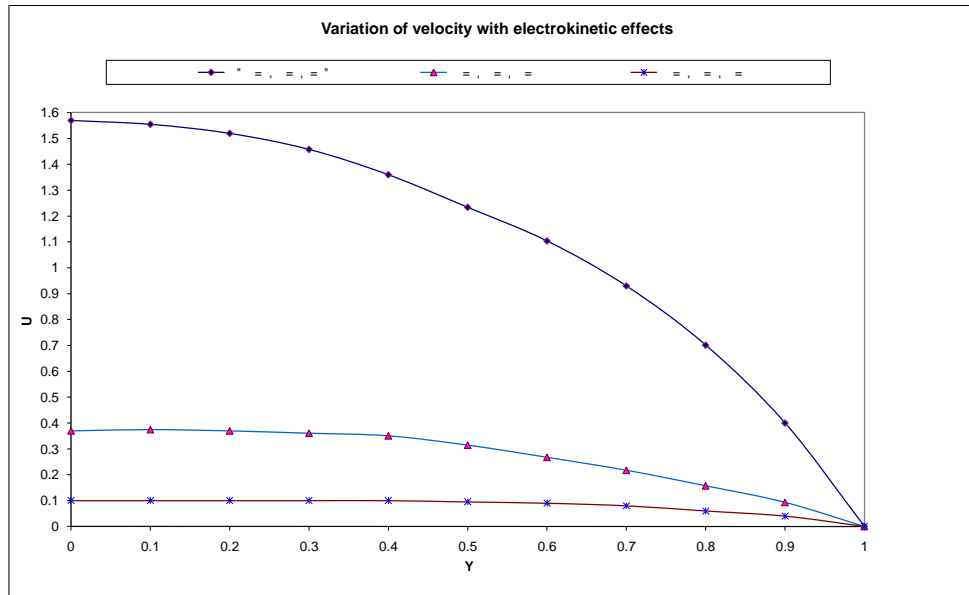


FIGURE 2 Variation of velocity with electrokinetic effects

REFERENCES

- [1] L.Zhang *et al.* *J.MEMS* 11(1), 2002.
- [2] Abhishek *et al.* *Int.Journal Heat& Mass Transfer* 50, 5161-5167, 2007.

EXPLICIT SOLUTIONS FOR HEAT AND FLUID FLOW IN CYLINDRICAL POROUS DOMAINS

Fausto Arpino

Dipartimento di Meccanica Strutture Ambiente e Territorio (DiMSAT), Università di Cassino, Via
G. Di Biasio 43, 03043 Cassino (FR), Italy. E-mail: f.arpino@unicas.it

Alberto Carotenuto, Nicola Massarotti, Alessandro Mauro

Dipartimento per le Tecnologie (DiT), Università degli Studi di Napoli "Parthenope", Centro
Direzionale, Isola C4, 80143 Napoli, Italy. E-mail: alberto.carotenuto@uniparthenope.it,
nicola.massarotti@uniparthenope.it, alessandro.mauro@uniparthenope.it

ABSTRACT

In this work, fully explicit numerical solutions for heat and fluid flow in cylindrical domains, completely or partially filled with a fluid saturated porous medium, are presented. Laminar natural convection in a vertical porous annulus and in a vertical annulus with a centrally located heat generating rod, and laminar forced convection in a pipe partially filled with a porous medium are numerically simulated. Novel stability conditions are carried out for the fully explicit Artificial Compressibility (AC) version of the Characteristic Based Split (CBS) algorithm, in order to effectively solve the above problems. The results presented in this paper are validated against experimental and numerical results available from the literature.

Key Words: *AC-CBS, stability, cylinder, annular, generalized porous medium model.*

1. INTRODUCTION

Interest in understanding the convective transport processes in porous materials is increasing owing to the development of geothermal energy technology, high performance insulation for building, drying processes, packed bed chemical reactors, porous heat exchangers, underground disposal of nuclear waste materials, food storage, electronic device cooling [1]. Many numerical and experimental studies on heat and fluid flow in porous domains have been carried out during the last decades. A comprehensive review concerned with this topic can be found in the references [2-4].

Laminar natural convection in vertical porous annuli has been widely investigated in the literature, both numerically and experimentally. Havstad and Burns [5] used a finite difference technique to analyze the heat transfer characteristics in a vertical annulus filled with a porous medium, and presented correlations for the heat transfer in the annulus. Natural convection in a vertical porous annulus has been studied for isothermal heating [6] as well as by considering a constant heat flux at the inner wall [7] for a wide range of Rayleigh numbers, aspect ratios and radius ratios. Prasad and Kulacki [6] employed a finite difference discretization technique and a point iterative method to solve the system of algebraic natural convection equations. The numerical results were validated against experimental data, carried out by building up a proper experimental apparatus and a measurement procedure described in reference [6].

Forced convection in ducts partially filled with a fluid saturated porous medium has been extensively studied mainly in relation with its practical application on heat transfer enhancement inside heat exchangers. Mohamad [8] analyzed the steady laminar flow in a conduit fully or partially filled with a porous layer for different values of permeability and porous layer thickness. A control volume, finite-difference discretization technique is used, and the SIMPLER algorithm is employed to solve the equations in primitive variables. The algebraic equations are solved by a line-

by-line iterative method. Yang and Hwang [9] studied numerically the turbulent heat transfer enhancement in pipes partially filled with porous media, by employing a $k-\varepsilon$ turbulence model. The conservation equations are discretized by employing a control volume based finite difference method. The numerical method used is based on the SIMPLE iterative algorithm.

To the authors' knowledge, a fully explicit finite element based scheme has not been employed in the literature to solve natural convection in porous annuli and forced convection in partially porous pipes. For this reason, the authors have further developed the AC-CBS scheme [10] to solve axisymmetric problems in fluid and porous domains. In order to obtain a stable and computationally efficient solution, the algorithm has been properly stabilized to solve the generalized porous medium model in a cylindrical coordinate system.

2. GOVERNING EQUATIONS

The non-dimensional form of the equations in a cylindrical coordinate system, solved in this paper, can be written as:

Mass conservation equation

$$\frac{\partial \rho}{\partial t} + \frac{1}{r} \frac{\partial (r \rho u_r)}{\partial r} + \frac{\partial (\rho u_z)}{\partial z} = 0 \quad (1)$$

Momentum conservation equation in r-direction

$$\frac{1}{\varepsilon} \frac{\partial u_r}{\partial t} + \frac{1}{\varepsilon^2} \left(u_r \frac{\partial u_r}{\partial r} + u_z \frac{\partial u_r}{\partial z} \right) = -\frac{\partial p_f}{\partial r} + \frac{J}{\varepsilon \text{Re}} \left[\frac{1}{r} \frac{\partial}{\partial r} \left(r \frac{\partial u_r}{\partial r} \right) - \frac{u_r}{r^2} + \frac{\partial^2 u_r}{\partial z^2} \right] - P u_r + G_r \quad (2)$$

Momentum conservation equation in z-direction

$$\frac{1}{\varepsilon} \frac{\partial u_z}{\partial t} + \frac{1}{\varepsilon^2} \left(u_r \frac{\partial u_z}{\partial r} + u_z \frac{\partial u_z}{\partial z} \right) = -\frac{\partial p_f}{\partial z} + \frac{J}{\varepsilon \text{Re}} \left[\frac{1}{r} \frac{\partial}{\partial r} \left(r \frac{\partial u_z}{\partial r} \right) + \frac{\partial^2 u_z}{\partial z^2} \right] - P u_z + G_z \quad (3)$$

Energy conservation equation

$$\sigma \frac{\partial T}{\partial t} + \left(u_r \frac{\partial T}{\partial r} + u_z \frac{\partial T}{\partial z} \right) = \frac{\lambda}{\text{Pr Re}} \left[\frac{1}{r} \frac{\partial}{\partial r} \left(r \frac{\partial T}{\partial r} \right) + \frac{\partial^2 T}{\partial z^2} \right] + S_e \quad (4)$$

The scales and the parameters used to derive the above non-dimensional equations, written for the general case of mixed convection, are:

$$\begin{aligned} x_i &= \frac{x_i^*}{L}; \quad u_i = \frac{u_i^* L}{\alpha_f}; \quad t = \frac{t^* \alpha_f}{L^2}; \quad p_f = \frac{p_f^* L^2}{\rho_f \alpha_f^2}; \quad T = \frac{T^* - T_c}{T_h - T_c}; \quad \alpha_f = \frac{\lambda_f}{(\rho c_p)_f}; \quad \nu_f = \frac{\mu_f}{\rho_f}; \\ \lambda &= \frac{\lambda_{\text{eff}}}{\lambda_f}; \quad J = \frac{\mu_{\text{eff}}}{\mu_f}; \quad \sigma = \frac{\varepsilon (\rho c_p)_f + (1-\varepsilon)(\rho c_p)_s}{(\rho c_p)_f}; \quad \text{Pr} = \frac{\nu_f}{\alpha_f}; \quad \text{Re} = \frac{\rho_f u_{\text{ref}} L}{\mu_f}; \quad \text{Da} = \frac{\kappa}{L^2}; \\ \text{Ra} &= \frac{g B_f (T_h - T_c) L^3}{\nu_f \alpha_f}; \quad P = \left(\frac{1}{\text{Re Da}} + \frac{F}{\sqrt{\text{Da}}} |\mathbf{u}| \right); \quad G_z = \frac{\text{Ra}}{\text{Pr Re}^2} T; \quad G_r = S_e = 0 \end{aligned} \quad (5)$$

3. AC-CBS STABILITY ANALYSIS FOR AXISYMMETRIC PROBLEMS

In order to solve the generalized porous medium model in axisymmetric domains, the stability analysis of the conservation equations, performed on the basis of the order of magnitude of all the terms [10], is here presented for a cylindrical coordinate system. The stability conditions are derived

by observing that the order of magnitude of each term must be smaller than one. This approach is applied to the steps of the AC-CBS scheme. The time-step restrictions obtained by adopting the present analysis are shown in the followings:

$$\begin{aligned}
 \text{Step 1: } \Delta t_{conv} &= \frac{\varepsilon h}{u_{conv}^n}; \Delta t_{diff} = \frac{Re h^2}{2}; \Delta t_b = \frac{Pr Re^2 h}{\varepsilon Ra T^n \Delta T^n}; \Delta t_{ax1} = Re \bar{r} h; \Delta t_{axr} = Re \bar{r}^2 \\
 \text{Step 2: } \beta &= u_{conv}^n + \frac{h}{\min(\Delta t_{conv}, \Delta t_{diff}, \Delta t_b)}; \Delta t_2 = \min\left(\frac{p^n \varepsilon h}{\beta^2 \tilde{u}^{n+1}}, \sqrt{\frac{\rho_f h^2}{2\beta^2}}\right) \\
 \text{Step 3: } \Delta t_3 &= \frac{h}{\beta}; \text{ Step 4: } \Delta t_{convT} \leq \frac{h}{u_{conv}^n}; \Delta t_{diffT} \leq \frac{Pr Re h^2}{2}
 \end{aligned} \tag{6}$$

4. RESULTS

The axial-symmetric version of the AC-CBS scheme is successfully applied to the following problems: i) natural convection in a vertical porous annulus; ii) forced convection in a pipe completely and partially filled with a saturated porous medium. The computational domains and the boundary conditions employed for the two problems considered are shown in Figure 1. The present results have been validated against numerical, analytical and experimental data available from the literature [6, 8], and an excellent agreement has been found. Figure 2 shows the velocity and temperature profiles for natural convection in a vertical porous annulus and forced convection in partially porous pipe, respectively. All the parameters employed in the present simulations can be found in references [6, 8].

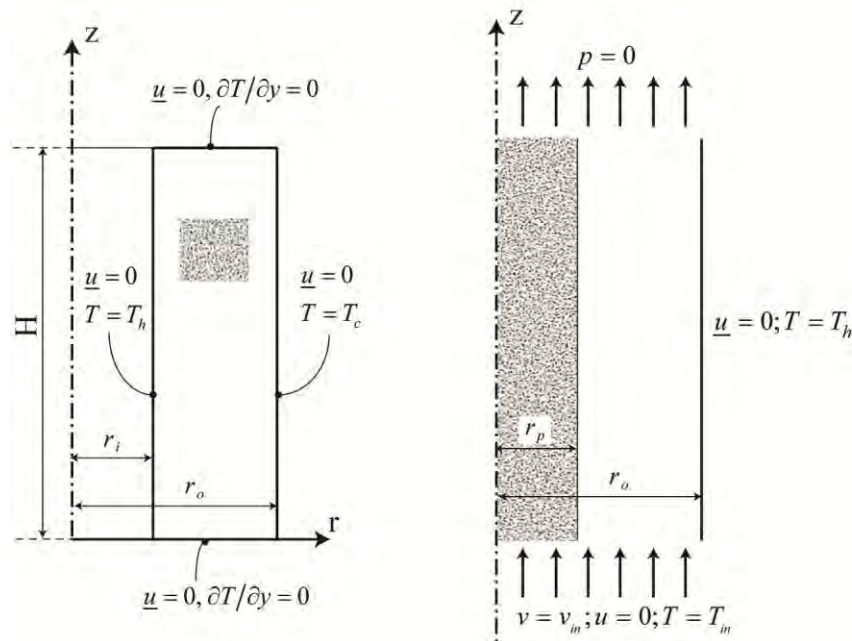


FIGURE 1. Computational domain and boundary conditions employed: (left) natural convection in a vertical porous annulus; (right) forced convection in a partially porous pipe.

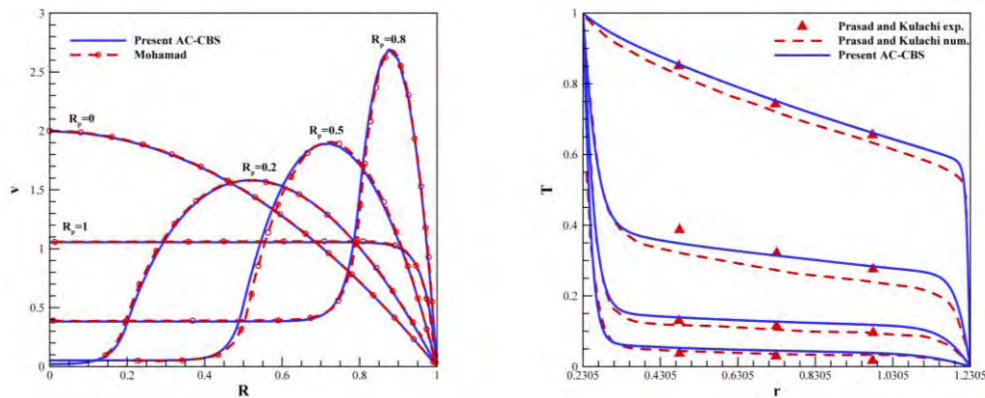


FIGURE 2. Natural convection in a vertical porous annulus (left); forced convection in a partially porous pipe (right).

5. CONCLUSIONS

The axisymmetric version of the AC-CBS algorithm has been successfully applied to natural and forced convection problems in porous and partially porous domains. The stability analysis developed for the scheme in cylindrical coordinate system has allowed to efficiently solve axisymmetric problems in presence of large source terms. The present results have been validated against analytical, numerical and experimental data available from the literature.

REFERENCES

- [1] M. Sankar, Y.Y. Park, J.M. Lopez, Y. Do, Numerical study of natural convection in a vertical porous annulus with discrete heating, *International Journal of Heat and Mass Transfer*, 54, 1493-1505, 2011.
- [2] P. Vadasz, *Emerging Topics in Heat and Mass Transfer in Porous Media*, Springer, New York, 2008.
- [3] D.A. Nield, A. Bejan, *Convection in Porous Media*, third ed., Springer, New York, 2006.
- [4] K. Vafai, *Handbook of Porous Media*, 2nd ed., Taylor & Francis, New York, 2005.
- [5] M.A. Havstad, P.J. Burns, Convective heat transfer in vertical cylindrical annuli filled with a porous medium, *International Journal of Heat and Mass Transfer*, 25, 1755-1766, 1982.
- [6] V. Prasad, F.A. Kulacki, Natural convection in porous media bounded by short concentric vertical cylinders, *Journal of Heat Transfer*, 107, 147-154, 1985.
- [7] V. Prasad, Numerical study of natural convection in a vertical, porous annulus with constant heat flux on the inner wall, *International Journal of Heat and Mass Transfer*, 29, 841-853, 1986.
- [8] A.A. Mohamad, Heat transfer enhancements in heat exchangers fitted with porous media Part I: constant wall temperature, *International Journal of Thermal Sciences*, 42, 385-395, 2003.
- [9] Y.T. Yang, M.L. Hwang, Numerical simulation of turbulent fluid flow and heat transfer characteristics in heat exchangers fitted with porous media, *International Journal of Heat and Mass Transfer*, 52, 2956-2965, 2009.
- [10] F. Arpino, N. Massarotti, A. Mauro, A stable explicit fractional step procedure for the solution of heat and fluid flow through interfaces between saturated porous media and free fluids in presence of high source terms, *International Journal for Numerical Methods in Engineering*, 83: 671-692, 2010.

NUMERICAL MODELLING OF GRAVITATIONAL CONVECTION IN THREE-COMPONENT GAS MIXTURES IN THE CYLINDRICAL CHANNEL

V.N. Kosov

Kazakh National Pedagogical University named after Abay, Dostyk, 13, Almaty, Kazakhstan,
050100, kosov_vlad_nik@list.ru

I.V. Poyarkov, O.V. Fedorenko

Al-Farabi Kazakh National University, Tole bi, 96, Almaty, Kazakhstan, 050012, p-igor@inbox.ru

ABSTRACT

The gravitational convection or diffusion instability under diffusive mixing in ternary gas mixture in a vertical cylindrical channel of finite size is numerically investigated. The arrangement of the transition boundaries between diffusion and gravitational convection is defined.

Key Words: *Diffusion, Convection, Instability of Mechanical Equilibrium, Linear Theory of Stability, Rayleigh Numbers.*

1. INTRODUCTION

Experimental measuring the diffusion coefficients in multicomponent gas mixtures is the time-consuming problem and requires certain level of proficiency from a researcher, particularly, when making the diffusion apparatus and devices as well as other necessary equipment. The experiments performed previously revealed unknown peculiarities of the multicomponent mass transfer, for example, the diffusion instability [1,2] and the circulation of diluent gas in a diffusion channel [3]. The study of diffusion instability (anomalous gravitation concentration convection) is of great interest for both the mass transfer theory and practical applications.

The systems with two and more independent gradients or thermodynamic forces exhibit complicated behaviour, when the convective flows occur. Such systems are called the systems with double-diffusive convection [4]. The stability paradox is characteristic of the systems with double-diffusive convection. Meanwhile, the instability in the gravity field can be arisen from the stable stratification of mass density, i.e. in the case when the density above is less than the one below. The process of diffusion instability depends on certain conditions and parameters, for example, pressure, concentration, temperature, viscosity, geometry of the diffusion channel etc. [5].

2. THE MODEL OF DIFFUSION INSTABILITY

Various kinetic, thermodynamic and semiempirical approaches to the definition of diffusion instability are used in the literature [1-4].

Application of the methods of the stability theory [1] made it possible to develop an approach for the study of the most general peculiarities to define the arrangement of transition boundaries between the diffusion and the concentration gravitation convection.

The macroscopic flow of the isothermal ternary gas mixture is described by the general system of the hydrodynamic equations, that includes the Navier-Stokes equations, equations for conservation of the number of particles in the mixture and the components. Taking into account the conditions of

independent diffusion, for which the equalities $\sum_{i=1}^3 \bar{j}_i = 0$ and $\sum_{i=1}^3 c_i = 1$ are valid, the system of equations takes the following form [1,5]:

$$\begin{aligned} \rho \left[\frac{\partial \bar{u}}{\partial t} + (\bar{u} \nabla \bar{u}) \right] &= -\nabla p + \eta \nabla^2 \bar{u} + \left(\frac{\eta}{3} + \xi \right) \nabla \operatorname{div} \bar{u} + \rho \bar{g}, \\ \frac{\partial n}{\partial t} + \operatorname{div}(n \bar{v}) &= 0, \quad \frac{\partial c_i}{\partial t} + \bar{v} \nabla c_i = -\operatorname{div} \bar{j}_i, \\ \bar{j}_i &= -(D_{ii}^* \nabla c_i + D_{ij}^* \nabla c_j), \end{aligned} \quad (1)$$

where D_{ij}^* are “practical” coefficients of three-component diffusion.

The equations (1) are supplemented by the environmental state equation

$$\rho = \rho(c_1, c_2, p), \quad T = \text{const},$$

relating the thermodynamic parameters entering Eq. (1).

The method of small perturbations [1,6] is used for solution of the system of Eq. (1). Taking into account that at $L \gg r$ (L, r are the length and the radius of the diffusion channel, respectively) the differences in the perturbations of the average \bar{v} and the weight-average \bar{u} velocities in the Navier-Stokes equations is negligible [5]. Then the final system of equations of the gravitational concentration convection, which is written in terms of the perturbed dimensionless parameters, takes the following form [6]:

$$\begin{aligned} P_{22} \frac{\partial c_1}{\partial t} - (\bar{u} \bar{\gamma}) &= \tau_{11} \nabla^2 c_1 + \frac{A_2}{A_1} \tau_{12} \nabla^2 c_2, \quad P_{22} \frac{\partial c_2}{\partial t} - (\bar{u} \bar{\gamma}) = \frac{A_1}{A_2} \tau_{21} \nabla^2 c_1 + \nabla^2 c_2, \\ \frac{\partial \bar{u}}{\partial t} &= -\nabla p + \nabla^2 \bar{u} + (R_1 \tau_{11} c_1 + R_2 c_2) \bar{\gamma}, \quad \operatorname{div} \bar{v} = 0 \end{aligned} \quad (2)$$

where $P_{ii} = \nu / D_{ii}^*$ is the Prandtl diffusion number, $R_i = g \beta_i A_i d^4 / \nu D_{ii}^*$ is the Rayleigh partial number, $\tau_{ij} = D_{ij}^* / D_{22}^*$ denote the parameters, which determine the relationship between the “practical” diffusion coefficients.

It is necessary to define exactly the boundary conditions for the solution of the system of Eq. (2). Therefore, we have considered the unstable diffusion mixing problem in the cylindrical channel of a finite size, which is distinct from the infinite case.

The equation system (2) is solved by the method given in [1]. As a result, we determine the concentration distribution along the length of the cylindrical channel of finite dimensions L, r :

$$c_i = \frac{11K_i (h^2 - z^2) (5h^2 - z^2) \cos n\varphi}{248\alpha^2 (k^2 + \alpha^2)} \left[\alpha^2 \frac{J_n(kr)}{J_n(k)} + \frac{I_n(\alpha r)}{\alpha I_n(\alpha)} \left\{ n(\alpha^2 + k^2) - \alpha^2 k \frac{J'_n(k)}{J_n(k)} \right\} - (k^2 + \alpha^2) r^n \right], \quad (3)$$

where $K_1 = \left(\frac{1 - \frac{A_2}{A_1} \tau_{12}}{\tau_{11} - \tau_{12} \tau_{21}} \right)$, $K_2 = \left(\frac{\tau_{11} - \frac{A_1}{A_2} \tau_{21}}{\tau_{11} - \tau_{12} \tau_{21}} \right)$, $\alpha^2 = \frac{153}{62h^2}$, J_n and I_n are the n-order Bessel functions of the first kind, and the parameter k can be found from the equation $k J_n''(k) = (n+1) J_n'(k)$.

In order to determine the monotonous stability boundary of the problem under consideration, the third equation of the system (2) can be scalarly multiplied by the vector \bar{u} and integrated all over the volume V of the diffusion channel. This can be done under the conditions, that $\nabla p = 0, \frac{\partial \bar{u}}{\partial t} = 0$.

Then we have:

$$\int \bar{u} \nabla^2 \bar{u} dV + R_1 \tau_{11} \int u_z c_1 dV + R_2 \int u_z c_2 dV = 0. \quad (4)$$

3. RESULTS OF NUMERICAL EXPERIMENTS

Study is carried out for ternary gas mixture $H_2+N_2-CH_4$. In our experiments, the binary mixture density is less than the density of the pure component. Calculations for the system $H_2+N_2-CH_4$ are made at a temperature 298.0 K under the pressure ranging from 1.0 to 5.0 MPa and the concentrations of gases in the initial binary mixtures for fractions from 0.1 to 0.9 moles.

The case describing the mixing of binary mixture $H_2+N_2-CH_4$ subject to the pressure and the various concentrations of light component is shown in Figures 1.a and 1.b. As seen in Figure 1.a, the point 3 corresponding to the pressure 2.0 MPa is situated practically at the curve MM. Thus, for the system $0.6H_2+0.4N_2-CH_4$ the transition into the area of unstable diffusion occurs under the pressure above 2.0 MPa. In accordance with Figure 1.b the increase of the hydrogen concentration to 0.75 mole fractions results in the transition from the stable area into the unstable one, which occurs under the pressure above 4.0 MPa (point 7). According to Figures 1.a and 1.b, the pressure increase leads to the fact that the stable diffusion process becomes unstable, but the increase of the light component concentration leads to the increase of transition pressure almost by the factor of two.

It follows from Figures 1.a and 1.b that, when changing the pressure, the systems can be both in the stable diffusion area and the unstable process one.

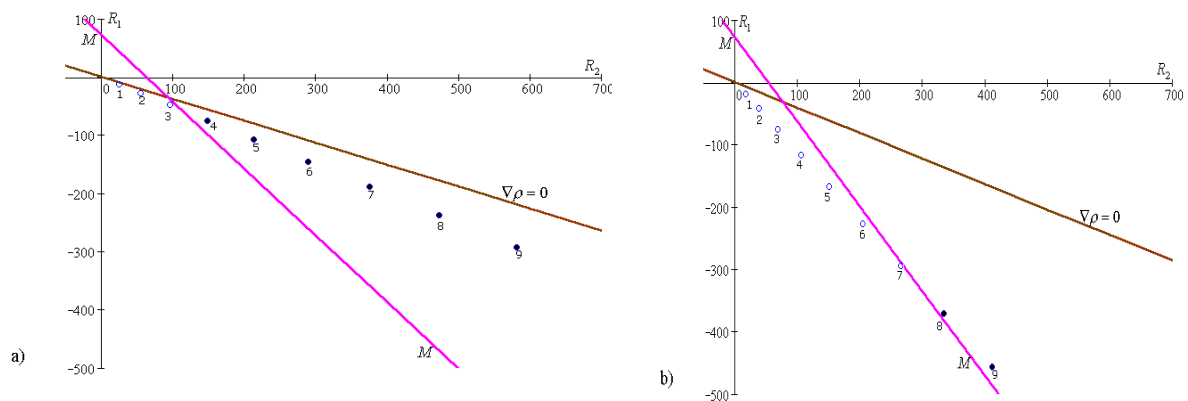


FIGURE 1. Regions of stable and unstable diffusion for the system $H_2+N_2-CH_4$. a) $0.6H_2+0.4N_2-CH_4$; b) $0.75H_2+0.25N_2-CH_4$. Symbols \circ, \bullet correspond to data that determine stable and unstable states respectively. The calculation is carried out at the pressure values: 1 – P=1, 2 – 1.5, 3 – 2, 4 – 2.5, 5 – 3, 6 – 3.5, 7 – 4, 8 – 4.5, 9 – 5 MPa; T = 298.0 K, d = 3.3 mm is the channel diameter; MM is a curve of monotonic disturbances, $\nabla \rho = 0$ is a curve of the zero density gradient

Thus, our studies show that the transition from the diffusion region to the unstable diffusion one occurs at the certain critical pressure P_* . The diffusion occurs in the system at the experiment pressure $P < P_*$.

Points represented on Figure 1 are calculated by the formulas:

$$R_1 = \frac{g n r^4 \Delta m_1}{\rho \nu D_{11}^*} \cdot \frac{\partial c_1}{\partial z}, R_2 = \frac{g n r^4 \Delta m_2}{\rho \nu D_{22}^*} \cdot \frac{\partial c_2}{\partial z}, \quad (5)$$

where m_i is the molecular mass of the i -th component, $\Delta m_1 = m_1 - m_3$, $\Delta m_2 = m_2 - m_3$.

The full circles correspond to the convective mixing process while the open circles conform to the diffusion one.

It can be noticed that on the plane (R_1, R_2) the regions exist, where the line MM is located below the curve of the zero density gradient. In this area the mixture condition is unstable though the mixture density in the lower part of the diffusion channel is more than in the upper one. The physical interpretation of instability for the isothermal mixture is the following. The element of the medium, which is shifted upwards, enters the mixture of the smaller density, but with the different composition. The variance in the interdiffusion coefficients of components results in the transversal diffusion of components, which leads to the equalizing of the light component concentration. Consequently, its insufficient amount is rapidly compensated. The shifted element becomes lighter than environmental and it continues to float up causing the instability [5].

4. CONCLUSIONS

The suggested method of calculation allows one to reveal the areas of both the stable and the unstable mass transfer on the Rayleigh number plane in three component gas mixtures depending on various thermodynamic parameters. The calculation procedure can be applied to determine thermodynamic parameters of gas systems and the geometry of the diffusive channel. The latter has an essential impact on the occurrence of the gravitational convection (diffusive instability). The mathematical model proposed in the current paper is also applicable for calculating of the multicomponent stable mass transfer.

REFERENCES

- [1] G.Z. Gershuni and E.M. Zhukhovitskii, *Convective Stability of an Incompressible Fluid*, Nauka, Moscow, 1972.
- [2] L. Miller and E.A. Mason, Oscillating instabilities in multicomponent diffusion, *Phys. Fluids*, 9(4), 711-721, 1966.
- [3] N.D. Kosov, Yu.I. Zhavrin and D.U. Kul'zhanov, Diffusion of two gases diluted equally by third gas, *Zh.T.F.*, 51(3), 654-649, 1981.
- [4] J.S. Turner, *Buoyancy effects in fluids*, Cambridge University Press, 1979.
- [5] V.N. Kosov and V.D. Seleznev, *An Arise of anomalous Free Gravitational Convection in Isothermal Three-Component Gas Mixtures*, Ural Branch of the Russian Academy of Sciences, Ekaterinburg, 2000.
- [6] V.N. Kosov, V.D. Seleznev and Yu.I. Zhavrin, The diffusion instability of isothermal three-component gas mixtures, *Thermophysics and Aeromechanics*, 7(1), 127-135, 2000.

A GENERALIZED NAVIER-STOKES CONSTITUTION RELATION FOR MULTISCALE GAS FLOWS

Zhaoli Guo, Chuguang Zheng

National Laboratory of Coal Combustion, Huazhong University of Science and Technology, Wuhan,
430074, China, zlguo@hust.edu.cn

ABSTRACT

As a gas flowing over a solid surface, there exists a kinetic boundary layer, also known as Knudsen layer (KL) near the surface in which the velocity changes rapidly. The KL is different from the viscous boundary layer usually encountered in hydrodynamic problems. The thickness of the KL is usually in the order of the mean-free path (MFP) of the gas system. Within the KL, the intermolecular collisions in the KL are much inefficient than that far from the wall so that the quasi-thermodynamic-equilibrium assumption, upon which the Navier-Stokes constitution depends, does not hold any more. Therefore, it is generally thought that this linear Navier-Stokes constitutive relation is invalid. For many engineering problems, the KL is negligible and the flow within the KL can be well described by the Navier-Stokes equation. However, for non-continuum flows where the KL takes a large portion, it becomes critical to capture the gas motion in the KL. This work aims to develop an extended Navier-Stokes constitution with an effective viscosity which considers the KL effect.

In order to capture the KL while keeping the simple form of the Navier-Stokes model, the following extended Navier-Stokes formulation is developed:

$$\boldsymbol{\tau}(\mathbf{r}) = -\mu_e(\mathbf{r})\dot{\boldsymbol{\gamma}}(\mathbf{r}), \quad (1)$$

where $\boldsymbol{\tau}$, μ_e , and $\dot{\boldsymbol{\gamma}}$ are the local shear stress, effective dynamic viscosity, and strain rate at position \mathbf{r} , respectively. The key point of this model lies in the definition of the effective viscosity μ_e . Based on the relationship between the viscosity and the mean-free-path in the gas kinetic theory [1]:

$$\lambda_e = \frac{\mu_e}{p} \sqrt{\frac{\pi RT}{2}}, \quad (2)$$

where $p = \rho RT$ is the pressure, with ρ the density, R the gas constant, and T the gas temperature. Therefore, once the effective mean-free-path λ_e is determined, the new Navier-Stokes model will be closed. The effective mean-free-path λ_e in a gas system bounded by a solid wall is always smaller than that in an unbounded system, because the free paths of some molecules will be cut off by the wall. The effect of wall-confinement on the mean-free-path can be expressed through a function Ψ ,

$$\lambda_e = \lambda \Psi(\mathbf{r}, \text{Kn}). \quad (3)$$

The exact expression of Ψ can be derived rigorously through the probability distribution function of the free-path of a gas molecule [2], and is usually dependent on the flow geometry. For instance, for a gas bounded between two parallel plates located at $y=0$ and $y=H$ respectively, the mean-free-path of the molecules in the plane located at $0 \leq y \leq H$ is [3]

$$\Psi(y) = \frac{1}{2} \left[\psi\left(\frac{y}{\lambda}\right) + \psi\left(\frac{H-y}{\lambda}\right) \right], \quad (4)$$

where λ is the mean-free-path for an unbounded system, and the function ψ is defined as

$$\psi(\alpha) = 1 + (\alpha - 1)e^{-\alpha} - \alpha^2 E_i(\alpha), \quad (5)$$

where $E_i(x)$ is the exponential integral function defined by

$$E_i(x) = \int_1^{\infty} t^{-1} e^{-xt} dt. \quad (6)$$

From Eqs. (2) and (3) we can obtain the effective geometry-dependent viscosity as

$$\mu_e(y) = \mu \Psi(y), \quad (7)$$

where μ is the viscosity for an unbounded gas or that far away from the wall.

It is noted that $\psi(x)$ is a monotonically increasing function satisfying $\psi(0) = 0$ and $\psi(\infty) = 1.0$. Therefore, if the top plate is removed, i.e. $H \rightarrow \infty$, the effective viscosity becomes

$$\mu_e(y) = \frac{\mu}{2} \left[\psi\left(\frac{y}{\lambda}\right) + 1 \right]. \quad (8)$$

This suggests that the effective viscosity will approach to the bulk one far away from the wall, but is exactly one half of the bulk one at the wall. The fact that $\mu_e(0) = \mu/2$ is consistent with some previous independent studies [4,5].

For a more complicated geometry, the exact formulation of the geometric function $\Psi(\mathbf{r}, \text{Kn})$ may be quite complicated. However, if the local curvature of the wall is not large, a more effective way may be to use the present formulation as a "wall function", just like that proposed in Ref. [5].

In practical applications the generalized Navier-Stokes equations with the extended constitution must be supplemented by some suitable boundary conditions. Generally, the true or microscopic velocity at the wall, u_s , is usually different from the virtual or macroscopic slip velocity u_s^{ns} extrapolated from the Navier-Stokes velocity in the bulk region. For instance, for the Kramer's problem these two slip velocities are given approximately by [6],

$$u_s = \frac{2 - \sigma}{\sigma} (1 - 0.1817\sigma) \lambda \frac{\partial u}{\partial y}, \quad (9)$$

$$u_s^{ns} = \frac{2 - \sigma}{\sigma} (1 + 0.1621\sigma) \lambda \frac{\partial u}{\partial y}, \quad (10)$$

where σ is the accommodation coefficient. As $\sigma = 1$, i.e., the wall is fully diffusive, both u_s and u_s^{ns} are in good agreement with the exact solutions of the linearized Boltzmann (BGK) equation [1]. The velocity outside the KL is linear for the Karmer's problem. Cercignani also proposed a second-order slip boundary condition for u_s^{ns} based on the solution of Boltzmann equation for the Poiseuille flow where the velocity outside the KL is nonlinear:

$$u_s^{ns} = \zeta \lambda' \partial_y u - \frac{1}{2} \left(\frac{1}{2} + \zeta^2 \right) \lambda'^2 \partial_y^2 u, \quad (11)$$

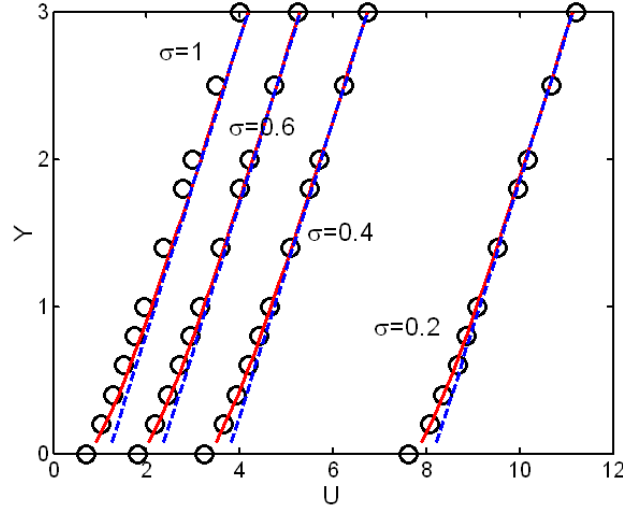


FIGURE 1. Velocity profiles of the Kramer problem. Solid line: Generalized Navier-Stokes model; Dashed line: linear extrapolation; Symbol: linearized Boltzmann equation [6]. Here $Y = y / \lambda'$ with $\lambda' = (2 / \sqrt{\pi})\lambda$, and $U = u / a\sqrt{2RT}$.

where $\zeta = 1.016$ and $\lambda' = (2 / \sqrt{\pi})\lambda$. Motivated by Eqs. (9), (10), and (11), we propose a heuristic second-order slip boundary condition for the microscopic slip velocity u_s :

$$u_s := u(0) - u_w = A_1 \left[\lambda_e \partial_y u \right] - A_2 \left[\lambda_e \partial_y (\lambda_e \partial_y u) \right], \quad (12)$$

where $u(0)$ is the gas velocity at the wall, u_w is the wall velocity, and the two slip coefficients are given by

$$A_1 = \frac{2 - \sigma}{\sigma} (1 - 0.1817\sigma), \quad A_2 = \frac{1}{\pi} + \frac{1}{2} A_1^2. \quad (13)$$

This is a generalization of the boundary condition proposed in Ref. [3] where the two parameters A_1 and A_2 are set to be 1.0 and 0.5, respectively. It should be emphasized that the mean-free-path appearing in the above boundary condition is a locally position-dependent variable. If we replace λ_e with the constant bulk mean-free-path λ , Eq. (12) is very similar to the second-order slip boundary condition that is widely used for the classical Navier-Stokes equations [7]. It is also noted that owing to the use of the local effective-mean-free-path, the slip velocity given by Eq. (12) is smaller than that of the classical one given by Eq. (11) as $\sigma = 1$. This is reasonable since the microslip velocity u_s is usually smaller than the extrapolated Navier-Stokes slip velocity u_s^{ns} .

The developed generalized Navier-Stokes constitution, together with a generalized slip boundary condition, is applied to several gas flows ranging from continuum to free-molecular regimes. It is shown that with this new model is able to capture the critical behaviors within the KL. The first test case is the Kramer problem, which is used to demonstrate the capability of the method for capturing the Knudsen layer. In this problem the gas fills the half space $y > 0$ bounded by a wall in the plane $y = 0$ and is sheared by a uniformly applied stress a at infinity [1]. For this problem, the second term on the right-hand side of the heuristic boundary condition (12) takes no effect since $\partial_y (\lambda_e \partial_y u) = 0$ everywhere, and therefore equation (12) essentially gives a first-order slip boundary condition.

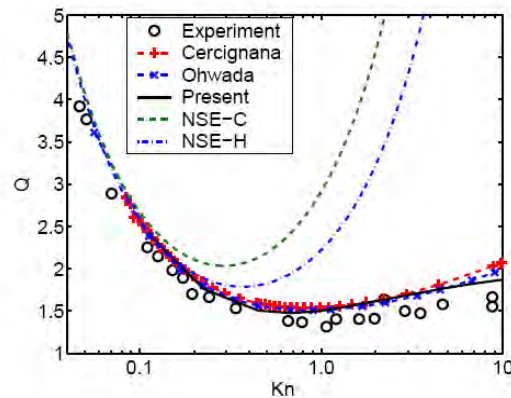


FIGURE 2. Normalized mass flow rate in a force driven channel flow.

In Fig. [1], the velocity profiles predicted by the present MRT-LBE as σ changes from 0.2 to 1.0 are shown and compared with the results of the linearized Boltzmann equation [6]. For comparison, the linear extrapolations from the velocity profiles outside the KL are also shown. It is clearly seen that the LBE results are in good agreement with the solutions of the Boltzmann equation, and the nonlinearity of the velocity profile within the Knudsen layer is successfully captured. These observations demonstrate the potential capability of the present MRT-LBE model for capturing the flows within KL.

The generalized Navier-Stokes model is also applied to the planar Poiseuille flow driven by a constant force a , which has a nonlinear velocity profile in the whole region. In Fig. 2 the nondimensional mass fluxes Q of several methods normalized by $\rho a H^2 / \sqrt{2RT}$. It is seen that all of the methods give accurate results as $Kn \leq 0.1$ in comparison with the solutions of the Boltzmann equation obtained and the experimental results [8]. Above this Kn , the other two methods (NSE-C and NSC-H), which use the classical Navier-Stokes model with the standard second-order slip boundary condition [1] or a modified one [9], produces unreasonable results. On the other hand, the present model predicts satisfied result in a rather larger region, and is able to capture the Knudsen minimum successfully.

REFERENCES

- [1] C. Cercignani, *Mathematical Methods in Kinetic Theory*, Plenum, New York, 1990.
- [2] D.W. Stops, *J. Phys. D: Appl. Phys.*, 3, 685, 1970.
- [3] Z.L. Guo, B.C. Shi, and C.G. Zheng, *Europhys. Lett.*, 80, 24001, 2007.
- [4] M. Fichman and G. Hetsroni, *Phys. Fluids*, 17, 123102, 2005.
- [5] D.A. Lockerby, J.M. Reese, and M.A. Gallis, *AIAA J.*, 43, 1391, 2005.
- [6] S.K. Loyalka, N. Petrellis, and T.S. Strovvick, *Phys. Fluids*, 18,1094, 1975.
- [7] G.E. Karniadakis and A. Beskok, *Micro Flows, Fundamentals and Simulation*, Springer, New York, 2001.
- [8] W. Dong, University of California Report, UCRL-3353, 1956.
- [9] N.G. Hadjiconstantinou, *Phys. Fluids*, 15, 2352, 2003.

MIXED CONVECTION FLOW IN A VERTICAL ANNULUS FILLED WITH VARIABLE POROUS MATERIAL

M.L. Kaurangini

Department of mathematical sciences Kano University of Science and Technology, Wudil, Nigeria,
kaurangini@yahoo.com

Basant K. Jha

Department of mathematics Ahmadu Bello University, Zaria, Nigeria, basant777@yahoo.co.uk

ABSTRACT

The present article deals with analytical solution of fully developed mixed convection flow of an incompressible and viscous fluid in a vertical annulus filled with porous material having variable porosity. The non-Darcian flow model derived by Vafai and Tien [13] is adopted for the momentum transfer in the porous domain. The inertia effect is neglected to derive the closed form solution for the governing equations. The influence of the porous matrix on the mass flow rate, pressure gradient, and shear stress at the duct surfaces is clearly demonstrated for isothermal and isoflux heating of the duct surfaces. The main objective is to investigate the influence of different parameters occurring in the present model, namely the Darcy number and the ratio of the radius of inner cylinder to the radius of outer cylinder, on the occurrence of flow reversal at the outer surface of inner cylinder or inner surface of outer cylinder for two different thermal boundary conditions at the outer surface of inner cylinder. During the course of numerical computation it was found that reverse flow occurs easily at the outer surface of inner cylinder for a small Darcy number when Isoflux heating of the duct surfaces.

Key Words: *Mixed Convection, Flow Reversal, Darcy Number, Porous Matrix.*

1. INTRODUCTION

Studies of fluid flow in a vertical annular have drawn the attention of scientists because of its wide application in chemical engineering, petroleum exploration, underground water studies and many others. A recent literature survey shows that, Nield and Bejan [12] found that majority of the works on convection heat transfer in porous media are based on Darcy law [6] where specific range of Darcy and Reynolds numbers are used to determine the accuracy of the results. Vafai and Tien [13] discussed the importance of Brickman and Forchheimer terms in the case of forced convection flow over a flat plate and presented the results when the viscous and inertia terms are negligible. Mishra *et al.* [11] studied the mixed convection in a vertical annulus filled with a porous matrix with constant porosity. Jha [9] studied free convection flow through an annular porous medium.

Studies carried out by several investigators disclosed that flow reversal as a significant phenomenon in ducts [1,2,4,5,7,8,10,14]. Buoyancy-assisted flow reversal in the entrance region of vertical rectangular ducts has been studied numerically by Cheng *et al.* [5]. Various asymmetric heating boundary conditions have been reported. Also it has been found that the flow reversal takes place when the ratio Gr/Re surpasses a threshold value. The threshold value of Gr/Re for the onset flow reversal under fully developed conditions for mixed convection in a vertical parallel plate ducts is also investigated by Barletta [1,2]. The same study also evaluated the effect of various boundary conditions on flow reversal analytically. Ingham *et al.* [7] have addressed a numerical method solution of mixed convection in vertical parallel plate ducts, including the condition for both negative and positive values of Gr/Re . They have focused on the situations that buoyancy effects are so significant that flow reversal occurs either at the centre of the duct or near the walls. Marcondes

and Maliska [10] have solved the elliptic natural convection flows in open-ended channels applying different boundary conditions for pressure and velocity at the channel inlet. They have found that for non-symmetrical flow conditions, flow reversal at the channel outlet depends on the pressure boundary condition applied at the entrance. Wang *et al.* [14] have investigated numerically mixed convection flow at low Peclet numbers within vertical and horizontal pipes, paying attention to the flow reversal taking place at the thermal entrance region of the pipes. The occurrence regime of flow reversal corresponding to Pe has been identified for both cooling and heating cases. Since for low Pr fluids the axial conduction plays a significant role in heat transfer, Pe is the relevant parameter whose effects on the occurrence of flow reversal have been studied. Bazdidi-Tehrani *et al.* [3] presented numerical analysis of combined mixed convection-radiation heat transfer in vertical channel where the radiative properties (i.e. emitting, scattering and absorbing) have been considered both for the walls and participating medium. The influence of two radiative parameters, namely, the conduction-radiation parameter and optical thickness on the flow reversal has been presented. None of the studies mentioned here have considered the flow reversal in vertical annulus filled with porous material. This motivated the present work to study flow reversal in mixed convective flow passing through vertical annulus filled with porous material. The fully developed mixed convection flow of an incompressible and viscous fluid in vertical concentric annuli filled with a porous material having variable porosity for isothermal or isoflux heating of duct surface was studied.

2. MATHEMATICAL ANALYSIS

A steady laminar fully developed mixed convection flow of an incompressible and viscous fluid is considered in a vertical concentric annulus of infinite length filled with porous material having variable porosity. A pressure gradient is taken along z-axis parallel to the axis of the cylinders and r-axis perpendicular to it. In formulating the problem, the following assumptions have been made:

- The fluid obeys Boussinesq approximation.
- The velocity of the fluid varies in the axial direction only.
- The heat transfer takes place by conduction only.
- The pressure gradient is taken into account.

Under these assumptions, flow of fluid through a vertical annulus filled with porous material having variable porosity is considered by heating the duct surface Isothermally or constant heat flux so that its temperature is different from the ambient temperature T_0^1 . Therefore, the basic equations and boundary conditions for this problem in dimensional form are in equations (1) and (2) respectively

$$\gamma_{eff} \left[\frac{d^2 u'}{dr'^2} + \frac{1}{r'} \frac{du'}{dr'} \right] - \gamma_f \frac{u'}{k} + g\beta(T' - T_0^1) - \frac{\partial p}{\partial z} \frac{1}{\rho} = 0 \quad (1)$$

$$\frac{d^2 T'}{dr'^2} + \frac{1}{r'} \frac{dT'}{dr'} = 0$$

Subject to the conditions:

$$\begin{aligned} u' = 0, T' = T_2' \text{ or } \frac{dT'}{dr'} = -\frac{q}{k^*} & \quad \text{at } r' = b \\ u' = 0, T' = T_0^1 & \quad \text{at } r' = a \end{aligned} \quad (2)$$

3. CONCLUSION

The fully developed flow characteristics including phenomena of reversal flow of the mixed convection in a vertical annulus filled with porous material having variable porosity are investigated theoretically. The most important outcome of the numerical calculations of the analytical result is that behaviour of the flow formation of the fluid, as a result of mixed convection between the cylinders, filled with porous material and saturated with same fluid, can be controlled by applying a suitable mode of heating process, and also by changing the gap between the cylinders. The occurrence of the reversal flow is found to be strongly dependent on the value of $Gr/Re=GR_e$.

REFERENCES

- [1] A. Barletta, Analysis of Flow reversal for Laminar mixed convection in a vertical Rectangular Duct with one or more Isothermal walls, *Int. J. Heat Mass Transfer*, 44, 3481-3497, 2001.
- [2] A. Barletta, Fully Developed mixed convection and flow reversal in a vertical Rectangular Duct with Uniform wall Heat Flux, *Int. J. Heat Mass Transfer*, 45, 641-654, 2002.
- [3] F. Bazdidi-Tehrani and M. Shahini, Combined mixed convection-Radiation Heat Transfer within a vertical channel: Investigation of Flow reversal, *Numerical Heat Transfer, Part A*, 55, 289-307, 2009.
- [4] A.J. Chamkha, On laminar Hydromagnetic Mixed Convection Flow in a vertical Channel with symmetric and Asymmetric Wall Heating Condition, *Int. J. Heat Mass Transfer*, 45, 2509-2525, 2002.
- [5] C.H. Cheng, C.J. Weng, and W. Aung, Buoyancy-Assisted flow reversal and Convective Heat Transfer in Entrance Region of a vertical Rectangular Duct, *Int. J. Heat Fluid Flow*, 21, 403-411, 2000.
- [6] H.P. Darcy, *Les fontins publiques de la ville de dijoin*, Victor Delmont, Paris, 1856.
- [7] D.B. Ingham, D.J. Keen, and P.J. Heggs, Two dimensional combined Convection in vertical Parallel Plate Ducts Including Situations of Flow Reversal *Int. J. for Numerical Methods in Eng.*, 26, 1645-1664, 1988.
- [8] Y.N. Jeng, J.L. Cheng, and W. Aung, On the Reynolds-Number Independence of mixed Convection in a vertical channel subjected to Asymmetric wall temperature with and without Flow reversal, *Int. J. Heat Fluid Flow*, 13(4), 329-339, 1992.
- [9] B.K. Jha, Free-convection flow through an annular porous medium, *Heat and mass Transfer Germany*, 41(8), 675-679, 2005.
- [10] F. Marcondes and C.R. Maliska, Treatment of the Inlet Boundary Conditions in Natural-convection flows in open-ended channels, *Numerical Heat Transfer B*, 35, 317-345, 1999.
- [11] A.K. Mishra, B.K. Jha, and A.K. Singh, Mixed Convection in a vertical Annulus filled with a porous matrix, *Thermal systems and Heat Transfer* (proceedings of third National conference on thermal system), 2001.
- [12] D.A. Nield and A. Bejan, *Convection in porous media*, second edition, Springer-Verlag, New York, 1999.
- [13] K. Vafai and C.L. Tien, Boundary and inertia effect on flow and heat transfer in porous media, *Int. J. of Heat and Mass Transfer*, 24, 195-204, 1981.
- [14] M. Wang, T. Tsuji and Y. Nagano, Mixed convection with flow reversal in the Thermal Entrance Region of Horizontal and vertical Pipes, *Int. J. Heat Mass Transfer*, 37(15), 2305-2319, 1994.

BENCHMARK SOLUTION OF 3D NATURAL CONVECTION FLOWS WITH SURFACE RADIATION IN AIR-FILLED CAVITY

Liyuan Hu^{a,b}, Shihe Xin^{a*}, Yvonne Chávez Chena^a, Jalel Chergui^c, Patrick Le Quéré^c

^aINSA-Lyon, Cethil, UMR5008, 20 av. Albert Einstein 69621 Villeurbanne, France

^bInst. of Thermal Energy Engineering, School of Mechanical Engineering, Shanghai Jiaotong University, Shanghai, 200240, P.R. China

^cLIMSI-CNRS, BP 133, 91403 Orsay, France

*Correspondence author: Fax: +00 33 472438811, Email: shihe.xin@insa-lyon.fr

ABSTRACT

A benchmark problem of 3D natural convection/surface radiation coupling in an air-filled square cavity is investigated. The benchmark problem and reference solutions are provided for $Ra=10^4, 10^5$ and 10^6 . The relationship between the two spatial resolutions (one for the Navier-Stokes and another for the surface radiation) is also discussed.

Key Words: *Natural Convection, Surface Radiation, Benchmark Problem*

1. INTRODUCTION

Natural convection in an air-filled square cavity became a reference problem for validating the CFD codes after the pioneering work of De Vahl Davis [1]. There was still no benchmark problem in an air-filled cavity for the coupling of natural convection with surface radiation in 3D cases, and it is difficult to validate the parallel 3D code developed [2]. Colomer *et al.* [3] have provided the 3D simulation results of convection and radiation in a differentially heated cavity, but according to the dimensionless parameters that he supplied, it is hard to determine the values of physical quantities such as averaged temperature T_0 , temperature difference ΔT , cavity height H and so on. The aim of this work is to provide the reference solutions on the purpose of validating numerical procedures developed for investigating the interaction of natural convection with surface radiation.

2. NUMERICAL METHODS AND BENCHMARK PROBLEMS

Spectral methods and MPI (Message Passing Interface) are used for both natural convection and surface radiation. Parallel DNS is performed for the coupling laminar natural convection with surface radiation in air-filled cavities. Parallel multi-domain has been implemented by using influence matrix technique for constructing Schur complement [2].

The Benchmark problem concerns a 3D air-filled cubic cavity of height H , width W and depth D , which is an extension of the 2D benchmark problem [2]. Air in the cavity is considered as a transparent medium. The two vertical walls at $x=0$ and W are maintained at constant but different temperatures (T_h, T_c and $\Delta T= T_h-T_c$) and other walls are adiabatic with the convection-radiation balance. No slip condition is applied on the cavity walls. Buoyancy-driven air flow in the cavity is governed by the Navier-Stokes equations under Boussinesq assumption. The representative parameters are the geometrical aspect ratios $A_x=H/W$ and $A_y=D/H$ ($A_x= A_y=1$), Prandtl number, $Pr=\nu/\alpha=0.71$, and Rayleigh number, $Ra=(g\beta\Delta TH^3)/(\nu\alpha)$. The six cavity walls (grey, diffuse and opaque) have the same emissivity, $\epsilon=0.1$. $T_0=(T_h+T_c)/2$ is set to 293.5K, then λ at T is $0.025W/(m.K)$. $g\beta/\nu k=1.08E8$. Table 1 displays the values of H and ΔT corresponding to each Rayleigh number investigated.

Ra	10 ⁴	10 ⁵	10 ⁶
H(m)	0.020	0.045	0.097
ΔT(K)	11.574074	10.1610527	10.1452100

TABLE 1. Ra investigated and the corresponding H and ΔT

3. RESULTS

At first, the simulation results are compared with that in [3](TABLE 2).Although Colomer *et al.* [3] did not give the clear physical parameters, we can estimate the value of ΔT according to the values of Ra, Pi, and Tc/ΔT. The estimated value of ΔT is 17.954K in case of T₀=278.29K, accordingly, H=0.03369m. TABLE 2 shows that our simulation results agree well with that of Colomer *et al.* [3]. For w_{max}(z=0.5), the sum of two y values approaches to 1 because the fluid field is symmetrical along y direction.

	U _{max} (x=0.5)	y	z	W _{max} (z=0.5)	x	y	Hot \overline{Nu}_c	Hot \overline{Nu}_r
Colomer <i>et al.</i> [3]	0.1869	0.285	0.869	0.2865	0.069	0.115	3.983	3.385
simulated	0.1874	0.2815	0.8746	0.2890	0.0744	0.8813	3.9761	3.6471

TABLE 2. Local extreme values for velocity and average Nusselt numbers in hot wall(Ra=10⁵, Pi = 0.043, Tc/ΔT=15 , ε=1 and Pr =0.71)

TABLE 3 shows average convection Nusselt numbers, maximum and minimum velocity and their positions when y=0.5 at Ra=10⁴. Numerical results are compatible with that in 2D cases [2].It indicates that (Ni*Nj*Nk)_r has almost no influence and they can be considered as converged solutions. Convection Nusselt numbers are more sensible to (Ni*Nj*Nk)_{NS}. TABLE 4 lists average Nusselt numbers in planes, maximum velocity in the cavity and their positions at Ra=10⁴. Numerical results also indicate that coarser (Ni*Nj*Nk)_r can be used as is shown in 2D cases [2]. TABLE 5 and 6 lists the numerical solutions in planes and in the cavity at Ra =10⁵ and Ra=10⁶.

(Ni*Nj*Nk) _{NS}	32*32*8			48*48*12		
(Ni*Nj*Nk) _r	16*16*4	32*32*8	48*48*12	16*16*4	24*24*6	48*48*12
Hot \overline{Nu}_c	2.2493E+00	2.2492E+00	2.2492E+00	2.2486E+00	2.2486E+00	2.2486E+00
W/2 \overline{Nu}_c	2.3151E+00	2.3152E+00	2.3152E+00	2.3152E+00	2.3152E+00	2.3152E+00
Cold \overline{Nu}_c	2.2549E+00	2.2549E+00	2.2549E+00	2.2543E+00	2.2543E+00	2.2543E+00
W/2 U _{max}	1.6967E-01	1.6967E-01	1.6967E-01	1.6967E-01	1.6967E-01	1.6967E-01
z	8.2796E-01	8.2796E-01	8.2796E-01	8.2796E-01	8.2796E-01	8.2796E-01
W/2 U _{min}	-1.6979E-01	-1.6979E-01	-1.6979E-01	-1.6979E-01	-1.6979E-01	-1.6979E-01
z	1.7186E-01	1.7186E-01	1.7186E-01	1.7185E-01	1.7185E-01	1.7185E-01
H/2 W _{max}	1.8774E-01	1.8774E-01	1.8774E-01	1.8774E-01	1.8774E-01	1.8774E-01
x	1.1651E-01	1.1651E-01	1.1651E-01	1.1653E-01	1.1653E-01	1.1653E-01
H/2 W _{min}	-1.8796E-01	-1.8796E-01	-1.8796E-01	-1.8796E-01	-1.8796E-01	-1.8796E-01
x	8.8353E-01	8.8353E-01	8.8353E-01	8.8355E-01	8.8355E-01	8.8355E-01

TABLE 3. Benchmark solutions at Ra=10⁴ in a cubic cavity (y=0.5)

(Ni*Nj*Nk) _{NS}	32*32*8			48*48*12		
(Ni*Nj*Nk) _r	16*16*4	32*32*8	48*48*12	16*16*4	24*24*6	48*48*12
Hot Nu_c	2.0914E+00	2.0913E+00	2.0913E+00	2.0907E+00	2.0907E+00	2.0906E+00
W/2 Nu_c	1.9541E+00	1.9541E+00	1.9541E+00	1.9541E+00	1.9541E+00	1.9541E+00
Cold Nu_c	2.0973E+00	2.0972E+00	2.0972E+00	2.0966E+00	2.0966E+00	2.0966E+00
Hot Nu_r	2.2754E-01	2.2747E-01	2.2746E-01	2.2754E-01	2.2749E-01	2.2746E-01
Cold Nu_r	2.2160E-01	2.2154E-01	2.2153E-01	2.2160E-01	2.2156E-01	2.2153E-01
Front Nu_r	-1.7197E-03	-1.7195E-03	-1.7195E-03	-1.7197E-03	-1.7196E-03	-1.7195E-03
Rear Nu_r	1.7197E-03	1.7195E-03	1.7195E-03	1.7197E-03	1.7196E-03	1.7195E-03
Bottom $\overline{Nu_r}$	-8.2632E-02	-8.2632E-02	-8.2632E-02	-8.2633E-02	-8.2633E-02	-8.2633E-02
Top $\overline{Nu_r}$	-8.0132E-02	-8.0132E-02	-8.0132E-02	-8.0132E-02	-8.0133E-02	-8.0133E-02
U_{max}	1.6987E-01	1.6987E-01	1.6987E-01	1.6987E-01	1.6987E-01	1.6987E-01
x	5.1791E-01	5.1791E-01	5.1791E-01	5.1791E-01	5.1791E-01	5.1791E-01
y	5.0000E-01	5.0000E-01	5.0000E-01	5.0000E-01	5.0000E-01	5.0000E-01
z	8.2670E-01	8.2670E-01	8.2670E-01	8.2672E-01	8.2672E-01	8.2672E-01
V_{max}	2.1908E-02	2.1908E-02	2.1908E-02	2.1909E-02	2.1909E-02	2.1909E-02
x	1.1926E-01	1.1926E-01	1.1926E-01	1.1926E-01	1.1927E-01	1.1926E-01
y	7.8080E-01	7.8080E-01	7.8080E-01	7.8081E-01	7.8081E-01	7.8082E-01
z	1.5452E-01	1.5452E-01	1.5452E-01	1.5448E-01	1.5447E-01	1.5447E-01
W_{max}	1.9105E-01	1.9105E-01	1.9105E-01	1.9105E-01	1.9105E-01	1.9105E-01
x	1.1774E-01	1.1774E-01	1.1774E-01	1.1773E-01	1.1773E-01	1.1773E-01
y	7.2637E-01	7.2637E-01	7.2637E-01	7.2636E-01	7.2636E-01	7.2636E-01
z	4.8360E-01	4.8358E-01	4.8358E-01	4.8358E-01	4.8358E-01	4.8358E-01

TABLE 4. Benchmark solutions at Ra=10⁴ in a cubic cavity

(Ni*Nj*Nk) _r	24*24*6	48*48*12	24*24*6	48*48*12
D/2 U_{max}	1.4646E-01	1.4646E-01	1.4493E-01	1.4493E-01
x	3.2116E-01	3.2116E-01	1.9983E-01	1.9983E-01
z	8.8920E-01	8.8920E-01	9.4030E-01	9.4030E-01
D/2 W_{max}	2.0862E-01	2.0862E-01	2.1892E-01	2.1892E-01
x	6.4433E-02	6.4433E-02	3.7136E-02	3.7136E-02
z	5.0388E-01	5.0388E-01	4.8592E-01	4.8592E-01
Hot Nu_{cmax}	8.9824E+00	8.9753E+00	1.8685E+01	1.8666E+01
y	4.9999E-01	4.9999E-01	7.8530E-01	7.8541E-01
z	0.0000E+00	0.0000E+00	0.0000E+00	0.0000E+00
W/2 Nu_{cmax}	1.1247E+01	1.1247E+01	2.5672E+01	2.5672E+01
y	6.3992E-01	6.3995E-01	7.7637E-01	7.7637E-01
z	8.7567E-01	8.7567E-01	1.1460E-01	1.1462E-01
Cold Nu_{cmax}	8.9710E+00	8.9642E+00	1.8684E+01	1.8666E+01
y	4.9999E-01	4.9999E-01	2.5770E-01	7.4233E-01
z	1.0000E+00	1.0000E+00	1.0000E+00	1.0000E+00
Hot Nu_{rmax}	5.3527E-01	5.3530E-01	1.1566E+00	1.1566E+00
y	5.0004E-01	5.0000E-01	5.0004E-01	5.0000E-01
z	2.8060E-01	2.8050E-01	2.3773E-01	2.3753E-01

TABLE 5. Benchmark solutions at Ra=10⁵ and 10⁶ in a cubic cavity ((Ni*Nj*Nk)_{NS}=48*48*12)

(Ni*Nj*Nk) _r	24*24*6	48*48*12	24*24*6	48*48*12
Hot Nu_c	4.2726E+00	4.2726E+00	8.3238E+00	8.3237E+00
W/2 Nu_c	4.0964E+00	4.0964E+00	8.1167E+00	8.1168E+00
Cold Nu_c	4.2848E+00	4.2848E+00	8.3500E+00	8.3499E+00
Hot Nu_r	5.1519E-01	5.1514E-01	1.1172E+00	1.1171E+00
Cold Nu_r	5.0300E-01	5.0295E-01	1.0904E+00	1.0903E+00
Front Nu_r	-3.8124E-03	-3.8123E-03	-8.5169E-03	-8.5167E-03
Rear Nu_r	3.8124E-03	3.8123E-03	8.5169E-03	8.5167E-03
Bottom Nu_r	-2.3525E-01	-2.3524E-01	-5.4921E-01	-5.4920E-01
Top Nu_r	-2.3066E-01	-2.3066E-01	-5.3942E-01	-5.3941E-01
U_{max}	1.4914E-01	1.4914E-01	1.4784E-01	1.4784E-01
x	3.2282E-01	3.2282E-01	2.0535E-01	2.0535E-01
y	2.7687E-01	2.7687E-01	7.9359E-01	7.9359E-01
z	8.9243E-01	8.9243E-01	9.4072E-01	9.4072E-01
V_{max}	3.3471E-02	3.3471E-02	3.2452E-02	3.2452E-02
x	8.5880E-02	8.5880E-02	5.5735E-02	5.5746E-02
y	8.3668E-01	8.3668E-01	8.9530E-01	8.9530E-01
z	1.1297E-01	1.1297E-01	6.6302E-02	6.6288E-02
W_{max}	2.2834E-01	2.2834E-01	2.4122E-01	2.4122E-01
x	7.0803E-02	7.0803E-02	4.0173E-02	4.0173E-02
y	8.7281E-01	8.7281E-01	7.0221E-02	7.0232E-02
z	5.0324E-01	5.0324E-01	4.7692E-01	4.7692E-01

TABLE 6. Benchmark solutions at $Ra=10^5$ and 10^6 in a cubic cavity ((Ni*Nj*Nk)_{NS}=48*48*12)

4. CONCLUSIONS

Benchmark solutions are provided for $Ra=10^4, 10^5$ and 10^6 by code coupling between Navier-stokes and surface radiation parallel codes. The simulation results indicate that (Ni*Nj*Nk)_r can be coarser than (Ni*Nj*Nk)_{NS} in 3D cases.

REFERENCES

- [1] G. de Vahl Davis and I.P.Jones, Natural convection in a square cavity: a comparison exercise, *Int. J. Num. Mech. in fluids*, 3, 227-248, 1983.
- [2] S.Xin, Benchmark problem of natural convection coupled with surface radiation in an air-filled square cavity: Part I Chebyshev collocation methods, *submitted to Int. J Therm. Sciences*, 2011.
- [3] G. Colomer, M. Costa, R. Consul and A. Oliva, Three-dimensional numerical simulation of convection and radiation in a differentially heated cavity using the discrete ordinates method, *Int. J Heat & Mass Trans.*, 47(2), 257-269, 2004.

NATURAL CONVECTION IN VITREOUS HUMOR DURING TRANSPUPILLARY THERMOTHERAPY (TTT) OF HUMAN EYE

Kaushal Kumar Jha, Sundarraj C, Arunn Narasimhan

Department of Mechanical Engineering, Indian Institute of Technology Madras, Chennai - 600036, India. E-mail: arunn@iitm.ac.in

ABSTRACT

Natural convection in vitreous humour and associated effects during TTT are studied numerically using two-dimensional full scale model of human eye. Both steady state and transient simulation are performed considering the laser irradiation and subsequent heating of retina. Cooling effect at retina due to natural convection is found to be significant.

Key Words: *Heat Transfer, Natural Convection, TTT, Vitreous Humor.*

1. INTRODUCTION

Increasing interest in the fluid dynamics of eye is prevalent owing to the difficulty in delivering drug effectively to the posterior segment of eye. The aqueous humour flow inside the anterior chamber of eye has been studied in detail by Canning *et al.* [1], Ooi *et al.* [2] and Fitt *et al.* [3]. However less attention is given for vitreous humour flow. The objective of the present study is to analyse the natural convection in vitreous humour undergoing transpupillary thermotherapy (TTT). TTT is a low retinal irradiance, long pulse IR diode laser photocoagulation treatment with a large laser spot diameter. TTT is routinely used in treatment of choroidal neovascularization. During TTT, the temperature of retina increases around 10 to 15 K as studied by Kandulla *et al.* [4]. The existing temperature difference across the eye tissues should induce natural convection in vitreous humour during TTT. Thus neglecting the vitreous humour flow may result in inaccurate temperature prediction and extent of thermal damage on the retinal surface.

2. NUMERICAL METHOD

Using numerical simulation, the steady state and transient temperature distribution in eye subjected to TTT is predicted. The temperature distribution for a stagnant vitreous humor is initially evaluated. Then it is contrasted with the temperature distribution inside the eye considering the natural convection in vitreous humour. The energy equation is numerically solved in the eye domain. The Boussinesq approximation is incorporated into the conservation equations. The density variation induced due to temperature variation is accounted by this approximation. The boundary conditions imposed are: Combined convection and radiation boundary condition at corneal surface ($h = 10 \text{ Wm}^{-2}\text{K}^{-1}$) and a convective boundary condition at the sclera ($h = 65 \text{ Wm}^{-2}\text{K}^{-1}$) which accounts for cooling effect of blood convection. Outside and body core temperature are assumed to be 298 K and 310 K respectively in the numerical simulations. The geometrical model is constructed using the commercial software GAMBIT 2.4.6. Quadrilateral finite volume (surface) elements are used for meshing the eye domain. The conservation equations are solved by FLUENT 6.3.26. A laser power of 300 mW and spot diameter of 4 mm is considered for numerical simulations.

3. RESULTS AND DISCUSSIONS

3.1 Steady state results:

3.1.1 Temperature distribution:

The steady state temperature distribution inside the eye during TTT considering the natural convection in the vitreous humour is presented in the Fig. 1(a). The cornea absorbs 5 % of the laser energy (15 mW). Between aqueous humour and vitreous humour including lens, another 5 % of laser energy (15 mW) is absorbed. Out of the remaining (270 mW) laser energy, 40 % is absorbed in retina. A summary of thermo-physical properties, the laser power distribution between the different eye tissues and resulting volumetric heat generation rates are presented in Table 1. As vitreous humour is composed of more than 99 % of water, the viscosity and coefficient of thermal expansion of vitreous humour are considered same as that of water.

The peak temperature of the retina is observed to be at 346 K for a stagnant vitreous humour during steady state simulation. Due to cooling effect of natural convection in vitreous humour, the peak temperature reduces to 330 K as shown in Fig. 1(a). As seen from the steady state isotherms (Fig. 1a), asymmetry exists in the temperature distribution due to vitreous humour flow. The natural convection flow enhances the retinal heat transfer in the direction of natural convection current. Thus effect of natural convection cannot be ignored during long duration surgery like TTT.

Eye tissue	κ (W/m-K)	c (J/kg-K)	ρ (Kg/m ³)	γ (%)	Absorbed power (mW)	Thickness (mm)	Volume (x10 ⁻⁹) (m ³)	Q''' (x10 ⁶) (W/m ³)
Cornea	0.58	4178	1050	5	15	0.52	6.534	2.295
Aqueous	0.58	3997	1000	1	3	3	37.699	0.0795
Lens	0.4	3000	1050	1	3	3.6	45.238	0.0663
Vitreous	0.603	4178	1000	3	9	15.88	199.553	0.0451
Retina	0.603	4178	1000	36	108	0.01	0.1256	859.87
Sclera	0.603	4178	1000	0	0			

TABLE 1. Thermo-physical properties and volumetric heat generation rates in the human eye tissue.

3.1.2 Velocity contours:

The velocity contour of the natural convection flow in vitreous humour is shown in the Fig. 1(b). From the Fig. 1(b), it is clear that the flow is concentrated more in the upper half of the vitreous humour chamber. The region adjacent to the heating zone gains sufficient buoyant force to rise into the upper half region. A substantial portion of the vitreous humour at the bottom remains un-heated due to lack of penetration from the heating provided by the local retinal heat source.

3.1.3. Velocity profile at pupillary axis:

The y-component velocity magnitude during steady state simulation and induced natural convection due to temperature gradient during TTT along the pupillary axis is shown in Fig. 2. The peak velocity is found to be near to the retina (in vitreous humour, approximately 1 mm away from the retina). The obtained velocity profile is similar to the velocity profile for natural convection in a heated vertical plate.

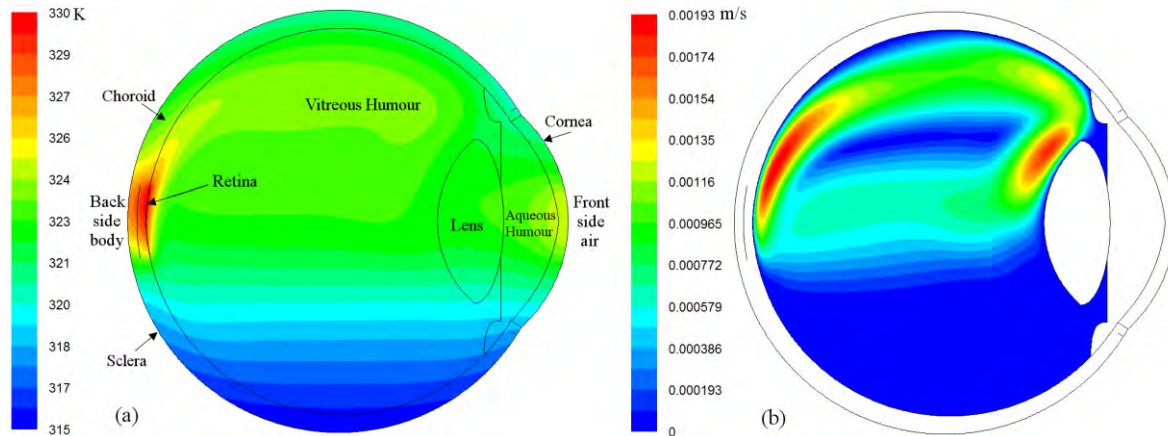


FIGURE 1. Steady state (a) isotherms and (b) velocity contour in eye during TTT for a laser power of 300 mW, laser spot diameter of 4 mm and natural convection in vitreous humour

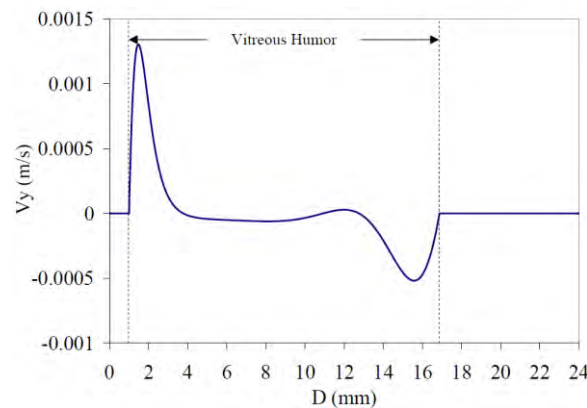


FIGURE 2. Y-component of velocity magnitude along the pupillary axis during steady state simulation of TTT considering natural convection in vitreous humour.

3.2 Transient results:

Considering the same parameters used in steady state simulations, transient simulations of TTT process are performed for a laser heating period of 60 seconds. The time of transient simulation (60 seconds) is the typical time considered for TTT process. The steady state simulation of the natural convection in the vitreous humour due to the temperature gradient developed from body core temperature and outside temperature, without laser heating is used as the initial condition for the transient simulations.

3.2.1 Transient temperature distribution:

Isotherms resulting from transient simulation of TTT process at 60 second are presented in Fig. 3(a). The peak temperature in the retina, reaches to 318 K after 60 seconds of laser heating during transient simulation of TTT process, whereas the peak temperature with same parameters is 330 K for steady state simulation. Thus an increase of 8 K above body core temperature is seen during transient simulation. This temperature rise is not sufficient to destroy the target tissue, but sufficient enough to induce the natural convection in vitreous humour as presented in the next subsection.

3.2.2. Transient velocity contour:

The contours of velocity magnitude during transient simulation of TTT process at 60 seconds are presented in Fig. 3(b). The natural convection flow of vitreous humor in human eye is developed

due to the transient heating of retina by laser. As stated in previous section, the magnitude of peak temperature is just 8 K above body core temperature which is not sufficient for irreversible cell damage, but well enough to induce natural convection in vitreous humor. It is interesting to see that the maximum velocity (0.00227m/s) attained in transient condition is more than that of steady state condition (0.00193 m/s). This can be attributed to the higher local temperature gradient between laser treated zone and the adjacent vitreous fluid. The higher velocity can further enhance the drug deposition rate at targeted tissue compared to steady state condition.

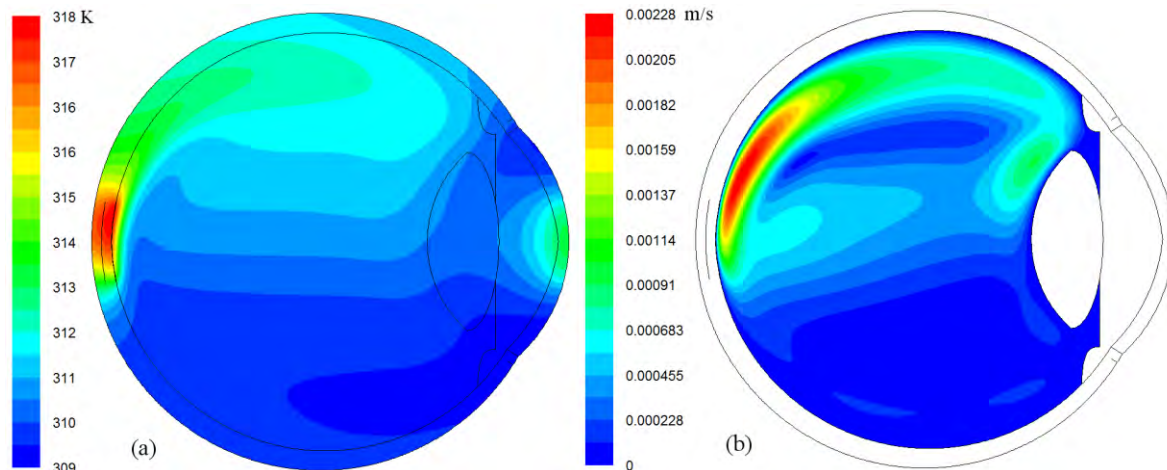


FIGURE 3. (a) Isotherms and (b) velocity contour in human eye during transient simulation of TTT process at 60 seconds for a laser power of 300 mW, laser spot diameter of 4 mm and natural convection in vitreous humour

4. CONCLUSIONS

Two-dimensional computational model of the human eye has been developed and numerical simulations for studying the natural convection in vitreous humour during TTT are performed. Temperature distribution and velocity contours have been presented for both the steady state and transient conditions. The velocity contour showed maximum velocity of transient case to be higher than the steady state case. Substantial vitreous humour at the bottom remained un-heated due to lack of penetration from the local retinal heat source. The simulation studies may be extended for varying laser power, laser heating time and laser spot diameter to characterize the extent of heat penetration on the retinal surface due to natural convection in the vitreous humour.

REFERENCES

- [1] C R Canning, M J Greaney, J N Dewynne, and A D Fitt. Fluid flow in the anterior chamber of a human eye. *IMA Journal of Mathematics Applied in Medicine and Biology*, 19:3160, 2002.
- [2] Ean Hin Ooi and Eddie Yin Kwee Ng. Simulation of aqueous humor hydrodynamics in human eye heat transfer. *Computers in Biology and Medicine*, 38(2):252–262, 2008.
- [3] A D Fitt and G Gonzalez. Fluid mechanics of the human eye: Aqueous humour flow in the anterior chamber. *Bulletin of Mathematical Biology*, 68:5371, (2006).
- [4] J Kandulla, H Elsner, R Birngruber, and R Brinkmann. Noninvasive optoacoustic online retinal temperature determination during continuous-wave laser irradiation. *Journal of Biomedical Optics*, 11(4):041111–1–13, 2006.

3D IHCP IN POOL BOILING: MATHEMATICAL FORMULATION, EFFICIENT COMPUTATIONAL STRATEGIES AND SOFTWARE TOOL

Yi Heng

AixCAPE e.V., D-52072, Aachen, Germany, Heng@aixcape.org

Adel Mhamdi, Wolfgang Marquardt

AVT - Process Systems Engineering, RWTH Aachen University, D-52064 Aachen, Germany,
{Adel.Mhamdi, Wolfgang.Marquardt}@avt.rwth-aachen.de

ABSTRACT

Among all kinds of studies on boiling processes, the efficient and accurate estimation of the local heat flux distribution at the boiling surface, beyond its average information which can be obtained by traditional approaches, is a crucial prerequisite in modern modeling of boiling heat transfer. For accurate predictions, the heat flux estimation task is formulated as a three-dimensional (3D) inverse heat conduction problem (IHCP). In case of a complex heater geometry, realistic boundary conditions and a nonuniformly measurement configuration, the solution of the 3D IHCP considered leads to a large-scale PDE-constrained optimization problem. Further, regularization-based techniques have to be applied to tackle the inherent severe ill-posedness of the 3D IHCP. This paper gives a brief summary of our recent developments in the efficient solution of the 3D IHCP which accomplishes the task of heat flux reconstruction in pool boiling. It incorporates an iterative regularization based on a conjugate gradient method for the normal equations (CGNE) and a multi level adaptive computational strategy. The novel method can efficiently cope with both idealized (high-resolution) and limited point-wise experimental data which are commonly available in most heat transfer experiments. The method has been applied to the evaluation of real temperature data obtained from two novel pool boiling experiments. For the first time, the computational effort of such tasks reduces to the order of minutes on standard desktop computers.

Key Words: *3D IHCP, Boiling Heat Transfer, Iterative Regularization, Adaptive Mesh Refinement.*

1. INTRODUCTION

From the mathematical point of view, the estimation of the temperature and heat flux distribution at the inaccessible boiling boundary from interior temperature observations belongs to the class of 3D boundary IHCP. The solution procedure of the IHCP is not trivial with respect to both its severe ill-posedness and the high computational effort. During the past decades, numerous numerical and application-oriented IHCP papers have been published. However, due to the high complexity, most of them are restricted to one or two space dimensions. Only a few publications are available for IHCP in three dimensions but on regular computational domains (cf. a literature review of previous works on 3D IHCP in [1]). To our knowledge, none of the existing IHCP solution techniques can cope with both more complex computational domains and non-uniformly measurement configurations employed in real experiments, which is considered in this paper.

2. MATHEMATICAL FORMULATION

This prototype IHCP to be investigated arise from two novel pool boiling experiments operated by our collaboration partners [2, 3] (cf. Figure 1 and Figure 2). Let Hilbert spaces X , Y , e.g. the set of L^2 functions, denote the solution and data spaces, respectively. Let unperturbed temperature data

corresponding to the true heat flux q at the boiling surface Γ_B be denoted by T_m and the noisy data be denoted by T_m^δ with an upper error bound δ , i.e., $\|T_m - T_m^\delta\|_Y \leq \delta$.

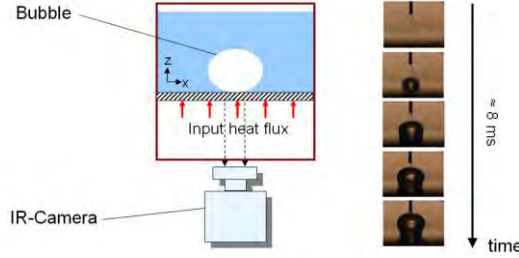


FIGURE 1. A single-bubble nucleate boiling experiment (adopted from [4])

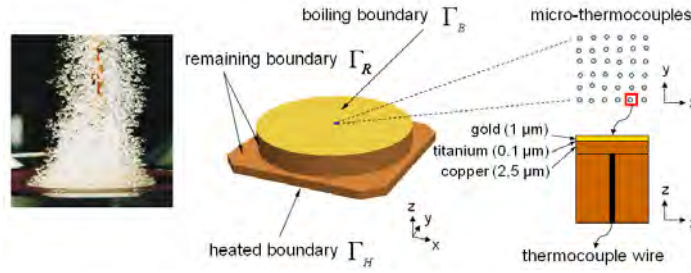


FIGURE 2. Experimental setup of the test heater and schematic of the MTC arrangement (adopted from [5] used in pool boiling experiments carried out at TU Berlin [2])

The IHCP under investigation corresponds to the reconstruction of the unknown heat flux q at Γ_B from noisy temperature observations T_m^δ measured inside the heater or on part of the boundary. The IHCP in the operator form can be formulated as follows:

$$\text{Find } q \in X \text{ such that } Kq = T_m^\delta \quad (1)$$

where the function operator K is implicitly given by eqs. (2)–(3):

$$\rho c_p \frac{\partial T}{\partial t} = \nabla \cdot (\lambda \nabla T), \quad \text{in } \Omega \times (0, t_f), \quad T(\cdot, 0) = 0, \quad \text{on } \Omega \quad (2)$$

$$\lambda \frac{\partial T}{\partial n} = 0, \quad \text{on } (\Gamma_H \cup \Gamma_R) \times (0, t_f), \quad \lambda \frac{\partial T}{\partial n} = q, \quad \text{on } \Gamma_B \times (0, t_f) \quad (3)$$

Ω represents the heater geometry with the boundary defined as $\partial\Omega := \Gamma_H \cup \Gamma_R \cup \Gamma_B$. The observation time interval is $[0, t_f]$ and n denotes the outer normal on the boundaries. Γ_H, Γ_B and Γ_R denote the heated boundary, the boiling boundary and the remaining boundary, respectively. ρ , c_p and λ denote the density, the heat capacity and the heat conductivity of the materials, respectively. It has to be mentioned that a general IHCP constrained by a linear heat equation system with non-homogeneous initial and boundary conditions can always be reduced to (1), cf. [5].

3. SOLUTION ALGORITHM

The IHCP stated in eq. (1) can be cast into the following minimization problem:

$$\min J(q) \text{ subject to } J(q) = \|Kq - T_m^\delta\|_Y^2 > (\tau\delta)^2, \quad \tau > 1 \quad (4)$$

Kq corresponds to the temperature predictions at the measurement locations for a given heat flux q which results from a solution of the model (2)–(3). The constraint in (4) is necessary to avoid an overfitting. It bounds the residual from below by the measurement error.

3.1. Single-level approach. In case K is a linear function operator, the minimization problem (4) can be solved by the CGNE algorithm efficiently (cf. Algorithm 1, [5]). L can be chosen as either the identity operator or the differential operator. For the implementation of Algorithm 1, it requires to realize the forward and adjoint operators K and K' . Detailed implementation issues can be found in [1, 5].

Algorithm 1 Modified CGNE Iteration

Let $q_0 \in X$, $\tau > 1$, δ , K and K' be given. Set $d_0 = T_m^\delta - Kq_0$, $p_1 = s_0 = K'd_0$.

For $k = 1, 2, \dots$, compute

$$u_k = Kp_k, \gamma_k = \|Ls_{k-1}\|_X^2 / \|u_k\|_Y^2, q_k = q_{k-1} + \gamma_k p_k, d_k = d_{k-1} - \gamma_k u_k,$$

$$\text{if } \|d_k\|_Y \leq \tau\delta, \text{ stop, otherwise, } s_k = K'd_k, \beta_k = \|Ls_k\|_X^2 / \|Ls_{k-1}\|_X^2, p_{k+1} = s_k + \beta_k p_k.$$

3.2. Multi-level adaptive approach. A further significant improvement in the computational efficiency can be obtained by using a type of multi-level adaptive approach (cf. Algorithm 2). Note that different types of a-posteriori error estimators can be applied in step 3, e.g. the temperature-based error estimation technique, which is efficient for point-wise measurements [6]. In our most recent work [4], a completely different but general heat flux-based error estimation technique was developed to tackle both high-resolution and point-wise measurement configuration. With this novel computational strategy, 3D IHCP in pool boiling previously considered computationally intractable can be solved for the first time in the order of minutes on standard desktop computers.

Algorithm 2 Multi-level adaptive regularization

1. Choose an initial coarse mesh M_h^1 and set $l = 1$, $q_{h,0}^1 = 0$
 2. Solve the IHCP on M_h^l to obtain the solution q_h^l (Algorithm 1)
 3. Evaluate the a-posteriori error estimator
 4. If the predefined stopping condition is fulfilled, stop
 5. Refine $M_h^l \rightarrow M_h^{l+1}$ and set initial value $q_{h,0}^{l+1} = \tilde{q}_h^l$, with \tilde{q}_h^l being the interpolation of the solution q_h^l on the finer mesh M_h^{l+1} ; increment l and go to 2
-

4. IHCP TOOL AND ITS APPLICATIONS

The CGNE minimization algorithm combined with the multi-level adaptive mesh refinement strategy is coded in C++ and integrated with the NETGEN/NGSolve software package. Only a few estimation results along the entire boiling curve are shown in Figure 3 for lack of space. Further related material can be found at <http://www.avt.rwth-aachen.de/AVT/index.php?id=780>.

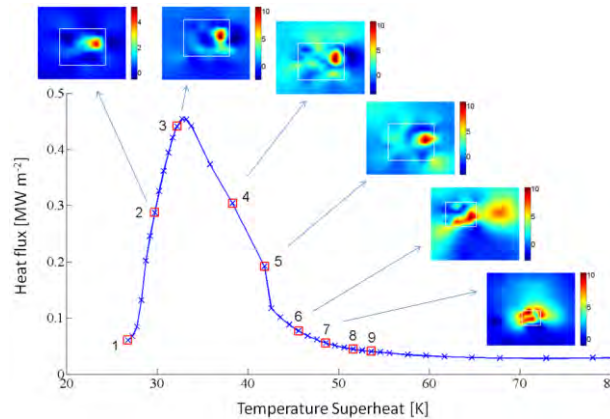


FIGURE 3. Boiling curve of isopropanol at $P_{sat} = 0.1$ MPa; Representative plots of estimated local boiling heat flux distribution in the different boiling regimes

5. CONCLUSIONS

In this paper, a mathematical formulation of 3D IHCP stemming from pool boiling experiments has been presented. The estimated local boiling heat fluxes, together with other experimental results, have provided a database for the development of realistic mechanistic heat transfer models for boiling regimes beyond low heat flux nucleate boiling. The proposed IHCP solution technique can also be viewed as an efficient soft sensor to deduce unmeasurable local boiling heat fluxes such that the evaluation of the experimental data can easily be integrated into the experimental work process.

Possible future works include the development and implementation of adaptive discretization algorithm also in time, the extension of the problem formulation to cover the wetting characteristics on the boiling surface.

ACKNOWLEDGEMENT

The authors acknowledge the financial support by German Research Foundation (DFG) through a joint research project on the fundamentals of boiling heat transfer. We particularly thank Prof. H. Auracher as well as Prof. P. Stephan for giving us access to data of their boiling experiments. We also thank Dr. H. Egger and Prof. J. Schöberl for providing the open source finite element code NETGEN/NGSolve for our development of the IHCP tool.

REFERENCES

- [1] Y. Heng, Mathematical Formulation and Efficient Solution of 3D Inverse Heat Transfer Problems in Pool Boiling, *Fortschritt-Berichte VDI, VDI Verlag, Reihe 3*, Nr. 922, 2011.
- [2] M. Buchholz, et al., Experimental investigation of local processes in pool boiling along the entire boiling curve, *Int. J. Heat Fluid Flow*, 25(2), 243–261, 2004.
- [3] E. Wagner, et al., Nucleate boiling at single artificial cavities: Bubble dynamics and local temperature measurements, *Proc. 6th Int. Conf. Multiphase Flow*, 2007.
- [4] Y. Heng, et al., Efficient reconstruction of local heat fluxes in pool boiling experiments by goaloriented adaptive mesh refinement, *Heat Mass Transfer*, 46(11), 1121–1135, 2010.
- [5] H. Egger, Y. Heng, et al., Efficient solution of a three-dimensional inverse heat conduction problem in pool boiling, *Inverse Prob.*, 25(9), 095006 (19pp), 2009.
- [6] Y. Heng, et al., A multi-level adaptive solution strategy for 3D inverse problems in pool boiling, *Int. J. Numer. Methods Heat Fluid Flow*, 21(5), 469-493, 2011.

RECONSTRUCTION OF THE STEFAN-BOLTZMANN COEFFICIENTS IN THE HEAT TRANSFER PROCESS

Jin Cheng

School of Mathematical Sciences, Fudan University, Shanghai 200433, China;
E-Institute of Scientific Computation, Shanghai Normal University,
Shanghai, China

Shuai Lu

School of Mathematical Sciences, Fudan University, Shanghai 200433, China, slu@fudan.edu.cn

Masahiro Yamamoto

Graduate School of Mathematical Sciences, University of Tokyo, Tokyo 153-8914, Japan

ABSTRACT

In this paper, we investigate an inverse problem on the determination of boundary coefficients within the framework of Stefan-Boltzmann radiation conditions for the heat transfer process.

The mathematical formulation for the forward and inverse problems is introduced and the uniqueness of the inverse problem is proved. The finite difference method is implemented for a discretization of the forward problem. Based on the feature of the problem, we propose a reconstruction method for solving the inverse problem. Some regularization techniques are implemented to overcome the ill-posedness of the problem. Numerical simulation shows that our reconstruction method is stable and effective.

Key Words: *Stefan-Boltzmann coefficients; Inverse problems; Heat transfer.*

1. INTRODUCTION

In modern engineering and manufacturing, a quality control is widely used in order to ensure whether products are designed to meet customers' requirements, and the quality control is usually done by detecting defects on the surface of products. The size of these kinds of defects is usually small and cannot be directly observed, for example, by some standard cameras. Nevertheless, in the laboratory experiments, it is observed that such kinds of defects significantly influence the heat radiation process on the surface of a product. This observation yields a possibly new quality control method, which will be discussed in the current paper, in order to detect defects by a thermal camera when the product is heated suitably.

Existing detection methods include computerized surface-colour comparison, manual observation, etc. These methods highly depend on the obvious colour difference induced by a defect on the surface of a material. However, the defects which do not have some obvious difference on the surface will usually be ignored by the mentioned methods above. By laboratory experiments on specimens, we observe that the heat transfer process near the defect is different from the normal region. More precisely, when we heat the specimens up to a certain temperature, the cooling process then shows a different temperature profile, which can be observed by thermal cameras. Mathematically, the changing cooling modes are modelled by different Stefan-Boltzmann radiation coefficients of the normal and the defective surface.

In this talk, we focus on the reconstruction of the coefficients in a Stefan-Boltzmann boundary condition for the heat transfer process without initial temperature value. Notice

differences between the coefficients are caused by defects, we thus expect to detect these defects on the surface of a material by reconstructing the coefficients and finding their locations with respect to the coefficient difference.

2. MAIN BODY

In this paper we consider a three-dimensional simply connected domain Ω , whose boundary $\partial\Omega$ is Lipschitz continuous. The main interest focuses on the heat transfer process, i.e., the temperature distributions $u(x, t)$ with $(x, t) \in \Omega \times [0, T]$. Thus the mathematical model for the forward problem is governed by

$$\begin{cases} \partial_t u(x, t) = \alpha \Delta u(x, t), x \in \Omega, t \in [0, T], \\ u(x, t) = u_0(x), x \in \Omega, \\ -\lambda \partial_n u(x, t) = \sigma(x)(u^4(x, t) - u_A^4), x \in \partial\Omega, t \in [0, T]. \end{cases} \quad (1)$$

Here we assume that the thermal conductivity α , λ are positive constants, $u_A > 0$ represents the constant air temperature outside of the domain Ω . Moreover the initial temperature $u_0(x)$ and the coefficient function $\sigma(x)$ of the Stefan-Boltzmann boundary condition are supposed to be two strictly positive functions depending on the spacial variable x . The nonlinear boundary condition in (1) is the Stefan-Boltzmann boundary condition, which represents the radiation phenomena of the heat transfer laws on the boundary.

The forward problem is to compute the temperature distributions $u(x, t)$ with the known domain Ω , constants α, λ, u_A and functions $u_0(x), \sigma(x)$. Such a kind of problems can be solved within the classical theoretical framework, and as for numeric of a related forward problem.

In this talk, we concentrate on an inverse problem, which aims at the determination of the coefficient $\sigma(x)$ in the Stefan-Boltzmann boundary condition by additional information of $u(x, t)$ on some part of the boundary. Based on the real situations in industry, one cannot expect an initial value of $u_0(x)$ since we only access the online testing on the surface.

Here we will provide a detailed description. Mathematically, a defect of a specified material usually presents a non-constant Stefan-Boltzmann coefficient function. Let us assume that the Stefan-Boltzmann coefficient function $\sigma(x)$ satisfies

$$\sigma(x) = \begin{cases} \sigma_u(x), x \in \Gamma, \\ \sigma_0, x \in \partial\Omega \setminus \Gamma, \end{cases} \quad (2)$$

where $\sigma_0 > 0, \sigma_u(x) > 0$, and $\sigma_0 \neq \sigma_u(x)$. We understand that $\partial\Omega \setminus \Gamma$ is defined as a normal surface where the value of $\sigma(x)$ is known to be a fixed constant σ_0 . At the same time, the coefficient function value on the defect area Γ is unknown and needs to be determined. We distinguish the defect area Γ and the anomalous coefficient $\sigma_u(x)$ where an inequality $\sigma_0 \neq \sigma_u(x)$ is satisfied.

In the talk, our main task is to analyse the inverse problem as follows.

Inverse problem (IP): Assume that $u(x, t)$ satisfies

$$\begin{cases} \partial_t u(x, t) = \alpha \Delta u(x, t), x \in \Omega, t \in [0, T], \\ -\lambda \partial_n u(x, t) = \sigma(x)(u^4(x, t) - u_A^4), x \in \partial\Omega, t \in [0, T], \end{cases} \quad (3)$$

where the domain Ω is fixed; $\alpha, \lambda, u_A > 0$ are known constants, and $\sigma(x)$ in the Stefan-Boltzmann boundary condition satisfies (2). In addition, the normal coefficient function value σ_0 is assumed to be known. Γ here is an observation surface satisfying $\Gamma \subset \partial\Omega$ and $\Gamma \neq \partial\Omega$. Then we would like to determine the unknown $\sigma(x)$ in (2) from the Dirichlet data $u(x, t)$ on the observation surface Γ :

$$u(x, t) = f(x, t), x \in \Gamma, t \in [0, T] \quad (4)$$

Notice that in the system (2)-(3) there is no initial value $u_0(x) (= u(x, 0))$ available due to the measuring difficulty. However, in order to assure that the heat transfer process we study here is a cooling-down process, we a priori assume that the initial value satisfies

$$u_0(x) > u_A > 0, x \in \Omega$$

which is consistent with our experimental condition and the requirements in the applications.

3. CONCLUSIONS

In this talk, we initialize researches for an inverse problem, which arises in an industry quality control process. It requires us to determine coefficients of some physical nature on the surface of materials, and these coefficients characterize the Stefan-Boltzmann boundary condition in heat transfer process.

We prove the uniqueness of the inverse problem, i.e., reconstruction of the coefficients, which provides a theoretical base for our ongoing numerical works. After that, we concentrate on the numeric, present an appropriate finite difference method of the forward problem, and introduce an effective reconstruction scheme for the inverse problem. The numerical results are provided, which give us a visible influence of the Stefan-Boltzmann coefficients in the heat transfer process, and show the validity of the proposed numerical method as well. Stability estimation of the inverse problem will be presented in a forthcoming paper.

REFERENCES

- [1] J.V. Beck, B. Blackwell and C.R. St. Clair, *Inverse Heat Conduction: Ill-posed Problems*, Wiley, New York, 1985.
- [2] A. Chambolle, R.A. DeVore, N.Y. Lee, B.J. Lucier, Nonlinear wavelet image processing: variational problems, compression, and noise removal through wavelet shrinkage, *IEEE Transactions on Image Processing*, 7, 319-335, 1998.
- [3] M.C. Delfour, G. Payre, J.P. Zolesio, Approximation of nonlinear problems associated with radiating bodies in space, *SIAM J. Numer. Anal.*, 24, 1077-1094, 1987.

- [4] P. Druet, Weak solutions to a stationary heat equation with non-local radiation boundary condition and right-hand side in L_p ($p \geq 1$), *Math. Methods Appl. Sci.*, 32, 135-166, 2009.
- [5] H.W. Engl, P. Fusek and S.V. Pereverzev, Natural linearization for the identification of nonlinear heat transfer laws, *J. Inv. Ill-posed Problems*, 13, 567-582, 2005.

IDENTIFICATION OF HEATING SOURCE IN AN ENCLOSURE DYNAMICALLY COUPLED WITH THERMAL TRANSPORT

Fu-Yun Zhao^{*ab}, Ernst Rank^a, Ralf-Peter Mundani^a, Jérôme Frisch^a,

Di Liu^b, Han-Qing Wang^b

a) Faculty of Civil Engineering and Geodesy, Technical University Munich, Munich, Germany

b) School of Civil Engineering, Hunan University of Technology, Zhuzhou, Hunan, China,

zfyfdnet@163.com, zhao@bv.tum.de

ABSTRACT

Natural convection occurring in high rise building space presents turbulent flow characteristics. Unknown boundary heat fluxes should be identified due to the control of building ventilation, i.e., inverse turbulent natural convection problems arising. An iterative Fletcher-Reeves conjugate gradient method is applied such that the gradient of the cost function is introduced when the appropriate sensitivity and adjoint problems are defined. The inverse problem of determining an unknown space dependent heat flux on the side of a square enclosure from temperature measurements by sensors within the flow is investigated to demonstrate the developed formulations. Noise data solutions are regularized by stopping the iterations with the discrepancy principle of Alifanov, before the high frequency components of the random noises are reproduced. The present method generally solves the inverse turbulent natural convection problem satisfactorily without any a priori information about the unknown heat flux to be estimated.

Keywords: *Inverse Heat Transfer, Adjoint Method, Turbulent Natural Convection*

1. INTRODUCTION

As people spend nowadays most of their time in enclosed spaces, there has been an increasing interest in the problems dealing with indoor air environment [1,2]. To achieve comfortable indoor air environment, it requires profound knowledge of air, heat and contaminant transports, upon which appropriate indoor air management strategies could be implemented. Consequently, computational fluid dynamics (CFD) has been extensively used to evaluate the air motion, thermal and pollutant distributions; and it appears to offer a competitive and flexible alternative comparing with physical modelling and field measurement [2,3].

These CFD numerical studies were generally concerned with the determination of flow velocity, temperature and concentration distributions within the enclosed space when the initial conditions, boundary conditions, internal thermal source, thermal sink, thermo-physical properties and geometries of the enclosed environment are specified. However, there are usual situations involving the determination of the initial or boundary conditions from the knowledge of airflow, temperature and concentration measurements at some points within the domain. This is also called inverse heat transfer problem and has drawn attentions in diverse fields, such as aerodynamic duct design, solidification process, and high temperature measurements [4]. Over the last two decades, the inverse heat conduction problem has been received much attention. Typical problems addressed include reconstruction of the boundary heat flux condition from temperature measurement within a conducting body, determining thermal properties (such as conductivity) as a function of temperature and the calculation of distributed heat sources from the knowledge of the temperature field at some points within the domain and/or on the boundary. Despite the relatively large interest expressed in inverse heat conduction problems, inverse heat transfer problems involving convection flow have not attracted much attention. Convection heat transfer problems are governed by a system of partial differential equations, namely the continuity, Navier-Stokes, and energy equations. These studies

were mainly focused on the channel flow and the temperature field is independent of fluid flow [4]. Comparing with the aforementioned investigations of inverse heat conduction problems, inverse natural convection problems in enclosures are more difficult to investigate as the flow field is dynamically coupled with the thermal convection. Fluid flow introduces new physics such as boundary layer and vortex formation, which in turn localizes the region where sensitive information is contained. Typically, Colaco and Orlande estimated two boundary conditions of natural convection in the irregular cavities, which are transformed into regular geometries by using an elliptic scheme of numerical grid generation [5]. Zhao and his co-authors have discussed the inverse natural convections in porous and conjugate medium [6,7].

It will be observed that these investigations are confined in the domain of laminar flow. Whereas, in the filed of building ventilation and air environment, air flow and thermal plumes tend to be turbulent. In addition, the measurements cannot be easily accessed, while the accurate control of air flow is essentially required. Several authors have dealt with the inverse problems to achieve indoor air environment safe and comfort. Murakami combined CFD technique with a CFD feedback system, which could modify the boundary conditions (supply of air temperature, supply of air volume, etc.) to maintain the target value of predicted mean vote. This process of decision-making however is empirical rather than deterministic [8]. Zhang and Chen solved the quasi reversibility equation for contaminant transport to identify the pollutant source locations in a two dimensional aircraft cabins and a three dimensional office. Their method works better for convection dominant flows than that for recirculation flow. Whereas, the thermal plumes did not develop such strong to twist the main stream dominated by the forced flow [9]. Zhao and his co-authors have investigated the inverse heat convections within a slot vented enclosure [10], however still confining in the laminar flow domain. As preliminary and essential step, presently, the turbulent natural convection in an enclosure modelling the high rise buildings or atrium will be investigated in terms of direct and inverse problems. A heat source distributed along the wall generates a thermal plume by natural convection. As it develops, this plume conveys an ambient airflow, which increases as it rises within the room.

The present inverse turbulent heat convection problem is the estimation of the surface heat flux given one or more measured temperature histories inside the fluid or on the boundaries. For the measurement of internal temperatures, errors are always present to some extent and they affect the accuracy of the unknown heat flux calculation. In many applications, the surface temperature is also desired in addition to the surface heat flux. The emphasis of this study is on the determination of heat flux, since surface temperature is generally a by-product of the heat flux calculation. Also, heat flux estimation is more sensitive to measurement errors than the surface temperature estimation because the heat flux is proportional to the temperature gradient.

2. DEFINITION OF TURBULENT NATURAL CONVECTION PROBLEM

An incompressible viscous fluid occupies the region shown in Fig. 1 and natural convection is induced from density variations within the domain. It is assumed in the analysis that the thermo-physical properties of the walls materials and of the air are independent of temperature. The fluid is viscous, heat-conducting, Newtonian, and the Boussinesq approximation is valid. The turbulent flow considered is described mathematically by the Reynolds averaged Navier-Stokes (RANS) equations, including the time averaged energy equation for the mean temperature fields that drives the flow by the buoyancy force. In the near wall regions, steep nonlinear gradients and relatively low level of turbulence exist. To account for these, the wall function method is adopted.

3. FUNCTIONAL OPTIMIZATION FOR INVERSE TURBULENT CONVECTION

For the inverse natural convection problem, we should determine the boundary heat flux $Q_u(Y)$ with the known boundary conditions and the measured or designed temperature due to the fact that

temperature field inside the domain can be easily measured at various locations. In the present work, a solution to the inverse problem would be assumed existed in the sense of Tichonov. Particularly, we look for the boundary heat flux Q_u that will minimize the following error,

$$E(Q_u) = \frac{1}{2} \int_0^{\tau_f} \sum_{i=1}^M [T(X_i, Y_i, \tau) - T_m(X_i, Y_i, \tau)]^2 d\tau \quad (1)$$

Where T and T_m are the predicted and given temperature at the sensor's position, respectively. M is the total number of sensors. The sequence of approximations for the unknown heat flux may be constructed following the steps of the conjugate gradient method, according to $Q_u^{K+1} = Q_u^K + \alpha^K ps^K$, where α is the step size and ps the conjugate search direction. The search direction is related to the gradient of the cost functional E with respect to Q_u , whose function shape is not available for general case. The gradient of the cost functional E and the step size α must be obtained respectively from the solution of the adjoint and sensitivity problems.

4. RESULTS OF INVERSE CONVECTIONS

The following well-defined triangular function of heat flux Q_u has been employed in the confirmation of the present algorithm for inverse natural convection problem,

$$Q_u(Y) = \begin{cases} -2Y, & 0 \leq Y \leq 0.5 \\ 2Y - 2, & 0.5 \leq Y \leq 1.0 \end{cases} \quad (2)$$

When the thermal Rayleigh number maintains at 10^{10} , the fluid and heat transport structures are plotted in Fig. 2 as functions of heat flux profiles. A counter-clockwise flow eddy is observed under the heat flux condition, as presented in Fig. 2.

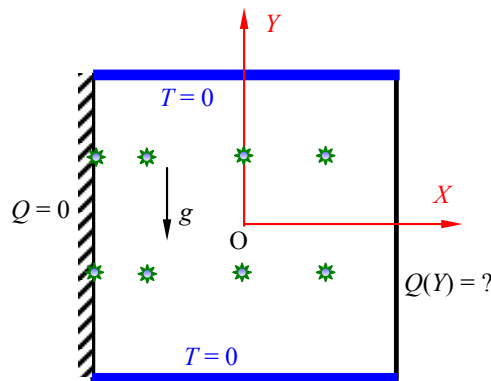


FIGURE 1 Configurations

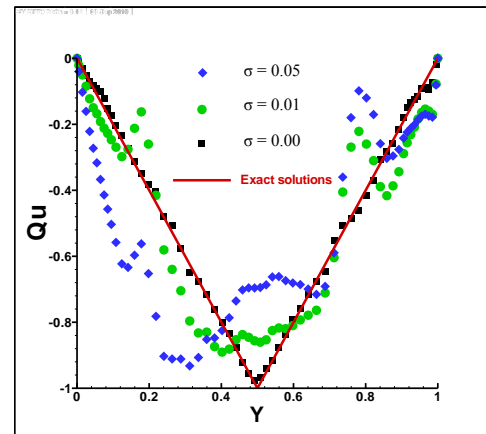


FIGURE 2. Inverse results

Observing from the heatlines shown in Fig. 2, the short-circuiting effect occurs, i.e., the hot fluid flowing in the vicinity of the right wall transfers a significant portion of its sensible heat to the sink of the top side instead of carrying it all the way to the top and bottom cold walls of the enclosure.

In practical experimental situations, it is expected that some errors will be introduced into the measurements. When inverse turbulent convection problems are solved using noisy data, the iterative regularization effect of the conjugate gradient on the solution can be detected just as well as in conduction, and used with much profit to optimize the final result.

The convergence speed of the inverse solution slows down as frequency increases. Bias remains in the solution, which could be reduced by taking the sensors closer to active boundary, but at the

expense of a greater sensitivity to the higher noise frequency components. Numerical solutions presented in Fig. 3 reveal that the accuracy of estimation deteriorates as the noise level increases.

ACKNOWLEDGMENTS

This work was partially supported by Alexander von Humboldt Foundation – Germany (2011-2013), Key Project of Hunan Science and Technology – Air Purification in Industrial Halls (2010-2012), and Twelve-Five National Supportive Plan from China Ministry of Science and Technology – building energy conservations in hot summer and cold winter regions in China (2011-2015).

REFERENCES

- [1] P. Wargocki, D.P. Wyon, J. Sundell, *et al.*, The effects of outdoor air supply rate in an office on perceived air quality, Sick Building Syndrome (SBS) symptoms and productivity, *Indoor Air*, 10, 222-236, 2000.
- [2] D. Liu, F.Y. Zhao, G.F. Tang, Numerical analysis of two contaminants removal from a three-dimensional cavity, *International Journal of Heat and Mass Transfer*, 51, 378-382, 2008.
- [3] F.Y. Zhao, D. Liu, G.F. Tang, Multiple steady fluid flows in a slot-ventilated enclosure, *International Journal of Heat and Fluid Flow*, 29, 1295-1308, 2008.
- [4] M.N. Ozisik, H.R.B. Orlande, *Inverse Heat Transfer: Fundamentals and Applications*, Taylor & Francis, New York, 2000.
- [5] M.J. Colaco, H.R.B. Orlande, Inverse natural convection problem of simultaneous estimation of two boundary heat fluxes in irregular cavities, *International Journal of Heat and Mass Transfer*, 47, 1201-1215, 2004.
- [6] F.Y. Zhao, D. Liu, G.F. Tang, Inverse determination of boundary heat fluxes in a porous enclosure dynamically with thermal transport, *Chemical Engineering Science*, 64, 1390-1403, 2009.
- [7] F.Y. Zhao, D. Liu, G.F. Tang, Determining boundary heat flux profiles in an enclosure containing solid conducting block, *International Journal of Heat and Mass Transfer*, 53, 1269-1282, 2010.
- [8] S. Murakami, Indoor/outdoor climate design by CFD based on the software platform, *International Journal of Heat and Fluid Flow*, 25, 849-863, 2004.
- [9] T.F. Zhang, Q. Chen, Identification of contaminant sources in enclosed environments by inverse CFD modeling, *Indoor Air*, 17, 167-177, 2007.
- [10] F.Y. Zhao, D. Liu, L. Tang, Direct and inverse mixed convections in an enclosure with ventilation ports, *International Journal of Heat and Mass Transfer*, 52, 4400-4412, 2009.

NUMERICAL SIMULATION OF ACOUSTIC STREAMING IN THE PISTON-DRIVEN RESONATOR BY GAS-KINETIC BGK SCHEME

Heying Feng, Xiaoqing Zhang, Huanxin Chen

School of Energy and Power Engineering, Huazhong University of Science and Technology,
Wuhan, 430074, Hubei, P. R. China, zhangxq@mail.hust.edu.cn

Yehui Peng

School of Mathematics and Computation Science, Hunan University of Science and Technology,
Xiangtan, 412001, Hunan, P.R.China.

ABSTRACT

This paper is focused on the numerical simulation of the acoustic field arising inside an acoustic resonator. The oscillatory flow field in the resonator is created by the piston at the left end of resonator. The fully compressible Navier–Stokes equations are considered. The formation of the wave fields in the resonator is numerically computed by the gas-kinetic BGK scheme. The interaction of the wave fields with viscous effects and the formation of streaming structures are revealed.

Key Words: *Numerical simulation, acoustic streaming, resonator, gas-kinetic BGK scheme.*

1. INTRODUCTION

The acoustic streaming in the resonator is one of the challenging problems of the interaction of acoustic waves in compressible fluids and solid boundaries. It is a well-known fact that the particle velocities in the resonator are not simply sinusoidal and a pattern of time-independent vortical flows or steady circulations is often found in the body of compressible media. Sound at high intensity levels in gases may be accompanied by many nonlinear second-order effects such as acoustic streaming. Although the streaming velocity magnitude is smaller than the primary oscillatory particle velocity magnitude, acoustic streaming may be effective in accelerating certain kinds of rate processes and has applications in devices like acoustic compressors, thermoacoustic refrigerators.

The study of acoustic streaming started with the theoretical work of Lord Rayleigh [1]. The effect of compressibility on acoustic streaming near a rigid boundary was investigated by Qi [2] with a theoretical study. Kawahashi and Arakawa [3] performed a numerical analysis of acoustic streaming induced by finite-amplitude oscillation in a closed duct driven by a piston applying a fourth order spatial difference method. Yano [4] investigated acoustic streaming excited by resonant oscillations with periodic shock waves in a gas-filled closed tube. His computational predictions demonstrated strong vortices localized near the tube wall that are quite different from Rayleigh streaming. Alexeev and Gutfinger [5] studied resonant gas oscillations in closed tubes numerically and experimentally. They considered a two-dimensional axisymmetric flow for a compressible gas with a turbulence model and reported shock waves traveling back and forth along the tube. They reported streaming motion at resonance having an opposite direction with that in nonresonant oscillations. Most of these analytical and numerical studies, the formation of acoustic streaming is analyzed with a simplified approach which assumes that is a perfectly sinusoidal primary standing wave field in the domain of interest.

In this study, an analytical model for the acoustic streaming is presented. The acoustic field in the resonator is investigated by solving the full two-dimension Navier-Stokes equations by gas-kinetic BGK scheme.

2. THE MODEL AND FINITE VOLUME GAS-KINETIC BGK SCHEME

Acoustic streaming formation can be described by the full two-dimension Navier–Stokes equations for compressible fluid. In a Cartesian coordinate system, these equations are expressed as

$$\frac{\partial \rho}{\partial t} + \frac{\partial \rho U}{\partial x} + \frac{\partial \rho V}{\partial y} = 0 \quad (1)$$

$$\frac{\partial \rho U}{\partial t} + \frac{\partial \rho U^2}{\partial x} + \frac{\partial \rho UV}{\partial y} = -\frac{\partial p}{\partial x} + \frac{\partial \sigma_{xx}}{\partial x} + \frac{\partial \sigma_{xy}}{\partial y} \quad (2)$$

$$\frac{\partial \rho V}{\partial t} + \frac{\partial \rho UV}{\partial x} + \frac{\partial \rho V^2}{\partial y} = -\frac{\partial p}{\partial y} + \frac{\partial \sigma_{yx}}{\partial x} + \frac{\partial \sigma_{yy}}{\partial y} \quad (3)$$

$$\frac{\partial E}{\partial t} + \frac{\partial (E+p)U}{\partial x} + \frac{\partial V(E+p)}{\partial y} = \frac{\partial (U\sigma_{xx} + V\sigma_{xy} - q_x)}{\partial x} + \frac{\partial (U\sigma_{yx} + V\sigma_{yy} - q_y)}{\partial y} \quad (4)$$

Here, t is time, x and y refer to the Cartesian coordinates, ρ is density, p is pressure, U and V are the velocity components, and E is the total energy defined as:

$$E = \frac{P}{\gamma - 1} + 0.5\rho(U^2 + V^2)$$

where the ratio of specific heats $\gamma = 1.4$ for ideal gas. The closure of the equations (1)-(4) is based on the ideal-gas law: $p = \rho RT$, where the specific gas constant R . In Eqs.(1)-(4), the viscous stress σ is defined as

$$\sigma_{xx} = \frac{4}{3}\mu \frac{\partial U}{\partial x} - \frac{2}{3}\mu \frac{\partial V}{\partial y}, \quad \sigma_{yy} = \frac{4}{3}\mu \frac{\partial V}{\partial y} - \frac{2}{3}\mu \frac{\partial U}{\partial x}, \quad \sigma_{xy} = \sigma_{yx} = \mu \frac{\partial U}{\partial y} + \mu \frac{\partial V}{\partial x}$$

where μ is the dynamic viscosity and takes the Sutherland's law. And the heat-flux vector are written as

$$q_1 = -\kappa \frac{\partial T}{\partial x}, \quad q_2 = -\kappa \frac{\partial T}{\partial y}$$

where T is temperature and k is thermal conductivity.

The following is the finite volume gas-kinetic BGK scheme used in the paper. In the finite volume method, the macro-values $W = (\rho, \rho U, \rho V, E)$ are updated as follows

$$W_{i,j}^{n+1} = W_{i,j}^n + \frac{1}{\Delta V_{i,j}} \sum_{l=1}^4 s_{i,j,l} F_{i,j,l}^n \quad (5)$$

where $\Delta V_{i,j}$ is the cell volume, $s_{i,j,l}$ is the length of the cell interface, and $F_{i,j,l}^n$ is the numerical flux along the outer normal of the cell interface at the n -the time level. In the gas-kinetic BGK scheme, the flux is computed by kinetic approach.

In the directional splitting method, the BGK model without external force in the x -direction is

$$\frac{\partial f}{\partial t} + u \frac{\partial f}{\partial x} = -\frac{f - g}{\tau} \quad (6)$$

where f is the gas distribution function and g is the equilibrium state approached by f . Both f and g are functions of space x , time t , particle velocities (u, v) , and internal variable ξ . The particle collision time τ is related to the viscosity and heat conduction coefficients. The equilibrium state is a Maxwellian distribution

$$g = \rho \left(\frac{\lambda}{\pi} \right)^{\frac{2+K}{2}} e^{-\lambda((U-u)^2+(V-v)^2+\xi^2)}$$

where $\xi^2 = \xi_1^2 + \dots + \xi_K^2$ and $K = 3$ for 2-dimension case. The Eq. (6) has the following integral solution at the interface $(x_{i+1/2}, y_j)$

$$f(x_{i+1/2}, y_j, t, u, v, \xi) = \frac{1}{\tau} \int_0^t g(x', y_j, t', u, v, \xi) e^{-(t-t')/\tau} dt' + e^{-t/\tau} f_0(x_{i+1/2} - ut, y_j) \quad (7)$$

Here, f_0 is the distribution function at t^n and $x' = x - u(t - t')$. Thus the flux along the x -direction at $(x_{i+1/2}, y_j)$ can be computed as $\int_{t^n}^{t^{n+1}} \int u f(x_{i+1/2}, y_j, t, u, v, \xi) du dv d\xi dt$. The flux along other directions can be computed similarly by coordinate transfer.

The gas-kinetic BGK scheme uses the macro-values at the time level t^n to construct the function g and f_0 , and obtains the flux in the (5). One can find the details in Ref. [7]-[8].

4. RESULTS

The physical object of this research is an air gas-filled tube closed at one end, and driven at another end by a piston in a sine law

$$u_0 = l\omega \sin \omega t \quad (8)$$

where l is the displacement amplitude and ω is the angular frequency of piston moving.

The following model is chosen from [9]. The resonance tube has a length of $L = 1.995\text{m}$ and a diameter is of $H = 0.036\text{m}$. The parameter values of gas as initial data in calculations, are taken at $\rho_0 = 1.165\text{kg} / \text{m}^3$, $T_0 = 295\text{K}$, $R = 287\text{J} / (\text{kg}\cdot\text{K})$, and the ratio of the specific heat $\gamma = 1.4$. The sound speed is defined as $C_s = \sqrt{\gamma RT_0}$. The fundamental resonant frequency Ω of the tube is $\Omega = \pi C_s / L$, L being the distance between the motionless end of the tube and the middle position of piston moving. The parameter l is chosen such that $l/L = 0.00186$. The sound field created by the piston is investigated in simulation. No-slip velocity and zero-gradient temperature boundary conditions were used for all the solid walls. The mesh is 206×160 .

Figure 1 gives the instantaneous oscillatory flow fields in the resonant at eight different moments $t_i = \left(40 + \frac{i}{4}\right) \times \frac{L}{C_s}$, $i = 0, 1, \dots, 7$ in the 20th cycle. In the figure, the streamtrace and the contour of pressure are denoted by solid line and dashed line, respectively. These are representative figures and although the flow directions change during the acoustic cycle due to periodic oscillations, the nature of the flow field is preserved. Figure 1 shows that at six different moments $t_1, t_2, t_3, t_5, t_6, t_7$ there are two-dimension flow patterns. And there is circulation pattern resulting from viscous interactions at a position for each moment $t_1, t_2, t_3, t_5, t_6, t_7$. Figure 1(d) and (h) show

that at some region the flow is uniform at the moment t_3 and t_7 . These results are consistent with those in [4]. Moreover, our results show that there are pressure disturbance at the moment t_0 and t_4 .

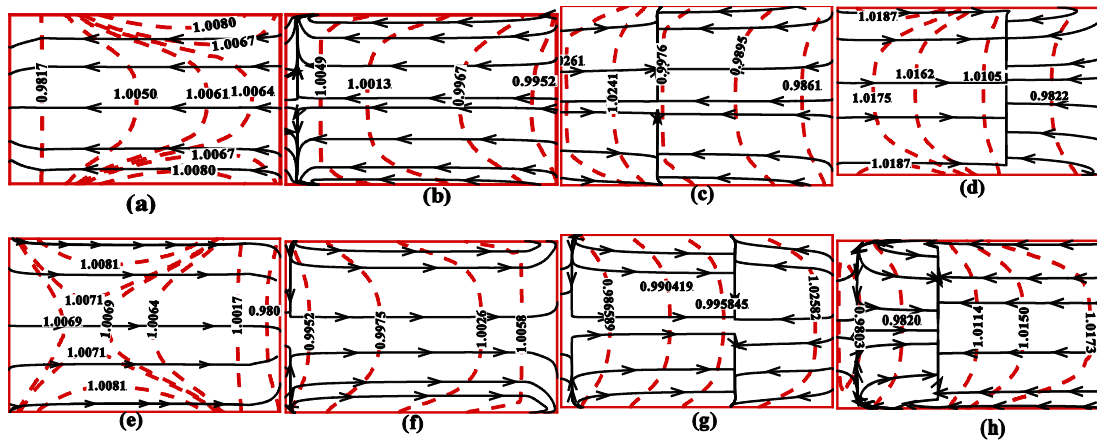


FIGURE 1. The instantaneous flow fields in the resonant at eight different moments in the 20th cycle.

5. CONCLUSIONS

Acoustic field in the resonator is simulated by the gas-kinetic scheme. The obtained results show that there is uniform flow in the tube. The present studies also demonstrated successfully the kinetic scheme is well capable of simulating acoustic field in a resonant tube.

REFERENCES

- [1] Lord Rayleigh, On the circulation of air observed in Kundt's tubes, *Philos. Trans. R. Soc. London, Ser. A*, 175, 1–21, 1884.
- [2] Q. Qi, The effect of compressibility on acoustic streaming near a rigid boundary for a plane traveling wave, *J. Acoust. Soc. Am.* 94, 1090–1098, 1993.
- [3] M. Kawahashi and M. Arakawa, Nonlinear phenomena induced by finite-amplitude oscillation of air column in closed duct, *JSME Int. J.*, 39, 280–286, 1996.
- [4] T. Yano, Turbulent acoustic streaming excited by resonant gas oscillation with periodic shock waves in a closed tube, *J. Acoust. Soc. Am.*, 106, L7–L12, 1999.
- [5] A. Alexeev and C. Gutfinger, Resonance gas oscillations in closed tubes: Numerical study and experiments, *Phys. Fluids*, 15, 3397–3408 ~2003.
- [6] Murat K. Aktas and Bakhtier Farouk, Numerical simulation of acoustic streaming generated by finite-amplitude resonant oscillations in an enclosure, *J. Acoust. Soc. Am.* 116 (5), 2822–2831, 2004
- [7] Xu K, Gas-Kinetic Schemes for Unsteady Compressible Flow Simulations. *VKI for Fluid Dynamics Lecture Series*, 1998
- [8] Xu K, A Gas-Kinetic BGK Scheme for the Navier–Stokes Equations and Its Connection with Artificial Dissipation and Godunov Method. *Journal of Computational Physics*, 171, 289–335, 2001.
- [9] X. Q. Zhang, *Investigation on Modeling and Optimization of Thermoacoustic Engine Systems*, Ph.D. Thesis, Huazhong University of Science and Technology (in chinese), 2001.

PARTICLE DEPOSITION EFFECTS ON HEAT TRANSFER FROM A POROUS HEAT SINK

Kamel Hooman, Mostafa Odabae

School of Mechanical and Mining Engineering, The University of Queensland, Australia,
k.hooman@uq.edu.au

Ali Tamayol

School of Engineering Science, Simon Fraser University, Canada

ABSTRACT

A novel thermal resistance approach, cross-validated with CFD simulation, is presented in this paper to investigate the effects of dust deposition on a metal foam heat sink. As one would expect, the deposition of dust with low thermal conductivity on the highly conductive solid phase of metal foam decreases the heat transfer rate from the surface. At the same time, pressure drop increases monotonically as pores are blocked and the permeability is reduced. CFD results for a 2D case of a metal foam-wrapped tube bundle are in close agreement to those of the analytical model

Key Words: *Heat Transfer, Metal Foams, Dust Deposition, Finite Volume, Thermal Resistance.*

1. INTRODUCTION

Metalfoams are a class of relatively new fibrous materials with novel thermophysical properties including low flow/thermal resistance, excellent surface-area-to-volume ratio, high temperature tolerance, low density, and corrosion resistance. Foams can be constructed from a wide variety of materials including metals (aluminum, nickel, copper, iron, and steel alloys), polymers, and carbon. More importantly, these micro structures can be tailored to meet a range of requirements.

In metalfoam heat sinks, heat transfer rate is enhanced by conducting the heat to the metallic ligaments with a large accessible surface area per unit volume. The ligaments highly interact with the passing fluid as the boundary layer separates and pore level turbulence is promoted. As a result of recent decrease in production costs, metalfoams have received a special attention as a candidate for designing compact heat exchangers in the past decade. As such, numerous studies have been conducted to determine the transport properties of metalfoams.

Despite such wonderful thermohydraulic performance of metalfoams, they are vulnerable to dust and particle deposition in the open pores. Depending on their size and density (as well as the cooling air flow rate), the particles can deposit on the heat sink surface and reduce the effective thermal conductivity of the heat sink. If not cleaned, the particles can block the pores and further reduce the permeability of the porous medium. Our literature review reveals a need to a model that can predict the dust deposition effect on the performance of the sink. Hence, proposing a thermal resistor network and conducting CFD simulations, this paper aims at filling this gap in the literature.

2. ANALYSIS

Forced convection over a metalfoam heat sink with constant wall temperature of T_s is considered. The metalfoam is sandwiched between a hot plate and an insulated wall; see Fig. 1. Laminar flow of an incompressible constant property fluid is investigated. Moreover, the side wall effects on the volume-averaged velocity (U_D) distribution are neglected and a uniform volume averaged velocity is assumed over the entire cross-section. The width of the heat sink is assumed to be long enough such that the problem can be analyzed two dimensionally. The solid matrix (metalfoam) is assumed to be isotropic and its thermo-physical properties are uniform over the entire area. A simple

approach for modeling the heat transfer is to adopt a thermal resistor network. The network shown in Fig. 1 is comprised of a lumped mass at the nodes that is connected to other side nodes through thermal resistors. The resistors depend on the conductive properties of the ligaments between the nodes and the convective interstitial heat transfer coefficient of the ligaments and the local fluid temperature. The actual resistor network of the matrix shown here is 2D but yet complex.

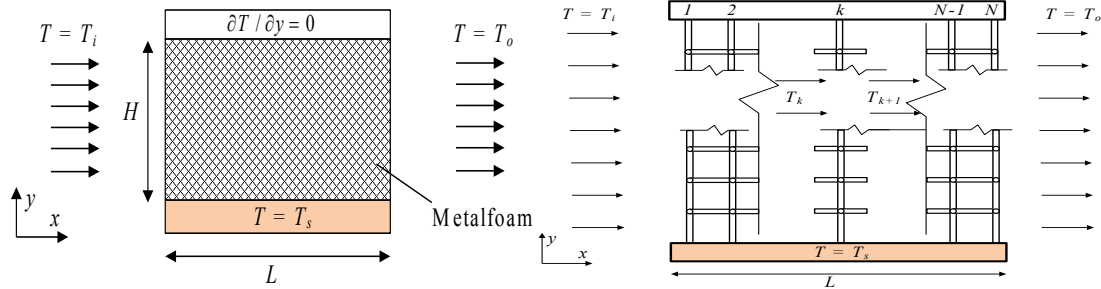


FIGURE 1. Schematic of the metalfoam heat sink (left) along with the network of ligaments (right).

The metalfoam microstructure described by a complex geometry prevents exact solution of transport equations. The geometrical parameters that describe such media are: porosity ε , fiber diameter, and pore density, which is typically expressed in the unit of pores per inch (PPI) [1-3]. Following Bhattacharya *et al.* [4] the random dodecahedron-like microstructure of metalfoams is modeled by a cubic unit cell, as shown in Fig. 2a, which is assumed to be repeated throughout the media. However, the cross-section of the ligaments are not circular and is a function of porosity, see [5-7] for more details. Bhattacharya *et al.* [4] proposed the following relationship between the fiber diameter d_f and pore diameter d_p :

$$\frac{d_f}{d_p} = \frac{1.18}{G} \sqrt{\frac{1-\varepsilon}{3\pi}}, \quad G = 1 - e^{-(1-\varepsilon)/0.04} \quad (1)$$

where G was a shape factor that took into account the variation of ligament cross-section with porosity. Bhattacharya *et al.* [4] did not provide an explicit equation for estimating the fiber's diameter. Our analysis showed that the following correlation can predict the experimental values of d_f in millimeter, for aluminum foams reported by others within 9% accuracy:

$$d_f = 0.431 - 0.0049PPI + \frac{2.43}{PPI^2} \quad (2)$$

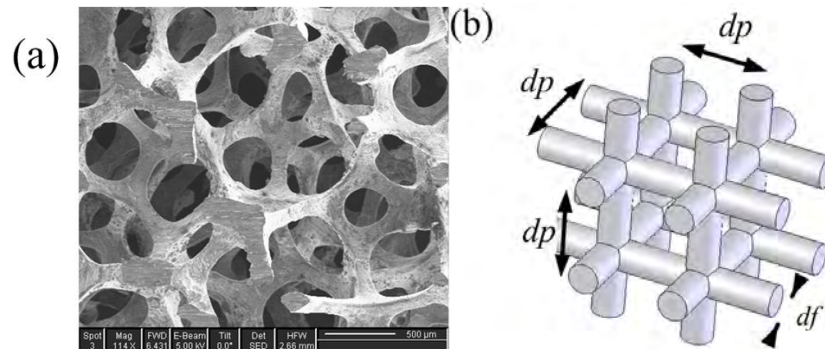


FIGURE 2. Metalfoam microstructure; a) the actual geometry, b) considered unit cell.

The current analysis seeks to estimate the overall heat transfer from a metal foam heat sink modeled as a network of interconnect ligaments allowing conduction and interfacial convection to the passing fluid. Here, $R_{conv, fiber}$ is associated with the interfacial convection from the fibers perpendicular to flow direction in each unit cell, calculated as:

$$R_{conv,fiber} = \frac{1}{h_{int} A_{int,pore}} = \frac{3}{2a_{sf} (d_f + dp)^2 W h_{int}} \quad (4)$$

where $A_{int,pore}$ is the surface area of fibers perpendicular to flow direction and h_{int} is the interstitial heat transfer coefficient given by [7]

$$h_{int} = 0.52 \frac{k_f}{d_f} Re^{0.5} Pr^{0.37} \quad (5)$$

The convective thermal resistance from the base plate is also calculated from:

$$R_{conv,plate} = \frac{1}{h_{plate} (d_f + d_p) W} \quad (7)$$

where the convective heat transfer coefficient is given by:

$$h_{plate,L} = 0.664 \frac{k_f}{L} Re_L^{0.5} Pr^{1/3} \quad (8)$$

The conductive resistance at each pore is calculated from:

$$R_{cond} = \frac{d_f + d_p}{k_s M \pi / 4 (d_f G)^2} \quad (9)$$

where M is the number of pores in the through-plane direction for a unit of length. The effect of the variation of ligament cross-section with porosity is included by using $d_f G$ instead of d_f .

3. RESULTS

The present approach [8] is compared with the experimental data reported in [7]; see Fig. 3. The heat sink studied in [7] has a height of 0.045 m and the length of 0.112 m. Thermal conductivity of solid phase was reported as 213 W/mK. The values of Nu_{keff} calculated using the present model for a clean heat exchanger are within 12% of the experimental data over a wide range of $Re_k Pr$. Adding a layer of dust, with either a uniform or non-uniform thickness, to the heat sink introduces an extra conduction resistance to our

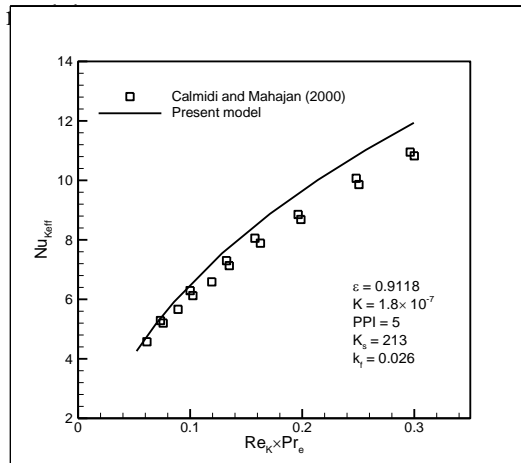


FIGURE 3. Comparison of the present model with experimental data of Calmidi and Mahajan [7].

An independent CFD simulation of the problem is also conducted by running ANSYS12.1 solver to get results from a four row tube bundle covered by metal foam [8]. Two extreme cases were considered. One assumes that the dust is accumulated on the front rows, case A, while the other one allows for uniform distribution and penetration of dust to the foam in such a way that all tubes are covered with the same amount of particles, case B.

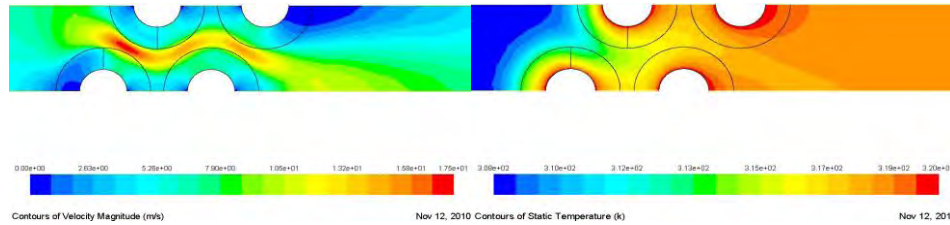


FIGURE 4. Velocity magnitude and isotherms for case A.

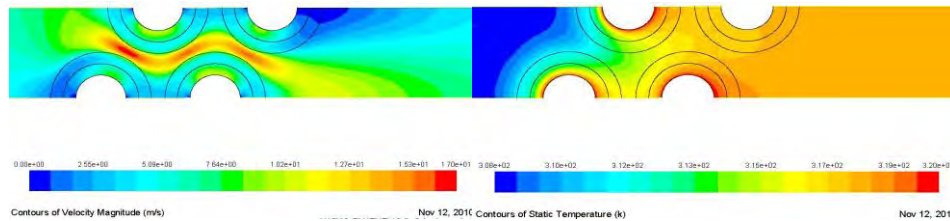


FIGURE 5. Velocity magnitude and isotherms for case B.

4. CONCLUSIONS

Based on the thermal resistance approach, a theoretical study has been conducted to investigate the effects of dust deposition on the exterior surface of a metal foam heat exchanger. The model tends to generate accurate results for the case of clean heat exchangers. However, due to lack of experimental data on fouled foam heat exchangers in the literature, such comparison under dusty condition was not possible in this study. The closed form solutions are then compared with CFD (finite volume) simulation of the heat exchanger under dusty conditions.

REFERENCES

- [1] A. Tamayol and M. Bahrami, Analytical determination of viscous permeability of fibrous porous media, *International Journal of Heat and Mass Transfer*, 52, 2407-2414, 2009.
- [2] S. Mahjoob and K. Vafai, A synthesis of fluid and thermal transport models for metal foam heat exchangers, *International Journal of Heat and Mass Transfer*, 51, 3701-3711, 2008.
- [3] V.V. Calmidi and R.L. Mahajan, The effective thermal conductivity of high porosity fibrous metal foams, *ASME-Journal of Heat Transfer*, 121, 466-471, 1999.
- [4] A. Bhattacharya, V.V. Calmidi and R.L. Mahajan, Thermophysical properties of high porosity metal foams, *International Journal of Heat and Mass Transfer*, 45, 1017-1031, 2002.
- [5] M. Wang and N. Pan, Modeling and prediction of the effective thermal conductivity of random open-cell porous foams, *International Journal of Heat and Mass Transfer*, 51, 1325-1331, 2008.
- [6] M. Odabae, K. Hooman and H. Gurgenci, Metal foam heat exchangers for heat transfer augmentation from a cylinder in cross-flow, *Transport in Porous Media*, 86, 911-923, 2011.
- [7] V.V. Calmidi and R.L. Mahajan, Forced convection in high porosity metal foams, *ASME-Journal of Heat Transfer*, 122(3), 557-565, 2000.
- [8] K. Hooman and A. Merrikh, Theoretical analysis of natural convection in an enclosure filled with disconnected conducting square solid blocks, *Transport in Porous Media*, 85, 641-651, 2010.

THERMAL MODELING OF POWER TRANSFORMER RADIATORS USING A POROUS MEDIUM BASED CFD APPROACH

Rebei Bel Fdhila, Jurjen Kranenborg, Tor Laneryd, Carl-Olof Olsson, Bertil Samuelsson
ABB Corporate Research, Västerås, Sweden, {rebei.bel.fdhila, jurjen.kranenborg, tor.laneryd, carl-
olof.olsson, bertil.samuelsson}@se.abb.com

Andreas Gustafsson, Lars-Åke Lundin
ABB Power Products Division / Transformers, Ludvika, Sweden, andreas.gustafsson@se.abb.com

ABSTRACT

In power transformer cooling applications, the heat transfer in large fan-cooled radiator batteries and their immediate surroundings can be successfully studied using a CFD model in which the mixed convection based oil and air flows and the heat transfer between these media in the radiators is modelled using an anisotropic porous medium approach and the area surrounding the radiators using a standard turbulent heat transfer model. The resulting model appears fast enough to allow a large number of realistic simulations to be run to study the effect of radiator design parameters like fan position, fan size and oil flow rate on the cooling capacity of the radiators. As an example the analysis of the effect of fan size on radiator cooling capacity is shown.

Key Words: *Heat Transfer, Radiators, Power Transformers, CFD, Porous Medium.*

1. INTRODUCTION

Power transformers are large products that are often cooled using large assemblies of radiators with fans. The footprint of these radiators is generally of similar size as the power transformer itself. The radiator configuration is tailor-made for each transformer and can be described using a number of design parameters like height and width, number of panels per radiator, number of radiators per assembly, the number and size of fans used as well as their position (horizontal, vertical) on the radiators. As a consequence, a radiator assembly is a complex geometrical entity with a cooling oil flow in small ducts in the radiator panels, a cooling air flow in the small sections between the panels as well as an air flow in a large area surrounding the radiator. Such a setup is well worth studying using a CFD model, an approach that has already been successfully used for the simulation of mixed convection in power transformer windings [1, 2].

In order to allow a large number of simulations as required for studying practical cooling scenarios, a porous medium approach has been chosen to model the radiators on a fine numerical grid, coupled with a turbulent heat transfer model on a much coarser grid for the heat and mass transport in the air surrounding the radiators. To this end the background literature on heat transfer in porous media has been reviewed [3, 4, 5] and published anisotropic models were used for porosity and thermal conductivity [6] to account for the radiator panel orientation.

2. TEST CASE AND CFD RADIATOR POROUS MEDIUM MODEL DESCRIPTION

A specific transformer design as shown in Figure 1 has been chosen as the reference case, serving as a starting point for many of the model variants studied. The thermal parameters that are relevant for radiator cooling (top oil and bottom oil temperatures, thermal losses and net oil flow rate through the radiators) were derived from the heat run test data and the design model. In the same figure the geometry of the CFD model is depicted. Only half of the radiator domain including two

radiator groups (each group having three radiators) needs to be modeled due to the symmetry that is present in this particular design.

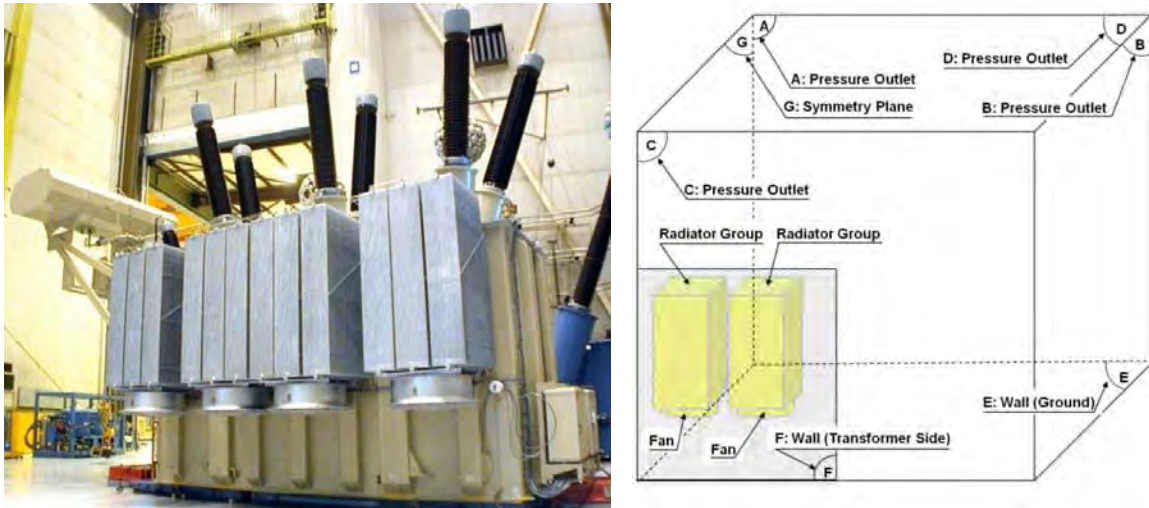


FIGURE 1. Reference transformer design (left) and corresponding CFD model geometry (right) that includes the radiators and a large surrounding area to minimize the effect of computational boundaries on the simulation results. The boundary conditions are included in the figure as well.

The CFD model was implemented using ANSYS Fluent 12.0. In the radiator groups domain, generalized porous medium equations for heat and mass transfer are solved for air using Fluent's porous model approach. The oil temperature in the radiator is modeled using a standard heat transport equation and the vertical oil velocity has been explicitly modeled based on a prescribed average value modulated by buoyancy due to the vertically averaged oil temperature field. The heat transfer from oil to air is modeled using a common heat transfer coefficient. The porous medium model coefficients (Darcy viscous loss term and effective thermal conductivity, published in [6]) that are used in the radiator domain are anisotropic to represent the parallel-panel structure of the radiators. The fans are modeled as a volume where a known velocity is specified on the boundary of the fans. The outer computational domain boundaries model the floor, the transformer tank wall (adiabatic in our simulations, so only affecting the flow) and open domain boundaries (the latter located far away from the radiators and using pressure outlet conditions, such as to minimize the effect on the computational result). Since the cooling oil flow in the transformer under study is driven by natural convection (as a consequence of the buoyancy difference between the warm oil inside the transformer tank and the colder oil in the radiators), the total oil flow rate through the radiator is fixed based on the reference design estimate and the oil inlet temperature is fixed as well (since the transformer itself is not modeled). In this way the main measure of the radiator cooling capacity we use is top-to-bottom oil temperature difference; for a given thermal loss a larger difference implies a larger cooling capacity.

In the final version of the simulation code, special care has been taken for parallelization of the code. As a consequence the model has shown to be efficient allowing a typical scenario case to be calculated in just a few hours on 32 nodes of the computational cluster at ABB Corporate Research.

3. RESULTS

Figure 2 shows the simulation results for the reference design case used to validate the model. In this figure the computational grid is shown at a horizontal cross-cut through the radiators, revealing the dense, accurate grid inside the radiators (allowed by use of the efficient porous medium approach), the coarse blue regular grid at the outside as well as the intermediate (pink) grid in between. The validation results show good agreement between measured and calculated results.

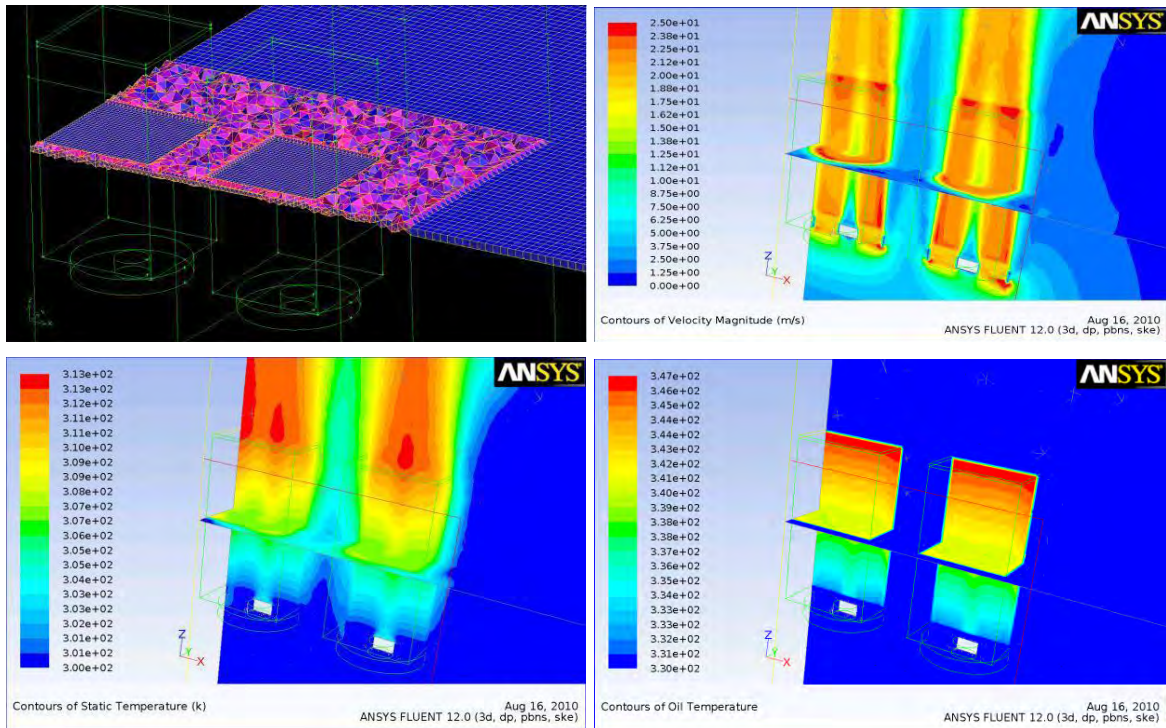


FIGURE 2. validation simulation results. Upper left: impression of computational grid (horizontal crosscut). Upper right: air flow magnitude (m/s). Lower left: Absolute air temperature (Kelvin). Lower right: oil temperature distribution in radiator.

The CFD model has proved to be very useful in generating a large database of solutions for analyzing various design scenarios, in which the effect of a radiator design parameter on cooling capacity is studied. One of these scenarios deals with the effect of radiator fan diameter. We have investigated whether smaller fans have an advantage over less but larger fans (assuming an equal net air flow through the radiators to allow the cases to be compared) since the smaller fans allow a better coverage of the lower radiator air inlet area. The fan diameter has been varied between 0.8 and 1.5 m, allowing two, three or four fans to cover the lower air inlet area of the radiator groups (with the two radiator assemblies as shown in figure 2 now modeled as a single group). As an example for the case with three fans, Figure 3 shows that the inlet coverage has a profound effect on the temperature distribution in the radiators and thus may be expected to affect the cooling capacity as well.

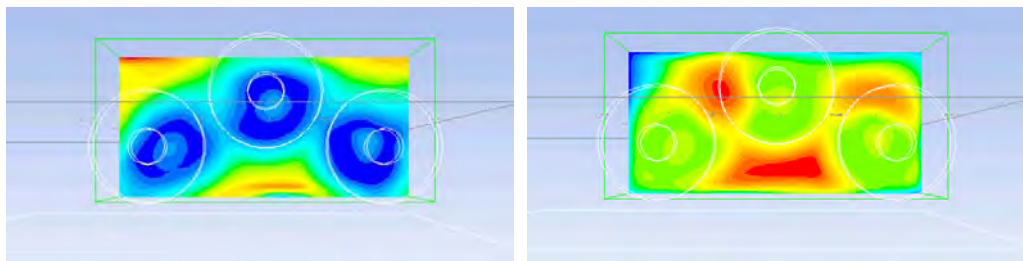


Figure 3. Air (left) and oil (right) relative temperature distribution in the radiators at horizontal mid-plane cross-section (same position as in Figure 2) for a radiator inlet coverage with three fans.

In Figure 4 the cooling capacity results for the different fan diameters have been collected. It reveals that the top-to-bottom temperature difference and thereby the cooling capacity increases if the same amount of air is spread more evenly with a larger number of smaller fans because of the

improved coverage. The figure also shows that the transformer tank wall has some influence on cooling capacity since the two configurations with three fans do not give exactly the same result. The maximum cooling capacity improvement obtained in this way is of the order of 5% – 10%, based on the investigated cases.

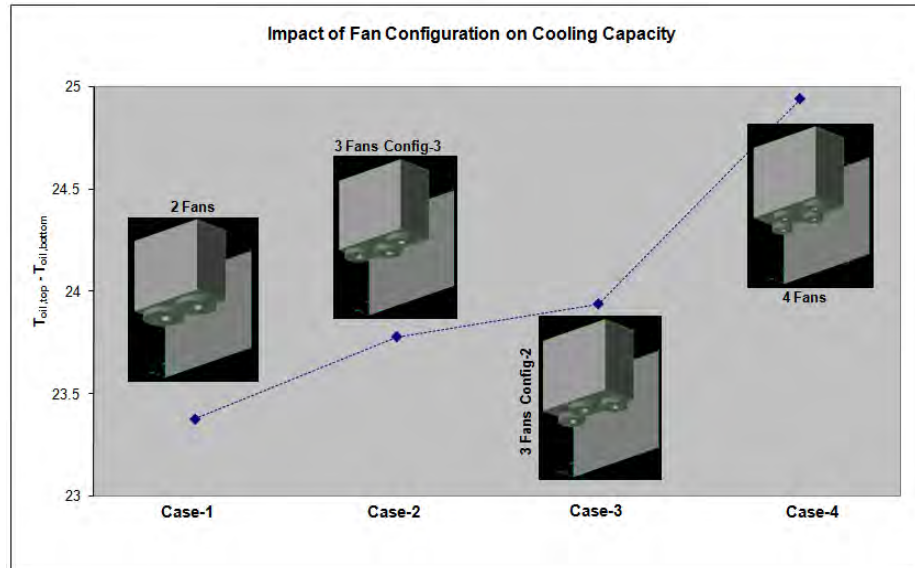


FIGURE 4. Cooling capacity (in terms of top-to-bottom oil temperature difference) for four different fan configurations with different fan diameter.

4. CONCLUSIONS

The CFD model presented here provides a fast yet accurate approach for performing realistic simulations on an important class of radiator cooling problems. Using the porous medium approach the execution time becomes small enough to allow design scenarios to be investigated that require a large number of simulations. Consequently, CFD methods can be applied directly to derive design guidelines for large industrial cooling equipment like fan-cooled transformer radiators.

REFERENCES

- [1] E.J. Kranenborg, C. O. Olsson, B. R. Samuelsson, L-Å. Lundin, R. M. Missing, Numerical study on mixed convection and thermal streaking in power transformer windings, *5th European Thermal-Sciences Conference (EUROTHERM 2008)*, The Netherlands, 2008.
- [2] P. Picher, F. Torriano, M. Chaaban, S. Gravel, C. Rajotte, B. Girard, Optimization of transformer overload using advanced thermal modeling, *CIGRE Biannual meeting 2010*, Paris, France, 2010
- [3] Ergun, S., Fluid Flow Through Packed Columns, *Chemical Engineering Progress*, pp. 89-94, vol. 48, No 2, 1952.
- [4] Bejan, A., Designed Porous Media: Maximal Heat Transfer Density At Decreasing Length Scales, *Int. J. Heat Mass transfer*, pp. 3073-3083, vol. 47, 2004.
- [5] Bejan, A., Dincer, I., Lorente, S., Miguel, A. F. and Reis, A. H., "*Porous and Complex Flow Structures in Modern Technologies*", Springer-Verlag, 2004.
- [6] Morega, A. M., Bejan, A. and Lee, S. W., Free Stream Cooling Of A stack Of Parallel Plates, *Int. J. Heat Mass transfer*, pp. 519-531, vol. 38, No 3, 1994.

NUMERICAL INVESTIGATION ON THERMAL STRATIFICATION PHENOMENON IN A SHUTDOWN COOLING SYSTEM PIPING

Sun-Hye Kim, Hee-Dong Sung, Young-Jin Kim

School of Mechanical Engineering, Sungkyunkwan University, Suwon 440-746 Republic of Korea,

E-mail: remote@skku.edu, hdsung@skku.edu, yjkim50@skku.edu

Jung-Soon Park, Young-Hwan Choi

Korea Institute of Nuclear Safety, Daejeon 305-338 Republic of Korea,

E-mail: k651pjs@kins.re.kr, k202cyh@kins.re.kr

ABSTRACT

Several piping failures caused by thermal stratification have been reported in several nuclear power plants since the early 1980s. However, this kind of thermal effect was not considered when the old vintage nuclear power plants were designed. Therefore, additionally, it is necessary to evaluate this unexpected thermal effect on structural integrity. Thermally stratified flow is usually generated by turbulent penetration from reactor coolant system to branch line or leakage through a damaged part of valve in branch line. In this paper, the characteristic of thermal stratification in a shutdown cooling system of pressurized water reactor (PWR) plant were investigated by using numerical method. First, CFD analyses were carried out considering in-leakage. Especially, the temperature distribution along the shutdown cooling system piping was simultaneously calculated based on conjugate heat transfer condition. Finally, thermal stress caused by stratified flow in piping was evaluated based on one-way sequential coupling method. This approach can reduce the effort to calculate heat transfer coefficient and lead more realistic and accurate results.

Key Words: *Conjugate Heat Transfer Analysis, Coupled Analysis, Thermal Stratification.*

1. INTRODUCTION

According to the increase of operating nuclear power plants, piping failures related to thermal stratification phenomenon have increased throughout the world. Usually, thermal stratification can lead to unexpected bending stresses and serious thermal fatigue cracking in piping system. Nevertheless, this kind of thermal effect was not considered when the old vintage nuclear power plants were designed [1]. Thus, United State Nuclear Regulatory Commission (USNRC) issued the Bulletin No. 88-11 to request evaluation on the main piping which has a possibility to experience thermal stratification [2]. Furthermore, Electric Power Research Institute (EPRI) published the guidance, MRP-146 [3] for thermal fatigue evaluation on the thermally stratified branch line. It means thermal stratification has become a significant concern for nuclear power plants because of its potential impact. Usually, thermal stratification phenomenon which causes unexpected thermal fatigue can be generated by turbulent penetration and valve leakage at the branch lines which are connected to reactor coolant system (RCS).

One of possible branch systems which can be affected by turbulent penetration and leaking is the shutdown cooling system (SCS) in pressurized water reactor (PWR) plants. In this study, thermal stress evaluation on SCS piping was performed using one-way sequential coupled analysis method. First, temperature distribution along a SCS piping in PWR was estimated by using CFD analysis. Especially, the temperature distribution caused by turbulent penetration and leaking flow was analyzed. Then, the results of thermal flow analysis were converted to the input file for thermal stress analysis. It means that thermal stress was calculated by directly considering the temperature

distribution. In this scheme, there is no need to calculate and define heat transfer coefficients for thermal stress analysis so that this method is more realistic and effective.

2. CFD ANALYSIS MODEL DESCRIPTION

The SCS of PWR plant operates to continually remove heat when the reactor shutdown occurs. During normal or start-up operating condition, the coolants of SCS are isolated since all valves in SCS are closed [1]. However, if a damaged part exists at the first isolation valve, leaking flow can generate from branch line to RCS (in-leakage). Fig. 1 shows the schematic diagram of a SCS piping which is connected to the bottom of hot leg. The nominal diameter of SCS piping is 0.406 m and wall thickness is 0.04 m. Also, additionally, reactor drain tank (RDT) line and high pressure safety injection (HPSI) line are linked with the SCS piping and the nominal diameters of each line are 0.076 m and 0.051 m. We excluded the RDT line from analysis scope because this line has too small diameter and long vertical part so that it is difficult to generate stratified flow. Fig. 2 presents the scope of thermal flow analysis, especially, pipe and valve disks of two valves (V652, V532) were considered as solid domain.

For CFD analysis, three dimensional unsteady, incompressible flows were assumed and the effect of viscous dissipation and radiation heat transfer was ignored. Because the flow in hot leg belongs to turbulent region so that shear stress transport (SST) model was considered as turbulent model. SST model is widely known to high accuracy of boundary layer simulation because this model applies a $k-\omega$ based model formulation in proximity of the wall and $k-\epsilon$ model in the bulk of flow [4]. To simultaneously calculate the temperature distribution across the pipe, conjugate heat transfer condition was applied. Furthermore, the temperature dependent density difference was directly considered to calculate buoyancy term. The properties of light water were estimated according to temperature variation. Consequently, in this study, Reynolds-averaged Navier-Stokes (RANS) equations was used as governing equations.

Since, thermal distribution is rapidly changed according to time, transient analysis was performed until 3000 seconds considering 0.1seconds time step. The material of piping and valve disk was assumed to ANSI SUS 304 steel and temperature dependent properties were imposed. The initial temperature condition was applied to 308 K and initial flow was supposed to stagnant. In addition, all outer surfaces of piping were assumed to be adiabatic and no-slip conditions was applied to all inner surfaces of piping. Temperature and flow rate of coolant at the inlet of hot leg are 586 K and 7718 kg/s. For the outlet, a zero average static pressure outlet condition has been applied. Also, the ends of each branch line were assumed to be isolated and to be a low temperature wall of 308 K. Finally, as a leakage rate, $7.5D^3/\text{day}$ (D represents the nominal diameter of piping) was applied to V652 interface based on guidelines for experiment.

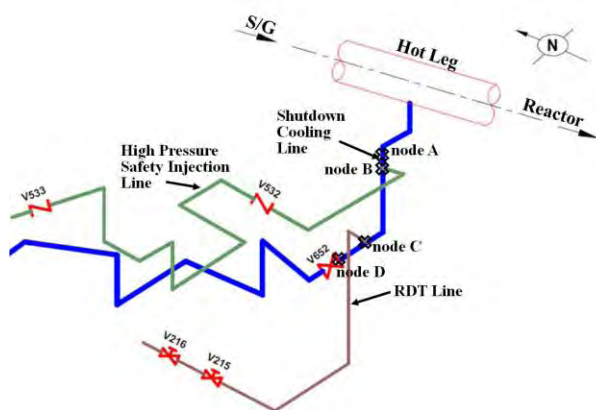


FIGURE 1. Schematic diagram of a SCS piping

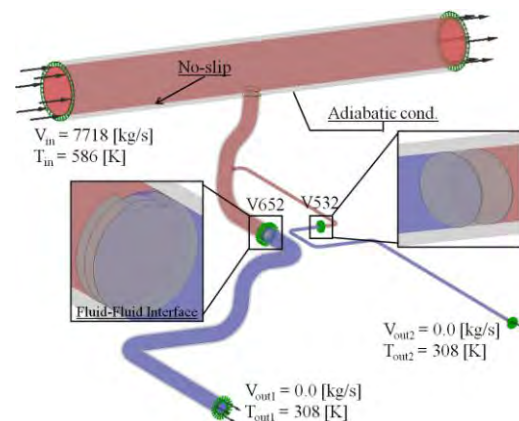


FIGURE 2. Illustration of CFD analysis model

3. ONE-WAY SEQUENTIAL COUPLED ANALYSIS APPROACH

From the results of unsteady thermal flow analysis, the history of temperature at each node and heat flux at each element was converted to the input file for structural analysis without any calculation of heat transfer coefficient. A series of this process is called one-way sequential coupled method. In previous studies, it was difficult to determine appropriate heat transfer coefficient around piping because thermal distribution is rapidly changed with geometry and flow characteristic. However, in this method, there is no need to define heat transfer coefficient so that it is more effective and correct. In this research, based on a converted input file, thermal stress analysis was carried out using a commercial FE analysis code, ANSYS ver. 12 [5].

For transient thermal stress analysis, first, we converted a grid model and temperature distribution data of pipe region into input format for FE analysis by some operation for mesh-based parallel code coupling interface (MPCCI) between CFX code and ANSYS mechanical code. The sensitivity analysis on grid size was not conducted since it is fairly small compare with general grid size for FE analysis. In the process of FE analysis, the initial temperature condition was set to be 308 K and the outer surface of piping was assumed to be adiabatic wall. At the both ends of the RCS hot leg, symmetric condition was imposed. In addition, at the end of each branch line, fixed support condition was applied and several support conditions were also imposed reflecting real support system. Above all, we were not considered any other loads except temperature loading condition. The temperature dependent material properties of piping, ANSI SUS 304 steel, were employed.

4. RESULTS

Fig. 3 (left) describes the velocity vectors and stream lines from the intersection between hot leg and SC line. Due to the strong turbulent penetration from the hot leg, a downward flow is generated near the connection between hot leg and SC line. Furthermore, since the length of turbulent penetration from hot leg reaches the connection of HPSI line, stream line is also developed near the first elbow of HPSI line. However, turbulent penetration cannot significantly influence to the horizontal part of SC line and the effect of leakage is relatively small. Fig. 3 (right) shows the temperature distribution in SCS flow and piping at 3000 seconds. Until the elapsed time, 3000 seconds, thermal stratification cannot be developed near the first valve, V 652, in the SC line. Because turbulence from the RCS can pervade into HPSI line which is horizontally connected to SC line, thermal stratification well develop into HPSI line and the effect of turbulent penetration is the most at the first elbow, section A-A'.

The temperature difference between top and bottom at the inner wall of section A-A' is represented in Fig. 4. The maximum temperature difference is 80 K and this value is larger than threshold temperature (89 °F) which is presented in EPRI MRP-146 [3]. Therefore, thermal stress evaluation should be conducted considering the effect of the stratified flow. The maximum thermal stress results at the critical location are indicated in Table 1. Similar to the result of thermal flow analysis, high thermal stratification stress, S_{TS} is developed near the intersection of HPSI line. Relatively, the thermal stress near the node C and D is very small due to stratification flow is not well developed near these regions. Therefore, to understand the effect of in-leakage and turbulence penetration near the V652, supplementary analysis considering extended elapsed time is needed. However lots of computational time will be requested to complete this analysis.

5. CONCLUSIONS

The one-way sequential coupled analysis approach is more effective and realistic than previous methods to predict thermally stratified flow induced thermal stress because there is no need to calculate and define heat transfer coefficient. In addition, to prevent excessive thermal stresses, the HPSI line should be relocated to avoid the influence of turbulent penetration.

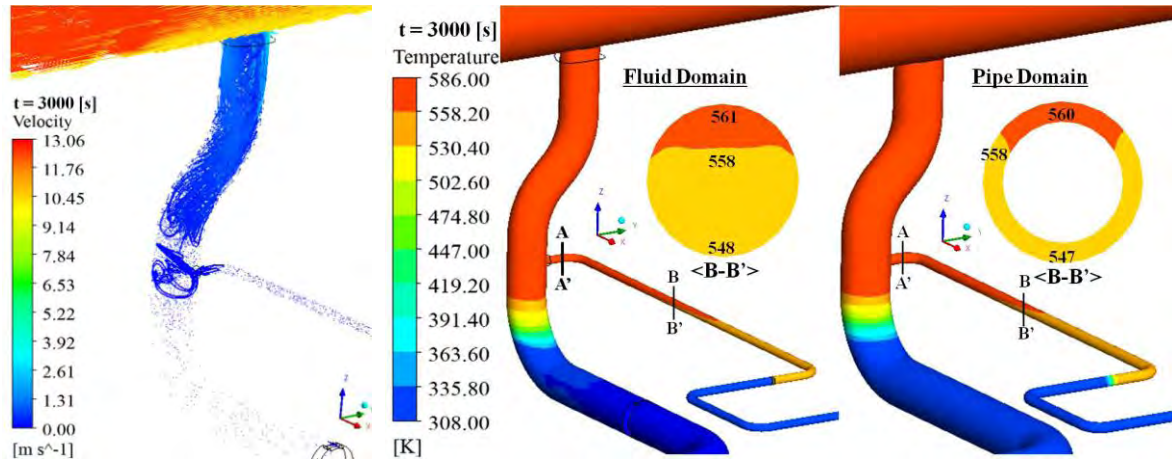


FIGURE 3. Vectors and streamlines plot (right) and temperature distribution (left) in branch lines

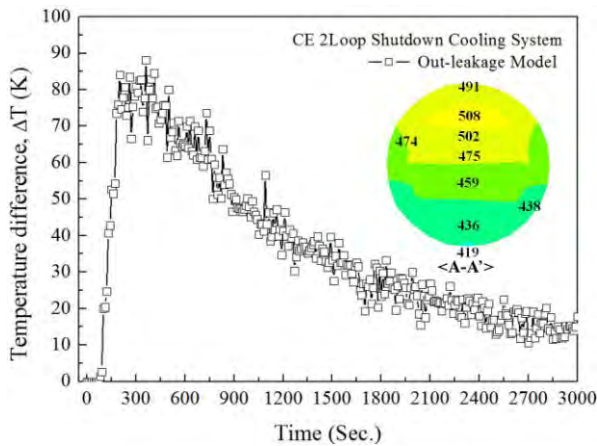


FIGURE 4. Temperature differences at section A-A'

Location	S_{TS} (MPa)
Node A (Vertical pipe)	430
Node B (SC connection)	170
Node C (HPSI connection)	0.275
Node D (RDT connection)	0.206

TABLE 1. Max. S_{TS} at critical location

6. ACKNOWLEDGEMENTS

This research was supported by WCU (World Class University) program through the Korea Science and Engineering Foundation funded by the Ministry of Education, Science and Technology (R33-2008-000-10027-0).

REFERENCES

- [1] K. C. Kim, J. H. Lim, and J. K. Yoon, Thermal fatigue estimation due to thermal stratification in the RCS branch line using one-way FSI scheme, *Journal of Mechanical Science and Technology*, 22, 2218-27, 2008.
- [2] USNRC, Thermal stresses in piping connected to reactor coolant systems, *Bulletin 88-08*, 1988.
- [3] EPRI, Material reliability program: management of thermal fatigue in normally stagnant non-isolable reactor coolant system branch lines, *MRP-146*, 2005.
- [4] Th. Frank, C. Lifante, H. M. Prasser, and F. Menter, Simulation of turbulent and thermal mixing in T-junctions using URANS and Scale-resolving turbulence models in ANSYS CFX, *Nuclear Engineering and Design*, 240, 2313-28, 2010.
- [5] ANSYS Inc., Mechanical APDL documentation, *ANSYS release 12.0*, 2009.

PERFORMANCE EVALUATION OF HEAT LEAK TO THE EVAPORATOR AND THE EFFECT OF LONGITUDINAL HEAT CONDUCTION FROM A COUNTER-FLOW CRYOGENIC HEAT EXCHANGER USING FINITE ELEMENT METHOD

V.Krishna, Pradeep G. Hegde, K. N. Seetharamu, T.R.Seetharam

Department of Mechanical Engineering, P.E.S. Institute of Technology, Bangalore - 560085, India, vkrishna@pes.edu; pghegde@gmail.com; knseetharamu@yahoo.com; tr_seetharam@yahoo.co.in

ABSTRACT

The performance of heat exchangers working in the cryogenic temperature range is strongly affected by factors such as longitudinal wall conduction, heat in leak from the surroundings, flow maldistribution, fluid property variations etc. In most heat exchanger analyses the common assumption is that the ends are insulated. However, in case of small J-T refrigerators longitudinal wall conduction is significant. The cold end of the heat exchanger is almost directly connected to the evaporator. This leads to appreciable heat leak to the evaporator leading to significant drop in performance. In this paper the governing equations for a counter-flow heat exchanger, with heat loss at the cold end, are solved by FEM and the methodology validated by comparing the results with numerical and experimental values published earlier. The analysis is further extended to understand the effects of variation of wall temperature at the cold end and the effect of NtuH not being the same as NtuC, on the performance of the heat exchanger.

Key Words: *Cryogenic Heat Exchangers; Heat Leak; Longitudinal heat conduction; Finite Element Method.*

1. INTRODUCTION

A common assumption made by most authors analyzing the performance of heat exchangers is that the walls of the heat exchanger are insulated at either end. Such an assumption is, however, not valid in the case of small J-T refrigerators such as micro-miniature refrigerators (MMR). Longitudinal conduction through the wall separating the two fluids will be much higher in this case compared to other cryogenic heat exchangers. Due to the small distance between the cold end of the refrigerator and the evaporator, a significant part of the heat conducted through the wall is leaked to the evaporator. The parasitic heat leak leads to significant loss of refrigeration. As such, the assumption of an insulated cold end cannot be applied to an MMR.

In the present paper the governing equations for a counter-flow heat exchanger, with heat loss at the cold end, are solved by FEM using the Galerkin's method. The results obtained are validated by comparison with values published by Narayanan and Venkatarathnam [2] and Gupta & Atrey [3]. The study is then extended to understand the effect of variation of the wall temperature at the cold end and the effect of NtuH not being the same as NtuC, and how it affects the exit temperatures of the two fluids and heat loss at the cold end.

2. GOVERNING EQUATIONS

The governing equations for the hot fluid, cold fluid and the wall are obtained by energy balance as follows:

$$\text{Hot Fluid: } \frac{d\theta_H}{dX} + Ntu_H(\theta_H - \theta_W) = 0 \quad (1)$$

$$\text{Cold Fluid: } \frac{d\theta_C}{dX} + Ntu_C(\theta_W - \theta_C) + \frac{\alpha(NTU)}{\gamma\mu}(\theta_{amb} - \theta_C) = 0 \quad (2)$$

$$\text{Wall: } -\frac{d\theta_H}{dX} + \gamma \frac{d\theta_C}{dX} + \frac{\lambda}{\mu} \frac{d^2\theta_W}{dX^2} = 0 \quad (3)$$

In the above expressions θ_h , θ_c and θ_w represent the dimensionless temperatures of the hot fluid, cold fluid and the wall respectively. The different non-dimensional terms used in the analysis are defined as mentioned below:

$$\theta = \frac{T - T_{C,in}}{T_{H,in} - T_{C,in}}; \quad X = \frac{x}{L}; \quad \gamma = \frac{C_C}{C_H}; \quad \mu = \frac{C_H}{C_{min}}; \quad \lambda = \frac{kA_c}{C_{min}}, \quad \alpha = \frac{U_oA_o}{U_iA_i}; \quad Ntu_H = \left(\frac{hA}{C_H}\right)_H;$$

$$Ntu_C = \left(\frac{hA}{C_C}\right)_C; \quad NTU = \frac{UA}{C_{min}} \quad (4)$$

In the absence of heat in leak $\alpha = 0$ and hence the equation for the cold fluid reduces to

$$\frac{d\theta_C}{dX} + Ntu_C(\theta_W - \theta_C) = 0 \quad (5)$$

Boundary Conditions

Assuming that the wall is insulated at the hot end, and conducting at the cold end, the boundary conditions can be expressed as follows:

$$X = 0: \theta_H = 1, \quad \frac{d\theta_w}{dX} = 0 \quad (6)$$

$$X = 1: \theta_C = 0, \quad \theta_W = \theta_w \quad (7)$$

The heat loss to the evaporator from the cold end will be maximum when wall temperature at the cold end of the heat exchanger is equated to zero. For this case the boundary conditions for the cold end may be modified as:

$$X = 1: \theta_C = 0, \quad \theta_W = 0 \quad (8)$$

The boundary condition expressed in Eq. (8) has been used in the present analysis and the results have been compared with those published by Narayanan et al [2].

3. FINITE ELEMENT METHOD

The heat exchanger is discretized into a number of elements. The method of minimizing the weighted residual (Lewis et al, (4)) is used to solve equations (1)-(5) as:

$$\int_0^1 W \left\{ \frac{d\theta_H}{dX} + Ntu_H(\theta_H - \theta_W) \right\} dX = 0 \quad (9)$$

$$\int_0^1 W \left\{ \frac{d\theta_C}{dX} + Ntu_C(\theta_W - \theta_C) \right\} dX = 0 \quad (10)$$

$$\int_0^1 W \left\{ -\frac{d\theta_H}{dX} + \gamma \frac{d\theta_C}{dX} + \frac{\lambda}{\mu} \frac{d^2\theta_W}{dX^2} \right\} dX = 0 \quad (11)$$

A linear variation of the hot and cold fluids as well as the wall in a is assumed in every single element for counter flow as:

$$\theta_h = Ni\theta_{hi} + Nj\theta_{ho}; \quad \theta_c = Nj\theta_{co} + Ni\theta_{ci}; \quad \theta_w = Ni\theta_{wi} + Nj\theta_{wo} \quad (12)$$

where the shape functions N_i and N_j are given by $N_i = 1 - X$ and $N_j = X$. Substitution of these approximations in equations (9) – (11) the set of algebraic equations can be obtained if the weighted parameter W is defined. In the present analysis the Galerkin's method is used, in which the weights are taken to be the shape functions N_i and N_j . The discretized governing equations are written in matrix form for each element as:

$$[K]\{\theta\} = \{f\} \quad (13)$$

Assembling the element matrix form of the governing equations for all the elements in the solution domain leads to the global matrix form of the governing equations in the whole solution domain. The resultant global matrix form is modified by the forcing boundary conditions chosen and solved by MATLAB for the dimensionless temperatures along the heat exchanger.

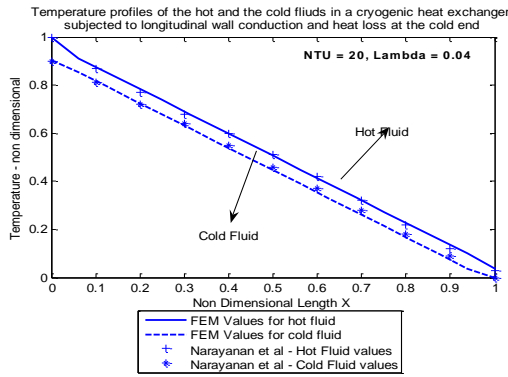


FIGURE 1

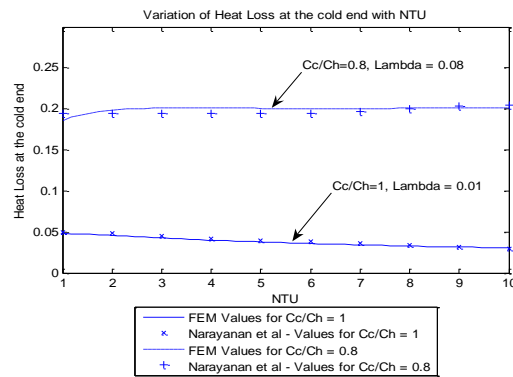


FIGURE 2

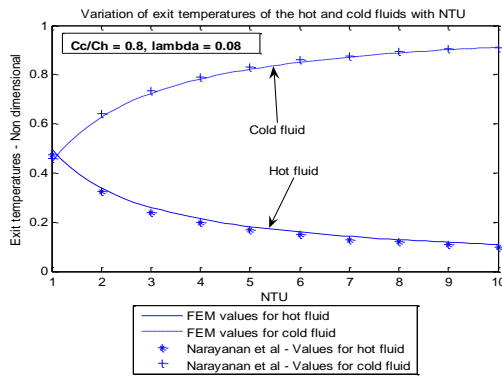


FIGURE 3

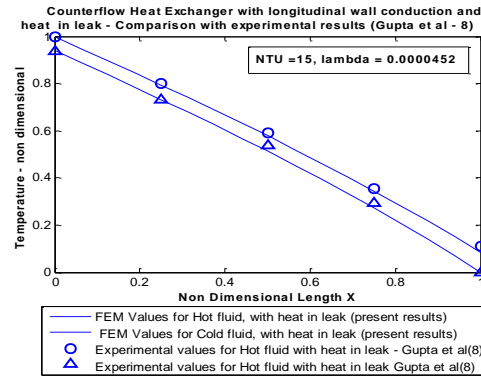


FIGURE 4

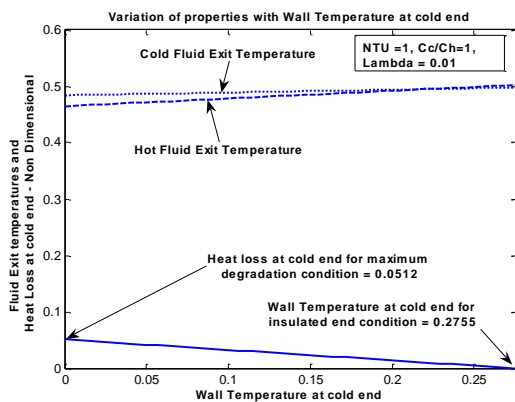


FIGURE 5

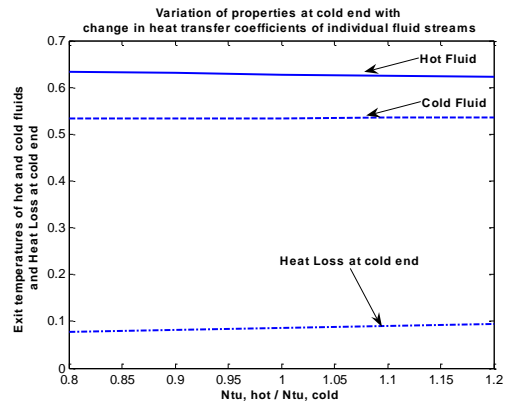


FIGURE 6

x (m)	Temperature of the hot fluid, (heat in leak parameter $\alpha = 0.003$)			Temperature of the cold fluid, (heat in leak parameter $\alpha = 0.003$)		
	Experimental Values – Published (3)	FEM Values	FDM Values – Published (3)	Experimental Values - Published (3)	FEM Values	FDM Values – Published (3)
	Th, K	Th, K	Th, K	Tc, K	Tc, K	Tc, K
0	297.00	297.00	297.00	283.40	287.88	289.89
2	252.30	255.22	261.50	244.90	245.69	252.90
4	211.40	210.31	218.20	204.30	199.79	207.10
6	162.20	159.47	165.80	153.30	147.29	151.60
8	104.50	99.48	102.60	84.90	84.90	84.90

TABLE 1. Comparison of temperature distribution for a counter-flow heat exchanger, with heat in leak and longitudinal wall conduction with values published by Gupta et al (3) for $NTU = 18$, $\lambda = 0.0000901$

4. RESULTS

In the present paper the governing equations have been solved by FEM and the results obtained compared with results published by Narayanan et al (2) and experimental results published by Gupta et al (3). Figs (1)-(4) and Table (1) show the comparisons. The work is then extended to understand (a) the variation of the wall temperature at the cold end and (b) the effect of Ntu_H not being the same as Ntu_C , and how it affects the exit temperatures of the two fluids and heat loss at the cold end. These have been shown in Fig(5) and Fig. (6).

5. CONCLUSIONS

The good comparison of the predictions from FEM with the numerical values (2) and experimental results (3) establish the validation of the present methodology. The method can be used for both balanced and unbalanced flow heat exchangers without any need for going in for separate numerical methods for the two types. Using the analysis it is possible to predict the heat loss at the cold end for a given wall temperature at the cold end or predict the wall temperature for a specified heat loss at the cold end. Further the analysis shows that with increasing values of ratio Ntu_H/Ntu_C the exit temperature of the hot fluid decreases while that of the cold fluid increases. The heat loss at the cold end of the heat exchanger increases with increasing values of Ntu_H/Ntu_C .

REFERENCES

- [1] P.G. Kroger, Performance deterioration in high effectiveness heat exchangers due to axial conduction effects, *Adv. Cryog. Eng.*, 12, 363-372, 1967.
- [2] S.P. Narayanan, G. Venkatarathnam, Performance of counter flow heat exchanger with heat loss through the wall at the cold end, *Cryogenics*, 39, 43-52, 1999.
- [3] P. Gupta, M.D. Atrey, Performance evaluation of counter flow heat exchangers considering the effect of heat in leak and longitudinal conduction for low temperature applications, *Cryogenics*, 40, 469-474, 2000.
- [4] R.W. Lewis, P. Nithiarasu, K.N. Seetharamu, *Fundamentals of Finite Element Method for Heat and Fluid Flow*, John Wiley and Sons, 2004.

EFFECTS OF ASPECT RATIO ON NATURAL CONVECTION IN A VERTICAL ANNULUS EMBEDDED WITH POROUS MEDIUM WITH DIFFERENT TYPES OF COLD WALL BOUNDARY CONDITIONS

Mukesh Patil, Pradeep G. Hegde, T.R.Seetharam, K.N.Seetharamu

Department of Mechanical Engineering, PES Institute of Technology, Bangalore - 560085, India,

patilmukesh@pes.edu; pghegde@gmail.com; tr_seetharam@yahoo.co.in;

knseetharamu@yahoo.com;

ABSTRACT

This paper deals with the numerical solution for effects of aspect ratio on natural convection in a vertical annulus embedded with porous medium for different types of cold wall boundary conditions. The heat transfer is assumed to take place by convection and radiation. The inner wall (hot wall) of the annulus is maintained at an isothermal temperature, which manifests the case of high heat transfer coefficient, thus indicating the heat source. The outer wall (cold wall) is subjected to different types of boundary conditions. The different types of cold wall boundary conditions include the uniform temperature, non uniform temperature and convective cases. The fluid is assumed to obey Darcy's law. The governing partial differential equations are non-dimensionalised and solved by finite element method. The porous medium is discretised with unstructured triangular elements. The effects of aspect ratio and Rayleigh number on the Nusselt number and Sherwood number are investigated. The results reveal that the Nusselt number and Sherwood number at hot wall increase initially with the aspect ratio and then decrease.

Key Words: *Radiation, Convection, Numerical Method, Porous Medium, Heat Transfer*

1. INTRODUCTION

In recent years, natural convection, heat and mass transfer through porous medium have received remarkable interest among the researchers. Porous medium plays important role in many geophysical and engineering applications such as heat exchangers, energy recovery from petroleum resources, thermal insulation of buildings, chemical reactors, nuclear waste disposal etc.

To the best knowledge of the authors there appears to be no study in the literature concerned with the combined effect of natural convection and radiation on a saturated vertical annular porous medium with different types of cold wall boundary conditions. The work carried out in the past corresponds to the case of non dimensional temperature (\bar{T}_0) to be zero, as observed from the literature. In the present work, three case studies have been carried out. The first case corresponds to the uniform temperature condition ($\bar{T}_0 = 0.1$), whereas in the second case the effect of non uniform temperature variation in accordance with the power law, along the cold wall of the vertical annulus is analysed. The third case deals with the convective cold wall boundary condition, which is the real case, as observed in practice.

The objective of the present work is to study the effect of aspect ratio on natural convection, heat and mass transfer for different types of boundary conditions at the cold wall. The effects of radiation and Rayleigh number on the heat and mass transfer in terms of average Nusselt number and average Sherwood number respectively are analysed. Also their effects on temperature, flow and concentration distributions are examined.

2. MATHEMATICAL FORMULATION

In the present study, a saturated vertical porous annulus of inner radius (r_i) and outer radius (r_o) is considered. Let the inner wall (hot wall) be at temperature T_i and outer wall (cold wall) be at temperature T_o such that $T_o < T_i$. The two horizontal walls are insulated, thus making them adiabatic.

The following assumptions are made in the present study:

- Porous medium is saturated with fluid
- The fluid is assumed to be gray emitting but non-scattering
- The fluid and medium are in local thermal equilibrium in the domain
- The porous medium is isotropic and homogeneous
- Fluid properties are constant except for the variation of density
- Darcy's law is assumed for the flow in the porous medium

For the problem under investigation the boundary conditions can be defined as:

at $r = r_i$, $\bar{T} = \bar{T}_i = 1$, $\bar{C} = 1$, $\bar{\Psi} = 0$ – General condition for all the three cases

at $r = r_o$, $\bar{T} = \bar{T}_o = [B(z)^\lambda]$, $\bar{C} = 0$, $\bar{\Psi} = 0$ – Condition for Case 1 corresponding to uniform temperature, here $\lambda = 0$, $B = 0.1$. Hence $\bar{T}_o = 0.1$.

at $r = r_o$, $\bar{T} = \bar{T}_o = [B(z)^\lambda]$, $\bar{C} = 0$, $\bar{\Psi} = 0$ – Condition for Case 2 corresponding to non uniform temperature, where B is a constant. In the present study, λ has been evaluated for a value of 0.25.

at $r = r_o$, $\left[-K \frac{\partial \bar{T}}{\partial r}\right]_{r_o} = h(T_{r_o} - T_\infty)$, $\bar{C} = 0$, $\bar{\Psi} = 0$ – Condition for Case 3 corresponding to convective boundary condition

Non-dimensionalised momentum equation:

$$\frac{\partial^2 \bar{\Psi}}{\partial \bar{y}^2} + \bar{r} \frac{\partial}{\partial \bar{r}} \left(\frac{1}{\bar{r}} \frac{\partial \bar{\Psi}}{\partial \bar{r}} \right) = \bar{r} Ra \left[\frac{\partial \bar{T}}{\partial \bar{r}} + N \frac{\partial \bar{C}}{\partial \bar{r}} \right]$$

Non-dimensionalised energy equation:

$$\frac{1}{\bar{r}} \left[\frac{\partial \bar{\Psi}}{\partial \bar{r}} \frac{\partial \bar{T}}{\partial \bar{z}} - \frac{\partial \bar{\Psi}}{\partial \bar{z}} \frac{\partial \bar{T}}{\partial \bar{r}} \right] = \left(\frac{1}{\bar{r}} \frac{\partial}{\partial \bar{r}} \left(\left(1 + \frac{4Rd}{3} \right) \bar{r} \frac{\partial \bar{T}}{\partial \bar{r}} \right) + \frac{\partial^2 \bar{T}}{\partial \bar{z}^2} \right)$$

Non-dimensionalised concentration equation:

$$\frac{1}{\bar{r}} \left[\frac{\partial \bar{\Psi}}{\partial \bar{r}} \frac{\partial \bar{C}}{\partial \bar{z}} - \frac{\partial \bar{\Psi}}{\partial \bar{z}} \frac{\partial \bar{C}}{\partial \bar{r}} \right] = \frac{1}{Le} \left(\frac{1}{\bar{r}} \frac{\partial}{\partial \bar{r}} \left(\bar{r} \frac{\partial \bar{C}}{\partial \bar{r}} \right) + \frac{\partial^2 \bar{C}}{\partial \bar{z}^2} \right)$$

3. RESULTS

Case 1: Effect of aspect ratio on \bar{Nu} and \bar{Sh} for uniform temperature cold wall boundary condition

As can be observed from Fig. 1, \bar{Nu} and \bar{Sh} initially increase with aspect ratio and then decrease. The increase in \bar{Nu} is due to the large thermal potential between the hot and cold walls whereas the the increase in \bar{Sh} is due to the velocity only.

Case 2: Effect of aspect ratio on \bar{Nu} and \bar{Sh} for non uniform temperature cold wall boundary condition

As can be observed from Fig. 2, this case is similar to the Case 1 except for the lower values of \bar{Nu} and almost same values of \bar{Sh} .

Case 3: Effect of aspect ratio \overline{Nu} and \overline{Sh} for convective boundary condition

As can be observed from Figs. 3 and 4, which indicate the effect of aspect ratio for $Bi=1$ and 10 respectively, \overline{Nu} and \overline{Sh} initially increase with aspect ratio and then decrease.

Figures. 5 and 6 indicate the isothermal lines for pure natural convection corresponding to Cases 1 and 2 respectively. Figures 7 and 8 indicate the isothermal lines for Biot numbers 1 and 10 respectively corresponding to Case 3.

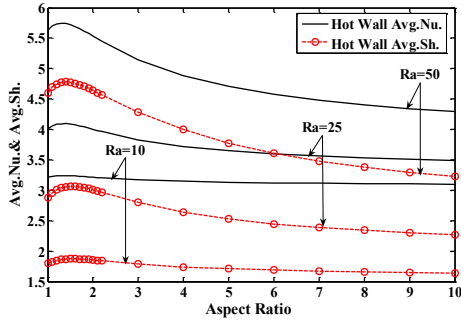


FIGURE 1.

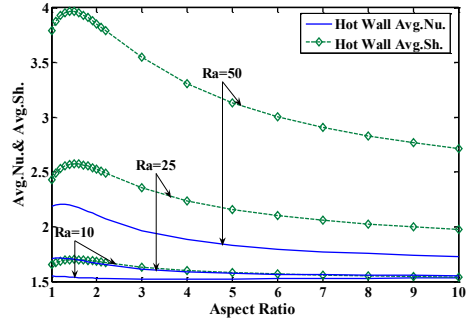


FIGURE 2.

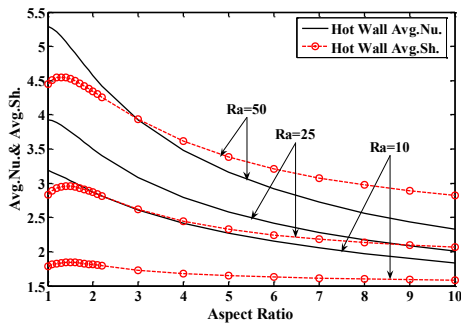


FIGURE 3.

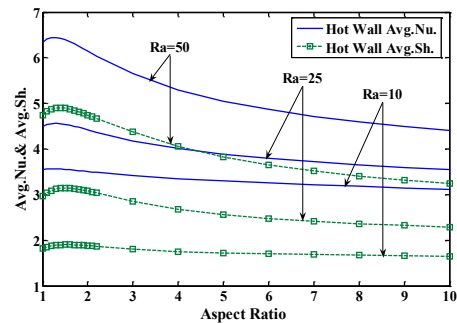


FIGURE 4.

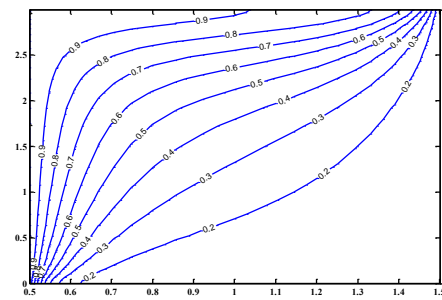


FIGURE 5.

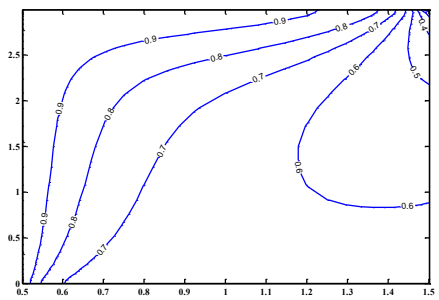


FIGURE 6.

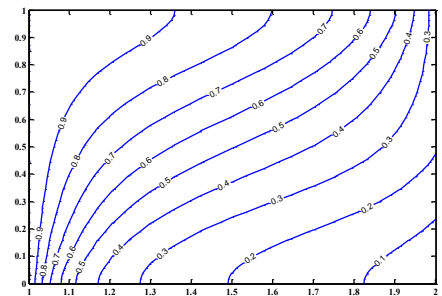


FIGURE 7.

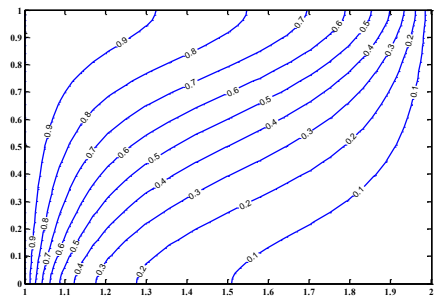


FIGURE 8.

4. CONCLUSIONS

The effect of aspect ratio and different types of cold wall boundary conditions on the natural convection in a saturated vertical porous medium is considered in the present study. The results for $\bar{T}_o = 0.1$ (uniform temperature), $\lambda=0.25$ (non uniform temperature) and $Bi=1$ and 10 (convective boundary condition) are shown in the present work. The governing equations are non-dimensionalised and solved using finite element method. It is found that the average Nusselt number and average Sherwood number increase initially with the aspect ratio and then decrease at the hot wall. They attain a maximum value at aspect ratio around unity, where the heat transfer changes from conduction to convection thus increasing the heat transfer coefficient. As the aspect ratio increases further, for a constant outer wall temperature, the heat fluxes will reduce along the height and consequently Nusselt number reduces. It is also found that the average Nusselt number and average Sherwood number increase with the Rayleigh number at the hot wall. The effect of Rayleigh number increases for the case of higher thermal potential between the hot wall and cold wall. Increase in Rayleigh number increases the fluid movement, which is due to the enhanced buoyancy effect. Hence the fluid velocity is increased along with the Nusselt number. Radiation has a considerable effect on Nusselt number indicating the increase in natural convection process.

REFERENCES

- [1] Ahmed, N. J. Salman, Z.A Zainal, Irfan Anjum, Hussain M.T. Khalid, Heat transfer analysis of porous medium in a conical cylinder with variable wall temperature. *International Journal of Mechanical and Materials Engineering*, 3(2), 145-152, 2008.
- [2] B. Cherif, and M.S. Sifaoui, Theoretical study of heat transfer by radiation, conduction and convection in a semi transparent porous medium in a cylindrical enclosure. *Journal of Quantitative Spectroscopy and Radiative Heat Transfer*, 83, 519-527, 2004.
- [3] A.B. Irfan, Z.A. Zainal, P.A. Aswatha Narayana, K.N. Seetharamu, Heat transfer by radiation and natural convection through a vertical cylindrical annular porous medium. *International Communications in Heat and Mass Transfer*, 33, 500-507, 2006.
- [4] R.C. Rajamani, C. Srinivas, P. Nithiarasu, K.N. Seetharamu, Convective heat transfer in axisymmetric porous bodies. *International Journal of Numerical Methods and Heat Fluid Flow*, 5, 829-837, 1995.
- [5] N. Srivastava, and A.K Singh, Mixed convection in a composite system bounded by vertical walls. *Journal of Applied Fluid Mechanics*, 3(2), 65-75, 2010.

FINITE ELEMENT APPLICATIONS IN HEAT EXCHANGERS

K N Seetharamu

Chair Professor in Thermal Engineering, PES Institute of Technology, 100 Feet Ring Road, BSK III Stage, Bangalore-560085. Email: knseetharamu@yahoo.com

ABSTRACT

A simple system analysis, originated from the early finite element methods, is considered first. The method of obtaining FEM equations from differential equations is illustrated next. Then design of micro compact heat exchanger is considered for illustration of FEM analysis, verification with experimental work and utilization of AI tools. Then FEM modeling approach to solve the momentum and energy equations to obtain the heat transfer coefficients and skin friction coefficients follows.

1. ANALYSIS OF HEAT EXCHANGER

The performance of a heat exchanger can be calculated in terms of its effectiveness for a given condition (Holman 1989; Incropera and Dewitt 1990). In order to determine the effectiveness of a heat exchanger, we have to calculate the outlet temperatures of both the hot fluid and the cold fluid for the given inlet temperatures. The overall heat transfer coefficient may be a constant or could vary along the heat exchanger. (Figure 1)

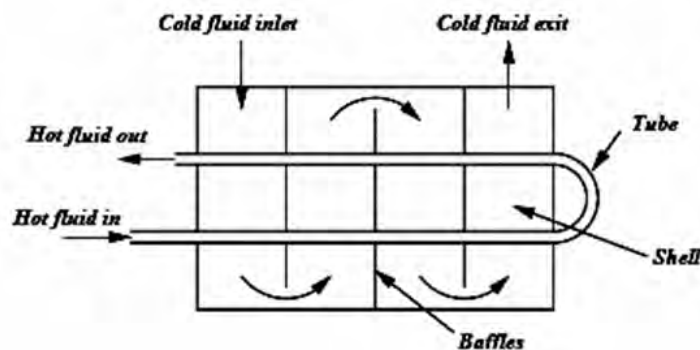


FIGURE 1. Schematic diagram of a shell and tube exchanger

2. THREE-FLUID PARALLEL AND COUNTER FLOW HEAT EXCHANGER

It may be difficult to derive the stiffness matrix and the loading terms from basics in a complicated heat exchanger system. Alternatively, we write down the differential equations for the fluids involved in the heat exchanger. We make use of Weighted Residual methods (sub-domain and Galerkin) to derive the element stiffness matrix and the loading terms. All these are illustrated through the example of a three fluid heat exchanger. (Figure 2). This can also be used to illustrate the effect of environment on two-fluid heat exchanger.

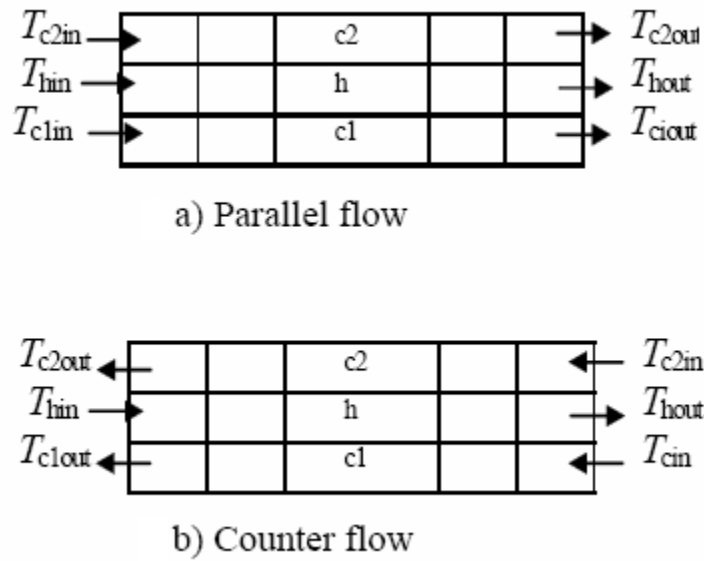


FIGURE 2. Schematic diagram for three fluid heat exchanger

Finite Element Method is used for solving the equations by minimizing the weighted residual with linear elements.

The discretized governing equations can be written in matrix form for each element as:

$$[\mathbf{K}]\{\boldsymbol{\theta}\} = \{\mathbf{f}\}$$

3. RESULTS AND DISCUSSION

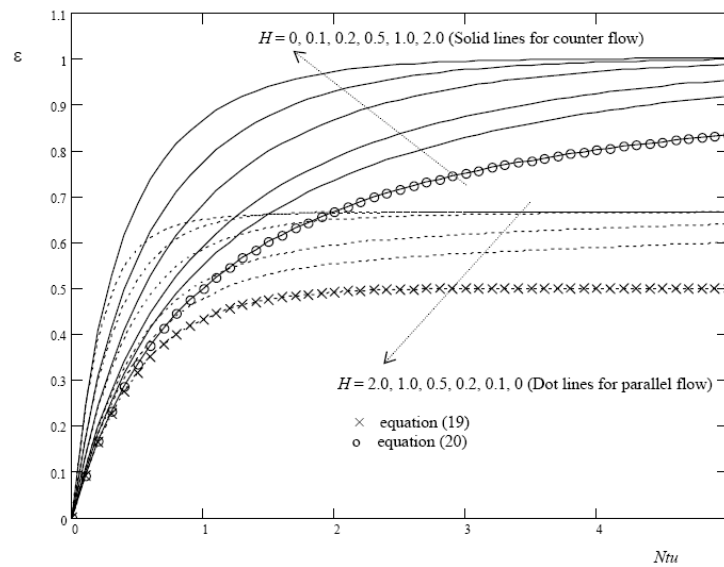


FIGURE 3. Variation of the effectiveness with ntu for different values of heat transfer coefficient ratio and fixed values of $r_1 = r_2 = 1.0$ and $\theta = 0$

4. MICRO COMPACT HEAT EXCHANGER

In recent years, with the rapid emerging of Micro-Electro-Mechanical Systems (MEMS), many micro-fabrication technologies have been developed and being introduced in the field of heat transfer engineering to realize micro-channel devices. One of the famous micro machining methods, LIGA process, has been adopted by Harris, et al. (2000, 2002) to fabricate micro-cross-flow heat exchanger. Generally micro heat exchanger can be applied in many important fields; namely micro-electronics, aviation and aerospace, medical treatment, biological engineering, materials sciences, cooling of high temperature superconductors, thermal control of film deposition and cooling of powerful laser mirrors. Compared with conventional heat-exchangers, the main advantage of micro heat exchanger is their extremely high heat transfer area per unit volume.

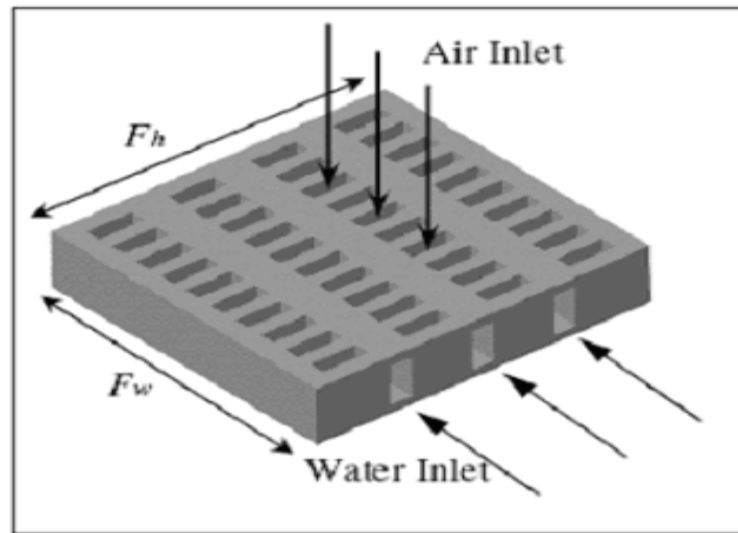


FIGURE 4. Schematic of micro-cross flow heat exchanger (MHE)

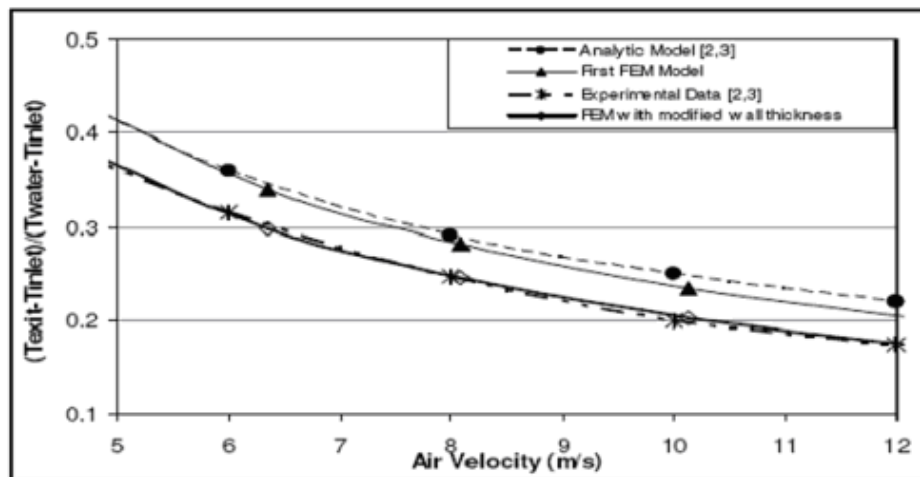


FIGURE 5. Temperature rise of air as a function of air velocity for the MHE

This MHE is designed based upon the performance criteria of a car radiator where its main function is for the dissipation of heat into air to prevent the engine from overheating. (figures 3, 4 and 5).

5. NEURO GENETIC METHODOLOGY FOR OPTIMIZATION

This work will present a neuro-genetic methodology to simulate and optimize the performance of the MHE for different working parameters and geometries. This methodology combines both the artificial neural network (ANN) and genetic algorithms (GA) together to achieve the optimization goal. ANN is capable of building up the quite complex and non-linear model through training by making use of available data obtained through finite element method (FEM) simulation.

6. ARTIFICIAL NEURAL NETWORK

In this work, the multi layer perceptron neural network has been trained using the back-propagation algorithm. The back-propagation algorithm uses supervised learning, which means that we provide the algorithm with examples of the inputs and outputs we want the network to compute, and then the error (difference between actual and expected results) is calculated. The idea of the back-propagation algorithm is to reduce this error until the ANN learns the training data. The training begins with random weights and the goal is to adjust them so that the error will be minimal.

7. GENETIC ALGORITHMS

Genetic Algorithms (GA) are adaptive search methods based on Darwinian's principles of natural selection, survival of the fittest and natural genetics. They combine survival of the fittest among string structures with a structured yet randomized information exchange to form a search algorithm with some of the innovative flair of human search. As in human genetics, GA exploits the fittest traits of old individuals to create a new generation of artificial creatures (strings). With each generation, a better population of individuals is created to replace the old population. Based on these principles, genetic algorithm is developed as a search tool that efficiently exploits historical information to speculate on new search points with expected improved performance.

8. CONCLUSIONS

Finite Element Method of predicting the performance of a heat exchanger is illustrated by an example of three fluid heat exchanger. FEM methodology is extended to a micro compact heat exchanger and the methodology to improve the modeling in a simple way to agree well with experimental values is illustrated. Application of Artificial intelligence tools like ANN and GA are applied to the Micro Compact Heat Exchanger to achieve maximum effectiveness by choosing the proper dimensions of the heat exchanger.

